AERODYNAMICS OF VARIABLE GEOMETRY WING / BODY COMBINATIONS

BY

ABDULMOHAMMAD - OSTADSAFFARI

B.Sc., M.Sc.

A THESIS SUBMITTED FOR THE DEGREE OF DOCTOR OF PHILOSOPHY

UNIVERSITY OF SALFORD

DEPARTMENT OF AERONAUTICAL AND MECHANICAL ENGINEERING

OCTOBER - 1983

TO MY FAMILY

ACKNOWLEDGEMENTS

The author wishes to express his sincere gratitude to a number of people.

First, to Dr. R.A. Sawyer, the project supervisor, for his invaluable advice, throughout the this project.

The author would like to thank Professor J.L. Livesey, the Professor of Fluid Mechanics of the Aeronautical and Mechanical Eengineering Department for this work. Also the author would like to thank Dr. D.F. Myring, for his invaluable help and encouragement, throughout the completion of his thesis.

The Hawker Siddeley Aviation for making available the subsonic computer programme for the use of this project, and the British Aerospace Warton division for some of their wind tunnel tests.

The author also wishes to express his gratitude to the following:- The Mechanical Engineering workshop staff, and the Civil Engineering Timberwood Workshop staff, for their help and constructive discussions, for making the wind tunnel test model, and Mr. R.A. Fowler for his cooperation and advice for the wind tunnel experimental set up and demonstrations in the Aerodynamics laboratory.

Without the use of the computing facilities of the University of Salford this work would not have been possible and the author wishes to thank the staff of the Salford University computer for their advice and the use of facilities.

The extremely patient and careful typing of Mrs. M. Hamilton for this thesis which has been exemplary and much appreciated.

Finally, the author is indebted to his family for their ceaseless encouragement and financial support, without which, he could not continue his work and he will never forget.

SUMMARY

A description of the experimental investigation of the aerodynamic characteristics of variable geometry of an aircraft model is presented. Aerodynamically, the model is tested for a sweep range of 0°, 12.5^o, 32.5^o, and 52.5^o and incidence range of 0° to 20° in 4° intervals. All the pressure distributions on the wing, glove, and body are recorded for each wind tunnel test. Aerodynamic forces and moments were also taken through a balance mechanism system which is attached to the model. This is connected to an independent computer terminal and a Teletype printer. Initially, a flow visualization to test the flow separation on the wing model was carried out.

A three-dimensional subsonic program, which was already developed by Hawker Siddeley Aviation Limited, was modified for our purposes in order to carry out numerical calculation of the aerodynamic characteristics and investigate the interference of wing and body.

This programme has also been developed to include the compressibility effects and compare these results with those for incompressible flow. The three-dimensional numerical solution was a Panel method for the subsonic case. This investigates the three-dimensional flow-field using a distribution of quadrilateral vortex panels, the effects of which are summed to calculate the aerodynamic characteristics of the model.

This subsonic theory was applied to calculate the characteristics of the wind tunnel model over a similar range of sweep and incidence to those tested, for Mach numbers of 0 and 0.5. As the only input data required is the configuration geometry and the flight condition, however, the program can be used to calculate the aerodymamics of any wing-body arrangement specified by the user. The program includes the capability of analysing both fixed-wing and variable sweep-wing configurations. This computational method is capable of being applied to general arbitrary subsonic three-dimensional potential flows, including inlet flow fields. In panel methods, the velocity potential at any point in a flow field is expressed in terms of the induced effects of source and doublet (or vortex) sheet distributed on the boundary surfaces. The configuration surfaces are divided into panels, and essentially, this is a general three-dimensional boundary value problem solver that is capable of being applied to most problems that can be modelled within the limitations of potential flow.Compressibility effects are approximated by the Göthert rule.

Comparisons were made between the subsonic calculations and the experimental results and some other theoretical results. Hence, an indication of agreement and accuracy among them is seen, which is good up to a certain degree of incidence (about 10°). Owing to viscous effects, the experimental results for lift coefficient show a signifident decline in size with respect to subsonic calculated results. Wing-body interference was calculated for subsonic flows and found to be favourable.

Similarly, a general supersonic program was developed for numerical analysis of the aerodynamic characteristics of a thin wing. The theory was extended to include wing-body interferences. This extended treatment consists of slender body theory combined with a thin wing solution using a "characteristic box" method for supersonic analysis. Streamwise pressure distributions on an aircraft wing are presented, and also some aerodynamic force and moment coefficients of this wing are presented.

Finally, for wing body interaction analysis, the Nielsen method was used. All the relevant computations including centre of pressure position and interferences of wing and body for a combined model are presented. Comparisons of the supersonic results with some theoretical and experimental results shows good agreement. The interference calculations in this case showed favourable effects, which very broadly tend to be lower than those calculated for subsonic flow.

C O N T E N T S

			PAGE
ACKNOWLEDGEMENTS		... .	i
SUMMARY		... ...	iii
CONTENTS		... ...	vi
NOTATIONS		... ...	xii
CHAPTER 1 :		INTODUCTION	1
	1.1	INTRODUCTION TO WING - BODY INTERFERENCE EFFECTS	5
	1.2	AERODYNAMIC PRINCIPLES FOR THE DESIGN OF SWEPT WINGS	9
	1.3	AERODYNAMIC INTERFERENCE IN SUPERSONIC AIRPLANE DESIGN	18
	1.4	VARIABLE GEOMETRY AIRCRAFT	26
		REFERENCES	28
CHAPTER 2 :		EXPERIMENTAL ANALYSIS	44
	2.1	INTRODUCTION	45
	2.2	EXPERIMENTAL PROGRAMME	45
	2.3	DESCRIPTION OF THE EXPERIMENTAL SET-UP	46
	2.4	THE WIND TUNNEL	47
	2.5	CALIBRATION OF THE WIND TUNNEL ...	48
	2.6	PRESSURE MEASURING TECHNIQUES	49
	2.7	CONVERSION OF READINGS TO WIND AXES ...	50
	2.8	MODEL SPECIFICATION	50
	2.9	THE GEOMETRY OF THE AIRCRAFT MODEL ...	51
	2.10	WING MODEL GEOMETRIES	52
	2.10.1	WING MODEL MANUFACTURING PROCEDURE ...	53

PAGE

2.11 GLOVE UNIT DETAILS 54
2.11.1 PRESSURE TUBES ON THE GLOVE UNIT ... 55
2.12 FUSELAGE MODEL SPECIFICATION ... 56
2.12.1 PRESSURE TAPPINGS ON THE FUSELAGE ... 56
2.13 DESCRIPTION OF THE LOAD BRACKET 57
REFERENCES 58
FIGURES 59

CHAPTER 3 : SUBSONIC FLOW ANALYSIS FOR A VARIABLE GEOMETRY WING 75
3.1 SUBSONIC WING/BODY INTERFERENCE 76
3.2 THE BASIC PROBLEM AND MAIN ASSUMPTION ... 77
3.3 QUADVORTEX DESCRIPTION 78
3.3.1 FEATURES OF THE QUADRILATERAL VORTEX RING 78
3.4 METHOD OUTLINE 79
3.5 GEOMETRY 80
3.5.1 SURFACE PANEL 80
3.5.2 WAKE GEOMETRY 81
3.5.3 ELEMENT PARAMETERS 81
3.6 INFLUENCE COEFFICIENTS 83
3.6.1 INDUCED VELOCITY 83
3.6.2 SEMI-INFINITE VORTICES 84
3.6.3 CASES OF SYMMETRY AND GROUND EFFECT ... 86
3.7 SOLVING FOR VORTEX-RING STRENGTHS ... 86
3.7.1 THE BOUNDARY CONDITION 86
3.7.2 METHOD OF SOLUTION 88
3.8 VELOCITIES AND FORCES 91
3.8.1 VELOCITIES AT POINTS OFF THE SURFACE ... 94
3.9 TWO-DIMENSIONAL FACTORS AFFECTING THE DISTRIBUTION OF SURFACE ELEMENTS ... 94
3.9.1 KUTTA CONDITION 94
3.10 QUADVORTEX ELEMENTS 95
3.11 VORTEX SHEET REPRESENTATION 96
3.12 THREE-DIMENSIONAL FACTORS 98

PAGE

	3.12.1	CONTROL POINT LOCATION	98
	3.12.2	WING TIP	99
	3.13	OUTLINE OF THE SUBSONIC PROGRAMME ... AND DATA PREPARATION	100
	3.13.1	SUBSONIC DATA PREPARATION	100
	3.13.2	SUBSONIC DATA INPUT	102
	3.14	COMPRESSIBILITY	108
	3.15	COMPRESSIBILITY CORRECTION	108
	3.15.1	LINEARIZED COMPRESSIBLE FLOW	108
		REFERENCES	112
		SKETCHES	115
		FIGURES	116
CHAPTER 4 :		AEROFOIL DESIGN AND AERODYNAMIC CALCULATIONS FOR THE WIND TUNNEL TEST MODEL	123
	4.1	INTRODUCTION	124
	4.2	DESIGN OF CAMBER LINE AND THICKNESS FUNCTION FOR THE WING	124
	4.3	SURFACE EQUATION FOR VARIABLE SWEEP ...	125
	4.3.1	SURFACE EQUATION FOR THE WING AT 12.5° SWEEP	127
	4.3.2	SURFACE EQUATION FOR THE WING AT 32.5° SWEEP	128
	4.3.3	SURFACE EQUATION FOR THE WING AT 52.5° SWEEP	128
	4.4	2-DIMENSIONAL THIN AEROFOIL THEORY FOR CAMBER LINE AT INCIDENCE	129
	4.5	SIMPLE SWEEP THEORY APPLIED TO CONSTANT SECTION WINGS AT SWEEP BACK ANGLE Λ	132
	4.6	IMPROVEMENTS IN LINEARISED THIN AEROFOIL THEORY FOR MODERATELY THICK SWEPT AND TAPERED WINGS(KUCHEMANN AND WEBER) ...	132
	4.6	FITTING OF CHORDWISE LOADING CURVES TO MEASURE VALUES OF ΔC_p	136

PAGE

REFERENCES 141
TABLES
FIGURES

CHAPTER 5 : SUPERSONIC INVESTIGATION ANALYSIS OF FLOW OVER AN ARBITRARY WING CONFIGURATION ... 142
5.1 INTRODUCTION 143
5.2 PRESSURE WAVES IN SUBSONIC-SUPERSONIC FLOW ... 144
5.3 INTEGRAL EQUATIONS FOR A NUMERICAL MODEL ... 146
5.3.1 EQUATIONS OF FLOW 146
5.3.2 DERIVATION OF BASIC INTEGRAL EQUATION 150
5.4 BASIC INTEGRAL EQUATION FOR STEADY FLOW ... 155
5.5 SOLUTION OF INTEGRAL EQUATION USING A CHARACTERISTIC MESH 158
5.6 NUMERICAL SOLUTION OF THE BASIC INTEGRAL EQUATIONS FOR THE PIVOTAL ϕ' 161
5.7 REGULAR PARABOLIC INTERPOLATION WEIGHTS FOR A LINEAR VARIATION OF POTENTIAL 162
5.8 THE REGULAR PARABOLIC INTERPOLATION WEIGHTS FOR A VARIATION OF POTENTIAL $\phi = a+by+cy^2+dx$ ... 167
5.9 IRREGULAR RHOMBUS WEIGHTS 169
5.9.1 FORMATION OF IRREGULAR WEIGHTS AT SUBSONIC LEADING EDGE 169
5.9.2 THE PIVOTAL WEIGHT $W_{(o,o)}$ FOR AN IRREGULAR RHOMBUS ADJACENT TO A SUPERSONIC LEADING EDGE ... 173
5.10 SOME COMMENTS ON THE TREATMENT OF IRREGULAR RHOMBUSES 175
REFERENCES 177
FIGURES

CHAPTER 6 : NUMERICAL ANALYSIS OF A SUPERSONIC FLOW FOR AN ARBITRARY WING-BODY USING 'THE CHARACTERISTIC BOX ' METHOD 178
6.1 INTRODUCTION 179
6.2 MESH DEFINITION 179
6.3 DEFINITION OF A WING GEOMETRY 180

PAGE

6.4 DEFINITION OF CELLS 182
6.5 NUMERICAL CALCULATION OF VELOCITY POTENTIAL Ø′ 184
6.6 NUMERICAL CALCULATION OF C_p 185
6.7 INVESTIGATION OF IRREGULAR RHOMBUSES ON THE BOUNDARY LEADING EDGE 187
6.7.1 SUBSONIC LEADING EDGE 187
6.7.2 SUPERSONIC LEADING EDGE 188
6.8 NUMERICAL SOLUTION FOR SMOOTHING DATA USING THE LEAST SQUARE METHOD 189
6.8.1 FORWARD SUBSTITUTION 192
6.8.2 BACKWARD SUBSTITUTION 193

CHAPTER 7 : EVALUATION OF AERODYNAMIC CHARACTERISTICS OF AN ARBITRARY WING IN A SUPERSONIC FLOW ... 195
7.1 INTRODUCTION 196
7.2 EVALUATION OF LIFT COEFFICIENT 196
7.3 EVALUATION OF PITCHING MOMENT COEFFICIENT 198
7.4 NUMERICAL SOLUTION FOR LIFT AND PITCHING MOMENT COEFFICIENTS 198
7.5 INTERPOLATION OR EXTRAPOLATION OF THE POTENTIALS AT THE TRAILING EDGE 200
7.6 CALCULATION OF PRESSURE COEFFICIENT C_p ON THE WING PLANFORM 202

CHAPTER 8 : SUPERSONIC WING-BODY INTERFERENCE ... 203
8.1 INTRODUCTION 204
8.2 DETERMINATION OF PRESSURE COEEFICIENT C_p ... 205
8.3 INTEGRATION OF THE LIFT ON WING WHEN THE BODY IS OF CONSTANT CROSS SECTION... 213
REFERENCES 216

CHAPTER 9 : RESULTS, COMPARISONS AND DISCUSSIONS 217
9.1 INTRODUCTION 218
9.2 SUBSONIC RESULTS 218
9.3 SUBSONIC RESULTS AND COMPARISONS 218
9.4 DISCUSSIONS OF FORCES AND MOMENTS FROM THE QUADVORTEX METHOD 221

			PAGE
	9.5	COMPARISONS AND VALIDATIONS FOR THE QUADVORTEX METHOD	223
	9.6	COMPARISONS OF ΔC_p FOR EXPERIMENTAL AND COMPUTED RESULTS	225
	9.7	COMPARISONS OF SUPERSONIC RESULTS ...	227
	9.8	OIL FLOW VISUALIZATION	230
	9.9	OVERALL EXPERIMENTAL FORCES AND MOMENTS	234
	9.10	COMPARISONS OF EXPERIMENTAL AND THEORETICAL RESULTS	237
		REFERENCES	239
		LIST OF FIGURES	
		FIGURES	
CHAPTER 10	:	CONCLUDING REMARKS AND SUGGESTIONS FOR FURTHER WORK	244
	10.1	CONCLUDING REMARKS	245
	10.2	SUGGESTIONS FOR FURTHER WORK	249
APPENDIX (A)	:	CONVERSION OF EXPERIMENTAL READINGS TO WIND AXES	A1
	A.1	CALIBRATION FACTORS FOR THE EXPERIMENTAL READINGS	A2
APPENDIX (B)	:	COMPRESSIBILITY IN SUBSONIC FLOW ...	B1
	B.1	EFFECT OF COMPRESSIBILITY ON AERODYNAMIC FORCES	B2
	B.1.1	LIFT COEFFICIENT CL_C	B2
	B.1.2	DRAG COEFFICIENT CD_C	B3
	B.1.3	SIDE FORCE COEFFICIENT CF_C	B4
	B.2	EFFECT OF COMPRESSIBILITY ON AERODYNAMIC MOMENTS	B5
	B.2.1	PITCHING MOMENT COEFFICIENT CMP_C	B5
	B.2.2	ROLLING " " CMR_C	B6
	B.2.3	YAWING " " CMY_C	B7

NOTATIONS

C_P	Pressure coefficient.
C_M	Coefficient of moment.
$\bar{C}_L$	Total lift coefficient.
C_l	Coefficient of Local Lift.
$[C_l \cdot C]/[\bar{C}_L \cdot \bar{C}]$	Spanwise Distribution Of Load.
g	The earth gravity.
$(C_l \cdot C / \bar{C})$	Spanwise Load Distribution.
K_1, K_2	Wind tunnel correction factors.
C_L / α	Slop of lift curve.(Load).
M	Mach number.
C_{MY}	Pitching moment coefficient.
a	Speed of sound.
U	Speed of air.
dx, dy, dz	Increment in x, y, z directions.
u, v, w	Velocity in x, y, z directions.
$W_{r,s}$	Integration weight.
$\lambda_{uv}(\ )$, $f_u(\ )$, $f_v(\ )$	Linear interpolation functions.
$\tau_{uv}(r,s)$	Contributions to weights from irregular rhombuses.

$G_0(\ ), G_{\frac{1}{2}}(\ ), G_1(\ )$	Parabolic functions.
$\bar{C}$	Wing mean chord.
C	Local Chord.
C_0	Wing root chord.
L	Reference length used in non-dimensionalising $\emptyset$.
ℓ	Length of side of basic rhombus.
L, M, N	Coefficients for an irregular rhombus.
ρ, σ	Characteristic coordinates based at pivotal point.
ρ', σ'	$\rho' = \rho - r, \quad \sigma' = \sigma - s$
x, y, z	Rectangular coordinates.
W_{oo}	Pivotal weights
$\omega = \frac{\partial \phi}{\partial z}$	Upwash
S	Planform area
s	Semi-span

A, B, C, D	Symbols used to label rhombuses relative to point (r,s).
C_1^P (r,s) (P=0,1,2)	Coefficient in parabolic fitting to $C_1(r,s,g)$

GREEK SYMBOLS

α	Angle of incidence.
Δ, δ	Increment
Λ, β	Wing sweep angle.
∞	Free-stream
γ	Ratio of specific heats
ξ, η, λ, μ	Non-dimensional axes.
ϕ	Velocity potential.
$\phi' = \frac{\phi}{UL}$	Non-dimensional potential
ψ	Stream function

i, c	Incompressible, compressible
-	Mean value
u. v	Local system of characteristic co-ordinates such that base point of current rhombus is u = o, v = o
r, s	values of ρ, σ the characteristic co-ordinates based at the pivotal point.

These notations and symbols only contain those which are commonly used throughout the work. Other notations and symbols, less widely used, are defined locally.

CHAPTER 1

INTRODUCTION

INTRODUCTION

This thesis is concerned with investigation and research directed towards the aerodynamics of variable geometry wing-body combinations. These studies lie in a very broad field of numerical work for subsonic and supersonic flow investigation. Some experimental tests were carried out on a scaled variable geometry wing-body model in low speed wind tunnel. For subsonic studies extensive efforts were made to extend, modify develope and validate a three-dimensional potential flow programme using a surface distribution of Quadrilateral Vortex-rings (or panels) for this purpose. This method was also developed for compressible flow using the Gothert transformation for wing-body combinations. Subsonic results are compared for wing-body combinations in Chapter (9). Effects of variable geometry wing are indicated on the overall wing-body lift coefficient C_L for 0°, $12{\cdot}5^\circ$, $32{\cdot}5^\circ$, $52{\cdot}5^\circ$ sweep wing for some selected low and high incidences.

Interference effects are also shown for the wing-body combinations and compared with the wing and body alone results. Effects of the V-notch on low sweep wings (0° and $12{\cdot}5^\circ$) are investigated for the wing body, and their combinations and compared with a similar sets of results for the wing-body cobinations with no V-notch on the wing. In subsonic calculations of forces and moments for the wing-body combinations are based on projected planform area and mean chord respectively. This reference area and mean chord are kept consistent for each wing sweep. Comparisons of subsonic results with experimental results for lift coefficient C_L for the wing-body combinations are shown in Chapter (9), and effects of viscous flow and inviscid flow are identified in these

comparisons. The modified panel method has a wide range of applications for calculation of aerodynamics of variable wings and mutual interference of wing-body combinations. Encouraging results from this subsonic method in comparison with the experimental results gives an indication of accuracy of panel method.

Nevertheless, the vortex strength, aerodynamic forces and moments calculations and study of this method is shown in Chapter (3). The present experimental work was carried out to provide a comparison with the theoretical prediction method. However, the results obtained provide useful experimental evidence of wing-body aerodynamics and form a positive contribution to knowledge in this area. In these wind tunnel tests, force and moment coefficients were derived for the same ranges of sweep angle as theoretical subsonic results.

Effects of tripping devices were investigated in order to create an attached turbulent flow on the wing surface. Some of these surface flow photos show at about what incidence angle the flow starts separating. In some cases a three-dimensional classical spiral separation was observed. Effects of tripping devices on the wing surface flow and consequently on the overall wing-body lift coefficients are identified and they are presented in Chapter (9), at the same time, the effects of tripping device on the wing pressure readings were recorded and found to be vertually independent of tripping device (minute changes in their readings). The pressure coefficients on the wing surfaces are compared with some other theoretical and experimental results and they are presented in Chapter (9). In order to fit the best curve through experimental C_p readings of the wing surface, thin aerofoil theory is used to shape the pressure distribution and hence to

determine section lift at any wing spanwise stations. The method is shown in Chapter (4) and section lift coefficient results are compared with some other experimental results and are shown in Chapter (9).

A supersonic two-dimensional potential flow theory was developed to perform a numerical integration to solve the integral equation for a wing planform. This is carried out by expressing the downwash as a summation of the velocity potential over the area of the wing in the Mach forecone for linearised, steady supersonic flow. Hence, the pressure coefficient distribution, and the lift coefficient, pitching moment coefficient were found on a wing planform. In the numerical calculations of velocity potential on the wing planform, several numerical techniques were developed for calculation of the pressure coefficient C_p . Some of these numerical techniques are shown in Chapter (6) to (8). Finally, this supersonic potential flow method is developed to calculate the mutual interference of wing-boby combinations. Comparisons of C_p distribution for a rectangular wing with some experimental and theoretical results are encouraging and are shown in the corresponding section of Chapter (9). Full study of this supersonic method for velocity potential, pressure coefficient, lift and pitching moment coefficients and mutual interference calculations and their procedures are shown in Chapter (6) to (8). This new development is a contribution to numerical solutions of supersonic potential flow theory and hence supersonic calculations of forces and moments and mutual interference of wing-boby combinations.

1.1 INTRODUCTION TO WING/BODY INTERFERENCE EFFECTS

"When we are considering the interference between a swept, or unswept, wing and fuselage, we should bear in mind that the basic design concept of such an aircraft starts from an assumption that these interference effects are small".

Thus D·Kuchemann introduces the topic of wing/body interference in a historical survey. This concept goes back to Cayley (1.1) who proposed in 1809 that human engineers, in contrast to nature, could do well to keep the organs for providing volume, lift, propulsion, and controls separate and largely independent. Present design trends run against this principle, especially with swept-winged aircraft; the flows past the wing and the fuselage tend to become less independent of one another and the interference effects tend to become large and significant. This means that we must try not only to know more about what the interference effects are but also to develop design methods where the interference effects are used to bring us back to those types of flow which would obtain if wings and bodies would still be largely independent. Therefore, we must concern ourselves with two problems: to determine the flow past given shapes; and to design shapes which give a prescribed flow.

In the reference paper he also shows the major effects that wing sweep angle and dihedral angle can have on the interference with the fuselage. In this case the method of singularities was applied for calculation of inviscid incompressible flow fields for some simple cases with and without lift.

A large volume of research has been carried out by D .Kuchemann into the aerodynamic design aspects of swept wings. Refs. (1.6) and (1.7) are concerned with the development of methods for calculating the flow over sweptback wings at subcritical speeds and for alleviating the adverse root and tip effects. In Ref (1.6) a linear theory solution for the flow at zero lift over a sheared wing and at the centre section of a semi-infinite sweptback wing is given. Then from a simple method for calculating the loading (1.7) over a sweptback wing of any aspect ratio, a method inspired by Prandtl's concept (1.8) of an effective and induced incidence for obtaining the loading over a wing of high aspect ratio but reducing to R.T. Jones' solution (1.9) for a wing of small aspect ratio, D .Kuchemann and his colleagues ultimately developed what came to be known as the "RAE Standard Method" (1.10). This enabled one to calculate the chordwise pressure distribution at any station on a cambered, twisted sweptback wing of arbitrary planform and section variation across the span.

Weber (1.11) has carried out some studies on interference effects

between a fuselage and a lifting wing, in inviscid incompressible flow. She has considered the special case of an infinite wing (swept or unswept) with constant chord, attached to a cylindrical fuselage of circular cross-section in the mid-wing position when the axis of the fuselage is parallel to the mainstream.

There has been much world-wide effort towards the design of swept wing aircraft cruising at low supersonic and high subsonic Mach numbers. Continuous improvement of the ML/D parameter has enabled the latest generation of subsonic high speed commercial jets to fly at higher cruise Mach numbers. To achieve these gains, a swept wing design gives the best possible type of wing flow.

A comprehensive design method intended to achieve this aim has been developed by Lock and Bridgewater (1.12), based on supersonic (or sonic) linearised theory but taking into account the principal non-linear effects in a crude but reasonably effective way.

Bridgewater, Lock and Lee (1.13) have performed some investigations on wing-body half-models. From combinations of two different body shapes and two distinct swept wings designed according to the principles of Ref (1.12), they have produced theoretical and experimental studies for swept-wing body configurations, and found conditions for the correct shaping of

the body waisting, etc. These studies lead to reductions in drag at high subsonic and low supersonic speeds.

A method has been described which permits the calculation of pressure distributions on lifting wing-body combinations in subcritical flow (1.14). Also Ref (1.15) is concerned with the general case of three-dimensional circulatory flow and the application to lifting wing-body combinations. To illustrate the applicability of the method in wing-body interference studies, a comparison of measured and calculated pressure distributions for three widely different wing-body combinations are shown in Ref (1.14). In order to be able to separate the effect of the body on the wing pressure distribution calculations have in all cases been performed for both the complete configuration and the wing alone.

1.2 AERODYNAMIC PRINCIPLES FOR THE DESIGN OF SWEPT WINGS

In the preliminary design of an aircraft it is necessary to decide upon which combination of sweep, thickness/chord ratio, and cruise C_L will satisfy the design requirements for a certain cruise Mach number and aircraft payload. The final choice is a compromise between aerodynamic performance at high and low speeds and structure weight. For instance, increasing the thickness/chord ratio, t/c, reduces the wing weight for a given strength but also reduces the drag rise Mach number. Increasing sweep allows a large t/c to be used, but also tends to reduce the low speed $C_{L_{max}}$ available and may make it necessary to use complex, and

expensive high-lift devices to obtain satisfactory airfield performance. Increasing sweep may also lead to larger torsional loads on the wing and possible aeroeleastic problems which may cancel some of the gains due to increased t/c. For any particular application the condition that shock waves on the wing should be absent or small in strength usually leads to a fairly narrow range of design variables. A further condition is the necessity to avoid boundary layer separation which in conjunction with the above, can be used in many cases to determine the optimum design pressure distribution for sub-critical flow.

Bagley (1.16) and (1.17) has given a general approach which enables the possible combinations of t/c, sweep angle ϕ, Mach number M, design lift coefficient C_L, thickness distribution and upper surface pressure distribution to be found approximately, to avoid the formation of strong shock waves. It is assumed that the wing will have suitable camber, twist and thickness variation across the span to maintain straight isobars and the aerodynamic performance will ideally be that of the sheared wing.

Lighthill (1.18), Thwaites (1.19), Eppler (1.20) and Sinnott, Osborne (1.21) in their methods use a general routine for two-dimensional calculation of conventional aerofoils on infinite sheared wings. They are generally used when thick or highly cambered aerofoils, or aerofoils with suction slots, are required, which are treated accurately.

In the general case, the flow over the wing at subsonic or supersonic speeds can be solved by a differential equation for the velocity potential. There is a discontinuity in the solutions for the differential equation in mixed transition flow. Sears (1.22) has discussed some of these problems in his report. Also, Bagley (1.23) in his paper, considered that it is this discontinuity solution which corresponds to a flow with shock waves and a pressure drag force on the body and which is due to change of entropy through the shock. In Section (4) he also shows the outcome of many investigations on aerodynamic design of aircraft, including the most effective use of swept wing principles. From experiment he showed that as the Mach number increases to achieve a better aerodynamic design, the angle of sweep needs to be increased and consequently there will be a fall in aspect ratio. Rogers and Hall's description (1.24) of the transonic flow development on swept wings shows that, although the obvious signs of the supercritical flow are manifest first on the outer part of the wing, the origins of these phenomena can be found near the centre of the wing. The basic aim is to preserve a low drag and a well-behaved flow up to as high a Mach number as possible.

The interference between a central fuselage, or other auxiliary bodies, and the swept wing can also be used to improve the isobar pattern of the wing. At subsonic speeds, Kuchemann (1.25) and Hartley (1.26) have shown how a properly shaped "waisted" body could be designed to produce a junction velocity distribution

similar to that on the corresponding infinite sheared wing. A different approach to the design of swept wings can be derived by considering the far field. Jones (1.27) showed that a necessary and sufficient condition for the drag due to lift to be a minimum on a wing of given planform and total lift was that the load should be distributed in such a fashion that the downwash in the combined forward and reverse flow fields should be uniform over the whole planform.

Another method of finding the appropriate loading, and the camber shape which produces it, has been developed by Ginzel and Multhopp (1.28), who use a polynomial expression for the loading.

Lomax (1.29) has shown how the "supersonic area rule" should be generalized to extend to lifting configurations. The drag according to linearized supersonic theory can then be expressed in terms of the lengthwise distributions of the areas and forces on sections intercepted by planes parallel to the waves of the Mach cone.

A wing-fuselage combination with low drag for high speeds can be constructed by utilising a wing of fairly high sweep. It is well known that a sheared wing of infinite span has zero wave drag below its critical Mach number, which has an upper bound of unity if the angle of sweep is high enough and the wing is thin enough. This was pointed out by Kuchemann and Weber (1.6), who

also showed how the extra wave drag of a swept wing of finite span could be avoided by combining it with a suitably shaped body. A practical method for designing the body in a supersonic mainstream, which was begun by Hartley, has been developed by Bagley (1.16).

Kuchemann and Hartley (1.26) have shown how the body might be designed to reduce the high subsonic drag rise by controlling the rate at which the shockwave on the upper surface of the wing moves back towards the trailing edge as the Mach number increases.

Whitcomb (1.30) has shown experimentally determined drag curves from two NACA tests, one on a wing with 45° sweepback whose Mach number M_{cs} was 1.08, and the other by Fischetti (1.31), on a 60° sweptback wing with M_{cs} approximately equal to 1.3. These two models were designed by the area rule, but Bagley (1.32) has shown that the junction shape of Whitcomb's model (1.30) does not in fact produce a pressure distribution in the junction which is substantially the same as that as the corresponding sheared wing.

Around 1970, Kuchemann illustrated some new methods of calculating wing-body interference. Kuchemann (1.5) distinguished between methods where the sources are put on the surface of the two interfering bodies as in the A.M.O. Smith

treatment (1.33) of the Neumann problem and his own approach in which the sources are placed either wholly inside the bodies or both inside and on the surface.

Consider first the case of a non-lifting configuration of given shape, where both the wing and fuselage can be represented by a distribution of sources and sinks. Two distinct approaches to the problem have been proposed:

(1) The sources are put on the surface of the two bodies

(2) The sources are either wholly inside the bodies or both inside and on the surface.

In the first case, the Neumann problem must be solved. This has been treated by A.M.O. Smith (1.33) who also provided a widely used computer program for obtaining numerical answers by using the panel method. In the second case discussed above, this could be effected by adding an image system of the wing sources inside the fuselage such that the latter remains a stream surface. The first theory of this kind was provided by Liese and Vaudrey (1.34) who added the source distribution along the axis of a fuselage to that over the chordal plane of a wing.

Among the numerical techniques available, the method of finite elements shows considerable promise because of its ability to handle configurations of arbitrary geometry (1.35). Many investigations have been carried out to write numerical programs

based on the superposition of finite elements. For example, there is the incompressible potential flow program developed by Hess and Smith at Douglas (1.33) and the "fan-in-wing" program developed by Rubbert and others at Boeing (1.36). There are also numerous planar and nonplanar lifting surface programs, a summary of which can be found in (1.37). Wing-body-nacelle interference at subsonic speeds is treated in (1.38) while supersonic nacelle-on-wing interference is described in (1.39). For wing-body interference, there is the procedure based on the subsonic-supersonic lifting surface elements described by Woodward (1.40) and the subsonic vortex-lattice procedures developed by Kalman, Rodden, and Giesing (1.41). This wealth of procedures indicates the essential soundness of the finite element approach and also illustrates the fact that special programs can be developed for special problems with reasonable effort.

Ref (1·42) gives an approach to the use of finite element methods for predicting the aerodynamics of wing-body combinations, which can be represented by a collection of line sources and doublets, and surface panels representing thickness and lift.

A.M.O. Smith, Ref (1.33) has represented the surface of the wing and body by a large number of quadrilateral panels, each carrying a source distribution of constant strength. In addition to this a system of horse-shoe vortices is applied, as in the method of Rubbert and Saaris (1.43), to cover the surface of discontinuity

behind the wing and body, the camber surface of the wing and its extension inside the body.

Stewartson (1.44) has carried out some extensive work on the interference between a body, consisting of an infinitely long circular cylinder aligned with the direction of motion, and a thin wing lying approximately in the diametral plane of the cylinder. In his numerical procedure, he used a panel distribution of sources with linear or non-linear hyperbolic equations.

Schneider (1.45) has experimentally investigated the effects of interference on wing-body combinations in the subsonic, transonic, and supersonic speed ranges. The wings he used for these investigations were a rectangular wing, a sweptback wing, and a delta wing.

Falkner (1.46) used the vortex-lattice method for the flow solution. The use of discrete horseshoe vortices with swept bound legs was demonstrated in a number of similar and independent developments of the vortex-lattice method by Rubbert (1.47), Dulmovits (1.48), Hedman (1.49), and Belotserkovskii (1.50). Later solutions for steady flow have replaced the horseshoe vortex system by a quadrilateral ring vortex system on the mean camber surface throughout the lifting surfaces except near the trailing edges, where a horseshoe vortex is placed. This approach has been taken by Monical (1.51), Rubbert and Saaris (1.43) and Tulinius (1.52).

Rubbert and Saaris also account for thickness effects by placing a system of source panels on the airfoil surface, whereas Tulinius treats thickness by using a source-lattice system on the mean camber surface. A rather different finite element is the constant pressure panel proposed by Woodward (1.40) in his study to unify the subsonic and supersonic analyses of wing-body combinations. Unfortunately, Woodwards unified approach does not have the accuracy at subsonic speeds that it achieves at supersonic speeds.

Some recent work by Kariappa and Smith (1.53) demonstrated the utility of a triangular facet, whose displacements could be made compatible with structural elements used for analysing the wing deformations. The Woodward (1.40) area element also appears adaptable to oscillatory, as well as steady, motion of lifting systems (see Ashley Part I, (1.98)). Woodward (1.54) used a potential panel method for calculation of interference in subsonic and supersonic flow. At Dornier a selection of numerical and semi-empirical methods in fluid mechanics has been established (1.55) which have application to the analysis and design of general aviation and transport aircraft as well as fighter type configurations and missile weapon systems in the subsonic and transonic speed regime. A great amount of effort and emphasis has been placed on the validation of these methods and on establishing limits for their applicability. In these works the panel method is also used to study the mutual interference between different components of a configuration.

Johnson and Rubbert (1.56) have recently developed curved panels with varying source and doublet strengths across the boundary surfaces, which are being incorporated in the PANAIR computation system and are described in Ref (1.56). Source and doublet strengths are assigned to each panel and are determined by the solution of a set of linear algebraic equations relating the singularity strengths to the boundary conditions. For computational convenience the boundary surfaces are divided into small panels.

1.3 AERODYNAMIC INTERFERENCE IN SUPERSONIC AIRPLANE DESIGN

In supersonic flow the aerodynamic interference between airplane components is strong owing to the confined zone of influence of supersonic pressure fields. There is a discussion of a method used to optimize the interference between wing and body, wing and engine nacelles, and between the wing and trimming surfaces by E.J. Kane and W.D. Middleton (1.57).

Early investigations (Refs 1.58 to 1.60) showed that significant supersonic aerodynamic interference could exist between a wing and body. Methods were developed to aid in exploiting this interference by Sheppard and Lomax (Refs 1.61 to 1.62). The efforts led to what is classically known as the area rule, which results from an examination of disturbances produced by a configuration far from its axis. Also, a complementary near field method, based upon the work of Lighthill (1.63) and Whitham (1.64), is presented, while the near field method is not specially suited

to the design problem, it is useful in the analysis of designs derived from area rule techniques. Lighthill suggested that the pressure field produced by a body of revolution can be computed using a variation of a linear method, this was developed by Witham. The technique, in essence, uses linear theory to predict the magnitude of disturbances produced in the flow field by a body of revolution, and then adjusts the location of these disturbances by modifying the characteristic lines emanating from the body.

Carlson and Middleton have shown in Ref (1.65) that through the use of a simple transformation the pressure field can be calculated using standard numerical techniques. Flow disturbances along characteristic lines produced by a body of arbitrary cross section are related to those produced by an axial source distribution whose strength is function of the body cross section area distribution. This technique, which gives to minimum drag shapes, leads to alterations in body cross section to compensate for the presence of wing so as to reduce wave drag. The interference of body on the wing and wing on the body are calculated as part of the procedure.

Sigalla and Hallstaff in Ref (1.66), Nichols in Ref (1.67), and Swan in Ref (1.68) have carried out some research on the aerodynamic interference between bodies adjacent to the wing and the wing itself. For instance, proper placement and shaping of engine nacelles and proper contouring of the local wing surface

can result in significant improvements in airplane drag and pitching moment.

Bagley, in Ref (1.23), has done some research on swept or M-wing planforms with about 55^{0} sweepback mounted on a waisted fuselage and cruising at about M=1.2.

TRANSONIC PROBLEMS

A recent method of solving flow by Hunt (1.69) such as the "panel method" is discussed for subcritical flow in the transonic regime. The aim is to cope with more complex geometries approaching that of the complete aircraft and other more complex flow situations such as shock-boundary layer interaction and areas of separating flow. The 'exact' method which solves the potential equation for the flow with exact boundary conditions has the advantage that there is only one dependent variable with a consequent saving of computer storage and computer time, but there is the disadvantage that the flow is assumed to be isentropic. In order to allow for the shocks correctly in inviscid flow and to produce a satisfactory model of the shock-boundary layer interaction, Rizzi (1.70) has solved the Euler equations, using a finite volume technique.

Refs (1.25) and (1.26) are concerned with how to eliminate or at least alleviate the loss in isobar sweep near the root of an untreated swept wing-body combination and thus, how to delay the

first appearance of a strong shockwave in the flow around a wing of a given sweepback and thickness/chord ratio. Haines has also carried out some extensive tests and investigations on the design of wing sections for a sweptback case at transonic speeds (1.71).

Ref (1.72) offers some numerical solutions for transonic flows past wing-body combinations. This inviscid transonic small perturbation program (1.72), treats the nett wing at low position with no other allowance for the body apart from an estimate for a mean increase of $\Delta M = 0.01$ due to the expansion around the body nose.

Lawrence and Flax, 1954, Ferrari 1957, also have published some of their survey (1.73), (1.74) articles in this field. Thwaites (1.75) (in Chapter XII) has summarised steady incompressible flow theory for both two-dimensional biplanes and infinite arrays of lifting airfoils. Garrick (1.76, 1.77), has also made early contributions using the exact method of conformal transformation. The extension of non-linear and small perturbation solutions for a compressible fluid appears in Chapter 12 of Woods (1.78). The theory of oscillating cascades was fully developed by Sohngen and Heister (1.79), for the incompressible case, and more recently, with inclusion of compressibility effects by authors such as Jones and Rao (1.80) and Bland (1.81). The interesting attempt to construct non-linear incompressible solutions for general unsteady

motions of interacting airfoils is typified by Giesing (1.82).

Djojodihardjo and Widnall (1·83) made some attempt to determine the evolution of the wake and loading of an isolated wing with finite thickness and incidence . The use of slender- body idealization was made the richest source of calculations for the interference of wing-body combinations by Ward (1·84) .

The most comprehensive exploitation of these concepts for forces and moment estimation appears in Nielsen (1.85), especially his Chapter 5 on interference. Chapter 2 of Ferrari (1.74) also summarizes the application to combinations of wings, bodies, and tails. From the extensive literature on slender-body methods adapted to interacting flows one other paper by Bryson(1.86)is singled out. His use of the momentum theorem of fluid mechanics to determine lateral forces and other stability derivatives is a landmark in the evolution of this subject.

Hayes and Probstein (1.87) developed many approximate schemes for non-linear numerical methods for supersonic flight. Typically

the elliptic field up to the sonic line was first determined by finite-difference integration of the governing equations behind some estimated position of the bow shock wave. At higher Mach numbers, the "shock layer" is thin, and quasi-one-dimensional approximations like the method of integral relations simplified this process and yielded the shock shape produced by a given body. The method of characteristics was the early choice for analysis of supersonic regions and still proves valuable for certain wholly supersonic flows (see e.g. Powers and Beeman (1.88)).

As of the present writing, none of the non-linear numerical schemes has been applied to general wing-body combinations. The most promising would seem to be that of Grossman, Marconi and Moretti (1.89), and Moretti and Abbett (1.90). The flow around blunt noses is rendered hyperbolic by introducing artificial time dependence, then conducting a finite-difference solution of the unsteady equations until the steady state is reached. For supersonic and hypersonic regions, a straightforward downstream "marching" computation is chosen in preference to characteristics.

Some recent research discussed at a meeting held at the NASA Ames Research Centre is given in Ref (1.91). AGARD (Advisory Group for Aeronautical Research and Development) have devoted some conference time to research in these fields, especially in interference, and this was organized by different panels of NATO (1.92) and (1.93). Also Ref (1.93) of AGARD contains extensive theory

and examples on unsteady motion of interacting systems of lifting surfaces (three-dimensional biplanes, wing-tail combinations, complete empennages, etc.), which are deemed to fall within the present scope.

An extension of Falkner's method to the oscillatory case was given by Runyan and Woolston (1.94) in an early form of the Kernel-function method. This solution was soon reconsidered in view of the successes of the newer vortex-lattice method. The extension of the vortex-lattice method has become known as the doublet-lattice method and resulted from similar and independent developments by Landahl and Stark (1.37), Albano and Rodden (1.95), Petkas (1.96), and Houbolt (1.97). A number of further developments and applications of the doublet-lattice method have been made by Rodden, Giesing and Kalman (1.41).

The history of finite-element methods for interacting lifting surfaces may be traced back to the work of Etkin (1.98) and Pines, Dugundji, and Neuringer (1.99) on planar wings. In Ref (1.99) authors divided the planform and the disturbed area ("diaphragm") of the xy plane off the planform into small square elements or facets. Each facet was covered with an oscillatory source sheet of constant strength amplitude. A matrix of aerodynamic influence coefficients was constructed, giving the upwash w at the centre of each facet due to each source element whose influence could be felt there. In the event that the wing motion is specified and the boundary condition as well, the loading can be predicted and the

source strengths may be determined from the boundary conditions. Once these source strengths are determined, pressure distributions and resultant loads will be found from a linearized theory.

Because of advances in computer technology there resulted a speed increase of benefit to computational analysis. Therefore, in 1975, Chapman and Mark (1.100) for the first time believed that it will be possible by the late 1980's to solve the full Navier-Stokes equations, in spite of the complexity and variation of scale in different regions of the flow which have rendered numerical solutions of these equations impracticable to date.

1.4 VARIABLE GEOMETRY AIRCRAFT

In the case of an aircraft which is required to operate efficiently in both the subsonic and supersonic regimes, variable wing sweep is a desirable feature.

Wings can then be swept back when the aircraft is being flown at high speeds and swept forward again when flying at low speeds. Some coutries, with advanced technologies such as America, Russia, United Kingdom, France, etc., have already been successful in constructing, flying, and even entering into military service, aircraft with variable-sweep wings designed to undertake important and difficult roles. Some of the variable geometry aircraft from different countries are listed below and for details refer to "Jane's All The World's Aircraft" Book.

(I) <u>AMERICA</u>

1) General Dynamics F-111
2) Grumman F-14 Tomcat
3) Rockwell International B-1
4) Bell X-5
5) Boeing 733 (SST)

(II) <u>RUSSIA</u>

1) Mikoyan MIG-23
2) Sukhoi SU-7B
3) Tupolev Backfire

(III) U.K.

1) Panavia-MRCA

2) Short SB5

(IV) FRANCE

1) Dassault Mirage G8

(V) GERMANY, ITALY

1) Panavia MRCA Tornado

REFERENCES FOR CHAPTER 1

(1.1) GIBBS-SMITH, C.H. "Sir George Cayley's Aeronautics". 1796-1855. London, 1962.

(1.2) KUCHEMANN, D. "Design of wing junction, fuselage and nacelles to obtain the full benefit of sweptback wings at high Mach number". R·A·E REPORT NO· AERO· 2219 (A·R·C 11035) 1947

(1.3) BUSEMANN, A. "Profilmessugen bei Geschwindigkeiten nahe der schallgeschwindigkeit". Jb. Wiss. Ges. Flugtechn. 1928, 95.

(1.4) BETZ, A. "Sonderaufgaben der aerodynamis chen Forschung". Schr. dtsch. Akad. Luftfahrtf. 1020/409 (1940).

(1.5) KUCHEMANN, D. "Some remarks on the interference between a swept wing and a fuselage". AGARD-Cp-71 Aerodynamic Interference, Sept. 1971.

(1.6) KUCHEMANN, D. and WEBER, J. "The subsonic flow past swept wings at zero lift without and with body". ARC R & M 2908, 1956.

(1.7) KUCHEMANN, D. "A simple method for calculating the span and chordwise loading on straight and swept wings of any given aspect ratio at subsonic speeds. ARC R & M 2935. 1956.

(1.8) PRANDTL, L. TRAGFLUGELTHEORIE and MITTEILUNG I — "Nachrichten der Konigliehan Gesellschaft der Wissenschaften zu Gottingen". Math. Phsy. Klasse, P451, 1918.

(1.9) JONES, R.T. — "Properties of low-aspect-ratio pointed wings at speeds below and above the speed of sound. NACA Rept 835. 1946.

(1.10) — "Method for predicting the pressure distribution on swept wings with subsonic attached flow". ESDU Transonic Data Memorandum 73012. June 1973.

(1.11) WEBER, J. — "Interference problems on wing-fuselage combinations". Part I. Lifting unswept wing attached to a cylindrical fuselage at zero incidence in mid-wing position". R.A.E. Technical Report 69130 (1969).

(1.12) LOCK, R.C. and BRIDGEWATER, J. — "Theory of aerodynamic design for swept-winged aircraft at transonic and supersonic speeds". Prog. Aero. Sciences, Vol. 8, 1967, Pergamon Press.

(1.13) BRIDGEWATER, J.
LOCK, R.C. and
LEE, G.F.

"Theoretical and Experimental Investigation of wing-body combinations at low supersonic speeds".
Aerodynamics Division, National Physical Laboratory, England.
AGARD-Cp-71, Sept. 1970.

(1.14) LOEVE, W.,
LABRUJERE, Th.E. and
SLOOFF, J.W.

"An approximate method for the calculation of the pressure distribution on wing-body combinations at subcritical speeds".
National Aerospace Laboratory NLR, Amsterdam, Netherlands.
(AGARD-Cp-71), Sept. 1970).

(1.15) LOEVE, W.
LABRUJERE, The. E. and
SLOOFF, J.W.

"An approximate method for the determination of the pressure distribution on wings in the lower critical speed range".
AGARD Conference Proceedings No.35, (1968).

(1.16) BAGLEY, J.A.

"An aerodynamic outline of a transonic transport aeroplane".
R.A.E. Tech Note. Aero. 2472. 1965.

(1.17) BAGLEY, J.A.

"Wing section design for a transonic aeroplane".
R.A.E. Tech. Note. 2498, 1965.

(1.18) LIGHTHILL, M.J. "A new method of two-dimensional aerodynamic design". A.R.C. R & M 2112.

(1.19) THWAITES, B. "A new family of low drag wings with improved C_L Ranges". A.R.C. R & M 2292.

(1.20) EPPLER, R. "Direkte Berechnung Von Tragflugelprofilen aus der Druckvertcilung". JNG.ARCH. 25, 56.

(1.21) SINNOTT, C.S. and OSBORNE, J. "Review and Extension of transonic aerofoil theory". A.R.C. R & M. 3156.

(1.22) SEARS, W.R. "General theory of high speed aerodynamics Vol. VI of high speed aerodynamics and jet propulsion". Princeton University and O.U.P. 1955.

(1.23) BAGLEY, J.A. "Some aerodynamic principles for the design of swept wings". RAE Report Aero. 2650, May 1961.

(1.24) ROGERS, E.W. and HALL, I.M. "An introduction to the flow about plane sweptback wings at transonic speeds". Journal of Royal Aeronautical Society, 64, 449, August 1960.

(1.25) KUCHEMANN, D. "Methods of reducing the transonic drag of swept-back wings at zero lift' Journal of the Royal Aeronautical Soc. Vol. 61, pp.37-42, Jan. 1957.

(1.26) KUCHEMANN, D. and HARTLEY, D.E. "The design of swept wings and wing-body combinations to have low drag at transonic speeds". RAE Report No. Aero. 2537, June 1955.

(1.27) JONES, R.T. "The minimum drag of thin wings in frictionless flow". J. Aero. Sci. 18, 75 (Feb. 1951).

(1.28) GINZEL, I. and MULTHOPP, H. "Wings with minimum drag due to lift in supersonic flow". J. Aero. Space. Sci. 27, 13 (Jan. 1960).

(1.29) LOMAX, H. "The wave drag of arbitrary configurations in linearized flow as determined by areas and forces in oblique planes". NACA.RM A55 A18 (March 1955).

(1.30) WHITCOMB, R.T. "A study of the zero lift drag-rise characteristics of wing-body combinations near the speed of sound". NACA RM L52M08 [NACA/TIB/3279] Sept. 1952.

(1.31) WHITCOMB, R.T. and FISCHETTI, T.L. "Development of a supersonic area rule and an application to the design of a wing-body combination having high lift to drag ratios". NACA RM L53 H31a [NACA/TIB/3912] October, 1953.

(1.32) BAGLEY, J.A. Unpublished Ministry of Aviation Report.

(1.33) HESS, J.L. SMITH, A.M.O. "Calculation of potential flow about arbitrary bodies". Progr. in Aeron. Sci. 8, 1 (1967).

(1.34) LIESE, J. VANDREY, F. "Theoretische Untersuchungen über die Druckverteilung eines Mitteldeckers in der Nahe des Rumpt-Flugelubergangs Jb. Dtsch. Luftfahrtf. 1942, I, 326.

(1.35) CARMICHAEL, RALPH L. "Recent experience in using finite element methods for the solution of problems in aerodynamic interference". Ames Research Centre, NASA Moffett Field, California, U.S.A. 94035.

(1.36) RUBBERT, PAUL E, SAARIS, GARY R, MICHAEL B, STANDEN, NEIL M, and WALLACE, RICHARD E. "A General Method for Determining the Aerodynamic Characteristics of Fan-in-wing Configurations". USAA VLABS-TR-67-61A, AD-667980, Dec. 1968.

(1.37) LANDAHL, M.T. and STARK, V.J.E. "Numerical lifting surface theory-problems and progress". AIAA, J, Vol. 6, No.11, Nov. 1968.

(1.38) SPANGLER, S.B. MENDENHALL, M.R. and DILLENIUS, M.F.E. "Theoretical Investigation of Ducted Fan Interence for Transport-type Aircraft". NASA SP-228, 1970.

(1.39) MACK, ROBERT J. "A Numerical Method for the Evaluation and Utilization of Supersonic Nacelle-wing Interference". NASA TN D-5057, 1969.

(1.40) WOODWARD, F.A. "Analysis and Design of Wing-Body Combinations at Subsonic and Supersonic Speeds". J.Aircraft, Vol.5, No.6, Nov-Dec.1968.

(1.41) KALMAN, T.P., RODDEN, W.P. and GIESING, J.P. "Application of the Doublet-lattice method to non-planar configurations in subsonic flow". AIAA Paper 70-539, 1970.

(1.42) CARMICHAEL, RALPH L. CASTELLANO, CHARLES R and CHEN, F.C. "The use of Finite Element Methods for predicting the Aerodynamics of Wing-Body Combinations". NASA SP-228, 1970.

(1.43) RUBBERT, P.E. and SAARIS, G.R. "A general three-dimensional potential flow method applied to V/STOL aerodynamics". SAE Paper 680304 (1968).

(1.44) STEWARTSON, K. "Wing-body interference at supersonic speeds". University College London, D.A. Threadgold, Aerodynamics Department, Royal Aircraft Establishment, Farnborough. AGARD-Cp-35 (Sept. 1968)

(1.45) SCHNEIDER, W. "Experimental investigation of wing-body interferences in the Mach number range from 0.5 to 2.0". AGARD-Cp-35. Transonic Aerodynamics, Sept. 1968.

(1.46) FALKNER, V.M. "The calculation of aerodynamic loading on surfaces of any shape". Aeronaut. Res. Coun. Rep. Mem. No. 1910, 1943.

(1.47) RUBBERT, P.E. "Theoretical characteristics of arbitrary wings by a non-planar vortex lattice method". Boeing Co. Rep: D-6-9244, 1964.

(1.48) DULMOVITS, J. "A lifting surface method for calculating load distributions and the aerodynamic influence coefficient matrix for wings in subsonic flow". Grumman Aircraft Engineering Corp. Rept. AGARD. 01-02-64.1, 1964.

(1.49) HEDMAN, S.G. "Vortex lattice method for calculation of quasi steady state loadings on thin elastic wings". Aeronauti. Res. Inst. Sweden, Rept. 105, 1965.

(1.50) BELOTSERKOVSKII, S.M. "The theory of thin wings in subsonic flow". New York: Plenum - 1967.

(1.51) MONICAL, R.E. "A method for representing fan-wing combinations for three-dimensional potential flow solutions". J. Aircraft. 2:527-30 - 1965.

(1.52) TULINIUS, J.R. "Theoretical prediction of thick wing and pylon-fanpod-nacelle aerodynamic characteristics at sub-critical speeds". North Am. Rockwell Corp. Rep. NA-71-447, 1971.

(1.53) KARIAPPA and SMITH, G.C.C. "Further developments in consistent unsteady supersonic aerodynamic coefficients". AIAA Paper No. 71-177, 1971.

(1.54) WOODWARD, F.A. "An improved method for the aerodynamic analysis of wing-body-tail configurations in subsonic and supersonic flow". NASA CR 2228, 1973.

(1.55) WOLFGA SCHMIDT "Aerodynamic subsonic/transonic aircraft design studies by numerical methods".
Dornier GmbH, theoretical Aerodynamics Dept. D-7990 Freiedrichshafen, Germany. AGARD-CP-285, May 1980.

(1.56) JOHNSON, F.T. and RUBBERT, P.E. "Advanced panel-type influence coefficient methods applied to subsonic flows".
AIAA Paper No. 75-50, Jan. 1975.

(1.57) EDWARD, J. KANE, and WILBUR, D. MIDDLETON "Considerations of Aerodynamic Interference in supersonic airplane design"
The Boeing Company, Sept.1970.
AGARD-Cp-71.

(1.58) WHITCOMB,R.T. "A study of the zero lift drag rise characteristics of wing body combinations near the speed of sound".
NACA Report 1273, 1956.

(1.59) HAYES, W.D. "Linearized Supersonic Flow",
Princeton Univ. AMS Report No. 852, Oct. 1968 (Reprinted from North American Report AL-222, 1947).

(1.60) HEASLET, M.A. LOMAX, H. and SPREITER, J.R. "Linearized compressible flow theory for sonic flight speeds".
NACA Report 456, 1950.

(1.61) SHEPPARD, L.M. "Methods for determining the wave drag of non-lifting wing body combinations", ARC Technical Report R & M No.3077, 1958.

(1.62) LOMAX, H. "The wave drag of arbitrary configurations in linearized flow as determined by areas and forces in oblique planes", NACA RM A55A18, March 1955.

(1.63) LIGHTHILL, M.J. "Higher approximations in aerodynamic theory", Princeton Univ. Press, 1960.

(1.64) WHITHAM, G.B. "The flow pattern of a supersonic projectile", Communications on Pure and Applied Mechanics, Vol.4, Pgs. 301-348, 1952.

(1.65) MIDDLETON, W.D. and CARLSON, N.W. "A numerical method for calculating near field sonic boom pressure signatures", NASA TN D-3082, Nov.1965.

(1.66) SIGALLA, A. and HALLSTAFF, T.H. "The aerodynamics of powerplant installations on supersonic aircraft", Journal of Aircraft, Vol. 4, No.4, July 1967.

(1.67) NICHOLS, M.R. "Aerodynamics of Airframe Engine integration of supersonic Aircraft", NASA TN D-3390, 1966.

(1.68) SWAN, W.C. "A Discussion of Selected Aerodynamic Problems on Integration of Propulsion System with the Airframe on Transport Aircraft", Agardograph No.103, Oct. 1965.

(1.69) HUNT, B. "The prediction of external store characteristics by means of the panel method." BAC(MAD) Report Ae/372, Jan. 1977.

(1.70) RIZZI, A. "Transonic solutions of the Euler equations by the finite volume method". IUTAM Symposium Transsonicum II. Gottingen, pp.567-574. Sept. 1975.

(1.71) HAINES, A.B. "Wing section design for swept-back wings at transonic speeds". Journal of the Royal Aeronautical Society. Vol.61. pp.238-244, Jan 1957.

(1.72) ALBONE, C.M., HALL, M.G. and JOYCE GAYNOR "Numerical solutions for transonic flows past wing-body combinations". IUTAM Symposium Transsonicum II, Gottingen 1975. Spr. Verlag. 1976.

(1.73) LAWRENCE, H.R. and FLAX, A.H. "Wing body interference at subsonic and supersonic speeds-survey and new developments". J. Aero. Sci. 21: 289-324, 328, 1954.

(1.74) FERRARI, C. "Intraction problems in high speed aerodynamics and jet propulsion". Ed. H.R. Lawrence, A.F. Donovan, Section C, Vol. VII, Princeton, N.J: Princeton Univ. Press.

(1.75) THWAITES, B. "Incompressible aerodynamics" OXFOR: Clarendon Press. Ed. 1960.

(1.76) GARRICK, I.E. "Potential flow about arbitrary biplane wing sections". NACA Rept. 542, 1936.

(1.77) GARRICK, I.E. "On the plane potential flow past a lattice of arbitrary airfoils". NACA. Rept. 788, 1944.

(1.78) WOODS, L.C. "The theory of subsonic plane flow". Cambridge: Cambridge Univ, Press, 1961.

(1.79) SOHNGEN, H. and MEISTER, E. "Beitrag zue Aerodynamik eincs schwingenden gitters". ZAMM 38: 443-65, 1958.

(1.80) JONES, W.P. and RAO, B.M. "Compressibility effects on oscillating rotor blades in hovering flight". AIAA J. 8:321-29, 1970.

(1.81) BLAND, S.R. "Two-dimensional oscillating airfoil in a wind tunnel in subsonic compressible flow". Ph.D. Thesis, North Carolina State Univ. 1968.

(1.82) GIESING, J.P. "Non-linear interaction of two lifting bodies in arbitrary unsteady motion". J. Basic Eng. 90:387:94, 1968.

(1.83) DJOJODIHARDJO,R.H. and WIDNALL, S.E. "A numerical method for the calculation of non-linear, unsteady lifting potential flow problems". AIAA J.7:2001-9.

(1.84) WARD, G.N. "Supersonic flow past slender pointed bodies". Quart. J. Mech. Appl. Maths, 2:75-97, 1965.

(1.85) NIELSEN, J.N. "Missile Aerodynamics". New York: McGraw-Hill, 1960.

(1.86) BRYSON, A.E. "Stability derivatives for a slender missile with application to a wing-body vertical tail configuration". J. Aeronaut. Sci. 20: 297-308, 1953.

(1.87) HAYES, W.D. and PROBSTEIN, R.F. "Hypersonic flow theory". New York, London Academic, 1959.

(1.88) POWERS, S.A. and BEEMAN, E.R. Jr. "Flow fields over sharp edged delta wings with attached shocks". NASA CR-1738, 1971.

(1.89) GROSSMAN, F. "A numerical procedure to calculate the inviscid flow field about a space shuttle orbiter travelling at a supersonic/hypersonic velocity". Paper 6, NASA Space Shuttle Technol. Conf. NASA TM X12272.

(1.90) MORETTI, G. and ABBETT, M. "A time-dependent computational method for blunt body flows". AIAA J. 4:2136, 1966.

(1.91) "Analytical methods in aircraft aerodynamics". NASA SP-228, 1969.

(1.92) "Aerodynamic interference" AGARD Conference Proceedings No. 71, 1970.

(1.93) "Symposium on unsteady aerodynamics for aeroelastic analyses of interfering surfaces". AGARD Conference Proceedings No. 80, (Part I and II) 1971.

(1.94) RUNYAN, H.L. and WOOLSTON, D.S. "Method for calculating the aerodynamic loading on an oscillating finite wing in subsonic and sonic flow". NASA Rept. 1322, 1957.

(1.95) ALBANO, E. and RODDEN, W.P. "A doublet lattice method for calculating lift distributions on oscillating surfaces in subsonic flows AIAA J.7:279-85,2192, 1969.

(1.96) PETKAS, J.S. "Oscillatory aerodynamic representation using discrete load line element (DLLE) method". Lockheed-Georgia Co. Unpublished Memo. 1969.

(1.97) HOUBOLT, J.C. "Some new concepts in oscillatory-lifting surface theory". USAF FDL-TR-69-2, 1969.

(1.98) ETKIN, B. "Numerical Integration Methods for supersonic wings in steady and oscillatory motion". Inst. Aero Phys., Univ. of Toronto, Rept. 36. 1955.

(1.99) PINES, S. DUGUNDJI, J. and NEURINGER, J. "Aerodynamic flutter derivatives for a flexible wing with supersonic and subsonic edges". J. Aeronaut. Sci. 22:693-700, 1955.

(1.100) CHAPMAN, D.R. MARK, H. and PIRTLE, M.W. "Computers vs wind tunnels for aerodynamic flow simulation". Astronautics and Aeronautics, pp.22-30, April 1975.

CHAPTER 2

EXPERIMENTAL ANALYSIS

(2.1) Introduction.

A scale model of a variable geometry aircraft was built for testing in the wind tunnel in order to determine the basic aerodynamic force and moment coefficients, together with pressure distributions. The effect of sweep angle on the aerodynamic forces and moments was investigated and comparisons between the experimental readings and theoretical predictions described in Chapter (3) were made. The corresponding results are shown in Chapter (9). Observations were made of the boundary layer behaviour on the wing surface. Effort were made to create an turbulent boundary layer on the wing surface by insertion of tripping devices. Some flow visualisation pictures are shown in Chapter (9). This chapter also contains a description of the construction of the model wing, glove, fuselage and othe parts. Description of the wind tunnel used for testing and the experimental arrangements are presented. The force and moment coefficients for the model were derived from measurements of the pressure distrubution over the surface of the model, using a numerical integration scheme.

(2.2) Experimental Programme.

The configuration that was selected for the model was similar to the B -1 bomber, variable sweep aircraft. The sweep angles tested were 0°, 12.5°, 32.5°, 52.5°. This range of sweep was selected to give a complete picture of aerodynamic forces and moments. The maximum incidence for the aircraft was selected to be 20°, although separation was occuring on the wing surface was about 10° incidence.

Therefore tests were carried out, starting from 0° incidence and proceeding to 20° incidence in steps of 4°. This range of incidence gives a good view of the effects on the aerodynamic forces and moments.

2.3 Descritption of the experimental set-up.

The general layout of the wind tunnel is shown in Fig (2.1).
A general view of the complete test equipment and the model is shown in Figs (2.2) to (2.6). A turntable was made to hold the model with the wing hanging vertically downwards. This table is attached to the 6 component balance (with electro - mechanical output system) situated on the top of working section of wind tunnel No.1 in the Aerodynamics Laboratory. An electric motor within the balance enables the table and attached model to rotate on an axis set at 1/4 root chord of the wing, perpendicular to the turntable. This rotation allows the model to have a variable angle of incidence, relative to the flow direction.
Pressure distributions on the wing, glove, and the body were measured. All the forces and moments acting upon the model were recorded in the form of electrical voltage signals by the independent computer system which was connected to the balance output system.

The wing carries four drilled holes for the four different sweep settings. There is a hole through the top and bottom of the glove surfaces, so that it is possible to lock the wing for each of the four sweep angles to the glove by a bolt. The pressure distributions were taken over the top and bottom wing surfaces, the top and bottom glove surfaces and the body surface. Finally, oil flow visualization tests were carried, and tripping devices were used to create a turbulent attach flow region on the wing surface.

(2.4) The Wind Tunnel.

The wind tunnel is one of the most important facilities available for experimental work in aerodynamics. Its purpose is to provide a region of controlled airflow into which models can be inserted. For this purpose the flow in the working section should be uniform in speed and direction and free from vorticity. Such perfections can never be achieved in practice, and the quality of a wind tunnel is related to the closeness to which the airflow in the working section approaches the ideal.

Usually, there are two types of working section, closed or open. There are some advantages and disadvantages associated with these two types of working section. Firstly the closed working section constrains the airflow within the solid walls. While the open working section lets the airflow expand because there are no solid walls. Secondly, for closed working section there is a greater efficiency (i.e. reduced power losses) and better control of the airflow. A closed working section enables measurement of pressures at points on the walls, while an open working section allows easier access to the model and easier visual study of the flow.

For the present work a closed working section wind tunnel was used. This tunnel is of a low speed, closed - return type. The working section is 3ft high (i.e. 91.44 cm), 4ft wide (i.e. 121.92 cm) and 5.9ft long (i.e. 179.83 cm.). The tunnel is fitted with a screen and honeycomb air-straightener in the settling chamber. The air is accelerated by a 3.5:1 contraction prior to entering the working section. The maximum airspeed of 40 m/sec (i.e. motor speed of 1,100 R.P.M.) is

produced by means of a 25 hp electric motor. The speed is continuously variable down to 17 m/sec. The velocity distribution across the empty working section is within $\pm$ 1 per cent of the mean velocity, and the variation in flow direction does not exceed $\pm$ 1/2 degree, and turbulence level is 0·3 % . The air is circulated by a 4 bladed wooden fan which is driven by the electric motor through a transmission system consisting of a pair of bevel gears and a flexible coupling. The Reynolds number in experimental tests was found to be about (0.82 to 1.64) x 10^6. Fig (2.1) shows a schematic view of the wind tunnel.

2.5 Calibration Of The Wind Tunnel.

To calibrate the working section of wind tunnel No. 1 which was used for the aerodynamic tests on the model, first the wind tunnel speed was set to 1,100 R.P.M. The tunnel was initially calibrated, using a Pitot-static tube in the working section. All the pressure readings were directed towards the determination of the calibration factors K_1 and K_2 which are defined as follows:-

$$K_1 = \frac{P_{Total} - P_{Static}}{P_A - P_B} \qquad K_2 = \frac{P_{Static} - P_{Atmos}}{P_{Total} - P_{Static}}$$

Where P_A = reference static pressure upstream of the contraction.

P_B = reference " " downstream of " " .

Hence K_1 and K_2 were found to be 1.137 and -0.18 respectively.

Pressure readings were converted to C_p values by use of these factors as follows:

$$C_p = \frac{1}{K_1}\left(\frac{P - P_{Atmos}}{P_A - P_B}\right) - K_2$$

and in this case.

$$C_P = \frac{1}{1{\cdot}137}\left(\frac{P - P_{Atmos}}{P_A - P_B}\right) + 0{\cdot}18$$

2.6 Pressure Measuring Techniques

The total number of points at which pressure readings were taken is 72 on the fuselage in six chordwise rows, and 48 on the glove in four chordwise rows. On the top and bottom surfaces there are 4 pressure holes along the wing chord for different sweep angle settings, in seven different spanwise positions. Therefore this constituted total of 112 holes on the top and 112 holes on the bottom of the wing surfce.

All the pressure tappings were connected to a paraffin multitube manometer. A total of 24 pressure tubes were used to take pressure readings on the model. The reference pressure readings P_A and P_B were taken in cm of paraffin on the paraffin manometer as well as on the Betz manometer in mm of water. Thus, it was possible to deduce, the values of pressure coefficients C_p from the values of the pressures, for each of the pressure tappings.

(2.7) Conversion Of Readings To Wind Axes.

The aerodynamic forces and moments acting on the model were recorded in forms of electrical voltages and then printed by a small teletype printer connected to the aerodynamic balance mechanism. Because the model was hanging down from the balance strut all forces and moments acting on the model have to be corrected and converted to the horizontal (conventional) principle ones of the aircraft. Some more details can be found in Appendix (A).

2.8 Model Specification

In this section, details of the model, which has a fuselage in the form of a slender body of revolution, are presented. The model was made in three main parts: a half fuselage, the glove, and the wing. As shown in Figs (2.2) to (2.4) the fuselage of this model is made of solid wood, and consists of three sections; an ellipsoidal part for the nose, semi-circular cylinder for the main middle section, and a body of revolution formed by rotating a circular arc for the tail position. Because of symmetry about the centre plane of the aircraft, a half model was used so that only a starboard glove and wing were made. Pressure holes were drilled along a single line on the surface of each part of the model parallel to the axis of symmetry and passing through the leading point. The surface distances between these pressure holes on each surface line are different. There are four holes on each streamwise line of tubing of the wing, and twelve holes on the glove and fuselage in the same direction on each line. These static pressure tapping were constructed by fitting brass tubes of 0.094 (3/32)in outside diameter into the pre-drilled pressure grooves.

In order to investigate the effect of the wind tunnel on the model and the static pressure readings, the model was first supported vertically downwards, and secondly horizontally. All the differences in static pressures for corresponding tubes were minute and negligible. Therefore tests with the model mounted vertically were used for the main results. This decision was mde because in the vertical position tests were simpler to conduct and the model could be mounted directly onto the balance with incidence changes being produced by the balance yaw motor. All the details of the individual parts of the model, are set out in the following sections.

(2.9) The Geomtry Of The Aircraft Model.

Research was carried out into some actual variable sweep aircraft designs and these studied for an ideal model. The investigations were carried out to find a suitable variable geometry wing aircraft having well defined and known geometry. Eventually, after a search, the geometry of the Bomber B - 1 was found to be set out in some detail in the aeronautical Journals Refs. (2.1) and (2.2).
The actual wing aerofoil section geometry chosen was NACA. 64. A210 which was selected from page 430 and 596 - 597 of Ref. (2.3). The dimensions and all the details are described in the following sections.

(2.10) Wing Model Geometries.

The wing planform was designed to be the same as the B-1 wing, as shown in Fig (2.7). It was necessary to have a v-notch gap between the root and glove to allow the wing to cover the full range of the variable sweep positions. The actual wing aerofoil section was selected to be rather thin in order to be suitable for subsonic and supersonic design conditions. The geometry of the wing is shown in Fig (2.8) and the details are as follows:

1) Leading Edge Semi-span = 27.2"
2) Trailing Edge Semi-span = 22.4"
3) Root chord = 12.1"
4) Tip chord = 3.2"
5) Maximum thickness chord ratio (t/c) = 6.3%
6) Aspect Ratio $\left(\frac{\bar{S}}{\bar{C}}\right)$ = 3.24

Cross-sectional geometries and some drawings across the chord are shown in Figs (2.16) for different positions along the span. The wing was made of three layers, the top layer of solid hardwood (mahogany), the middle a thin plate of aluminium and the lower also of the same hardwood material. First the wing was cut in a rectangular shape, then machined into a triangular shape, and finally into the appropriate geometry. As shown in Fig (2.8), the apex angle of the wing was about 16.14^{o}. The angles of tip with leading edge and trailing edge are 112° and 84° and the angles between the root and the L.E. and T.E. are 31° and 133° respectively. Near the root leading edge on

the 1/4 chordline, the pivot pin was located for the variable sweep and the leadind edge close to the ping was machined to follow circular arc shape with its centre at the pin centre. The location of this centre is 1.9" below the leading edge, and with a radius of 2.3" for an 149° arc angle as shown in Fig (2.8).

Four pressure tubes were sunk inside the top surface of the wing along the four spanwise grooves shown in Fig (2.10), see also Figs (2.2) to (2.6) of the model photographs for a better view. These four tubes were set in the wing, so that their chordal position ratios were 3/16, 7/16, 11/16, and 15/16 of the chord length, all the way along the span.

(2.10.1) Wing Model Manufacturing Procedure.

Owing to the lack of suitable equipment such as a tilting table etc., which are used for making three dimensional wing and aerofoil models in industry, there was some difficulty in manufacturing accurately the wing geometry specified. Therefore a method was decided upon for making the aerofoil shape which was chosen for the wing. In this method, to make the wing aerofoil sections, two perpendicular axes were used to enable the milling machine operation to be simplified. One horizontal axis was located on the ox-axis of the wing, perpendicular to the wing leading edge, as shown in Fig (2.9). The other horizontal axis was located on the oy-axis, along the leading edge span. The wing section geometry was recalculated in terms of sections at right angle to the leading edge. When the wing is rotated through angles θ about a vertical axis (i.e. which is perpendicular to the wing plane)

the streamwise wing sections change. For each different angle of rotation θ, corresponding coordinates x,y, of the wing, and the corresponding values of thickness ratio were specified for these streamwise sections.

There are seven spanwise stations along the wing with pressure tappings. At each station along the chord four pressure tappings were drilled through the wing, for different sweep settings. Therefore at each station A to G in Fig (2.10) , there were sixteen pressure tappings on the upper surface and the lower surface of the wing. However, these pressure tappings were reduced to fourteen for some stations, because of small distances between the first tube tappings for different sweep settings. Details of these pressure tappings allowed us to take static pressure readings for different angles of sweep and different angles of incidence, on the wing surface.

(2.11) Glove Unit Details.

This unit is originally made of mahogany, with a chord length of 28.2" and 5" span in a rectangular block shape 3" thick. It then was machined into an aerofoil shape, approximately that of NACA.64.A210 Ref (2.3), with a total root chord of 28.2" and a tip chord of 16.2" and then it was tapered down from 3" thickness at the root to about 2.2" at the tip.

All the coordinates and aerofoil shapes are shown in Figs (2.11). Once the outer glove shape had been completed, then the inside of the glove was sawn out, so that it made room for the wing to be swept inside it as shown in Figs (2.2), (2.4). (2.5), (2.6), and (2.12). A pin hole

of about ½" was drilled through the top and bottom surfaces of the glove for a sweep pin (hinge). This hole is located on the glove mid-span chord line at a chord-wise distance of 14" from the tip of the root chord.

A mild steel load bracket was designed to act as a cantilever and this takes all the load from the glove and the wing. This load bracket is fitted inside the fuselage at one end, and passes throuth the glove at the other end, holding the wing.

(2.11.1) Pressure Tubes On The Glove Unit

Two sets of pressure tubes on the top and two sets on the bottom surfaces of the glove unit are sunk inside four pregrooved channels. After the pressure tubes were inserted inside the grooves, they were covered by a quick setting epoxy adhesive, namely ARALDITE. This epoxy adhesive became clear after drying out and then five holes were drilled in (i.e. drill no. 16). The pressure tubes on each surface of the glove were divided into two halves, the leading edge half and the trailing edge half. These two halves were taken out from the flat side of the fuselage through a slot and by a right angle turn at the glove root, through the body-glove junction. Every pressure tube on the glove surface carries twelve pressure tapping holes in the chordwise direction.

(2.12) Fuselage Model Specification.

The fuselage model is made of a solid mahogany. It consists of three sections, a semi-elliptical shape at the nose, a semi-circular cylinder for a body section, and a rotated circular-arc shape for the tail section. However, owing to symmetry of the model with its centre plane, it was initially decided to make only one half of the aircraft model and hence only starboard half was tested in the wind tunnel for the experimental purposes.

(2.12.1) Pressure Tappings On The Fuselage.

There were 6 chordwise pressure tubes on the fuselage surface. All the tubes were taken out through a slot in the fuselage. Therefore the static pressure distribution on the fuselage could be recorded. Figs (2.2), (2.4), (2.12), (2.14), and (2.15) show some geometry and details of the fuselage. Also photographs of the model are shown in Figs. (2.2) to (2.6) which present a better view. Fig (2.15) shows the positions of pressure tubes on the fuselage surface, and also it shows details of the pressure tapping holes on the fuselage,. These pressure tubes were located on the fuselage at angles of 2°, 30°, 71°, 154°, 165°, and 178° in a clockwise direction. Each of these tubes carries 12 pressure holes. After all the pressure tapping were installed on the model it was left to dry out and eventually it was smoothed down, in order to reduce the skin drag. Drilling of the pressure tapping holes was carried out along the chord. Finally, the load bracket was assembled by locating it inside the slot inside the fuselage. The location

of this slot in the fuselage is at 42.5% length from the nose, and ½" from the fuselage centre line.

(2.13) Description Of The Load Bracket.

This bracket was made of mild steel, with dimensions of 6.1" length, 2" width, and 1.7" height. One end of this bracket was attached to the flat side of the fuselage, and the other end was fixed inside the glove slot. Fig (2.13) shows all the dimensions of the bracket.

REFERENCES FOR CHAPTER 2

2.1 TAYLOR, J.W.R. (EDITOR) "Journal of Jane's All the World Aircraft". Jane's. Year Book, 1980.

2.2 ALLWARD, MAURICE "Rockwell International's B-1 Strategic Bomber". Air Pictorial, Jan. 1974.

2.3 ABBOTT, AND VON DOEN HOFF "Theory of Wing Section", Doner Publications Ltd., New York, June, 1958.

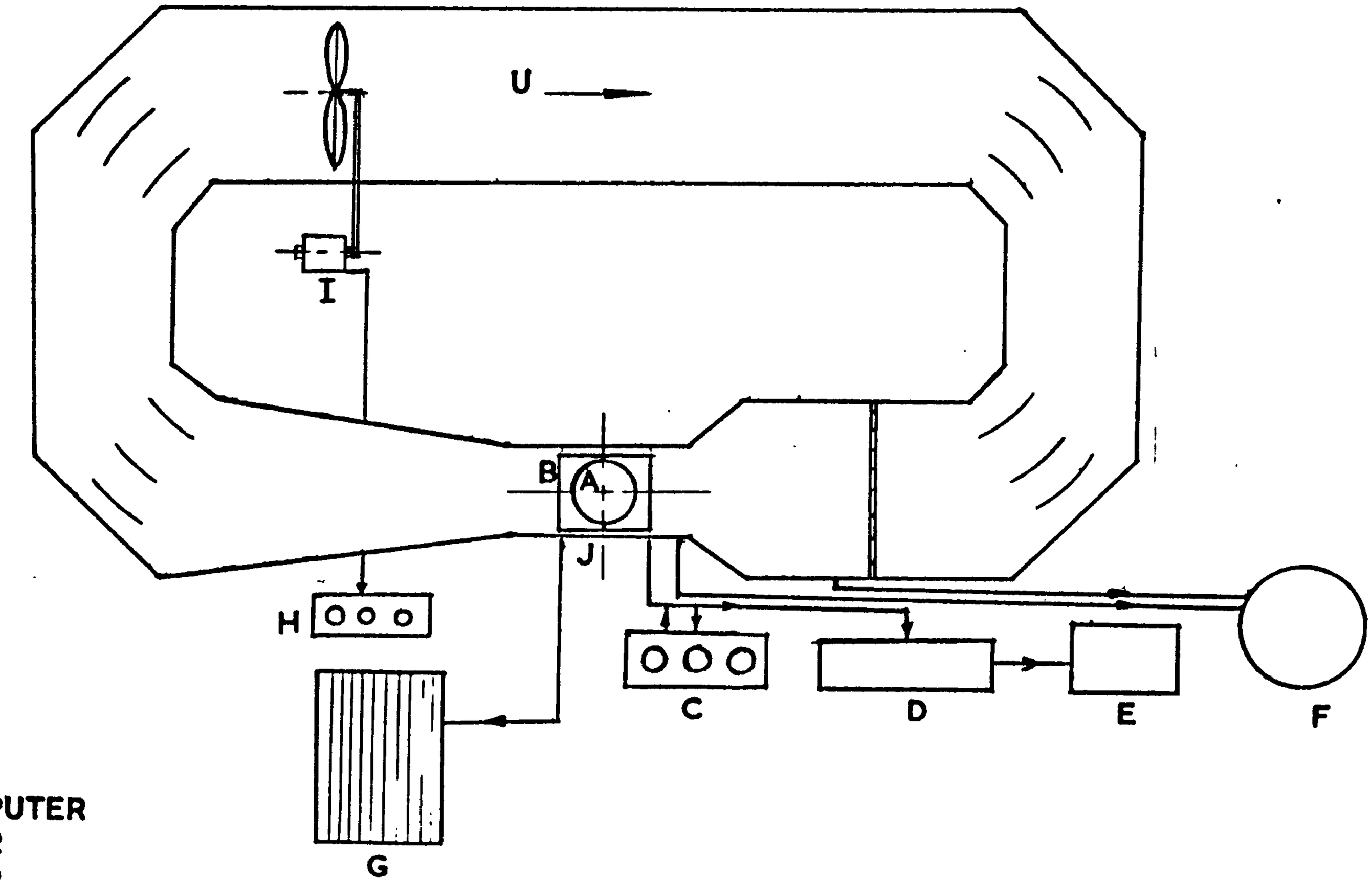

A- TURN TABLE
B- BALANCE
C- YAW METER
D- INDEPENDENT COMPUTER
E- TELETYPE PRINTER
F- BETZ MANOMETER
G- MULTITUBE PARAFFIN MANOMETER
H- WIND TUNNEL CONTROL PANEL
I- ELECTRIC MOTOR
J- WIND TUNNEL WORKING SECTION

FIG.(2.1) SCHEMATIC VIEW OF THE WIND TUNNEL

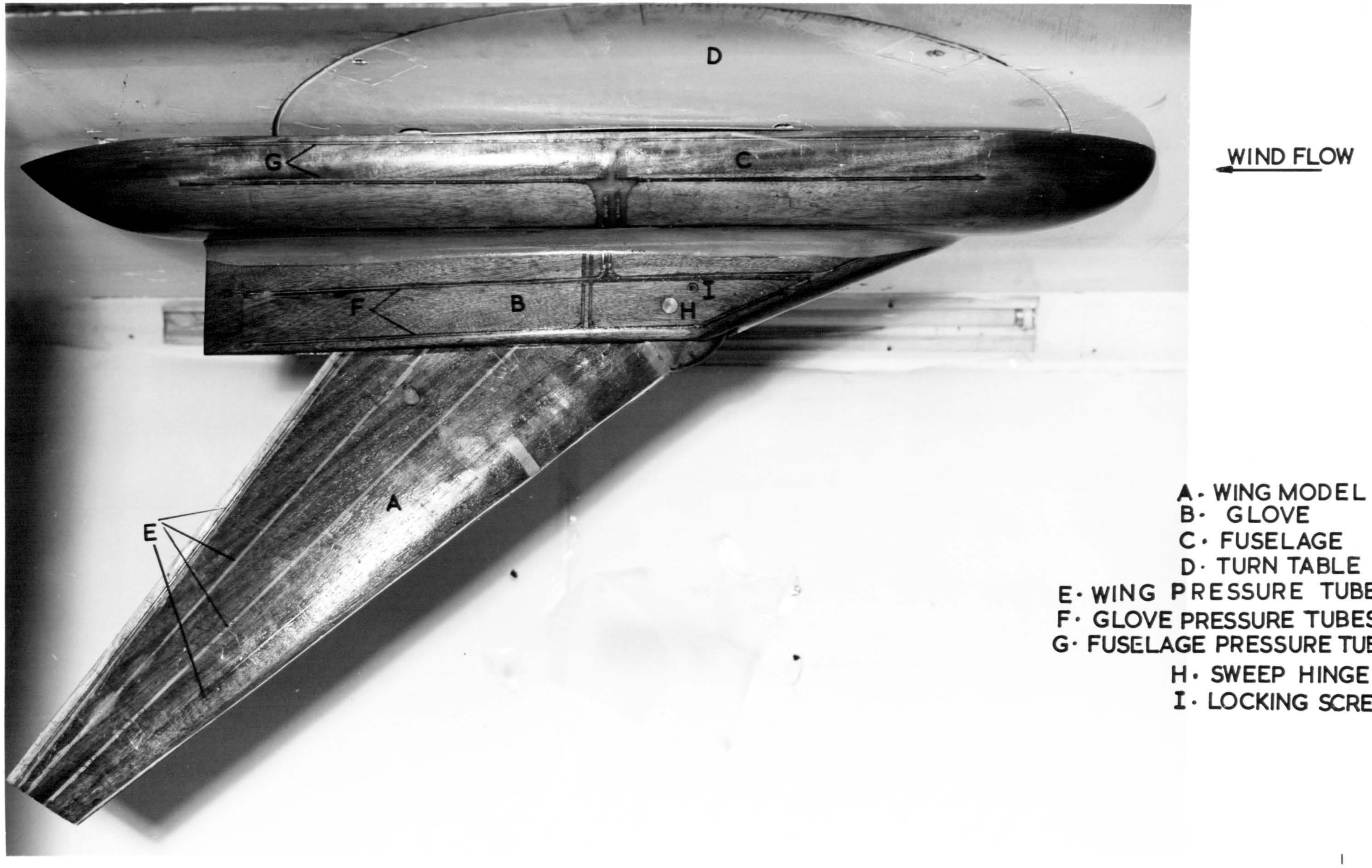

FIG [2.2] A GENERAL VIEW OF THE MODEL COMPONENTS INSIDE THE WIND TUNNEL NO·1

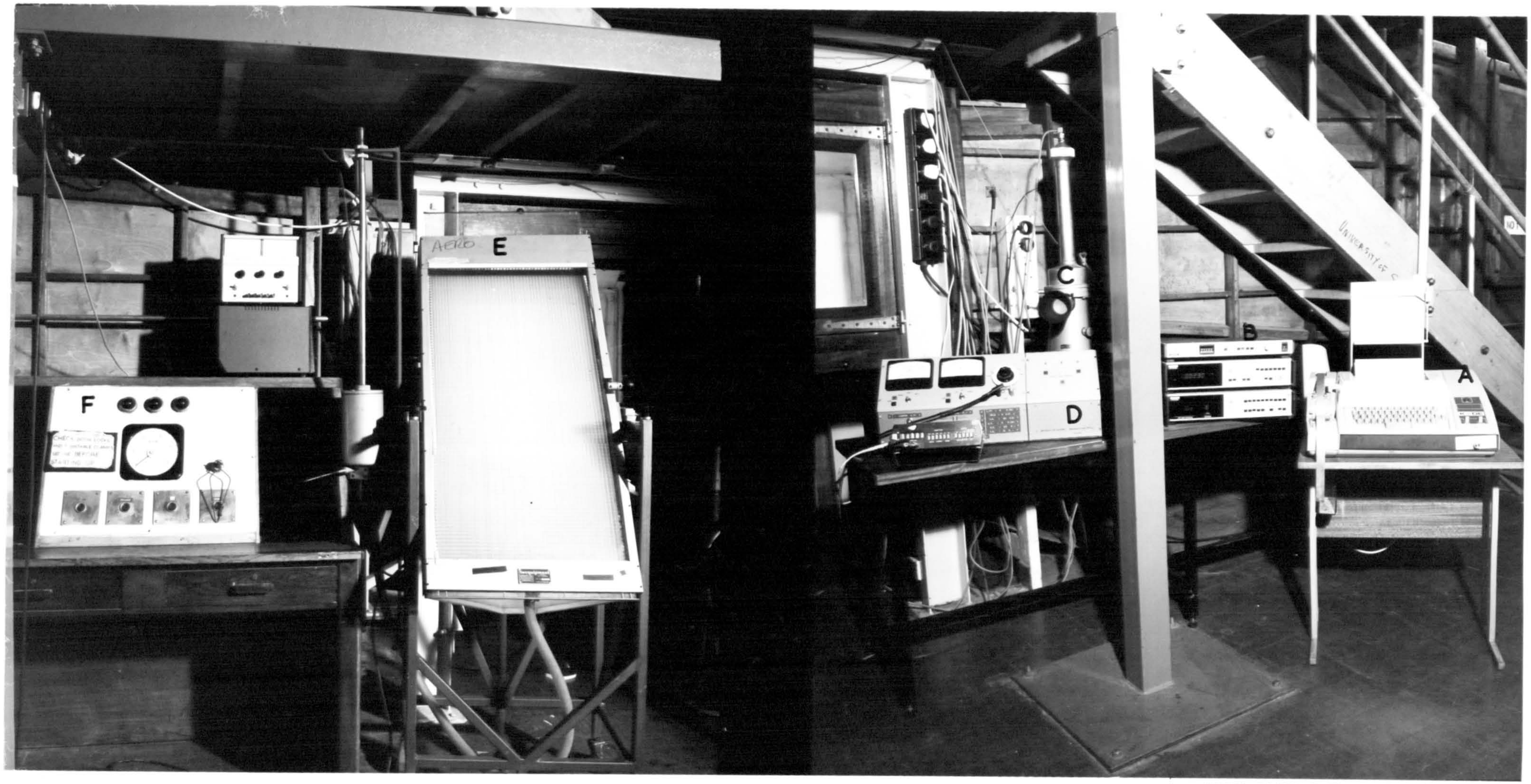

FIG [2 · 3] A GENERAL VIEW OF THE EXPERIMENTAL EQUIPMENTS

A · TELETYPE PRINTER
B · INDEPENDENT COMPUTER
C · BETZ MANOMETER
D · YAW METER
E · MULTITUBE PARAFFIN MANOMET
F · WIND TUNNEL CONTROL PANE

FIG [2 . 4] A SIDE VIEW OF THE WIND TUNNEL MODEL FOR HORIZONTAL TESTING WITH SWEPT WING

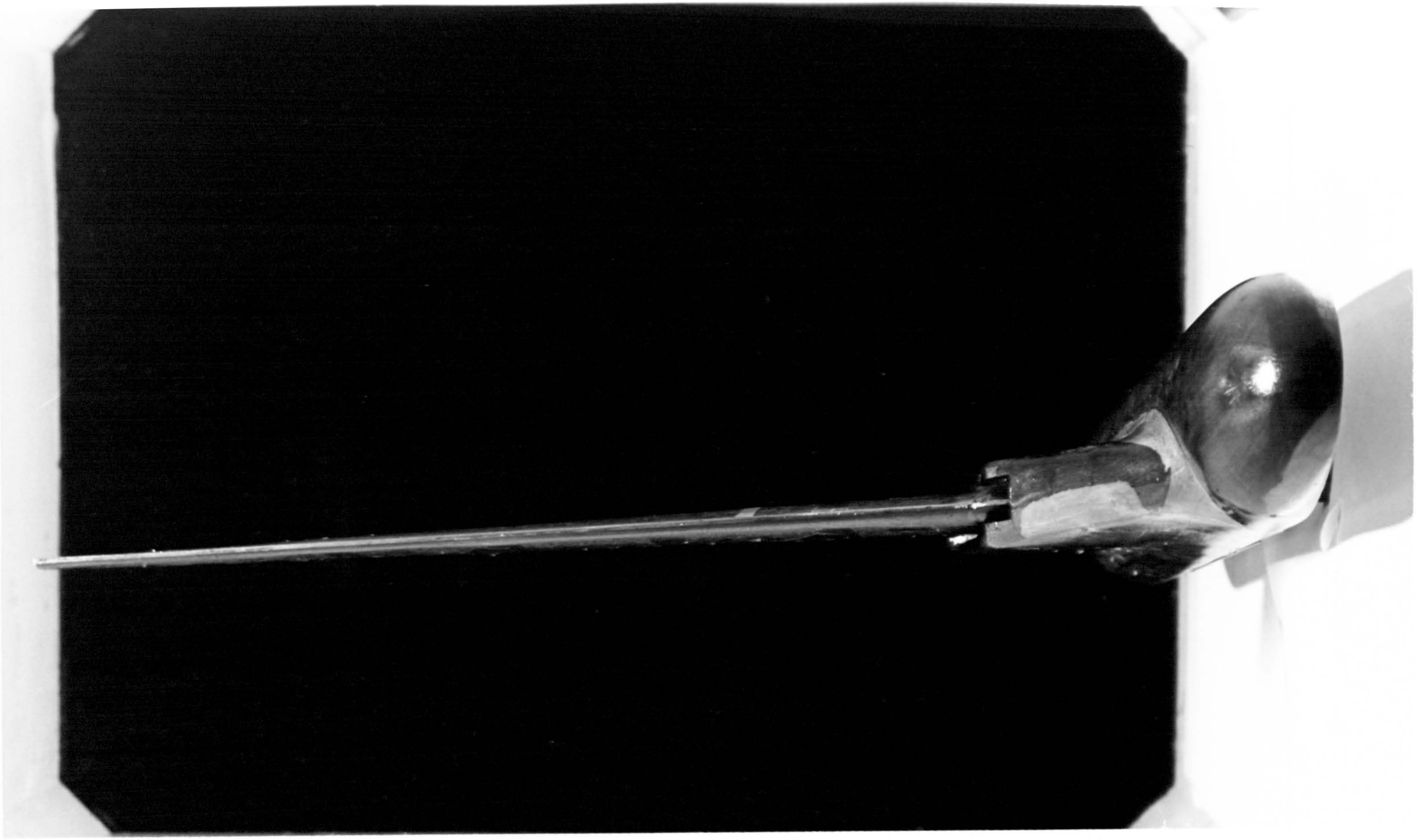

FIG [2 · 5] A FRONT VIEW OF THE WIND TUNNEL MODEL WITH A FORWARD SWEPT WING AND ITS TIP POSITION RELATIVE TO THE WALL

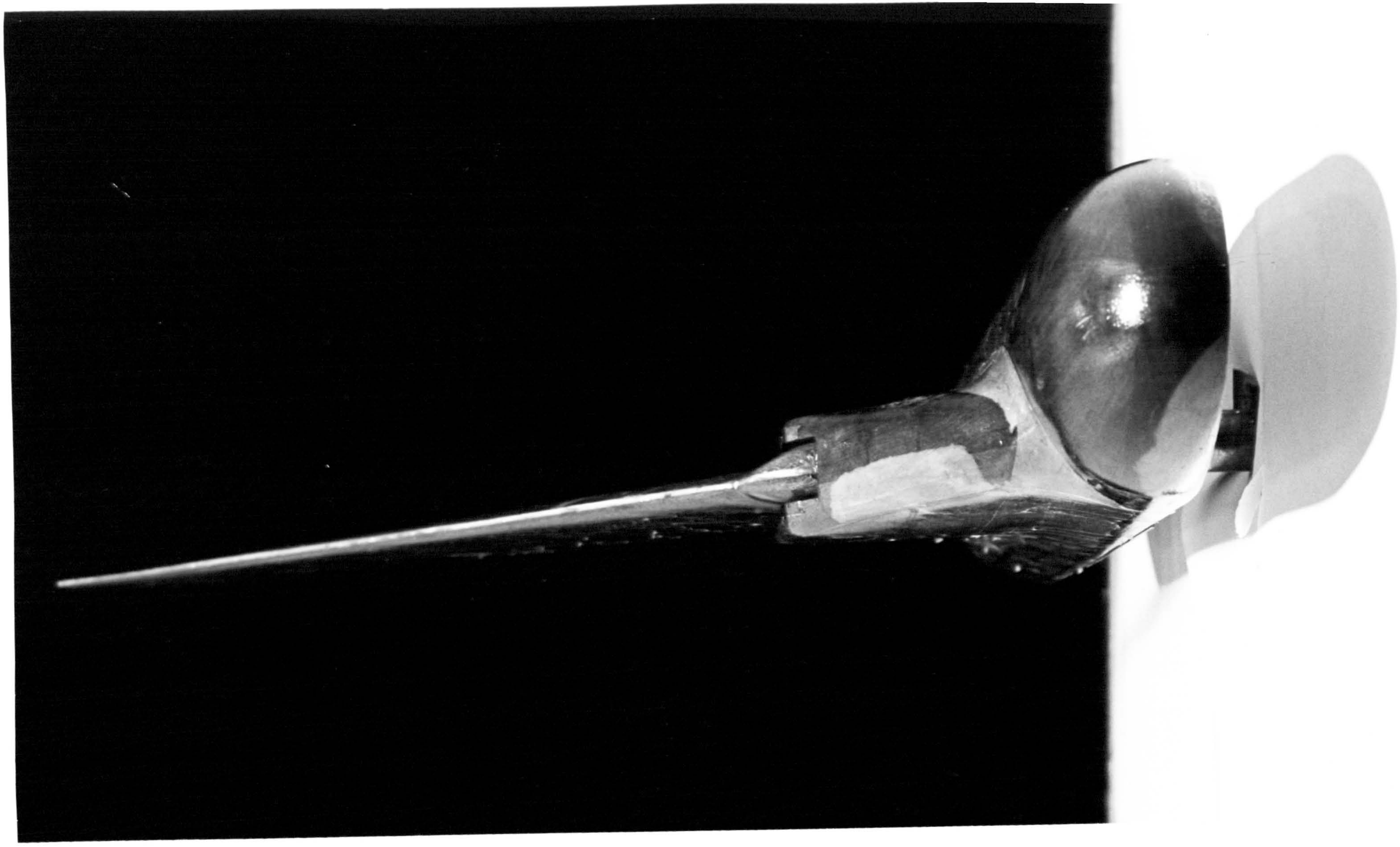

FIG [2·6] A FRONT VIEW OF THE WIND TUNNEL MODEL WITH A SWEPT BACK WING

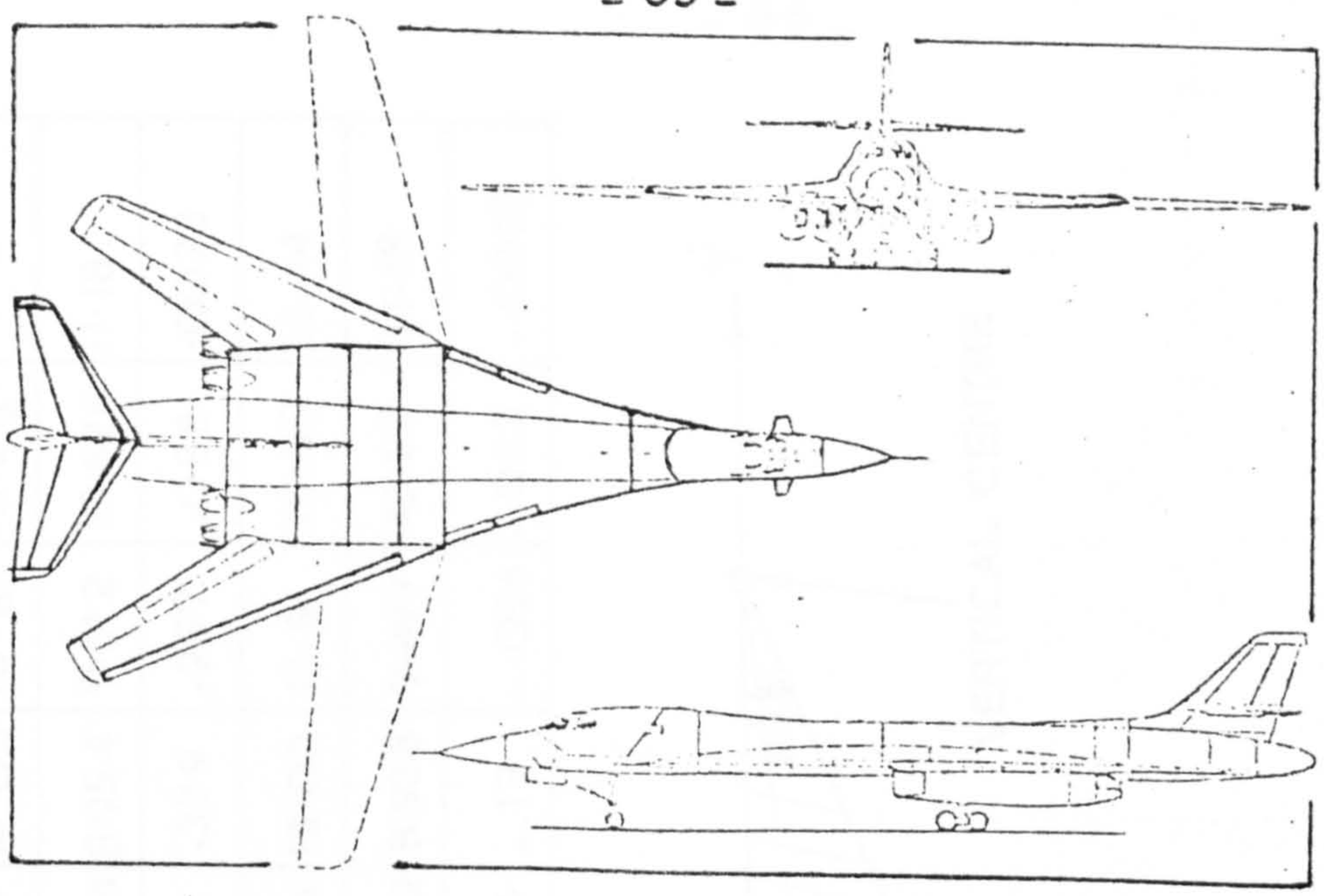

FIG.(2.7) THE B-1 BOMBER (VARIABLE SWEEP WING)

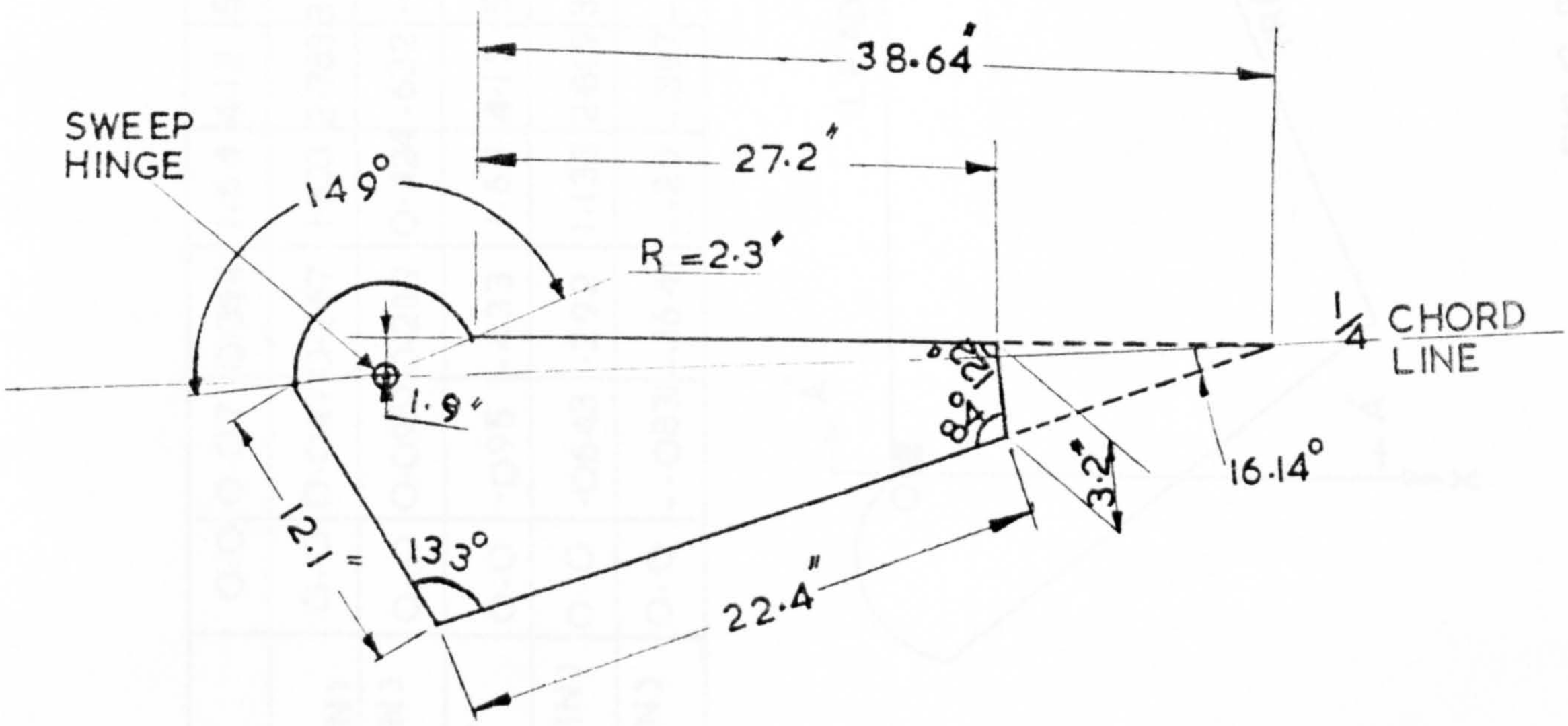

FIG.(2.8) PLANFORM OF THE WING MODEL (IN SCALE)

UPPER SURFACE	θ°	0.0	0.07	0.394	1.64	4.12	5.77	7.42	8.23	9.86	11.46	13.05	13.83	15.38	16.14
	X (IN)	0.0	0.047	0.267	1.103	2.783	3.907	5.03	5.59	6.713	7.834	8.954	9.512	10.626	11.18
	Y (IN)	0.0	0.0957	0.2119	0.424	.632	.692	.694	.672	.594	.481	.339	.257	.088	.0023
LOWER SURFACE	θ°	0.0	.095	.433	1.68	4.15	5.79	7.42	8.23	9.85	11.44	13.02	13.81	15.37	16.14
	X (IN)	0.0	.0643	.292	1.133	2.807	3.92	5.035	5.591	6.706	7.822	8.938	9.497	10.62	11.18
	Y (IN)	0.0	-.0831	-.1641	-.29	-.397	-.418	-.40	-.375	-.304	-.216	-.13	-.096	-.033	-.0023

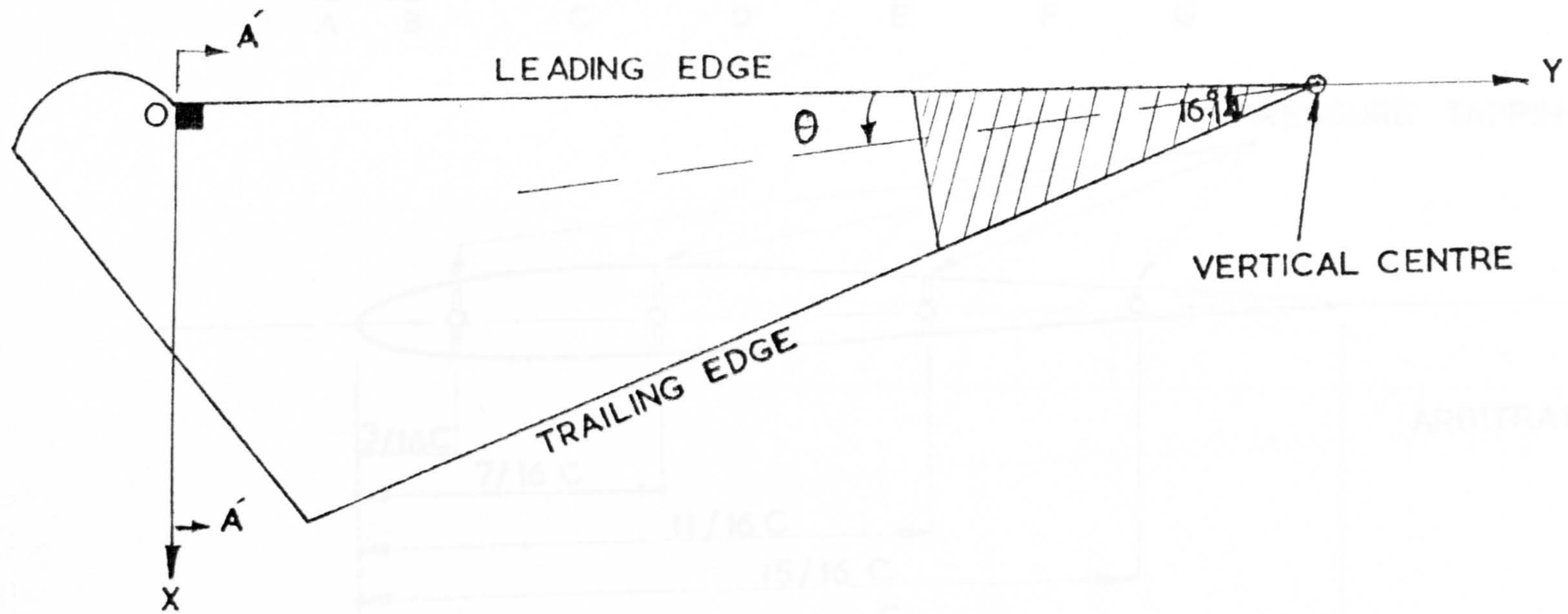

FIG (2.9) COORDINATES FOR SECTION A'-A' OF THE WING MODEL

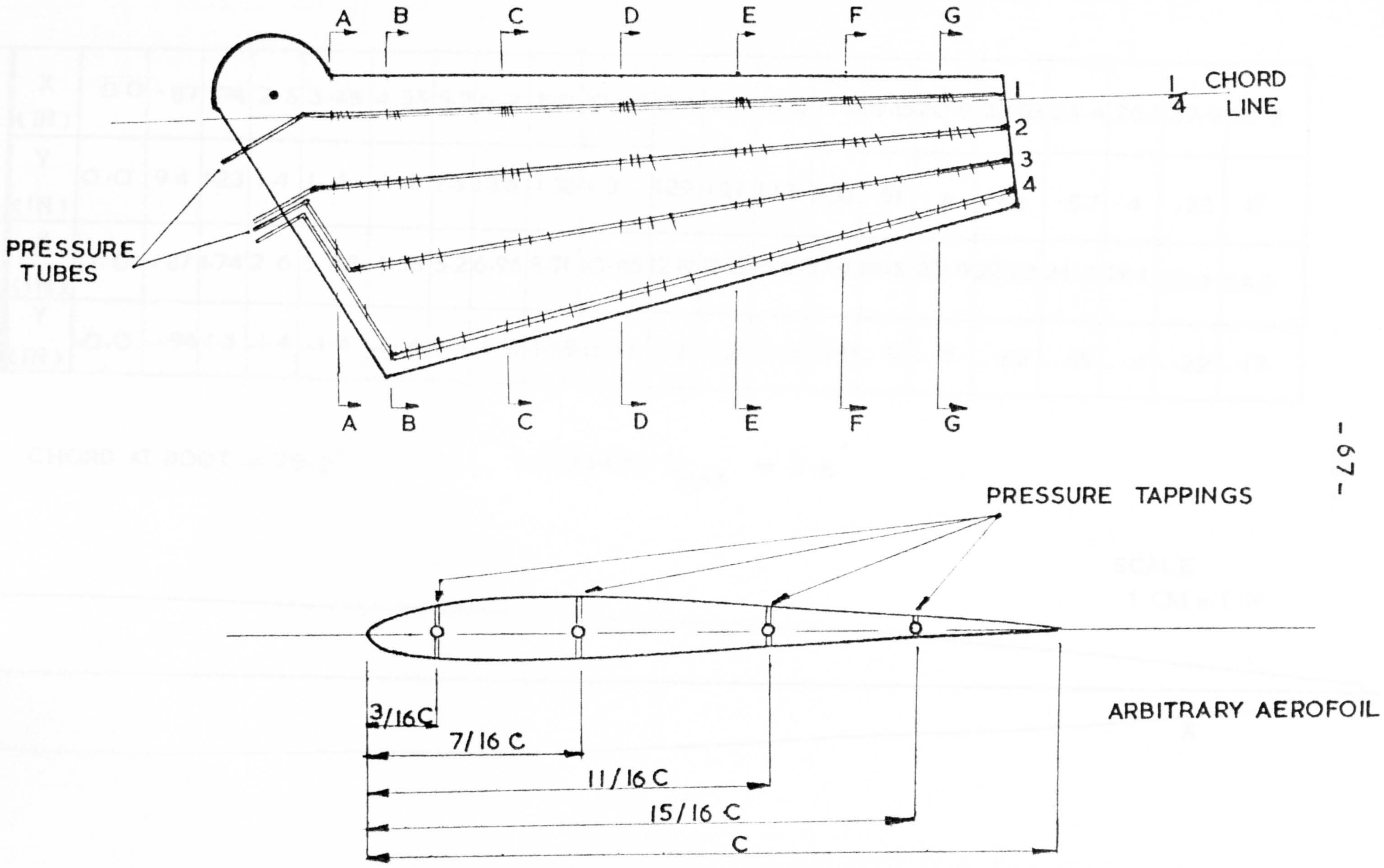

FIG (2·10) PRESSURE TUBE POSITIONS IN THE WING AND THEIR TAPPING LOCATIONS.

UPPER SURFACE	X (IN)	0.0	.87	1.74	2.6	3.48	4.35	5.2	6.2	8.71	10.45	12.19	13.93	15.67	17.4	19.15	20.9	22.63	24.4	26.1	27.9	28.2
	Y (IN)	0.0	.94	1.23	1.4	1.4	1.4	1.4	1.36	1.36	1.3	1.29	1.21	1.13	1.03	.91	.8	.68	.57	.4	.23	.17
LOWER SURFACE	X (IN)	0.0	.87	1.74	2.6	3.48	4.35	5.2	6.96	8.71	10.45	12.19	13.93	15.67	17.4	19.15	20.9	22.63	24.4	26.1	27.9	28.2
	Y (IN)	-0.0	-.94	-1.3	-1.4	-1.4	-1.4	-1.4	-1.4	-1.35	-1.31	-1.3	-1.21	-1.13	-1.03	-.91	-.8	-.68	-.55	-.4	-.22	-.17

CHORD AT ROOT = 28.2″ , THICKNESS t_{MAX} = 2.8″

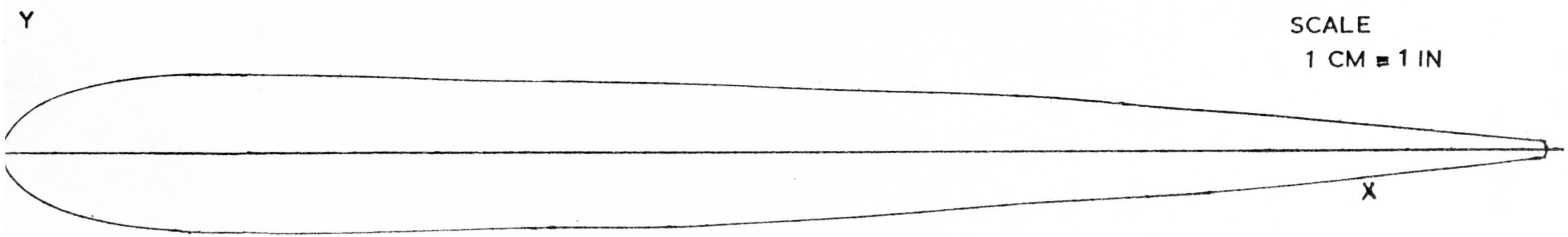

(a)

FIG (2.11) AEROFOIL SECTION AND COORDINATES FOR THE GLOVE ROOT.

UPPER	X (IN)	0	.5	1.0	1.5	2.0	2.5	3.0	4.0	5.0	6.0	7.0	8.0	9.0	10.0	11.0	12.0	13.0	14.0	15.0	16.0	16.2
SURFACE	Y (IN)	0	.8	1.05	1.2	1.2	1.2	1.2	1.19	1.19	1.17	1.13	1.06	.99	.9	.8	.7	.6	.5	.35	.2	.15
LOWER	X (IN)	0	.5	1.0	1.5	2.0	2.5	3.0	4.0	5.0	6.0	7.0	8.0	9.0	10.	11.	12	13	14	15	16	16.2
SURFACE	Y (IN)	0	-.94	-1.13	-1.2	-1.2	-1.2	-1.2	-1.2	-1.18	-1.15	-1.12	-1.1	-.98	-.9	-.8	-.7	-.6	-.48	-.33	-.19	-.15

CHORD LENGTH = 16.2" AT TIP , THICKNESS $t_{MAX.} = 2.8''$

SCALE

1 CM ≡ 1 IN

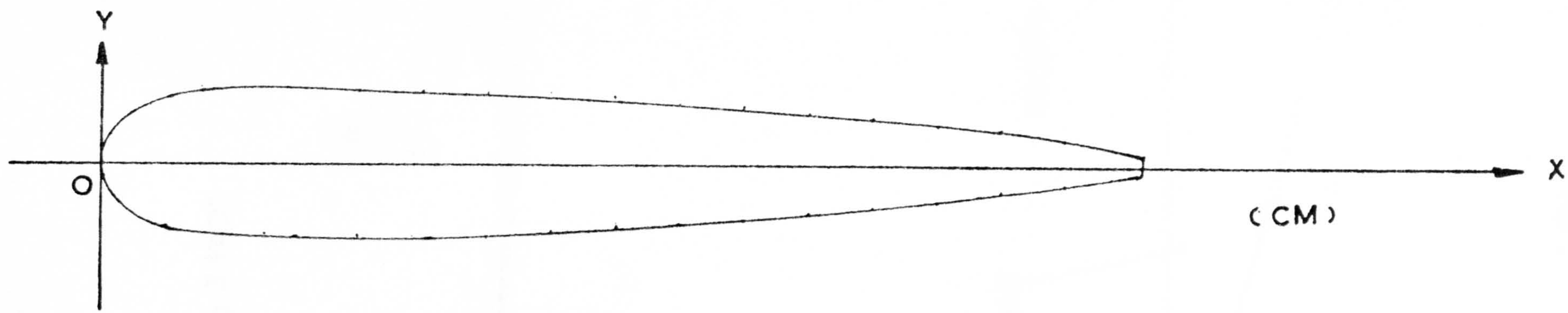

(b)

FIG (2.11) AEROFOIL SECTION AND COORDINATES FOR THE GLOVE TIP.

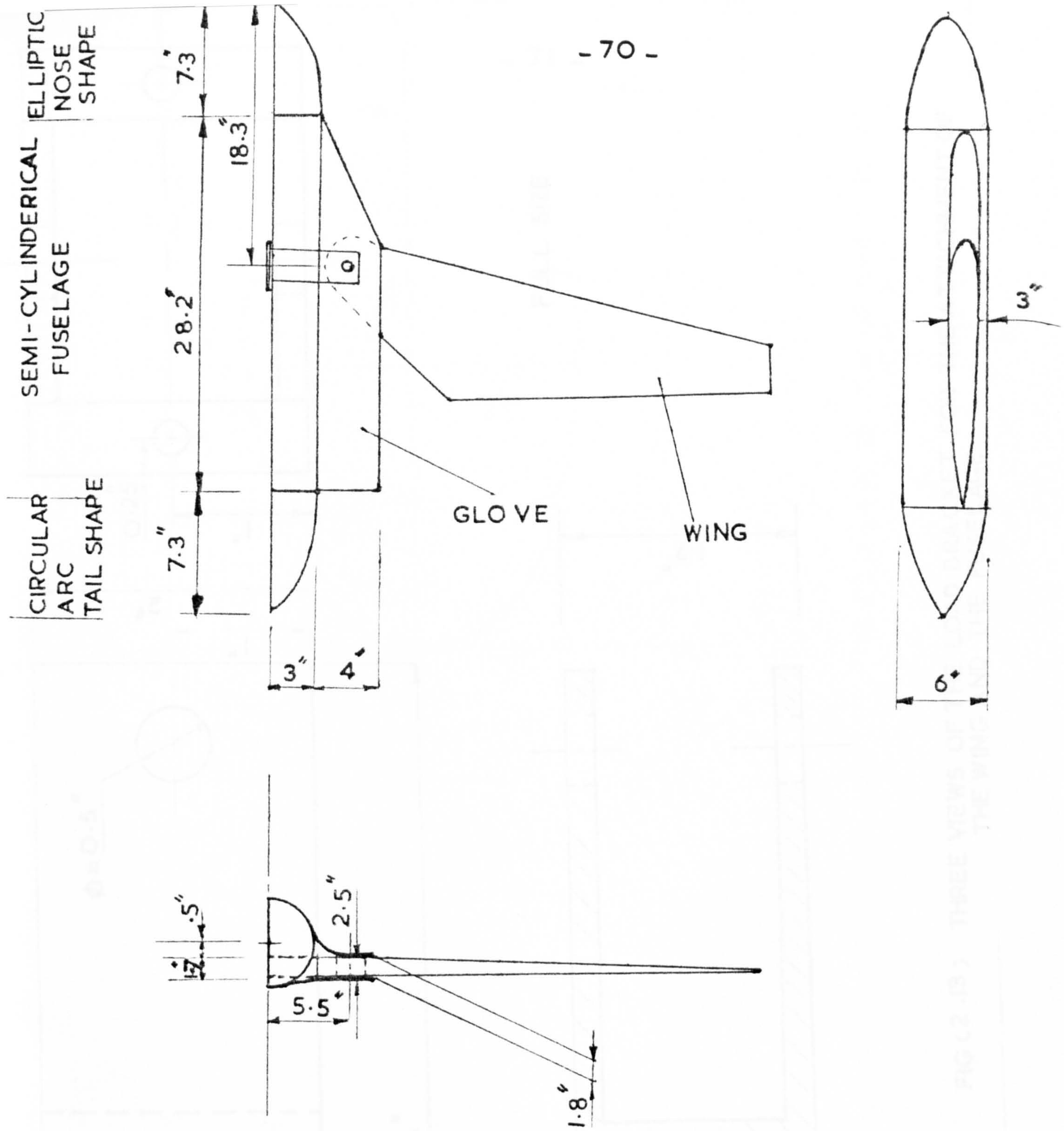

SCALE 1/10 OF THE TEST MODEL

FIG (2.12) THREE VIEWS OF THE AIRCRAFT MODEL.

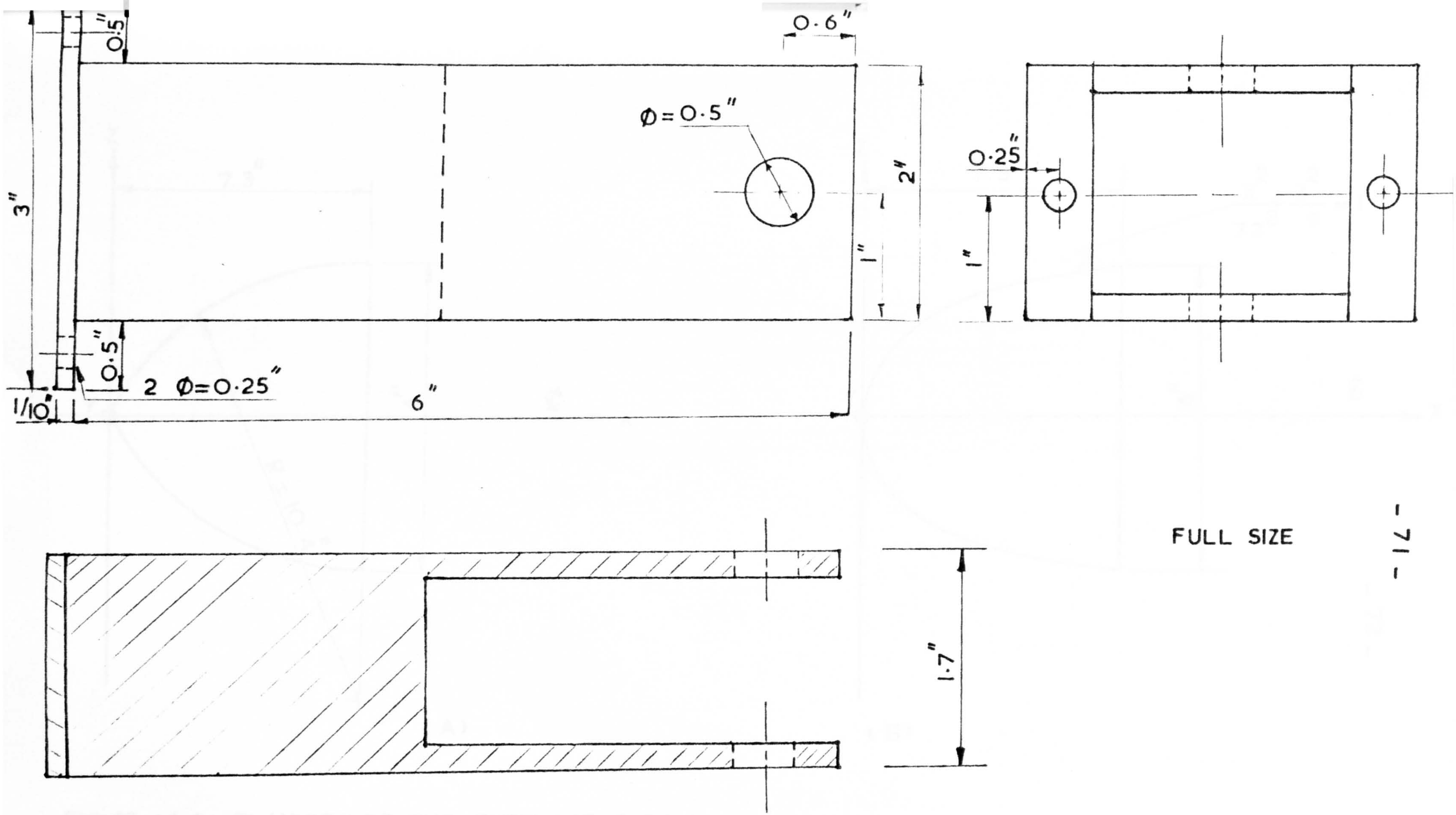

FIG (2.13) THREE VIEWS OF THE LOAD BRACKET FOR THE ATTACHMENT OF THE WING AND THE FUSELAGE.

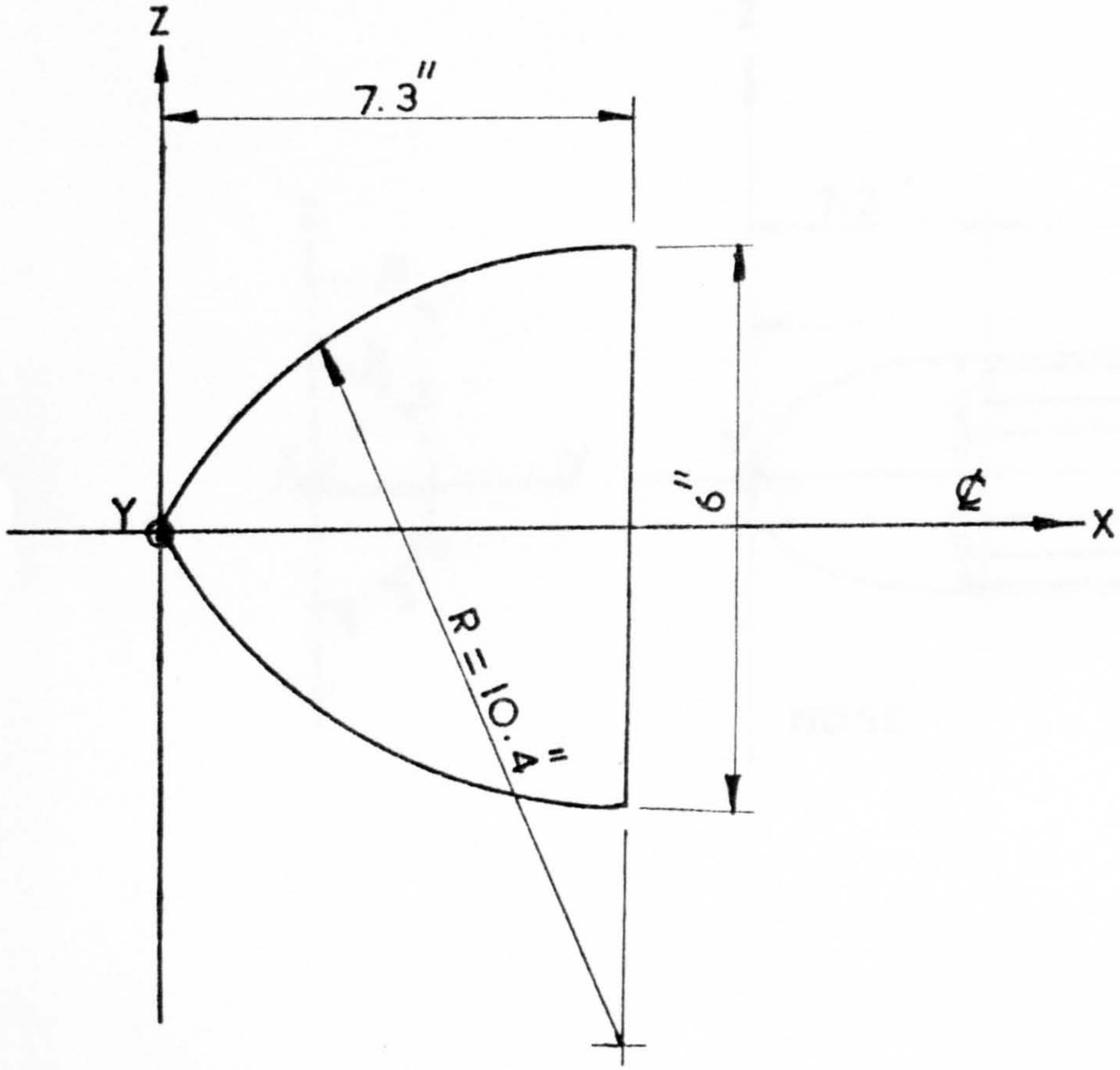

(A)

FIG (2.14) PLANVIEW OF THE FUSELAGE CIRCULAR ARC - TAIL

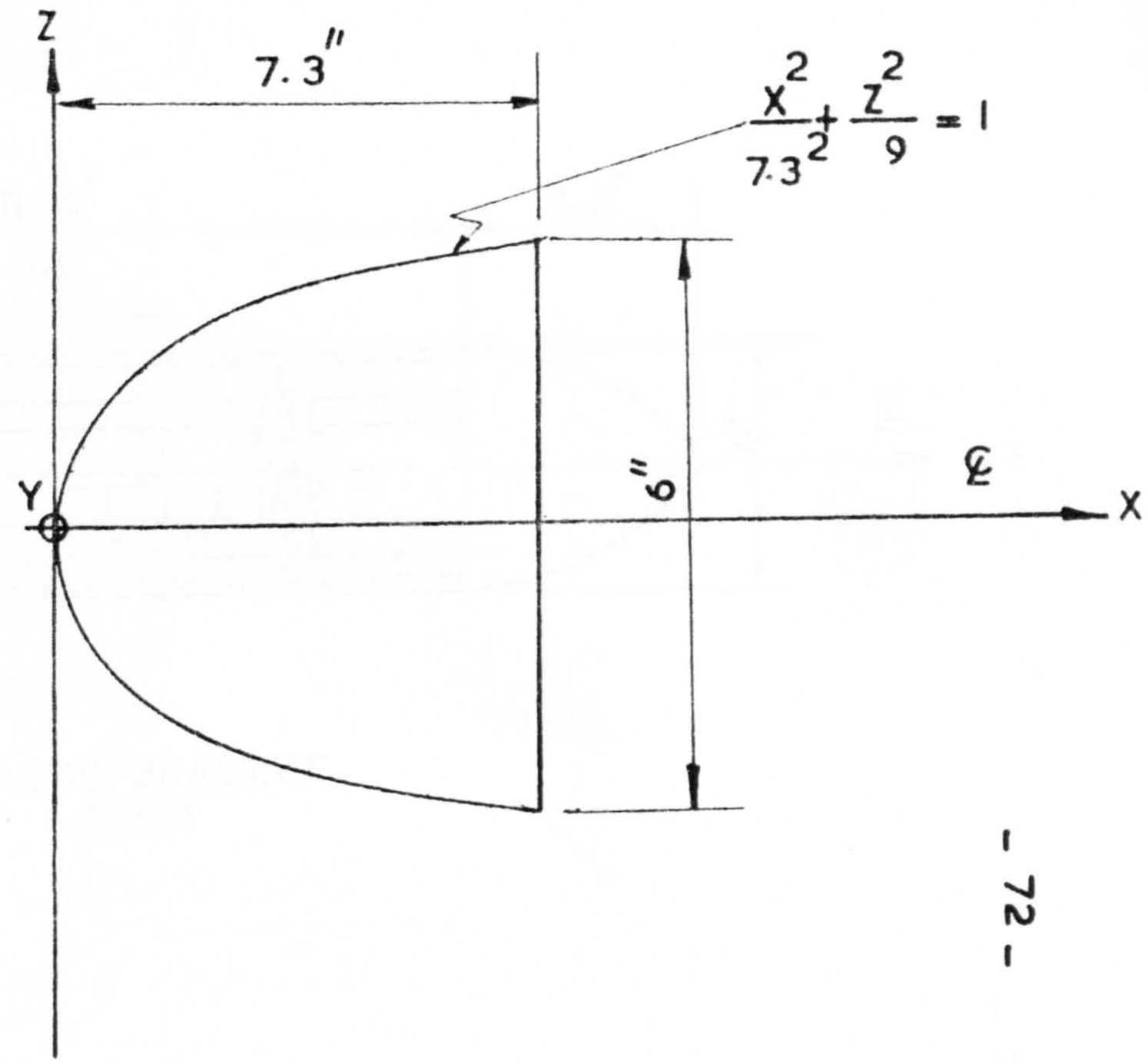

(B)

FIG (2.14) PLANVIEW OF THE FUSELAGE - ELLIPTICAL NOSE

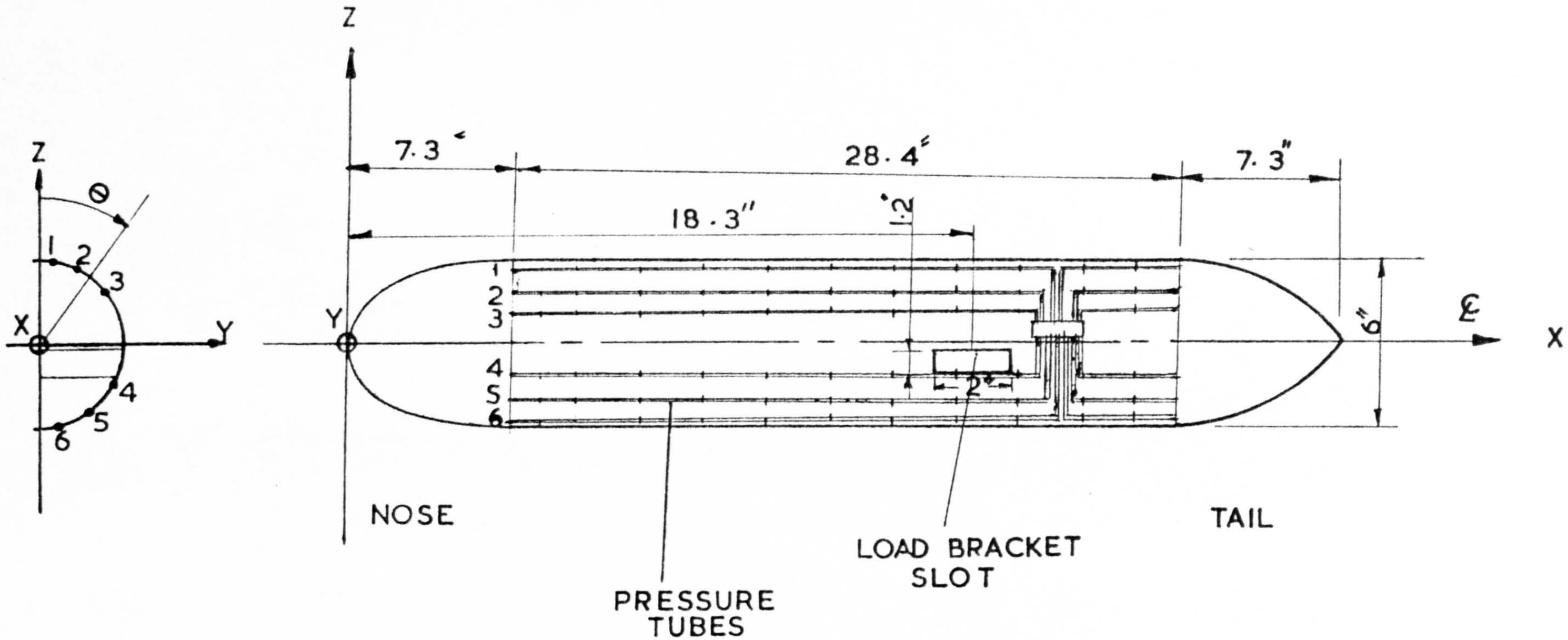

(C)

FIG (2.14) FUSELAGE MODEL VIEWS

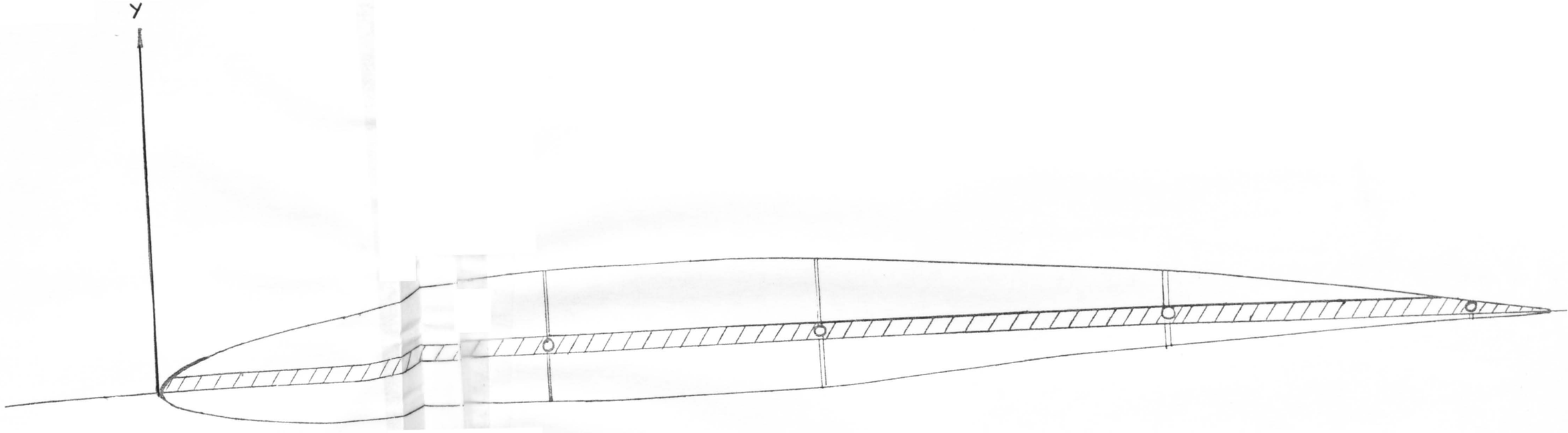

FULL SIZE
CHORD LENGTH = 13.4"

FIG [2.15] (a) WING ROOT AEROFOIL SECTION

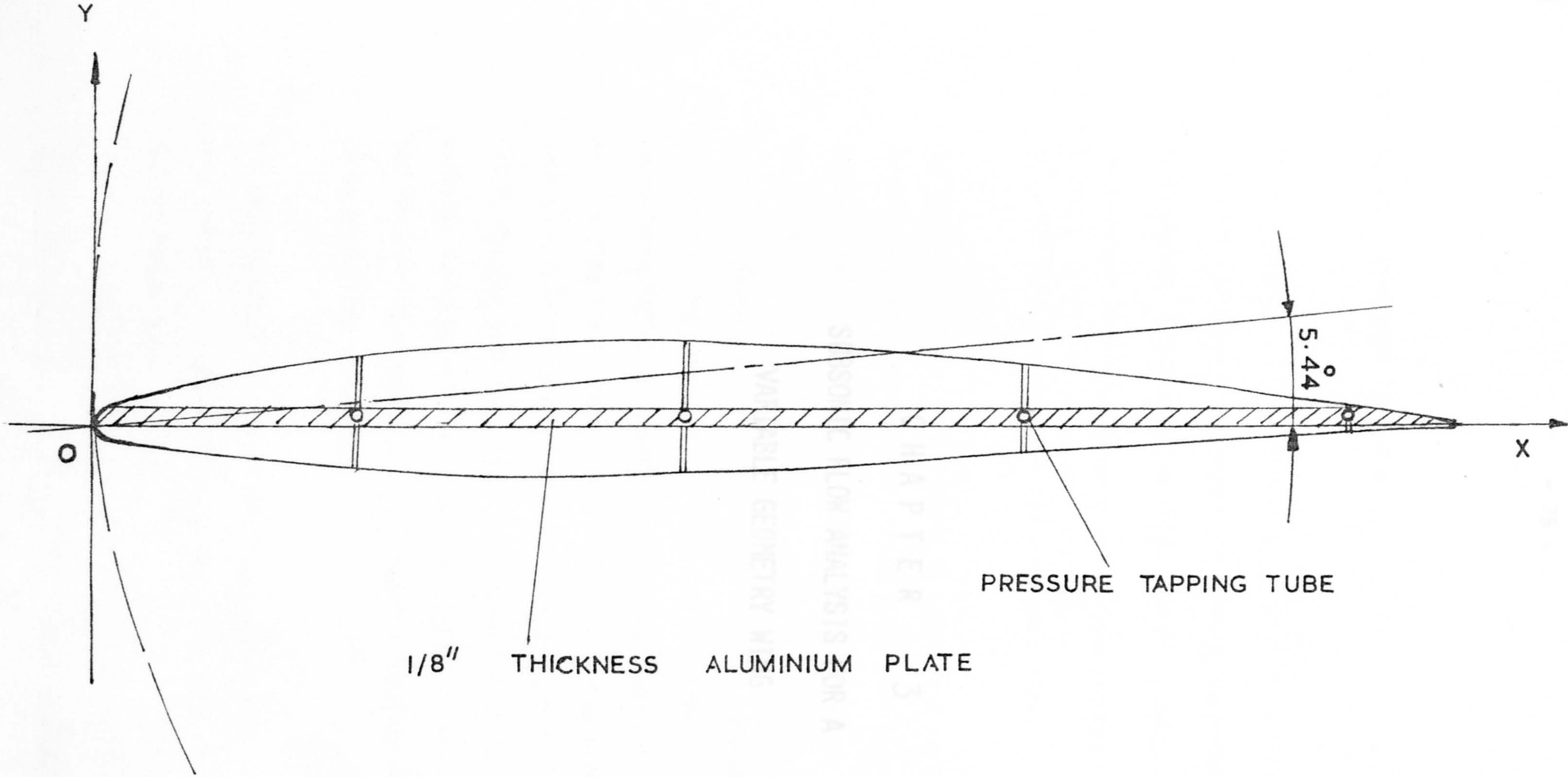

FIG [2.16] (b) AEROFOIL SHAPE

CHAPTER 3

SUBSONIC FLOW ANALYSIS FOR A VARIABLE GEOMETRY WING

3.1 SUBSONIC WING/BODY INTERFERENCE

The main object of this chapter is to describe a method used to calculate the steady three dimensional potential flow around lifting non-planar configurations. A program based on this method is used later to investigate the effects of different wing sweep angles on the aerodynamic characteristics of wing/body combinations for a subsonic flow.

The method for these calculations is based on a surface distribution of quadrilateral vortex rings (for convenience it shall be referred to here as QUADVORT). Each quadrilateral element has a control point at which the boundary condition of zero flow (vortex induced plus free stream) through the surface is specified. The vortex ring strengths are solved after evaluating all the vortex-ring influence coefficients for each control point in turn and applying the boundary condition. The vortex strengths are then used to obtain surface velocities, pressures, forces and moments. The method has been programmed in Fortran for an I.C.L.1904S Computer using University of Salford facilities which can handle 150 vortex-ring elements at this stage. The program is not yet up to production standard.

The results which are presented, include the cases of a thin wing only and of a wing/body plus the glove for both the compressible and the incompressible cases.

At preliminary stages of numerical work on this program, some problems involving the main program, compilations and other difficulties were encountered. In some cases these difficulties were in the actual numerical work associated with input of different configurations, number of elements etc.

3.2 THE BASIC PROBLEM AND MAIN ASSUMPTIONS

The basic problem is the calculation of the velocity distribution on and around lifting wing and wing/body configurations together with the force and moment vectors. The geometry of such configurations may be reasonably arbitrary in the sense that under real flow conditions, regions of separation should be small and lines of separation well defined (e.g. the wing trailing edge).

The main assumptions which were used for this purpose are as follows:

(1) The flow is subsonic and steady.

(2) Viscous regions are approximated by (or enclosed within) vortex sheets, external to which potential flow exists.

(3) The position and shape of free vortex sheets are specified at the outset.

3.3 QUADVORT DESCRIPTION

3.3.1 FEATURES OF THE QUADRILATERAL VORTEX-RING

The basis of the theoretical model is a system of quadrilateral vortex-rings (each of constant strength) covering the entire surface of a given geometry, e.g. wing, wing-fuselage, FIG (3.1a) - and extending to infinity downstream from the line of separation. Vortex-rings representing the wake close at infinity downstream since the conditions in the wake are constant (in steady flow). This system of vortex-rings is a discrete representation of the vortex sheet which, in classical theory, replaces the surface and wake.

Adjacent sides of quadrilateral elements are coincident, hence the effect of using closed vortex-rings is the same as that of a vortex lattice; the strength of each vortex element in the lattice is given by the difference in the strengths of adjacent vortex-rings. However, a closed vortex-ring is self sufficient, since it satisfies all the vortex laws, and provides a more suitable basis for numerical handling on a computer, particularly for complicated shapes.

The velocity potential due to vortex-ring (of any shape) is identical to that due to a uniform distribution of doublets over any surface bounded by the ring (Art. 150 Reference 3.2) the doublet axes being normal to the surface. Thus the vortex-ring

model is equivalent to a piecewise constant distribution of (normal) doublets over the surface and wake. The vortex model, however, provides a more intuitive physical picture of the flow.

3.4 METHOD OUTLINE

There are four distinct steps in the method:-

(I) Geometry: reduction of the input surface coordinates into quadrilateral vortex-ring element parameters.

(II) Influence Coefficients: a control point is taken in each element in turn and the induced velocity influence coefficients at that point are evaluated for all the vortex-ring elements.

(III) Vortex-Ring Strength : the vortex-ring strengths are calculated such that the zero normal velocity condition (vortex induced + free stream) is satisfied at all the control points. Trailing vortices, which for the first solution are assumed streamwise, are then divided into a number of straight line segments which are relaxed into the local flow directions. The change in the vortex wake influence at the control points is then evaluated and a second solution obtained for the vortex-ring strengths. The process is repeated by iteration. The number of iterations is an input

parameter and generally two iterations are sufficient for practical purposes.

(IV) After vortex-ring strengths are evaluated the lift, vortex drag and moments are calculated. Velocity-field calculations are performed at the end of the programme if required.

3.5 GEOMETRY

3.5.1 SURFACE PANELS

The input of surface coordinates for 3-D problems can be extremely lengthy and can give rise to mistakes which can be expensive in terms of delays and computer re-runs. An attempt has been made here to simplify the input by dividing the surface up into a number of panels and to generate as many of the surface points as possible within the Computer. At this stage linear interpolation between input points has been used; more sophisticated schemes may be introduced later.

Two basic panels are provided for:

(i) Double curvature panels require all vortex quadrilateral corner points to be input.

(ii) Single curvature panels are defined only at the "root"

and "tip": intermediate vortex quadrilateral corner points are derived within the program by linear interpolation.

Surfaces can be built up from a number of such panels FIG (3.1b). The distribution of quadrilateral elements in these panels must follow certain rules and these are discussed later.

3.5.2 WAKE GEOMETRY

Trailing vortex lines are approximated by a number of straight line segments, the last segment being semi-infinite. They are defined at the "root" and "tip" of each wing panel and intermediate lines are obtained by linear interpolation.

3.5.3 ELEMENT PARAMETERS

Each quadrilateral vortex-ring element is specified by a number of parameters:

(I) The x, y, z coordinates of the four corner points.

(II) The control point, at which the boundary condition is specified.

(III) The element area, S.

(IV) The components of the unit vector n, normal to the surface at the control point.

The element area and unit normal vector are obtained, i.e. referring to Sketch (3.1)

$$\text{Area of parallelogram} = \frac{1}{2}.S$$

$$= \frac{1}{2}\left|\underline{R}_1\right| \times \frac{1}{2}\left|\underline{R}_2\right| \times \sin\theta$$

$$\therefore\ S = \frac{1}{2}.\left|\underline{R}_1\right|.\left|\underline{R}_2\right|.\sin\theta$$

vector or cross product $\underline{R}_1 \times \underline{R}_2 = \left|\underline{R}_1\right|.\left|\underline{R}_2\right|\sin\theta.\underline{n}$ where $\underline{n}$ is unit vector normal both vectors $\underline{R}_1$ and $\underline{R}_2$.

Hence $\frac{1}{2}\,\underline{R}_1 \times \underline{R}_2 = S.\underline{n}$

Therefore $S^2 = S\underline{n}.\ S\underline{n} = \frac{1}{4}\,\underline{R}_1 \times \underline{R}_2.\ \underline{R}_1 \times \underline{R}_2$

$$S = \frac{\sqrt{(\underline{R}_1 \times \underline{R}_2).(\underline{R}_1 \times \underline{R}_2)}}{2}$$

Hence $$\underline{n} = \frac{\underline{R}_1 \times \underline{R}_2}{2.S}$$

The control point is taken as the mean of the four corner points at this stage - this is discussed later.

3.6 INFLUENCE COEFFICIENTS

3.6.1 INDUCED VELOCITY

The induced velocity due to a line vortex segment in vector notation is, referring to Sketch (3.2):

$$\underline{q} = \frac{1}{4\pi}\int_{\underline{a}}^{\underline{b}} \frac{\underline{r} \times (\Gamma.\underline{ds})}{|\underline{r}|^3} \qquad \ldots\ldots (3.1)$$

Reference (3.3)

where Γ is the density of vorticity per unit length of filament, and:

$$\underline{r} = \underline{a} + \alpha\underline{s}$$

$$\underline{ds} = \underline{s}d\alpha$$

Thus $\underline{q}$ reduces to:

$$\underline{q} = \frac{\Gamma}{4\pi} \quad \frac{\underline{a} \times \underline{b}}{\underline{a} \times \underline{b}.\underline{a} \times \underline{b}} \left\{ |\underline{a}|+|\underline{b}| \right\} \left\{ 1 - \frac{\underline{a}.\underline{b}}{|\underline{a}|.|\underline{b}|} \right\} \quad \ldots\ldots\ldots \quad (3.2)$$

where $|\underline{a}| = \sqrt{\underline{a}.\underline{a}}$, the modulus of vector $\underline{a}$, etc.

For a quadrilateral vortex-ring equation (3.2) is used four times. Since most vortex line elements belong to two neighbouring quadrilaterals (with opposite vorticity signs), the induced velocity coefficient for each line segment need only be evaluated once and the contribution added to or subtracted from the neighbouring quadrilateral coefficients.

A feature which has not been included in the program at this stage, but which should eventually provide a useful reduction in run times, is the possibility of considering vortex-ring elements which are well removed from a control point as elemental doublets.

3.6.2 SEMI-INFINITE VORTICES

Vector $\underline{b}$ in equation (3.2) can be written

$$\underline{b} = b.\underline{t}$$

where $\underline{t}$ being a unit vector.

Equation (3.2) then becomes:

$$\underline{q} = \frac{\Gamma}{4\pi} \frac{\underline{a} \times \underline{t}}{\underline{a} \times \underline{t}.\underline{a} \times \underline{t}} \frac{1}{b} \left\{ |\underline{a}| + b \right\} \left\{ 1 - \frac{\underline{a}.\underline{t}}{|\underline{a}|} \right\}$$

Thus the semi-infinite line vortices:

$$\underline{q} = \lim_{b \to \infty} \left[\frac{\Gamma}{4\pi} \frac{\underline{a} \times \underline{t}}{\underline{a} \times \underline{t}.\underline{a} \times \underline{t}} \left\{ \frac{|\underline{a}|}{b} + 1 \right\} \left\{ 1 - \frac{\underline{a}.\underline{t}}{|\underline{a}|} \right\} \right]$$

i.e. $$\underline{q} = \frac{\Gamma}{4\pi} \frac{\underline{a} \times \underline{t}}{\underline{a} \times \underline{t}.\underline{a} \times \underline{t}} \left\{ 1 - \frac{\underline{a}.\underline{t}}{|\underline{a}|} \right\} \qquad \text{..... (3.3)}$$

and in the limit as b tends to ∞, $\underline{t}$ is the unit vector in the direction of the vortex.

The vortex-ring adjacent to the trailing edge or any line from which a free sheet springs, is thus treated in a special way: the induced velocity for such elements is the sum of the influence of a number of straight line segments (equation (3.2)) and two semi-infinite lines (equation (3.3)) as shown in Sketch (3.3).

Thus the velocity induced at a control point by a given vortex-ring - whether closed on the surface or extending to infinity can be written:-

$$\underline{q} = \Gamma \underline{Q}$$

where $\underline{Q}$ is the <u>induced velocity coefficient</u> for the influence of the vortex-ring acting at that control point.

3.6.3 CASES OF SYMMETRY AND GROUND EFFECT

In many problems, e.g. wings and wing-fuselages at zero side-slip , considerable advantage can be taken in terms of number of elements by the fact that surface elements are reflected across the plane (or planes) of symmetry. Thus only one half of the problem need be represented by surface elements (for one plane of symmetry). The influence coefficients of image elements are evaluated by considering the velocity induced at the control point <u>image</u> by the <u>real</u> element and reversing the sign of the velocity component normal to the plane. The influence coefficients of corresponding real and image elements are added together since the vortex strengths are equal. The same procedure can be applied to the reflection across the ground plane in ground-effect problems.

3.7 SOLVING FOR VORTEX-RING STRENGTHS

3.7.1 THE BOUNDARY CONDITION

If there are N vortex-ring elements, each element control point is taken in turn and the induced velocity coefficients evaluated for all N vortex-rings.

The total velocity at the j control point is therefore:

$$\underline{V}_j = \underline{U}_\infty + \sum_{k=1}^{N} \{\Gamma_k \, \underline{Q}_{jk}\} \qquad \text{..... (3.4)}$$

where $\underline{U}_\infty$ is the onset velocity

$\underline{Q}_{jk}$ is the induced velocity coefficient for the influence of the kth vortex-ring acting at the jth control point.
(These vectors are stored on magnetic tape for later use in the program).

Γ_k is the "strength" of the kth vortex-ring

The boundary condition of zero flow through the surface is now specified

$$\underline{V}_j \cdot \underline{n}_j = 0$$

where $\underline{n}_j$ being the unit normal vector to the surface at the jth control point.

Thus from equation (3.4)

$$\sum_{k=1}^{N} \{\Gamma_k \, \underline{Q}_{jk} \cdot \underline{n}_j\} + \underline{U}_\infty \cdot \underline{n}_j = 0$$

There are N such equations, one for each control point, i.e.:

$$\sum_{k=1}^{N} \{\Gamma_k . A_{jk}\} + B_j = 0 \qquad j = 1, 2, ----, N \quad ..... (3.5)$$

A_{jk}, j, k = 1, 2, --- N are now (scalar) influence coefficients for the normal components of induced velocity.

B_j, j = 1, 2, ----, N are the normal components of free stream velocity at the control points.

3.7.2 METHOD OF SOLUTION

Equation (3.5) could be solved by standard matrix inversion schemes. For N greater than about 100 however, storage space in the computer becomes a major problem and matrix partitioning would have to be used. An alternative procedure would be to adopt a successive approximation scheme, but this has often shown a slow convergence for aerofoil section problems using a 2-D version of the A.M.O. Smith method (3.4).

For QUADVORT a <u>direct</u> method has been developed which appears to offer advantages in terms of computer storage requirement and in speed of solution (particularly for this type of problem where matrix A_{jk} is conveniently formed row by row). The procedure is based on the successive orthogonalisation (or vector) method for solving simultaneous equations by Purcell (3.5)

Briefly, take the jth equation:

$$\Gamma_1 A_{j1} + \Gamma_2 A_{j2} + \Gamma_3 A_{j3} + --- + \Gamma_N A_{jN} + B_j = 0$$

This can be considered as the dot product of two vectors:

i.e. $\underline{C}_j . \underline{D} = 0$

where $\underline{C}_j = (A_{j1}, A_{j2}, ---, A_{jN}, B_j)$

$\underline{D} = (\Gamma_1, \Gamma_2, \Gamma_3, ---. \Gamma_N, 1)$

The dot product of vectors is zero if the vectors are orthogonal. Thus, in the procedure, sets of linearly independent vectors are constructed which are successively orthogonal to each row $\underline{C}_j$. When all rows have been considered there is one vector, $\underline{D}$, which is orthogonal to all $\underline{C}_j$, j = 1,2,---,N and which thus contains the solution for Γ.

The computer storage requirement is low because only one row of the matrix A is required at a time (and once operated on can be over written) and an area of size $(\frac{N}{2})^2$ is sufficient to hold the relevant data for the intermediate sets of vectors. The procedure has been developed to hold this area on disc so that in principle a very large number of equations can now be solved directly.

The presence of the trailing vortex sheet makes the problem non-linear since two basic unknowns - the geometrical shape of the

trailing sheet (which is a streamline surface) and the overall distribution of vorticity - are independent.

Linearised solutions of the wing-problem have assumed the trailing sheet to lie in the plane of the wing, this is reasonable for problems having small angle of incidence. For more general solutions, however, the trailing vortex sheet can be greatly distorted and displaced from the wing plane.

An iterative scheme has been developed whereby the free trailing vortex sheet is progressively relaxed into local streamline directions: an initial guess for the vortex sheet location enables a vortex-ring strength solution to be obtained, this solution is then used to calculate streamline directions in the vicinity of the wake; the vorticity vectors can then be relocated and a second vortex-ring strength solution obtained and so on.

At each stage of the iteration only the new set of free vortex sheet influence coefficients need be calculated - the solid surface coefficients remain constant. (A wake relaxation scheme has been demonstrated for lifting line models by Butter (3.6), and also Joppa (3.7), and should be feasible for the lifting surface method).

The above discussion mainly applies to the wing wake. Treatment of the fuselage wake is less clear, although it should be included in a wake iteration procedure. The fuselage can be represented either by an infinite vortex tube or by an annular wing. In our

case the latter method is used, and here the vortex-ring distribution starts at the front of the fuselage and ends in semi-infinite line vortices, FIG (3.2); the set of trailing vortex lines is considered as a crude representation of the fuselage wake.

3.8 VELOCITIES AND FORCES

Substitution of Γ_k, k = 1,2,---,N in equation (3.4), (after recalling the induced velocity coefficients Q_{jk} from the magnetic tape store) gives the tangential velocity at each control point due to the free stream and vortex-ring elements. To this must be added the contribution $\Delta\underline{v}$ from the local velocity sheet which the concentrated vortices were assumed to replace initially. This further contribution arises from the difference in tangential velocity across the vortex sheet-only the mean, value, $\underline{v}_m$ has been computed at this stage, see Sketch (3.4)

ie

$$\underline{V}_U = \underline{V}_m + \Delta\underline{V}$$

$$\underline{V}_L = \underline{V}_m - \Delta\underline{V}$$

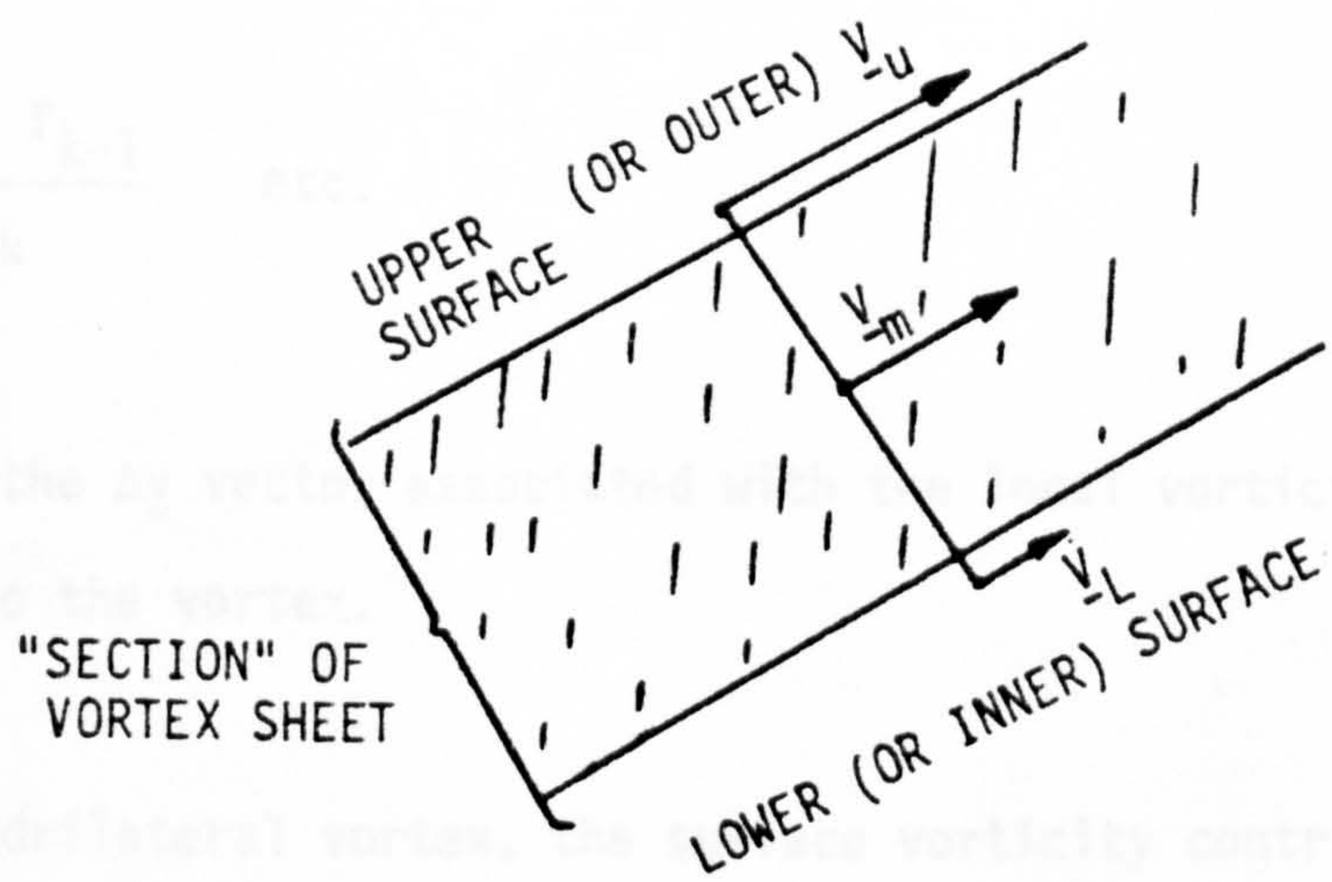

SKETCH (3.4)

The magnitude of vorticity at the control point is

$$\gamma = \left|\underline{v}_u - \underline{v}_L\right| = 2\left|\Delta\underline{v}\right|$$

i.e. $\left|\Delta\underline{v}\right| = \gamma/2$

γ is derived from the vortex-ring strengths by assuming each vortex to be spread evenly across its 'element width', Sketch (3.5).

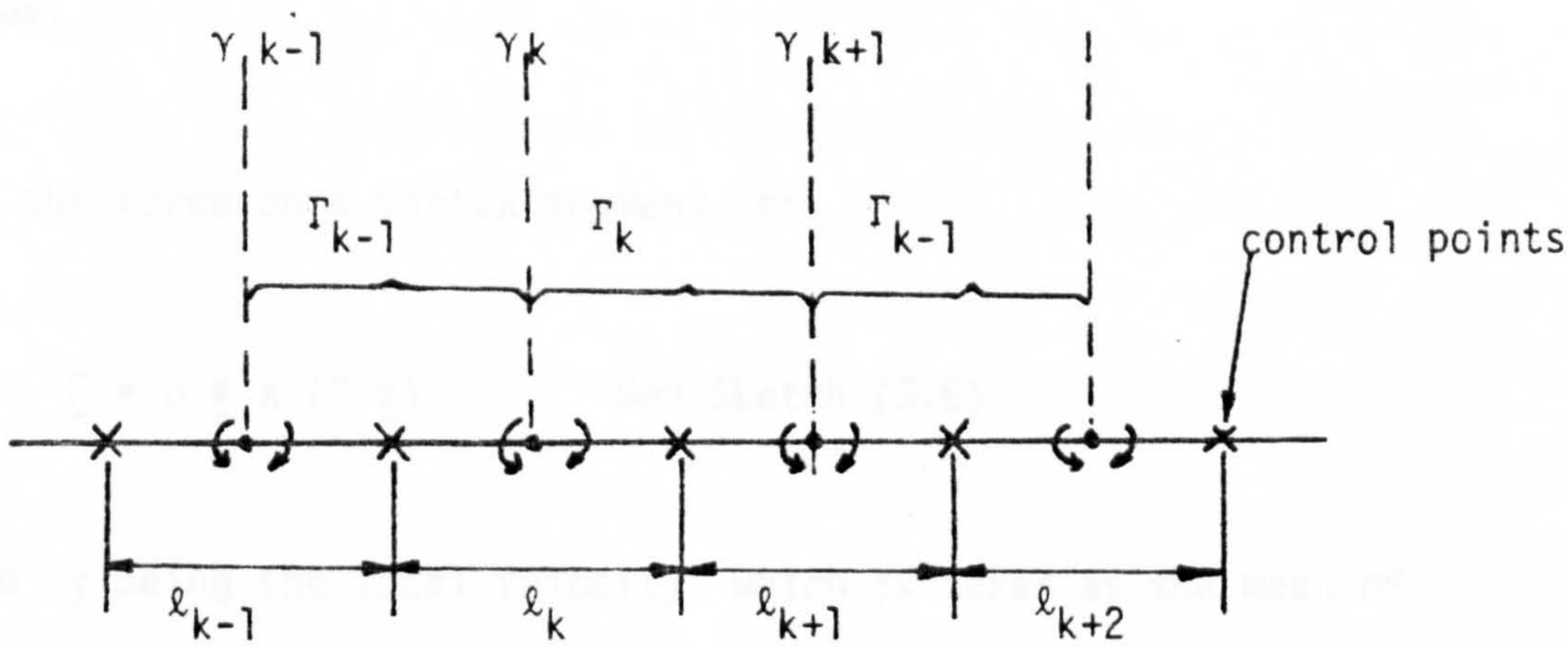

SKETCH (3.5)

i.e. $\gamma_k = \dfrac{\Gamma_k - \Gamma_{k-1}}{\ell_k}$ etc.

The direction of the $\Delta\underline{v}$ vector associated with the local vorticity is taken normal to the vortex.

Thus for each quadrilateral vortex, the surface vorticity contribution can be calculated at the mid-point of each side. A linear

interpolation between the sides provides the contribution at the control point, where the final velocity vectors (upper and lower or inner and outer) are thus obtained. Alternatively the local vorticity contribution could be obtained directly at the control point by considering the vortices as replacing segments of linear vorticity, rather than uniform, and solving for the corner γ values directly. (SKETCH 3.8).

The forces and moments can be obtained directly from a summation of the forces and moments of each surface vortex segment in the system:

Here the force on a vortex segment is:

$$\underline{F} = \rho\, \underline{v} \times (\Gamma\, \underline{s}) \qquad \text{See Sketch (3.6)}$$

where $\underline{v}$ being the local velocity, which is taken as the mean of the control point values on either side of the segment.

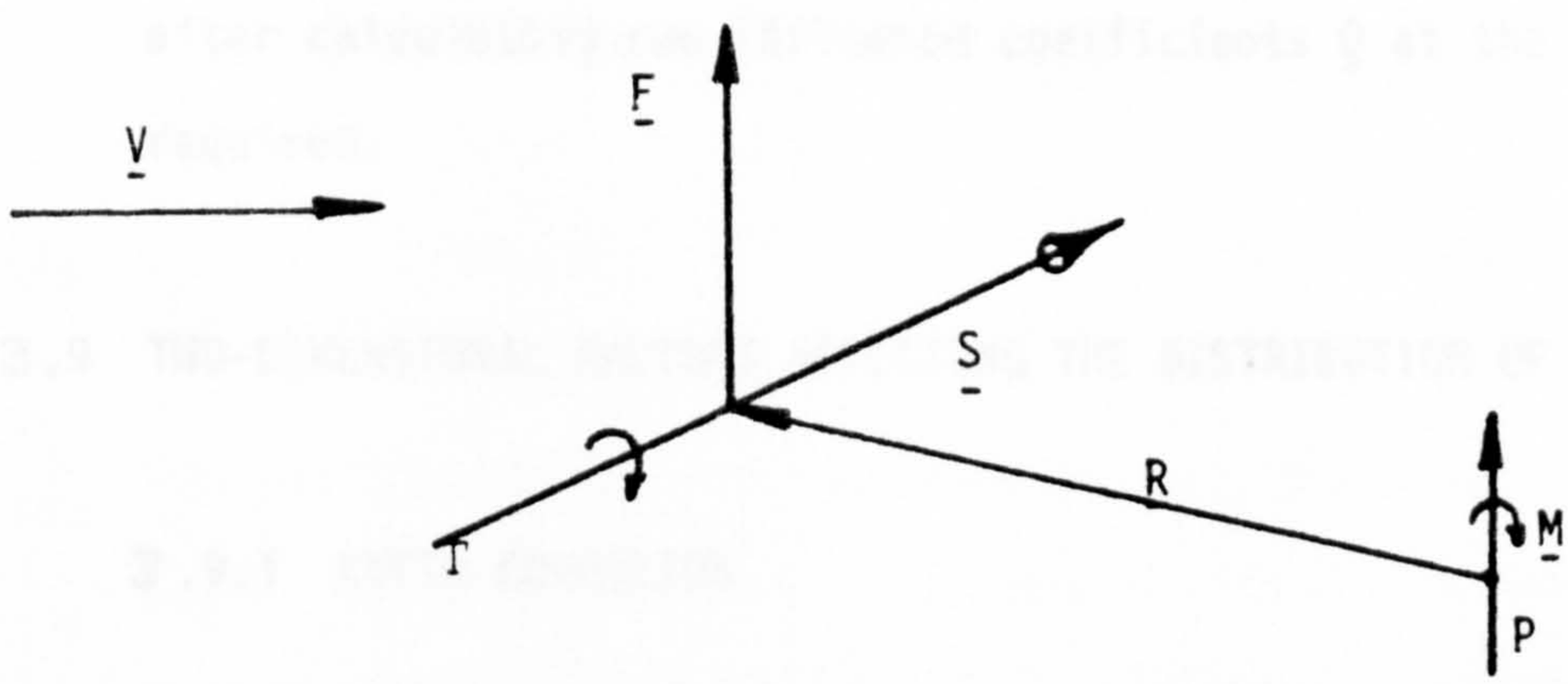

SKETCH (3.6)

The moment of this force about a point $\underline{P}$ is

$$\underline{M} = \underline{R} \times \underline{F}$$

$\underline{R}$ being the position vector of the centre of the vortex, say, with respect to $\underline{P}$.

Summing all such contributions gives the overall forces and moment vectors. If the summation is done in strips say across the wing chord, then the spanwise load distribution and centre of pressure locations can be derived. In fact the total circulation at a section on thin wings is the trailing edge vortex-ring element, strength (for thick wings it is the resultant of trailing edge element strengths).

3.8.1 VELOCITIES AT POINTS OFF THE SURFACE

The Γ solution can be used to obtain velocities at any point in the field of flow away from the vortex sheets. Equation (3.4) is used after calculating new influence coefficients $\underline{Q}$ at the points required.

3.9 TWO-DIMENSIONAL FACTORS AFFECTING THE DISTRIBUTION OF SURFACE ELEMENTS

3.9.1 KUTTA CONDITION

In Falkner's (3.8) vortex lattice method the Kutta condition was

satisfied by a suitable choice of chordwise loading functions. Later vortex lattice methods due to Hedman (3.9), Belotserkovskii (3.10) and Rubbert (3.11) solve the vortex lattice strengths directly without the aid of loading functions; the Kutta condition is now satisfied (on a 2-D basis at least) by a suitable placing of the bound vortex elements and the points at which the boundary condition is specified. It has been shown Refs. (3.9), (3.10) for 2-D conditions that if the chord is divided into a number of equal elements then this aerofoil theory lift and pitching moment values are obtained when the bound vortices are placed at panel quarter chord points and the boundary condition is specified at each element three quarter chord point (see Sketch 3.7).

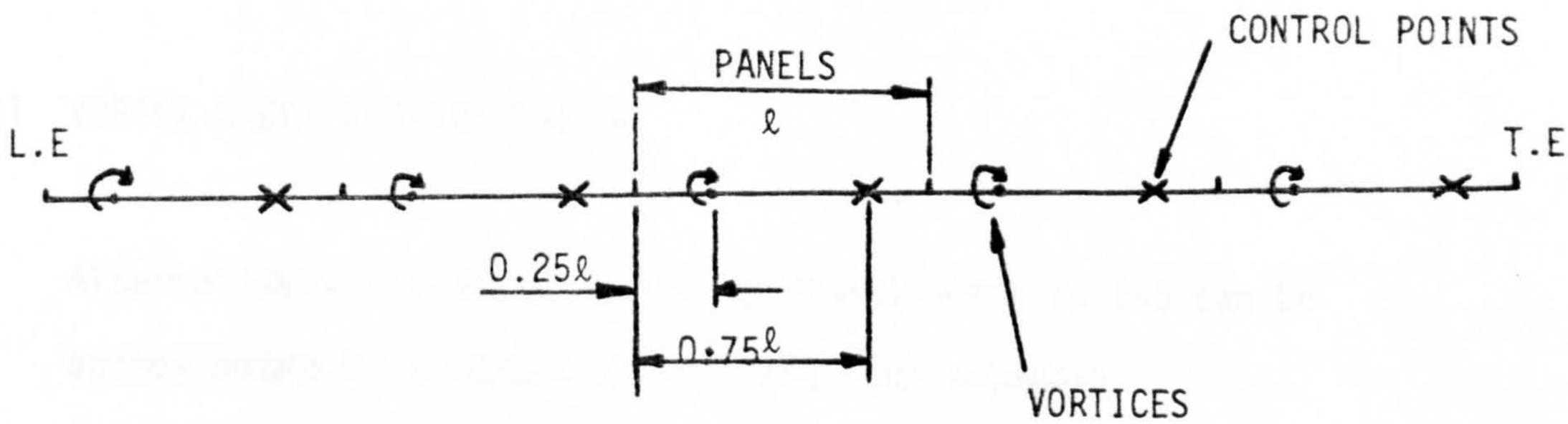

SKETCH 3.7

3.10 QUADVORT ELEMENTS

For the QUADVORT model it is more logical to consider each quadrilateral as an element of surface rather than forming a separate system of panel elements. In this case control point location is discussed in relation to the quadrilateral corners.

Also the local normal vector at the control point is taken as the normal to the quadrilateral and approximates very closely to the actual surface normal vector at the control point location. (Special care must be taken when considering the normal vectors for the panel system on curved surfaces since the slope of a panel does not approximate to the slope of the actual surface at the control point).

For thin wings the vortex-ring distribution can be arranged to follow standard vortex lattice practice in that the leading element vortex is set back a quarter element width from the leading edge and the last control point is placed a quarter element width upstream of the trailing edge.

3.11 VORTEX SHEET REPRESENTATION

Alternatively the basic vorticity distribution in 2-D can be approximated by a number of straight line segments (Sketch 3.8) which in turn can be approximated by 'point' vortices positioned at the mid-point of each segment. It can be shown that with equal segments control points should be placed mid-way between vortices.

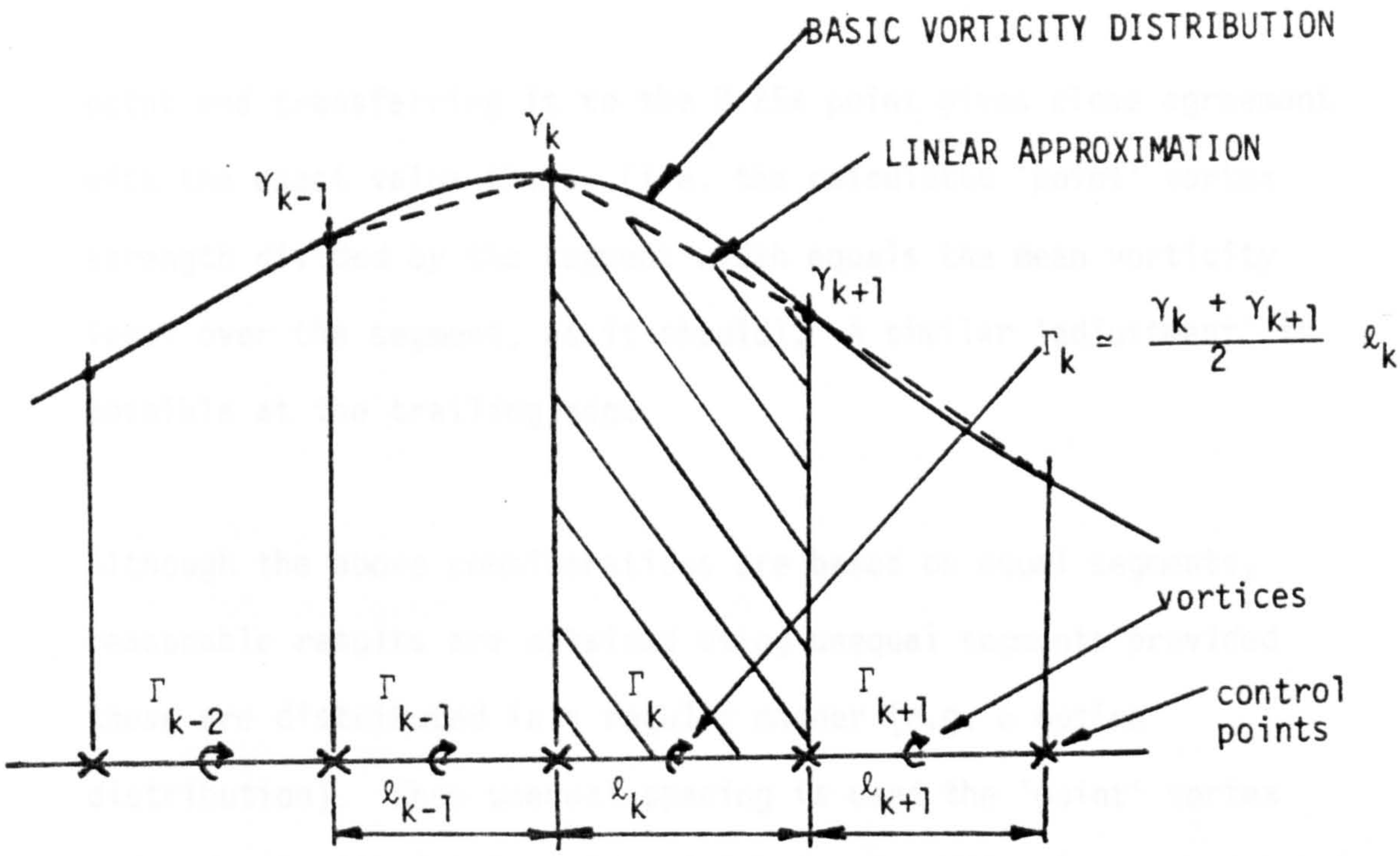

SKETCH 3.8

This approach has been applied to the 2-D thin aerofoil problem using 20 equal segments across the chord and the result compared with that of exact thin aerofoil theory. The error in C_L was 0.5% and the general order of error in vorticity values was 1.5%. The largest errors in vorticity occurred at the first and last segments where the linear approximation to the exact distribution ($\gamma \propto \sqrt{\frac{1-x}{x}}$) is poor unless a very large number of segments are used. Considering the exact distribution it is found that the <u>mean</u> value of vorticity over the leading edge segment actually occurs at 0.25ℓ of the segment (which is in close agreement with the 25% panel width adopted for standard vortex lattice work). Taking the vorticity value which was calculated from the vortex at the first segment mid-

point and transferring it to the 0.25ℓ point gives close agreement with the exact value there. (i.e. the calculated 'point' vortex strength divided by the segment width equals the mean vorticity level over the segment, as it should). A similar 'adjustment' is possible at the trailing edge.

Although the above considerations are based on equal segments, reasonable results are obtained using unequal segments provided these are distributed in a regular manner (e.g. a cosine distribution). When unequal spacing is used the 'point' vortex induced velocity (at the mid-point between vortices) does not match exactly the velocity induced by the linear vorticity segments. A small control point displacement, which is a function of the ratio of neighbouring element widths, is being considered in the hope of reducing the error so that more general element distributions may be used.

3.12 THREE-DIMENSIONAL FACTORS

3.12.1 CONTROL POINT LOCATION

The two-dimensional vorticity considerations have been used as the basis for control point location in QUADVORT, with the result that control points are placed at the mean of the four corner points of each quadrilateral vortex-ring. Thus the 2-D considerations are satisfied at least for rectangular shaped elements. However, for more general quadrilateral shapes this may not be the correct

location. In the case of a rectangular element the mean point is also the interior point at which the velocity induced by the vortex-ring is a minimum. It is possible that the minimum induced velocity point is a better criterion for control point location than the means of the corner points: a velocity rather than geometrical criterion would seem to provide a more logical basis for the control points location.

3.12.2 WING TIP

The spanwise distribution of elements on thin wings requires special treatment. Rubbert (3.11) has demonstrated that with the vortex lattice method the tip vortices should be inset by one quarter element width from the actual tip to maintain consistent results. This has not been proved rigorously. It could be argued however, that since each panel element of the wing is in effect being represented by a lifting line and since such representation for an isolated panel would have trailing vortices spring from approximately a quarter panel semi-span in-board from its tips ($1-\pi/4$) of the semi-span for elliptic loading), then such an inset should apply to all elements which have a free tip.

The inset of tip vortices also applies for thick wings in which the tip has been left open.

3.13 OUTLINE OF THE SUBSONIC PROGRAM AND DATA PREPARATION

The subsonic program can be applied to a wide range of problems in principle e.g. wing/flap with or without tailplane or fuselage in free air or in ground effect or inside a wind tunnel.

The wing is represented by a mean surface distribution of quadrilateral vortex-ring element as previously described, shown in Fig (3.4) the strengths of which are determined after applying the boundary conditions of zero normal components of velocity (i.e. free-stream plus vortex induced) at a control point in each equadrilateral element.

Trailing vortices, which for the first solution are assumed streamwise, are then divided into a number of straight line segments which relaxed into the local flow directions. The change in the vortex wake influence at the control points is the evaluated and a second solution obtained for the vortex ring strengths.

The process is repeated by iteration. The number of iterations is an input parameter and generally two iterations are sufficient for practical purposes. After the vortex ring strengths are evaluated the program calculates lift, vortex drag and moments.

3.13.1 SUBSONIC DATA PREPARATION

A problem may be represented by up to 3 components (e.g. a wing,

tailplane and pylon) on which up to 150 vortex ring elements and up to 31 trailing vortices may be placed (total). For symmetrical problems the coordinate system is shown in FIG (3.3). Each component is defined at a number of spanwise stations (up to 10 per component). Figure (3.4) and linear interpolation is employed within the program to generate additional points on the surface between the stations spanwise intervals may be either equal (and generated within the program) or unequal (and input separately). The maximum total number of spanwise intervals (columns) on a component is 30.

At each station x, y, z, coordinates of the leading and trailing edges are either generated within the program (using linear interpolation) or input separately. The maximum total number of chordwise intervals (Rows) on a component is 20. The number of Rows (NR) and number of columns (NC) on a component should be chosen to give an element aspect ratio of one or higher.

Generally the minimum values for NR and NC should be 4 and 10 respectively. If a component is close to another (i.e. within 2 or 3 element width) then the elements should be closely matched across the gap so that the control points on one surface lie approximately equi-distant from the nearest vortices on the other surface. A similar restriction is necessary when a component lies close to the wake from another component.

The length of trailing vortex segments should be of the order 1 to

3 times the distance apart of their upstream ends. This is to ensure a convergence of the vortex movements. The segment representation should go a short distance beyond the region of interest.

Flaps are defined (if required) by the hinge line(i.e. row)and by the spanwise one(i.e. columns)which contains the flap-edges FIG (3.5). Within the program additional vortex ring elements are generated at the flap edges FIG (3.6) and the flaps deflected to the specified angle.(Note that this deflection opens a gap at the centre-line when the hinge-line is swept). Also velocity field calculations are carried out (if required) over a 'box' defined by four position vectors FIG (3.8). The vectors between the first point and the other three points defined the base edges of the scanning box and are divided into a number of intervals. The intervals define grid lines within the box FIG (3.8) and the velocity vector is calculated at every point where grid lines cross. The local velocity contribution (tangential to sheet) at trailing vortex sheet intersections is included in this calculation.

3.13.2 SUBSONIC DATA INPUT

The data is input on paper tape which is in free format, or can be punched on cards or could be documented in a file. The subsonic program is dumped on magnetic tape. All the corresponding results

are saved separately during the program loading in three

stages. Whichever results are needed for any calculation purpose can be accessed. The following control cards (data input) must be kept in order, because each control card (or line) corresponds to a certain specific input which corresponds to "Read" statements in the main program. The square bracketed items may be input either on separate lines or together on one line for the bracket.

CARD NO.	READ STATEMENT	SPECIFIC PURPOSE
1	NCAS	Number of cases. All the following data must be input for each case. (i.e. wing, tailplane, fuselage).
2	HEADING	Up to 50 characters of text.
3	ALPHA>0	Angle of Incidence (of x-axis) in degrees.
4	PHI = 0.0	Side slip angle in degrees (not yet tested)
5	SW	Reference area (Total effective area of the wings)
6	CBAR	Reference chord (mean chord)
7	Semispan	Reference semispan
8	(RMP(I),I=1,2,3)	x,y,z coordinates of reference moment point.

CARD NO.	READ STATEMENT	SPECIFIC PURPOSE
9	D_{max}, AMACH	D_{max} = 1000.0 (This controls the use of a simple for field equation to reduce run times (see Reference 3.12) (AMACH is Mach number for compressible flow)
10.	NWT	Number of components (up to 3) (wing must be component 1)
11	IT_{max}	Number of iterations for wake shape (suggest 2)
12	IS	(=0 for no symmetry (=1 if z-x plane is plane of symmetry).
13	IG	(=0 for free air (=1 for ground effect.
14	NX	(=0 if velocity field calculation not required. (=1 if velocity field calculation is required.
15	H	If IG=1, height of origin above, the ground FIG (3.4). If IG=0; No input.

CARD NO.	READ STATEMENT	SPECIFIC PURPOSE
Input these two cards only If NX=1 — 16	(NXP(I),I=1,2,3)	Number of intervals on each edge of scan box.
17	((RX(I,N),I=1,2,3), N=1,2,3,4)	Four position vectors defining the scan box

Then for each component (i.e. wing or fuselage) all the following data must be input. (Items 18 to 30).

CARD NO.	READ STATEMENT	SPECIFIC PURPOSE
18	NST	Number of stations defined on component, $2 \leq NST \leq 10$
19	NPT	Number of vortex ring corner points chordwise across the component, $2 \leq NPT \leq 21$ (=NR+1)
20	For each station (1 to NST) input A, B and C below	
A)	XL YL ZL XT YT ZT	Leading edge and trailing edge coordinates.
B)	Input =	1 - All vortex corner points, x, y, z coords. input (with quarter-element chordwise shift). 2 - input x, z coords. only - y constant. 3 - input x coords. only - y and z constant 4 - no coords. input; program generates corner points using linear interpolation between L.E. and T.E.; equal segments and quarter segment shift are automatic.

CARD NO.	READ STATEMENT	SPECIFIC PURPOSE
C)	(X(I) Y(I) Z(I), I = 1, ----, NPT)	if INPUT = 1
	(X(I) Z(I), I = 1, ----, NPT)	if INPUT = 2
	(X(I), I = 1, ----. NPT)	if INPUT = 3
	NO INPUT	if INPUT = 4
21	SEG, NPVT (on one line)	SEG: Trailing vortex segment length (suggested value 0.5); NPVT: Number of points defining a trailing vortex (up to 30 - but watch the run time) suggested value 2
22	TIP, NTIP (on one line)	TIP: Tip edge inset in element 'spans' (suggested value 0.25); NTIP: Number of additional trailing vortices at wing tip edge. (i.e. for tip edge separations at large incidence).
23	INTERP	= 1 program assumes equal intervals between defined stations, and sets tip vortex in from the edge by the TIP value = 2 leading edge column point y values must be input. The tip inset is performed in the program as for INTERP=1 = 3 As for 2 but input z values (e.g. for a tin) (See Item 29)

CARD NO.	READ STATEMENT	SPECIFIC PURPOSE	
24	(NINT(I),I=1,----,(NST-1))	Number of intervals between stations I and I+1. Maximum total number of intervals on a component is 30.	
25	NFT	Number of flaps on the component. (up to 5 but 2 is the maximum tried so far)	
26	MF_1 MF_2	Inboard and outboard columns which contains flap edges.	only if NFT ≥ Repeat for each flap on the component
27	NRFH	Row which contains flap hinge at upstream edge.	
28	δ_f	Flap deflection normal to hinge line, in degrees. Positive downwards.	
29	No input if INTERP = 1 Y(I) if INTERP = 2 I=1,----, (TOTAL no. of columns plus 1) Z(I) if INTERP = 3		
30	X Y Z	Coordinates of 2nd point on vortex No. 1 when defining wing geometry only.	

3.14 COMPRESSIBILITY

In order to introduce compressibility effects, use may be made of transformation methods which can extend the application of incompressible flow methods within the subcritical Mach number range. One of a number of existing approximate compressibility corrections may be employed, for example the Prandtl-Glauert rule on aerofoil sections and Göthert transformation for wings and fuselages. The simple Göthert transformation is accurate enough for a linearised compressible flow in the range of $0.4 < M_\infty < 0.8$, thus this theory is employed here for both fuselage and wing. Refs (3.13), (3.14), (3.15).

3.15 COMPRESSIBILITY CORRECTIONS

3.15.1 LINEARIZED COMPRESSIBLE FLOW

To derive the Göthert linearized compressible flow correction (Ref. 3.13), consider the velocity perturbation potential ϕ which satisfies the equation

$$(1 - M_\infty^2)\frac{\partial^2\phi}{\partial x^2} + \frac{\partial^2\phi}{\partial y^2} + \frac{\partial^2\phi}{\partial z^2} = 0 \quad (M_\infty < 1 \text{ for subsonic flow}) \qquad \ldots\ldots\ldots\ldots\ldots\ldots (3.6)$$

We note that in compressible flow the linearized pressure coefficient is given by:

$$Cp_c = -\frac{2}{U_\infty}\frac{\partial\phi}{\partial x} \qquad \ldots\ldots\ldots (3.7)$$

where U_∞ is velocity of undisturbed flow.

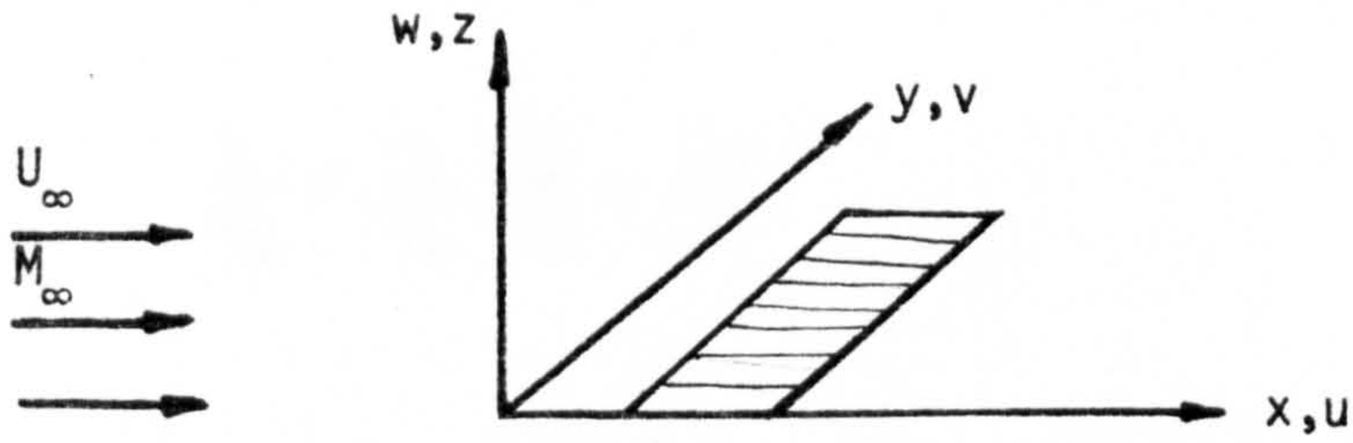

SKETCH (3.9)

Also the velocity components are:

$$u = U_\infty + \frac{\partial\phi}{\partial x}$$

$$v = \frac{\partial\phi}{\partial y}$$

$$w = \frac{\partial\phi}{\partial z}$$

If the x coordinate is transformed by writing $\xi = \dfrac{x}{\sqrt{1 - M_\infty^2}}$, leaving y, z alone and ϕ is changed to ϕ_i (suffix i stands for incompressible), then the basic equation of flow potential becomes:

$$\frac{\partial^2\phi_i}{\partial\xi^2} + \frac{\partial^2\phi_i}{\partial y^2} + \frac{\partial^2\phi_i}{\partial z^2} = 0 \qquad \text{..... (3.8)}$$

Using the flow tangency condition then, we have

$$\frac{w}{U_\infty} = \frac{1}{U_\infty}\frac{\partial\phi}{\partial Z} = \frac{\partial f}{\partial x} \qquad \text{..... (3.9)}$$

where $z = f(x,y)$ is the equation of the wing surface.

Transforming equation (3.7) to the incompressible state will give

$$Cp_i = -\frac{2}{U_\infty}\frac{\partial\phi_i}{\partial\xi} \qquad \text{..... (3.10)}$$

For the boundary condition that flow should be tangential to the surface of wing we must have

$$\frac{w}{U_\infty} = \text{Slope of surface}$$

Now the tangency condition becomes $\left(\xi = \frac{x}{\sqrt{1 - M_\infty^2}}\right)$

$$\frac{1}{U_\infty}\frac{\partial\phi_i}{\partial Z} = \frac{\partial f}{\partial\xi} = \sqrt{1 - M_\infty^2}\,\frac{\partial f}{\partial x} \qquad \text{..... (3.11)}$$

If $\lambda = \frac{1}{\sqrt{1 - M_\infty^2}}$, then equation (3.11) can be modified to

$$\frac{1}{U_\infty}\frac{\partial\phi_i}{\partial Z} = \frac{1}{\lambda}\,\frac{1}{U_\infty}\frac{\partial\phi_c}{\partial Z} \qquad \text{..... (3.12)}$$

Therefore the pressure coefficient for an incompressible condition will become:

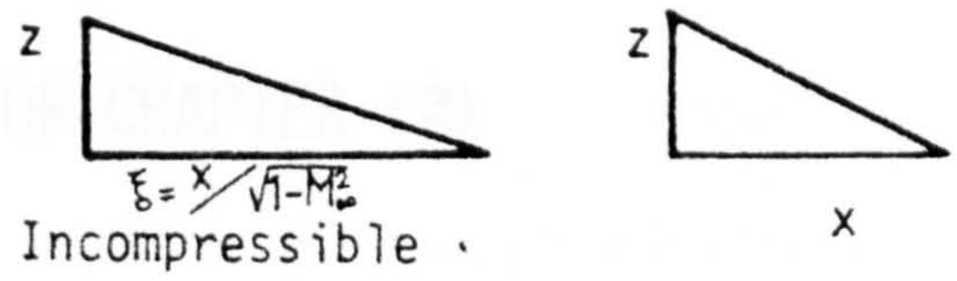

SKETCH 3.10

$$Cp_i = -\frac{2}{U_\infty}\frac{\partial\phi_i}{\partial\xi} = -\frac{2}{U_\infty}\frac{\sqrt{1-M_\infty^2}}{\lambda}\frac{\partial\phi_i}{\partial x}$$

$$= (1 - M_\infty^2)\left(-\frac{2}{U_\infty}\frac{\partial\phi_c}{\partial x}\right) = (1 - M_\infty^2)\, Cp_c$$

Hence

$$\underline{\underline{Cp_c = 1/(1 - M_\infty^2)\, Cp_i}} \qquad \ldots\ldots\ (3.13)$$

For further details of compressibility corrections on subsonic forces and moments refer to Appendix (B).

REFERENCES FOR CHAPTER (3)

(3.1) B. MASKEW "Calculation of the three dimensional potential flow around lifting non-planar wings and wing bodies using a surface distribution of quadrilateral vortex-rings". Loughborough University of Technology, TT 7009, Sept. 1970.

(3.2) H. LAMB "Hydrodynamics", Cambridge University Press, 1932.

(3.3) L.M. MILNE-THOMSON "Theoretical Aerodynamics". The Macmillan Co., London, 1952.

(3.4) A.M.O.SMITH, J.L. HESS "Calculation of potential flow about arbitrary bodies". Progress in Aeronautical Sciences, Vol. 8, Pergamon Press, London, 1966.

(3.5) E.W. PURCELL "The vector method of solving simultaneous linear equations". Journal of Math. Physics, Vol. 23, 180, 1953.

(3.6) D.J. BUTTER "Downwash fields behind swept wings". M.PHIL: Thesis, University of London, 1968.

(3.7) R.G. JOPPA "Wind-tunnel testing of S.T.O.L. aircraft". Journal of Aircraft, May-June, 1969.

(3.8) V.M. FALKNER "Calculation of aerodynamic loading on surfaces of any shape". A.R.C. Technical Report. R. and M. No. 1910, 1943.

(3.9) S.G. HEDMAN "Vortex lattice method for calculation of quasi-steady state loadings of thin elastic wings in subsonic flow". F.F.A. Report 105, 1965.

(3.10) S.M. BELOTSERKOVSKII "The theory of thin wings in subsonic flow". Plenum Press, New York, 1967.

(3.11) P.E. RUBBERT "Theoretical characteristics of arbitrary wings by a non-planar vortex-lattice method". The Boeing Co. Report. D6-9244, 1964.

(3.12) B. MASKEW An investigation into the use of a simple for field equation in the vortex-ring lifting surface method. Hawker Siddeley Aviation Ltd., Note No. YAD.3184, 1974.

(3.13) E.L. HOUGHTON AND R.P. BOSWELL. "Further Aerodynamics for Engineering Students". Edward Arnold (Publishers) Ltd. London - 1969.

(3.14) R.A. SAWYER "Aerofoil Design Methods". Part 2.3. MSc. Unit in computation methods and fluid mechanics. University of Salford, May, 1973.

(3.15) ROBERT, T. JONES AND DORIS COHEN "High Speed wing theory". Princeton, New Jersey. Princeton University Press, 1960.

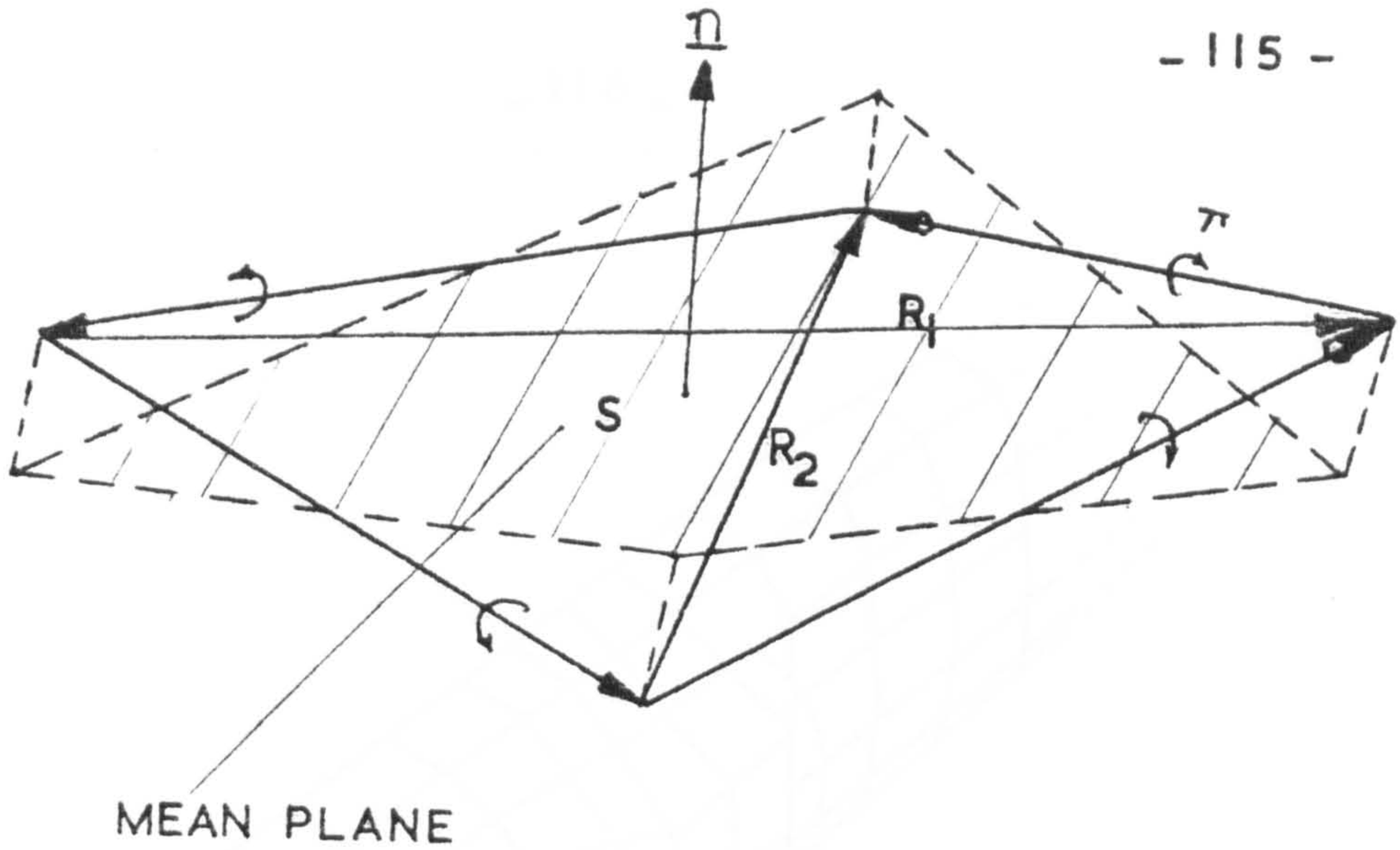

SKETCH (3·1)

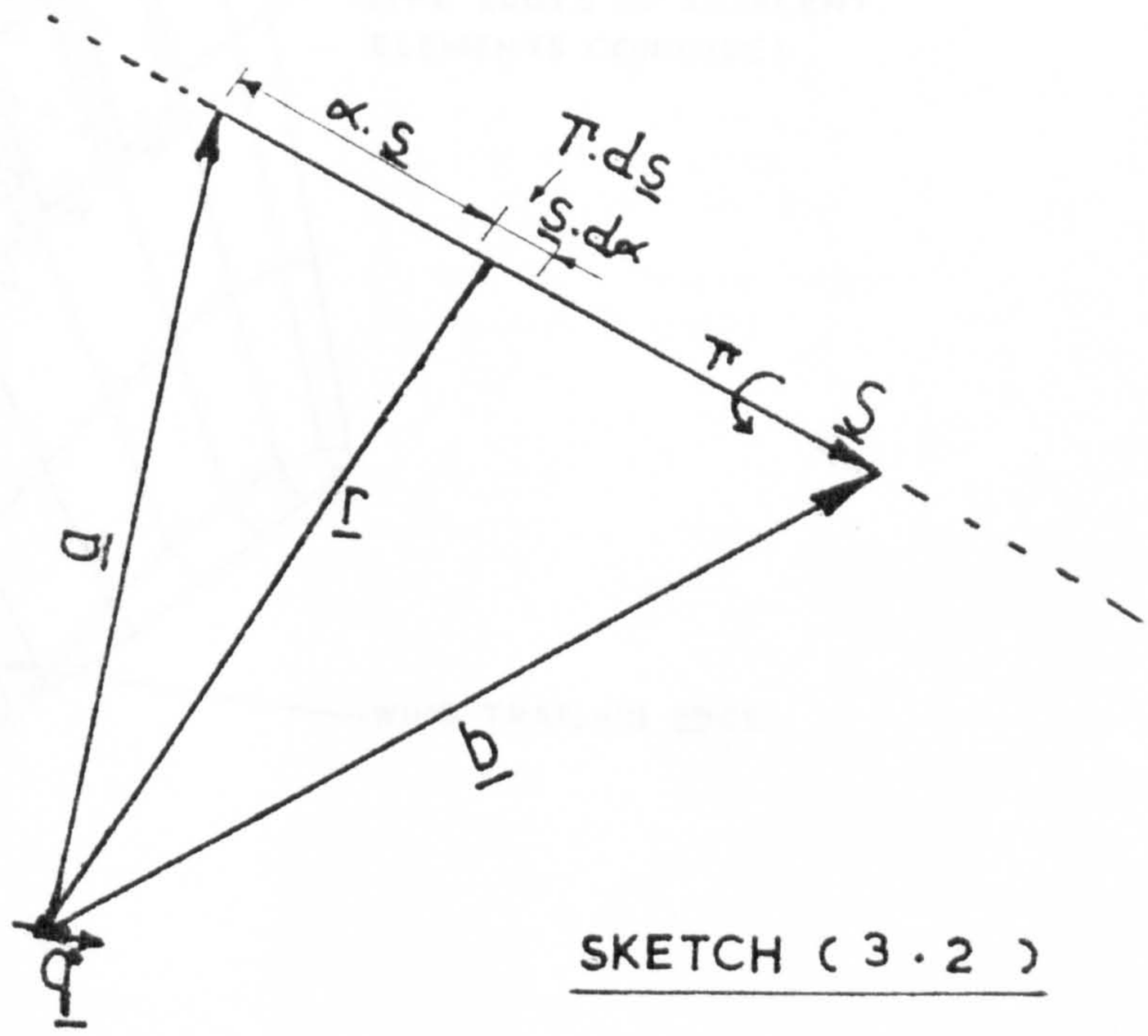

SKETCH (3·2)

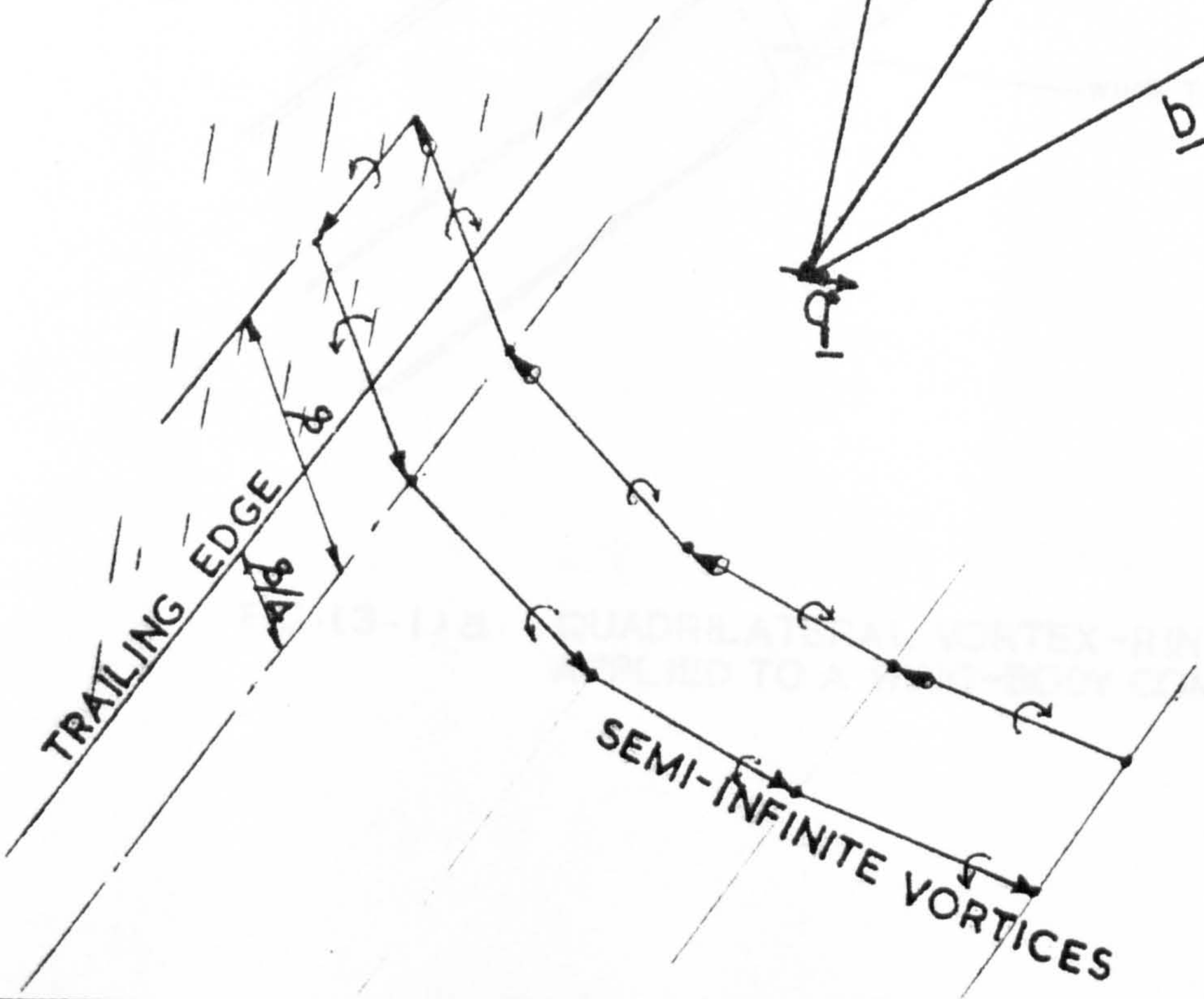

SKETCH (3·3)

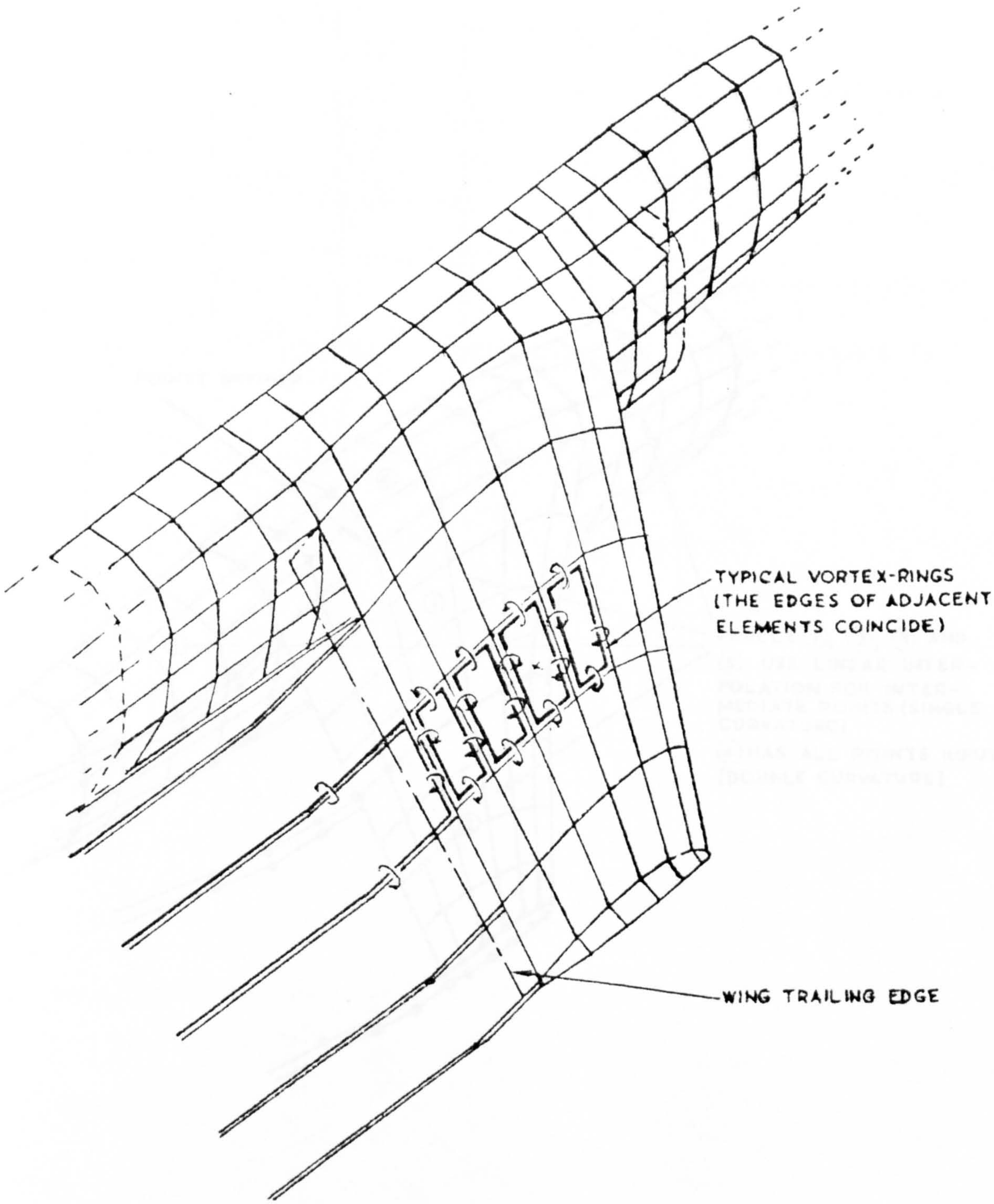

FIG.(3.1)a. QUADRILATERAL VORTEX-RING MODEL APPLIED TO A WING-BODY COMBINATION

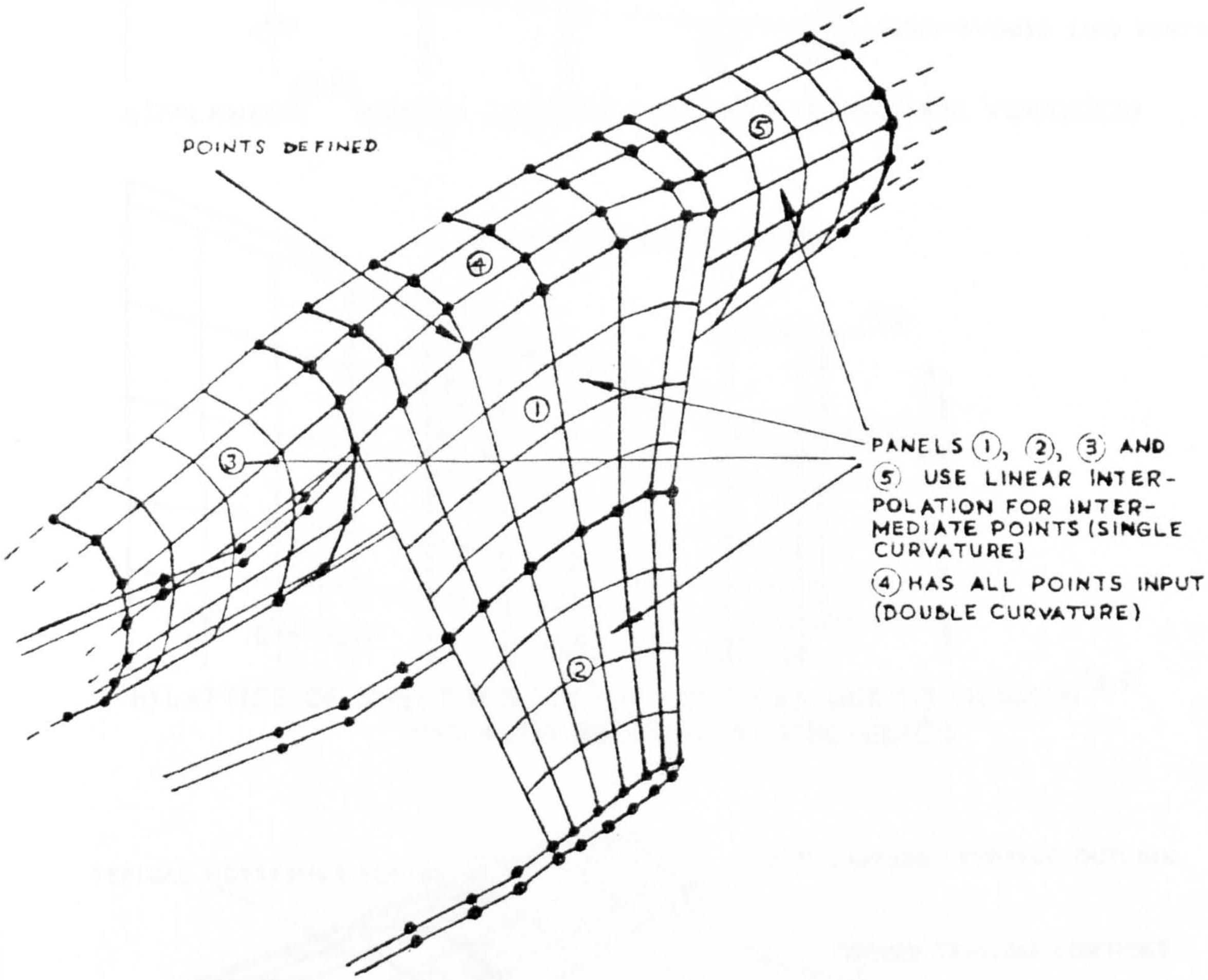

FIG. (3.1) b SURFACE PANELS FOR SIMPLIFIED INPUT

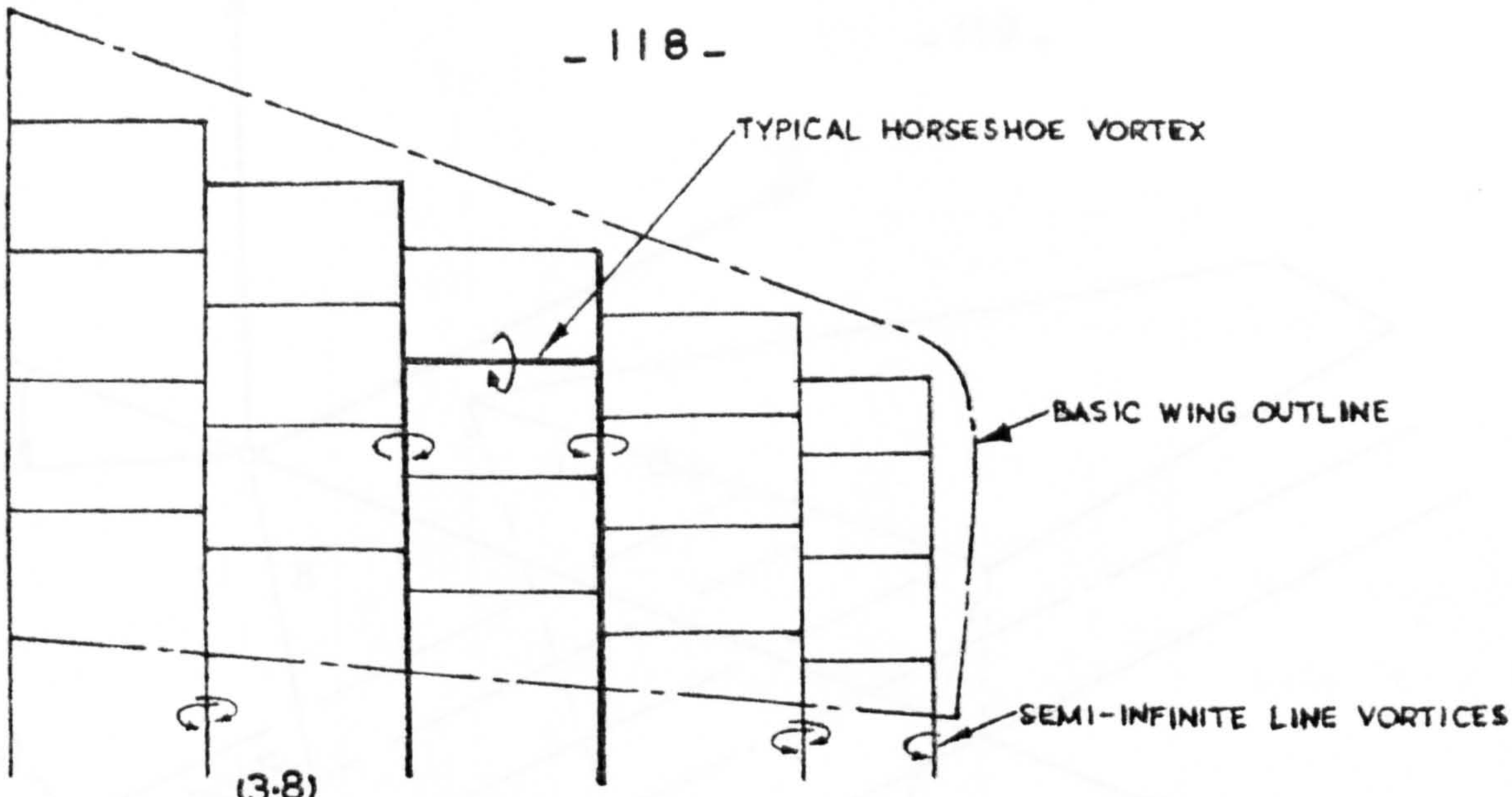

a) FALKNER'S[3.8] VORTEX LATTICE (UNSWEPT HORSESHOE VORTICES)

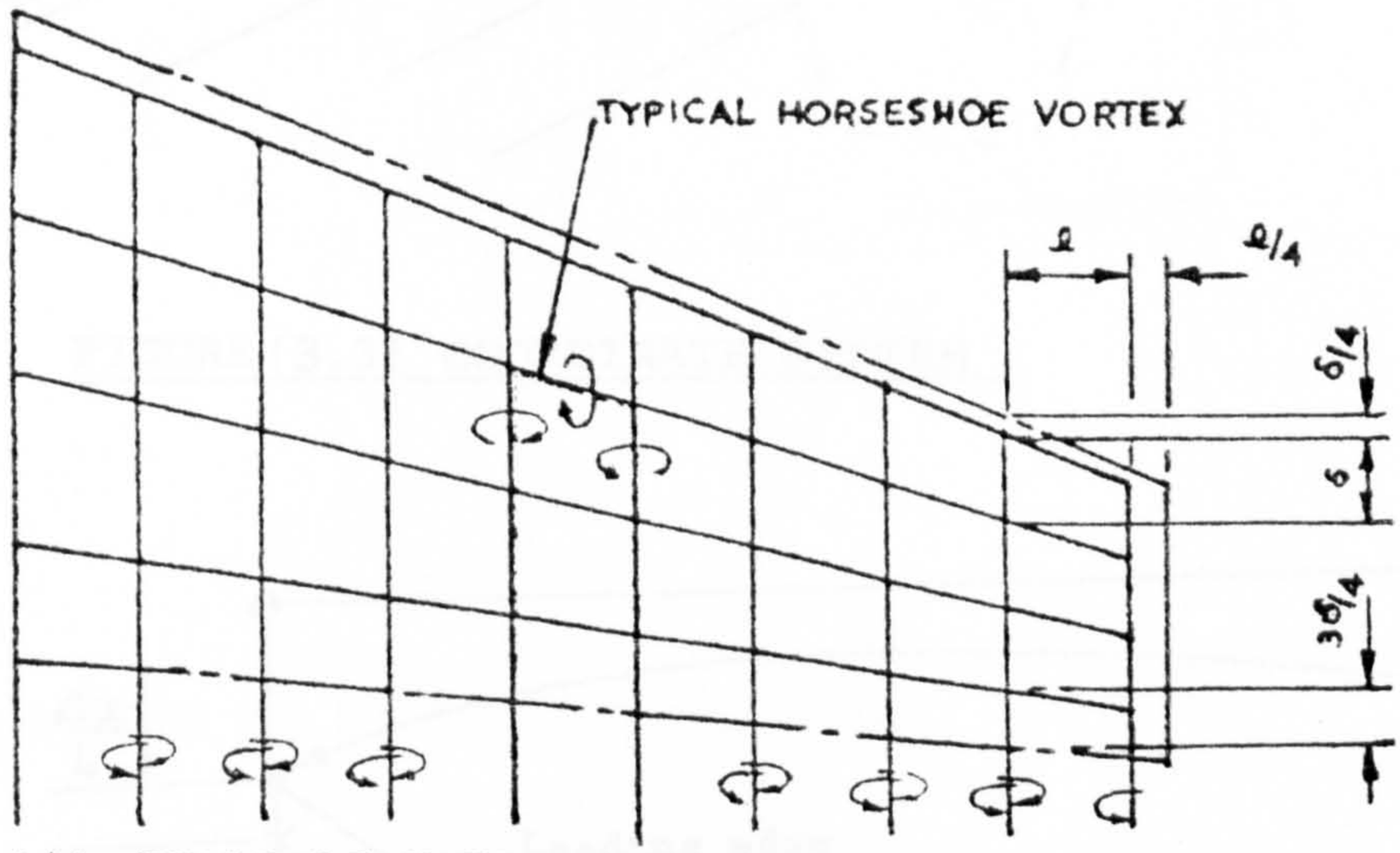

b) LATTICE OF SWEPT HORSESHOE VORTICES DUE TO HEDMAN[3.9] AND ALSO BELOTSERKOVSKII[3.10]

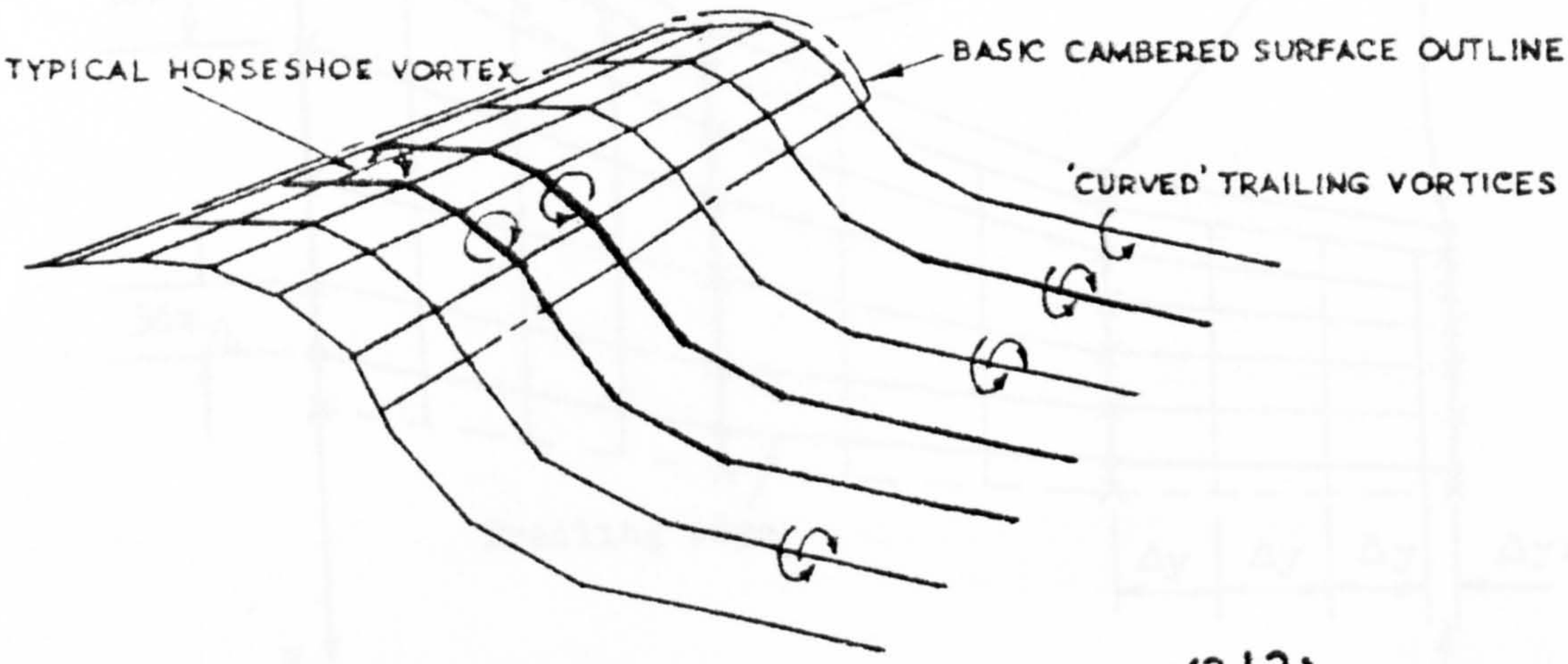

c) NON-PLANAR VORTEX LATTICE DUE TO RUBBERT[3.12]

FIG. (3.2) PREVIOUS VORTEX LATTICE ARRANGEMENTS.

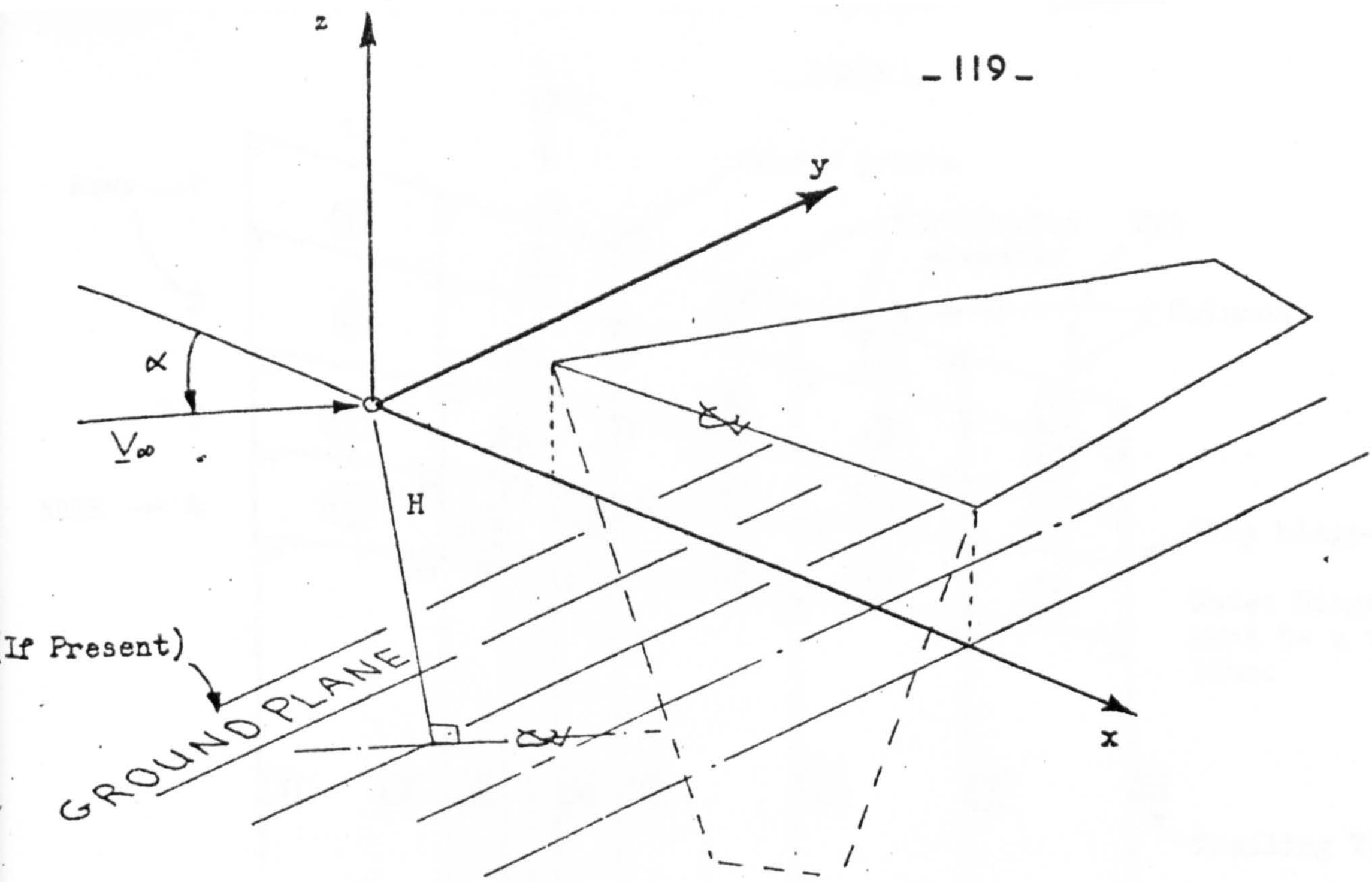

FIGURE (3.3) COORDINATE SYSTEM

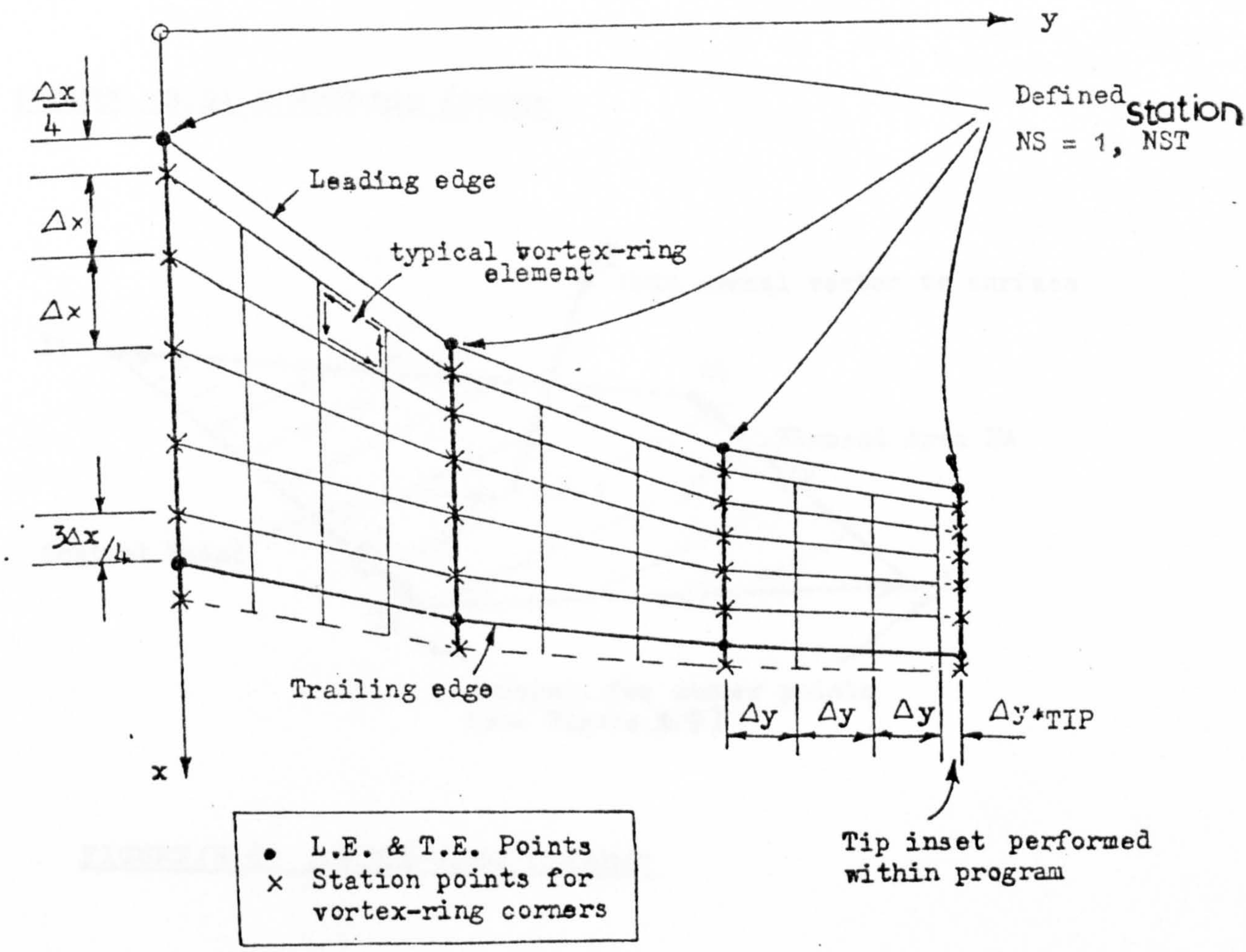

FIGURE (3.4) BASIC COMPONENT GEOMETRY

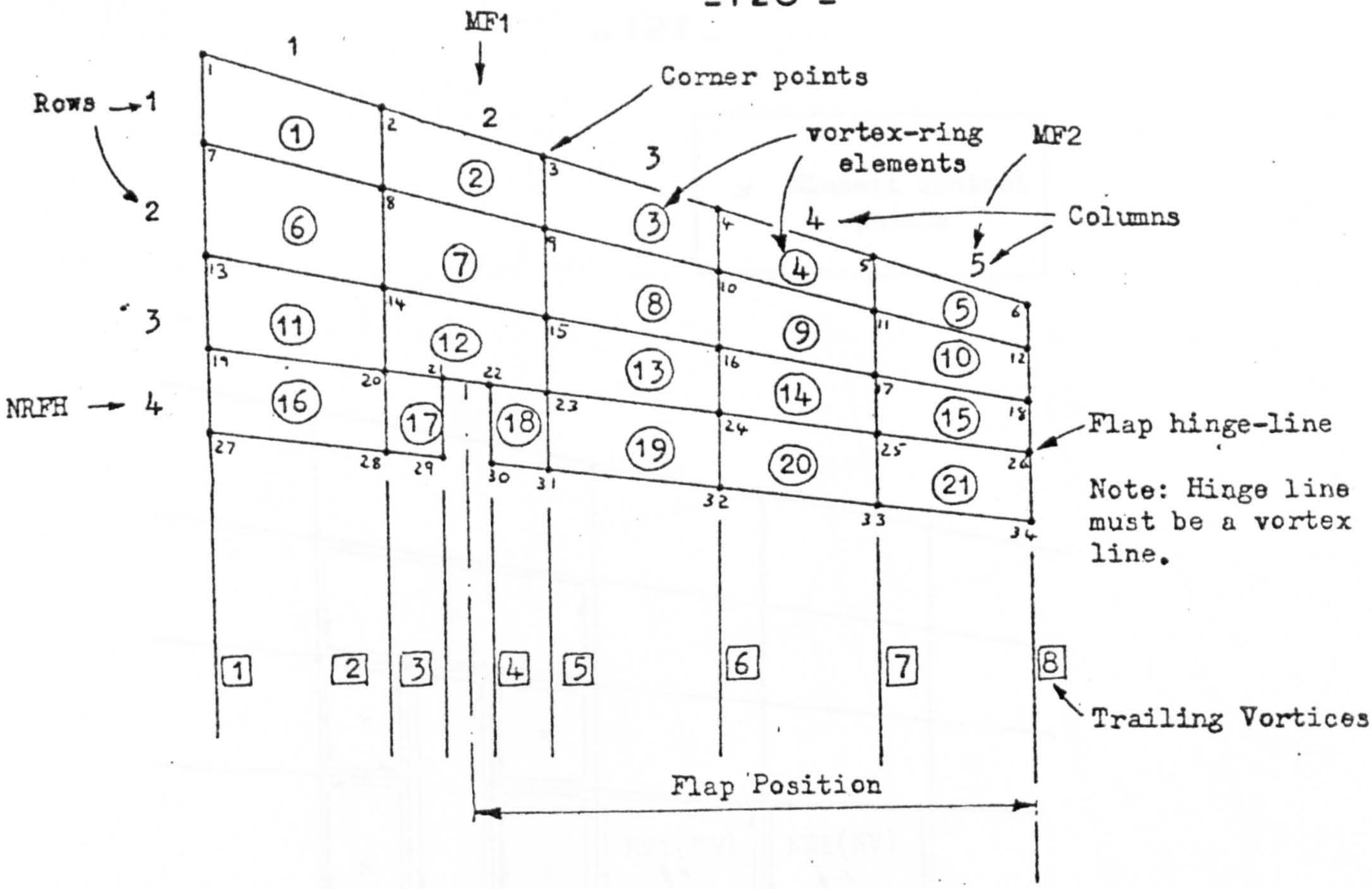

FIGURE (3.5) NUMBERING SYSTEM

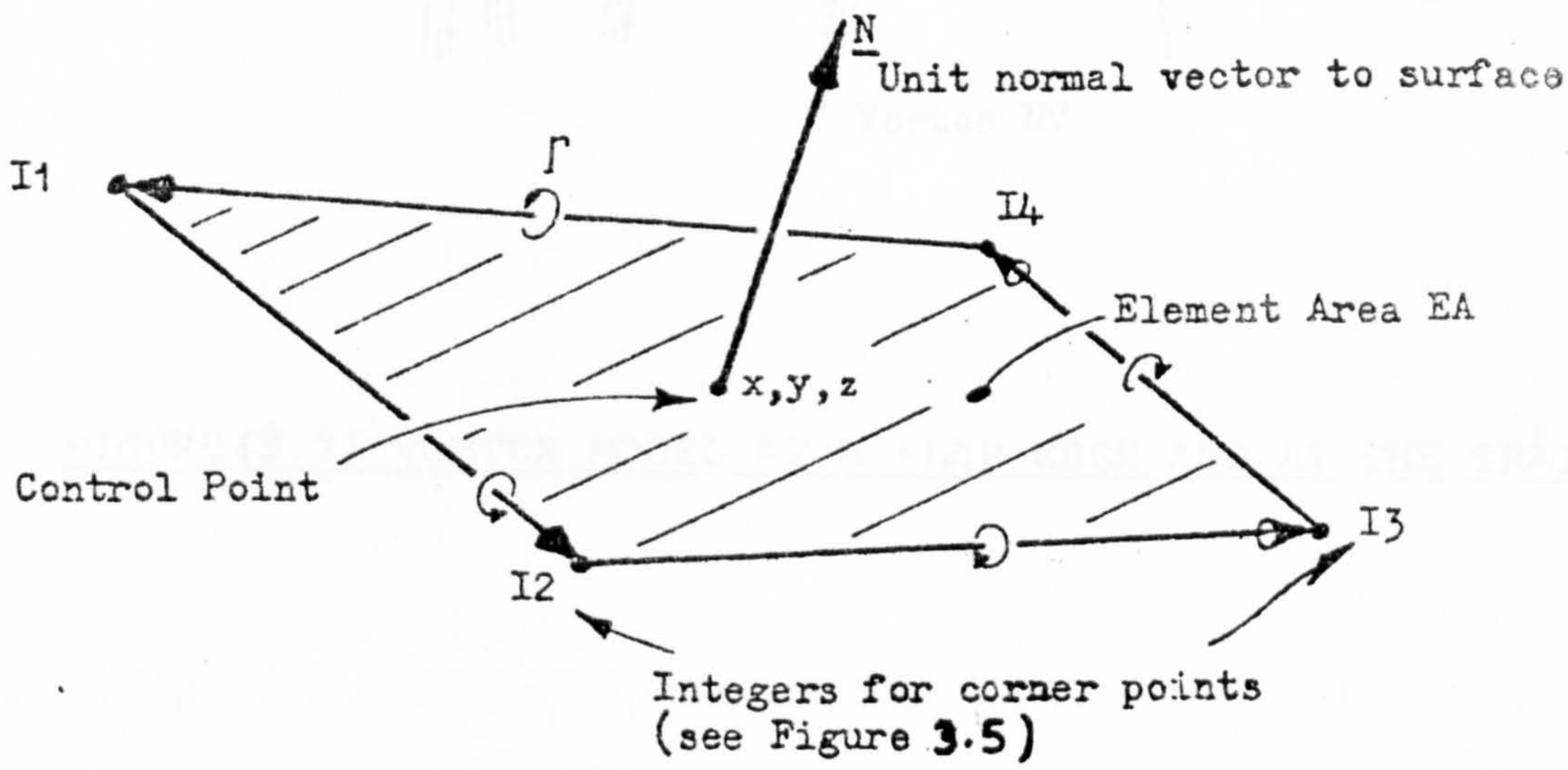

FIGURE (3.6) VORTEX-RING ELEMENT

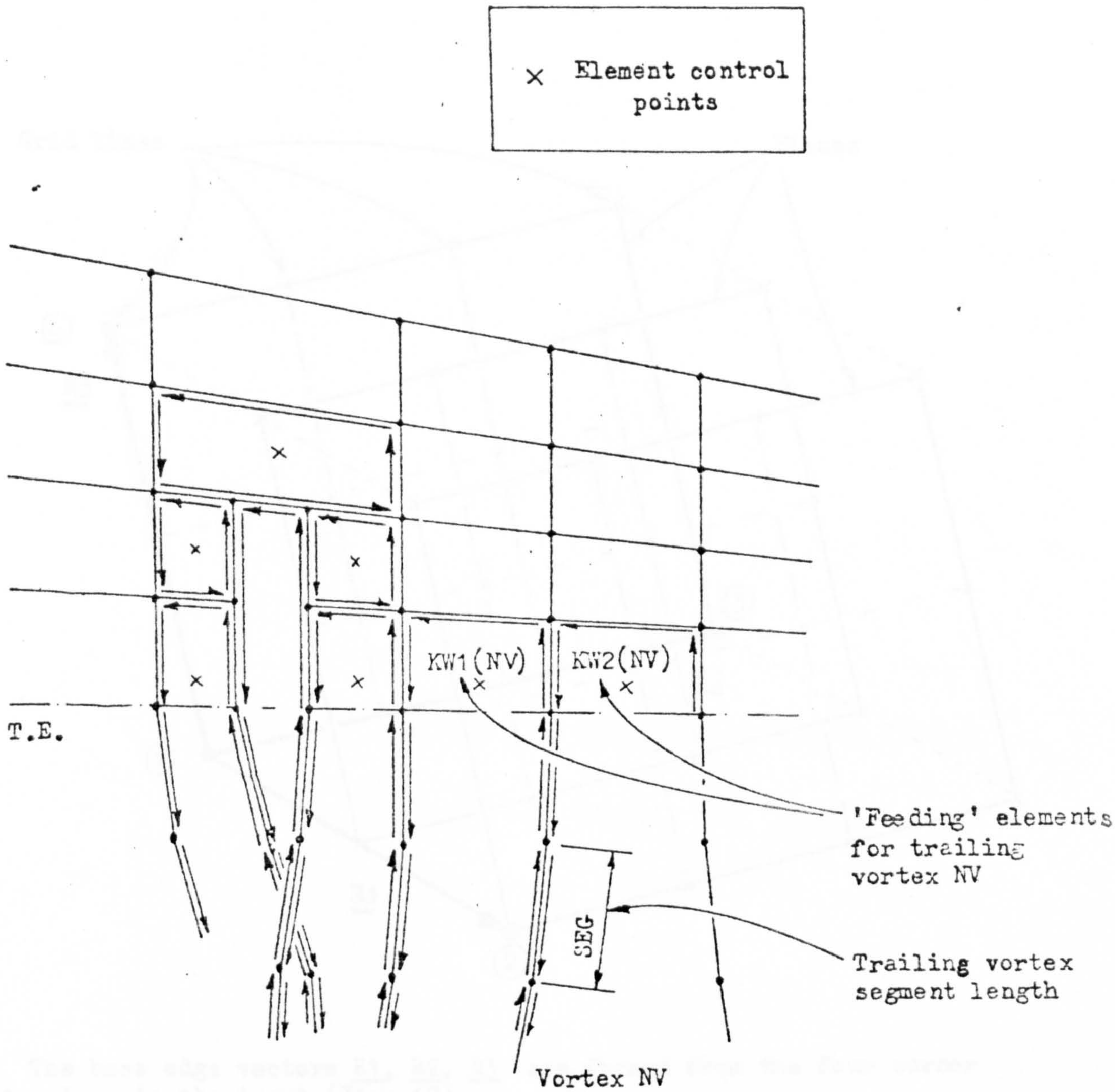

FIGURE (3.7) VORTEX MODEL AT A FLAP EDGE AND AT THE TRAILING EDGE

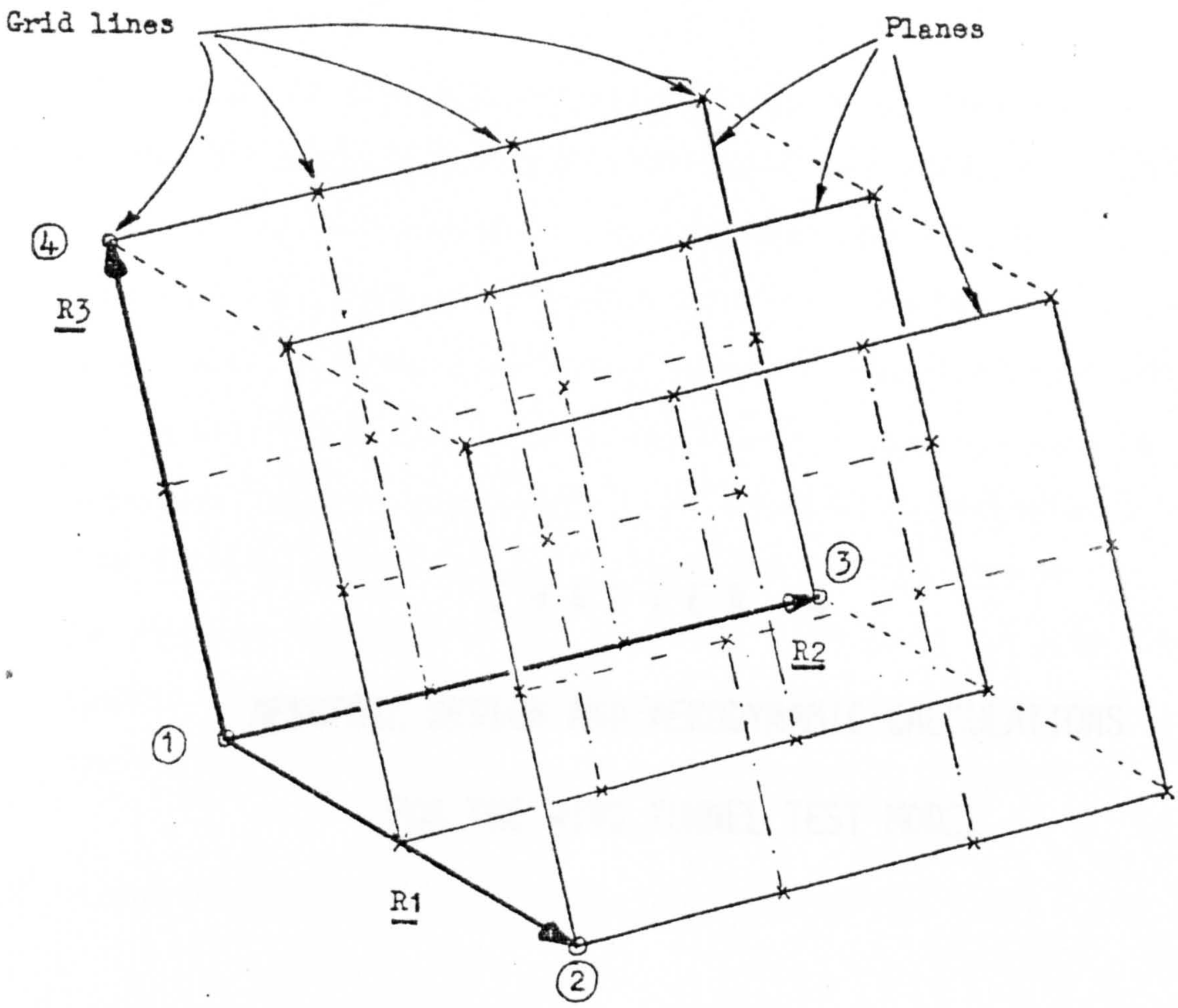

The base edge vectors R1, R2, R3 are formed from the four corner points given in the input (Item 17).

R1, R2, R3 are divided into a number of equal intervals according to the input values of NXP_1, NXP_2, NXP_3 respectively (Item 16).

All the points generated within the box by these intervals are scanned; the scan moves along grid lines parallel to R3 and intervals on R2 change next followed by those on R1.

FIGURE (3.8) THE 'BOX' FOR VELOCITY FIELD CALCULATION

CHAPTER 4

AEROFOIL DESIGN AND AERODYNAMIC CALCULATIONS FOR THE WIND TUNNEL TEST MODEL

4.1 INTRODUCTION

This chapter is devoted mainly to the design of the aerofoil section for the wing model and to the use of thin aerofoil theory in the final aerodynamic calculations. The aerofoil camber line and thickness distributions for all the variable sweep cases are used, in which to find the best curve fitting for the experimental pressure difference coefficients in order to evaluate section lift along the wing span. A programe is written for this purpose which evaluates the pressure distributions from the experimental data and to feed them into the program for the final calculations of lift force. All the other aerodynamic forces and moments were measured experimentally and their corresponding graphs are shown in the results chapter.

4.2 DESIGN OF CAMBER LINE AND THICKNESS FUNCTION FOR THE WING

In order to calculate the camber line equation and the thickness function for the wing, we need to find the equation of the wing surfaces for all angles of sweep. To do this, first of all the general equation is derived and then the surface equation for our chosen angles of sweep is found. Now, the camber line and thickness function ordinates are given by

Camber Line $= (Y_U+Y_L)/2xC$ ..... (4.1)

Thickness Function $= (Y_U-Y_L)/2xC$ ..... (4.2)

where Y_U and Y_L are the surface equations for the upper and lower surfaces respectively, and C is the chord length.

4.3 SURFACE EQUATION FOR VARIABLE SWEEP

Considering the wing planform shown in Sketch (4.1)

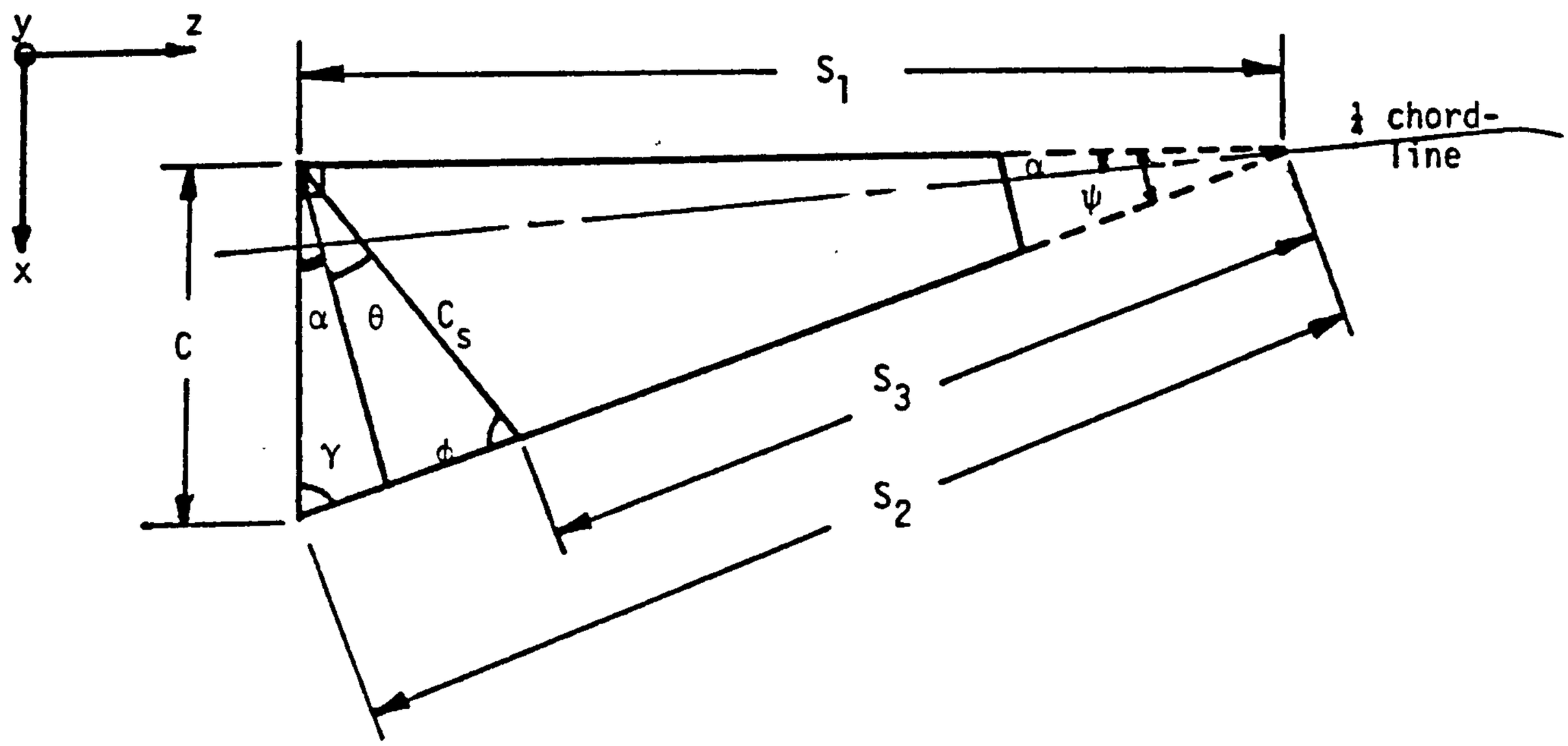

SKETCH 4.1

In this case $\psi = 16.14^o$, $\alpha = 4.035^o$, $\gamma = 90 - 16.14 = 73.86^o$, $\phi = 102.105^o - \theta^o$.

The angle of sweep is measured at the ¼-chord line, so that chord length will vary as the angle of sweep θ changes. Thus their dependence can be represented by the following equation:

$$C_s = (C \times \sin\gamma)/\sin(\phi) \qquad \text{..... (4.3)}$$

Knowing that the geometry of the wing can be represented as

$$S_1 = C \times \mathrm{Cot}(\psi^o) \qquad \text{..... (4.4),}$$

where S_1 is the leading edge length, and

$$S_2 = C \times \mathrm{Cos}\ (\psi^o) \qquad \text{..... (4.5),}$$

where S_2 is the trailing edge length,

$$S_3 = S_2 - C \times \mathrm{Sin}(\alpha+\theta)/\mathrm{Sin}\phi \qquad \text{..... (4.6),}$$

equation (4.6) can be modified by substituting S_2 and non-dimensionalising as follows:

$$\frac{S_3}{S_2} = 1 - (\mathrm{Sin}(\psi) \times \mathrm{Sin}(\alpha+\theta))/\mathrm{Sin}(\phi)$$

Here θ is angle of sweep, which in the experiments is chosen to be 12.5^o, 32.5^o, and 52.5^o.

The wing surface coordinates can be given by the following equation for any angle of sweep:

$$\frac{Y_s}{C_s} = \frac{Y}{C} \times \frac{C}{C_s} \left\{ 1 - \left[\frac{\mathrm{Sin}\psi \times \mathrm{Sin}(\alpha+\theta)}{\mathrm{Sin}\phi} \right] \frac{X}{C} \right\} \qquad \text{..... (4.7)}$$

Equation (4.7) can be simplified by substituting from equation (4.3), so that the surface coordinates can be evaluated from a 2-Dimensional aerofoil section as follows:

$$\frac{Y_s}{C_s} = \frac{Y}{C} \times \frac{\sin\phi}{\sin\gamma} \times \left[1 - \frac{\sin\psi.\sin(\alpha+\theta)}{\sin\phi} \times \frac{X}{C}\right]$$

or

$$\frac{Y_s}{C_s} = \frac{Y}{C} \left[\sin\phi - \sin\psi \times \sin(\alpha+\theta) \frac{X}{C}\right] / \sin\gamma \quad \ldots\ldots (4.8),$$

where $\frac{Y}{C}$ % and $\frac{X}{C}$ % values are shown in Table (4.1) from Ref (2.3). This equation at a 0° sweep can be shown to be:

$$\frac{Y_s}{C_s} = \frac{Y}{C} \left[1.01788 - 0.02036 \times \frac{X}{C}\right] \quad \ldots\ldots\ldots (4.9)$$

In this case values of Y_s/C_s % are shown in Table (4.2) for the upper and lower surface in Y_U/C and Y_L/C form respectively. Equation (4.8) can be applied for selected values of sweep angle as follows:

4.3.1 SURFACE EQUATION FOR THE WING AT 12.5^o SWEEP

The corresponding equation will be :

$$\frac{Y_s}{C_s} = \frac{Y}{C} \times \left[1.041 - 0.08232 \frac{X}{C}\right] \quad \ldots\ldots\ldots (4.10)$$

For this case all the new values of Y_U and Y_L are shown for the upper and lower surface are shown in Table (4.3).

4.3.2 SURFACE EQUATION FOR THE WING AT 32.5° SWEEP

Similarly equation of surface coordinates for $\theta = 32.5^o$ sweep can be deduced to be:

$$\frac{Y_s}{C_s} = \frac{Y}{C} \times (0.976 - 0.1723 \frac{X}{C}) \qquad \text{..... (4.11)}$$

All the surface geometries, i.e. $Y_{U/C}$ and $Y_{L/C}$ are shown for the upper and lower surface in Table (4.4).

4.3.3 SURFACE EQUATION FOR THE WING AT 52.5° SWEEP

Finally, the surface equation for a sweep angle of 52.5° can be represented by the following form:

$$\frac{Y_s}{C_s} = \frac{Y}{C} \times (0.793 - 0.24142 \frac{X}{C}) \qquad \text{..... (4.12)}$$

The corresponding values of $Y_{U/C}$ and $Y_{L/C}$ are shown in Table (4.5).

By evaluation of equations (4.9) to (4.12) all the corresponding surface coordinates for different sweep can be deduced, and

consequently the corresponding thickness functions and camber lines can be evaluated by evaluation of equations (4.1) and (4.2). In Figs. (4.1) and (4.2), the thickness/chord $\frac{t}{c}$ ratios are shown about 6% and the corresponding camber lines have an approximately parabolic behaviour.

4.4 2-DIMENSIONAL THIN AEROFOIL THEORY FOR CAMBER LINES AT INCIDENCE

A camber line $y = y_c(x)$, where $o \leqslant x \leqslant c$, at incidence α to a stream of speed U can be represented by a vortex distribution of strength K(x) per unit length along the chord line $y = o$, for $o \leqslant x \leqslant c$.

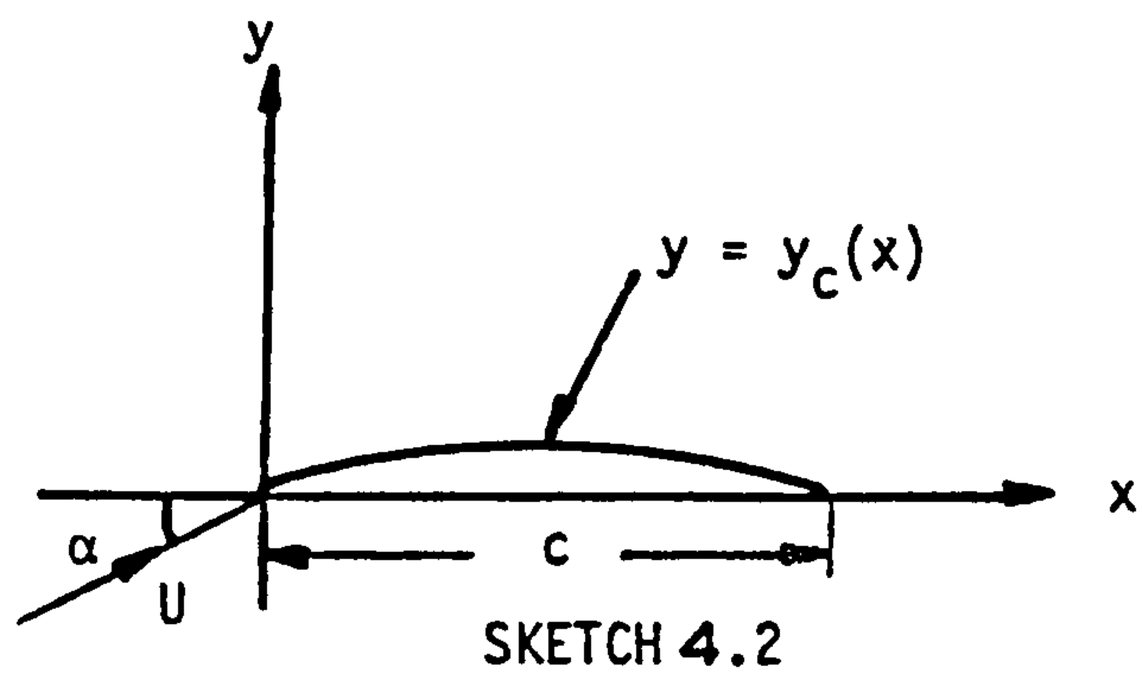

SKETCH 4.2

Under the transformation of the x-coordinate given by $x = \frac{1}{2}\, c(1-\cos\theta)$, it is possible to expand the chordwise vortex distribution K in the form as follows. Ref. (4.1).

$$K = 2U\left(A_o.\cot\frac{1}{2}\,\theta + \sum_{n=1}^{\infty} A_n.\sin n\theta\right) \qquad \ldots\ldots\ (4.13)$$

where each term gives zero loading at the trailing edge (c,o) and the leading term in $\cot\frac{1}{2}\theta$ represents the distribution of vorticity found for a flat plate $y = o$, for $o \leqslant x \leqslant c$. This latter distribution has a leading-edge singularity so that for any

incidence α which gives $Ao \neq o$, there will be a leading edge suction term giving a component of total force on the camber line in the direction of negative x.

By applying flow tangency conditions at the chord line it is possible to show that the 'A' coefficients are related to the camber-line shape by the equation.

$$\frac{dy_c}{dx} = \alpha - Ao + \sum_{n=1}^{\infty} An.Cosn\theta \qquad \text{..... (4.14)}$$

Equation (4.14) can be modified and the following equations can be derived for the 'A' coefficients:

$$\begin{cases} Ao = \alpha - \dfrac{1}{\pi} \displaystyle\int_o^{\pi} \frac{dy_c}{dx}.\ d\theta & \text{..... (4.15)} \\ \\ An = \dfrac{2}{\pi} \displaystyle\int_o^{\pi} \frac{dy_c}{dx}\ .Cos.n.\theta.d\theta, & \text{..... (4.16)} \end{cases}$$

where n = 1, 2, 3, ----

The resulting lift and moment coefficients are given by the following equations:

$$\begin{cases} CL = 2\pi\ (Ao + \frac{1}{2} A_1), \\ \\ CM_{\frac{1}{4}} = \frac{1}{4}\pi\ (A_2 - A_1), \end{cases} \qquad \text{..... (4.17)}$$

where the resulting moment is taken about the ¼-chord point. Substituting for the 'A' coefficients in the Fourier Expansion for K gives: Ref (3.13).

$$K = 2U\left\{\alpha\sqrt{\frac{1-x/c}{x/c}} + \frac{1}{\pi}\sqrt{\frac{1-x/c}{x/c}}\int_0^c \frac{dy_c}{d\xi}\sqrt{\frac{\xi/c}{1-\xi/c}}\;\frac{d\xi}{(x-\xi)}\right\} \qquad \text{..... (4.18)}$$

The chordwise velocity increment u due to the vortex distribution is given by

$u = \pm\frac{K}{2}$ where $\pm$ refer to upper and lower surfaces respectively, and the linearised value of pressure coefficient will be given by

$$Cp = \mp\frac{2u}{U} = \mp 2\left\{Ao\cot\frac{1}{2}\theta + \sum_{n=1}^{\infty} An.\mathrm{Sin}n\theta\right\} \qquad \text{..... (4.19)}$$

So the pressure difference across the camber line is given by

$$\Delta Cp = 4\left\{Ao\cot\frac{1}{2}\theta + \sum_{n=1}^{\infty} An.\mathrm{Sin}n\theta\right\} \qquad \text{..... (4.20)}$$

4.5 SIMPLE SWEEP THEORY APPLIED TO CONSTANT SECTION WINGS AT SWEEP BACK ANGLE Λ

This theory shows that on the wing the pressure coefficient is given by:

$$Cp = Cp_{2-D} \cos\Lambda \qquad \text{..... (4.21)}$$

where Cp_{2-D} refers to the pressure coefficient on the unswept wing having identical streamwise section and incidence.

4.6 IMPROVEMENTS IN LINEARISED THIN AEROFOIL THEORY FOR MODERATELY THICK SWEPT AND TAPERED WINGS (KUCHEMANN AND WEBER)

The vortex distribution used in linearised thin aerofoil theory for camber lines at incidence together with the source distribution used to represent thickness effects, are used as the basis of a method to predict the pressure distribution Ref (4.3) over a moderately thick aerofoil section under 2-dimensional incompressible flow conditions. An additional vortex distribution is necessary to allow for the effect of thickness, so that it is the surface velocity which should be calculated not the chordwise velocity increment.

Also due to the effect of slope of the aerofoil surface, particularly near a rounded leading edge, it is necessary to use the Weber

$$\text{factor} \quad \sqrt{\frac{1}{\left[1 + \left(\frac{dy_c}{dx} \pm \frac{dy_t}{dx}\right)^2\right]}}$$

to convert total chordwise velocity to surface velocity, and then to use a full Bernoulli's expression to calculate the Cp distribution as follows:

$$Cp = 1 - \left[\frac{V_{surface}}{U}\right]^2 \qquad \text{..... (4.22)}$$

where U is the undisturbed velocity, and $y_t(x)$ is the thickness distribution.

With wing sweep and taper, three dimensional effects are introduced so that the final expression obtained by Kuchemann and Weber (Ref·(4.3)) for surface velocity in incompressible flow is

$$\left[\frac{V_{surface}}{U}\right]^2 = \left\{\cos\alpha_e \left[1+f_1+f_2\right] D\left(\frac{U}{\ell}\right)^{-\frac{1}{2}} \pm \left[f_3 \cos\alpha_e + f_4 \sin\alpha_e\right] D\left(\frac{U}{\ell}\right)^{-n^*}\right\}^2$$

$$+ \left\{g_1 \cos\alpha_e D\left(\frac{U}{\ell}\right)^{-\frac{1}{2}} \pm \left[g_3 \cos\alpha_e + g_4 \sin\alpha_e\right] D\left(\frac{U}{\ell}\right)^{-n^*}\right\}$$

$$- h_1 \cos^2\alpha_e \left\{1 - D\left(\frac{U}{\ell}\right)^{-1}\right\} \qquad \text{..... (4.23)}$$

where

$$D\binom{u}{\ell} = 1 + \left[\left\{ \frac{dy_c}{dx} \pm \frac{dy_t}{dx} \right\} / \mathrm{Cos}\Lambda \right]^2 \qquad \ldots\ldots\ (4.24)$$

is the Weber factor, and α_e is the effective incidence of the section given by $\alpha_e = \alpha - \alpha_i$, where the induced incidence α_i is due to the trailing vortex distribution.

If wing thickness effects are small and the Cp values are required over that portion of the wing not too close to the centre section or tips, equation (4.23) may be simplified by writing

$f_1 = 0$ (a thickness term)

$f_2 = 0$ (a centre section thickness term)

$$f_3 = \mathrm{Cos}\Lambda . \frac{1}{\pi} . \sqrt{\frac{1-x/c}{x/c}} \int_0^c \frac{dy_c}{d\xi} \left(\frac{\xi/c}{1-\xi/c} \right)^{\frac{1}{2}} \frac{d\xi}{(x-\xi)}$$

$$f_4 = \mathrm{Cos}\Lambda \left(\frac{1-x/c}{x/c} \right)^{\frac{1}{2}}$$

$g_1 = 0$ (a thickness term)

$$g_3 = -\ \mathrm{Sin}\Lambda . \frac{1}{\pi} \left(\frac{1-x/c}{x/c} \right)^{\frac{1}{2}} \int_0^c \frac{dy_c}{d\xi} \left(\frac{\xi/c}{1-\xi/c} \right)^{\frac{1}{2}} \frac{d\xi}{(x-\xi)}$$

$$g_4 = -\sin\Lambda\cdot\left(\frac{1-x/c}{x/c}\right)^{\frac{1}{2}}$$

$$n^* = \tfrac{1}{2}$$

$h_1 = 0$ (a correction to the spanwise velocity term due to the thickness term g_1)

Thus for small incidence and camber

$$1-\left(\frac{V_{surface}}{U}\right)^2 = 1-\left\{1 \pm \cos\Lambda\left[\alpha_e\sqrt{\frac{1-x/c}{x/c}}+\frac{1}{\pi}\sqrt{\frac{1-x/c}{x/c}}\int_0^c\frac{dy_c}{d\xi}\sqrt{\frac{\xi/c}{1-\xi/c}}\frac{d\xi}{(x-\xi)}\right]\right\}^2$$

$$/D(\tfrac{U}{\ell}) - \left\{\sin\Lambda\left[\alpha_e\sqrt{\frac{1-x/c}{x/c}}+\frac{1}{\pi}\sqrt{\frac{1-x/c}{x/c}}\int_0^c\frac{dy_c}{d\xi}\sqrt{\frac{\xi/c}{1-\xi/c}}\frac{d\xi}{(x-\xi)}\right]\right\}^2/D(\tfrac{U}{\ell})$$

:..... (4.25)

and if $D(\frac{U}{\ell})$ has values which are appreciably different from 1 only where $\frac{dy_t}{dx}$ is significant, then we obtain the result

$$\Delta Cp = \frac{4\cos\Lambda}{\left[1+\left(\frac{dy_c}{dx}\right)^2/\cos\Lambda\right]}\cdot\left[\alpha_e\sqrt{\frac{1-x/c}{x/c}}+\frac{1}{\pi}\sqrt{\frac{1-x/c}{x/c}}\int_0^c\frac{dy_c}{d\xi}\sqrt{\frac{\xi/c}{1-\xi/c}}\frac{d\xi}{(x-\xi)}\right]$$

:..... (4.26)

which is equation (4.24), the 2-dimensional thin aerofoil result,

multiplied by the factor $\dfrac{\cos\Lambda}{\left[1+\left(\frac{dy_c}{dx}\right)^2/\cos\Lambda\right]}$

Now over the rest of the aerofoil chord $\left(\frac{dy_c}{dx}\right)^2/\cos\Lambda$ will be negligible so that a fairly accurate value of section lift coefficient will be obtained from the following formula

$$C_L = 2\pi\left(A_0' + \frac{1}{2}A_1'\right) \qquad \text{..... (4.27)}$$

$$\text{where } \Delta Cp = 4\left\{A_0' \cot\frac{1}{2}\theta + \sum_{n=1}^{\infty} A_n'.\sin n\theta\right\} \qquad \text{..... (4.28)}$$

and $$A_0' = \left\{\alpha_e - \frac{1}{\pi}\int_0^{\pi}\frac{dy_c}{dx}\,d\theta\right\}\cos\Lambda$$

$$A_n' = \left\{\frac{2}{\pi}\int_0^{\pi}\frac{dy_c}{dx}\cos n\theta.d\theta\right\}\cos\Lambda$$

(where n = 1, 2, 3, ---)

4.7 FITTING OF CHORDWISE LOADING CURVES TO MEASURE VALUES OF ΔCp

For a general parabolic camber line of maximum camber λ_c, the camber line equation is

$$y_c = 4\lambda \frac{x}{c}\left(1 - \frac{x}{c}\right)$$

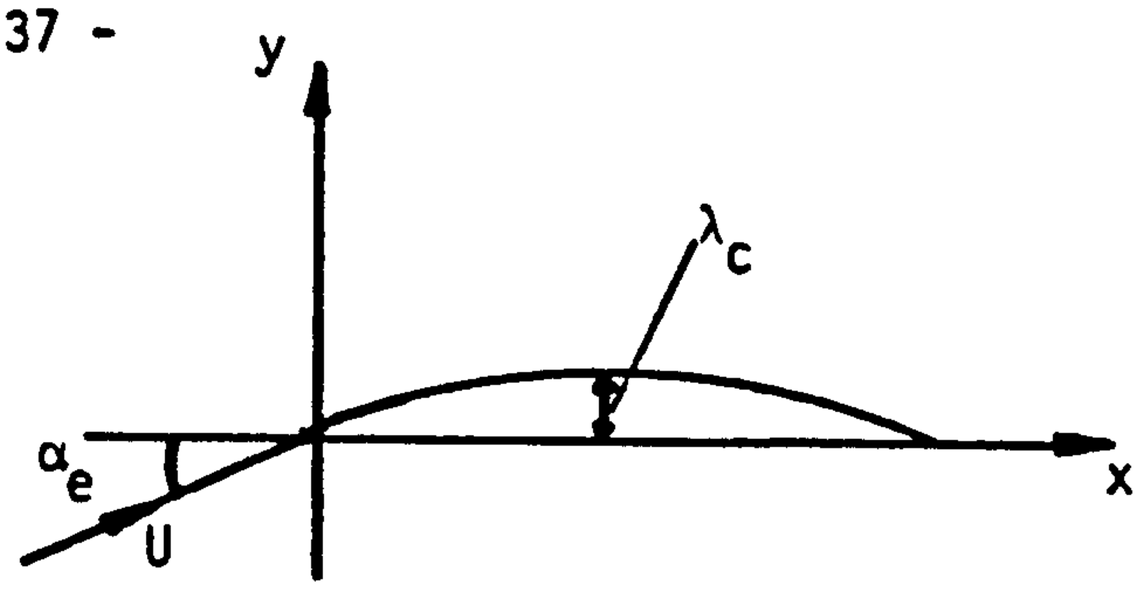

and the Glauert coefficients

A_0', A_1', A_2' --- etc. have the values $A_0' = \alpha_e.\text{Cos}\Lambda$,

$A_1' = 4\lambda.\text{Cos}\Lambda$, $A_2' = A_3' = A_4' = \text{------} = 0$

If the values of ΔCp are formed from experiment at four locations $\frac{x}{c} = \frac{3}{16}, \frac{7}{16}, \frac{11}{16}, \frac{15}{16}$, then we can fit the pressure difference distribution into a curve of the following form:

$$\Delta Cp = 4\left(A_0' \text{Cot}\frac{1}{2}\theta + \sum_{n=1}^{\infty} A_n'.\text{Sin}n\theta\right) \qquad \text{.....} \quad (4.29)$$

$$= 4\left(A_0'.\text{Cot}\frac{1}{2}\theta + A_1' \text{Sin}\theta\right)$$

for a general parabolic camber line through the 4 points, which will correspond to

$$\text{Cos}\theta_1 = \frac{5}{8}, \quad \text{Cos}\theta_2 = \frac{1}{8}, \quad \text{Cos}\theta_3 = -\frac{3}{8}, \quad \text{Cos}\theta_4 = -\frac{7}{8}$$

Now a least squares fit can be used for values of A_0' and A_1'. The least squares values of A_0' and A_1' will be found by minimising the following expressions by using the equation (4.29):

$$S = \sum_{i=1}^{4}\left\{\Delta Cp_i - 4\left(A_0' \text{Cot}\frac{1}{2}\theta_i + A_1' \text{Sin}\theta_i\right)\right\}^2 \qquad \text{.....} \quad (4.30)$$

This minimum will occur when $\frac{\partial s}{\partial A_0'} = \frac{\partial s}{\partial A_1'} = 0$

i.e. when

$$\begin{cases} A_0' \sum_{i=1}^{4} \mathrm{Cot}^2 \frac{1}{2}\theta_i + A_1' \sum_{i=1}^{4} \mathrm{Cot} \frac{1}{2}\theta_i \, \mathrm{Sin}\theta_i = \frac{1}{4} \sum_{i=1}^{4} \Delta Cp_i \, \mathrm{Cot} \frac{1}{2}\theta_i & \vdots \ldots\ldots (4.31) \\ A_0' \sum_{i=1}^{4} \mathrm{Cot} \frac{1}{2}\theta_i \, \mathrm{Sin}\theta_i + A_1' \sum_{i=1}^{4} \mathrm{Sin}^2\theta_i = \frac{1}{4} \sum_{i=1}^{4} \Delta Cp_i \, \mathrm{Sin}\theta_i & \vdots \ldots\ldots (4.32) \end{cases}$$

Solution of the above equations can be determined by matrix analysis by solving the two simultaneous equation. The solution is as follows:

$$A_0' = \frac{1}{4} \begin{bmatrix} S_{11} & S_{12} \\ S_{21} & S_{22} \end{bmatrix} / \Delta$$

$$A_1' = -\frac{1}{4} \begin{bmatrix} S_{11} & S_{12}' \\ S_{21} & S_{22}' \end{bmatrix} / \Delta$$

where
$$\Delta = \begin{bmatrix} S'_{12} & S_{12} \\ S'_{22} & S_{22} \end{bmatrix} ,$$

and
$$S_{11} = \sum_{i=1}^{4} \Delta Cp_i . \mathrm{Cot}\, \frac{1}{2}\, \theta_i \quad ,$$

$$S_{12} = \sum_{i=1}^{4} \mathrm{Cot}\, \frac{1}{2}\, \theta_i . \mathrm{Sin}\theta_i \quad ,$$

$$S_{21} = \sum_{i=1}^{4} \Delta Cp_i . \mathrm{Sin}\theta_i \quad ,$$

$$S_{22} = \sum_{i=1}^{4} \mathrm{Sin}^2\theta_i \quad ,$$

$$S'_{12} = \sum_{i=1}^{4} \mathrm{Cot}^2\, \frac{1}{2}\, \theta_i \quad ,$$

$$S'_{22} = \sum_{i=1}^{4} \mathrm{Cot}\, \frac{1}{2}\, \theta_i . \mathrm{Sin}\theta_i \quad .$$

Now using the values of A'_0 and A'_1, we can evaluate the lift coefficient as follows:

$$C_L = 2\pi \left(A'_0 + \frac{1}{2} A'\right) \qquad \text{..... (4.33)}$$

Therefore

$$C_L = \frac{\pi}{4\Delta}\left\{\sum_{i=1}^{4}\Delta Cp_i \ \mathrm{Cot}\,\frac{1}{2}\,\theta_i \ \left(2\sum_{i=1}^{4}\mathrm{Sin}^2\theta_i - \sum_{i=1}^{4}\mathrm{Cot}\,\frac{1}{2}\,\theta_i \ \mathrm{Sin}\theta_i\right)\right.$$

$$\left. + \sum_{i=1}^{4}\Delta Cp_i.\mathrm{Sin}\theta_i \ \left(-2\sum_{i=1}^{4}\mathrm{Cot}\,\frac{1}{2}\,\theta_i.\mathrm{Sin}\theta_i + \sum_{i=1}^{4}\mathrm{Cot}^2\frac{1}{2}\,\theta_i\right)\right\}$$

$$\vdots \ldots\ldots \quad (4.34)$$

All the summations in the equation (4.34) are calculated and tabulated in Table (4.6). Using values from this table, equation (4.34) can be modified as follows:

$$C_L = \frac{385 \times \pi}{4 \times 1637}\sum_{i=1}^{4}\Delta Cp_i\left\{\frac{15}{8}\,\mathrm{Cot}\,\frac{1}{2}\,\theta_i - \frac{331}{385}\,\mathrm{Sin}\theta_i\right\},$$

or

$$C_L = 0.596996\ \Delta Cp_1 + 0.235152\ \Delta Cp_2 + 0.086285\ \Delta Cp_3$$

$$+ 0.012543\ \Delta Cp_4$$

$$\vdots \ldots\ldots \quad (4.35)$$

where ΔCp_i is the static pressure difference between the top surface and lower surface taken from the experimental wind tunnel tests.

This equation gives a general parabolic camber line fit to measured ΔCp's.

REFERENCES FOR CHAPTER 4

(4.1) SAWYER, R.A. "Thin wing theory" M.Sc. Unit in Computation Methods and Fluid Mechanics. Department of Mathematics and Mechanical Eng., Salford University, April 1974.

(4.2) HOUGHTON, E.L. "Aerodynamics for Engineering Students". Edward Arnold Ltd., 1970.

(4.3) KUCHEMANN D AND WEBER, J. "Method for predicting the pressure distribution on swept wings with subsonic attached flow". R. Ae. S.T.D.M. 6312, 1963.

TABLE (4.1)

NACA 64A210

Slope of Radius through L.E = 0.095

L.E. Radius = 0.687

T.E. Radius = 0.023

(STATIONS AND ORDINATES GIVEN IN PER CENT OF AEROFOIL CHORD)

UPPER SURFACE		LOWER SURFACE	
STATION $\frac{x}{c}\%$	ORDINATE $\frac{y}{c}\%$	STATION $\frac{x}{c}\%$	ORDINATE $\frac{y}{x}\%$
0	0	0	0
0.424	0.856	0.576	-0.744
0.665	1.044	0.835	-0.886
1.153	1.342	1.347	-1.100
2.387	1.895	2.613	-1.473
4.874	2.685	5.126	-1.963
7.369	3.288	7.631	-2.316
9.868	3.792	10.132	-2.60
14.874	4.592	15.126	-3.030
19.885	5.200	20.115	-3.340
24.900	5.656	25.100	-3.554
29.917	5.984	30.083	-3.688
34.935	6.192	35.065	-3.744
39.955	6.274	40.045	-3.716
44.975	6.208	45.025	-3.580
49.994	6.014	50.006	-3.354
55.012	5.714	54.988	-3.062
60.028	5.323	59.972	-2.719
65.042	4.852	64.958	-2.342
70.054	4.310	69.946	-1.944
75.063	3.702	74.937	-1.542
80.076	3.037	79.924	-1.167
85.074	2.301	84.926	-0.859
90.052	1.551	89.948	-0.571
95.027	0.785	94.974	-0.295
100.00	0.021	100.00	-0.021

TABLE (4.2)

NEW GEOMETRY OF THE WING AEROFOIL SECTION, CAMBER LINE AND THICKNESS FUNCTION AT 0.0^{o} SWEEP

$$\frac{Y_s}{C_s} = \frac{Y}{C}\left\{1.018 - 0.0202\,\frac{x}{c}\right\}$$

STATION NO.	UPPER SURFACE % $\frac{Y_s}{C_s}$	LOWER SURFACE % $\frac{Y_s}{C_s}$	CAMBER LINE % $\frac{(Y_U + Y_L)}{2}/C$	THICKNESS FUNCTION % $\frac{(Y_U - Y_L)}{2}/C$
1	0.0	0.0	0.0	0.0
2	0.871	-0.76	0.056	0.816
3	1.93	-1.499	0.216	1.715
4	3.85	-2.64	0.61	3.25
5	5.27	-3.386	0.942	4.33
6	5.73	-3.60	1.065	4.67
7	6.26	-3.79	1.235	5.03
8	6.263	-3.61	1.327	4.94
9	6.06	-3.38	1.34	4.72
10	5.35	-2.73	1.31	4.04
11	4.33	-1.95	1.19	3.14
12	3.04	-1.17	0.935	2.105
13	2.3	-0.86	0.72	1.58
14	0.784	-0.29	0.25	0.54
15	0.021	-0.021	0.0	0.021

TABLE (4.3)

NEW GEOMETRY OF THE WING AEROFOIL SECTION, CAMBER LINE, AND THICKNESS FUNCTION AT 12.5° OF SWEEP

$$\left\{\frac{Y_s}{C_s} = \frac{Y}{C}\left[1.041 - 0.08232\,\frac{x}{c}\right]\right\}$$

STATION No.	UPPER SURFACE % $\frac{Y_s}{C_s}$	LOWER SURFACE % $\frac{Y_s}{C_s}$	CAMBER LINE % $\frac{(Y_U + Y_L)}{2}/C$	THICKNESS FUNCTION % $\frac{(Y_U - Y_L)}{2}/C$
1	0.0	0.0	0.0	0.0
2	0.891	-0.77	0.061	0.831
3	1.97	-1.53	0.22	1.75
4	3.92	-2.69	0.615	3.31
5	5.33	-3.42	0.96	4.38
6	5.77	-3.63	1.07	4.70
7	6.27	-3.79	1.24	5.03
8	6.23	-3.59	1.32	4.91
9	6.01	-3.35	1.33	4.68
10	5.28	-2.69	1.295	3.99
11	4.24	-1.91	1.165	3.08
12	2.96	-1.14	0.91	2.05
13	2.23	-0.83	0.70	1.53
14	0.756	-0.28	0.238	0.52
15	0.02	-0.02	0.0	0.02

TABLE (4.4)

NEW GEOMETRY OF THE WING AEROFOIL SECTION, CAMBER LINE, THICKNESS FUNCTION AT 32.5° OF SWEEP

$$\left[\frac{Y_s}{C_s} = \frac{Y}{C} \{0.976 - 0.1722 \frac{X}{C}\} \right]$$

STATION No.	UPPER SURFACE % Y_s $\left(\frac{Y_s}{C}\right)$	LOWER SURFACE % Y_s $\left(\frac{Y_s}{C}\right)$	CAMBER % LINE $\frac{(Y_U + Y_L)}{2C}$	THICKNESS % FUNCTION $\frac{(Y_U - Y_L)}{2C}$
1	0.0	-0.0	0.0	0.0
2	0.8348	-0.7254	0.053	0.783
3	1.8417	-1.431	0.205	1.6364
4	3.637	-2.49	0.57	3.06
5	4.89	-3.14	0.875	4.02
6	5.27	-3.32	0.975	4.30
7	5.67	-3.43	1.12	4.55
8	5.58	-3.22	1.175	4.4
9	5.35	-2.98	1.18	4.165
10	4.65	-2.37	1.14	3.51
11	3.69	-1.66	1.01	2.65
12	2.55	-0.97	0.79	1.745
13	1.910	-0.705	0.607	1.31
14	0.63	-0.24	0.195	0.44
15	0.017	-0.017	0.0	0.017

TABLE (4.5)

GEOMETRY OF THE WING AEROFOIL SECTION, CAMBER LINE, THICKNESS FUNCTION AT 52.5° SWEEP

$$\left\{\frac{Y_s}{C_s} = \frac{Y}{c}\left[0.793 - 0.2414\,\frac{x}{c}\right]\right\}$$

STATION No	UPPER % SURFACE $\left(\frac{Y_U}{C}\right)$	LOWER % SURFACE $\left(\frac{Y_L}{C}\right)$	CAMBER % LINE $\frac{(Y_U + Y_L)}{2C}$	THICKNESS % FUNCTION $\frac{(Y_U - Y_L)}{2C}$
1	0.0	0.0	0.0	0.0
2	0.68	-0.590	0.045	0.635
3	1.492	-1.160	0.166	1.326
4	2.92	-1.998	0.461	2.459
5	3.87	-2.49	0.69	3.18
6	4.15	-2.603	0.774	3.38
7	4.39	-2.65	0.87	3.52
8	4.25	-2.45	0.9	3.35
9	4.04	-2.26	0.89	3.15
10	3.45	-1.76	0.845	2.605
11	2.69	-1.21	0.74	1.95
12	1.82	-0.70	0.56	1.26
13	1.35	-0.505	0.423	0.928
14	0.44	-0.17	0.135	0.305
15	0.012	-0.012	0.0	0.012

TABLE (4.6)

i	1	2	3	4	$\sum_{i=1}^{4}$
$\cos\theta_i$	$\frac{5}{8}$	$\frac{1}{8}$	$\frac{-3}{8}$	$\frac{-7}{8}$	—
$\cot\frac{1}{2}\theta_i$	$\sqrt{\frac{13}{3}}$	$\frac{3}{\sqrt{7}}$	$\sqrt{\frac{5}{11}}$	$\frac{1}{\sqrt{15}}$	—
$\sin\theta_i$	$\frac{\sqrt{39}}{8}$	$\frac{\sqrt{63}}{8}$	$\frac{\sqrt{55}}{8}$	$\frac{\sqrt{15}}{8}$	—
$\cot^2\frac{1}{2}\theta_i$	$\frac{13}{3}$	$\frac{9}{7}$	$\frac{5}{11}$	$\frac{1}{15}$	$\frac{2364}{385}$
$\cot\frac{1}{2}\theta_i \sin\theta_i$	$\frac{13}{8}$	$\frac{9}{8}$	$\frac{3}{8}$	$\frac{1}{8}$	$\frac{7}{2}$
$\sin^2\theta_i$	$\frac{39}{64}$	$\frac{63}{64}$	$\frac{55}{64}$	$\frac{15}{64}$	$\frac{43}{16}$

$$\Delta = \frac{2364}{385} \times \frac{43}{16} - \frac{49}{4} = \frac{1637}{385}$$

$$\Delta = \frac{1637}{385}$$

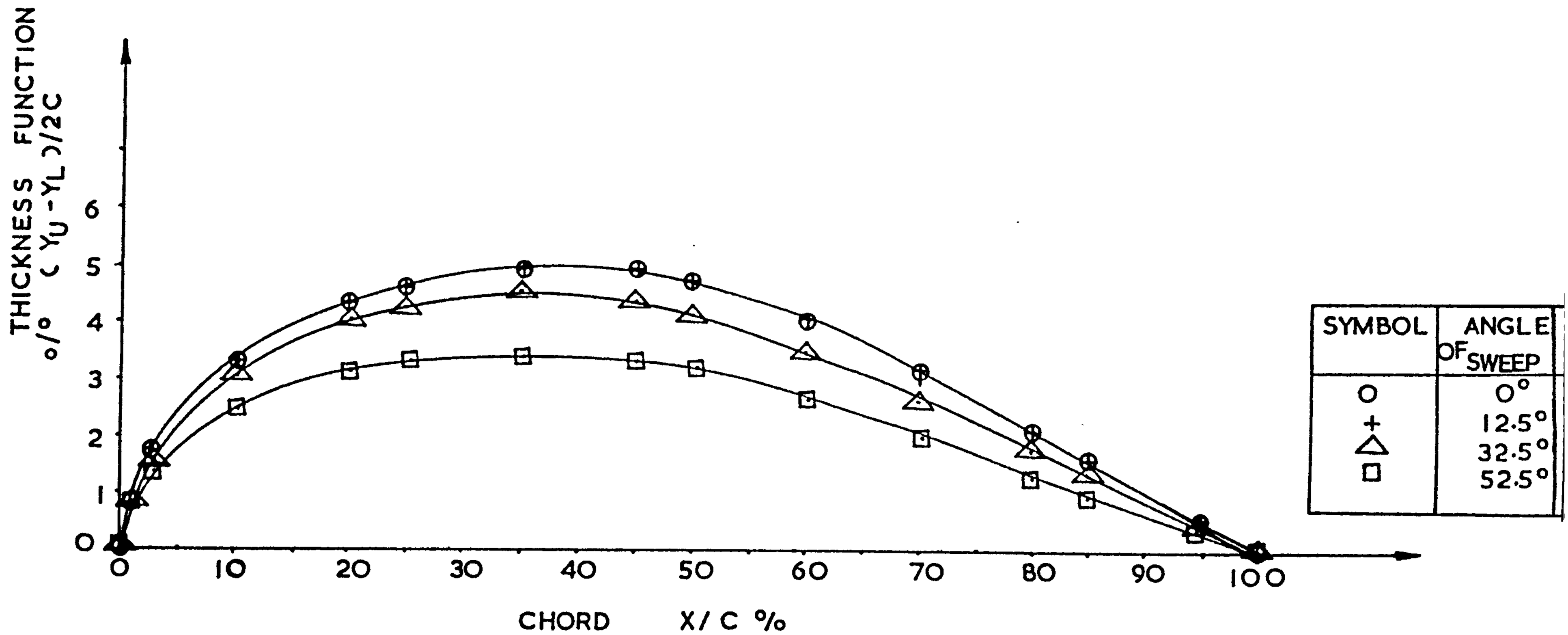

FIG. (4.1) GRAPH OF THICKNESS FUNCTION FOR THE WING AEROFOIL

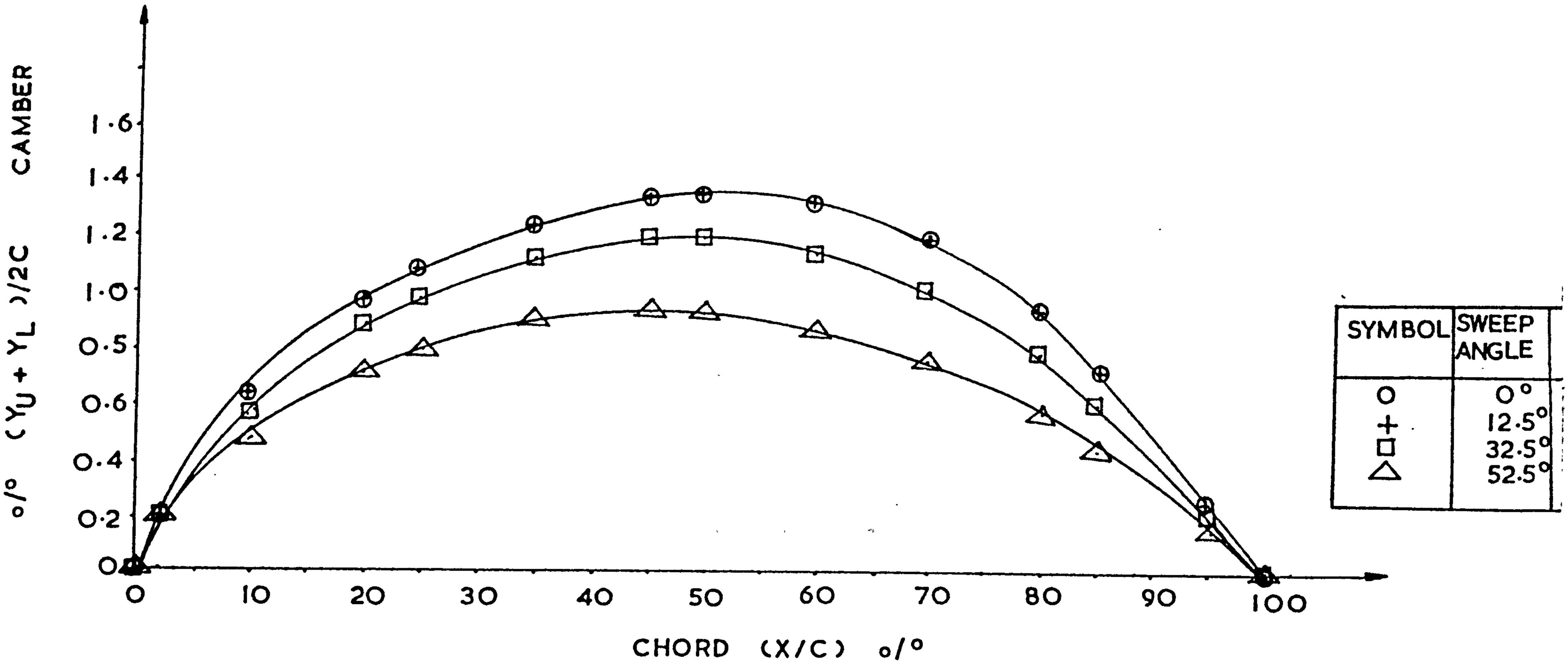

FIG·(4.2) GRAPH OF CAMBER LINE DISTRIBUTION FOR THE WING AEROFOIL

CHAPTER 5

SUPERSONIC INVESTIGATION ANALYSIS OF FLOW OVER AN ARBITRARY WING CONFIGURATION

5.1 INTRODUCTION

This work involves writing a general program which performs a numerical integration to solve the integral equation for a wing of any planform. This is done by expressing the downwash as a summation of the potential over the area of the wing in the Mach forecone for linearised, steady supersonic flow. Hence, once the potential has been obtained, the pressure coefficient distribution, and the lift coefficient, pitching moment coefficient etc. can be found. In the next chapter a method is used to calculate interference due to the body and wing using a modification of this wing procedure.

There are various computational methods for evaluating the pressure coefficient distribution on a wing in supersonic flow.

1) Richardson's collocation method (ARC R & M 3157)
2) Integrated Downwash method
3) Integrated Potential method (ARC R & M 3415)

The first method has the disadvantage that it does not cater for kinks in the leading edge. The second method has the disadvantage that you have to calculate the downwash over certain regions forward of the leading edge, consequently for certain Mach numbers it takes a long time to compute and will require a large storage space in the computer.

The third method (written by D.J. Allen and D.S. Sadler for oscillating flow problems) is the one used in this chapter (but evaluated for steady flow only). It uses the equation which gives the downwash at any point as an integral which involves the potential summed over the Mach fore-cone of the point concerned. Forward of the leading edge, the potential is zero so that the integration only uses values of the potential on the planform (except for the wake region) which makes it superior to method (2) both as regards speed and the storage space required.

This is done by constructing a characteristic mesh and determining the potential for the most upstream rhombus first. Consecutive potentials can be then determined by working down each row of characteristics, as each potential is dependent on the potentials upstream in its fore-cone. It is necessary to determine each potential very accurately, because if one potential has a slight error, it produces further errors downstream of that point.

In this case the mesh was arranged in a way that all the rhombuses were coded in R and S direction and corner points of each element were numbered. All the details of numerical analysis are described in the later sections of this chapter.

5.2 PRESSURE WAVES IN SUBSONIC-SUPERSONIC FLOW

In a subsonic flow a small pressure disturbance moving at some speed produces a pressure wave that will propogate throughout the

region of flow. Applied to an aerofoil this principle means that a pressure wave is advancing ahead of the wing and in accordance with the gas laws the streamlines of the air begin to diverge and position themselves in readiness for the wing. Obviously the faster the rate of flow, the smaller is the distance that the pressure waves can advance ahead of the wing in a given time and the shorter the time available for the air ahead to change its direction of flow. See FIG. (5.1), (a,b).

When the flow is supersonic, small pressure disturbances have their areas of influence restricted since they cannot advance ahead of the cause of the disturbance. The exact region of influence is dependent on the size of the disturbance and the speed of flow. A very small disturbance producing corresponding small pressure waves travelling at sonic velocity in a supersonic flow of M = 2.0 would produce the pattern shown in FIG . (5.1) (e).

If the cause of the disturbance was larger the wave pressure amplitude would be larger and the velocity of propagation (a´) would be correspondingly greater than local sonic speed (a). In this case the Mach wave would set itself at a larger angle, and since the Mach wave is a pressure wave of finite amplitude then it is a surface of sudden pressure discontinuity, in other words a shock wave. Therefore the Mach cone angle μ can be represented as:

$$M = \frac{u}{a} = \frac{1}{\sin\mu} \qquad \text{..... (5.1)}$$

5.3 INTEGRAL EQUATIONS FOR A NUMERICAL MODEL

5.3.1 EQUATIONS OF FLOW

Assuming an invicid flow condition, then Euler's equations for 3-D flow are:

$$u \frac{\partial u}{\partial x} + v \frac{\partial u}{\partial z} + w \frac{\partial u}{\partial z} = - \frac{1}{\rho} \frac{\partial p}{\partial x} \qquad \text{..... (5.2)}$$

$$u \frac{\partial v}{\partial x} + v \frac{\partial v}{\partial y} + w \frac{\partial v}{\partial z} - \frac{1}{\rho} \frac{\partial p}{\partial y} \qquad \text{..... (5.3)}$$

$$u \frac{\partial w}{\partial x} + v \frac{\partial w}{\partial y} + w \frac{\partial w}{\partial z} = - \frac{\partial p}{\rho \partial z} \qquad \text{..... (5.4)}$$

The continuity equation for a steady 3-D flow is:

$$\frac{\partial (u\rho)}{\partial x} + \frac{\partial (v\rho)}{\partial y} + \frac{\partial (w\rho)}{\partial z} = 0 \qquad \text{..... (5.5)}$$

Therefore for an irrotational flow case, we will have;

$$\frac{\partial u}{\partial y} = \frac{\partial v}{\partial x}, \quad \frac{\partial v}{\partial z} = \frac{\partial w}{\partial y}, \quad \frac{\partial u}{\partial z} = \frac{\partial w}{\partial x} \qquad \text{..... (5.6)}$$

For adiabatic flow we have

$P = K\rho^{\gamma}$, $\frac{\partial p}{\partial \rho} = a^2 = \frac{\gamma p}{\rho}$, where a is speed of sound.

For steady flow equation (5.5) for a 3-D becomes:

$$u\frac{\partial\rho}{\partial x} + v\frac{\partial\rho}{\partial y} + \rho\frac{\partial u}{\partial x} + \rho\frac{\partial v}{\partial y} + \boxed{w\frac{\partial\rho}{\partial z} + \rho\frac{\partial w}{\partial z}} = 0 \quad \ldots\ldots\ (5.7)$$

where

$$\frac{\partial\rho}{\partial x} = \frac{1}{a^2}\frac{\partial p}{\partial x} \text{ or } \frac{\partial\rho}{\partial y} = \frac{1}{a^2}\frac{\partial p}{\partial y} \text{ or } \frac{\partial\rho}{\partial z} = \frac{1}{a^2}\frac{\partial p}{\partial z}$$

Substituting these equations into (5.7) and simplify it as: (For simplicity and less work from this stage only 2-D flow analysis has been considered, that the same procedure can be applied to 3-D flow).

Therefore equation (5.7) for a 2-D flow is

$$\frac{u}{a^2}\frac{\partial p}{\partial x} + \frac{v}{a^2}\frac{\partial p}{\partial y} + \rho\frac{\partial u}{\partial x} + \rho\frac{\partial v}{\partial y} = 0 \quad \ldots\ldots\ (5.8)$$

where $\frac{\partial p}{\partial x}$ and $\frac{\partial p}{\partial y}$ can be substituted into equation (5.8) from equations (5.2), (5.3).

Cancelling ρ this gives

$$-\frac{u^2}{a^2}\frac{\partial u}{\partial x} - \frac{uv}{a^2}\frac{\partial u}{\partial y} - \frac{uv}{a^2}\frac{\partial v}{\partial x} - \frac{v^2}{a^2}\frac{\partial v}{\partial y} + \frac{\partial u}{\partial x} + \frac{\partial v}{\partial y} = 0$$

or, collecting like terms,

$$(1 - \frac{u^2}{a^2}) \frac{\partial u}{\partial x} - \frac{uv}{a^2} (\frac{\partial v}{\partial x} + \frac{\partial u}{\partial y}) + (1 - \frac{v^2}{a^2}) \frac{\partial v}{\partial y} = 0 \quad ..... (5.9)$$

For an irrotational case substitute equations (5.6) into (5.9) giving:

$$(1 - \frac{u^2}{2}) \frac{\partial u}{\partial x} - \frac{2uv}{a^2} \frac{\partial u}{\partial y} + (1 - \frac{v^2}{a^2}) \frac{\partial v}{\partial y} = 0 \quad ..... (5.10)$$

Since $u = \frac{\partial \phi_1}{\partial x}$, $v = \frac{\partial \phi_1}{\partial y}$, $w = \frac{\partial \phi_1}{\partial z}$, where ϕ_1 is velocity potential, equation (5.10) partially becomes:

$$(1 - \frac{u^2}{a^2}) \frac{\partial^2 \phi_1}{\partial x^2} - \frac{2uv}{a^2} \frac{\partial^2 \phi_1}{\partial x \partial y} + (1 - \frac{v^2}{a^2}) \frac{\partial^2 \phi_1}{\partial y^2} = 0 \quad .... (5.11)$$

Finally the energy equation provides the relation between u, v and acoustic speed as follows:

$$\frac{u^2 + v^2}{2} + \frac{a^2}{\gamma - 1} = \text{const.}$$

or $$\left(\frac{\partial \phi_1}{\partial x}\right)^2 + \left(\frac{\partial \phi_1}{\partial y}\right)^2 + \frac{2}{\gamma - 1} a^2 = \text{const.}$$

The local velocity components u and v can be written

$$u = U_\infty + u' \quad , \quad v = v'$$

where u' and v' are small compared to the undisturbed stream

velocity, and are termed the perturbation velocities. This may be expressed non-dimensionally in the form

$$\frac{u'}{U_\infty} << 1 \ , \ \frac{v'}{U_\infty} << 1$$

Similarly, $\frac{\partial^2\phi}{\partial x^2} = \frac{\partial u'}{\partial x}$, $\frac{\partial^2\phi}{\partial y^2} = \frac{\partial v'}{\partial y}$ are small.

By neglecting the square terms which are very small quantities and knowing that $\phi_1 = \phi_\infty + \phi$, where ϕ is perturbation potential, the equation (5.11) becomes

$$(1 - M_\infty^2)\frac{\partial^2\phi}{\partial x^2} + \frac{\partial^2\phi}{\partial y^2} = \frac{M_\infty^2}{1-(1-\gamma)M_\infty^2\frac{u'}{U_\infty}}\left[(2+(\gamma-1)M_\infty^2)\frac{u'}{U_\infty}\frac{\partial^2\phi}{\partial x^2} + \frac{2v'}{U_\infty}\frac{\partial^2\phi}{\partial x\partial y}\right]$$

Therefore for a 3-D flow equation of flow for subsonic condition would become;

$$(1 - M_\infty^2)\frac{\partial^2\phi}{\partial x^2} + \frac{\partial^2\phi}{\partial y^2} + \frac{\partial^2\phi}{\partial z^2} = 0 \qquad \text{..... (5.12)}$$

or for supersonic case becomes:

$$(M_\infty^2 - 1)\frac{\partial^2\phi}{\partial x^2} - \frac{\partial^2\phi}{\partial y^2} - \frac{\partial^2\phi}{\partial z^2} = 0 \qquad \text{..... (5.13)}$$

5.3.2 DERIVATION OF BASIC INTEGRAL EQUATION

Following the development of Allen and Sadler, in the unsteady flow case the general equation for the pertubation potential may be non-dimensionalised by substituting $X = \frac{x}{L}$, $Y = \frac{y\beta}{L}$, and $Z = \frac{\beta z}{L}$, $T = \frac{ut}{L}$ where L is a reference length, and $\beta = (M^2-1)^{\frac{1}{2}}$ and $M = \frac{u}{a}$ (M is Mach No.)

Therefore the disturbance potential ϕ satisfies the equation

$$\frac{\partial^2\phi}{\partial t^2} + 2u\frac{\partial^2\phi}{\partial x\partial t} + u^2\frac{\partial^2\phi}{\partial x^2} = a^2\left\{\frac{\partial^2\phi}{\partial x^2} + \frac{\partial^2\phi}{\partial y^2} + \frac{\partial^2\phi}{\partial z^2}\right\}$$

or $$M^2\frac{\partial^2\phi}{\partial T^2} + 2\frac{M^2}{\beta^2}\frac{\partial^2\phi}{\partial x\partial T} = \frac{\partial^2\phi}{\partial y^2} + \frac{\partial^2\phi}{\partial z^2} - \frac{\partial^2\phi}{\partial x^2} \qquad \text{..... (5.14)}$$

For harmonic oscillations put $\phi = \phi_2 e^{i\omega t}$ and $\Phi = \phi_2 e^{i\frac{M^2\omega x}{U\beta^2}}$ giving

$$\frac{\partial^2\Phi}{\partial y^2} + \frac{\partial^2\Phi}{\partial z^2} - \frac{\partial^2\Phi}{\partial x^2} - K^2\Phi = 0 \quad \text{where} \quad K = \frac{\omega LM}{U\beta}$$

Assuming $L(\Phi) = -\frac{\partial^2\Phi}{\partial x^2} + \frac{\partial^2\Phi}{\partial y^2} + \frac{\partial^2\Phi}{\partial z^2} - K^2\Phi$

and let Ψ denote a particular solution of the above equation. Using the generalised Green's Theorem, gives the following integral relation between the required solution Φ and Ψ, namely

$$\iiint_V \left[\Psi L(\Phi) - \Phi L(\Psi)\right] d\tau = \iint_S \left[\Phi \frac{\partial\Psi}{\partial\nu} - \Psi \frac{\partial\Phi}{\partial\nu}\right] ds \quad \ldots\ldots (5.15)$$

The integral on the left is taken over the volume enclosed by the surface s excluding, however, any points of singularity which may be within the region. The integral on the right is taken over the external surface S and the surfaces enclosing the singularities. In equation (5.15), the symbol ν refers to the co-normal which has direction cosines $(-\ell,m,n)$, where ℓ,m,n are the direction cosines of the inward-drawn normal at any point of the surface. Therefore the operator can be given by

$$\frac{\partial}{\partial\nu} \equiv -\ell \frac{\partial}{\partial x} + m \frac{\partial}{\partial y} + n \frac{\partial}{\partial z} \quad \ldots\ldots\ldots (5.16)$$

The normal and the co-normal have the same projection on the $x = o$ plane.

Suitable particular solutions for Ψ are $\Psi_{n+1} = (x_o-x)\ f(q)\ g(\theta)$ where $q^2 = K^2\{(x_o-x)^2 - (y_o-y)^2 - (z_o-z)^2\}$, $\theta = (x_o-x)/\{(y_o-y)^2+(z_o-z)^2\}^{\frac{1}{2}}$ where, corresponding to $n = 0,1$

$$\left.\begin{aligned} \Psi_1 &= \frac{\sin q}{q}\log_e\{\theta+(\theta^2-1)^{\frac{1}{2}}\}, \\ \text{and}\quad \Psi_2 &= -\frac{(x_o-x)}{q}\frac{\partial}{\partial q}\left(\frac{\sin q}{q}\right)\left\{\log_e\left[\theta+(\theta^2-1)^{\frac{1}{2}}\right]-\frac{(\theta^2-1)^{\frac{1}{2}}}{\theta}\right\} \end{aligned}\right\} \quad \ldots (5.17)$$

Now apply equation (5.15) with the above elementary solutions to the volume V bounded by the Mach fore cone of the point P, the plane z = o, and the wave front generated by the wing leading edges, as shown in FIG (5.2)

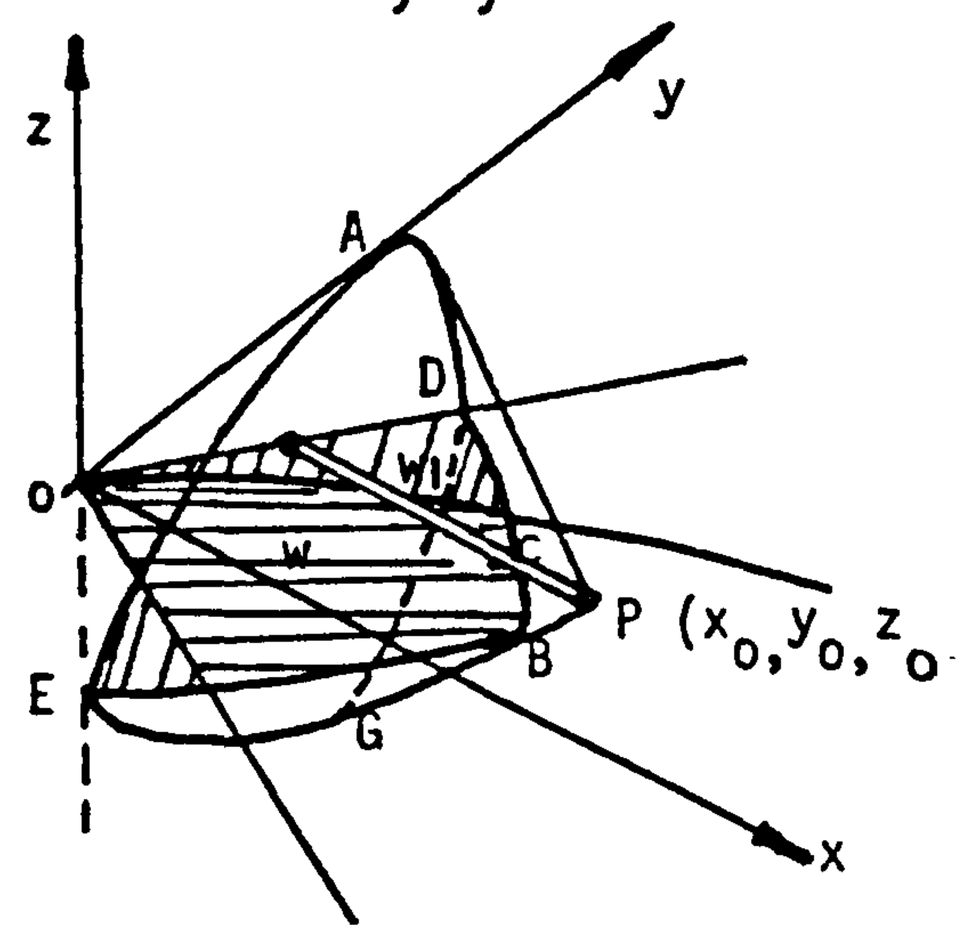

FIG (5.2)

It is necessary to exclude from V the volume enclosed by the cylinder C of small radius r and with axis through P parallel to the x axis.

Over the cylinder C, as $r = \{(y_o-y)^2 + (z_o-z)^2\}^{\frac{1}{2}} \to o$
if $\bar{x} = (x_o-x)$, then

$$\begin{cases} \Psi_1 \to -\dfrac{\sin(K\bar{x})}{K\bar{x}}\log_e r\ , \quad \dfrac{\partial\Phi_1}{\partial r} \to -\dfrac{\sin(K\bar{x})}{K\bar{x}}\cdot\dfrac{1}{r} \\[2ex] \Psi_2 \to -\dfrac{1}{K^2}\dfrac{\partial}{\partial x}\left\{\dfrac{\sin(K\bar{x})}{K\bar{x}}\right\}\log_e r\ , \quad \dfrac{\partial\Phi_2}{\partial r} \to -\dfrac{1}{K^2}\dfrac{\partial}{\partial x}\left\{\dfrac{\sin(K\bar{x})}{K\bar{x}}\right\}\dfrac{1}{r} \end{cases}$$

Thus in the limit $\iint_C \left\{ \Phi \frac{\partial \Psi_1}{\partial \nu} - \Psi \frac{\partial \Phi}{\partial \nu} \right\} ds \rightarrow -2\pi \int_{x_s}^{x_n} \Phi \frac{\sin K(x_o - x)}{K(x_o - x)} dx.$

where $x = x_s$ corresponds to the point of intersection of the axis of C with the wave front, with a related result for Ψ_2.

Over the surface of the fore cone from P, $\Psi_1 = \Psi_2 = 0 = \frac{\partial \Psi_1}{\partial \nu} = \frac{\partial \Psi_2}{\partial \nu}$ (since the co normals lie along the fore cone). Over the wave front $\Phi = \frac{\partial \Phi}{\partial \nu} = 0$.

Applying equation (5.15) to volumes GBDOE and PADOEB, and substracting the results using anti-symmetry of Φ with z at the wing w and continuity of Φ across the area w_1 outside the wing area, gives

$$\pi \int_{x_s}^{x_o} \Phi \frac{\sin[K(x_o - x)]}{K(x_o - x)} dx = \iint_W \Phi_W \frac{\partial \Psi_1}{\partial x} dxdy \qquad \text{..... (5.18)}$$

where $\Phi_W = \Phi\ (z=o)$

The corresponding results for Ψ_2 is

$$-\frac{\pi}{K^2} \int_{x_s}^{x_o} \Phi \frac{\partial}{\partial x_o} \left\{ \frac{\sin[K(x_o - x)]}{K(x_o - x)} \right\} dx = \iint_W \Phi_W \frac{\partial \Phi_2}{\partial x} dxdy \quad \text{.... (5.19)}$$

Then $\frac{\partial}{\partial x_o}$ (Equation 5.18) + K^2 (equation 5.19), gives

$$\pi\,\phi\,(x_0,y_0,z_0) = \iint_W \Phi_W \frac{\partial}{\partial z}\left\{\frac{\partial \Psi_1}{\partial x_0} + K^2\,\Psi_2\right\} dxdy$$

$$= \frac{-\partial}{\partial z_0}\left\{\iint_W \Phi_W \frac{\partial \Psi_1}{\partial x_0} + K^2\,\Psi_2\right\} dxdy$$

But $$\frac{\partial \Psi_1}{\partial x_0} + K^2\,\Psi_2 = \frac{\mathrm{Cos}\left\{K\left[(x_0-x)^2 - (y_0-y)^2 - (z_0-z)^2\right]^{\frac{1}{2}}\right\}}{\left[(x_0-x)^2 - (y_0-y)^2 - (z_0-z)^2\right]^{\frac{1}{2}}}$$

Therefore

$$\frac{\partial \Phi}{\partial z_0} = -\frac{1}{\pi}\,\frac{\partial^2}{\partial z_0^2}\left\{\iint_W \Phi_W \frac{\mathrm{Cos}\left[K(x_0-x)^2 - (y_0-y)^2 - (z_0-z)^2\right]^{\frac{1}{2}}}{\left[(x_0-x)^2 - (y_0-y)^2 - (z_0-z)^2\right]^{\frac{1}{2}}}\,dxdy\right\} \quad \ldots\ldots (5.20)$$

Substituting Φ in terms of ϕ and using the original coordinates gives

$$w(x,y) = \frac{\partial \phi}{\partial z}\bigg|_{z=0} = \mathrm{Lt}_{z\to 0}\left\{-\frac{1}{K}\,\frac{\partial^2}{\partial z^2}\iint_W \phi(\xi,\eta).A.B.d\eta.d\xi\right\} \quad \ldots\ldots (5.21)$$

$$w = \frac{\partial \phi}{\partial z}$$

where $A = \exp\left\{-\frac{iM^2.\omega(x-\xi)}{\beta^2.U}\right\}$

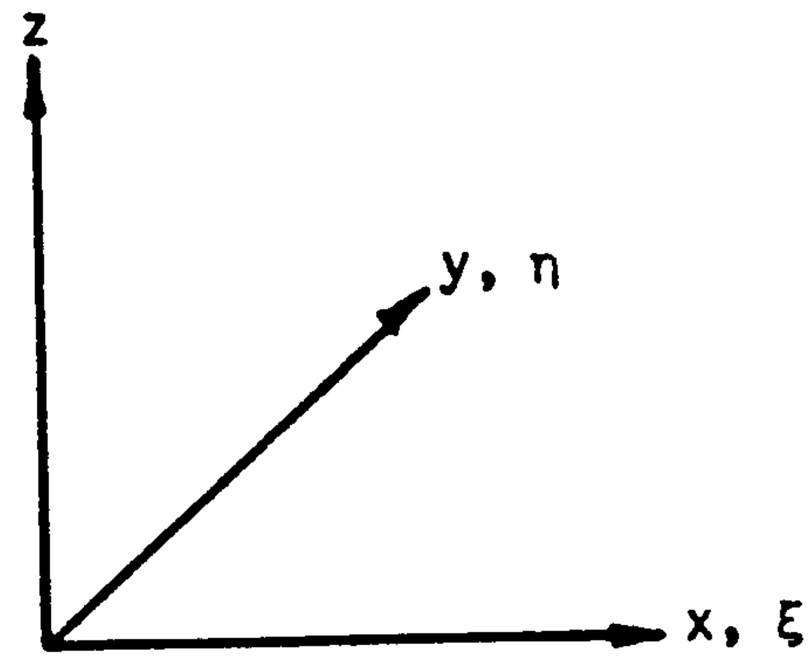

$$B = \cos\left(\frac{M\omega R}{\beta^2 U}\right)$$

$$R = \left[(x-\xi)^2 - \beta^2(y-\eta)^2 - \beta^2 z^2\right]^{\frac{1}{2}}$$

$$\beta = (M^2 - 1)^{\frac{1}{2}}$$

ϕ = velocity potential

ω = circular frequency of harmonic oscillation

S' is that part of the plane $z = o$ cut off by the cone $R = o$ for which $\xi < x$

M = free-stream Mach number

U = Free-stream velocity

5.4 BASIC INTEGRAL EQUATION FOR STEADY FLOW

Using the general basic integral equation (5.21), for a case of steady flow with a non-oscillatory assumption (i.e. $\omega = o$) would become

$$w(x,y) = \frac{\partial\phi}{\partial z} = -\frac{1}{\pi} \operatorname*{Lt}_{z\to o} \frac{\partial^2}{\partial z^2} \iint_{S'} \frac{\phi(\xi,\eta)}{R}\, d\xi d\eta$$

Substitute $\lambda = x - \xi$ and $\mu = y - \eta$ into the above equation

becomes:

$$w(x,y) = \frac{\beta^2}{\pi} \iint_{S'} \frac{\phi(\lambda,\mu)}{\left[\lambda^2 \ \beta^2\mu^2\right]^{3/2}} \, d\lambda d\mu \qquad \ldots\ldots\ (5.22)$$

But

$$w(x,y) = U \frac{\partial g}{\partial x} = - xU$$

where $z = g(x,y)$ is the equation of the lifting surface.

Changing coordinates to $\lambda = (\rho + \sigma) \frac{\ell\beta}{M}$, $\mu = (\rho-\sigma) \frac{\ell}{M}$, where ℓ is the side of a basic rhombus in the characteristic mesh, and writing $\phi' = \frac{\phi}{UL}$ where L is a reference length scale, and ϕ' is a non-dimensionalized velocity potential. Therefore the equation (5.22) can be simplified as follows:

$$\frac{\alpha \ \pi \ \ell}{M.L.} = \iint \frac{\phi'}{4(\rho\sigma)^{3/2}} \, d\rho d\sigma \ , \qquad \ldots\ldots\ (5.23)$$

where α is the angle of incidence.

Or equation (5.23) can be modified (Ref5.2). equations 23, 24) by using an interpolation functions over each Mach rhombus, becomes:

$$\frac{\alpha.\pi.\ell}{M.L} = \sum_{r=0} \sum_{s=0} (W_{r,s} \ \phi'_{r,s}) \qquad \ldots\ldots\ (5.24)$$

$$\text{or} \quad \phi'_{0,0} = \frac{1}{W_{0,0}} \left\{ \frac{\alpha.\pi.\ell}{M.L} - \sum_{(r,s\neq 0,0)} \Sigma\, W_{r,s}.\phi'_{r,s} \right\} \qquad \ldots\ldots (5.25)$$

where

$$W_{r,s} = \sum_{u=0}^{1} \sum_{v=0}^{1} \left[\sum_{i=0,\frac{1}{2},1} \sum_{j=0,\frac{1}{2},1} \lambda_{u,v}(i,j).G_i(r-u).G_j(s-v) \right]$$

$$\vdots \ldots\ldots (5.26)$$

($W_{r,s}$ are called the parabolic interpolation weights)

and where

$$G_i(r) = \int_0^1 \frac{g_i(\rho')}{2(\rho'+r)^{3/2}}\, d\rho' \quad \text{and} \quad \rho' = \rho - r$$

$$\sigma' = \sigma - s$$

$$\text{OR} \quad \left.\begin{aligned} g_0(\rho') &= 2\,(\rho'-\tfrac{1}{2})\,(\rho'-1) \\ g_{\frac{1}{2}}(\rho') &= -\,4\rho'\,(\rho'-1) \\ g_1(\rho') &= 2\rho'\,(\rho'-\tfrac{1}{2}) \end{aligned}\right\} \qquad \ldots\ldots (5.27)$$

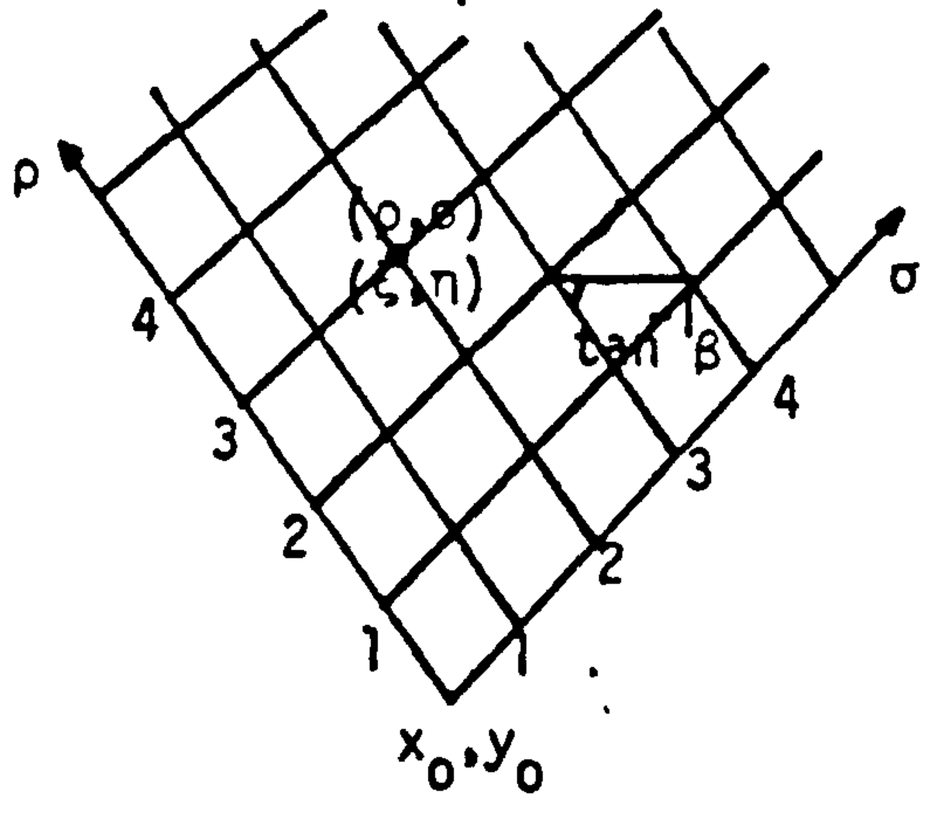

FIG (5.3)

$$\xi = x - \frac{\rho\ell\beta}{M} - \frac{\sigma\ell\beta}{M}$$

$$\eta = y - \frac{\rho\ell}{M} + \frac{\sigma\ell}{M}$$

$$\lambda = (\rho+\sigma)\,\frac{\ell\beta}{M}$$

$$\mu = (\rho-\sigma)\,\frac{\ell}{M}$$

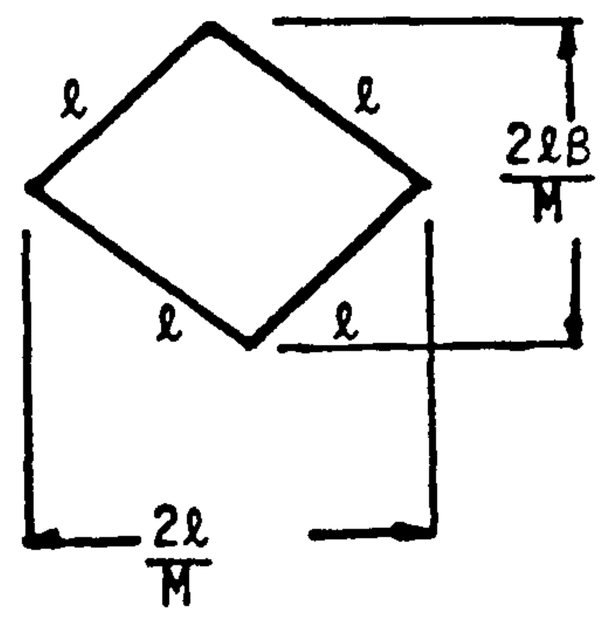

For numerical solution, the wing is divided into rhombic areas of side ℓ with edges parallel to the Mach direction.

Introducing characteristic coordinates ρ and σ having an origin at the pivotal point (x,y) as shown in FIG (5.3)

Therefore $\left|\frac{\partial(\lambda,\mu)}{\partial(\beta,\sigma)}\right| = \frac{2\ell^2\beta}{M^2}$

5.5 SOLUTION OF INTEGRAL EQUATION USING A CHARACTERISTIC MESH

If we assume only full rhombuses occur in the fore-cone of the pivotal point concerned, equation 5.23) becomes:

$$\iint \frac{\phi'}{4(\rho\sigma)^{3/2}} \cdot d\rho d\sigma = \sum_{r=o} \sum_{s=o} \int_r^{r+1} \int_s^{s+1} \frac{\phi'}{4(\rho\sigma)^{3/2}} \cdot d\rho d\sigma$$

Consider the contribution to the integral of the rhombus with base point (r,s), To make the integration possible some assumption has to be made about the variation of $\phi'(\rho,\sigma)$ over the rhombus.

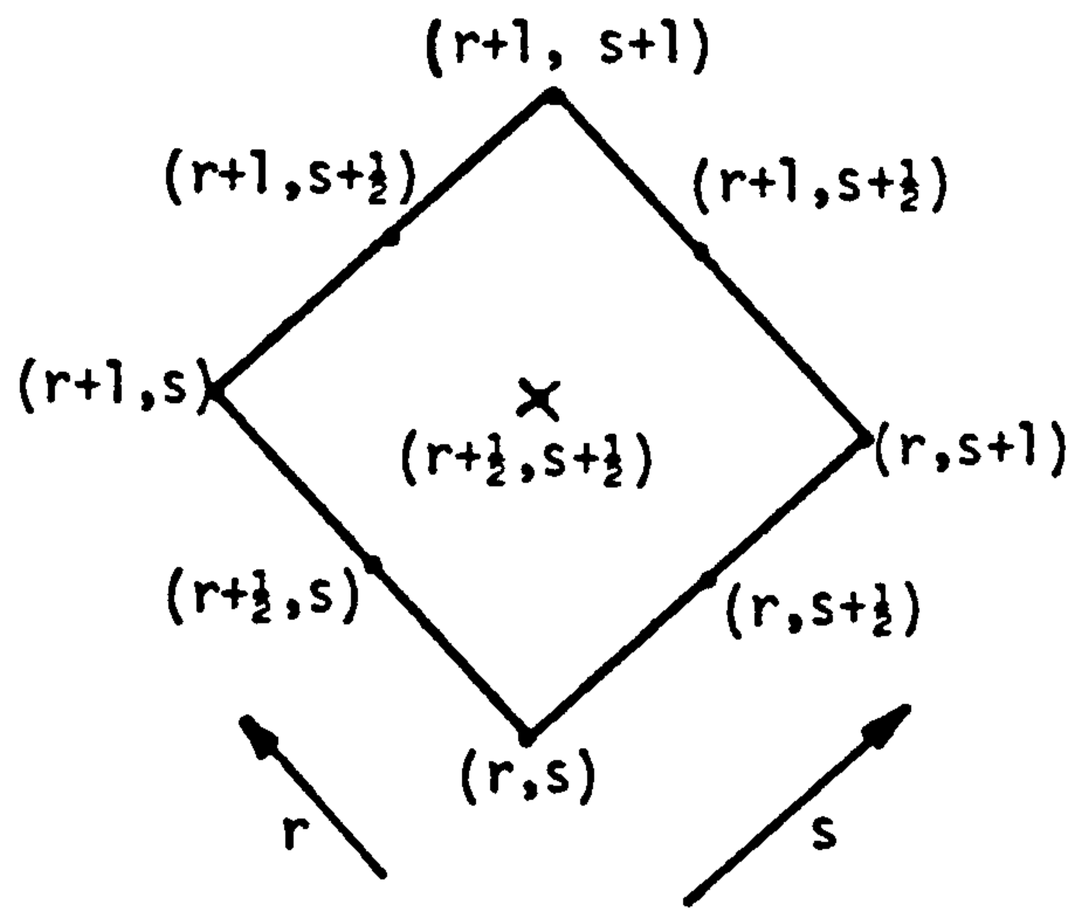

FIG (5.4)

Thus $\phi'(\rho,\sigma)$ can be represented as:

$$\phi'(\rho,\sigma) = \lambda_{00}(\rho',\sigma')\,\phi'_{r,s} + \lambda_{10}(\rho',\sigma')\,\phi_{r+1,s} + \lambda_{01}(\rho'\sigma')\,\phi_{r,s+1}$$

$$+ \lambda_{11}(\rho'\sigma')\,\phi_{r+1,s+1} \cdots\cdots \quad (5.27)$$

where $\rho' = \rho - r$, $\sigma' = \sigma - s$,

and $\lambda_{uv}(\rho',\sigma')$ is an interpolation function such that $\lambda_{uv}(\rho',\sigma') = 1$ at the vertex and equals zero at the other vertices of the rhombus.

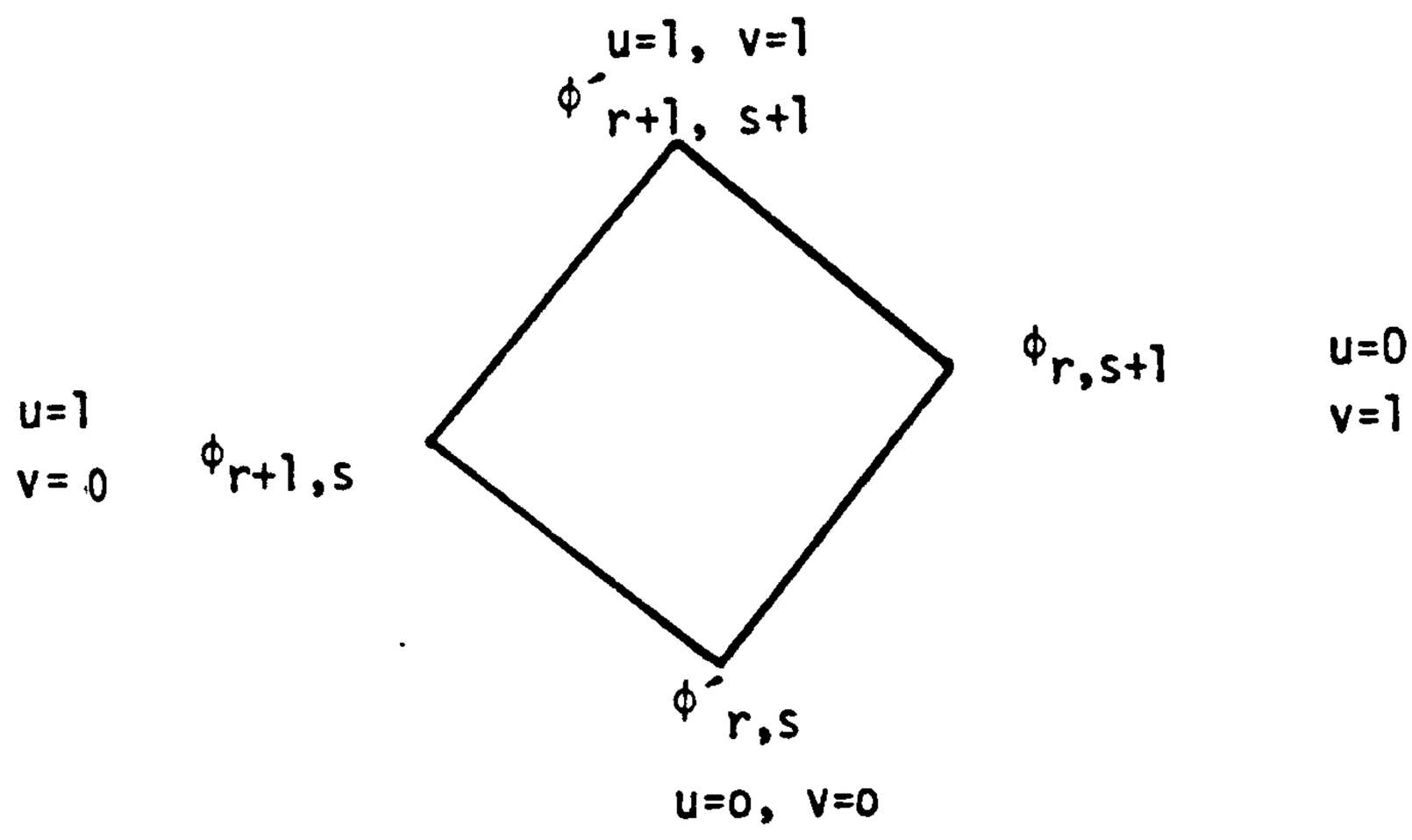

FIG (5.5)

Introduce a system of parabolic interpolation functions $g_i(\rho')$. As shown in equation (5.26) this leads to a system of a parabolic interpolation weights, which are used as coefficients for $\phi'_{(r,s)}$ distribution on the wing.

From Equations (5.27) it can be shown the actual parabolic functions

can be expressed in the following ways.

$$G_0(r) = \int_0^1 \frac{(\rho'-\frac{1}{2})(\rho'-1)}{(\rho'+r)^{3/2}}\, d\rho'$$

$$G_{\frac{1}{2}}(r) = -\int_0^1 \frac{2\rho'(\rho'-1)}{(\rho'+r)^{3/2}}\, d\rho'$$

$$G_1(r) = \int_0^1 \frac{\rho'(\rho'-\frac{1}{2})}{(\rho'+r)^{3/2}}\, d\rho'$$

performing these integrations give the results:

$$G_0(r) = \frac{2(r+1)(r+\frac{1}{2})}{r^{\frac{1}{2}}(r+1)^{\frac{1}{2}}\left[(r+1)^{\frac{1}{2}}+r^{\frac{1}{2}}\right]} - \frac{4r+3}{r^{\frac{1}{2}}+(r+1)^{\frac{1}{2}}} + \frac{2r^2+2r+2/3}{(r+1)^{3/2}+r^{3/2}}, \quad r \geq 1$$

$$G_0(o) = \frac{-10}{3} \qquad \text{..... (5.28)}$$

$$G_{\frac{1}{2}}(r) = 2\left[\frac{-2r(r+1)}{r^{\frac{1}{2}}(r+1)^{\frac{1}{2}}\{(r+1)^{\frac{1}{2}}+r^{\frac{1}{2}}\}} - \frac{-2(2r+1)}{r^{\frac{1}{2}}+(r+1)^{\frac{1}{2}}} - \frac{2r^2+2r+2/3}{(r+1)^{3/2}+r^{3/2}}\right], \quad r \geq 1$$

$$G_{\frac{1}{2}}(o) = \frac{8}{3} \qquad \text{..... (5.29)}$$

$$G_1(r) = \frac{r(2r+1)}{r^{\frac{1}{2}}(r+1)^{\frac{1}{2}}\left[(r+1)^{\frac{1}{2}}+r^{\frac{1}{2}}\right]} - \frac{4r+1}{r^{\frac{1}{2}}+(r+1)^{\frac{1}{2}}} + \frac{2r^2+2r+2/3}{(r+1)^{3/2}+r^{3/2}}, \quad r \geq 1$$

$$G_1(o) = -\frac{1}{3} \qquad \text{..... (5.30)}$$

For the case $r = o$, the integrated forms are singular at the lower limit, and in supersonic aerodynamics the singular parts are always ignored.

5.6 NUMERICAL SOLUTION OF THE BASIC INTEGRAL EQUATIONS FOR THE PIVOTAL ϕ'

As an example of the method of solution let us consider the simple planform shown in FIG. (5.6), which is symmetric about an axis in the free-stream direction. We assume that ϕ' are either symmetric or anti-symmetric functions of y, so that the potentials need only be computed on the starboard side of the wing.

We first find that row of rhombuses on the starboard side of the planform which has the lowest σ coordinate. In this row we start with that rhombus on the starboard side of the wing (including the centre-line) which has the lowest ρ coordinate. After computing the first ϕ' we work down this row σ =const. decreasing ρ each time. At each stage, if the current rhombus is on the planform, we compute ϕ'. If it is not on the planform, i.e. if it is forward of the leading edge, we jump down the row until a rhombus is encountered which is on the planform. This procedure is continued until the row is finished. It will be noted that, as shown in the diagram FIG. (5.6), when the row is finished the symmetric row on the port side of the wing can be filled in. The same procedure is now followed for the next downstream row σ = const. and it will be seen that the rhombuses will be dealt with in the order shown on

diagram. Proceeding in this way it can be seen that, at any given stage, all the upstream potentials in the fore-cone are known and it remains each time to determine the potential ϕ'.

Equation (5.25) will become,

$$w_{o,o} \cdot \phi'_{o,o} = \frac{\alpha\pi\ell}{ML} - \Sigma\Sigma\ (w_{r,s} \cdot \phi_{r,s})$$

or

$$\phi'_{o,o} = \frac{1}{w_{o,o}} \left[\frac{\alpha\pi\ell}{ML} - \sum_{s=1}^{m} \sum_{r=1}^{n} w_{r,s} \cdot \phi_{r,s}\right] \qquad \text{..... (5.31)}$$

5.7 REGULAR PARABOLIC INTERPOLATION WEIGHTS FOR A LINEAR VARIATION OF POTENTIAL

Assuming that the lines σ = constant or ρ = constant, then ϕ' varies linearly in the other variable. Therefore we must take

$$\lambda_{uv}\ (\rho',\sigma') = f_u(\rho')f_v(\sigma') \qquad \text{..... (5.32)}$$

where $f_u(\rho')$ and $f_v(\sigma')$ are linear interpolation functions (u and v take the values 0 or 1),

and $\quad f_u(\rho') = 1 \quad \text{for} \quad \rho' = u$

$\qquad\qquad\quad = 0 \quad \text{for} \quad \rho' \neq u$

Thus $f_0(\rho') = 1 - \rho'$

$f_1(\rho') = \rho'$

consequently

$$\left.\begin{aligned} \lambda_{00}(\rho',\sigma') &= (1-\rho')(1-\sigma') \\ \lambda_{10}(\rho',\sigma\rho) &= \rho'(1-\sigma') \\ \lambda_{01}(\rho',\sigma') &= (1-\rho')\sigma' \\ \lambda_{11}(\rho',\sigma') &= \rho'\sigma' \end{aligned}\right\} \quad \ldots\ldots\ldots (5.33)$$

Therefore the requisitive values for $\rho' = i = 0, \frac{1}{2}, 1$ and $j = \sigma' = 0, \frac{1}{2}, 1$ are:

TABLE (5.1)

	λ_{00}			λ_{10}			λ_{01}			λ_{11}		
i \ j	0	$\frac{1}{2}$	1	0	$\frac{1}{2}$	1	0	$\frac{1}{2}$	1	0	$\frac{1}{2}$	1
0	1	$\frac{1}{2}$	0	0	0	0	0	$\frac{1}{2}$	1	0	0	0
$\frac{1}{2}$	$\frac{1}{2}$	$\frac{1}{4}$	0	$\frac{1}{2}$	$\frac{1}{4}$	0	0	$\frac{1}{4}$	$\frac{1}{2}$	0	$\frac{1}{4}$	$\frac{1}{2}$
1	0	0	0	1	$\frac{1}{2}$	0	0	0	0	0	$\frac{1}{2}$	1

For example $w_{00} = \sum_{i=0,\frac{1}{2},1} \sum_{j=0,\frac{1}{2},1} \lambda_{00}\, G_i(o)\, G_j(o)$

$$= \left(\frac{-10}{3}\right)\left(\frac{-10}{3}\right) + \left(\frac{1}{2}\right)\left(\frac{-10}{3}\right)\left(\frac{8}{3}\right) + \left(\frac{1}{2}\right)\left(\frac{8}{3}\right)\left(\frac{-10}{3}\right) + \left(\frac{1}{4}\right)\left(\frac{8}{3}\right)\left(\frac{8}{3}\right)$$

i.e. $\underline{w_{00} = 4}$

Alternatively, from linear interpolation weights which will be explained in a later section the same result can be derived:

$$\underline{w_{oo} = E(o).\ E(o) = -2 \times -2 = +4}$$

Now considering A, B, C, D contributions in turn, then

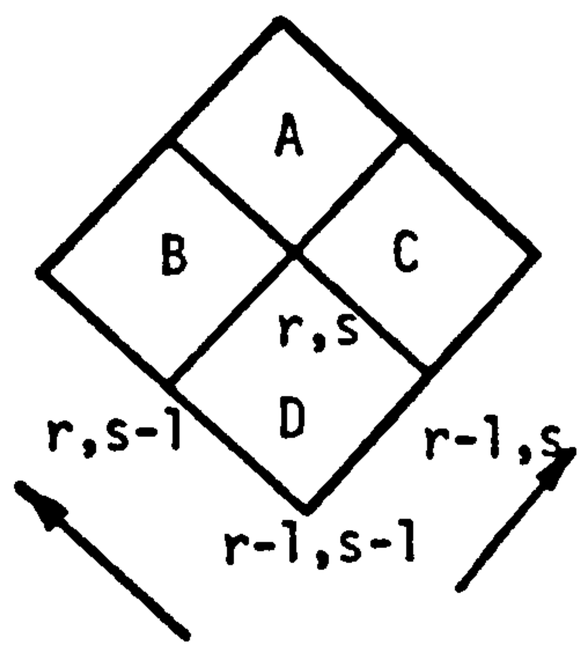

$$w_{(r,s)} = \Big[G_o(r)\ G_o(s) + \tfrac{1}{2}\ G_{\frac{1}{2}}(r)\ G_o(s) + \tfrac{1}{2}\ G_o(r)\ G_{\frac{1}{2}}(s) + \tfrac{1}{4}\ G_{\frac{1}{2}}(r)\ G_{\frac{1}{2}}(s)\Big] \qquad (1)$$

$$+ \Big[G_o(r)\ G_1(s-1) + \tfrac{1}{2}\ G_o(r)\ G_{\frac{1}{2}}(s-1) + \tfrac{1}{2}\ G_{\frac{1}{2}}(r)\ G_1(s-1) + \tfrac{1}{4}\ G_{\frac{1}{2}}(r)\ G_{\frac{1}{2}}(s-1)\Big] \qquad (2) \qquad \ldots\ldots\ (5.34)$$

$$+ \Big[G_o(s)\ G_1(r-1) + \tfrac{1}{2}\ G_o(s)\ G_{\frac{1}{2}}(r-1) + \tfrac{1}{2}\ G_{\frac{1}{2}}(s)\ G_1(r-1) + \tfrac{1}{4}\ G_{\frac{1}{2}}(s)\ G_{\frac{1}{2}}(r-1)\Big] \qquad (3)$$

$$+ \Big[G_1(r-1)\ G_1(s-1) + \tfrac{1}{2}\ G_1(r-1)\ G_{\frac{1}{2}}(s-1) + \tfrac{1}{2}\ G_{\frac{1}{2}}(r-1)\ G_1(s-1) + \tfrac{1}{4}\ G_{\frac{1}{2}}(r-1)\ G_{\frac{1}{2}}(s-1)\Big] \qquad (4)$$

OR $\quad w_{(r,s)}$ = TERM (1) + TERM (2) + TERM (3) + TERM (4)

Equation (5.34) represents a numerical solution for calculation of weights. It is important to make note that along line s=i=o OR j=r=o OR r=s=o we need to skip terms (2) + (4) or terms (3) + (4) or (2) + (3) + (4) respectively.

However for a small ν' i.e. $\frac{\ell\omega}{\beta U}$ which applies in this case since ν'=o, it may be sufficiently accurate to allow only a linear variation of the ϕ'. Now as it is shown, this simplifies the formulae for the weights considerably.

$$W_{(r,s)} = E(r) \times E(s) \qquad \text{..... (5.35)}$$

where

$$E(r) = F_o(r) + F_1(r-1) \qquad \text{..... (5.36)}$$

The contribution to the net coefficient of ϕ' will be

$C_{r+u,s+v}$ for u = o, v = o from rhombus A = $F_o(r)\ F_o(s)$

$C_{r+u,s-1+v}$ for u = o, v = o from rhombus B = $F_o(r)\ F_1(s-1)$

$C_{r-1+u,s+v}$ for u = 1, v = o from rhombus C = $F_1(r-1)\ F_o(s)$

$C_{r-1+u,s-1+v}$ for u = 1, v = 1 from rhombus D = $F_1(r-1)\ F_1(s-1)$

Thus the net coefficient of $\phi'_{(r,s)}$ will be

$$E(r) = \Big[F_0(r)\,F_0(s) + F_0(r)\,F_1(s-1) + F_1(r-1)\,F_0(s) +$$

$$F_1(r-1)\,F_1(s-1)\Big] = \underline{\underline{F_0(r) + F_1(r-1)}}$$

where $F_0(r) = \int_0^1 \frac{1-\rho'}{2(\rho'+r)^{3/2}}\,d\rho' = \int_r^{r+1} \frac{1+r-\rho}{2(\rho^{3/2})}\,d\rho = (1+r)\left[\frac{1}{(r+1)^{\frac{1}{2}}} - \frac{1}{r^{\frac{1}{2}}}\right]$

$$- \left[(r+1)^{\frac{1}{2}} - r^{\frac{1}{2}}\right] \quad \ldots (5.37)$$

$$F_1(r) = \int_0^1 \frac{\rho'}{2(\rho'+r)^{3/2}}\,d\rho' = \int_r^{r+1} \frac{\rho-r}{2\rho^{3/2}}\,d\rho = \left[(r+1)^{\frac{1}{2}} - r^{\frac{1}{2}}\right]$$

$$+ r\left[\frac{1}{(r+1)^{\frac{1}{2}}} - \frac{1}{r^{\frac{1}{2}}}\right] \quad \ldots\ldots (5.38)$$

and hence

$$E(r) = \left[r^{\frac{1}{2}} - (r-1)^{\frac{1}{2}}\right] + (r-1)\left[\frac{1}{r^{\frac{1}{2}}} - \frac{1}{(r-1)^{\frac{1}{2}}}\right] - (r+1)\left[\frac{1}{(r+1)^{\frac{1}{2}}} - \frac{1}{r^{\frac{1}{2}}}\right]$$

$$- \left[(r+1)^{\frac{1}{2}} - r^{\frac{1}{2}}\right] \quad \ldots\ldots\ldots (5.39$$

Also $E(o) = -2$, $E(1) = 4 - 2\sqrt{2}$

In evaluating $E(r)$, for $r = o$ or 1, the rule is that any singular

terms must be ommitted. For r = o, the terms stemming from F_1 must also be omitted.

For example $W_{(o,o)} = E(o) \times E(o) = -2 \times -2 = 4$

5.8 THE REGULAR PARABOLIC INTERPOLATION WEIGHTS FOR A VARIATION OF POTENTIAL $\phi = a + by + cy^2 + dx$.

This variation of potential was introduced in dealing with delta wings of low aspect ratio,where it seems desirable to allow the potential to have some curvature in the spanwise direction.

Now introduce an x,y system which has a different origin and scale from the usual one. The x,y coordinates and their relation to the points i = 0, ½, 1; j = 0, ½, 1 are illustrated in the diagram below

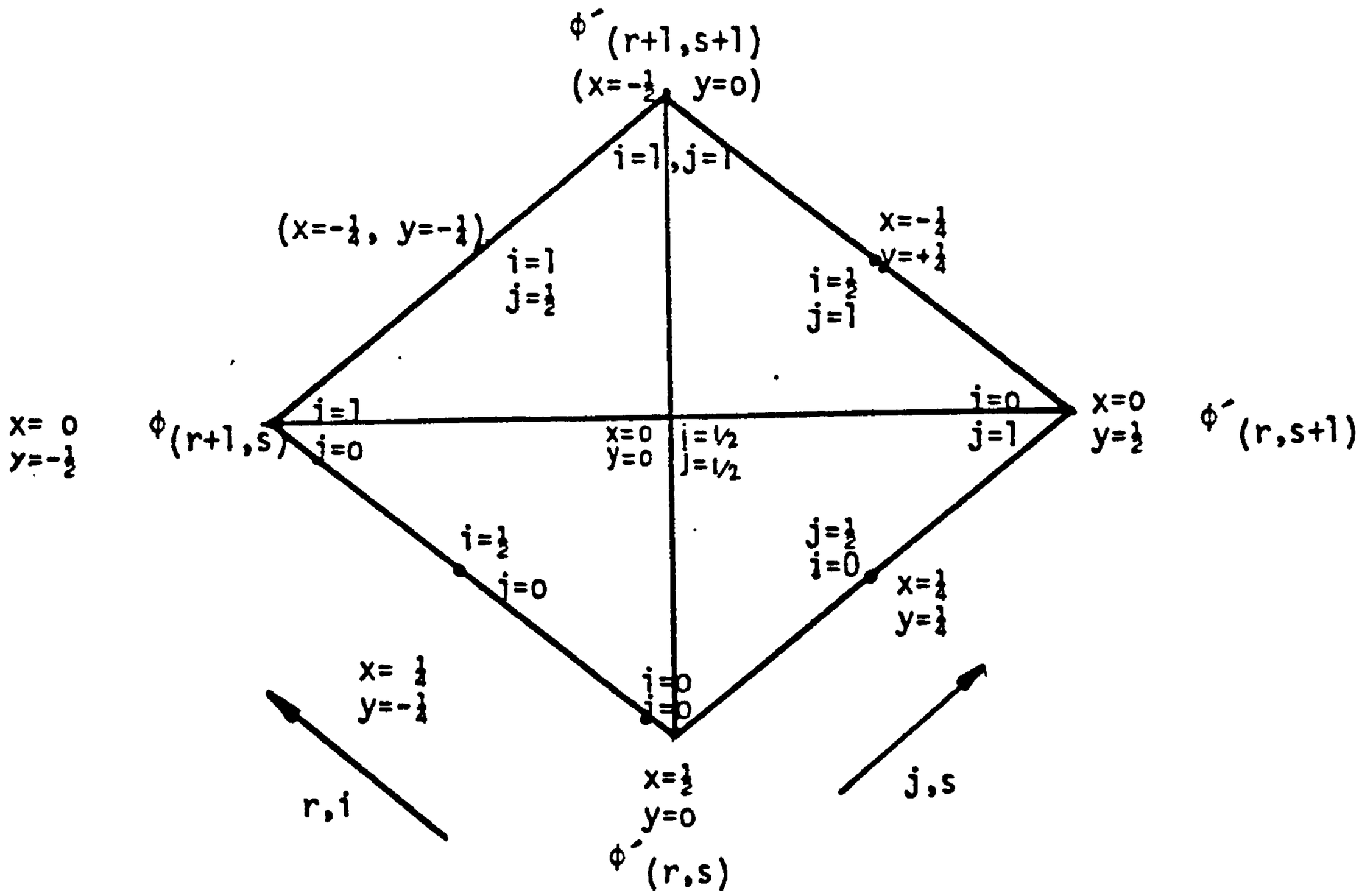

Now, consider first the contribution of A, B, C, D in turn for the weight functions

$$\text{Term 1} = G_0(r)\,G_0(s) + \tfrac{5}{8}\,G_{\frac{1}{2}}(r)\,G_0(s) + \tfrac{1}{8}\,G_{\frac{1}{2}}(r)\,G_1(s) + \tfrac{5}{8}\,G_0(r)\,G_{\frac{1}{2}}(s) + \tfrac{1}{2}\,G_{\frac{1}{2}}(r)\,G_{\frac{1}{2}}(s) + \tfrac{1}{8}\,G_1(r)\,G_{\frac{1}{2}}(s) \qquad \text{..... (5.40)}$$

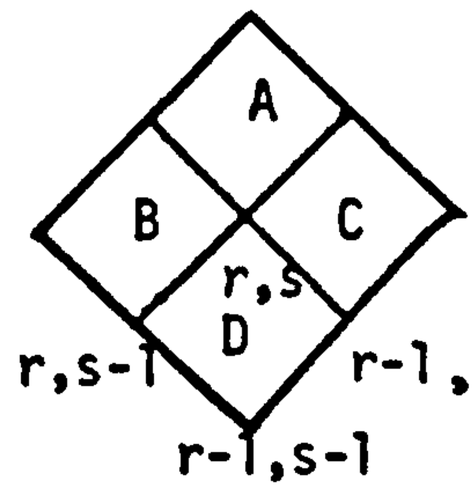

$$\text{Term 2} = -\tfrac{1}{8}\,G_0(s-1)\,G_{\frac{1}{2}}(r) + \tfrac{3}{8}\,G_0(r)\,G_{\frac{1}{2}}(s-1) - \tfrac{1}{8}\,G_1(r)\,G_{\frac{1}{2}}(s-1) + G_0(r)\,G_1(s-1) + \tfrac{3}{8}\,G_{\frac{1}{2}}(r)\,G_1(s-1) \qquad \text{..... (5.41)}$$

$$\text{Term 3} = +\tfrac{3}{8}\,G_{\frac{1}{2}}(r-1)\,G_0(s) + G_1(r-1)\,G_0(s) - \tfrac{1}{8}\,G_0(r-1)\,G_{\frac{1}{2}}(s) + \tfrac{3}{8}\,G_1(r-1)\,G_{\frac{1}{2}}(s) - \tfrac{1}{8}\,G_{\frac{1}{2}}(r-1)\,G_1(s) \qquad \text{..... (5.42)}$$

$$\text{Term 4} = \tfrac{1}{8}\,G_{\frac{1}{2}}(r-1)\,G_0(s-1) + \tfrac{1}{8}\,G_0(r-1)\,G_{\frac{1}{2}}(s-1) + \tfrac{1}{2}\,G_{\frac{1}{2}}(r-1)\,G_{\frac{1}{2}}(s-1) + \tfrac{5}{8}\,G_1(r-1)\,G_{\frac{1}{2}}(s-1) + \tfrac{5}{8}\,G_{\frac{1}{2}}(r-1)\,G_1(s-1) + G_1(r-1)\,G_1(s-1) \qquad \text{..... (5.43)}$$

To calculate $W_{(r,s)}$ for all the pivotal points, it is important to note that if r=o or s=o or s=r=o we need to operate as follows:

if r=o $\quad W_{(r,s)}$ = Term (1) + Term (2) ..... (5.44)

if s=o $\quad W_{(r,s)}$ = Term (1) + Term (3) ..... (5.45)

if $s \neq o$, $r \neq o$ then $W_{(r,s)}$ = Term (1) + Term (2) + Term (3)

+ Term (4) ..... (5.46)

5.9 IRREGULAR RHOMBUS WEIGHTS

For treatment of irregular rhombus weights, in general we need to look at two typical cases.

1) subsonic leading edge irregular rhombus weights

2) supersonic leading edge irregular rhombus weights

5.9.1 FORMATION OF IRREGULAR WEIGHTS AT SUBSONIC LEADING EDGE

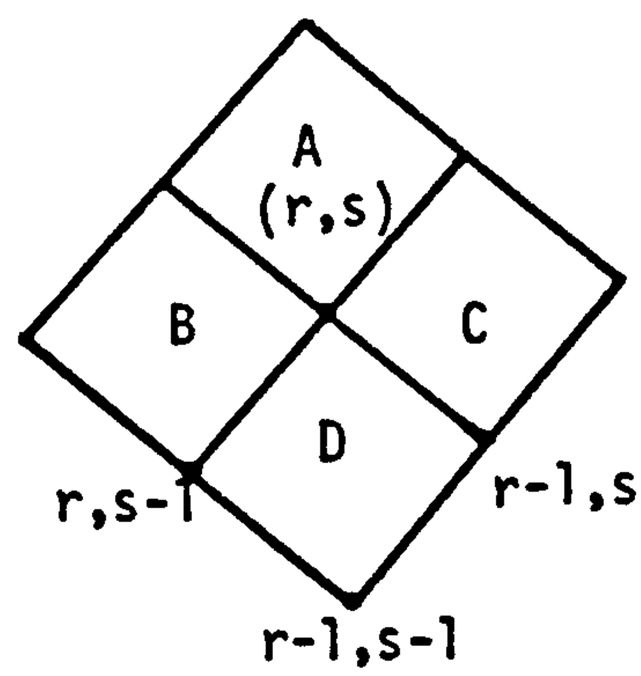

In this case in general, some irregular rhombuses will occur near the subsonic leading edges in the integration mesh.
These irregular rhombuses will be bounded, in general, by three characteristics and the planform edge.

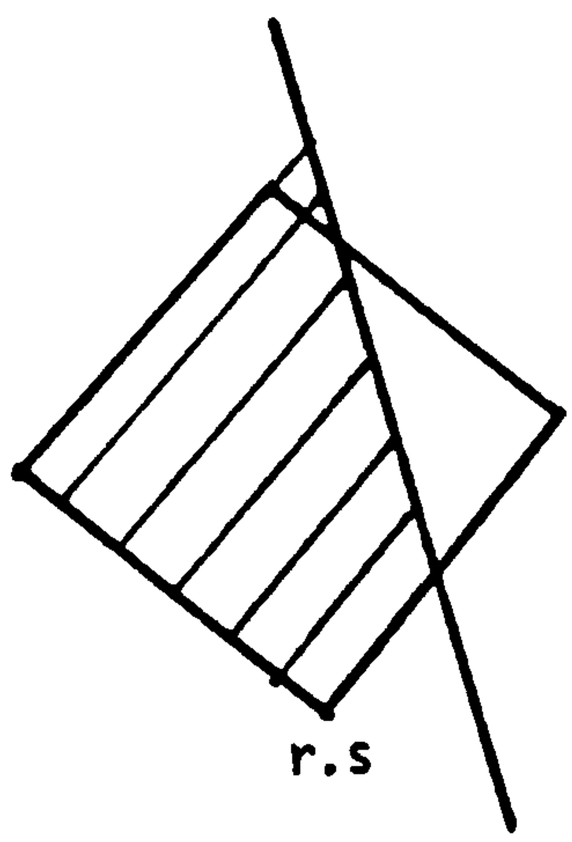

Subsonic L.E

$\sigma_{L.E}$ - σ near a supersonic edge.

Substituting equation (5.48) in equation (5.47) and performing the requisite integrations, the contribution of the irregular rhombus whose least point is (r,s) can be written as

$$\phi'(\rho,\sigma) = \tau_{00}(r,s)\ \phi'(r,s) + \tau_{10}(r,s)\ \phi'(r+1,s)$$

$$+ \tau_{01}(r,s)\ \phi'(r,s+1) + \tau_{11}(r,s)\ \phi'(r+1,s+1) \quad \ldots \quad (5.49)$$

where

$$\tau_{uv}\ (r,s) = \int_{r}^{r+1}\int_{s}^{\sigma_{L.E}(\rho)} \frac{\lambda_{uv}(\rho',\sigma')}{4(\rho\sigma)^{3/2}}\ d\rho.d\sigma \quad \ldots\ldots\ldots \quad (5.50)$$

and this requisite integration can be solved numerically for λ_{uv} as shown in Appendix (A). Equations (A.7) to (A.30) of Ref. (5.1).

Considering the way the regular weight is formed up from A, B, C, D contributions, we arrive at the following formula for the weight at the point (r,s) assuming any one or more of A, B, C, D to be irregular.

As we had

$$W_{(r,s)} = W_{(r,s)_A} + W_{(r,s)_B} + W_{(r,s)_C} + W_{(r,s)_D} \quad \ldots\ldots\ldots \quad (5.51)$$

For regular

where suffixes A, B, C, D represents the relevant rhombus.

Then,

$$W_{(r,s)_{irregular}} = W_{(r,s)_{reg.}}$$

$$- W_{(r,s)_A} + \tau_{00}(r,s) \quad \text{if A is irregular}$$

$$- W_{(r,s)_B} + \tau_{01}(r,s-1) \text{if B is irregular}$$

$$- W_{(r,s)_C} + \tau_{10}(r-1,s) \text{if C is irregular}$$

$$- W_{(r,s)_D} + \tau_{11}(r-1,s-1) \text{if D is irregular}$$

$$\ldots\ldots\ldots \quad (5.52)$$

From equation (5.52), the pivotal weights of an irregular rhombus adjacent to a subsonic leading edge can be found as follows:

$$W_{(o,o)} = \tau_{(o,o)} = C_{1(o,o)} = \frac{\pi}{\sqrt{g}}$$

Hence for a 3 vortex case, its contribution is

$$C_{1(o,o)}\,\phi'_{(o,o)} + C_{2(o,o)}\,\phi'_{(1,o)} + C_{3(o,o)}\,\phi'_{(1,1)}$$

and for a 2 vortex case

$$C'_{1(o,o)}\,\phi'_{(o,o)} + C'_{2(o,o)}\,\phi'_{(1,o)}$$

where

C_1, C_2, C_3, C_1', C_2' are calculated in Appendix (A) of Ref (5.1)

5.9.2 THE PIVOTAL WEIGHT $W_{(o,o)}$ FOR AN IRREGULAR RHOMBUS ADJACENT TO A SUPERSONIC LEADING EDGE

From equation (5.52) putting r=o, s=o we have

$$\left.\begin{array}{lll} & W_{(o,o)} = \tau_{oo\,(o,o)} = C_{1(o,o)} & \text{for 3 vortex case} \\ \text{or} & W_{(o,o)} = C_{1(o,o)}' & \text{for 2 vortex case} \\ \text{or} & W_{(o,o)} = C_{1\,(o,o)}'' & \text{for 1 vortex case} \end{array}\right\} \quad \ldots\ldots (5.53)$$

where coefficients C_1, C_1', and C_1'' are set out in Appendix B of Ref (5.1)

Thus

$$C_{1(o,o)} = \frac{1}{g}\left[- L_{(o,o)} - M_{(o,o)} + N_{(o,o)}\right] \quad \text{3 vortex} \ldots\ldots (5.54)$$

and from Appendix (B) of Ref (5.1) equations (B.1) to (B.21), the following coefficients can be evaluated:

$$C'_{1(o,o)} = \frac{1}{g}\left[- M_{(o,o)} + N_{(o,o)}\right] \quad \text{2 vortex} \quad \ldots\ldots\ (5.55)$$

$$C''_{1(o,o)} = \frac{N_{(o,o)}}{g} \quad \text{1 vortex} \quad \ldots\ldots\ (5.56)$$

where (from Appendix (B) of Ref. (5.1))

$$L_{(o,o)} = - \frac{1}{3}\left[2g(g+K)^{\frac{1}{2}} + 3g(-K)^{\frac{1}{2}}\left\{\frac{\pi}{2} - \sin^{-1}\left(\frac{g+K}{g}\right)^{\frac{1}{2}}\right\} - K(g+K)^{\frac{1}{2}}\right] \quad \ldots\ldots\ (5.57)$$

$$M_{(o,o)} = - \left[\frac{g}{(-K)^{\frac{1}{2}}} \sin^{-1}\left(\frac{-K}{g}\right)^{\frac{1}{2}} + (g+K)^{\frac{1}{2}}\right] \quad \ldots\ldots\ (5.58)$$

$$N_{(o,o)} = 2\left[(-K)^{\frac{1}{2}} \sin^{-1}\left(\frac{-K}{g}\right)^{\frac{1}{2}} + (g+K)^{\frac{1}{2}}\right] \quad \ldots\ldots\ (5.59)$$

If equations (5.59), (5.58), (5.57) are substituted into equations (5.54) to (5.56), the following results can be achieved:

$$W_{(o,o)} = \frac{1}{g}\left[(g+K)^{\frac{1}{2}}\ (2/3g-1/3\ K+3) + \left\{\frac{g}{(-K)^{\frac{1}{2}}} + 2(-K)^{\frac{1}{2}}\right\} \sin\left(\frac{-K}{g}\right)^{\frac{1}{2}} + g(-K)^{\frac{1}{2}}\left\{\frac{\pi}{2} - \sin^{-1}\left(\frac{g+K}{g}\right)\right\}\right] \quad \text{3 vortex} \quad \ldots\ldots\ (5.60)$$

OR $$W_{(o,o)} = \frac{1}{g}\left[(-K)^{\frac{1}{2}} \operatorname{Sin}^{-1}\left(\frac{-K}{g}\right)^{\frac{1}{2}} + (g+K)^{\frac{1}{2}}\right] \text{ 2 vortex} \quad \ldots\ldots \quad (5.61)$$

OR $$W_{(o,o)} = \frac{2}{g}\left[(-K)^{\frac{1}{2}} \operatorname{Sin}^{-1}\left(\frac{-K}{g}\right)^{\frac{1}{2}} + (g+K)^{\frac{1}{2}}\right] \text{ 1 vortex} \quad \ldots\ldots \quad (5.62)$$

5.10 SOME COMMENTS ON THE TREATMENT OF IRREGULAR RHOMBUSES

It is important to consider the following points concerning the treatment of irregular rhombuses:

1) For each given value of K (i.e. for a given Mach number and for each linked portion of the leading edge), the functions C_1, C_2, C_3, C_1', C_2', C_1'' should be evaluated before the main computation work, in order to save computational time and have a faster process. Then a parabola can be fitted over the appropriate range of g by the least squares method and we obtain, for instance, for the given K.

$$C_1\ (r,s,g) = C_1\ (r,s)\ g^2 + C_1\ (r,s)\ g + C_1\ (r,s)$$

Therefore the coefficient can be smoothed for each value of K.

2) In the formulae for the total irregular weight, it will be seen that, if we start with the regular weight, not only we must add to it the appropriate irregular A, B, C or D contribution, but we must also subtract from it the appropriate regular A, B, C or D contribution.

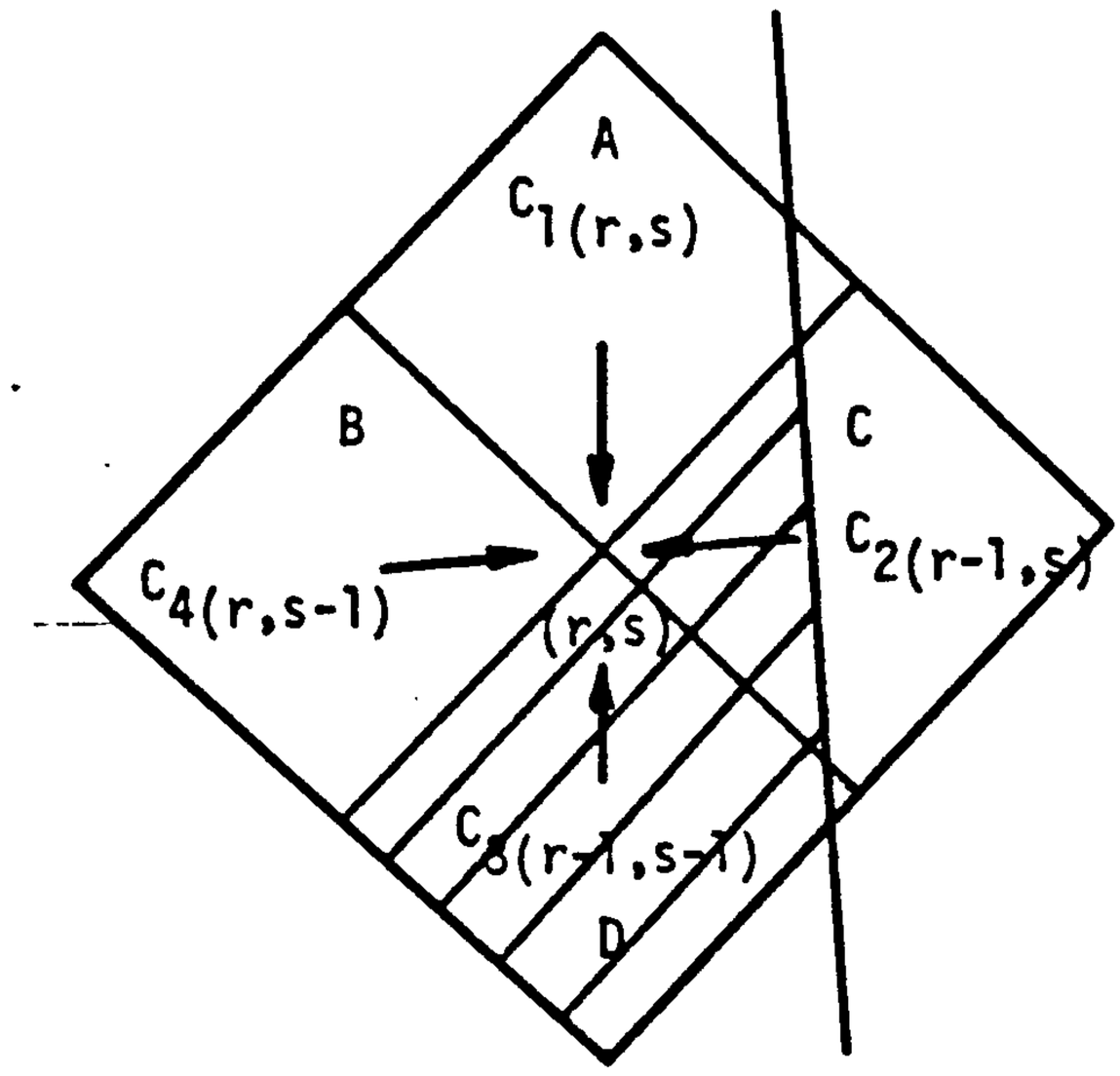

Therefore, it can be seen that, in effect, the appropriate subtractions can be carried out by replacing

$C_1(r,s)$ by $C_1(r,s) - F_0(r)\ F_0(s)$ if A is irregular

$C_2(r-1,s)$ by $C_2(r-1,s) - F_1(r-1) \times F_0(s)$ if C is irregular

$C_3(r-1,s-1)$ by $C_3(r-1,s-1) - F_1(r-1)\ F_1(s-1)$ if D is irregular

$C_4(r,s-1)$ by $C_4\ (r,s-1) - F_0(r).\ F_1(s-1)$ if B is irregular

For a swept wing B is never irregular, so C_4' (r,s-1) would not exist. Hence when D is irregular replace

$$C_3(r-1,s-1) \text{ by } C_3(r-1,s-1) - \underbrace{F_1(r-1)\ F_1(s-1)}_{\text{Due to D}} - \underbrace{F_1(r-1) - F_0(s)}_{\text{Due to C}}$$

This approach which has been described, is strictly only consistent when used with regular linear interpolation weights.

REFERENCES FOR CHAPTER (5)

(5.1) ALLEN, D. J. and SADLER, D.S. "Oscillatory Aerodynamic Forces in Linearised Supersonic Flow for Arbitrary Frequencies, Planforms and Mach Numbers". Aeronautical Research Council, Reports and Memoranda, R. & M. No. 3415, January 1963.

(5.2) W.P. JONES "Supersonic Theory for Oscillating Wings of any Planform". A.R.C. Report and Memoranda No. 2655, June 1948.

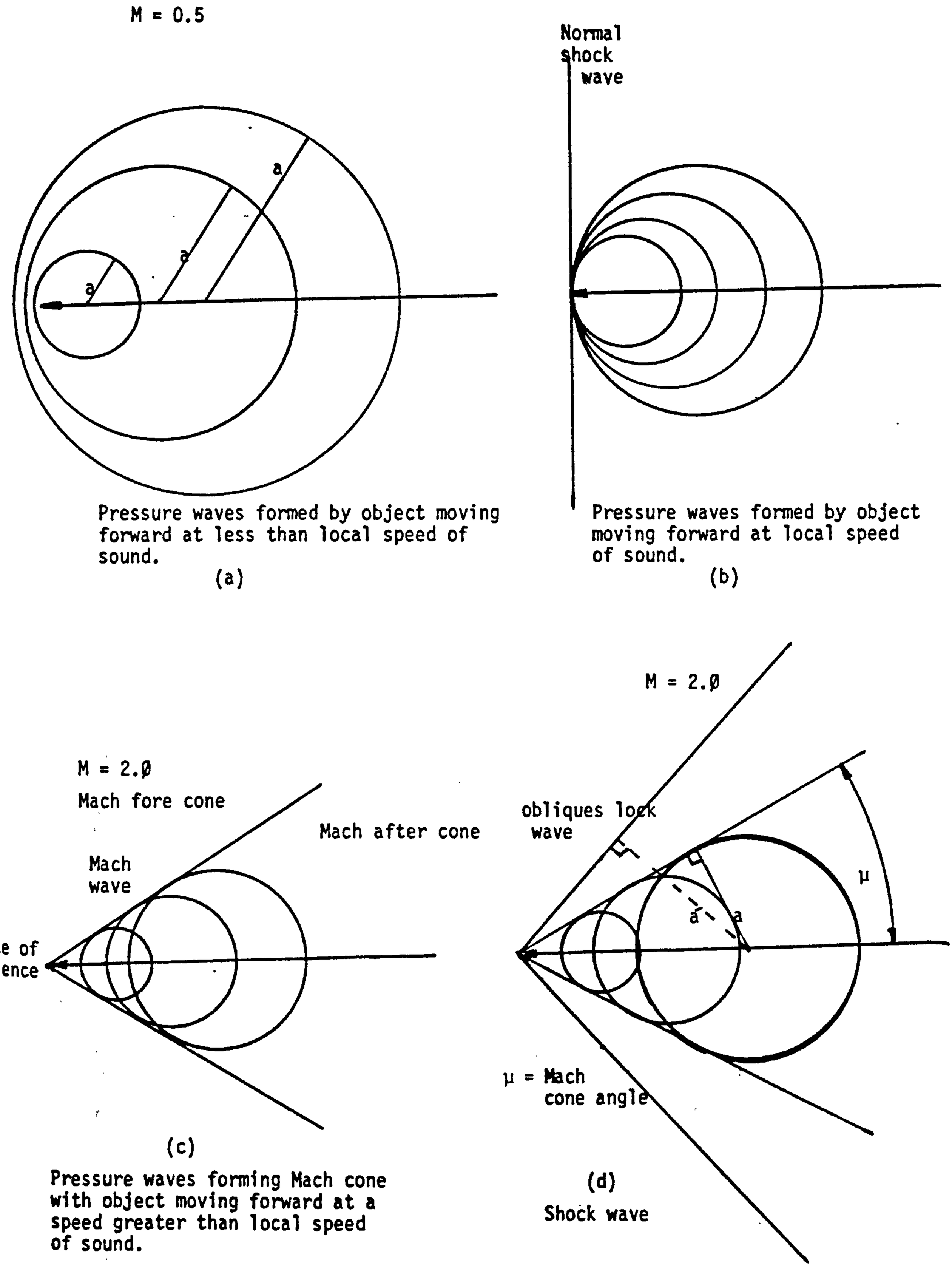

FIGURE (5.1) PRESSURE WAVE MOVEMENT REPRESENTATION

FIG(5.6) MESH SYSTEM &WING PLANFORM FOR CALCULATION OF ϕ' AND W

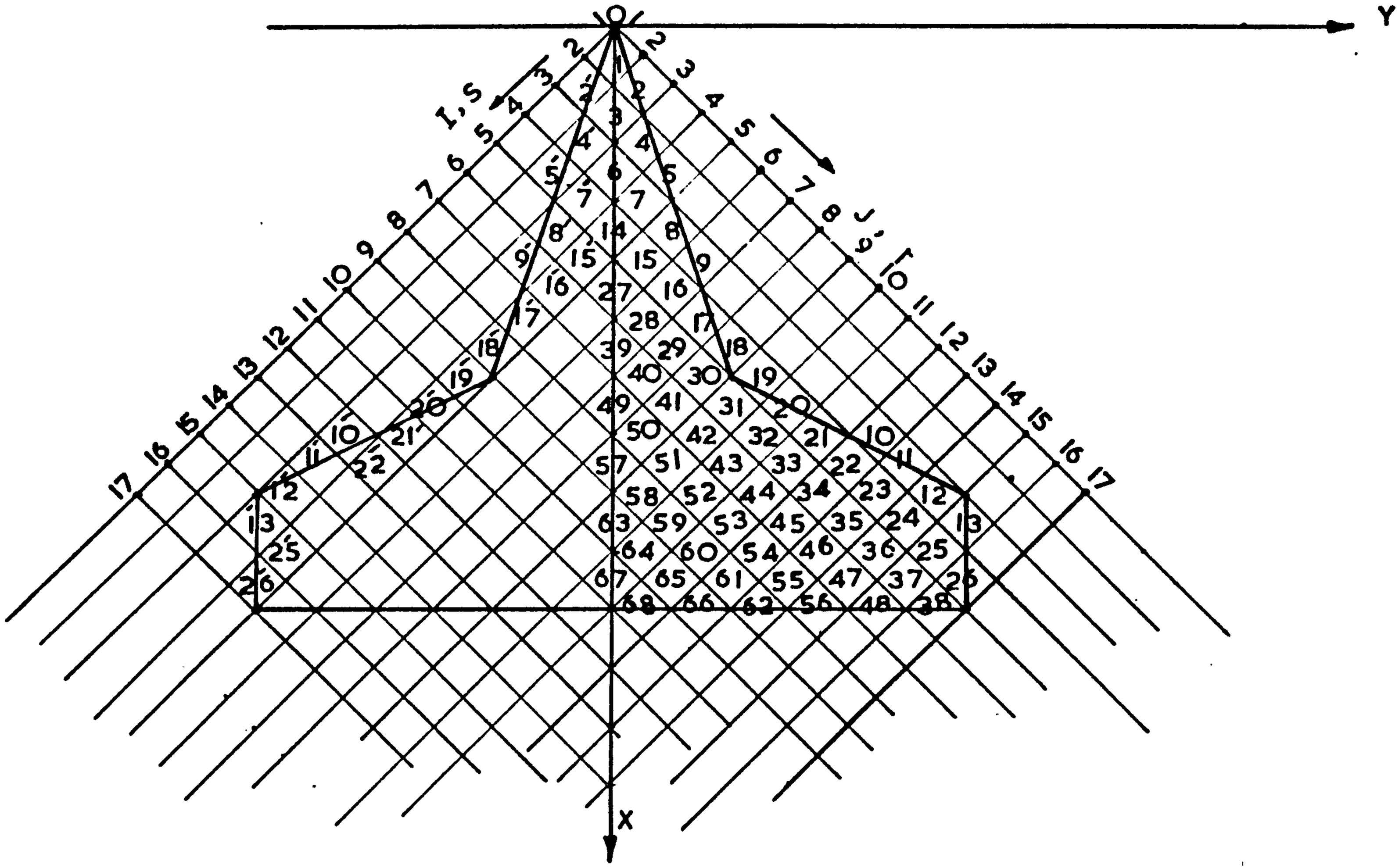

CHAPTER 6

NUMERICAL ANALYSIS OF A SUPERSONIC FLOW FOR AN ARBITRARY WING-BODY USING 'THE CHARACTERISTIC BOX' METHOD

6.1 INTRODUCTION

This chapter describes the analysis of the numerical work that has been carried out for calculation of velocity potential ϕ', pressure coefficient C_p, lift and pitching moment coefficients C_L and C_M, respectively, over an arbitrary wing. In order to do so, the Allen and Sadler method Ref. (5.1) was used by employing a characteristic mesh i.e. a rhombus with edges along the direction of Mach lines, which from now on will be referred to as the "characteristic box" method. To define an arbitrary wing planform, it is necessary to proceed as set out in the following sections.

6.2 MESH DEFINITION

To define a rhombic mesh in this case, consider an arbitrary point, say P(x,y). Then generate a mesh of JxI size parallel to the Mach cone from this point within the fore cone. In this case, the generated mesh will have (J-1) x (I-1) rhombuses, where J=2,3,---,n, and I=2,3,---,n. Now, as shown in Sketch (6.1) using symmetry about ox for an arbitrary wing planform, point P(x,y) will be selected on the ox-axis, and therefore only one half of the wing and generated mesh will be considered. But the effects of L.H.S. mesh need to be counted for the velocity potential summation calculations. Therefore as shown in Sketch (6.2) a modified mesh can be employed which can be used for later meshes. In Sketch (6.2) also all the central rhombuses which are laid down on ox-axis are considered as full rhombuses.

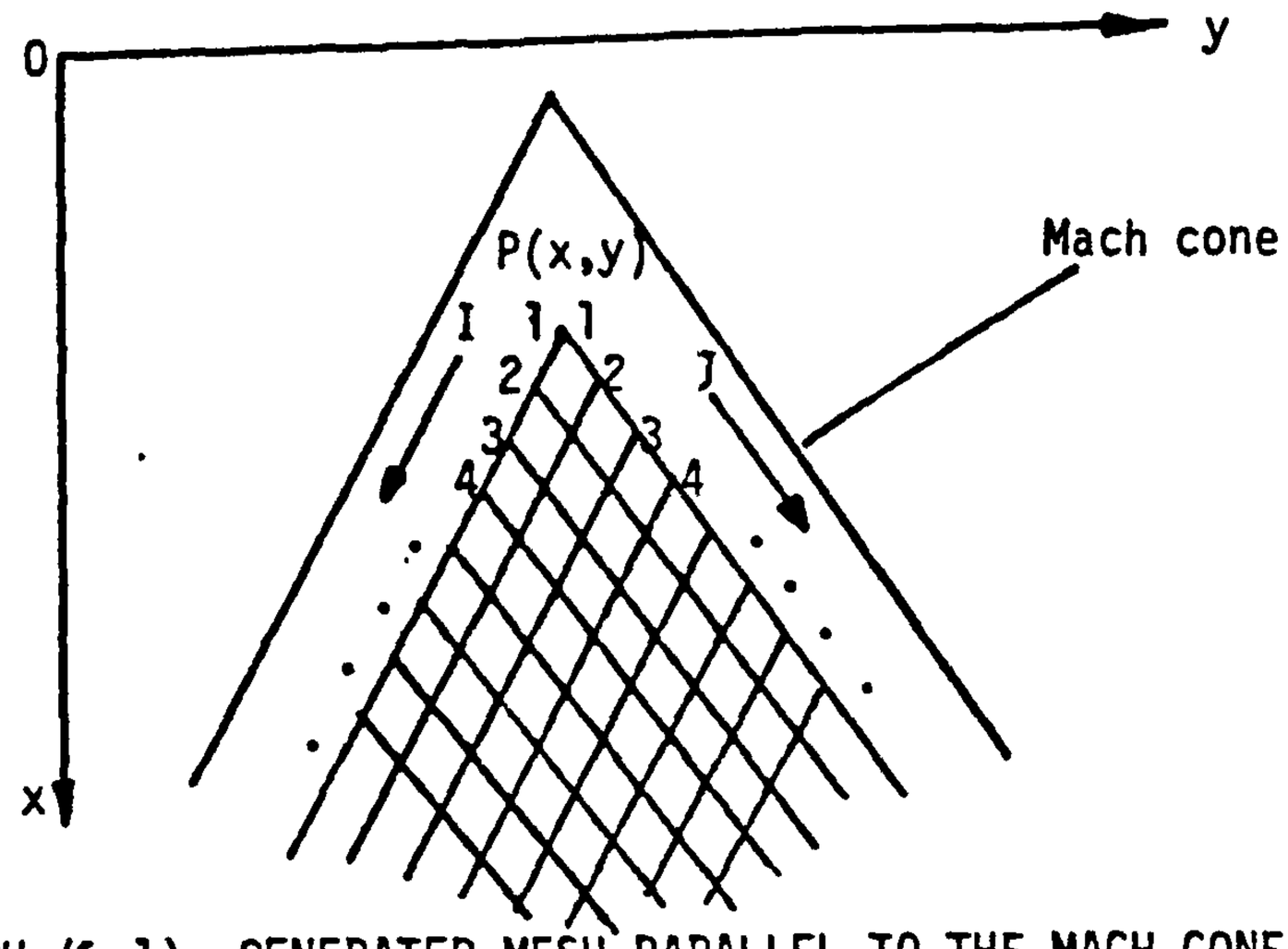

SKETCH (6.1) GENERATED MESH PARALLEL TO THE MACH CONE

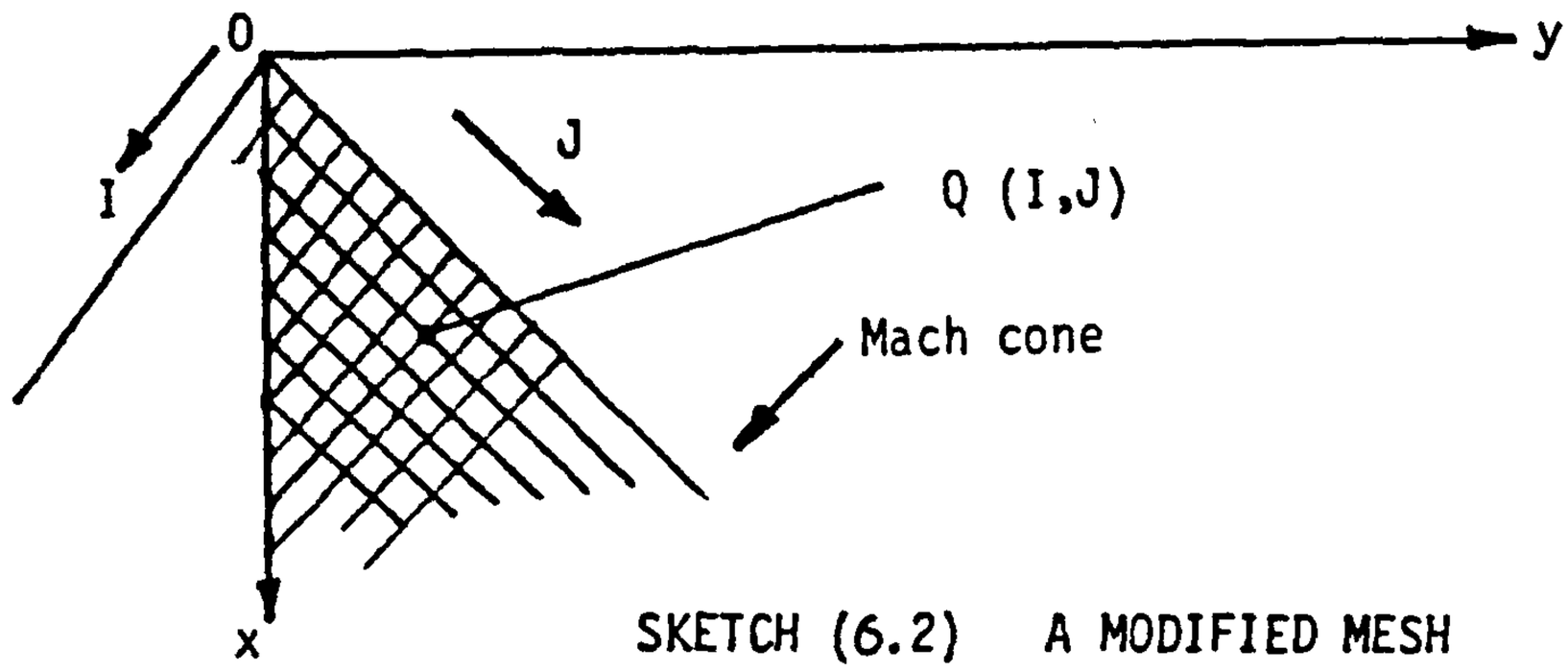

SKETCH (6.2) A MODIFIED MESH

Now, the coordinates of any point say Q(I,J) can be found in the new coordinate system with origin 0 as:

$$XQ\ (I,J) = \left[(J-1) + (I-1)\right] \cdot \frac{DX}{2} \qquad \ldots\ldots\ (6.1)$$

$$XQ\ (I,J) = \left[J-I\right] \cdot \frac{DY}{2} \qquad \ldots\ldots\ (6.2)$$

where DX and DY are diagonal length of a rhombus along ox and oy axes respectively.

6.3 DEFINITION OF A WING MODEL GEOMETRY

To define an arbitrary wing geometry, first it is advisable to

select a particular planform then it is necessary to define each vertex coordinate in a clockwise or anticlockwise direction round the planform. These coordinates can initially be input as input data. --Once all the coordinates are known all the leading edges or trailing edge equations can be found in the new coordinate system, e.g. as shown in Sketch (6.3). It is important to make a note that each line or point can have two different coordinates in two different systems, e.g. vertices, O, A, B, C, D, E coordinates can be represented by $O(X_0,Y_0)$, $A(X_1,Y_1)$ $B(X_2,Y_2)$, $C(X_3,Y_3)$, $C(X_3,Y_3)$, $D(X_4,Y_4)$, $E(X_5,Y_5)$ in XOY coordinate system or $O(I_0,J_0)$, $A(I_1,J_1)$, $B(I_2,J_2)$, $C(I_3,J_3)$, $D(I_4,J_4)$, $E(I_5,J_5)$ in IJ coordinate system respectively.

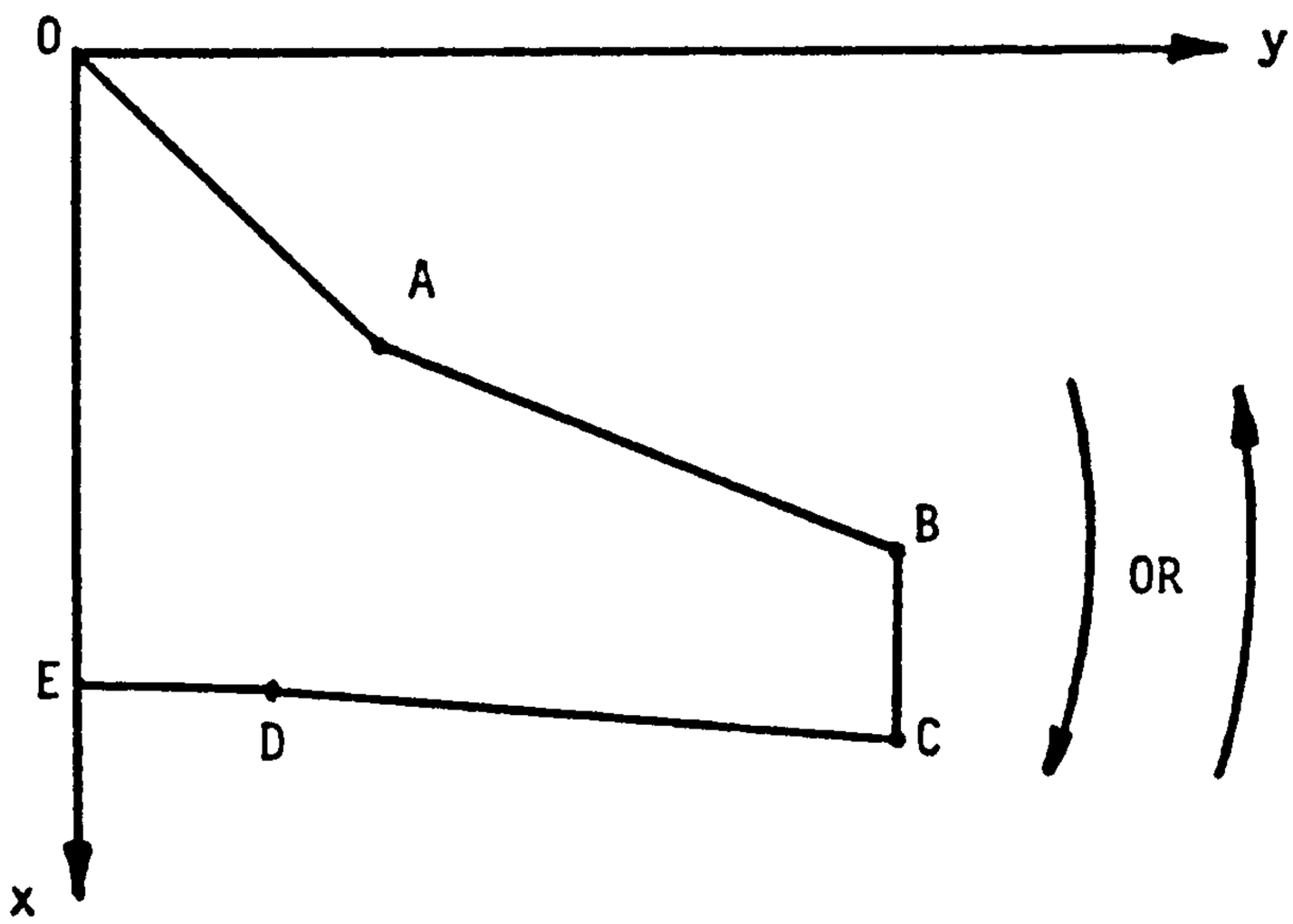

SKETCH (6.3) COORDINATE SYSTEM FOR AN ARBITRARY WING PLANFORM

All the coordinates of vertices must originally be input in forms of (I,J) coordinates, then using equations (6.1) and (6.2), they can be converted into (X,Y) coordinates. Equations of the leading edges

can be expressed as follows:

Equations of OA and AB (L.E) will be:

$$\underline{AO}\ \text{L.E.}\quad Y(I,J) - Y_0 = \frac{Y_A - Y_0}{X_A - X_0}\ (X(I,J) - X_0), \ldots\ldots (6.3)$$

$$\underline{AB}\ \text{L.E.}\quad Y(I,J) - Y_A = \frac{Y_B - Y_A}{X_B - X_A}\ (X(I,J) - X_A), \ldots\ldots (6.4)$$

and the equations of CD and ED (T.E) will be:

$$\underline{CD}\ \text{T.E.}\quad Y(I,J) - Y_D = \frac{Y_D - Y_C}{X_D - X_C}\ (X(I,J) - X_D), \ldots\ldots (6.5)$$

$$\underline{ED}\ \text{T.E.}\quad Y(I,J) - Y_D = \frac{Y_E - Y_D}{Y_E - X_C}\ (X(I,J) - X_D), \ldots\ldots (6.6)$$

$$\underline{Tip}\quad Y(I,J) - Y_C = \frac{Y_B - Y_C}{X_B - X_C}\ (X(I,J) - X_C) \ldots\ldots (6.7)$$

6.4 DEFINITION OF CELLS

In order to define all the cells generated by the mesh, and to investigate whether they are within the planform or not, it is necessary to use a set of coding system for each cell independently.

To do so, it is important to use a set of pivotal points so as to check whether a point Q(I,J) is within the planform, or on the boundary, or outside the planform. See Sketch (6.4) for a better view, as shown the pivotal points for each sections are as follows:

Section 1	Pivot Point	(X_0,Y_0)
Section 2	" "	(X_{P1},Y_{P1})
Section 3	" "	(X_{B1},Y_{B1})
Section 4	" "	(X_{D1},Y_{D1})

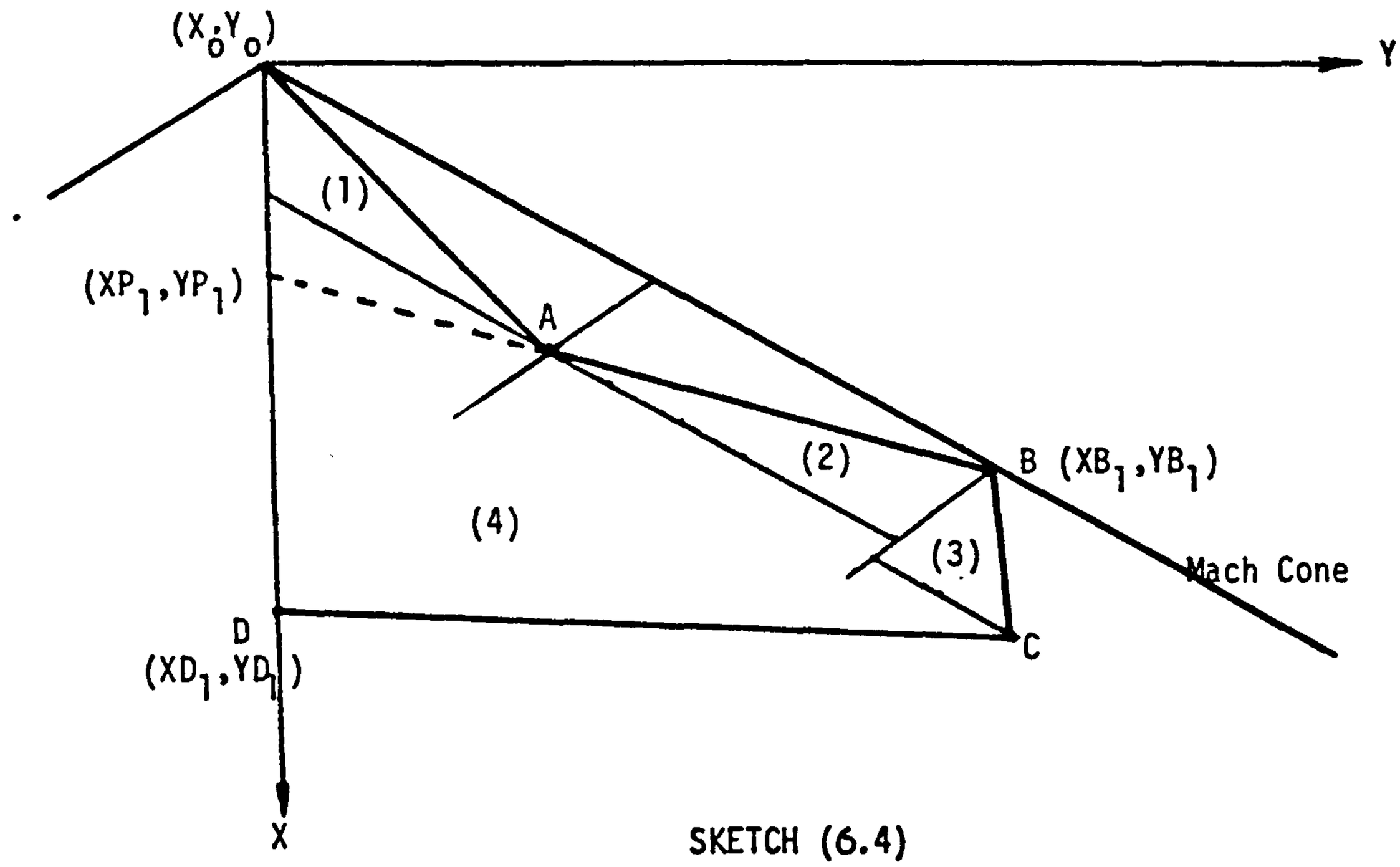

SKETCH (6.4)

Now considering a cell with its four corner points, say cell A with corner points (I_{P1},J_{P1}), (I_{P2},J_{P2}), (I_{P3},J_{P3}) and (I_{P4},J_{P4}) The angles made by the lines joining the four vertices of each cell

with point (X_0,Y_0) can be compared with their corresponding pivotal angle. If these four angles are equal or less than the corresponding pivotal angle, then the cell is within the planform. If they are greater than or equal to their corresponding pivotal angle, then the cell is located outside the planform, otherwise the cell is located on the boundary of planform.

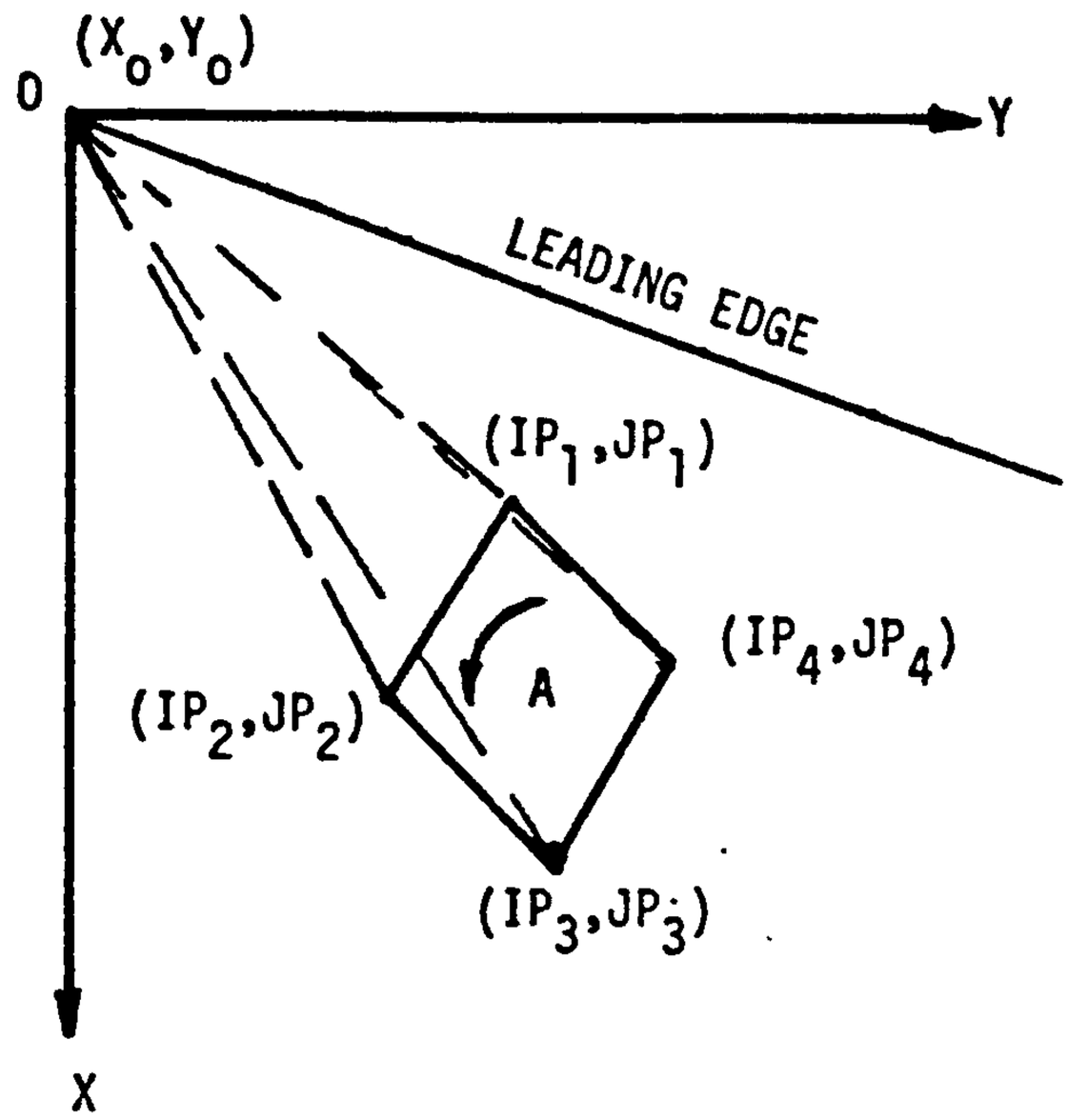

SKETCH (6.5)

If in a case the cell is inside the planform, then it can be coded as '1'. If it is outside the planform, it can be coded as '0'. And if it is on the boundary it can be coded as '2'. All the angles are measured with the vertical line of OX in an anticlockwise direction.

6.5 NUMERICAL CALCULATION OF VELOCITY POTENTIAL ϕ'

As it is explained in Chapter (5), Section (5.6) using equation (5.31) the velocity potential can be calculated numerically. Care should be taken on the leading edge where there could be a formation of irregular rhombuses. Treatments of these irregular rhombuses are laid down in Sections (5.9) and (5.10) of Chapter (5).

6.6 NUMERICAL CALCULATION OF Cp

To calculate the pressure coefficient Cp at each cell it is necessary to find out derivatives of velocity potential as follows:

$$\phi'_x = \frac{\partial(\phi', y)}{\partial(i,j)} \Big/ J$$

where J is Jacobian

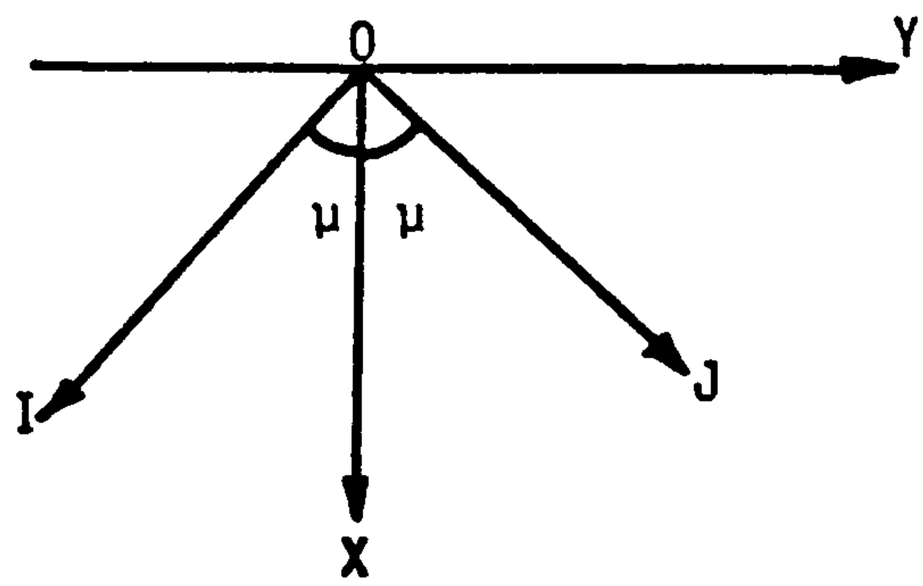

SKETCH (6.6)

$$\text{or} \quad \phi'_x = \begin{vmatrix} \phi_j & \phi_i \\ y_j & y_i \end{vmatrix} \Bigg/ \begin{vmatrix} x_j & x_i \\ y_j & y_i \end{vmatrix} \qquad \ldots\ldots\ldots (6.8)$$

$$\text{where} \quad \begin{cases} y(j) = j\ \text{Sin}\mu & \text{or}, \ \dfrac{\partial y(j)}{\partial j} = y_j = \text{Sin}\mu \\ x(j) = j\ \text{Cos}\mu & \text{or}, \ \dfrac{\partial x(j)}{\partial j} = x_j = \text{Cos}\mu \\ x(i) = i\ \text{Cos}\mu & \text{or}, \ \dfrac{\partial x(i)}{\partial i} = x_i = \text{Cos}\mu \\ y(i) = -\ i.\ \text{Sin}\mu & \text{or}, \ \dfrac{\partial y(i)}{\partial i} = y_i = -\text{Sin}\mu \end{cases}$$

Therefore equation (6.8) can be simplified as:

$$\phi_x' = \frac{\phi_j\, y_i - \phi_i\, y_j}{x_j\, y_i - x_i\, y_j} = \frac{-\phi_j \operatorname{Sin}\mu - \phi_i \operatorname{Sin}\mu}{\operatorname{Cos}\mu \operatorname{Sin}\mu - \operatorname{Cos}\mu \operatorname{Sin}\mu} = \frac{\phi_j + \phi_i}{2\operatorname{Cos}\mu}$$

thus,

$$\phi_x' = \frac{\partial\phi}{\partial x} = \frac{\phi_j' + \phi'_i}{2\operatorname{Cos}\mu} \qquad \text{..... (6.9)}$$

where

$$\phi_j' = \frac{\partial\phi}{\partial j} \text{ and } \phi_i \frac{\partial\phi'}{\partial i}$$

In order to evaluate ϕ_j' and ϕ_i' on the wing planform a central difference interpolation equation can be used such as:

$$\phi_j' = \frac{\phi'_{j+1} - \phi'_{j-1}}{2\ell}, \qquad \text{..... (6.10)}$$

where ℓ is rhombus side length, and on the boundary leading or trailing edges a backward or forward difference interpolation equation can be used as:

<u>Backward Interpolation</u>

$$\phi_j' = \frac{\phi_j - \phi'_{j-1}}{\ell} \qquad \text{..... (6.11)}$$

Forward Interpolation

$$\phi_j' = \frac{\phi''_{j+1} - \phi_j}{\ell} \qquad \text{..... (6.12)}$$

ϕ_i' derivatives can similarly be determined using equations (6.10) to (6.12).

6.7 INVESTIGATION OF IRREGULAR RHOMBUSES ON THE BOUNDARY LEADING EDGE

To treat irregular rhombuses it is necessary to investigate whether the leading edge which cuts through the boundary rhombuses is subsonic or supersonic and also to determine the irregular rhombus type. In this case both types of leading edge flow, i.e. subsonic and supersonic, were considered separately.

6.7.1 SUBSONIC LEADING EDGE

Here there is a subsonic leading edge which cuts through boundary rhombuses. There are only two distinct types of irregular rhombuses. In Sketch (6.7) the two types of rhombuses are shown.

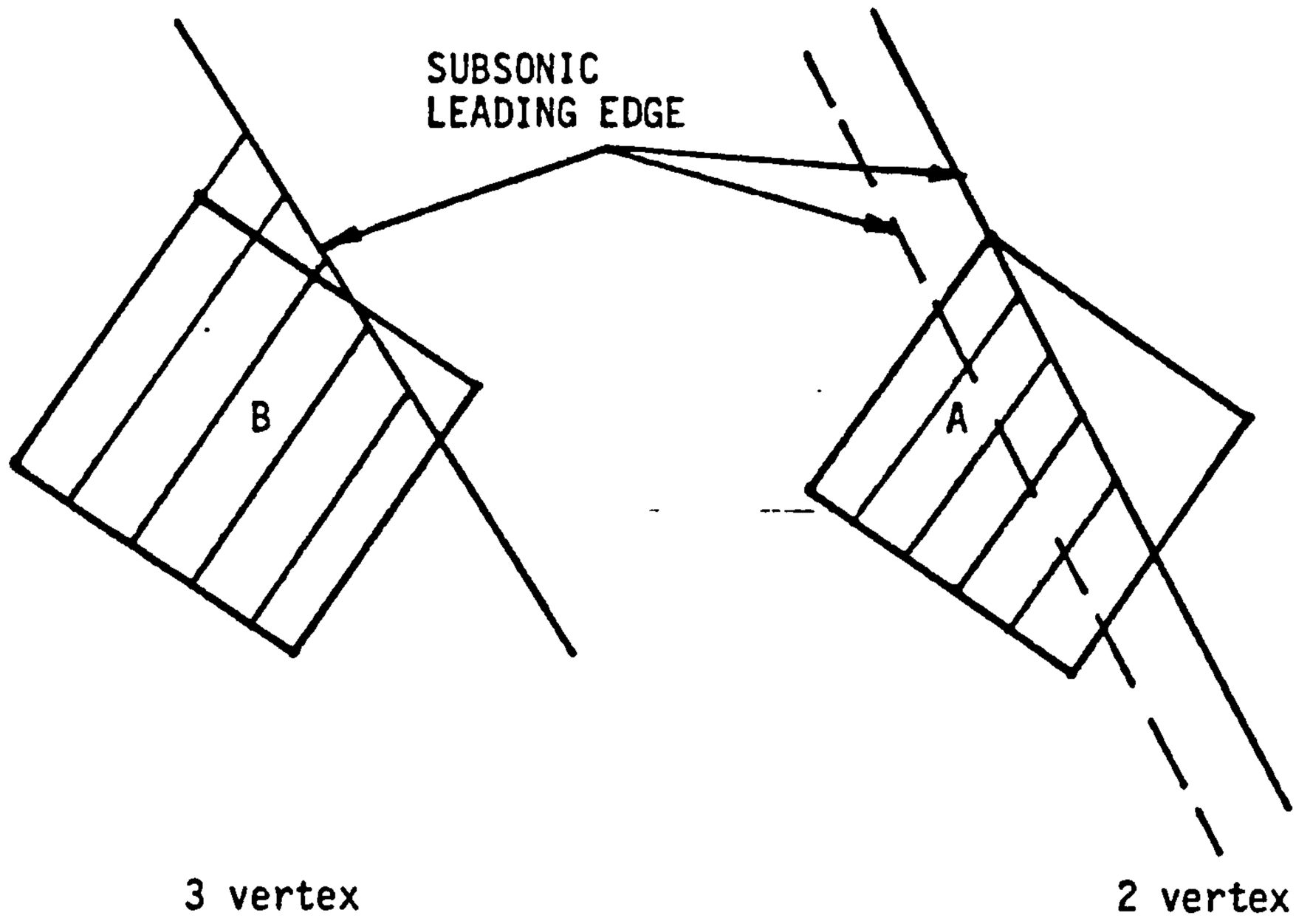

SKETCH (6.7)

In Sketch (6.7) rhombus (A), cut by a subsonic leading edge, has only 2 vertices. And rhombus (B), also cut by a subsonic leading edge, has 3 vertices. In rhombus A the leading edge can have two locations as shown.

6.7.2 SUPERSONIC LEADING EDGE

For supersonic leading edge, three types of irregular rhombuses can be obtained, as shown in Sketch (6.8). Rhombus A has 3 vertices within the planform boundary, rhombus B has 2 vertices, and rhombus C has only 1 vertex within the planform boundary.

As this sketch shows the leading edge can have two different locations in rhombuses B and C.

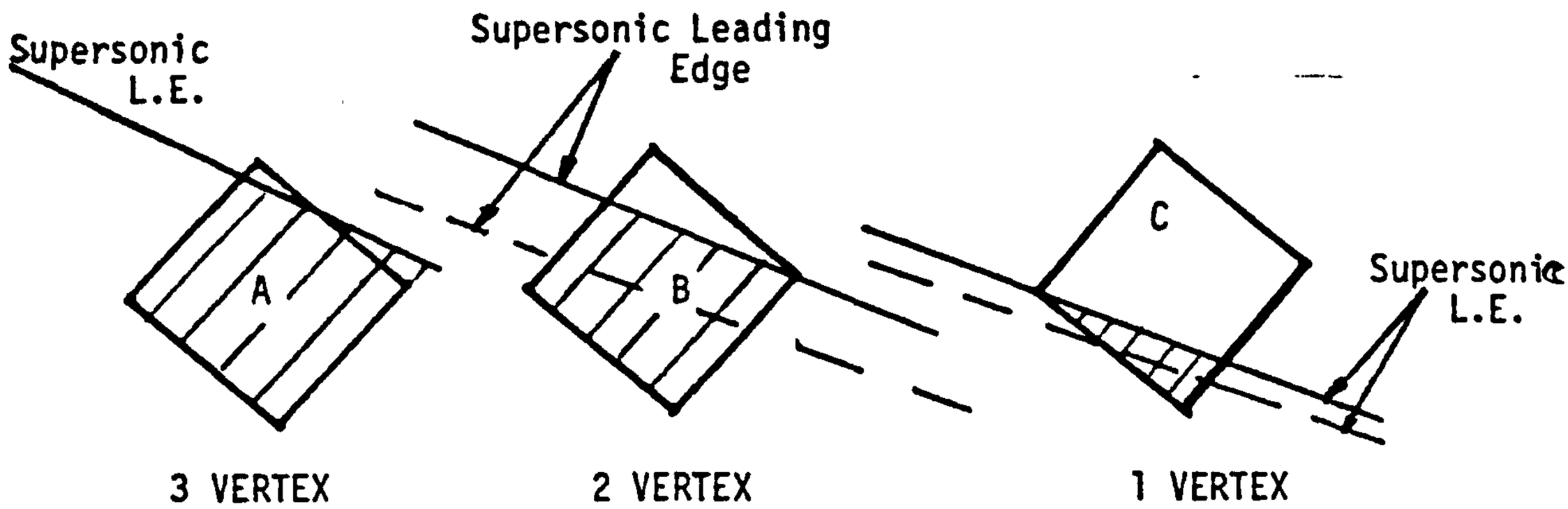

SKETCH (6.8)

Once all the three types of irregular rhombuses are distinguished i.e. type A, B, or C, then for their treatments, Sections (5.9) to (5.10) of Chapter (5) can be applied, for a parabolic or linear weight interpolation function. See Appendix (B) of Ref (5.1).

6.8 NUMERICAL SOLUTION FOR SMOOTHING DATA USING THE LEAST SQUARES METHOD

Considering a general case using the least squares method in order to smoothen a set of data. Representing a polynomial P(x) as a general solution for a best curve to be fitted into our data as:

$$P(x) = A_0 + A_1x + A_2x^2 + --- + A_m.x^m \qquad \text{..... (6.13)}$$

To find P(x), the following simultaneous equations for n points

with (x_i, y_i), $i=1,---,n$, coordinates should be solved.

$$\begin{cases} n A_o + A_1 \sum_{i=1}^{n} x_i + A_2 \sum_{i=1}^{n} x_i^2 + \dots + A_m \sum_{i=1}^{n} x_i^m = \sum_{i=1}^{n} y_i \\ A_o \sum_{i=1}^{n} + A_1 \sum_{i=1}^{n} x_i^2 \dots\dots\dots + A_m \sum_{i=1}^{n} x_i^{m+1} = \sum_{i=1}^{n} x_i y_i \\ \vdots \\ A_o \sum_{i=1}^{n} x_i^m + A_1 \sum_{i=1}^{n} x_i^{m+1} + \dots\dots + A_m \sum_{i=1}^{n} x_i^{2m} = \sum_{i=1}^{n} x_i^m y_i \end{cases}$$

Rearranging these equations and rewriting into matrix notation as:

$$\begin{bmatrix} n & \sum_{i=1}^{n} x_i & \dots\dots\dots & \sum_{i=1}^{n} x_i^m \\ \sum_{i=1}^{n} x_i & \sum_{i=1}^{n} x_i^2 & \dots\dots\dots & \sum_{i=1}^{n} x_i^{m+1} \\ \sum_{i=1}^{n} x_i^2 & \sum_{i=1}^{n} x_i^3 & \dots\dots\dots & \sum_{i=1}^{n} x_i^{m+2} \\ & & & \\ \sum_{i=1}^{n} x_i^m & & \dots\dots\dots & \sum_{i=1}^{n} x_i^{2m} \end{bmatrix} \begin{bmatrix} A_o \\ A_1 \\ A_2 \\ \vdots \\ A_m \end{bmatrix} = \begin{bmatrix} \sum_{i=1}^{n} y_i \\ \sum_{i=1}^{n} y_i x_i \\ \sum_{i=1}^{n} y_i x_i^2 \\ \vdots \\ \sum^{n} x_i^m y_i \end{bmatrix} \quad \dots\dots (6.14)$$

where n is the no. of points,

m is the degree of polynomial,

$x_i (i=1,---n)$ is x-coordinate from data,

$y_i (i=1,---n)$ is y-coordinate from data.

Now, equation (6.14) can be simplified as:

$$B.\underline{A} = \underline{R} \qquad \text{..... (6.15)}$$

where $\underline{A}$ and $\underline{R}$ are vectors and B is the matrix on L.H.S. of equation (6.14).

In order to solve the equation for P(x), it is initially necessary to find out coefficients $A_0, A_1, \text{---}\ A_m$, or on the other hand to solve equation (6.15) for unknown vector $\underline{A}$.

Now, to solve equation (6.15) matrix B can be split into two tridiagonal matrices as:

$$B = L.U = \begin{bmatrix} 1 & 0 & 0 \ldots & 0 \\ L_{21} & 1 & 0 \ldots & 0 \\ . & & 1 & . \\ L_{m1} & & L_{m2} \ldots & 1 \end{bmatrix} . \begin{bmatrix} U_{11} & .. & U_{12} & \ldots & U_{1m} \\ 0 & & U_{22} & \ldots & U_{2m} \\ 0 & & . & & \\ 0 & \ldots & \ldots & \ldots & U_{mm} \end{bmatrix} \qquad \text{.. (6.16)}$$

where elements of matrices L and U can easily be determined from equation (6.16). Therefore equation (6.15) can be simplified as:

$$L.\boxed{U.\ \underline{A}} = \underline{R} \qquad \text{..... (6.17)}$$

where $U.\underline{A}$ can be replaced by a vector say $\underline{f}$, then equation (6.17)

can be modified as:

$$L.\ \underline{f} = \underline{R} \qquad \text{..... (6.18)}$$

6.8.1 FORWARD SUBSTITUTION

Equation (6.18) can be solved for the unknown vector $\underline{f}$ and all the elements evaluated in the following sequence (i.e. forward substitution).

From equation (6.18)

$$\begin{bmatrix} 1 & 0 & 0 \ldots & 0 \\ L_{21} & 1 & & 0 \\ L_{31} & L_{32} & 1 & 0 \\ \vdots & & & \\ L_{m1} & & & 1 \end{bmatrix} \begin{bmatrix} f_0 \\ f_1 \\ f_2 \\ \vdots \\ f_m \end{bmatrix} = \begin{bmatrix} R_0 \\ R_1 \\ R_2 \\ \vdots \\ R_m \end{bmatrix}$$

$$\begin{cases} f_o = R_0 \\ f_1 = R_1 - L_{21} \cdot f_0 \\ f_2 = R_2 - L_{31}\, f_0 - L_{32} - f_1 \\ f_3 = R_3 - L_{41}\, f_0 - L_{42}\, f_1 - L_{43}\, f_2 \\ f_m = R_m - L_{m1}\, f_0 - L_{m2}\, f_1 - L_{m3}\, f_2 - L_{m,m-2}\, f_{m-1} \end{cases} \qquad \text{..... (6.19)}$$

The set of equations (6.19) must be kept in sequence in order to solve numerically for vector $\underline{f}$.

6.8.2 BACKWARD SUBSTITUTION

Once vector $\underline{f}$ elements have been determined from equations (6.19), then using a Backward Substitution process, vector $\underline{A}$ can be solved as follows:

We know that U. $\underline{A} = \underline{f}$

OR
$$\begin{bmatrix} U_{11} & U_{12} & \cdots & U_{1m} \\ 0 & U_{22} & \cdots & U_{2m} \\ \vdots & & & \vdots \\ 0 & \cdots & \cdots & U_{mm} \end{bmatrix} \begin{bmatrix} A_0 \\ A_1 \\ \vdots \\ A_m \end{bmatrix} = \begin{bmatrix} f_0 \\ f_1 \\ f_2 \\ \vdots \\ f_m \end{bmatrix}$$

Thus vector $\underline{A}$ which is unknown and represents the coefficients of the polynomial P(x) can be determined in sequence as follows:

$$\begin{cases} A_m = \dfrac{f_m}{U_{mm}} \\ A_{m-1} = \dfrac{f_{m-1} - A_{m-1} \cdot U_{m-1;m}}{U_{m-1,m-1}} \\ A_{m-2} = \dfrac{f_{m-2} - A_{m-1} \cdot U_{m-2;m-1} - U_{m-2,m} \cdot A_m}{U_{m-2,m-2}} \\ \vdots \\ A_0 = (f_0 - A_m \cdot U_{1m} - A_{m-1} \cdot U_{1m-1} - \cdots - U_{12} \cdot A_1)/U_{11} \end{cases} \qquad \cdots\cdots\cdots (6.20)$$

Once all the coefficients i.e. A_m have been determined from equation

(6.20), then the polynomial equation P(x) which can represent a better approximation for a set of data, can be solved and the new coordinates for (x_i, y_i), i=1, ---, n, determined.

CHAPTER 7

EVALUATION OF AERODYNAMIC CHARACTERISTICS OF AN ARBITRARY WING IN A SUPERSONIC FLOW

7.1 INTRODUCTION

In this chapter the procedure is described in which the values of velocity potentials which are calculated on the wing planform (previously described in Chapters (5) and (6)) are used to calculate the aerodynamic characteristics of wing planform at a particular Mach number. In order to achieve this, the following sections will provide the necessary formulea for this.

7.2 EVALUATION OF LIFT COEFFICIENT

Using Bernouilli's equation:

$$P - P_\infty - -\rho_\infty \left(U_\infty \frac{\partial}{\partial x} + i\omega\right) (\phi_R + i\phi_I),$$

in the form appropriate for unsteady sinusoidally oscillating flow of frequency ω modifying the above equation by ignoring the complex port gives:

$$\frac{P - P_\infty}{\rho U_\infty^2} = - \frac{1}{U_\infty} \frac{\partial \phi}{\partial x} \qquad \text{..... (7.1)}$$

Since ϕ is an anti-symmetric function of Z we have the lift per unit area given by

$$\ell(x,y) = -2\ (P - P_\infty) \text{ positive up} \qquad \text{..... (7.2)}$$

Now using equation (7.1) we can write:

$$C_L = \frac{\text{Lift}}{\frac{1}{2}\rho U^2 S} = \frac{1}{\frac{1}{2}\rho U^2 S} \iint_S \ell\,(x,y)\,dxdy \qquad \ldots\ldots\ (7.3)$$

where S is the planform area. Equations (7.1), (7.2) with $\phi' = \frac{\phi}{UL}$, give (L is a Reference length)

$$C_L = \frac{4L}{S} \iint_S \left[\frac{\partial \phi'}{\partial x}\right] dxdy \qquad \ldots\ldots\ (7.4)$$

$$= \frac{4L}{S} \int_{-\sigma}^{+\sigma} \phi_{T.E.}\, dy,$$

where σ is the semi-span, and using the fact ϕ' is zero along the leading edge. Now we introduce

$$\xi = \frac{x}{C_o}\ ,\ \eta = \frac{y}{\sigma} \qquad \ldots\ldots\ (7.5)$$

where C_o is the root chord. Therefore equation (7.4) becomes

$$C_L = \frac{8\sigma L}{S} \int_0^1 \phi'_{T.E}\, d\eta \qquad \ldots\ldots\ (7.6)$$

7.3 EVALUATION OF PITCHING MOMENT COEFFICIENT

The pitching-moment coefficient C_{MP}, positive nose up, about an axis through the wing vertex is

$$C_{MP} = -\frac{1}{\frac{1}{2}\rho U^2 S\bar{c}} \iint_S x.\ell(x,y)\, dxdy \qquad \ldots\ldots\ (7.7)$$

where $\bar{c}$ is the mean chord. Using equations (7.1), (7.2), (7.5) equation (7.7), can be modified to give:

$$C_{MP} = \frac{8\sigma L C_o}{S\bar{c}} \int_0^1 \left[\int_{L.E}^{T.E} \phi'.d\xi - \xi_{T.E} \cdot \phi'_{T.E} \cdot \right] d\eta \qquad \ldots\ldots\ (7.8)$$

7.4 NUMERICAL SOLUTION FOR LIFT AND PITCHING MOMENT COEFFICIENTS

It will be seen that all the spanwise integrations which occur, are of the same type, i.e. $\int_0^1 P(\eta)\, d\eta$. We begin by discussing a method of evaluating this type of integral. It is assumed initially that the same mesh used in obtaining the potentials is also used in obtaining the relevant integrals. The diagram shows that the characteristic mesh can be used to define a set of equally spaced spanwise stations. The number of spanwise stations can be odd or even, and Simpson's rule is used for the summations of the trailing edge potentials. Therefore Simpson's rule can be shown to be:

(putting $\phi_{T.E}(\eta) = P(\eta)$)

$$\int_0^1 \phi'(\eta)d\eta = \frac{1}{3}\Delta\eta\left[2\phi'(0) + 2\phi'(1) + 4\phi'(2) + 2\phi'(3) + \text{---} + \phi'(n)\right]$$

n is odd ..... (7.9)

OR

$$= \frac{1}{3}\Delta\eta\left[\phi'(0) + 4\phi'(1) + 2\phi'(2) + 4\phi'(3) + \text{----} + \right.$$

$$\left. + 4\phi'(n-1) + \phi(n)\right]$$

n is even ..... (7.10)

Therefore using equations (7.9) or (7.10), the lift coefficient can be evaluated.

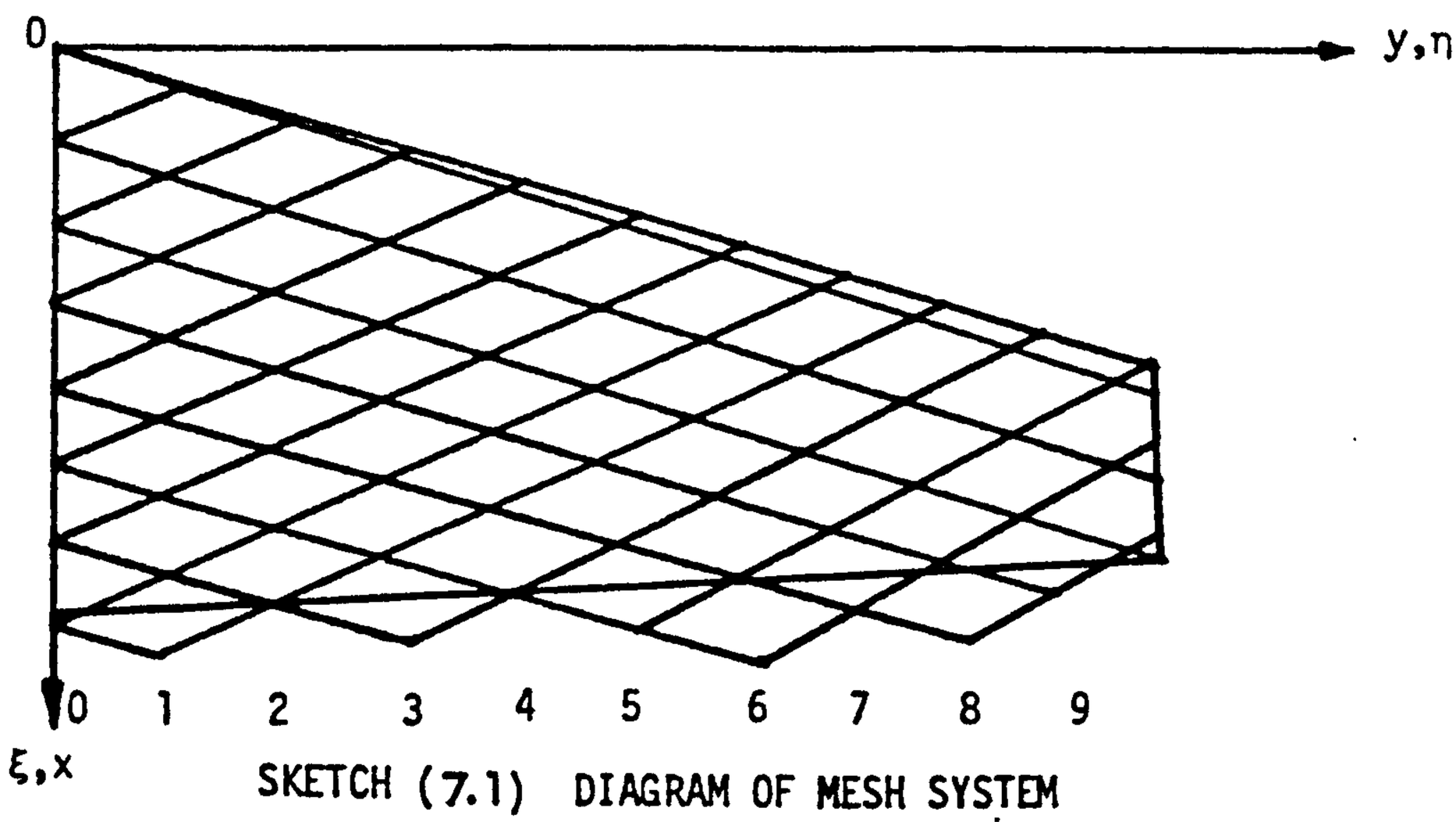

SKETCH (7.1) DIAGRAM OF MESH SYSTEM

Now, similarly using Simpson's rule once more to evaluate the double integral of equation (7.8) in the form:

$$C_{MP} = \frac{A}{3}\,\Delta\eta.\left[2P_0 + 2P_1 + 4P_2 + 2P_3 + --- + P_n\right]$$

n is odd ..... (7.11)

OR $$= \frac{A}{3}\,\Delta\eta.\left[P_0 + 4P_1 + 2P_2 + 4P_3 + --- + 4P_{n-1} + P_n\right]$$

n is even ..... (7.12)

where

$$P_n = \int_{L.E}^{T.E} \phi'(n)\, d\xi - \xi_{T.E}\cdot\, \phi'_{T.E} \qquad \text{..... (7.13)}$$

and $$A = \frac{8.\sigma.L.C_o}{S.\bar{c}} \qquad \text{..... (7.14)}$$

Similarly (7.13) can be evaluated by using Simpson's Rule, and hence C_{MP}.

7.5 INTERPOLATION OR EXTRAPOLATION OF THE POTENTIALS AT THE TRAILING EDGE

Considering the potentials at the trailing edge. For this case

there is no integration, but due to the fact that in general the characteristic mesh does not fit exactly on the planform, it will be necessary to obtain $\phi'_{T.E}$ by interpolation or extrapolation. As shown in the diagram, for instance, at spanwise station 3 interpolation is needed. and if the mesh point was on the planform extrapolation would have to be used.

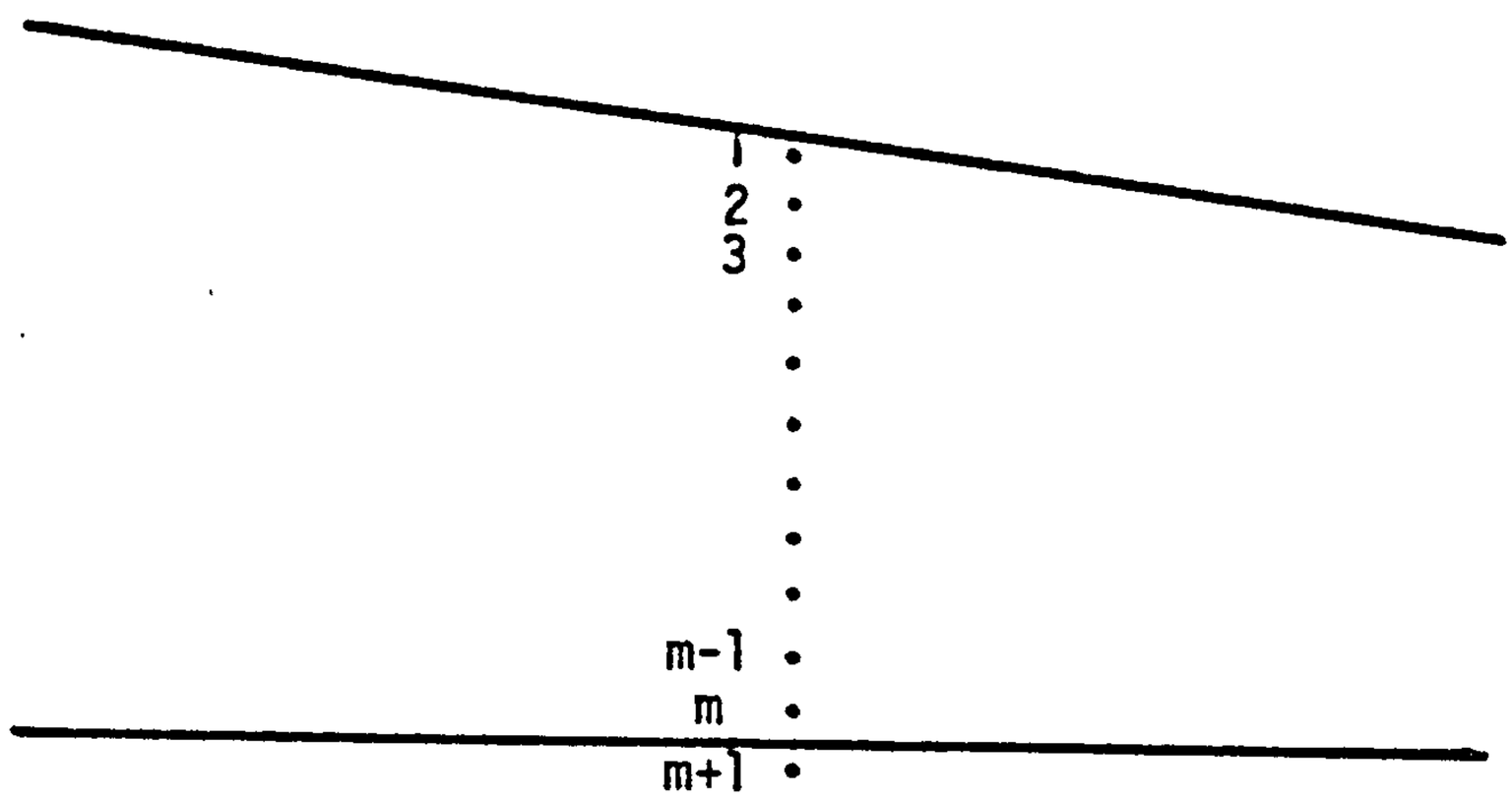

Thus, the scheme which was used for linear interpolation of potentials at trailing edge is:

$$\phi'_{T.E} = \phi'_m + \frac{(\phi'_{m+1} - \phi'_m)}{\Delta\xi} \cdot (\xi_{T.E} - \xi_m) \qquad \ldots\ldots\ (7.15)$$

and similarly for a linear extrapolation the appropriate formula which was used is:

$$\phi'_{T.E} = \phi'_m + \frac{(\phi'_m - \phi'_{m-1})}{\Delta\xi} (\xi_{T.E} - \xi_m) \qquad \ldots\ldots\ (7.16)$$

7.6 CALCULATION OF PRESSURE COEFFICIENT C_p ON THE WING PLANFORM

This can be done by finding derivatives for ϕ. To do this inside the planform a central difference equation can be used, and on the boundary a first order difference equation can be used, as shown below:

$$C_p = (\phi'_{m+1} - \phi'_{m-1})/2\Delta \qquad \text{..... (7.17)}$$

where Δ is unit length along the direction of movement

or on the leading edge C_p is taken to be given by:

$$C_p = (\phi'_{m+1} - \phi'_m)/\Delta \qquad \text{..... (7.18)}$$

and on the trailing edge C_p is given by

$$C_p = (\phi'_m - \phi_{m-1})/\Delta \qquad \text{..... (7.19)}$$

CHAPTER 8

SUPERSONIC WING-BODY INTERFERENCE

8.1 INTRODUCTION

The purpose of this chapter is to present methods for predicting the aerodynamic characteristics of configurations formed by the addition of lifting surfaces to a body. The primary focus here is on the wing-body calculations which are the wing-only results is obtained from Allen and Sadler's method in the previous chapters. The method which was set out by Allen and Sadler, only considered the wing aerodynamic characteristics without the effect of the body. However, the method that has been employed for the interference calculations is that outlined by J. Nielsen (Ref. 8.1). As shown in Section 5.6 of (Ref 8.1), the results are summarized for a complete wing-body configuration, and also Section (5.7) shows applications of these results to non-slender configurations and a calculative example illustrating the theoretical methods. From Section (5.7) (Ref 8.1), this method for wing-body combinations for a non-slender configuration can be used with confidence.

For this purpose, the aerodynamic characteristics of the wing above, which is found by the Allen and Sadler (Ref. 6.1), method, was used to calculate lift for a slender body combination. This can be done by calculating lift on the wing due to the body, and lift on the body due to the wing. And finally the position of the new centre of pressure due to presents of body, which is suppose to be sufficiently near to the value of centre of pressure location for wing alone,can be determined.

Before consideration of the application of slender-body theory to wing-body interference, it is probably as well to mention that wing-body interference problems can in certain instances be solved by full linear theory. For rectangular wings and circular bodies, for instance, the formal boundary-value problem presented by the full linear theory has been solved by Nielsen J.N. (Ref. 8.2). Also another solution for part of the interference field is given by Morikawa (Ref. 8.3).

However, these methods are generally too complex for actual engineering use, but they do serve as useful yardsticks for evaluating more approximate but simpler engineering methods. One such method is the essential subject matter of this chapter. A general survey of the subject of wing-body interference has been presented by Lawrence and Flax. (Ref. 8.4).

8.2 DETERMINATION OF PRESSURE COEFFICIENT C_p

Using energy equation in wind coordinates:

$$\frac{\gamma}{\gamma-1}\frac{P}{\rho} + \frac{1}{2}\left[(U_\infty + u_1)^2 + v_1^2 + w_1^2\right] = \frac{\gamma}{\gamma-1}\frac{P_\infty}{\rho_\infty} + \frac{1}{2}U_\infty^2 \quad \ldots\ldots (8.1)$$

Knowing $\frac{P}{P_\infty} = \left(\frac{\rho}{\rho_\infty}\right)^\gamma$ for an isentropic flow, then substitution into equation (8.1) gives:

$$\frac{\gamma}{\gamma-1}\cdot\frac{P_\infty}{\rho_\infty}\left(\frac{P}{P_\infty}\right)^{\frac{\gamma-1}{\gamma}} + \frac{1}{2}\left(u_1^2 + v_1^2 + w_1^2 + 2u_1U_\infty\right) = \frac{\gamma}{\gamma-1}\cdot\frac{P_\infty}{\rho_\infty} \quad \ldots (8.2)$$

Therefore simplifying equation (8.2):

$$\left(\frac{P}{P_\infty}\right)^{\frac{\gamma-1}{\gamma}} = 1 - \frac{\gamma-1}{2\gamma}\cdot\frac{\rho_\infty}{P_\infty}\left(u_1^2 + v_1^2 + w_1^2 + 2u_1U_\infty\right)$$

$$= 1 - \frac{\gamma-1}{2} M_\infty^2\left(\frac{2u_1}{U_\infty} + \frac{u_1^2 + v_1^2 + w_1^2}{U_\infty^2}\right) \quad \ldots\ldots\ldots (8.3)$$

Knowing that

$$C_p = \frac{P - P_\infty}{\frac{1}{2}\rho_\infty U_\infty^2} = \frac{P - P_\infty}{\gamma/2M_\infty^2 P_\infty} = \frac{2}{\gamma M_\infty^2}\cdot\left[\frac{P}{P_\infty} - 1\right] \quad \ldots\ldots\ldots (8.4)$$

Substituting (8.3) into (8.4) and expanding using binomial theorem results in:

$$C_p = \frac{2}{\gamma M_\infty^2}\left\{\left[1 - \frac{\gamma-1}{2} M_\infty^2\left(\frac{2u_1}{U_\infty} + \frac{u_1^2 + v_1^2 + w_1^2}{U_\infty}\right)\right]^{\frac{\gamma}{\gamma-1}} - 1\right\}$$

$$= \frac{2}{\gamma M_\infty^2}\left\{-\frac{\gamma M_\infty^2}{2}\left(\frac{2u_1}{U_\infty} + \frac{u_1^2 + v_1^2 + w_1^2}{U_\infty^2}\right) + \frac{\gamma M_\infty^4}{8}\left(\frac{2u_1}{U_\infty} + \frac{u_1^2 + v_1^2 + w_1^2}{U_\infty^2}\right)^2 + 0\left(M_\infty^6\left(\frac{u_1}{U_\infty}\right)^3\right)\right\}$$

$$= -\left[\frac{2u_1}{U_\infty} + \frac{u_1^2 + v_1^2 + w_1^2}{U_\infty^2}\right] + \frac{M_\infty^2}{2}\left[\frac{2u_1}{U_\infty} + \frac{u_1^2 + v_1^2 + w_1^2}{U_\infty^2}\right]^2 +$$

$$O\left(M_\infty^4 \left(\frac{u_1}{U_\infty}\right)^3\right) \cdots\cdots$$

$$C_p = -\frac{2u_1}{U_\infty} + \frac{u_1^2(M_\infty^2 - 1) - v_1^2 - w_1^2}{U_\infty^2} + O\left(\left(\frac{u_1}{U_\infty}\right)^3\right) \cdots\cdots \quad (8.5)$$

Transferring the wind axes system to body-axes gives:

$$\begin{cases} u_1 = u + w\alpha \\ v_1 = v \\ w_1 = -u\alpha + w \end{cases}$$

for small incidence α at zero bank angle

Therefore modifying C_p, gives:

$$C_p = -2\left(\frac{u + w\alpha}{U_\infty}\right) + \frac{(u + w\alpha)^2 (M_\infty^2 - 1) - v^2 - (-u\alpha + w)^2}{U_\infty^2}$$

$$+ O\left(\left(\frac{u}{U_\infty}\right)^3\right) \quad \cdots\cdots\cdots (8.6)$$

In slender body theory if α is $O(t)$, $\frac{v}{U_\infty}$ and $\frac{w}{U_\infty}$ are $O(t)$, $\frac{u}{U_\infty}$ is $O(t^2 \log_e t)$

Therefore

$$C_p = -2\ \frac{u}{U_\infty} + \frac{w}{U_\infty}\alpha - \frac{v}{U_\infty}^2 - \frac{w}{U_\infty}^2 + \text{small terms}$$

$$\vdots \ldots\ldots\ldots (8.7)$$

Not put
$$\begin{cases} \dfrac{u}{U_\infty} = \alpha u_\alpha + u_t \\ \dfrac{v}{U_\infty} = \alpha v_\alpha + v_t \\ \dfrac{w}{U_\infty} = \alpha w_\alpha + w_t \end{cases}$$

where u_α is due to unit incidence and u_t is due to unit thickness

$$\ldots\ldots\ldots (8.8)$$

Substituting equations (8.8) into equation (8.7) gives:

$$C_p = -2\ \{\alpha u + u_t + \alpha^2 w_\alpha + \alpha w_t\} - (\alpha v_\alpha + v_t)^2 - (\alpha w_\alpha + w_t)^2$$

$$= -2\ \{\alpha u_\alpha + \alpha^2 w\alpha\} - \alpha^2 v_\alpha^2 - \alpha^2 w_\alpha^2 - 2\ u_t - v_t^2 - w_t^2 - 2\alpha v_\alpha . v_t$$

$$- 2.\alpha.w_\alpha.w_t - 2\alpha.w_t \ldots\ldots\ldots (8.9)$$

Denote by $(\ )^+$ the upper surface and by $(\ )^-$ the low surface values.

Then $u_\alpha^+ = -u_\alpha^-$, $v_\alpha^+ = -v_\alpha^-$, $w_\alpha^+ = w_\alpha^-$

$u_t^+ = u_t^-$, $v_t^+ = v_t^-$, $w_t^+ = w_t^-$

For an axisymmetric body, it can be shown that

$v_\alpha v_t + w_\alpha w_t + w_t = 0.$

Hence the loading on the body due to the wing is:

$$(\Delta C_p)_{B(w)} = (C_p^- - C_p^+)_{B(w)}$$

$$\underline{\underline{(\Delta C_p)_{B(w)} = 4\alpha\, u_\alpha^+}} \qquad \ldots\ldots\ (8.10)$$

On a thin wing $w_\alpha^+ = w_\alpha^- = -1$, $w_t^+ = -w_t^- = 0$

Hence the loading on the wing due to the body is:

$$(\Delta C_p)_{w(B)} = (C_p^- - C_p^+)_{w(B)}$$

$$\underline{\underline{(\Delta C_p)_{w(B)} = 4\alpha\, u_\alpha^+ + 4\alpha\, v_\alpha^+ v_t^+}} \qquad \ldots\ldots\ (8.11)$$

The complex perturbation potential for flow about an axisymmetric body of radius a(x) with a flat wing of semispan s(x) at incidence α to a stream of speed U_∞ is:

$$w = U_\infty \Bigg[\underbrace{b_0(x) + a\frac{da}{dx}\log_e\zeta}_{\text{THICKNESS}} \underbrace{- i\alpha\left\{\left[\left(\zeta + \frac{a^2}{\zeta}\right)^2 - \left(s + \frac{a^2}{s}\right)^2\right]^{\frac{1}{2}} - \zeta\right\}}_{\text{INCIDENCE}}$$

$$\vdots \ldots\ldots\ (8.12)$$

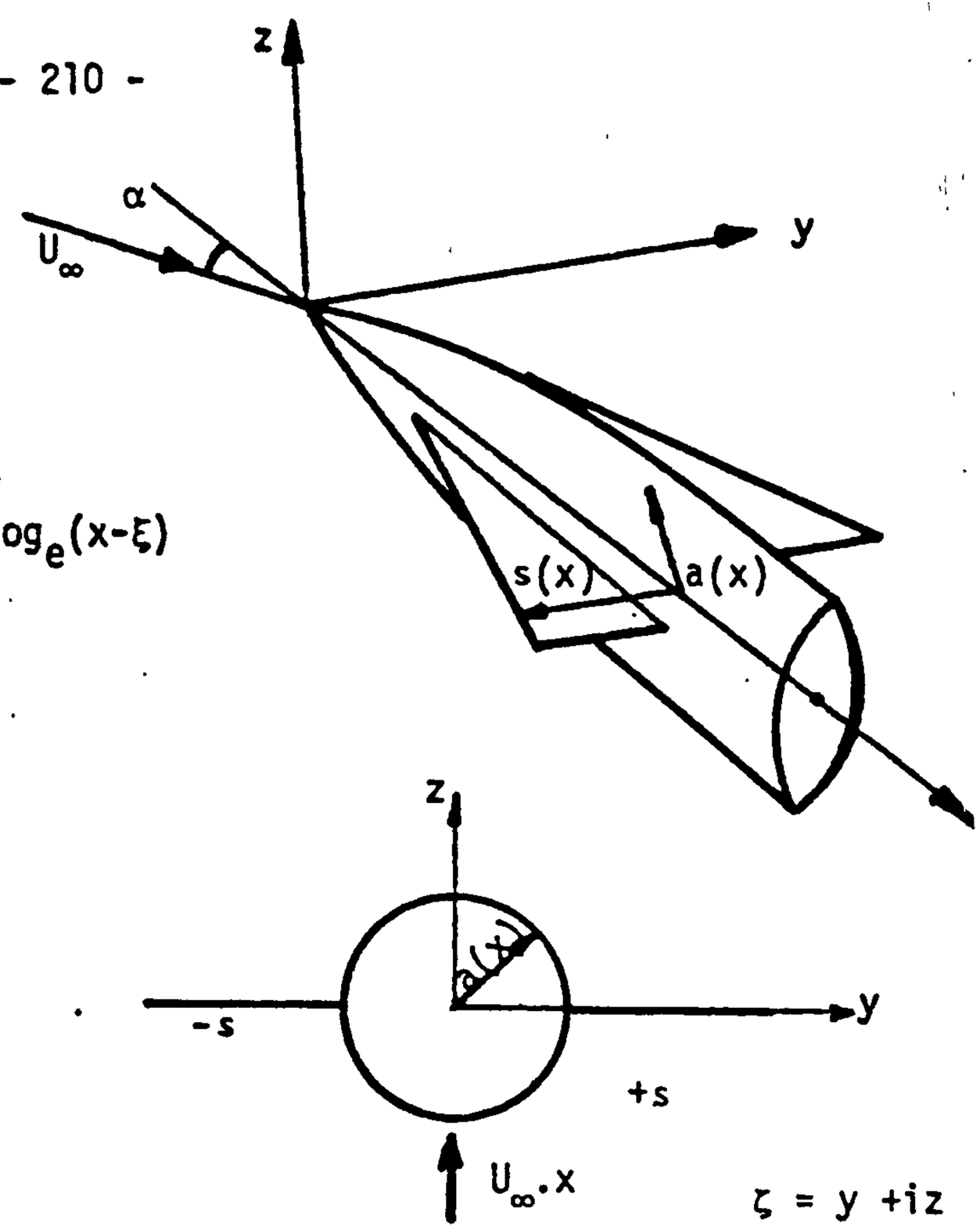

SKETCH (8.1)

where:

$$b_o(x) = \frac{1}{2\pi}\left\{ s'(x)\log_e\frac{B}{2} - \int_o^x \log_e(x-\xi)\, s''(\xi)\,d\xi \right\}$$

and where

$$s(x) = \pi a^2(x),\ B^2 = M_\infty^2 - 1$$

Putting the perturbation potential $\phi = R(w)$

$$\phi = U_\infty\left\{ b_o(x) + a\frac{da}{dx}\log_e\sqrt{y^2+z^2} + \alpha R\left\{\left[\left(s+\frac{a^2}{s}\right)^2 - \left(y+iz+\frac{a^2}{y+iz}\right)^2\right]^{\frac{1}{2}}\right\} - \alpha z \right\} \quad \ldots\ldots\ (8.13)$$

$$\therefore\ u = \frac{\partial\phi}{\partial x} = U_\infty\left\{\frac{db_o}{dx} + \left(a\frac{d^2a}{dx^2} + \left(\frac{da}{dx}\right)^2\right)\log_e\sqrt{y^2+z^2}\right\} + U_\infty.\alpha.R\ \{A\}$$

where

$$A = \left\{\frac{\left(s+\frac{a^2}{s}\right)\left(\left(1-\frac{a^2}{s^2}\right)\frac{ds}{dx} + \frac{2a}{s}\frac{da}{dx}\right) - \left(y+iz+\frac{a^2}{(y+iz)}\right)\frac{2a}{(y+iz)}\frac{da}{dx}}{\left[\left(s+\frac{a^2}{s}\right)^2 - \left((y+iz)+\frac{a^2}{(y+iz)}\right)^2\right]^{\frac{1}{2}}}\right\} \quad \ldots\ldots\ (8.14)$$

On the body $y = a \cos\theta$, $z = a \sin\theta$

and

$$u = U_\infty \left\{ \frac{db_o}{dx} + \left(a \frac{d^2a}{dx^2} + \left(\frac{da}{dx}\right)^2\right) \log_e a + \alpha \frac{\left(s+\frac{a^2}{s}\right)\left[\left(1-\frac{a^2}{s^2}\right)\frac{ds}{dx}+\frac{2a}{s}\frac{da}{dx}\right] - 2a\cos\theta \; 2\cos\theta\frac{da}{dx}}{\left[\left(s+\frac{a^2}{s}\right)^2 - (2a\cos\theta)^2\right]^{\frac{1}{2}}} \right.$$

$$\vdots \ldots\ldots \quad (8.15)$$

On the wing $z = o$, therefore equation (8.14) will become:

$$u = U_\infty \left\{ \frac{db_o}{dx} + \left(a \frac{d^2a}{dx^2} + \left(\frac{da}{dx}\right)^2\right) \log_e y + \alpha \frac{\left(s+\frac{a^2}{s}\right)\left[\left(1-\frac{a^2}{s^2}\right)\frac{ds}{dx}+\frac{2a}{s}\frac{da}{dx}\right] - \left(y+\frac{a^2}{y}\right)\frac{2a}{y}\frac{da}{dx}}{\left[\left(s+\frac{a^2}{s}\right)^2 - \left(y+\frac{a^2}{y}\right)^2\right]^{\frac{1}{2}}} \right\}$$

if $y \leqslant s$ ..... (8.16)

Also

$$v = \frac{\partial\phi}{\partial y} = U_\infty \left\{ a \frac{da}{dx} \frac{y}{(y^2+z^2)} + \alpha R. \left[\frac{-\left((y+iz) + \frac{a^2}{(y+iz)}\right)\left(1 - \frac{a^2}{(y+iz)^2}\right)}{\left[\left(s+\frac{a^2}{s}\right)^2 + \left((y+iz) + \frac{a^2}{(y+iz)}\right)^2\right]^{\frac{1}{2}}} \right] \right\}$$

$$\vdots \ldots\ldots \quad (8.17)$$

On the body $y = a \cos\theta$, $z = a \sin\theta$

and

$$v = U_\infty \left\{ \frac{da}{dx} \cos\theta - \alpha \frac{2a \cos\theta (1 - \cos 2\theta)}{\left[(s + \frac{a^2}{s})^2 - (2a\cos\theta)^2 \right]^{\frac{1}{2}}} \right\} \quad \ldots\ldots (8.18)$$

For the wing $z = o$, therefore

$$v = U_\infty \left\{ \frac{a}{y} \frac{da}{dx} - \alpha \frac{(y + \frac{a^2}{y})(1 - \frac{a^2}{y^2})}{\left[(s + \frac{a^2}{s})^2 - (y + \frac{a^2}{y})^2 \right]^{\frac{1}{2}}} \right\} \quad \text{if } y \leq s$$

$$\vdots\ldots\ldots (8.19)$$

Therefore the body pressure distribution can be found due to the wing by using equations (8.10) and (8.16) in the form:

$$(\Delta C_p)_{B(w)} = 4\alpha\, u_\alpha^+ = \frac{4\alpha . (1 - \frac{a^4}{s^4}) \frac{ds}{dx} + \frac{2a}{s} (1 - \frac{a^2}{s^2} - \frac{2y^2}{a^2}) \frac{da}{dx}}{\left[(1 + \frac{a^2}{s^2})^2 - 4 \frac{y^2}{s^2} \right]^{\frac{1}{2}}}$$

$$\vdots\ldots\ldots (8.20)$$

Also by substitution of equation (8.19) into equation (8.11), the pressure distribution can be found on the wing due to the body:

$$(\Delta C_p)_{w(B)} = 4\alpha\, u_\alpha^+ + 4\alpha\, v_\alpha^+ \; v_t^+$$

$$= 4\alpha . \frac{(1-\frac{a^4}{s^4})\frac{ds}{dx} + \frac{a}{s}\frac{da}{dx}\left[2(1+\frac{a^2}{s^2}) - 2(1+\frac{a^2}{y^2}) - \frac{s}{y}\frac{y}{s}(1-\frac{a^4}{y^4})\right]}{\left[(1+\frac{a^4}{s^2}) - \frac{y^2}{s^2}(1+\frac{a^4}{y^4})\right]^{\frac{1}{2}}}$$

$$(\Delta C_p)_{w(B)} = 4\alpha . \frac{(1-\frac{a^4}{s^4})\frac{ds}{dx} + \frac{a}{s}\frac{da}{dx}\left[2(\frac{a^2}{s^2}-1) + (1-\frac{a^2}{y^2})^2\right]}{\left[(1+\frac{a^4}{s^2}) - \frac{y^2}{s^2}(1+\frac{a^4}{y^4})\right]^{\frac{1}{2}}}$$

..... (8.21)

8.3 INTEGRATION OF THE LIFT ON WING WHEN THE BODY IS OF CONSTANT CROSS SECTION

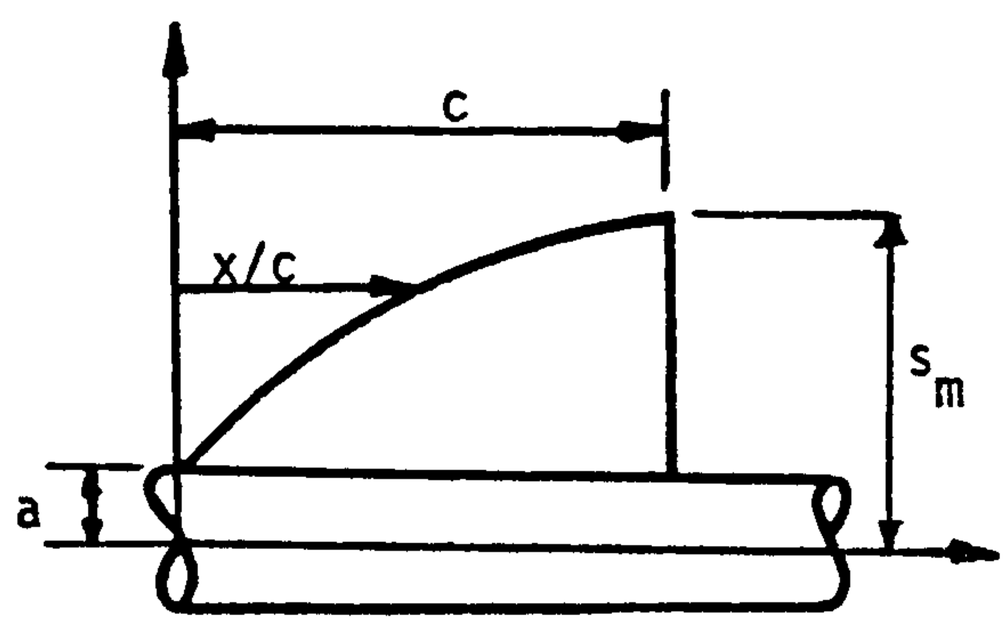

If $\frac{da}{dx}$ = o over the portion corresponding to the wing position, then equation (8.21) will become

$$(\Delta C_p)_{w(B)} = \frac{4\alpha\,(1-\frac{a^4}{s^4})\,\frac{ds}{dx}}{\left[(1+\frac{a^4}{s^4}) - \frac{y^2}{s^2}(1+\frac{a^4}{y^4})\right]^{\frac{1}{2}}}$$

..... (8.22)

Therefore lift on one wing $L_{w(B)}$ (due to the body) is given by:

$$\frac{L_{w(B)}}{\frac{1}{2}\rho U_\infty^2} = \int_a^{s_m}\left\{\int_{x\ell_c}^{c}(\Delta C_p)_{w(B)}.dx\right\}dy = \int_a^{s_m} 4\alpha\left[(s_m+\frac{a^2}{s_m})^2 - (y+\frac{a^2}{y})^2\right]^{\frac{1}{2}} dy$$

..... (8.23)

And also the lift on the wing alone in the absence of the body is given by:

$$\frac{L_W}{\frac{1}{2}\rho_\infty U_\infty^2} = 2\pi\alpha\,(s_m - a)^2 \qquad \ldots\ldots (8.24)$$

Assuming $\lambda = \frac{s_m}{a}$, using equations (8.23) and (8.24) the following result can be obtained:

The lift ratio,

$$K_W = \frac{L_{W(B)}}{L_W} = \frac{1}{\pi(\lambda-1)^2}\left[\frac{\pi}{2}\left(\frac{\lambda^2-1}{\lambda}\right)^2 + \left(\frac{\lambda^2+1}{\lambda}\right)^2 \sin^{-1}\left(\frac{\lambda^2-1}{\lambda^2+1}\right) - 2\left(\frac{\lambda^2-1}{\lambda}\right)\right]$$

$$\vdots\ldots\ldots (8.25)$$

Similarly, the lift ratio $K_B = \frac{L_{B(W)}}{L_W} = \frac{L_C - L_{W(B)} - L_N}{L_W}$

$$\vdots\ldots\ldots (8.26)$$

where L_C is total lift of a combined wing and body,

L_N is lift on nose section ahead of wing.

K_B can be found from the following equation:

$$K_B = \left(1 + \frac{1}{\lambda}\right)^2 - K_W \qquad \ldots\ldots (8.27)$$

Now from slender theory $\frac{L_W}{\frac{1}{2}\rho_\infty U_\infty^2} = 2\pi\alpha(s_m - a)^2$, $\frac{L_C}{\frac{1}{2}\rho_\infty U_\infty^2} = 2\pi\alpha.s_m^2\left(1 - \frac{a^2}{s_m^2} + \frac{a^4}{s_m^4}\right)$

and, $L_N = 2\pi.\alpha.a^2$ ..... (8.28)

Finally, from equation (8.26), we can write:

combined lift $L_C = L_{W(B)} + L_{B(N)} + L_N$ ..... (8.29)

For our purpose, using the lift and pitching moment coefficients which have been derived by Allen and Sadler method Ref (6.1), substitute lift for the wing alone into equation (8.25) and derive the lift on the wing due to presence of the body. Finally, the lift on the body due to presence of the wing can be calculated from equation (8.26), and also the total combined lift can be determined from equation (8.28) and equation (8.29).

REFERENCES FOR CHAPTER 8

(8.1) NIELSEN, JACK N. "Missile Aerodynamics". McGraw-Hill Book Company, Inc. New York, Toronto, London, 1960. H. Guyford Stever (Editor).

(8.2) NIELSEN, JACK N. "Quasi-cylindrical theory of wing-body interference at supersonic speeds and comparison with experiment, NACA. Tech. Report, 1252, 1956.

(8.3) MORIKAWA, G.K. "The wing-body problem for linearized supersonic flow', Doctoral thesis, California Institute of Technology, Pasadena, 1949.

(8.4) LAWRENCE, H.R. AND FLAX, A.H. "Wing-body interference at subsonic and supersonic speeds". Survey and new developments, J. Aeronautical Sci, Vol. 21, No. 5, 1954.

CHAPTER 9

RESULTS, COMPARISONS AND DISCUSSIONS

9.1 INTRODUCTION

This chapter is concerned with the results of subsonic and supersonic computations and of the wind tunnel tests, with discussions of results and comparisons. These are set out in the following sections.

9.2 SUBSONIC RESULTS

Extensive numerical computation work using the Quadvort method was carried out for three specified wing geometries corresponding to sweep angles of 12.5^{o}, 32.5^{o}, and 52.5^{o} over the range of incidence 2° to 20° with 2° intervals. But in this chapter only some of the incidence angle results and graphs are presented for each swept wing. The rest of these results are kept in a file for reference. See Figs (9 .3), (9 .4), and (9 .5) for the three specified swept wing geometries.

9.3 SUBSONIC RESULTS AND COMPARISONS

The combination of wing and body vortex-ring distributions is a logical step forward. The mutual interference effects as well as the individual characteristics of the components are now simultaneously by applying the boundary condition at control points on the combined surfaces. For a comparison of the Quadvort method with other methods, a test case of an infinite cylinder having 2:1 elliptical section was considered. The Quadvort method as

programmed can accomodate arrangements which have a plane of symmetry. Considering one half of the cylinder, the semi-ellipse section is represented by 6 vortex-rings. Closed vortex ring elements cover the fuselage over a length of 4 wing chords, and fore and aft of this the fuselage is represented by constant strength semi-infinite line vortices, Fig (9 .1). The basic fuselage was considered with three different wings as shown in Fig (9.1). Case WB_1 has an unswept wing, case WB_2 has a 45° swept wing, and case WB_3 has a cranked wing 45° sweep on the inboard panel and zero sweep on the outboard panel (from 0.6 semi-span). In each case the wing has constant chord, an aspect ratio of 5 and is centrally mounted, also the body width is 0.2 of the span and the wing and body are set at 5° incidence. The resulting spanwise load distributions and centre of pressure locus are presented in Figs. (9.2) and compared with results from a Brough Composite Computer programme (A10A) based on Kuchemann (9.1) (basic wing), Weber, Kirby and Kettle (9.2) (wing-fuselage), and Brebner (9.3) (wing cranks).

WB_1 results (Fig (9.2a)) for spanwise loading ($C_L \cdot C/\bar{C}$) show excellent agreement over the inboard part of the wing but Quadvort results show a much earlier fall in load towards the tip and also a lower value of lift carried by the fuselage. As a result Quadvort overall $\bar{C}_L$ is lower than that from the A10A programme (0.353 compared with 0.369) The centre of pressure locus due to Quadvort shows a forward shift at the fuselage side and also at the tip. At mid-semispan the Quadvort curve coincides with the constant value from the A10A

program. Fig (9.2b) shows the results for Case WB_2. The Quadvort spanwise loading curve in this case shows an increase over that of the A10A program on the middle semi-span but still shows a lower fuselage lift. The overall $\bar{C}_L$ values are thus almost the same (0.297 and 0.296 for Quadvort and A10A program respectively). The centre of pressure locus due to Quadvort gives a slight rearward shift at the body side compared with the wing alone result. This rearward shift is considerably smaller than that from the A10A programme. Outboard of mid-semispan the Quadvort curve shows a much earlier forward shift than that of the A10A program.

The cranked wing results (Case WB_3) are shown in Fig (9.2c) Agreement between the two methods for the loading curve is good near the body side, but Quadvort shows a more gradual effect on the kink and a much earlier fall in loading towards the tip. Again Quadvort shows a small lift over the fuselage. The overall $\bar{C}_L$ from Quadvort and the A10A program are 0.315 and 0.334 respectively. Fig (9.2c) shows a smaller rearward shift in centre of pressure locus at the body side from Quadvort than is given by the A10A program but the curves rapidly converge to good agreement up to the kink. Outboard of the kink the curves diverge, the A10A curve moving rearwards a constant value and the Quadvort curve moving first rearward and then forward to converge, in fact, towards the unswept wing curve (WB_1) near the tip.

(9.4) Discussion of forces and moments from the Quadvortex method.

Some forces and moments distributions along the wing span are shown in Figs (9.6) to (9.11) for 0°, 12.5°, 32.5°, and 52.5° sweep wing. (geometries shown in Figs (9.3) to (9.5)). Figs (9.6) show the load distributions (local lift x local chord/overal lift x mean chord) $(\frac{C_L \cdot C}{C_L \cdot \bar{C}})$ along the wing span which show that generally load increases as the wing sweep angle increases. Figs (9.7) represent the spanwise lift distributions (C_L/α) for different incidence and sweep angle. These clearly indicate the rise in lift curve slope due to reduction in angle ofsweep. Spanwise lift C_L distributions show a fall near the tip for different sweep angles in Figs (9.8).

Figs (9.9) show the overall lift coefficient $\bar{C}_L$ for the wing and body combinations for variable sweep wings. The trend of these curves for $\bar{C}_L$ shows a significient and expected reduction with sweep angle. From these results it can be seen that as the angle of incidence α increases the aerodynamic coefficients of the wing-body combinations gernerally tend to increase with lift approximately proportional to α. Drag coefficients were determined, but not presented here shown to be proportional to α^2. Above a certain value of incidence these relations can not be found in practice due to flow separation of the wing and body surfaces. The separation pattern changes with the wing separation moving further towards the leading edge as the angle of incidence increases and effects of viscous flow consequently play a major rule on the wing -body aerodynamic forces. In some sweep cases theseeffects were seen experimentally for angle of incidence beyond 8° shown on the photos 4, 10, 14, 20, and 24 which indicate a 3-D classical spiral separation on the wing surface.

Nevertheless, these effects are neglected in the subsonic programme which simply treats the flow as an attached flow for any angle of incidence, and this produces some inaccuracies in the computational results at higher values of α.

Figs (9.10) show the overall lift coefficient against angle of incidence for the wing $C_{L(W)}$, body $C_{L(B)}$,and total wing and body $C_{L(W+B)}$ for the geometries shown in Figs (9.3) to (9.5) for the four wing sweep angles as mentioned. From these comparisons it can be seen that $C_{L(W+B)}$ has values of 1.59, 1.52, 1.33 and 1.07 at 20° incidence for the selected sweep angle ranges respectively. Wing lift coefficient $C_{L(W)}$ similarly has values of 1.23, 1.15, 0.94, 0.67 and for the body lift values of 0.36, 0.38, 0.394, 0.395 are noted for $C_{L(B)}$.

Pitching moment C_{MY} distributions are shown along the wing span for the selected sweep ranges, in Figs (9.11). These graph show that pitching moment coefficient decreases negatively as sweep angle increases.

9.5 Comparisons and Validations for the Quadvortex Method

A rectangular planform wing was tested for various aspect ratios by dividing the span and the chord into a number of elements. For this purpose, starting from very low aspect ratio wings (i.e. AR = 0.2), to rather high aspect ratio wings (i.e. AR = 5), those tested gave quite stable and consistent results, showing that the Quadvortex method is consistent within itself. Figs (9.12) to (9.17) shows some of these results.

Rectangular planform wings with aspect ratios of 4 and 0.5 were also tested and results were compared with Kuchemann and Multhopp from Reference (1) in Ref. (9.5), showing a very good agreement between Quadvortex results and Multhopp in both cases. In the case of the wing with aspect ratio AR = 4 (in Fig 9.18(a)), it can be deduced that the overall C_L/α from Quadvortex is 3.598 and from Multhopp is 3.56 which are close enough. In the other case with aspect ratio AR = 0.5, results shown in Fig (9.18(a)), the Quadvortex method gives a value of 0.778 for overall lift coefficient C_L/α, and by Multhopp's method the corresponding figure is 0.770 for overall lift coefficient C_L/α. Also the trend of these distributions are very close to each other and encouraging since ten spanwise stations were used in Quadvortex method.

Results for a constant chord swept back wing of 45° sweep angle with aspect ratio of 5 and 10 were compared with calculated results from Ref (9.6) by Multhopp, Falkner and others. Fig (9.19(a)) shows the spanwise loading comparisons and Fig (9.19(b)) gives spanwise

distributions of lift C_L/α. These graphs demonstrate an encouraging agreement between Quadvortex results and Multhopp calculated results. Fig (9.20) shows chordwise centre of pressure locations along the span for a rectangular wing planform with aspect ratio of 4 for various numbers of elements along the wing chord and span. From these graphs it can be seen that both the compatibility and the consistency of the Quadvortex results are quite encouraging. Fig (9.21) show the comparisons of Quadvortex results of spanwise distributions of lift C_L/α and centre of pressure locus, with experimental results by Kuchemann of Ref (9.5). The spanwise distributions of lift C_L/α in Fig (9.21(a)) shows slightly higher values in C_L/α up to mid-span for the experimental results, slightly lower values for η between 0.5 and 0.8 and, the variation for greater values of η up to the wing tip, for the experimental and Quadvortex results. Fig (9.21(b)) shows a good agreement of centre of pressure locus for experimental values by Kuchemann in Ref (9.5) with Quadvortex results. Although, there is a slightly more shift back near the wing root given by the experimental results, and slightly more forward shift given by the Quadvortex results near the wing tip.

(9.6) Comparisons of ΔC_p for experimental and computed results.

Two different wing-body geometries (12.5° and 52.5° sweep wings) were selected for comparisons of ΔC_p results. The trend of ΔC_p distributions are shown for seven spanwise stations for the wing sweep of 12.5° in Fig (9.22). These show a good agreement in experimental distributions ΔC_p from the wind tunnel tests with the computed results form Quadvortex along the wing chord. Nevertheless, these graphs show that ΔC_p near the wing tip from the experimental results has lower values, but this can be explained due to closeness of the wing tip to the wind tunnel wall. This effect which could be due to incorrect modelling of the tip can be studied from the flow visualization photographs (no. 14, 20), which indicate that at this incidence angle $\alpha = 12°$ there is a three-dimensional classical spiral separatins on the wing surface. There is also an image reflection of the tip vortex from the wind tunnel wall which could have some effect on the experimental readings. However, the tunnel effects were calculated to be small enough to be neglected.

Careful study of Figs (9.23), for the wing at 52.5 sweep and 10° incidence produces the following comparions: distributions for column 1, 2 and 3 (i.e. $\eta_1 = 0.3175$, $\eta_2 = 0.378$, and $\eta_3 = 0.502$ respectively) from computed results are the same as the wind tunnel experiments, while there is only a shightly higher value in ΔC_p from experiments near the leading edge. Columns 4 and 5 for $\eta_4 = 0.6258$, $\eta_5 = 0.7497$, which are in the vicinity of mid-span, give larger ΔC_p values than the computed results. Column 6 ($\eta_6 = 0.8735$) gives a good agreement in ΔC_p distribution between experimental and computed results. Finally column 7 ($\eta_7 = 0.9368$) at the wing tip gives a lower value in ΔC_p distributions than the computed results due to tip effects (some incorrect modelling perhaps).

Flow visualization photographs show that there is a strong slender wing vortex flow, and the extra lift near mid-chord (column 4 and 5) corresponds to expected extra lift under the core of the vortex. There is considerable spanwise flow at the tip and this indicates a loss of lift in these regions. The effects of the interference of wing and body as preedicted by the computer programme are to a large degree confirmed by the good agreement with experimental results for columns 1, 2 and 3 in each case. For these inboard regions flow visualization showns that the flow at the surface is more nearly streamwise and attached.

In order to improve the computational results in a case where the elements are very large in chord length and narrow in span, the number of elements can be increased so that a better accuracy may be achieved in the final results and vortex strength calculation for the wing. There is evidence that the vortex representation used in the computer programme near the tip is not sufficiently accurate to predict local values of Cp in these regions. It should be remembered that the $^1/_4$ element inset at the tip is employed to give best agreement of total vortex drag of the wing, and has not been optimised for best ΔC_p prediction. A more detailed representation with a closer mesh at the tip (particularly near the leading edge) could give better agreement with exact ideal flow theory. However, the complicated rolling up of tip vortices and viscous effects at the tip might require even more sophisticated treatment. These points mentioned are illustrated in the following sketch.

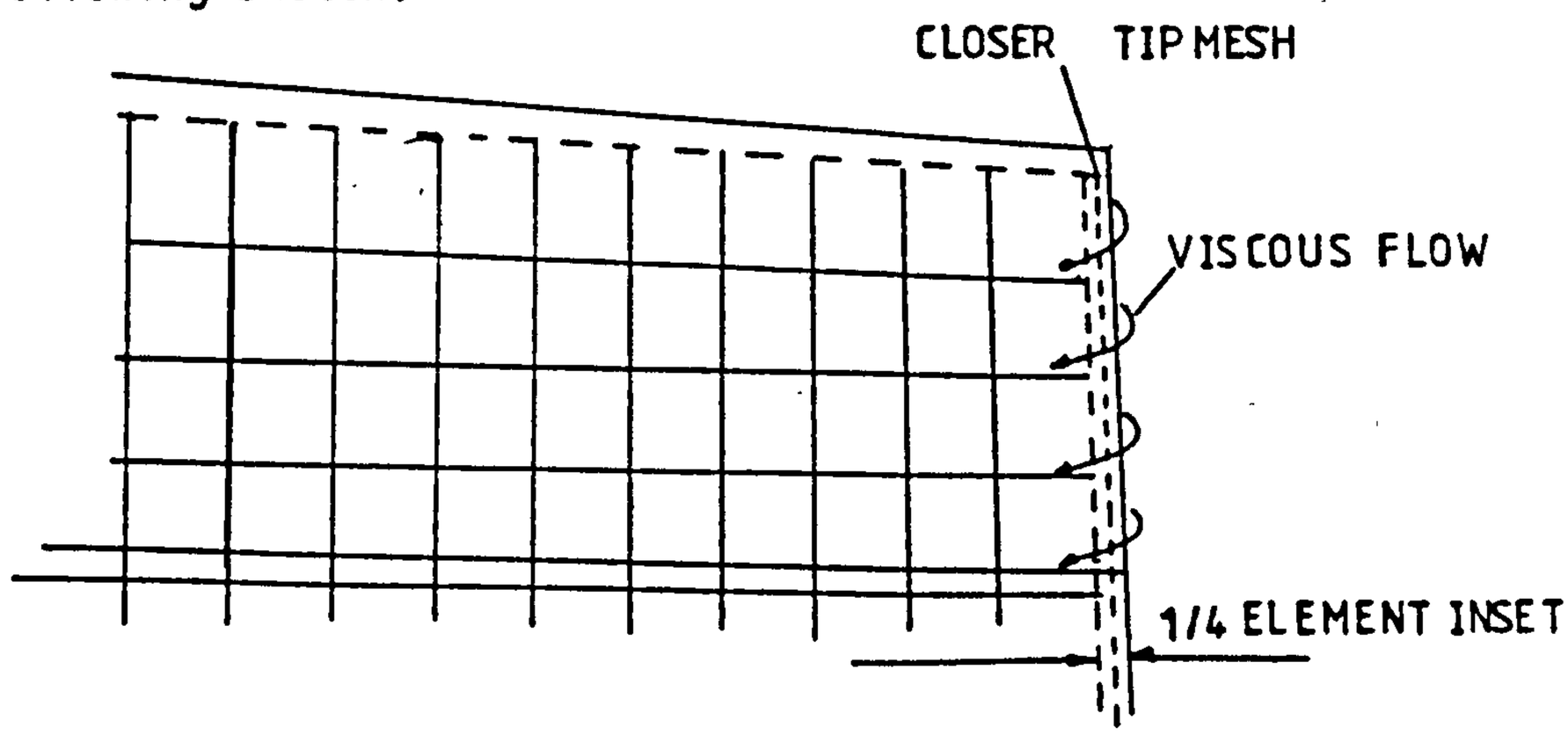

9.7 Comparisons of Supersonic Results

Figs (9.24) and (9.27) show a good comparison between our supersonic results using the Allen and Sadler method of solution for the potential flow theory, and experimental results. In this case a rectangular wing was considered with an aspect ratio of AR = 1.1 for a range of Mach numbers. The theoretical method used was exact conical flow theory and in each case the corresponding results of this method have been produced and are compared as shown on the graphs. Experimental results were obtained from the wind tunnel tests carried out by Tarbuck (final year project, University of Salford, Department of Aeronautical Engineering Science, 1980). These graphs show encouraging comparisons of our computed results with the theoretical and the experimental ones. Also it can be seen that the computed results (by use of Allen and Sadler) show greater accuracy as the Mach number increases from 1.7 to 2.4. The spanwise distributions of pressure coefficient on a rectangular wing are shown across the full span for different angles of incidence in these graphs. Finally, these comparisons indicate that the computational results (using the Allen and Sadler method) are quite acceptably accurate, and can be used for supersonic prediction of pressure coefficients over a general wing planform, over a large range of Mach numbers.

Two different planform wings are considered for the supersonic computer tests. Figs (9.27) show these planforms. Wing (1) is tested at 2° incidence, with Mach number M = 1.8 and a transonic

leading edge. Wing (2) has been tested for 2° incidence and Mach number M = 1.414 with a subsonic and supersonic leading edge. The pressure distributions were plotted in chordwise direction on both the wing planforms. Figs (9.29) to (9.33) show these distributions on the Wings (1) and (2) for a supersonic flow. These graphs show the pressure distribution Cp at some positions along the wing span. As these distributions of Cp show, for points approaching the tip, there is a sharper decrement in pressure coefficient Cp near the wing trailing edge and this effect increases near the tip. This can be explained, by considering the propogation of tip shock waves along the wing planform (Figs.9.31).

Figs (9..32) and (9.33) show the pressure distributions along the Wing (2) chord at root, mid-span, and the tip respectively. These graphs show a sudden drop in pressure coefficient Cp near the trailing edge, which is due to interference of the subsonic leading edge shock wave and the supersonic leading edge shock wave, and the interference and wave drag induced at the tip.

Figs (9.34) show the aerodynamic characteristics of Wing (2) and the interference effects of the body on the wing and vice-versa. From these graphs the centre of pressure locus can be seen for the wing alone, wing and body, wing with body and nose.

There is also a shift back in centre of pressure locus due to presence of body and nose. Figs (9.34) show the lift coefficients for the wing alone, wing plus body, and wing plus body and nose.

These graphs show the total effective lift on the wing and body for the wing-body-nose, i.e. $C_{L_{FT}}$ as shown on the graphs. The graph of lift curve shows these distributions for different incidence angles noting behave linearly. It can also be seen that there is an increase in total lift coefficient $C_{L_{FT}}$ due to the presence of nose by about 13% and due to the presence of body by about 12%.

From these graphs the total pitching moment coefficient for the combination of wing-body-nose for different incidence angle. This has a linear variation with incidence angle.

9.8 Oil Flow Visualization

From the photographs of oil flow for the wing surface, the flow patterns seem to originate from a laminar separation near the rounded leading edge; it can be suppressed or at least delayed at model Reynolds number (i.e. $R_e = 0.82 \times 10^6$ swept case, and $R_e = (1.64 \times 10^6$ unswept case) by a device for tripping the boundary layer. Flow separation from the surface of a swept wing, forward of the trailing edge, is well known to be a critical factor in the performance and controllability of the wing. At low speeds, separation is responsible for stall and wing tip drop. Separation takes many forms and all are to some degree subject to scale effect. The position of separation will vary with Reynolds number for both turbulent and , laminar , boundary layers . If a separated shear layer is not already turbulent , it usually becomes turbulent rapidly .

For weak interactions , the reattachment process may vary only slowly with Reynolds number. But once strong interactions with the external flow are admitted, very large variations with Reynolds number become possible, i.e. small increases of Reynolds number can produce large regions of separated flow over a swept wing. In this case for all the swept wings for several of incidence cases, oil flow patterns were observed. Photos (1) to (6) shows the flow patterns (i.e. without any transition band or

wire on) for 0° to 20° incidence at 0° sweep wing. From these flow patterns it was observed that the flow structure started disintegrating after 8° incidence and stall starts appearing on the wing. This can be seen clearly on Photos (5) and (6). A tripping device was used to the boundary layer to simulate a higher Reynolds number (i.e. attached turbulent flow) shown in Photos (7) to (10). This device effects only the first leading edge pressure readings due to the interference of the tripping device (which is close to the leading edge pressure holes). Stall effect are shown in some details in Figs (9.35) to (9.45), chordwise pressure distributions on the several spanwise positions for the variable sweep wings. These graphs show that beyond 8° incidence trailing edge separation occurs and stall starts. This phenomena occurs for 12.5^o, 32.5^o and 52.5^o sweep. But for 32.5^o sweep a track of vortex separation can be seen on the wing surface at 8° incidence, which starts spreading and widening on the wing surface as incidence angle increases (i.e. $\alpha = 12^o$) and stall occurs at higher angles of incidence (see Photos 23 to 26). For 52.5^o sweep stall occurs at lower incidences (i.e. about $\alpha = 6^o$) and the behaviour shown by the flow patterns is typical of slender wing flows, where the flow patterns are shown on the Photos (30) to (35). The change from attached flow to a conical separated vortex flow is that usually found on low aspect ratio wings at moderate incidences. For each case the tripping device was used but only some small changes in pressure readings were noticable which were mainly due to closeness of the leading edge pressure holes to the tripping

device. In some other cases this device caused a slight delay in commencement of conical vortex flow, a secondary separation, or a trailing edge separation. Some of the patterns are shown with the tripping device on the wing surface on photos (7) to (10), (17) to (20), and (27) to (29). The flow patterns on the glove surface and fuselage body during the operation had almost the same behaviour irrespective of wing sweep. Pressure distribution graphs are shown for different spanwise positions for the wing at different angles of sweep with the tripping device on and off for a range of incidence angles. Some of the static pressure distributions are shown on the upper wing surface in Figs (9.35) to (9.45) for variable sweep and variable incidence. Also in Fig (9.46) shows the stall curve for this case.

Finally, in Figs (9.48) the effect of tripping device is shown on the overall lift coefficients for the experimental tests. These results are compared with the theoretical ones from the Quadvortex method. Good agreement is evident between the experimental and theoretical results. The tripping device has cuased some rise in the overall lift coefficients. Flow was turbulent detached on the wing surface and presence of this device changed the flow to turbulent attached, and boundary layer started thickening owing to viscous flow effect and made the final rise in the overall lift coefficient, see Figs (9.35) to (9.38) and (9.41) to (9.43). Nevertheless, different types of tripping devices (different width and different roughness) were experimentally and visually tested and the roughest tripping device were used for this purpose.

However, the effect of tripping device as shown on the static pressure (suction) readings in Figs (9.35) to (9.45) is not so significiant, while it has some effects on the model overall lift coefficient readings especially at about 10° incidence for lower sweep angle ($\beta = 0°, 12.5°$) and at about 8° incidence for higher sweep angle ($\beta = 32.5°, 52.5°$). The effect of viscous flow is shown by Kuchemann in Fig (9.65) for several types of flow.

9.9 Overall Experimental Forces and Moments

From the graph of lift C_L.v.α, Fig (9.47) for variable sweep wing it can be deduced that the gradient of these distributions, i.e. $dC_L/d\alpha$, gradually declines from 0° to 52·5° sweep wing. This agrees with the lifting line theory which predicts $\frac{dC_L}{d\alpha}$ is proportional to the cosine of the sweep angle. Also, the linearity of the lift coefficient v. α curves are limited to a certain angle of incidence. These graphs show the effect of the tripping device which simulates a high Reynolds number state. In some cases, due to changes in flow separation and reattachment on the wing surface, there is more lift with the tripping device present than when tripping device is removed from the model surface. One of the distinguishing features of the oil flow visualizations is that the flow patterns stayed nearly the same on the aircraft body with and without tripping devices for all angles of sweep. Therefore the slope of the lift coefficient distributions shown in Fig (9.47) can be explained by considering the combined flow of the wing (which stalls) and the body (which does not), the interaction between the two leading to the decrease in $\frac{dC_L}{d\alpha}$ at about 8° for wings up to 32.5^o sweep. But for a higher angle of sweep (i.e. 52.5^o) it can be seen that there is a reduction in $\frac{dC_L}{d\alpha}$, which this is true and compatible with the cosine of sweep angle theory, and the more gradual change in lift curve slope indicates that the wing and body are more closely linked aerodynamically.

Figs (9.50) show distributions of lift coefficient C_L against angle of incidence from the computed results for 0° sweep wing-body combination (shown in Fig 9.3). These results indicate lift distributions for the wing in presence of body C_L(WB), body in presence of wing C_L(BW), and wing + Body C_L(WB+BW). Another set of results are calculated for lift on the wing alone C_L(W), body alone C_L(B) and their total C_L(W+B), in order to estimate the total mutual interference (positive in this case) between C_L(W+B) and C_L(WB+BW). These tests were also carried out to indicate the effect of V-notch on the wing-body overall lift coefficient. These graphs Figs (9.50) show that there is a favourable interference for the wing-body combinations. The amount of interference in terms of percentage lift for the wing in presence of body is about 27% and for the body is 39% at 20° incidence. Therefore the total interference for 0°sweep wing with V-notch is calculated to be about 30% and for 0° sweep without V-notch is about 26% as can be found from Figs (9.50).

Similarly, interference for 12.5° sweep wing with V-notch is 30% and for the sweep wing with no V-notch is 29% as can be found in Figs (9.51). Interference for 32.5° sweep wing is about 23% of the overall lift coefficient and for 52.5° sweep wing is about 19% as seen in Figs (9.52). In subsonic flow, the total favourable interference derived to be varying between 19% to 30% for the highest and the lowest wing sweep combinations.

The interference in supersonic flows was calculated from Figs (9.28) to be about 25% for the wing W_2-- body combination. These interference comparisons can give valuable informations towards aerodynamic design of a wing - body combination. However, from the theoretical interference

calculations useful evidence of wing - body contributions can be obtained which on their own rights can be a positive contribution to knowlege in this area.

9.10 Comparisons of Experimental and Theoretical Results

Comparisons were made between our experimental Cp distributions with some experimental and theoretical results from a report produced by British Aerospace Warton Division (Ref 9..7). Graphs (9.53) to (9.63) show the chordwise comparisons of Cp for several spanwise locations. From the graphs it can be deduced that there is a quite close agreement in the Cp distributions in most cases, which is encouraging, although at certain spanwise locations and angles of incidence and sweep there are significant differences in the Cp distributions. Graphs (9.58) and (9.59) give a good indication of the closeness in the Cp results in comparison with the B.Ae's results (experimental and theoretical).

In this comparison a theoretical sheared wing with 23° sweep angle is used by B.Ae for comparison with their experimental results for a swept wing model of 27°, while in our case the angle of sweep used is 32.5^{o} (or 30° at the L.E.) Graphs (9.64) and (9.65), represent the B.Ae lift distributions of C_L for the section lift on the wing, and also show our experimental results. These graphs show a good comparison between spanwise lift distributions at location $\eta = 0.333$ to our results with the corresponding B.Ae results at $\eta = 0.332$. In this case the effect of viscous flow can be seen in the experimental results with the non-viscous flow from theoretical subsonic results (Quadvortex) as they are indicated in Figs (9·49). This effect is more significiant

beyond 8° incidence for the overall lift coefficients of the wing-body combinations. These comparisons give encouraging evidences of the good degree of accuracy which we achieve in our experimental and theoretical (i.e. Quadvortex) investigations. However, some of the differences in Cp distributions can be explained between experimental and theoretical results as follows. Fig (9 .65) which is taken from Ref (9 .6) illustrates how non-zero thickness and viscosity effects influence the chordwise loading. First we can begin with the loading of the thin wing in inviscid flow at an incidence which is equal to the given geometric incidence, curve (a); the effect of the streamwise vortices on the wake is then to reduce the incidence by the amount of α_i, which this leads to curve (b); curve (c) is obtained by taking the thickness of the aerofoil section (t/c which in this case taken as 0.12 Ref 11.6) into account; and finally, the effect of viscosity is calculated by measuring values of the displacement thickness of the boundary layer as shown on curve (d).
This final result shows that the effects of aerofoil thickness and viscosity are quite distinct and cannot be neglected as is sometimes supposed.

Viscous flow effect also can be noticed near the trailing edge owing to thickening of boundary layer on the wing surface for the wing-body combinations, see Figs (9.53) to (9.63).

REFERENCES FOR CHAPTER 9

(9..1) KUCHEMANN, D. "A simple method for calculating the span and chordwise loadings on thin swept wings". R.A.E. Report. Aero. 2392, 1950.

(9.2) WEBER, J.
KIRBY, D.A. and
KETTLE, D.J. "An extension of Multhopp's method of calculating the span-wise loading of wing fuselage combinations". R.A.E. Report. Aero. 2446, 1951.

(9.3) BREBNER, G.G. "The calculation of the loading and pressure distribution on cranked wings". R.A.E. Report. Aero. 2483, 1953.

(9.4) MASKEW, B. "Calculation of the three-dimensional potential flow around lifting non-planar wings and wing-bodies using a surface distribution of quadrilateral vortex-rings". TT 7009, September 1970.

(9.5) BREBNER, G.G.
WYATT, L.A.
GLADYS P ILOTT

"Low speed wind tunnel tests on a series of rectangular wings of varying aspect ratio and aerofoil section".
R.A.E. TR. no. 65236, Oct, 1965.

(9.6) KUCHEMANN, D.

"A simple method for calculating the span and chordwise loading on straight and swept wings of any given aspect ratio at subsonic speeds".
A.R.C. R & M no. 2935, 1956.

(9.7) BRITISH AEROSPACE AIRCRAFT GROUP, WARTON DIVISION

"Low speed wind tunnel pressure plotting on wing, wing-fuselage configurations, including comparisons with a recent theoretical method".
Unclassified Report No. AX.322 Part 1 and 2. Lancashire PR4 1AX.

LIST OF FIGURES FOR CHAPTER 9

(9.1) Details of subsonic models for numerical calculations

(9.2)a,b,c Comparisons of Spanwise loading and centre of pressure locus.

(9.3),(9.4),(9.5) Subsonic model views.

(9.6) Quadvortex spanwise loading for variable sweep, variable incidence.

(9.7) Quadvortex spanwise lift C_L/α for variable sweep, variable incidence.

(9.8) Quadvortex spanwise lift C_L for variable sweep, variable incidence.

(9.9) Quadvortex lift coeff. C_L for variable sweep, variable incidence.

(9.10) Quadvortex overall lift coefficient C_L for variable sweep, variable incidence.

(9.11) Quadvortex spanwise pitching moment C_{M_y} for variable sweep, variable incidence.

(9.12),(9.13) Quadvortex spanwise lift for different no of elements for Rectangular wing of AR = 4.

(9.14),(9.15) Quadvortex spanwise loading and drag for different no. of elements for Rectangular wing of AR = 4.

(9.16),(9.17) Quadvortex spanwise wave drag and pitching moment for different no. of elements for Rectangular wing of AR = 4.

(9.18),(9.19) Quadvortex comparisons of lift C_L/α for different aspect ratios.

(9.20) Quadvortex spanwise centre of pressure locus for Rectangular wing for different elements with AR = 4.

(9.21) (a) Quadvortex comparisons of lift with Kuchemann theory.
(b) Quadvortex comparisons of centre of pressure locus with experiment.

(9.22) (9.23) Quadvortex chordwise comparisons of ΔCp with wind tunnel results for different spanwise locations (for $\beta = 12.5^0$ and 52.5^0 sweep at $\alpha = 10^0$).

(9.24) to (9.27) Supersonic spanwise comparisons of Cp for rectangular wing AR = 1.1

(9.28) Supersonic wing models for computational calculations.

(9.29) to (9.31) Supersonic chordwise Cp distributions for wing model 1.

(9.32) to (9.33) Supersonic chordwise Cp distributions for wing model 2.

(9.34) Supersonic aerodynamic forces,moments for wing model 2.

(9.35) to (9.39) Experimental chordwise static pressure for upper wing surface for $\beta = 0^0$ sweep at different spanwise locations.

(9.40) to (9.41) Experimental chordwise static pressure for upper wing surface for $\beta = 12.5^0$ sweep at different spanwise locations.

(9.42) to (9.43) Experimental chordwise static pressure for upper wing surface for $\beta = 32.5^0$ sweep at different spanwise locations.

(9.44) to (9.45) Experimental chordwise static pressure for upper wing surface for $\beta = 52.5^0$ sweep at different spanwise locations.

(9.46) Graph of stall curve for the wind tunnel test model.

(9.47) Graph of lift coefficient v. angle of incidence for the W.T. tests.

(9.48) Graph of comparisons of lift coeff. C_L v. angle of incidence for the W.T. tests, with Quadvortex .

(9.49) Graph of lift C_L coefficient v angle of incidence for the W.T. tests and Quadvortex.

(9.50) Graph of overall lift C_L coefficient v angle of incidence for the Quadvortex.

(9.51) Graph of lift force C_L coefficient v angle of incidence for the Quadvortex.

(9.52) Graph of overall lift C_L coefficient v angle of incidence for the Quadvortex.

(9.53) to (9.63) Experimental comparisons of chordwise Cp with theoreticals of the B.Ae's for different incidence and different spanwise locations.

(9.64) Experimental comparisons of lift coefficients C_L v angle of incidence with the B.Ae's.

(9.6) A chordwise load distributions curve for a wing of 45^0 sweep, AR = 3 and constant chord.

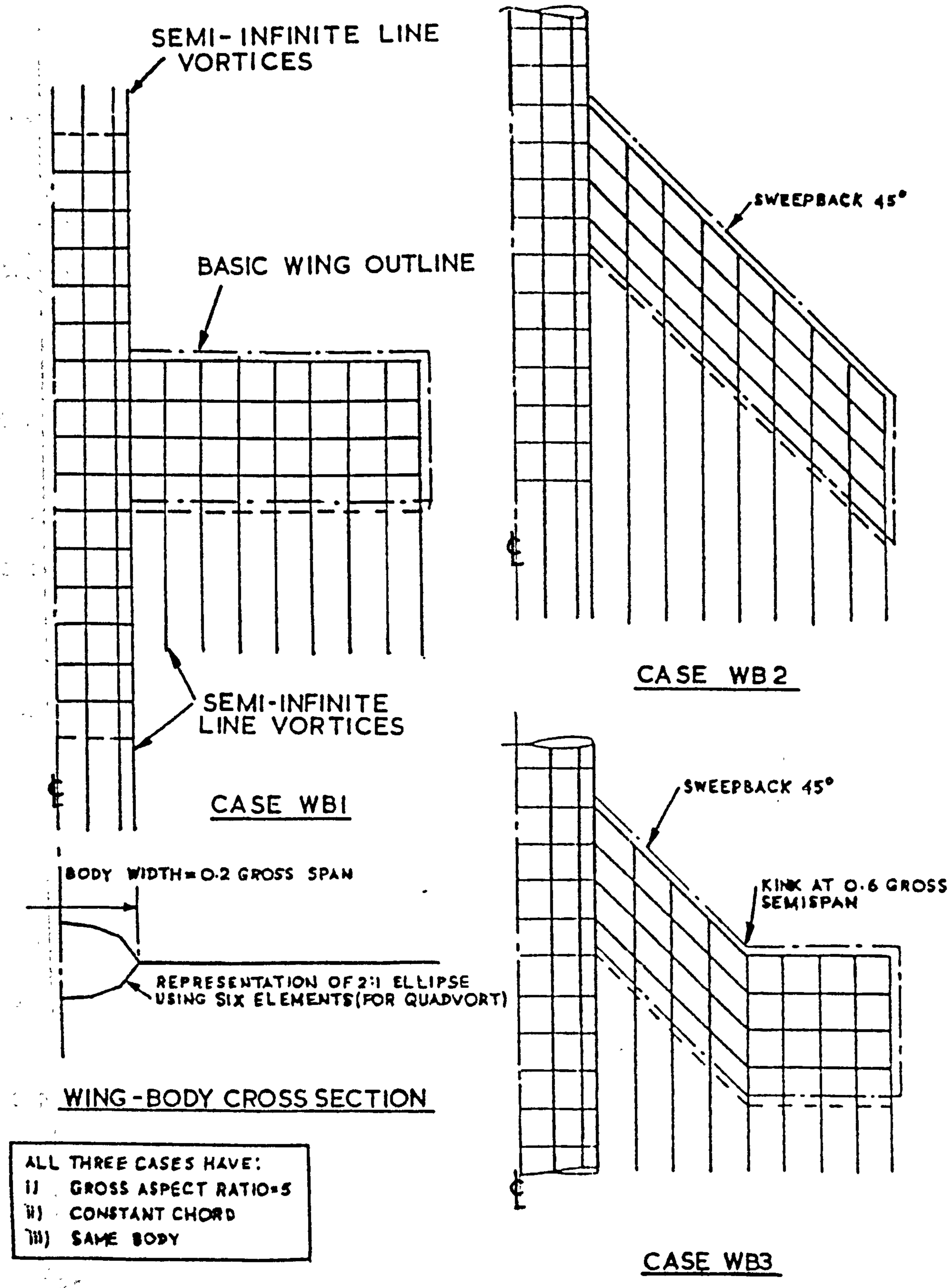

FIG. 9.1 DETAILS OF THIN WING-BODY COMBINATIONS WB1, WB2, WB3 SHOWING VORTEX-RING ELEMENT DISTRIBUTIONS

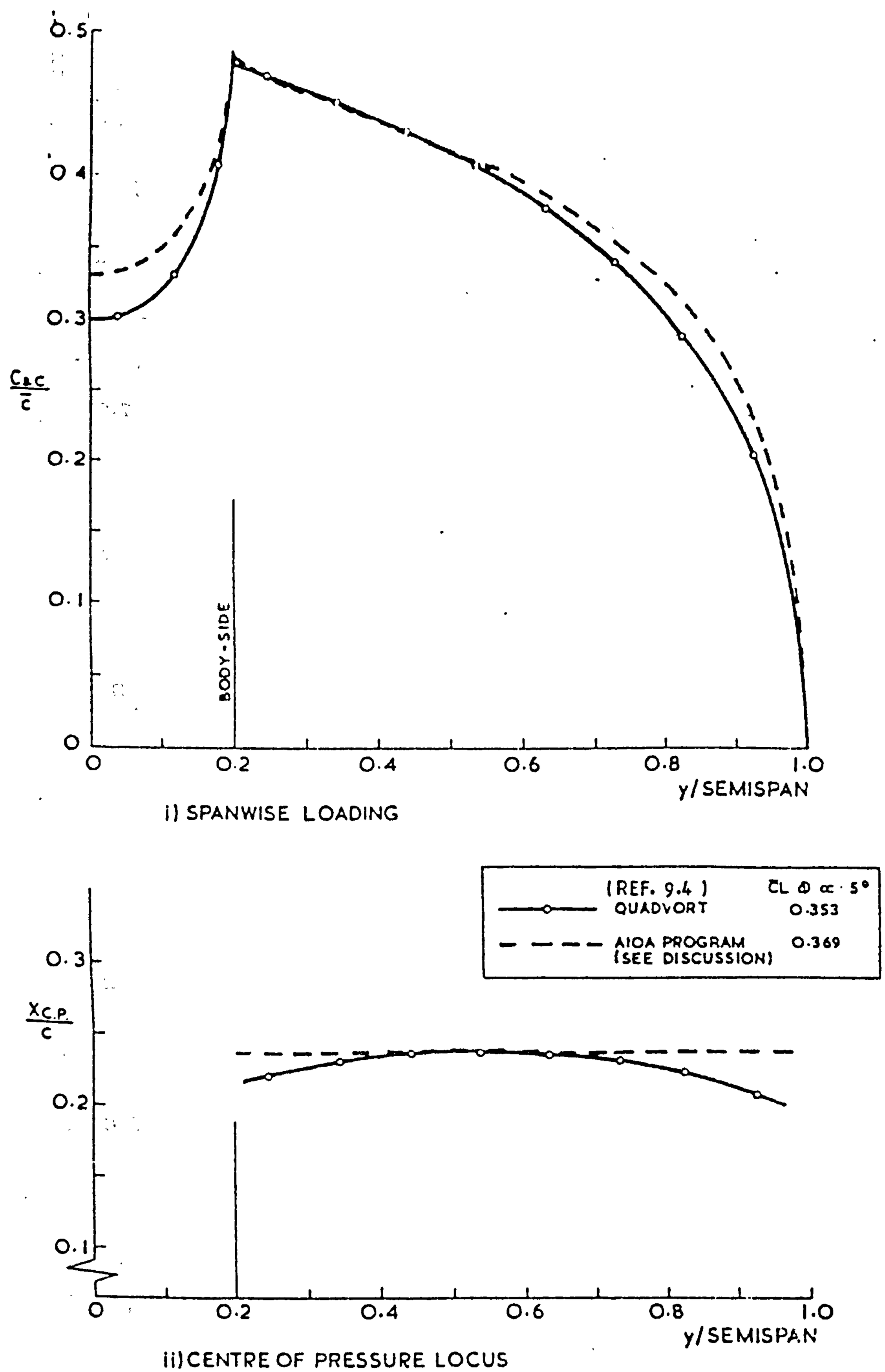

FIG. 9.2a COMPARISONS OF CALCULATED SPANWISE LOADING AND ALSO CENTRE OF PRESSURE LOCUS:
WING-BODY WB1

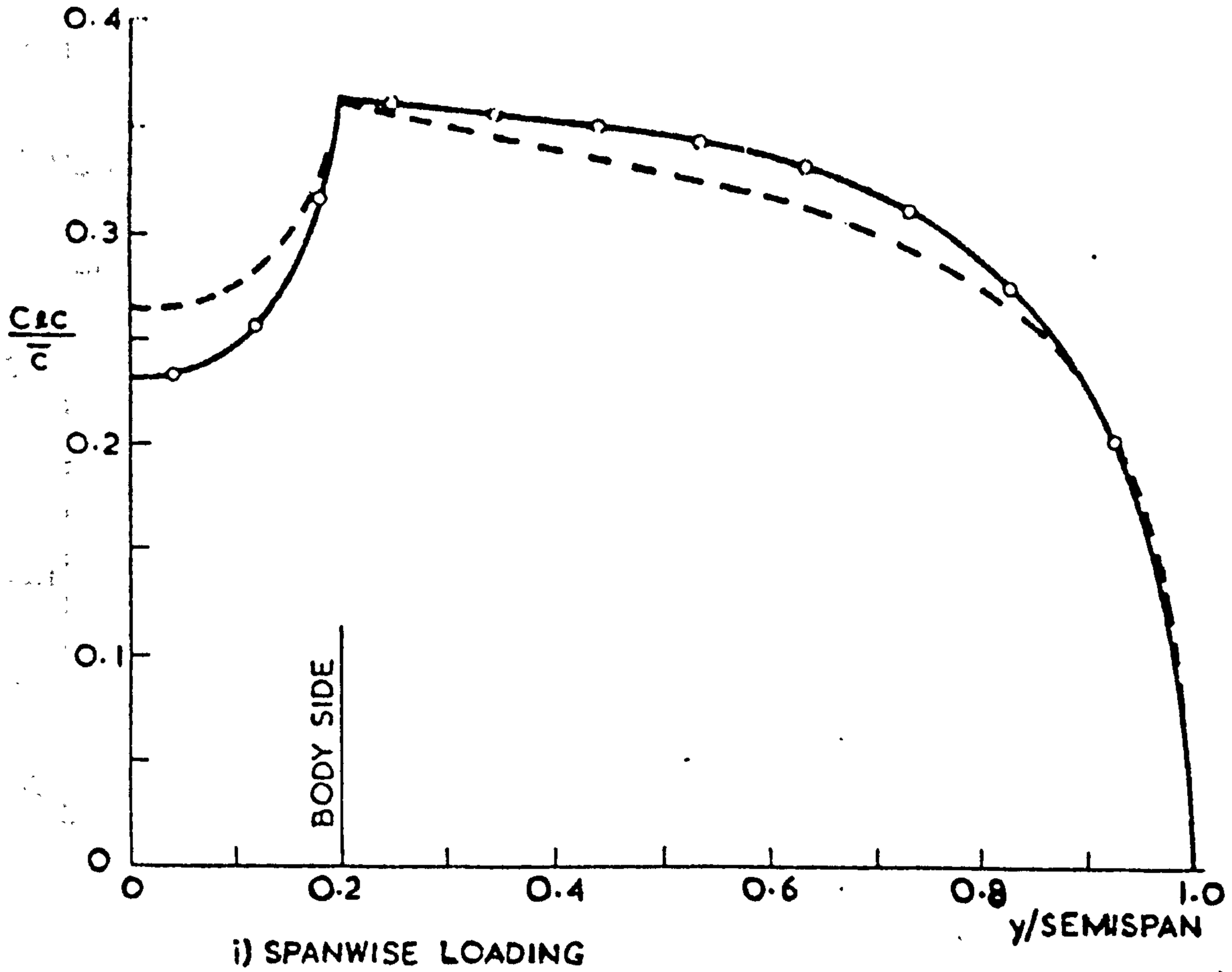

i) SPANWISE LOADING

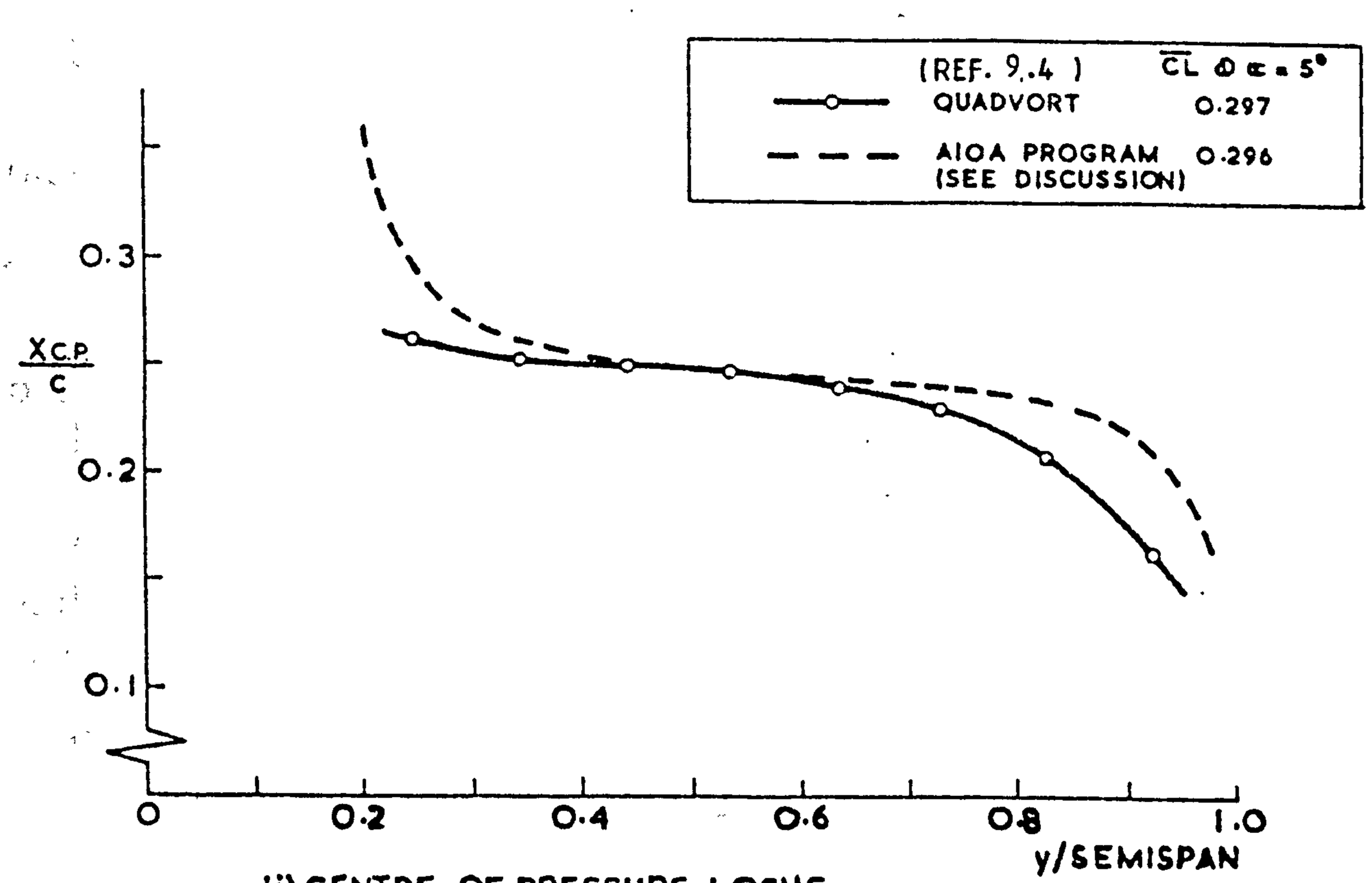

ii) CENTRE OF PRESSURE LOCUS

FIG.9.2 b COMPARISONS OF CALCULATED SPANWISE LOADING AND ALSO CENTRE OF PRESSURE LOCUS (continued)

WING-BODY WB2

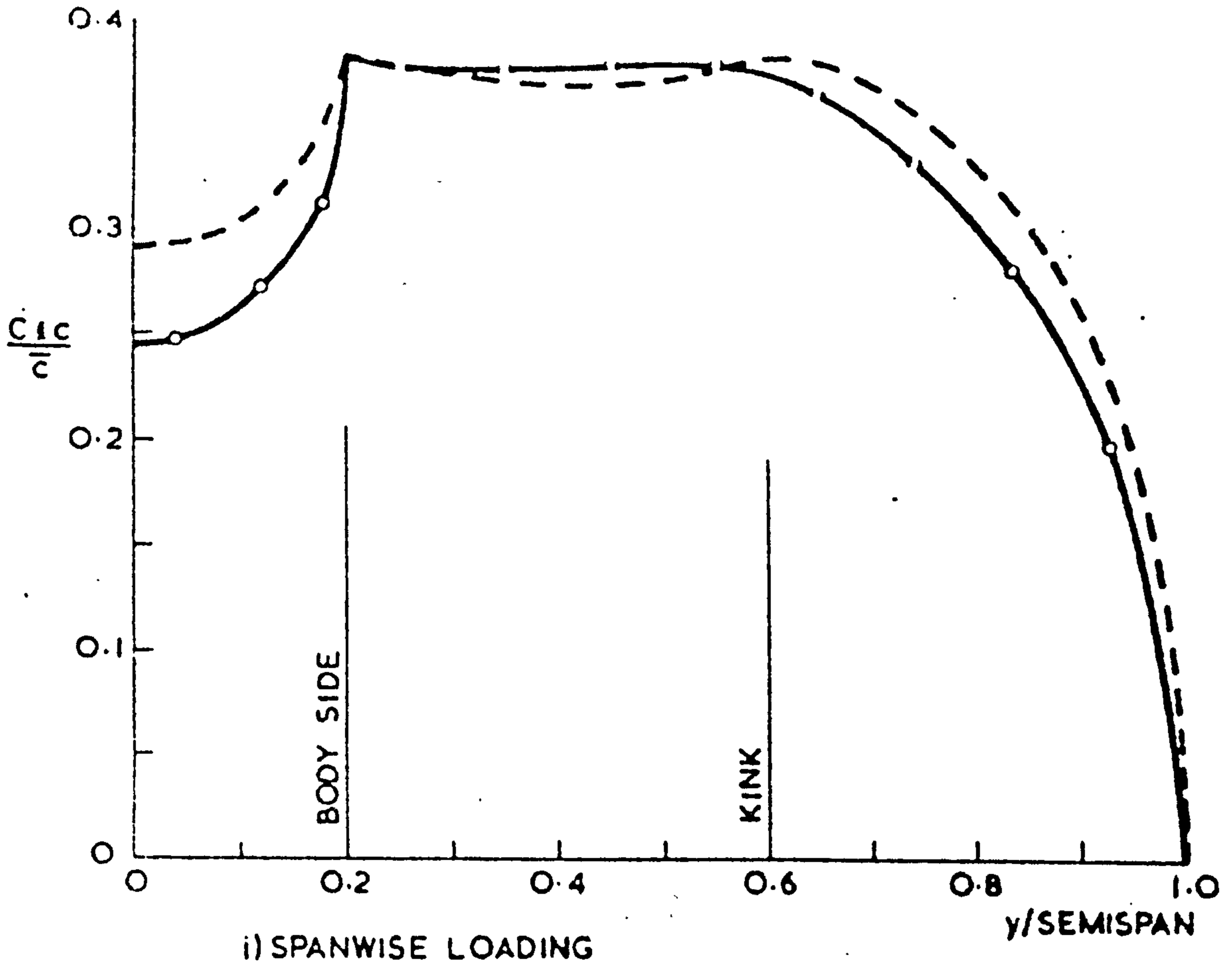

i) SPANWISE LOADING

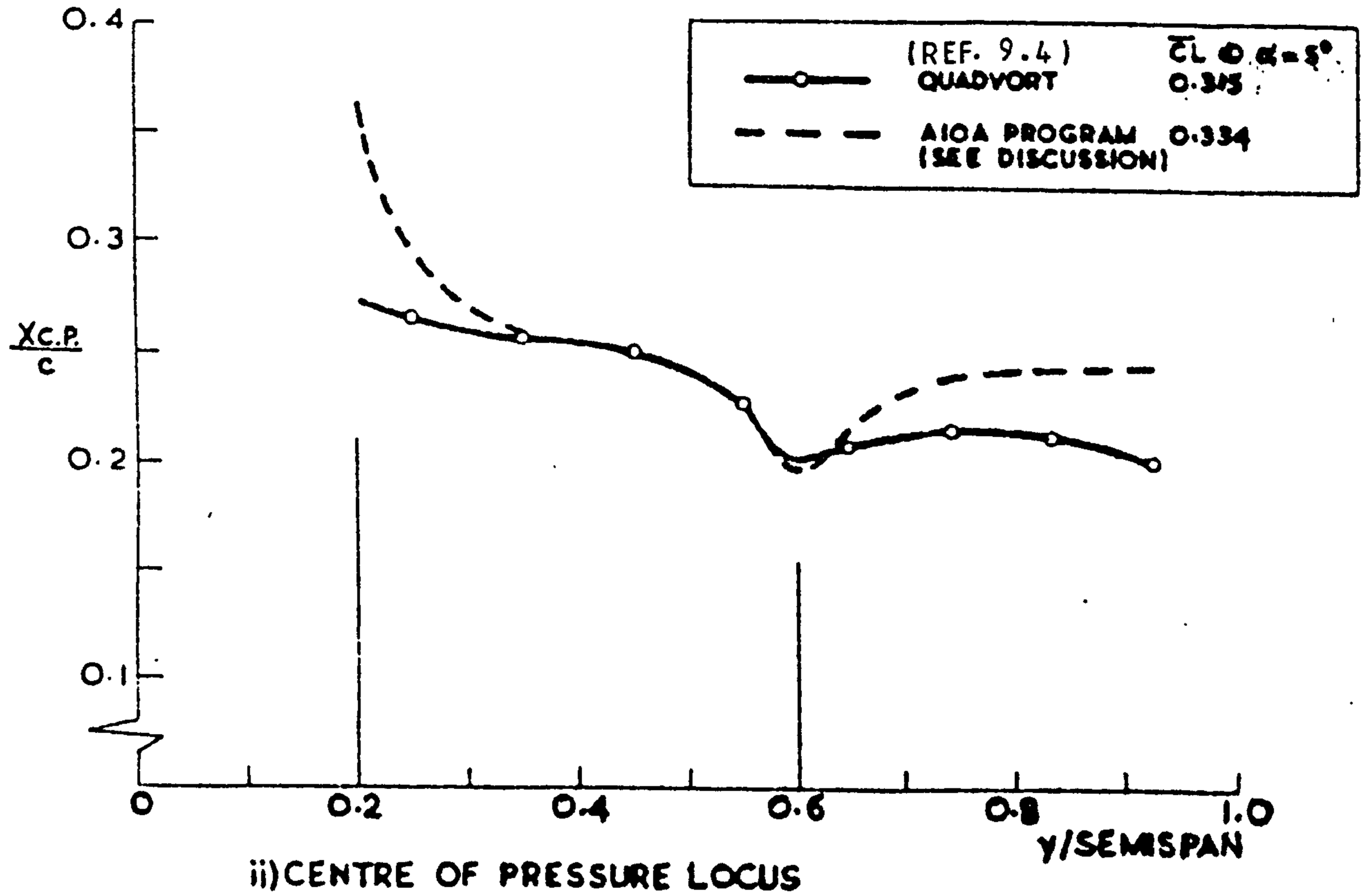

ii) CENTRE OF PRESSURE LOCUS

FIG. 9.2C COMPARISONS OF CALCULATED SPANWISE LOADING AND ALSO CENTRE OF PRESSURE LOCUS (continued)
WING-BODY WB3

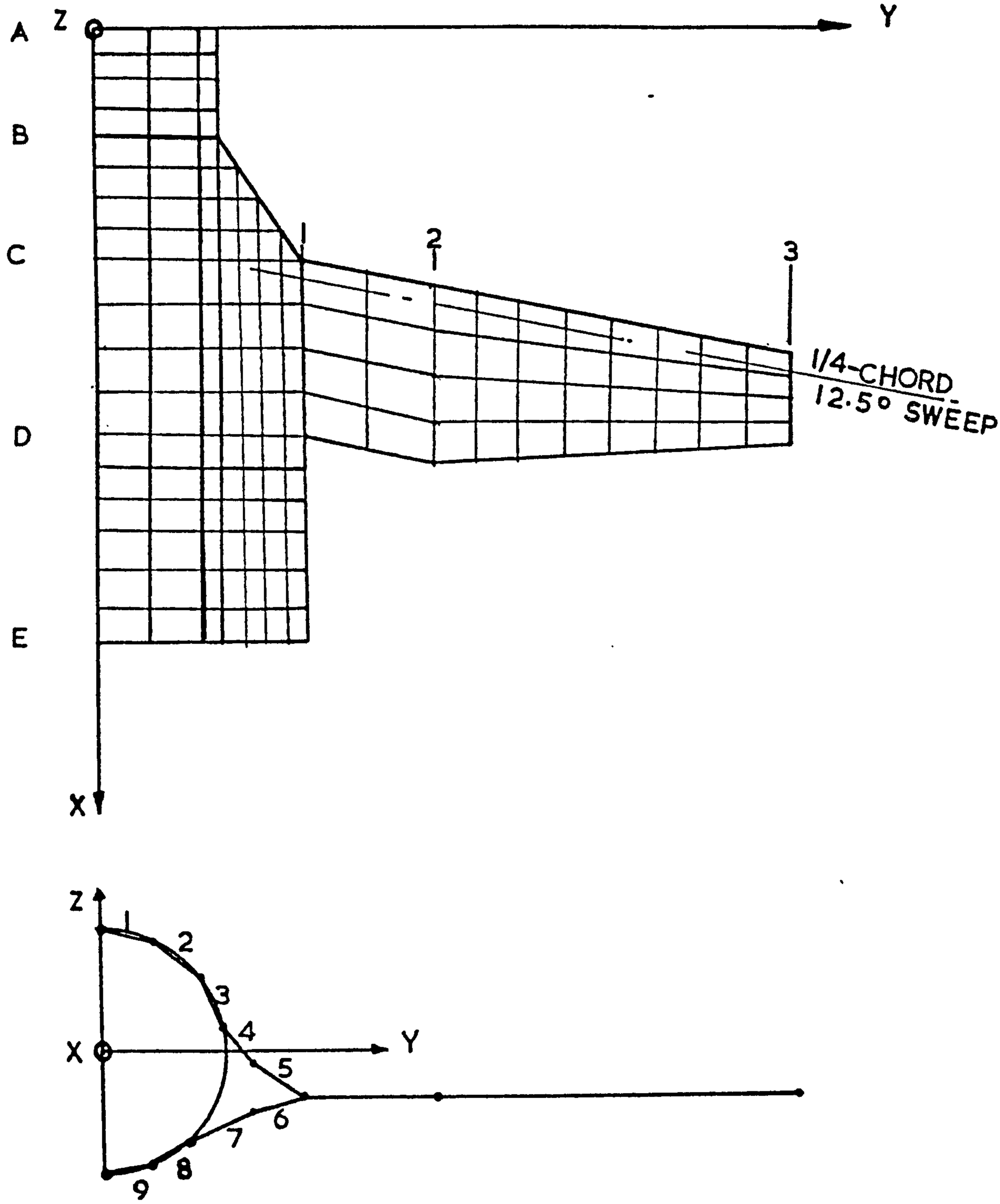

FIG. 9.3 A VIEW OF THE SUBSONIC MODEL WITH 12.5° WING - SWEEP ANGLE

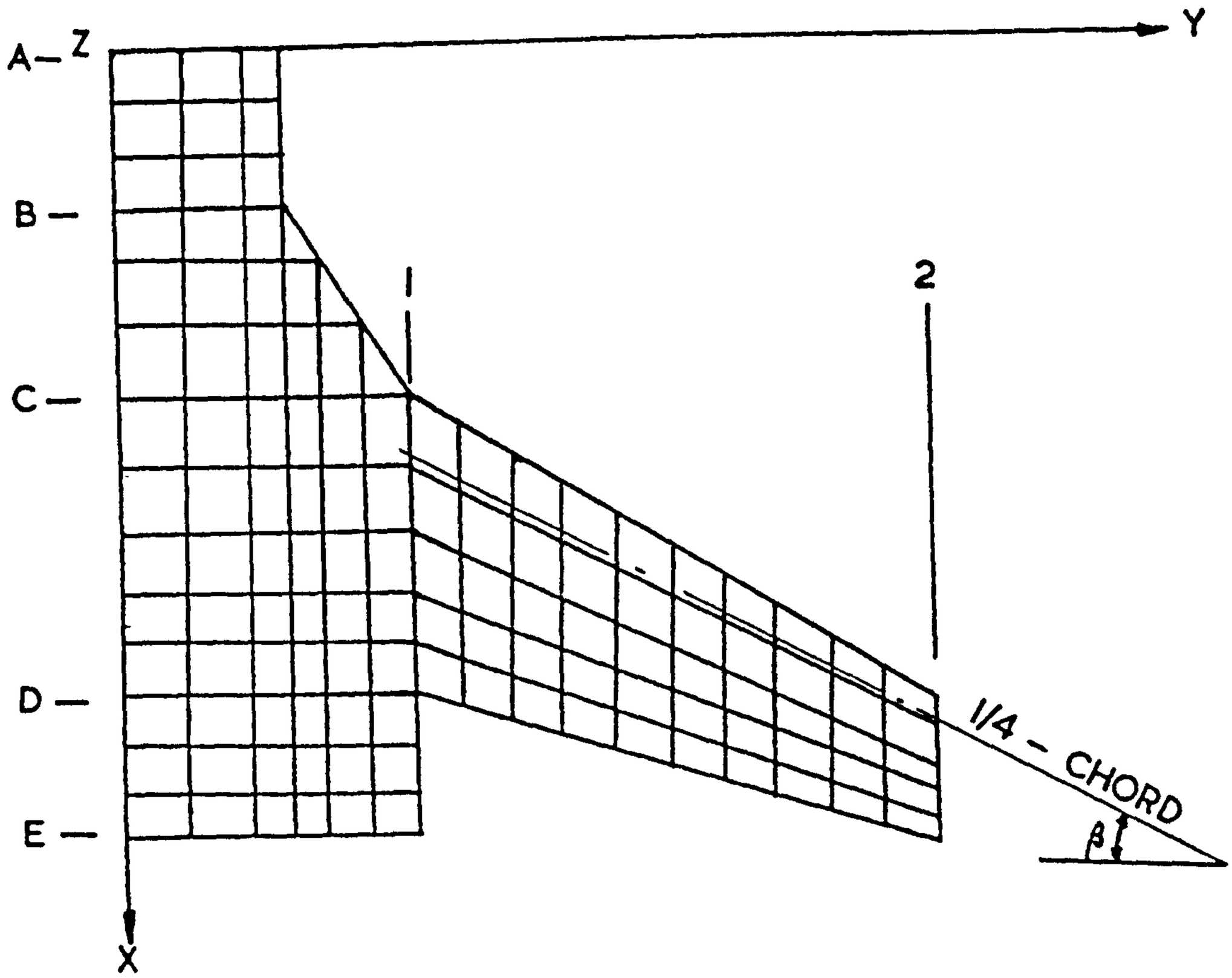

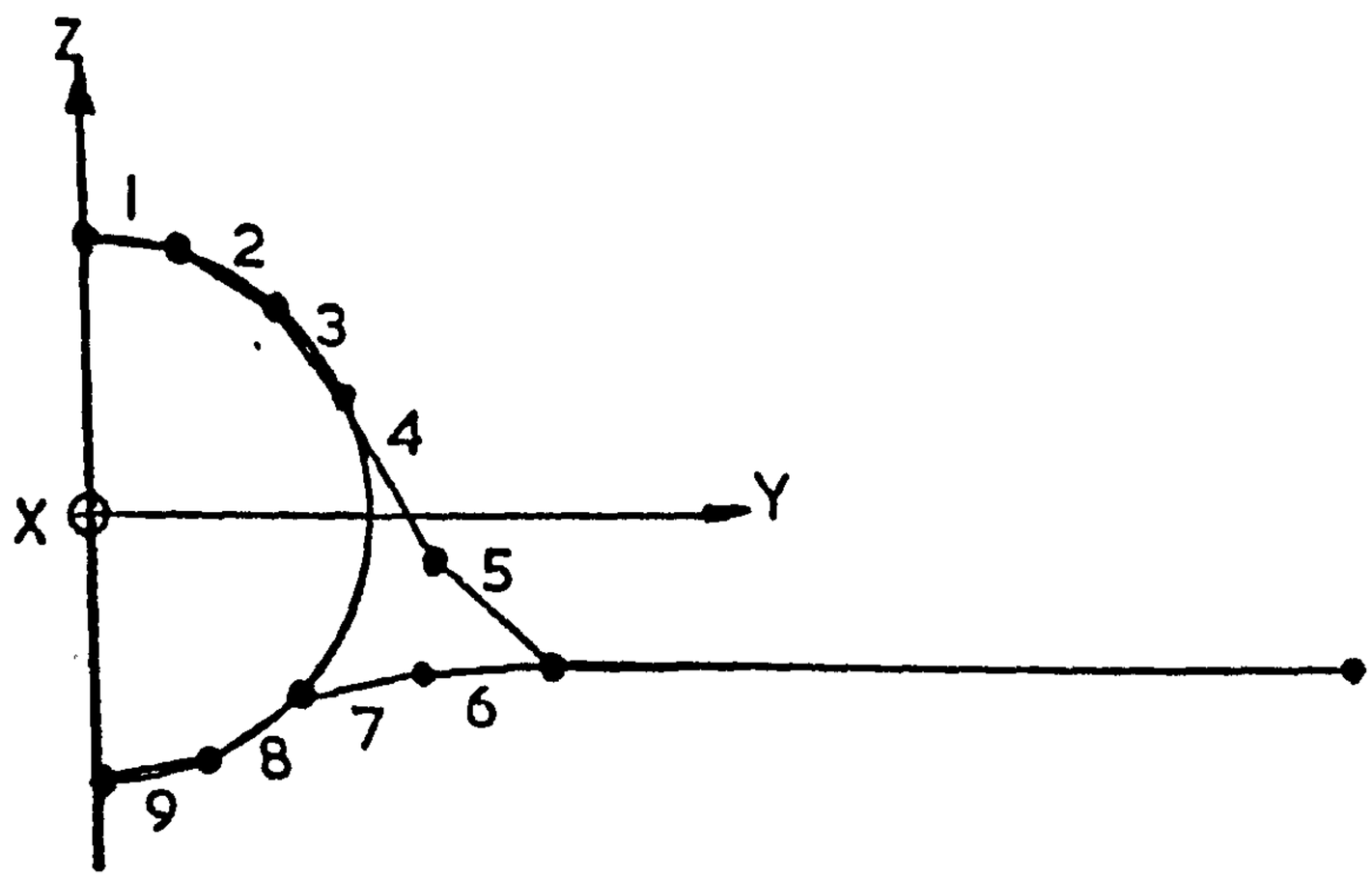

FIG. 9.4 A VIEW OF THE SUBSONIC MODEL WITH THE WING SWEEP $\beta = 32.5^\circ$ OR 52.5°

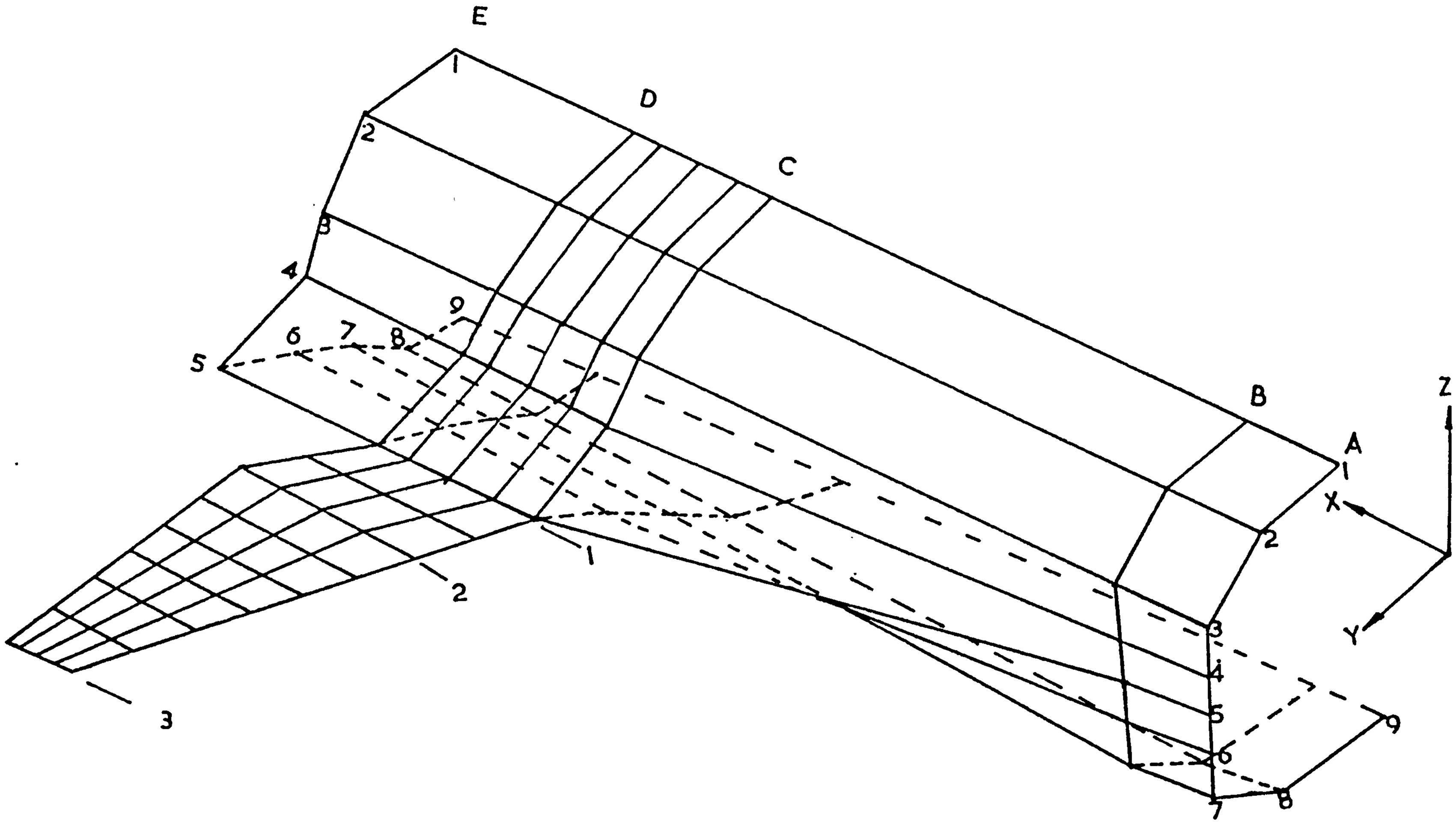

FIG · 9.5 A VIEW OF FUSELAGE AND WING COORDINATES SYSTEM AND NUMBERING SYSTEM FOR THE SUBSONIC MODEL

FIG.(9. 6) SPANWISE DISTRIBUTIONS OF LOAD ($C_\ell \cdot c/\bar{C}_L \cdot \bar{c}$) (From Quadvortex Method)

($C_\ell \cdot c$ is local lift , $\bar{C}_L \cdot \bar{c}$ is overall lift) For Geometries Shown In Figs.(9.3) to(9.5)

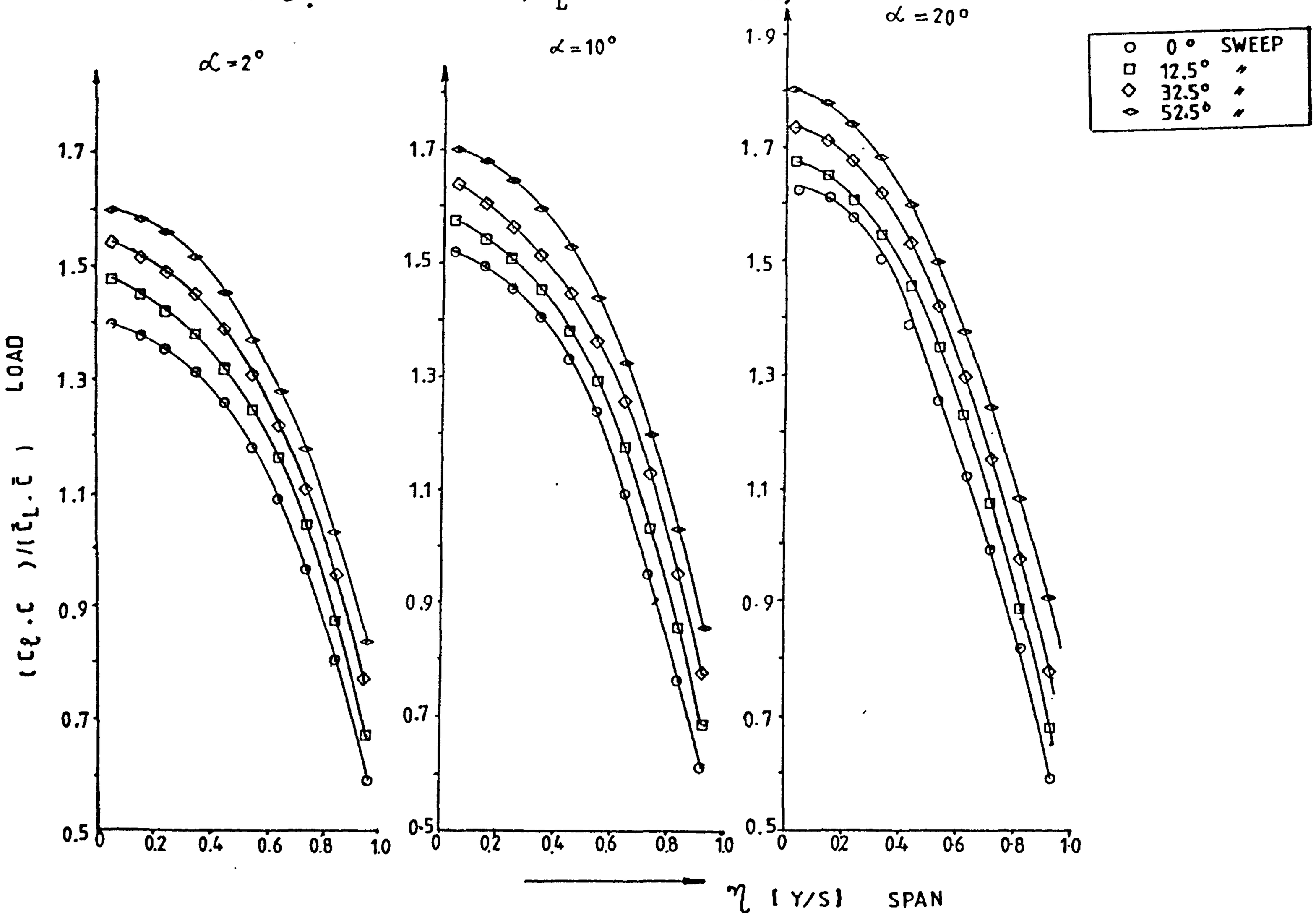

FIG.(9 . 7) SPANWISE DISTRIBUTIONS OF LOAD C_L/α (Quadvortex method)
FOR GEOMETRIES IN FIGS.(9.3) to (9.5)

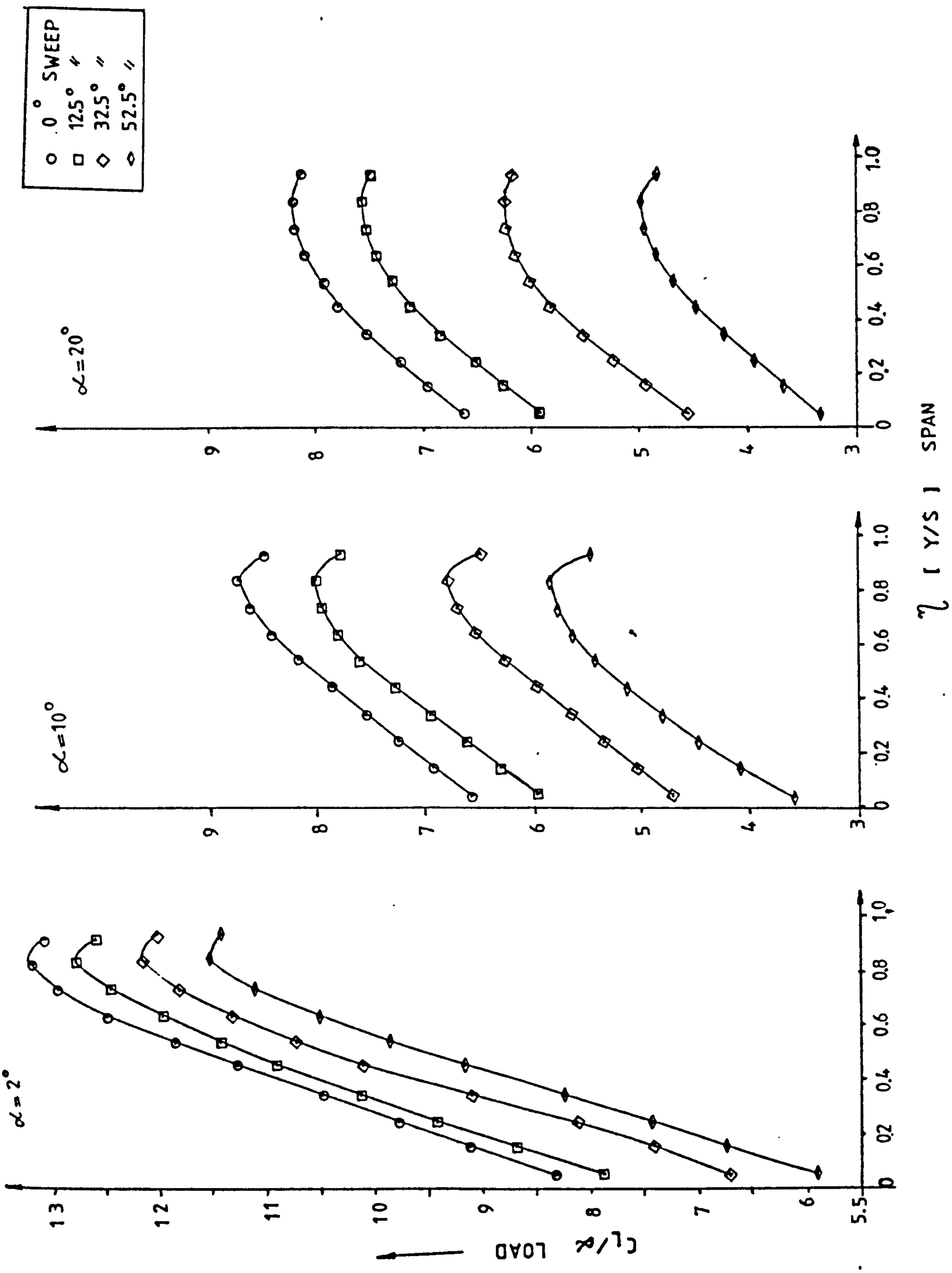

FIG.(9.8) SPANEWISE DISTRIBUTIONS OF LIFT C_L FOR GEOMETRIES SHOWN IN FIGS.(9.3) TO (9.5)
(Quadvortex Method)

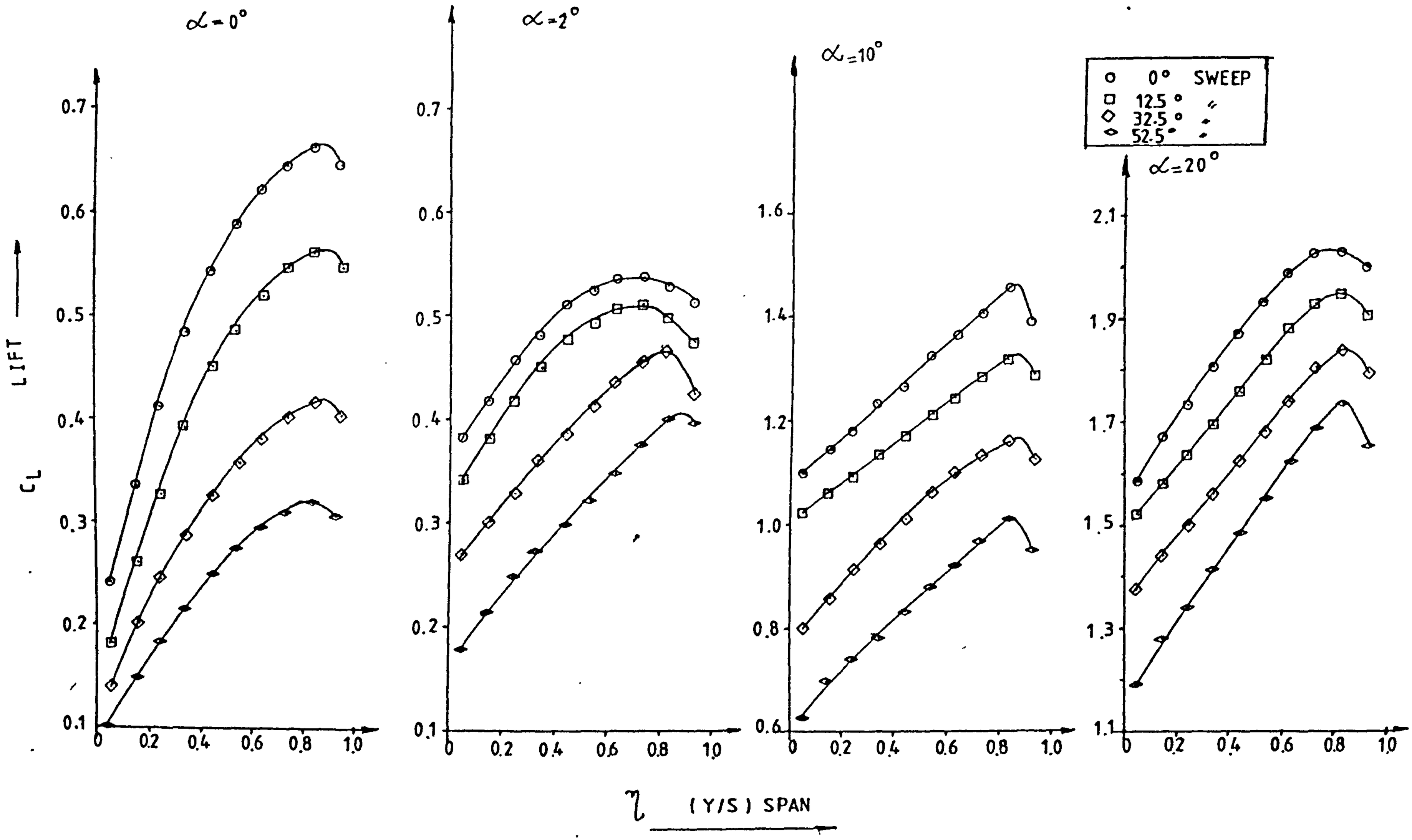

FIG.(9.9) OVERALL (WING+ BODY) LIFT C_L FOR GEOMETRIES SHOWN IN FIGS.(9.3) to (9.5) (From Quadvortex method)

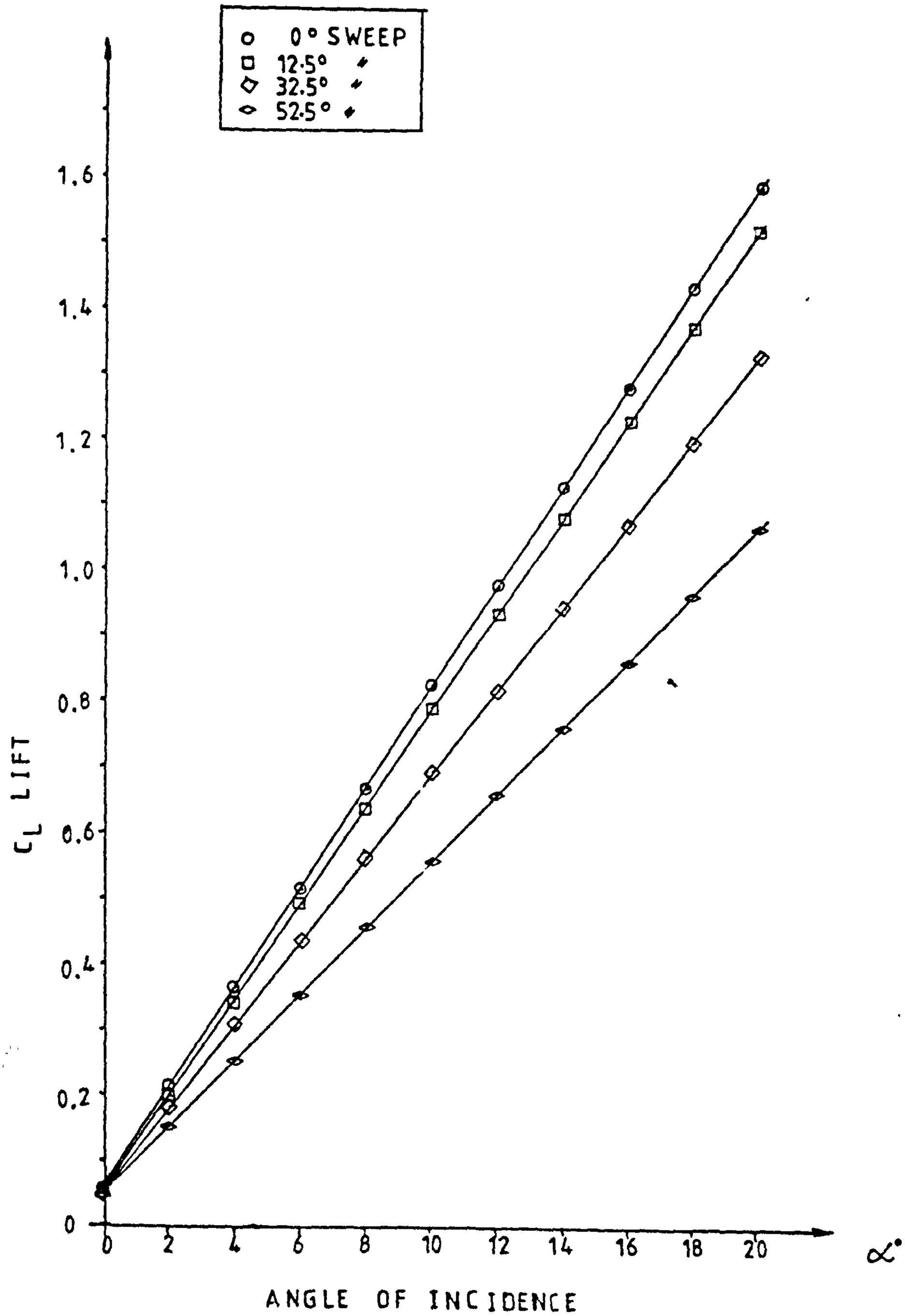

FIG.(9.10) LIFT DISTRIBUTIONS V ANGLE OF INCIDENCE FOR WING , BODY, AND WING + BODY FOR GEOMETRIES SHOWN IN FIGS.(9.3) to (9.5) FROM QUADVORTEX METHOD

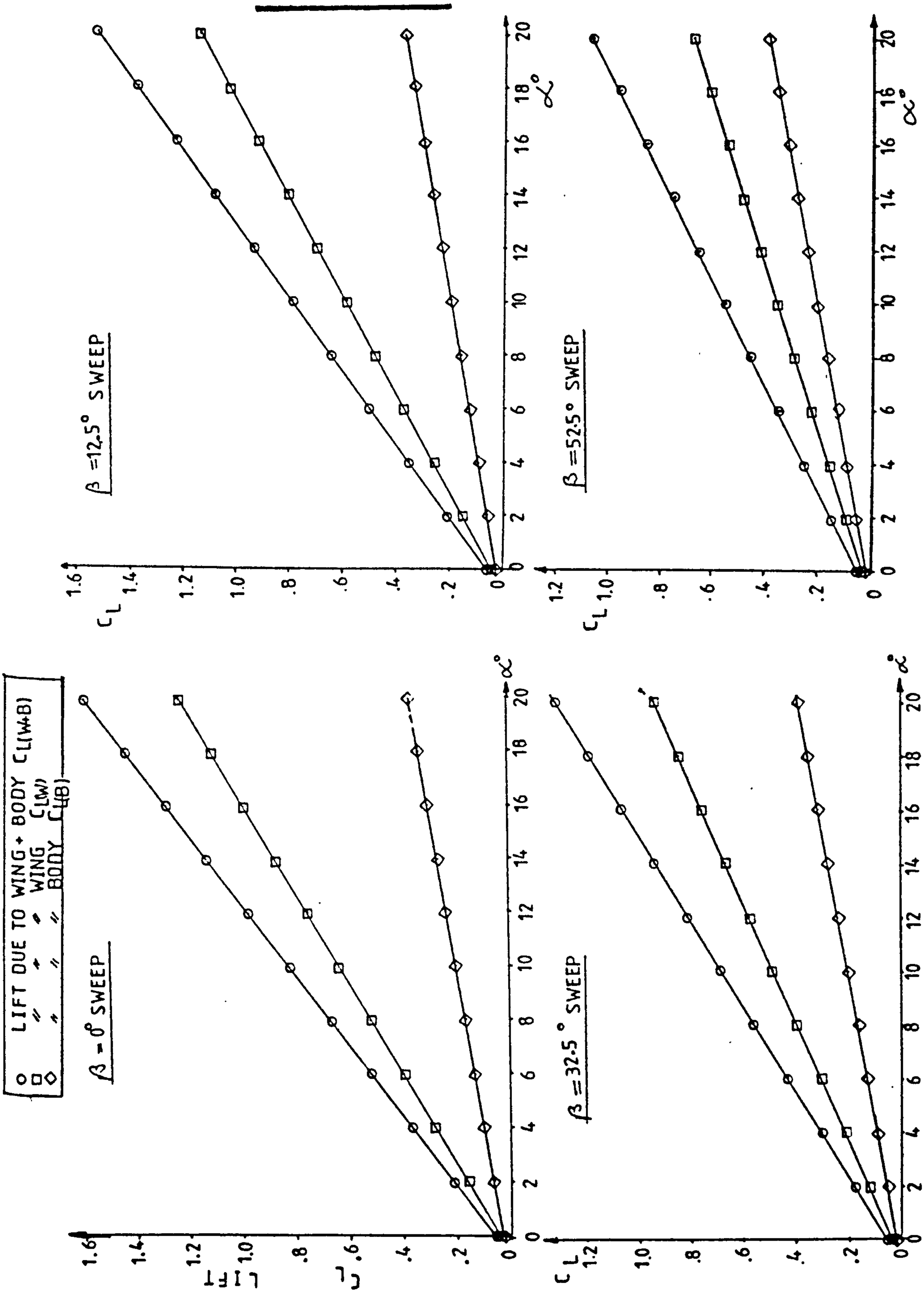

FIG.(9.11) SPANWISE DISTRIBUTIONS OF PITCHING MOMENT COEFFICIENT C_{MY} FOR GEOMETRIES SHOWN IN FIGS.(9.3) to (9.5) FROM QUADVORTEX METHOD

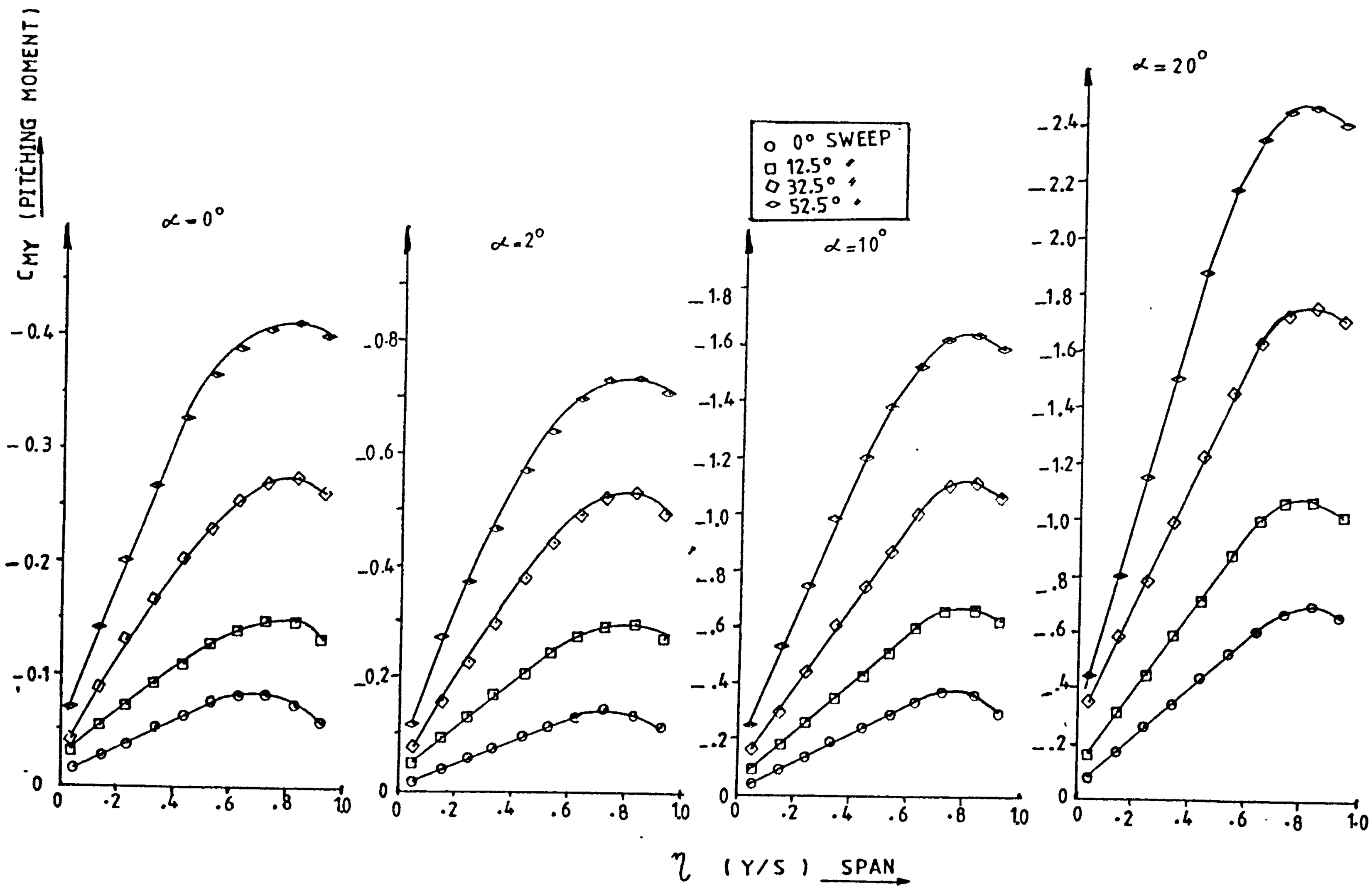

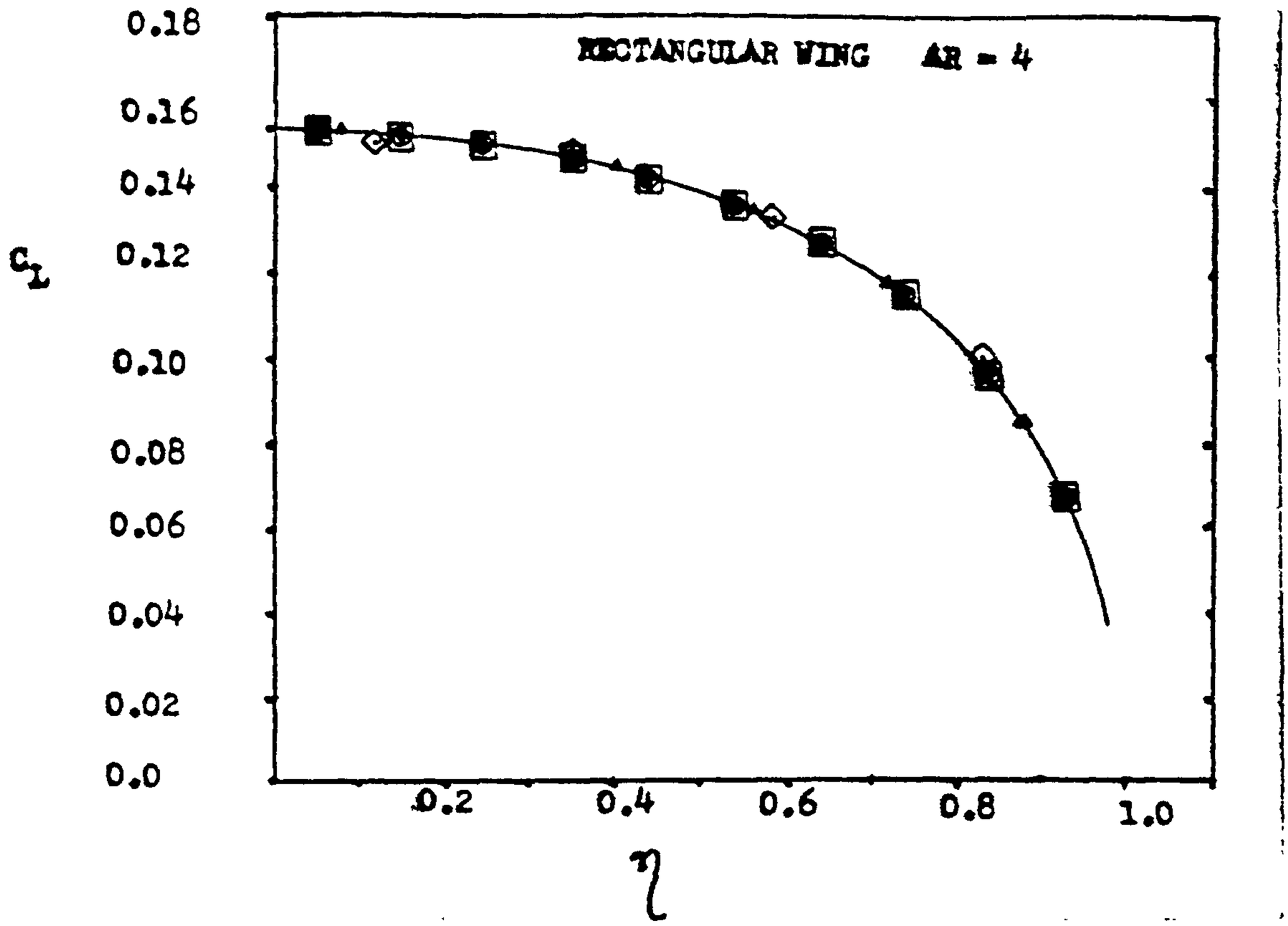

FIG. (9.12) SPANWISE DISTRIBUTIONS OF LIFT COEFFICIENTS C_L · V · η

	No. of elements Along Chord	Along Span	Total Elements	Aspect Ratio
○ ——	10	10	100	2
□ ——	5	10	50	1
◇ ——	10	4	40	5
△ ——	8	6	48	2.7
▽ ——	2	10	20	0.4

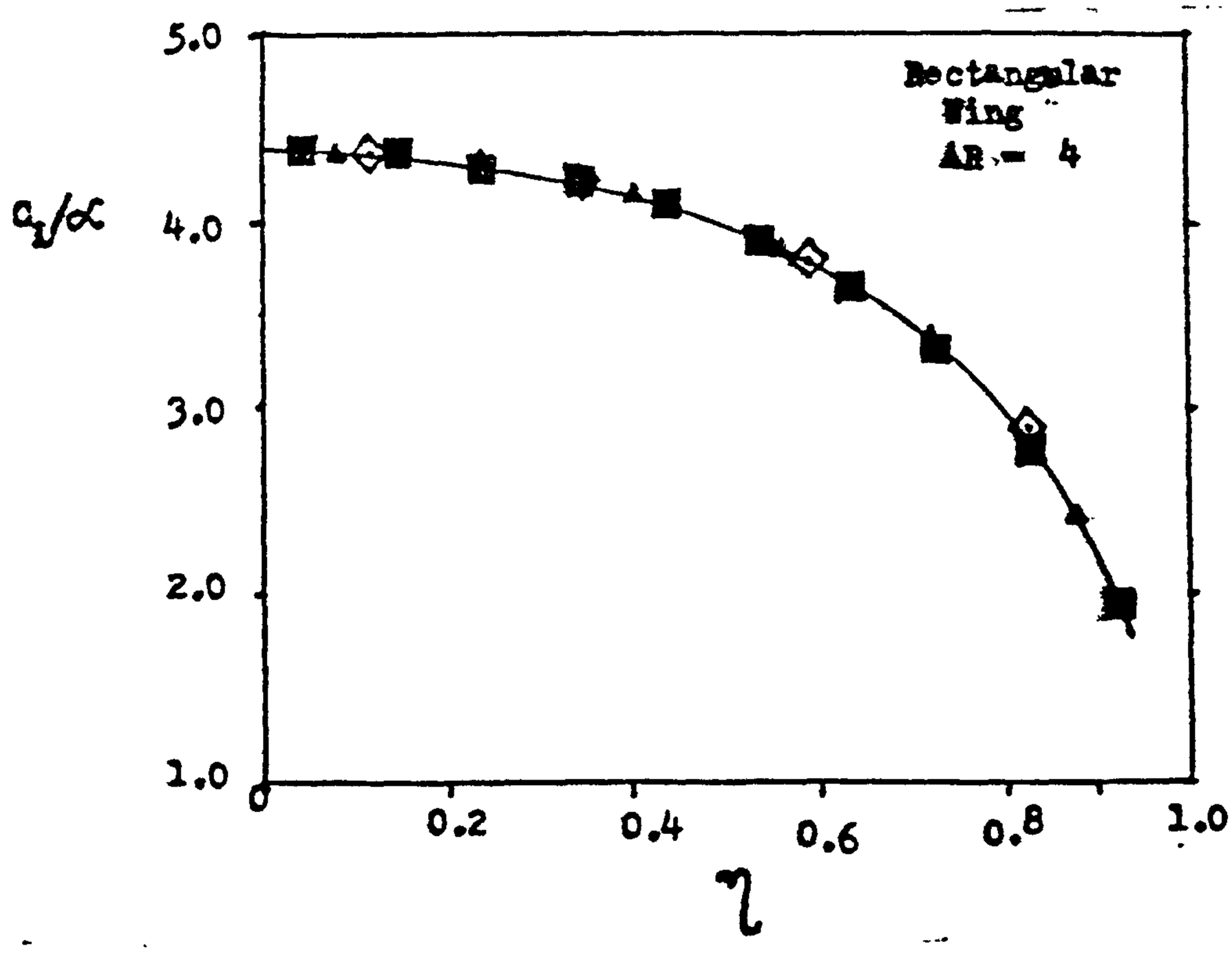

FIG. (9.13) SPANWISE DISTRIBUTIONS OF LIFT C_L/α · V · η

	No. of elements along Chord	Span	Total Elements	Aspect Ratio
○	10	10	100	2
□	5	10	50	1
◇	10	4	40	5
△	8	6	48	2.7
▽	2	10	20	0.4

FIG.(9.14) SPANWISE DISTRIBUTIONS OF DRAG C_D ·V·η

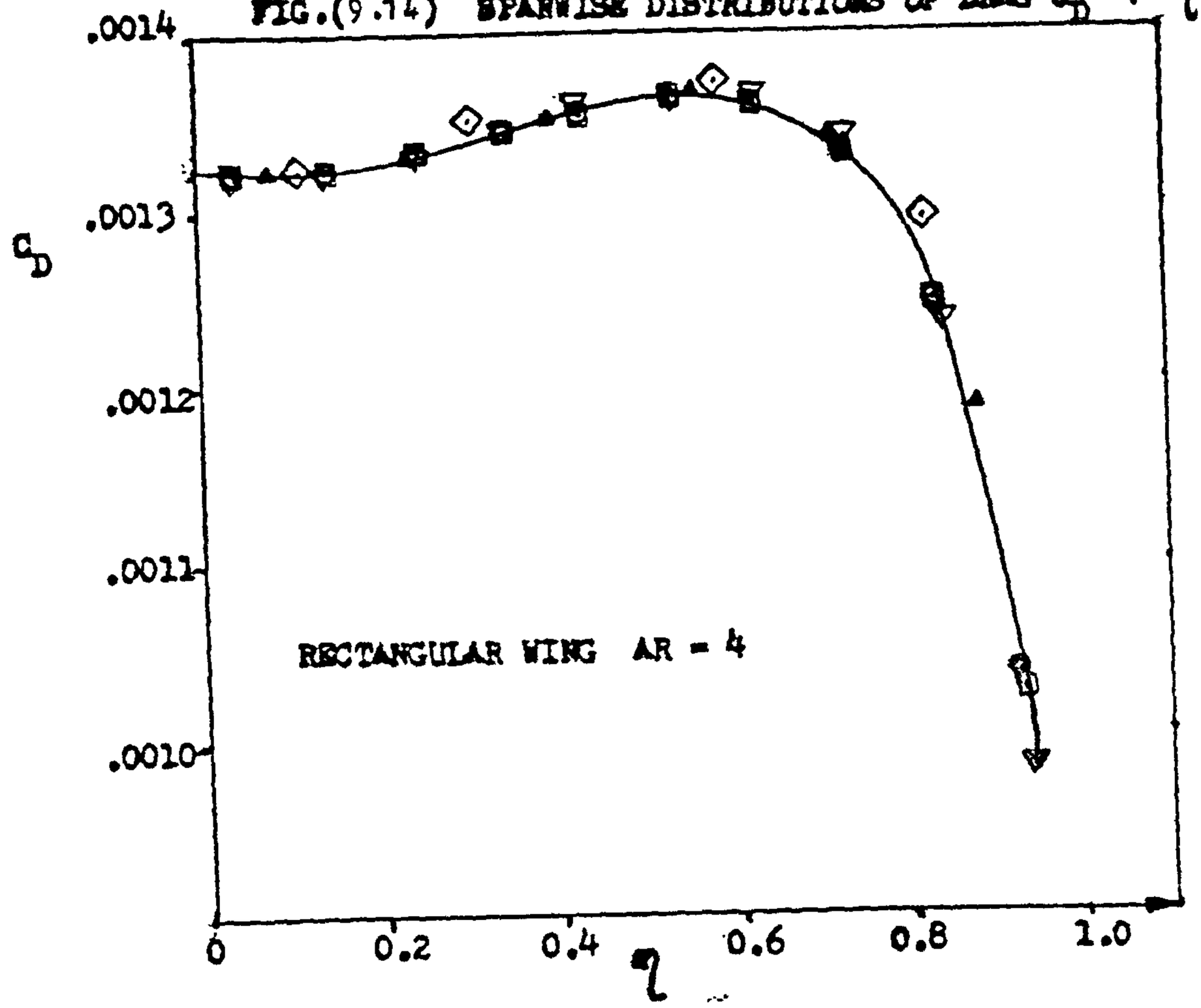

FIG.(9·15) SPANWISE DISTRIBUTIONS OF LOAD C_{LC} / $C_{L\bar{C}}$ ·V· η

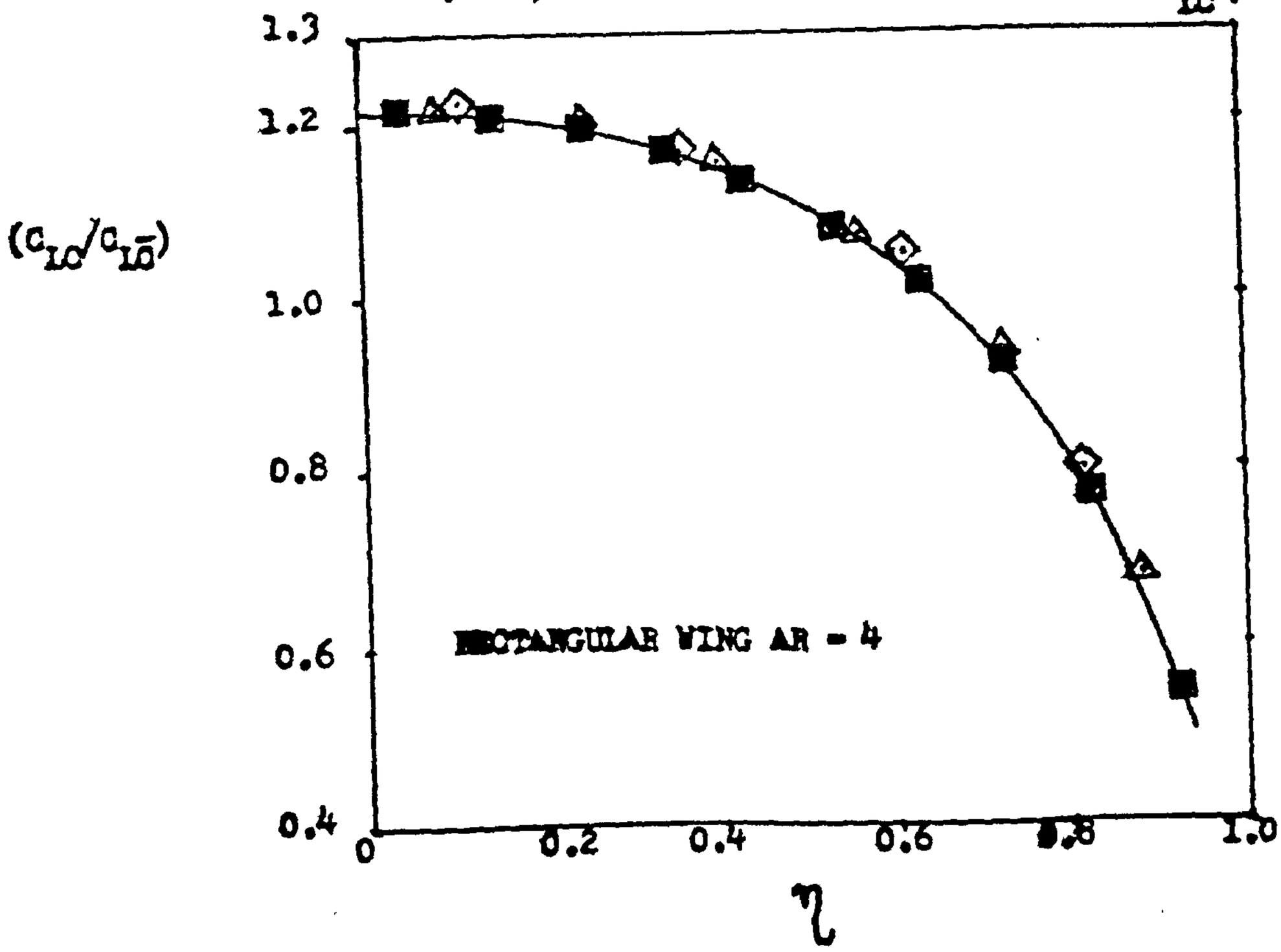

	No. of elements Along Chord	Span	Total Elements	Aspect Ratio
○ ———	10	10	100	2
□ ———	5	10	50	1
◇ ———	10	4	40	5
△ ———	8	6	48	2.7
▽ ———	2	10	20	0.4

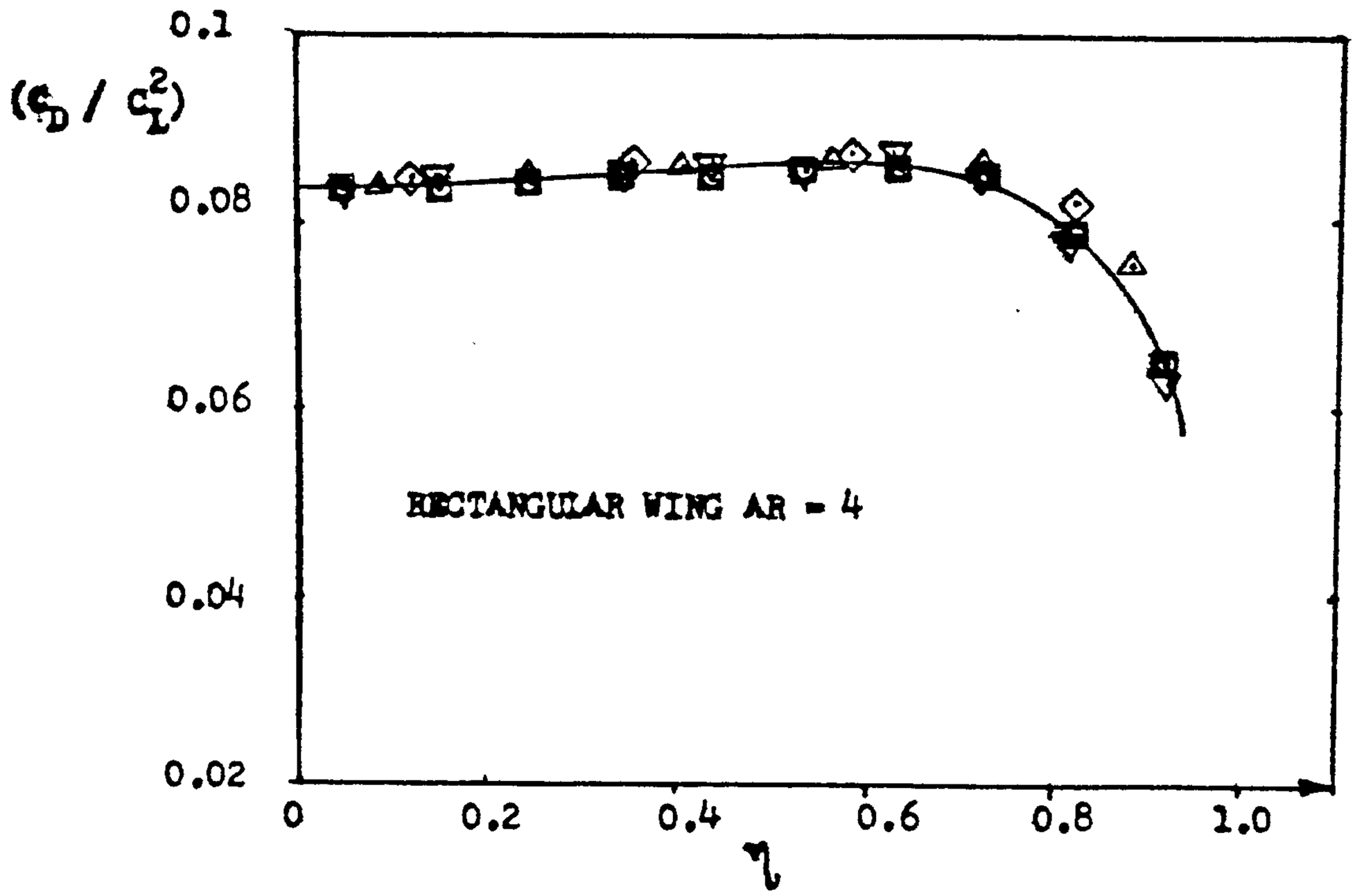

FIG.(9.16) SPANWISE DISTRIBUTIONS OF $C_D / C_L^2 \cdot Y \cdot \eta$

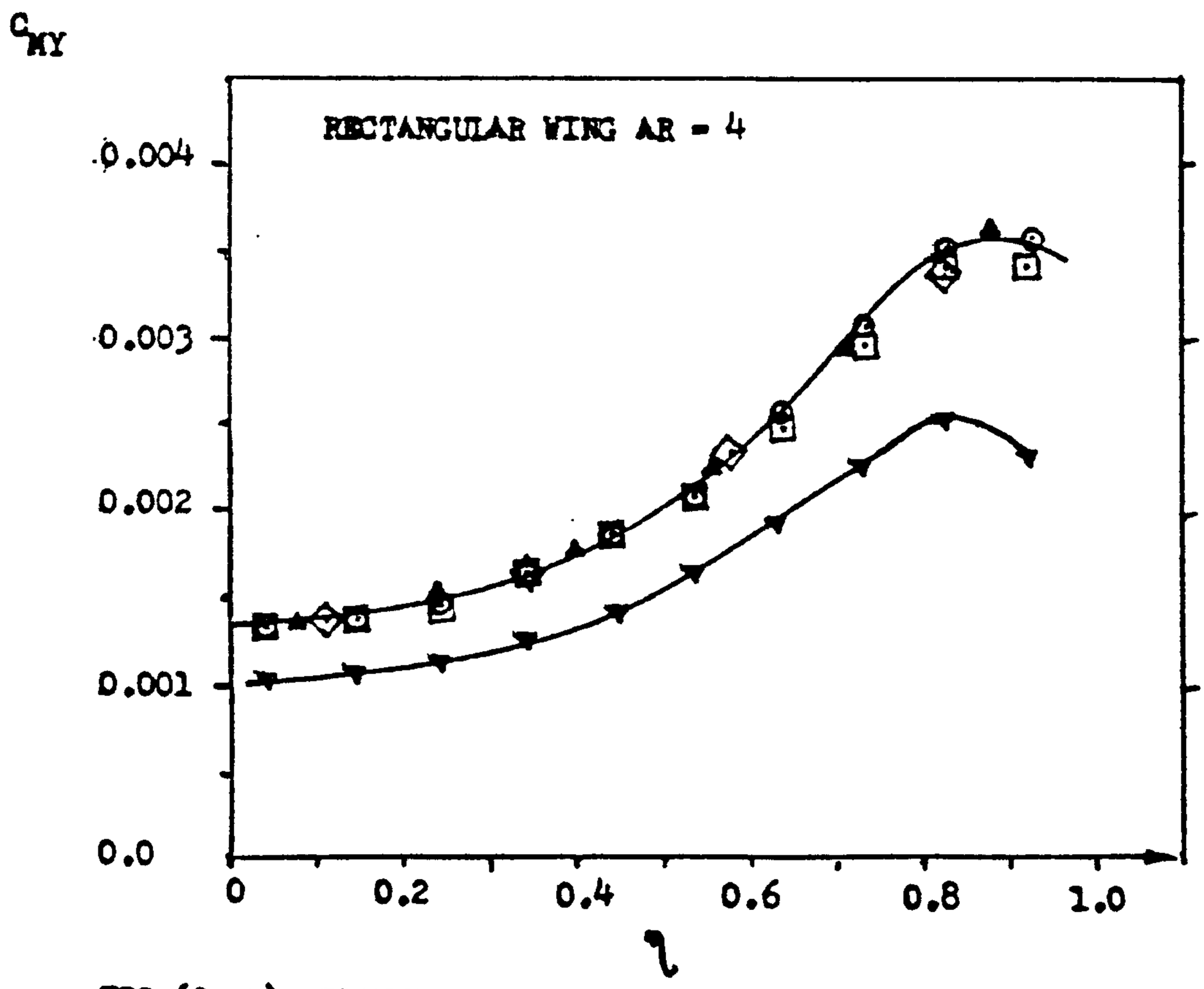

FIG.(9.17) SPANWISE DISTRIBUTIONS OF PITCHING MOMENT COEFFICIENTS

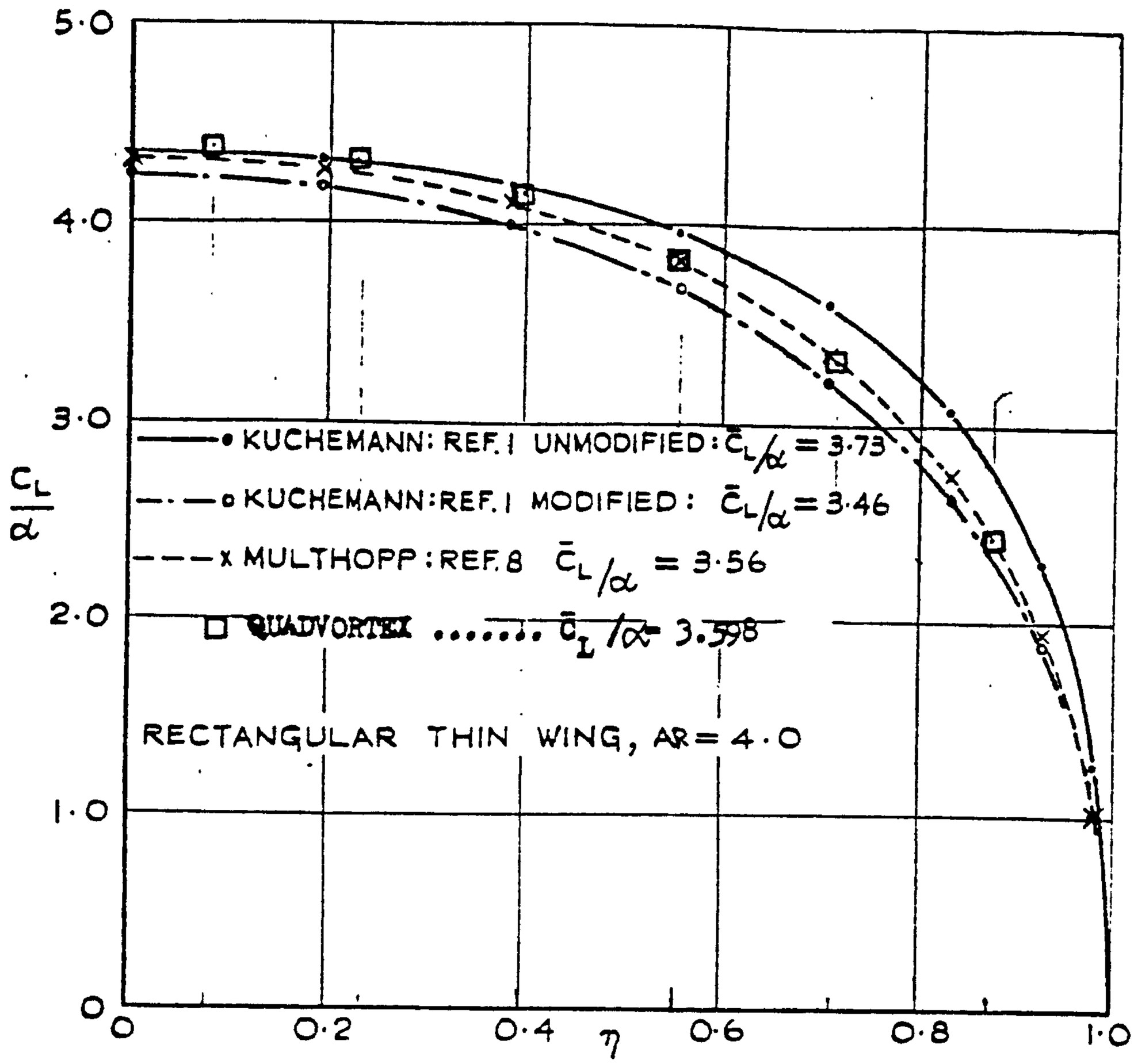

(a) ASPECT RATIO = 4·0

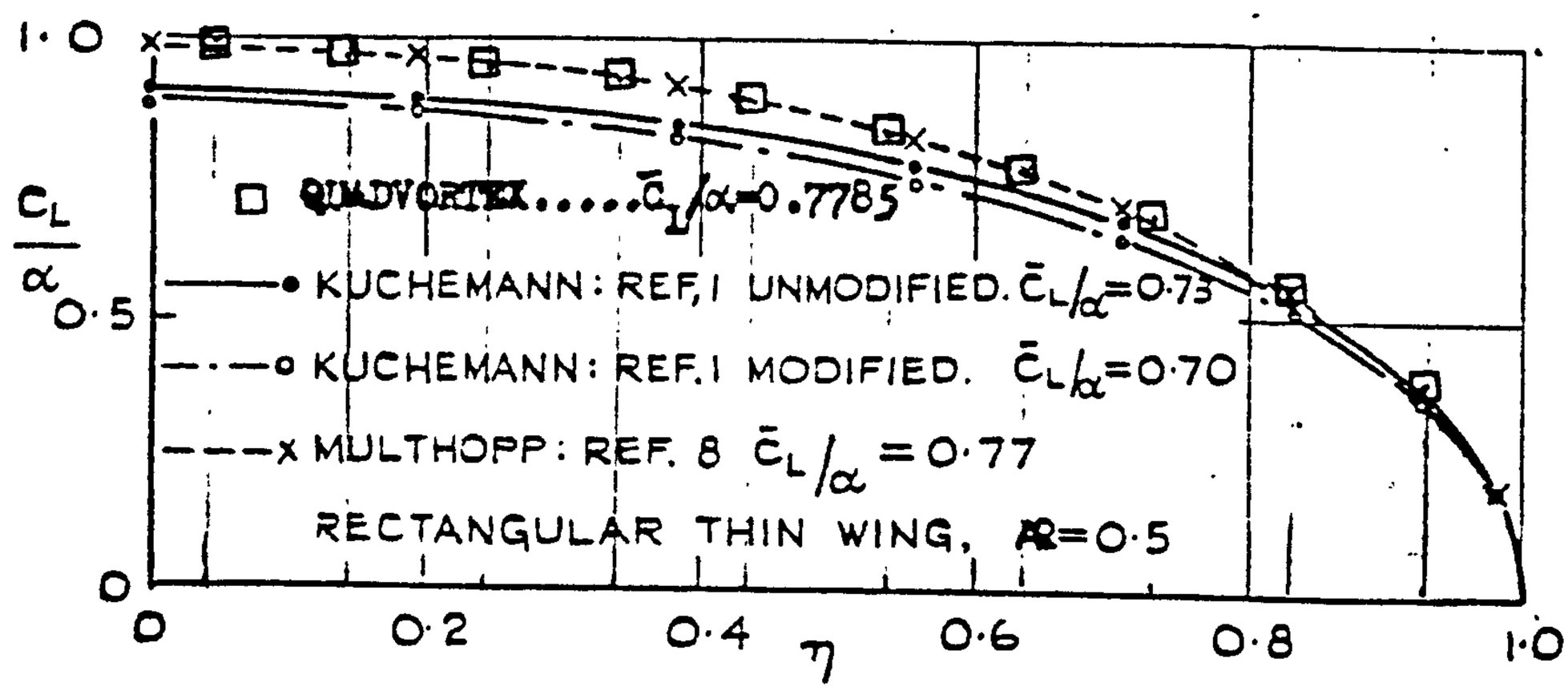

(b) ASPECT RATIO = 0·5

FIG. (9.18) COMPARISONS OF QUADVORTEX RESULTS WITH SOME CALCULATED RESULTS FOR SPANWISE LIFT DISTRIBUTION

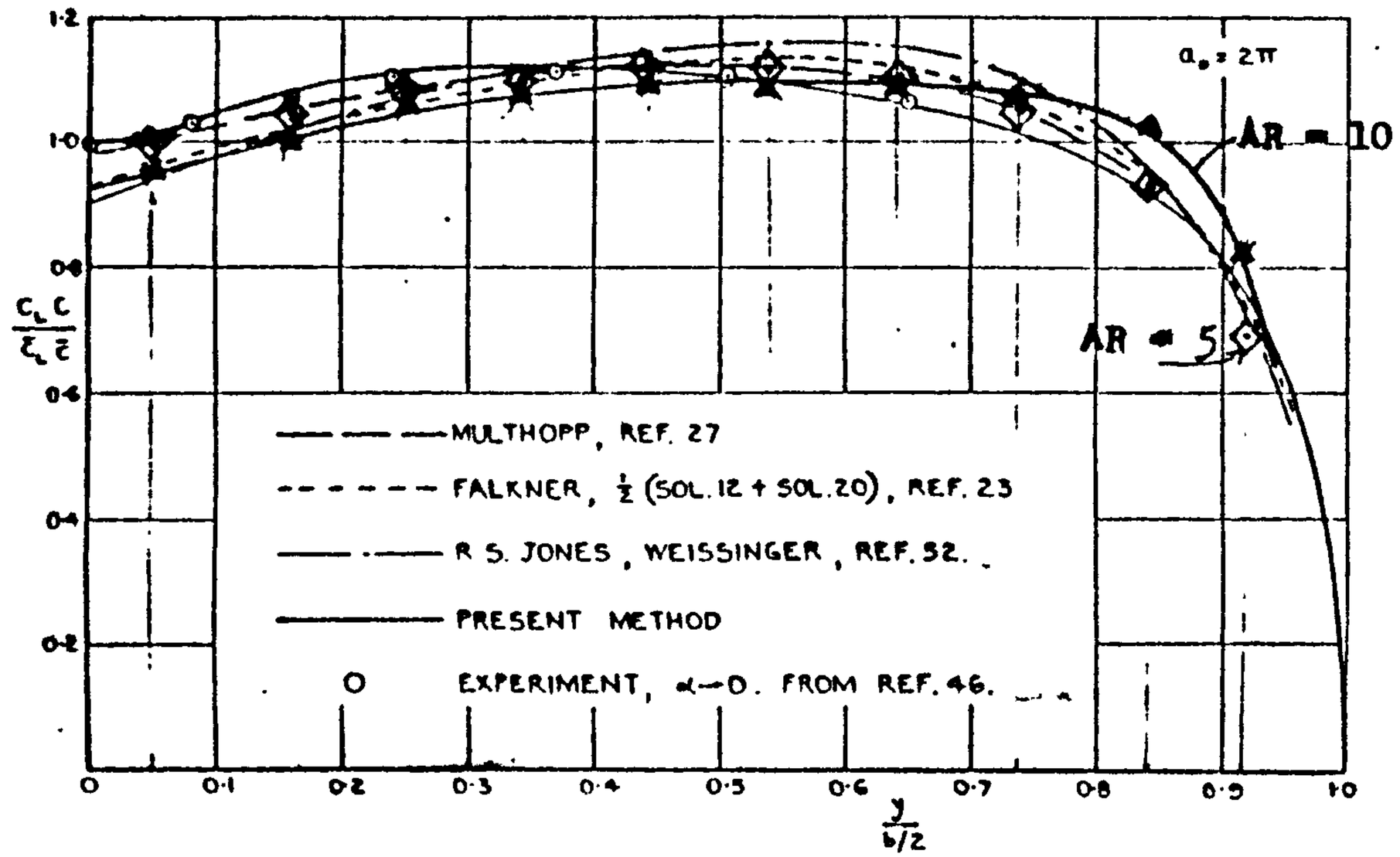

Span loadings for a 45-deg swept-back constant-chord wing. $A = 5$.

(a)

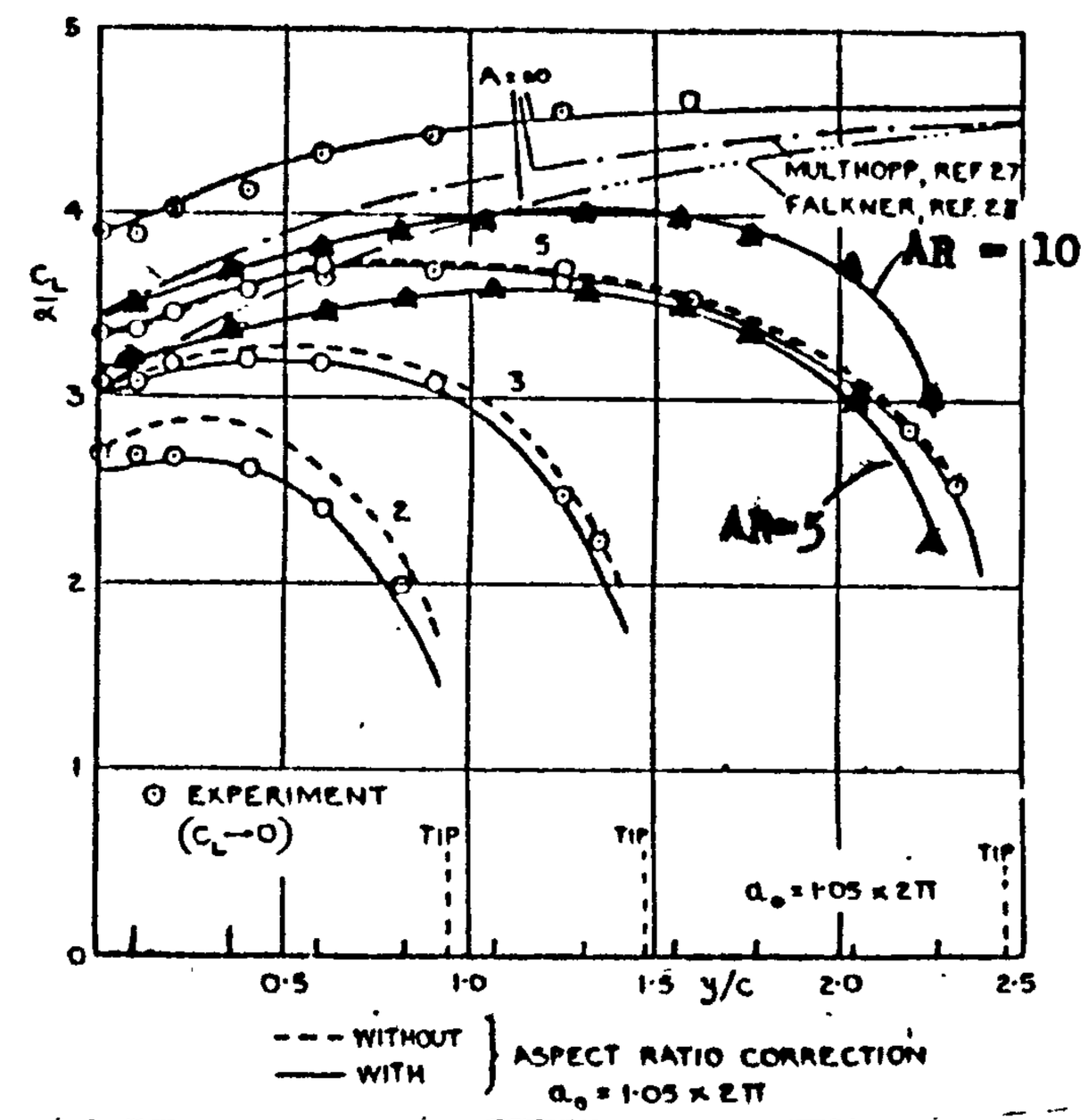

(b)

◇ △ — QUADVORTEX RESULTS

FIG.(9.19) COMPARISONS OF QUADVORTEX RESULTS FOR LIFT AND LOAD WITH SOME PUBLISHED RESULTS FOR A SWEPT WING AT 45° AND AR=5

FIG.(9.20) SPANWISE LOCATIONS OF C_p POSITION FOR A RECTANGULAR WING

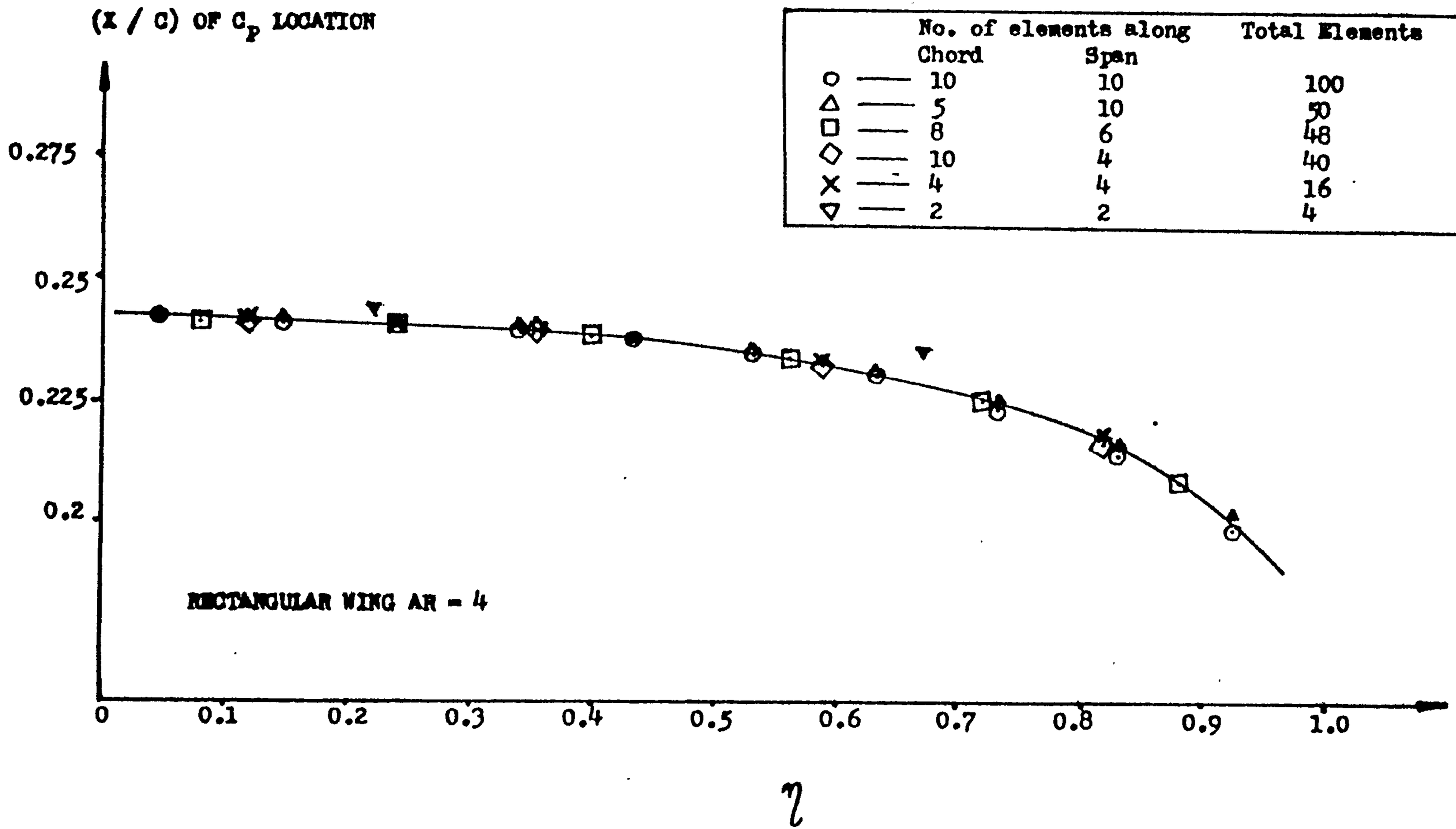

	No. of elements along Chord	Span	Total Elements	Aspect Ratio
○ ——	10	10	100	2
△ ——	5	10	50	1
□ ——	8	6	48	2.7
◇ ——	10	4	40	5
× ——	4	4	16	2
▽ ——	2	2	4	2

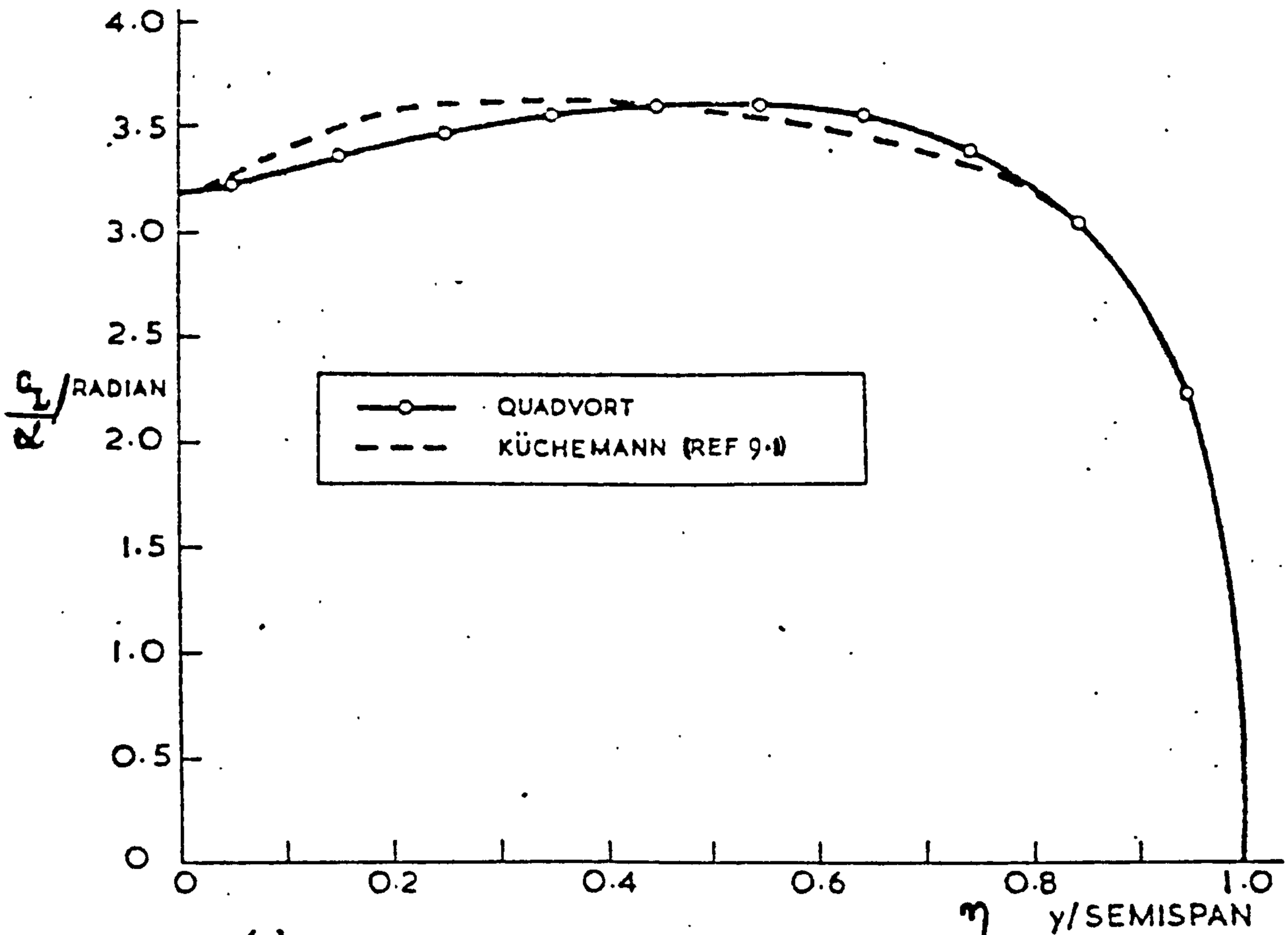

(a) SPANWISE DISTRIBUTION OF LIFT – COMPARISON WITH KÜCHEMANN'S THEORY

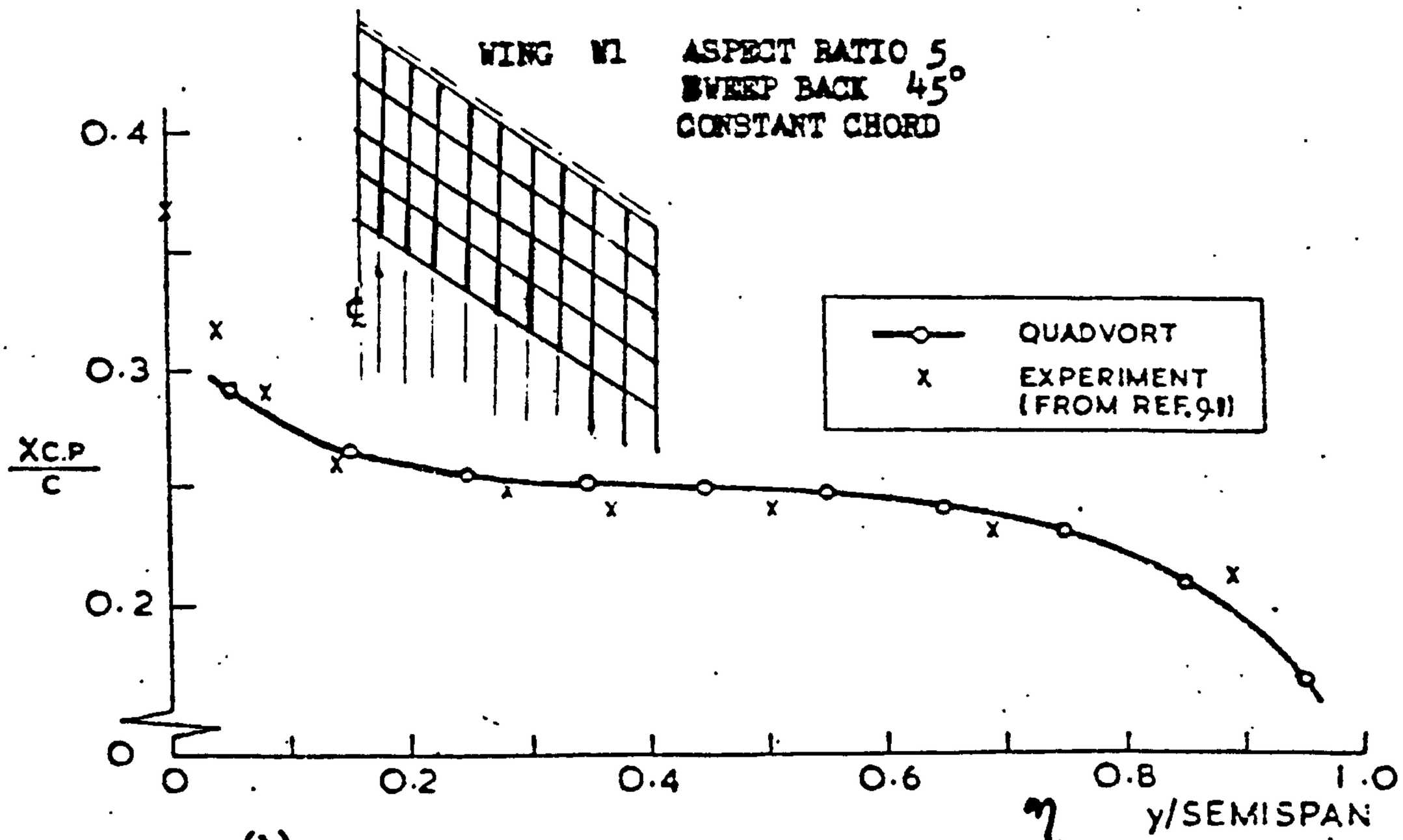

(b). CENTRE OF PRESSURE LOCUS – COMPARISON WITH EXPERIMENT.

FIG.(9·21) RESULTS FOR THIN WING W1

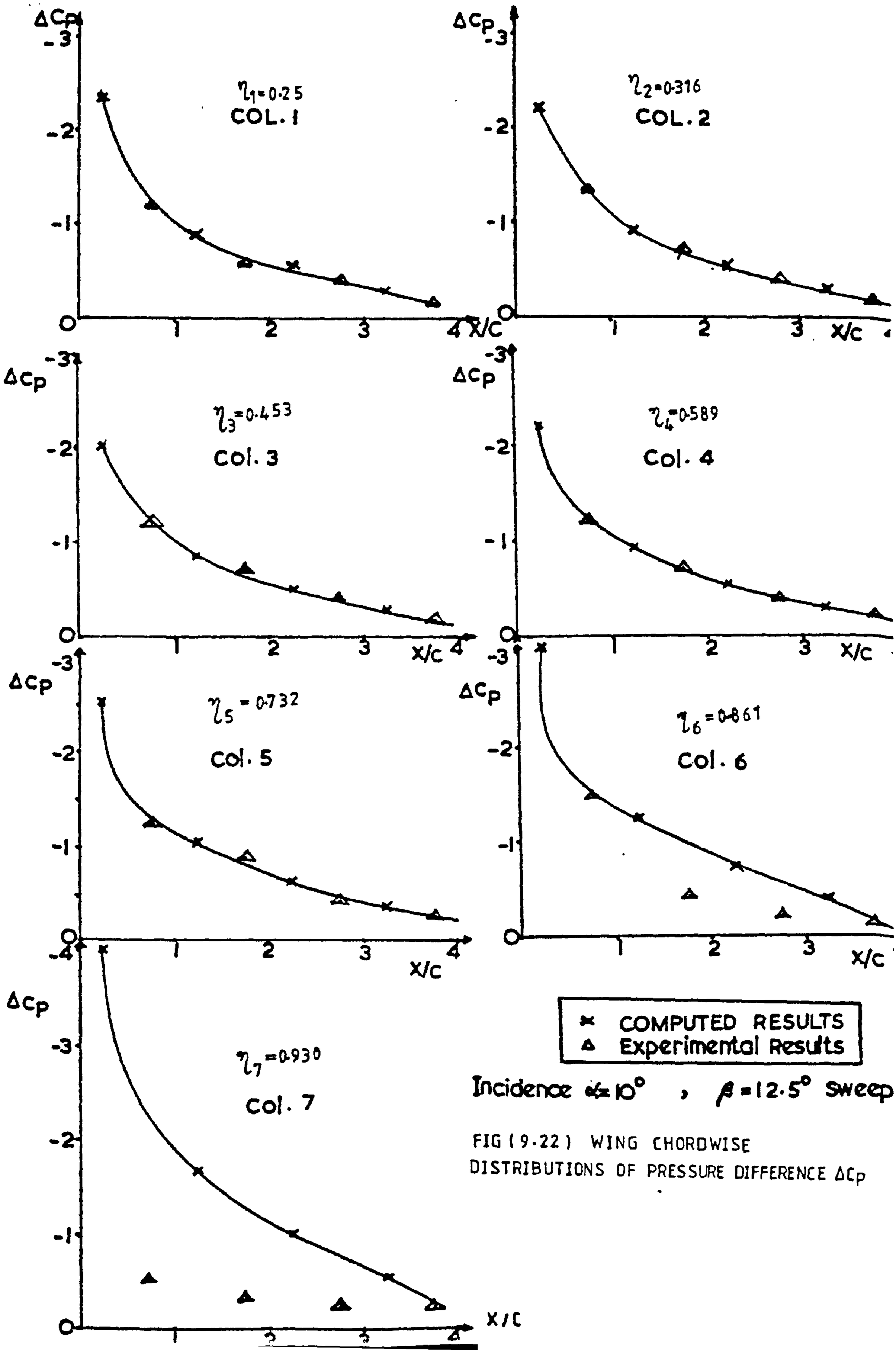

FIG (9.22) WING CHORDWISE DISTRIBUTIONS OF PRESSURE DIFFERENCE ΔCp

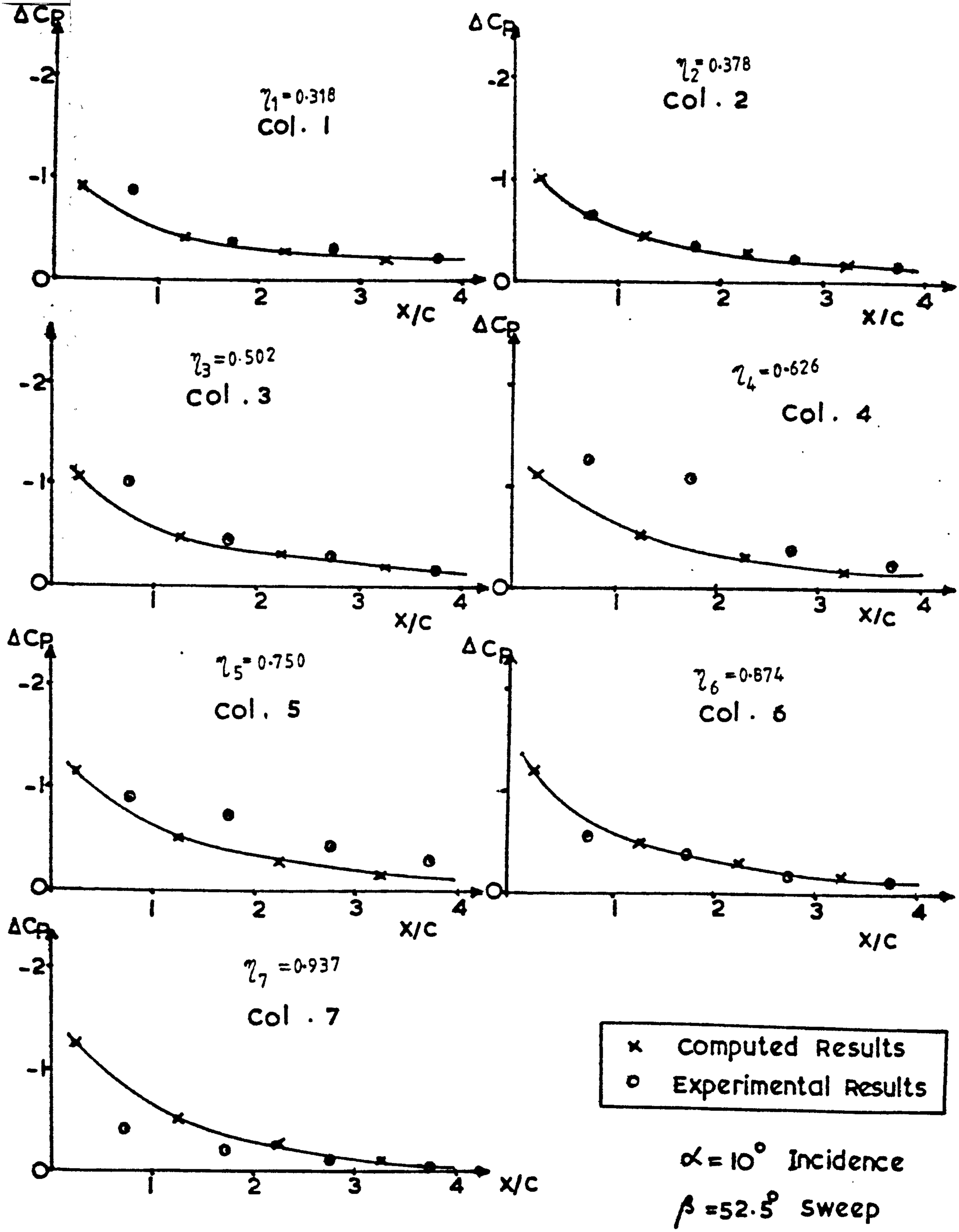

FIG. (9.23) Wing Chordwise Distributions Of Pressure Differences ΔC_p

FIG-(9.24) COMPARISONS OF SPANWISE DISTRIBUTIONS OF PRESSURE COEFFICIET FOR RECTANGULAR WING

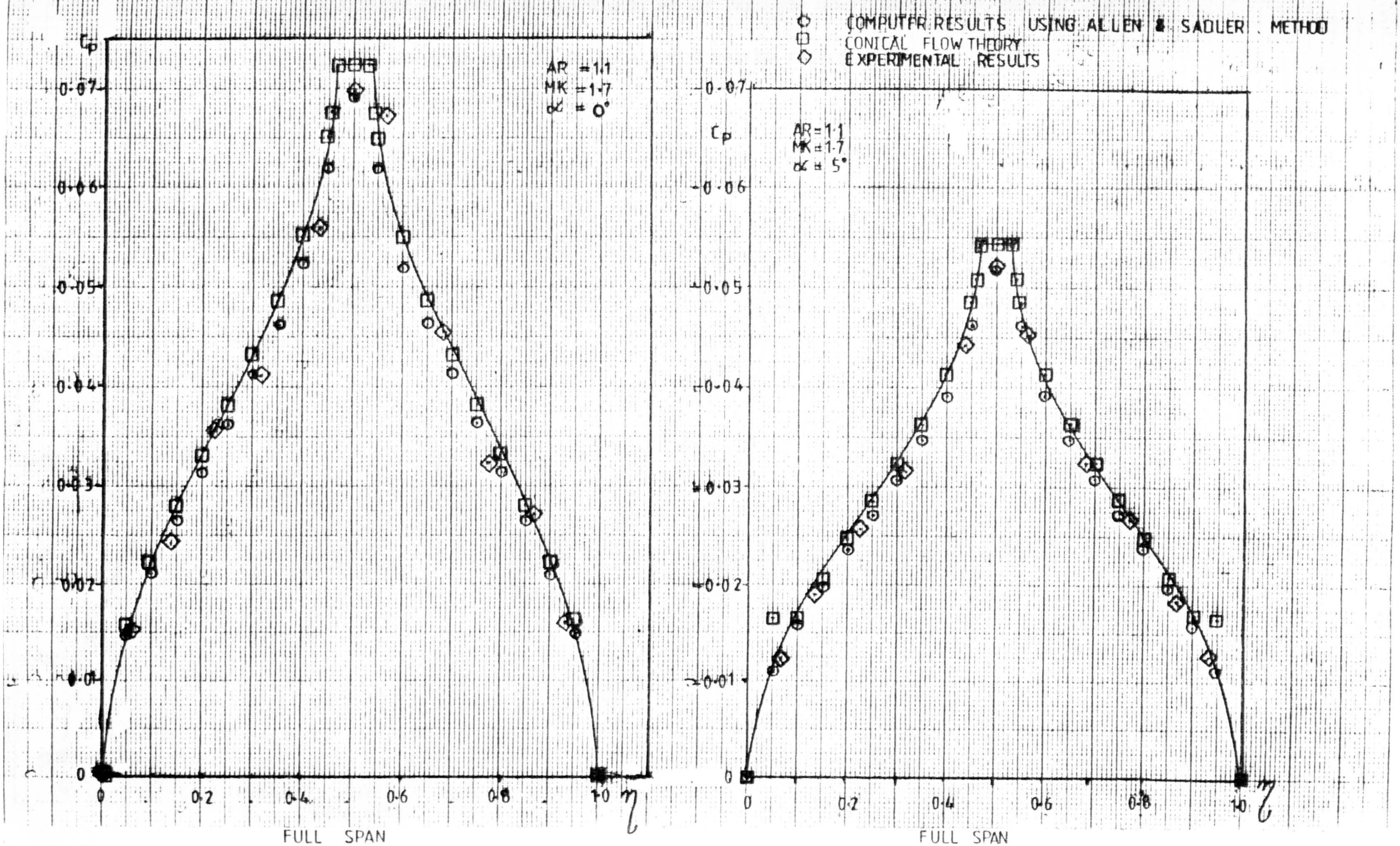

FIG.(9-25) COMPARISONS OF SPANWISE DISTRIBUTIONS OF PRESSURE COEFFICIENTS FOR RECTANGULAR WING

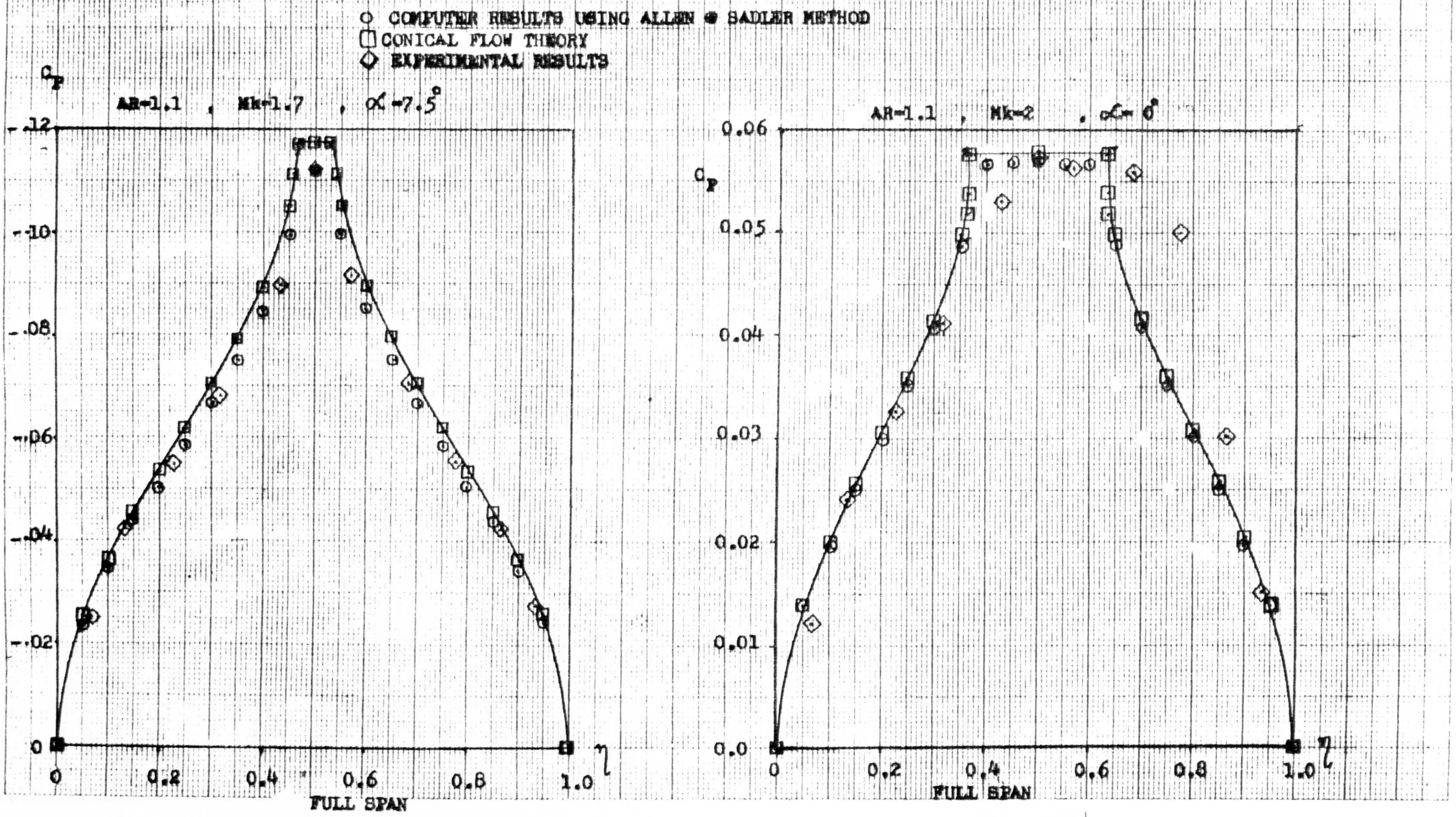

FIG.(9.26) COMPARISONS OF SPANWISE DISTRIBUTIONS OF PRESSURE COEFFICIENTS FOR RECTANGULAR WING

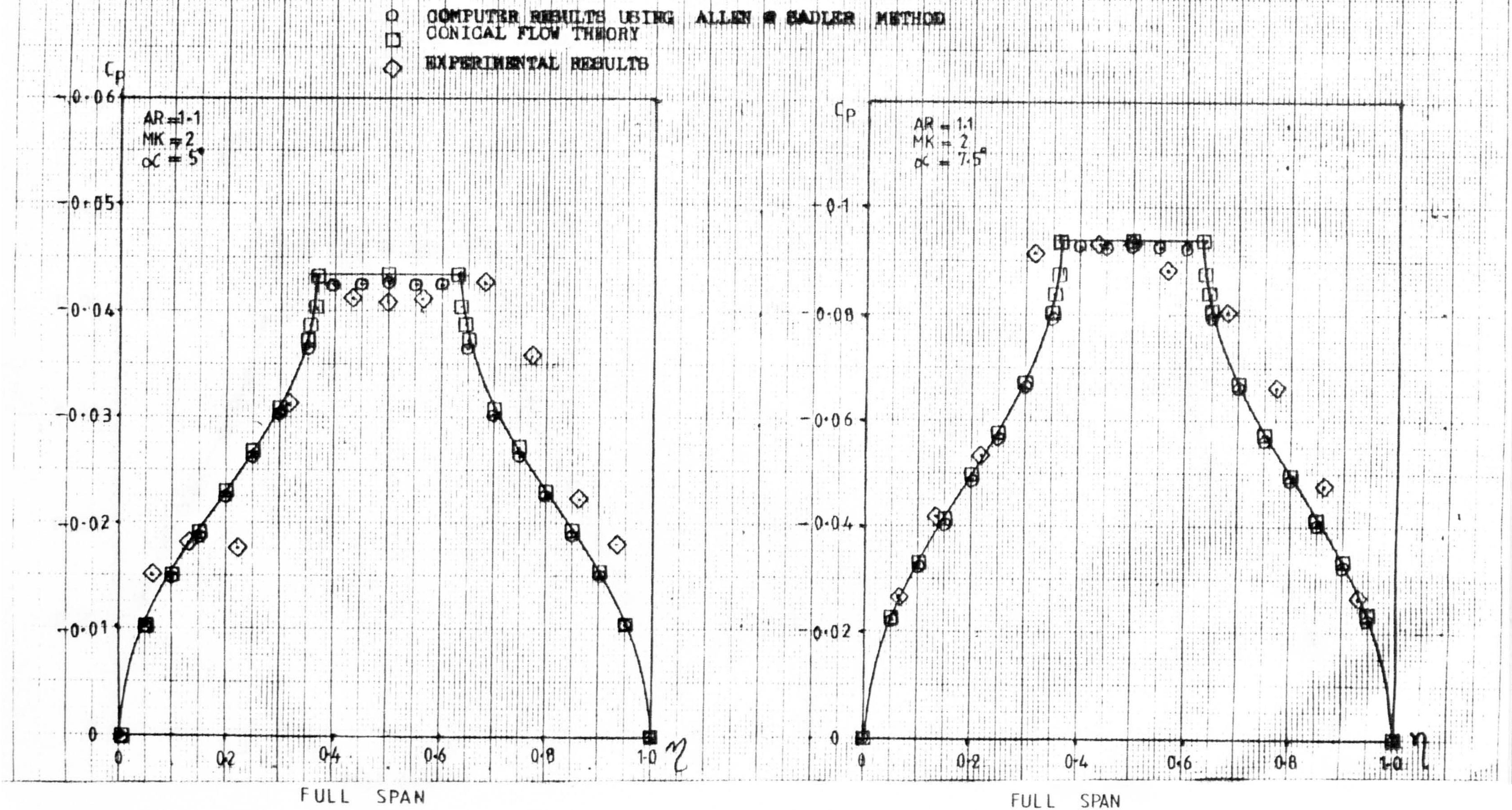

FIG.(9-27) COMPARISONS OF SPANWISE DISTRIBUTIONS OF PRESSURE COEFFICIENT FOR RECTANGULAR WING

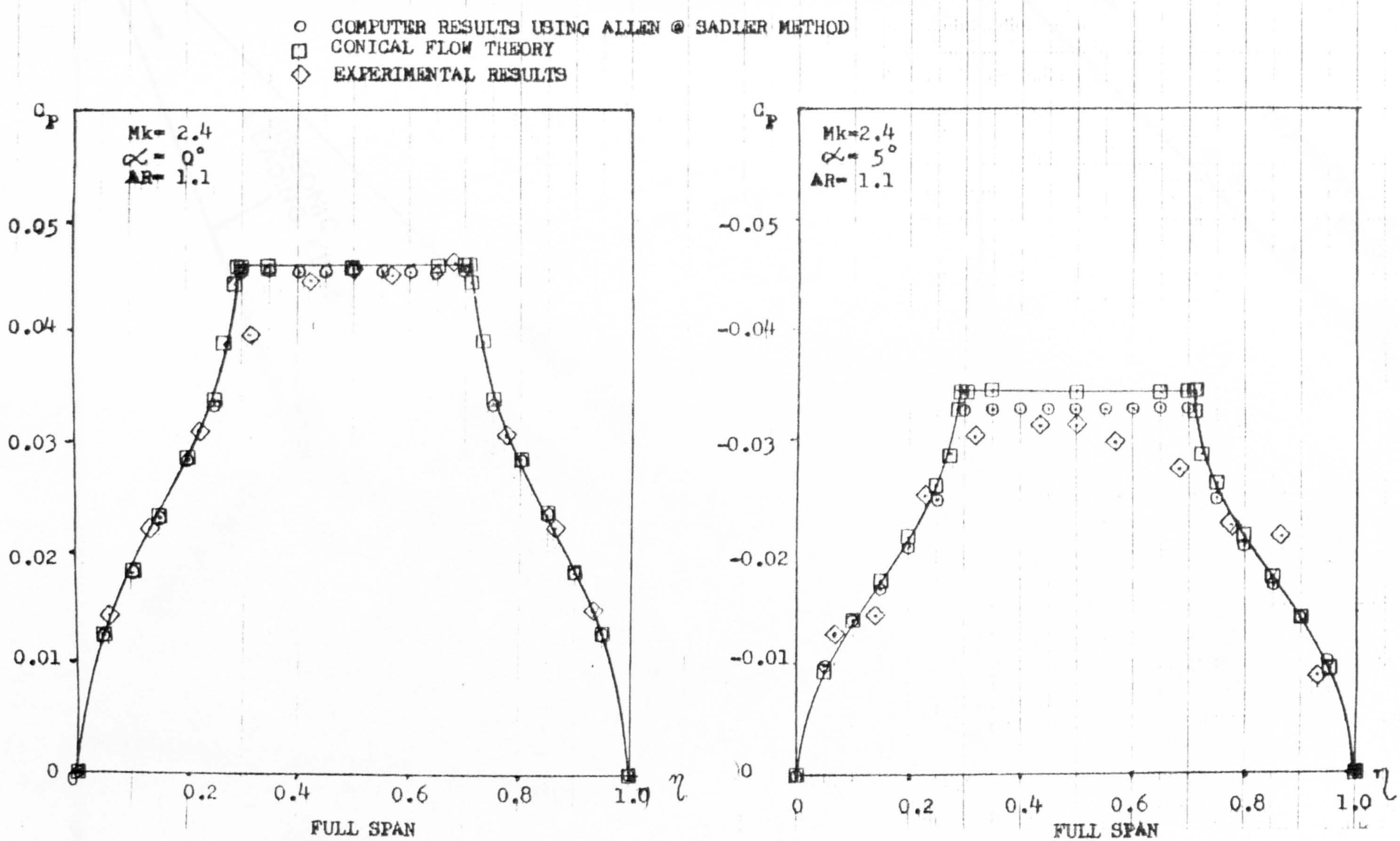

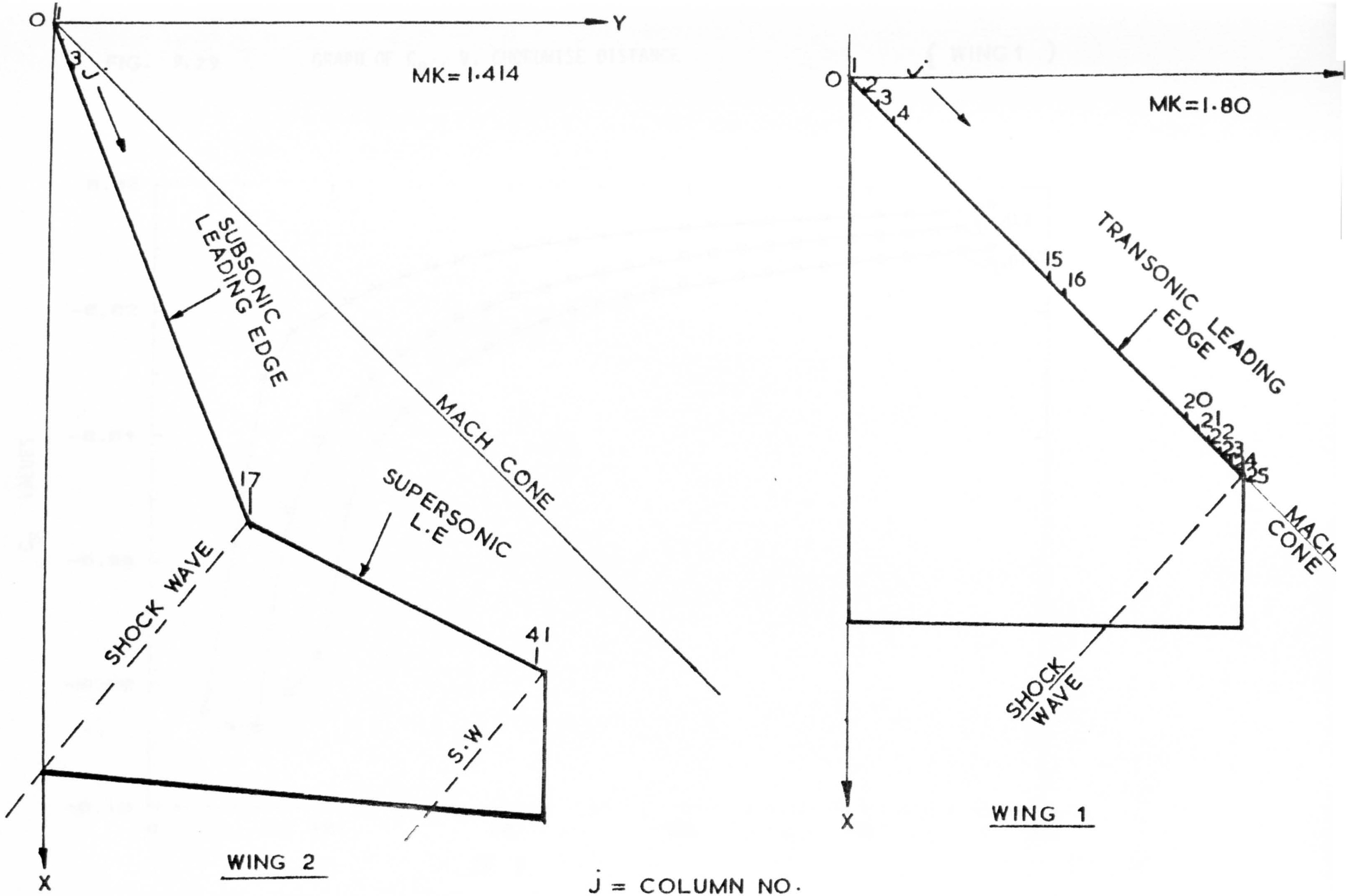

FIG. (9·28) SUPERSONIC WING PLANFORMS

FIG. 9.29 GRAPH OF C_p . V. CHORDWISE DISTANCE (WING 1)

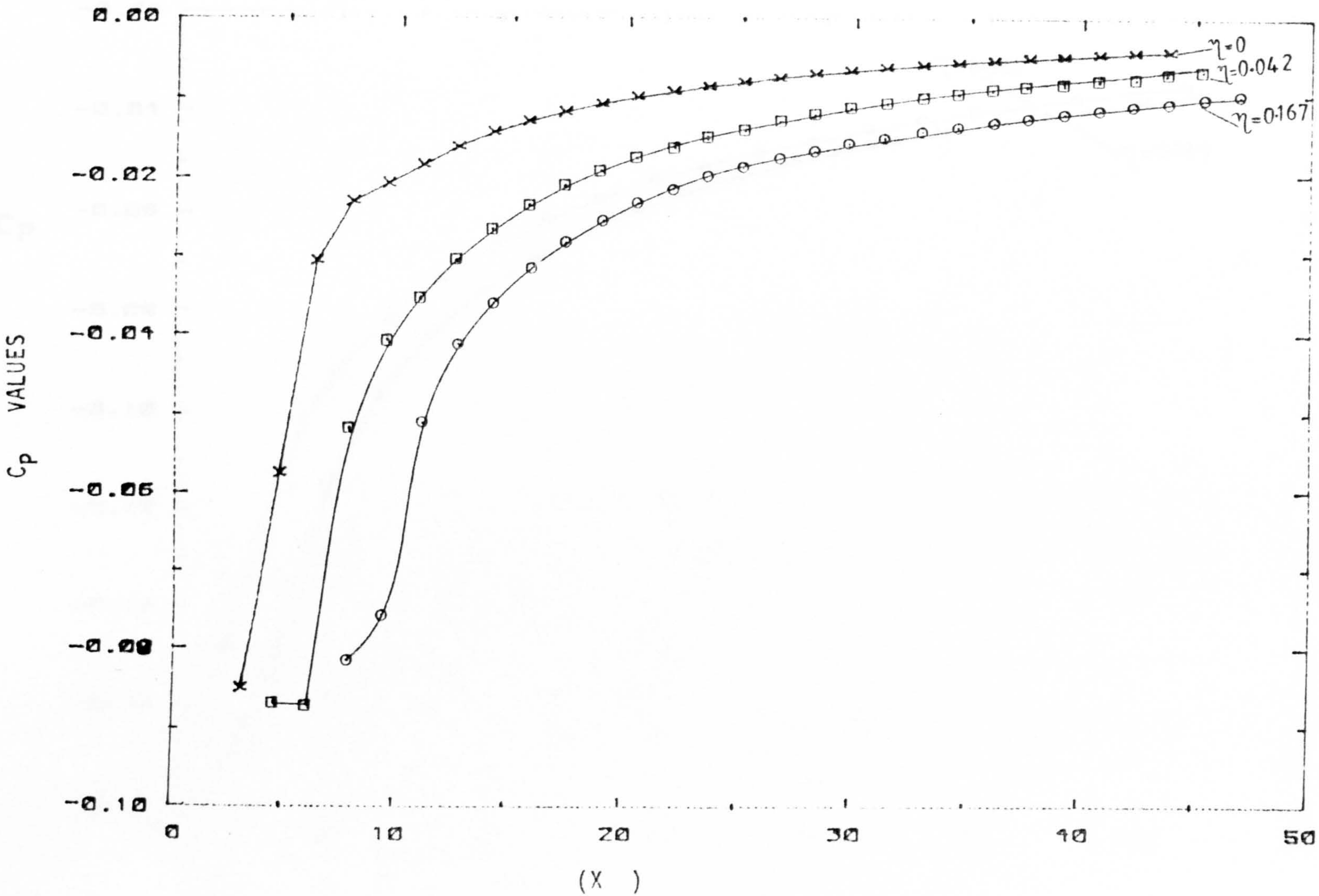

FIG. 9.30 GRAPH OF C_p · V · CHORDWISE DISTANCE (WING 1)

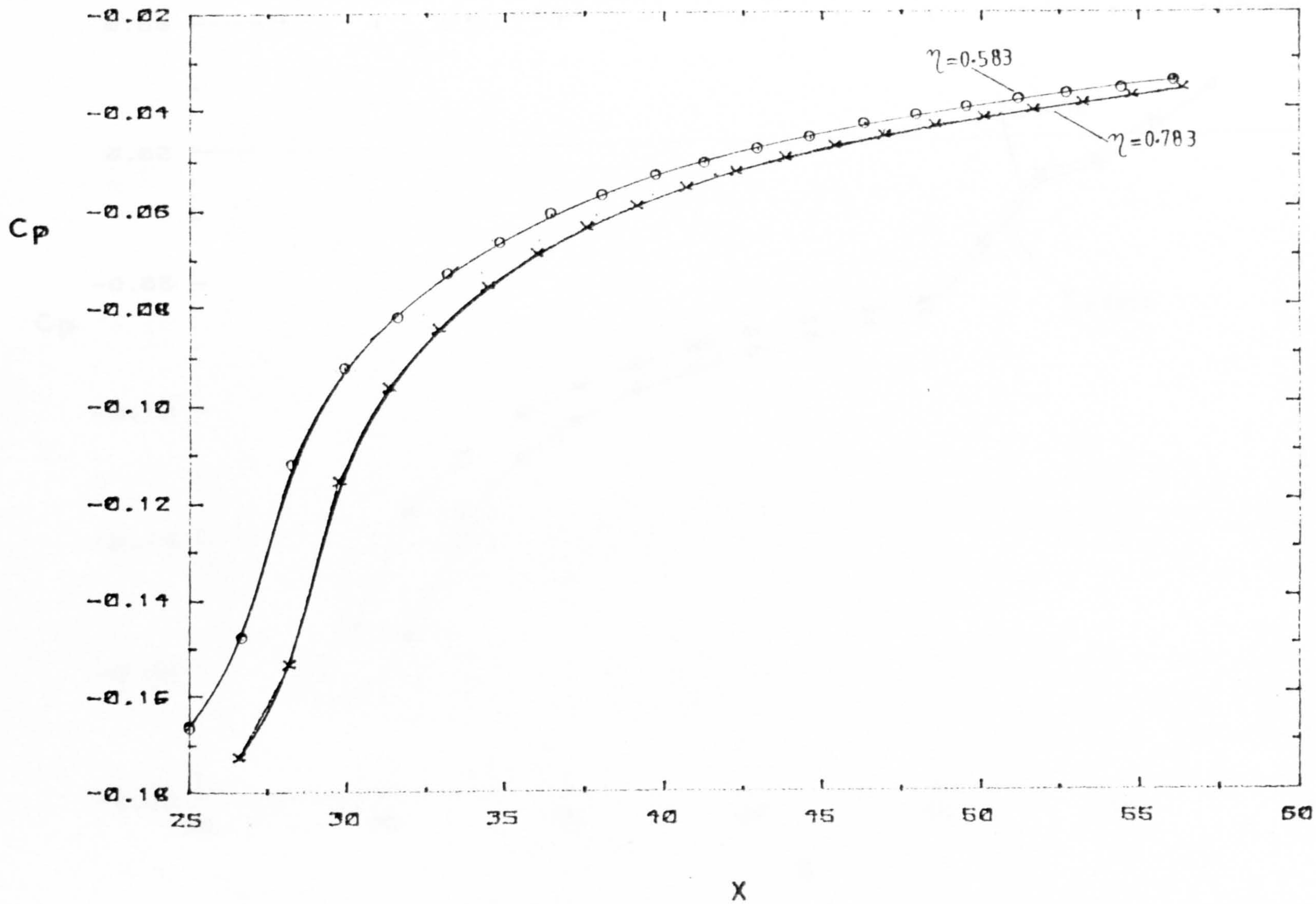

FIG. 9.31 GRAPH OF PRESSURE COEFFICIENT . V . CHORD (WING 1)

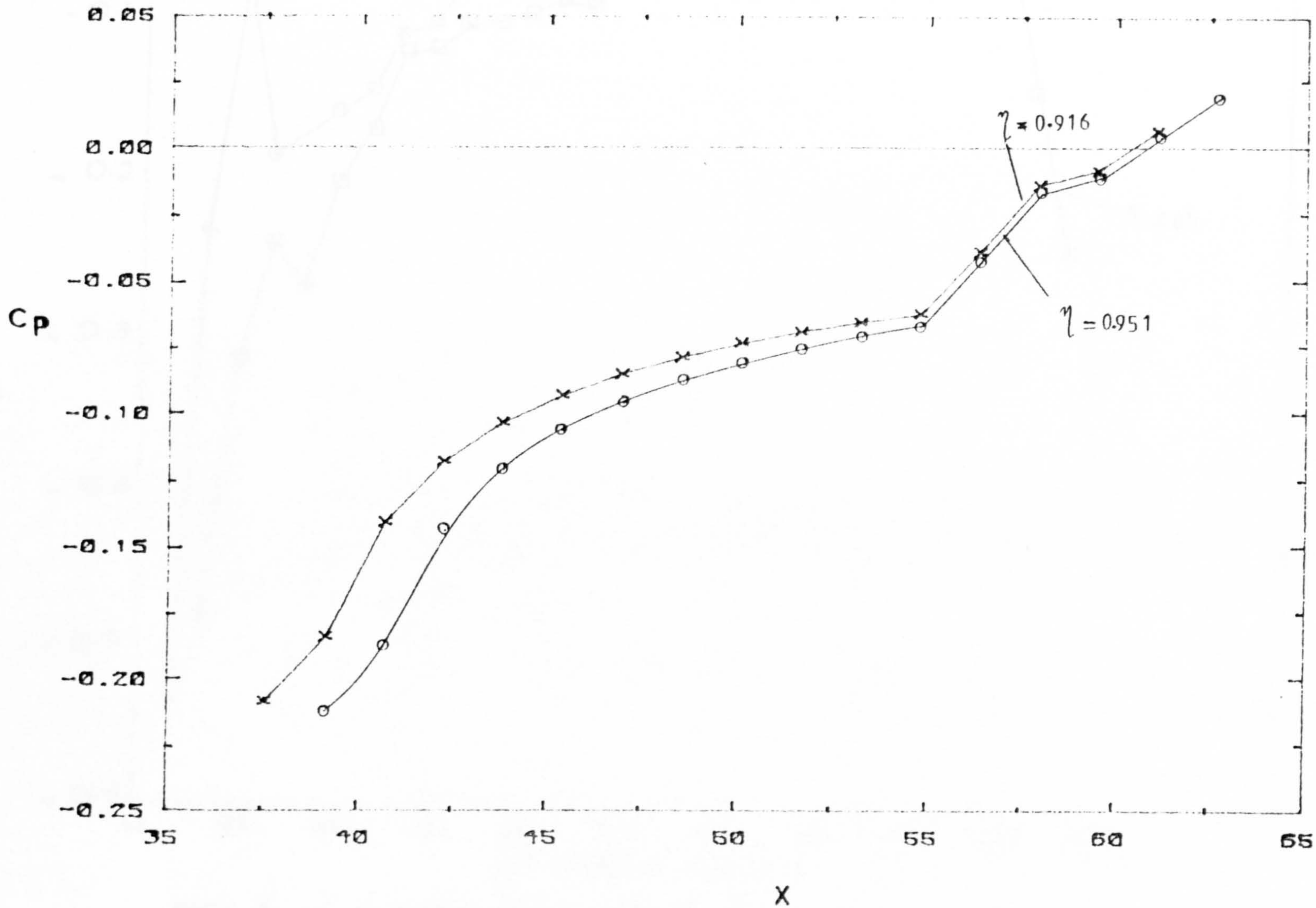

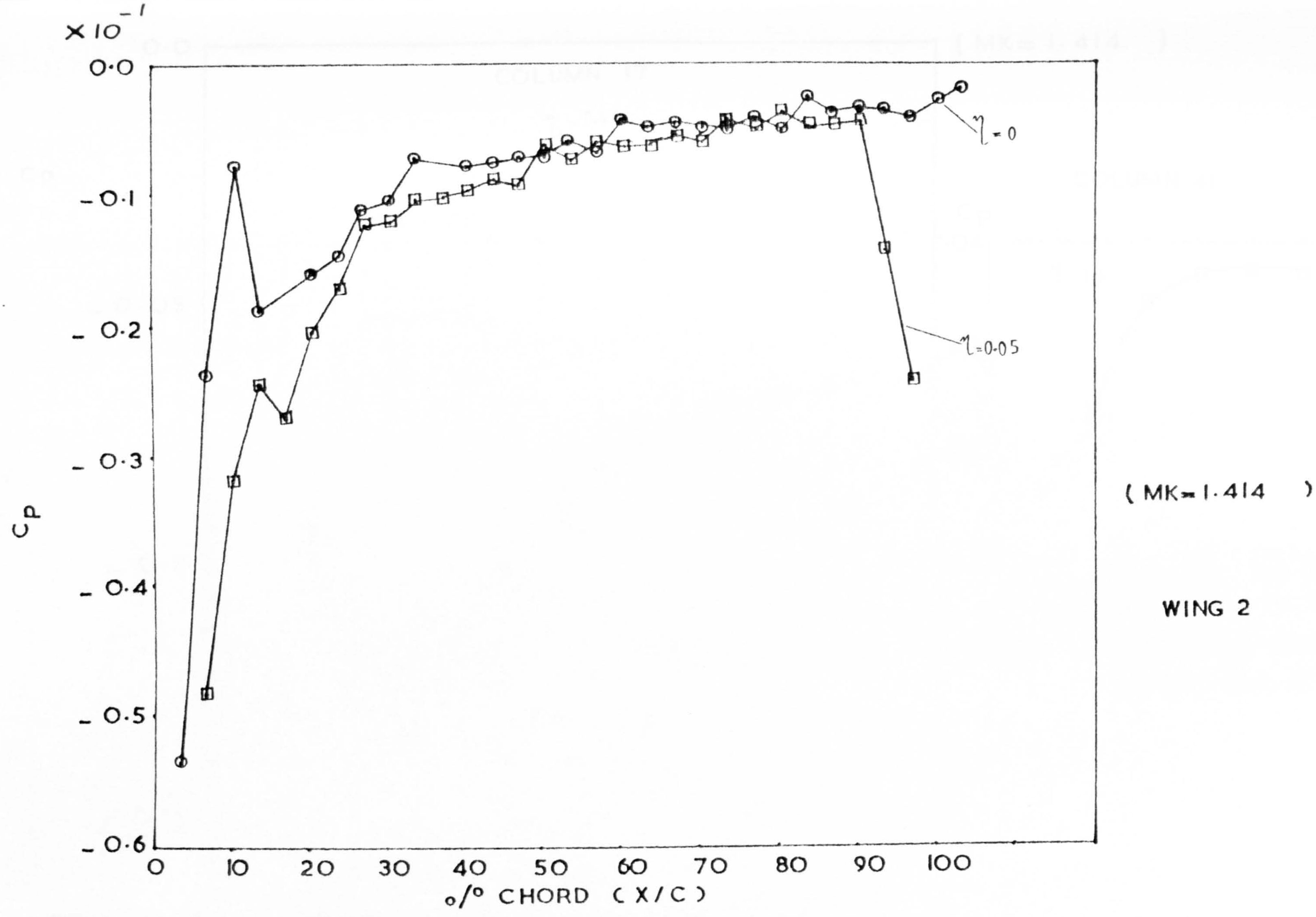

FIG (9. 32) CHORDWISE DISTRIBUTIONS OF PRESSURE COEFFICIENT C_p AT WING ROOT IN SUPERSONIC FLOW

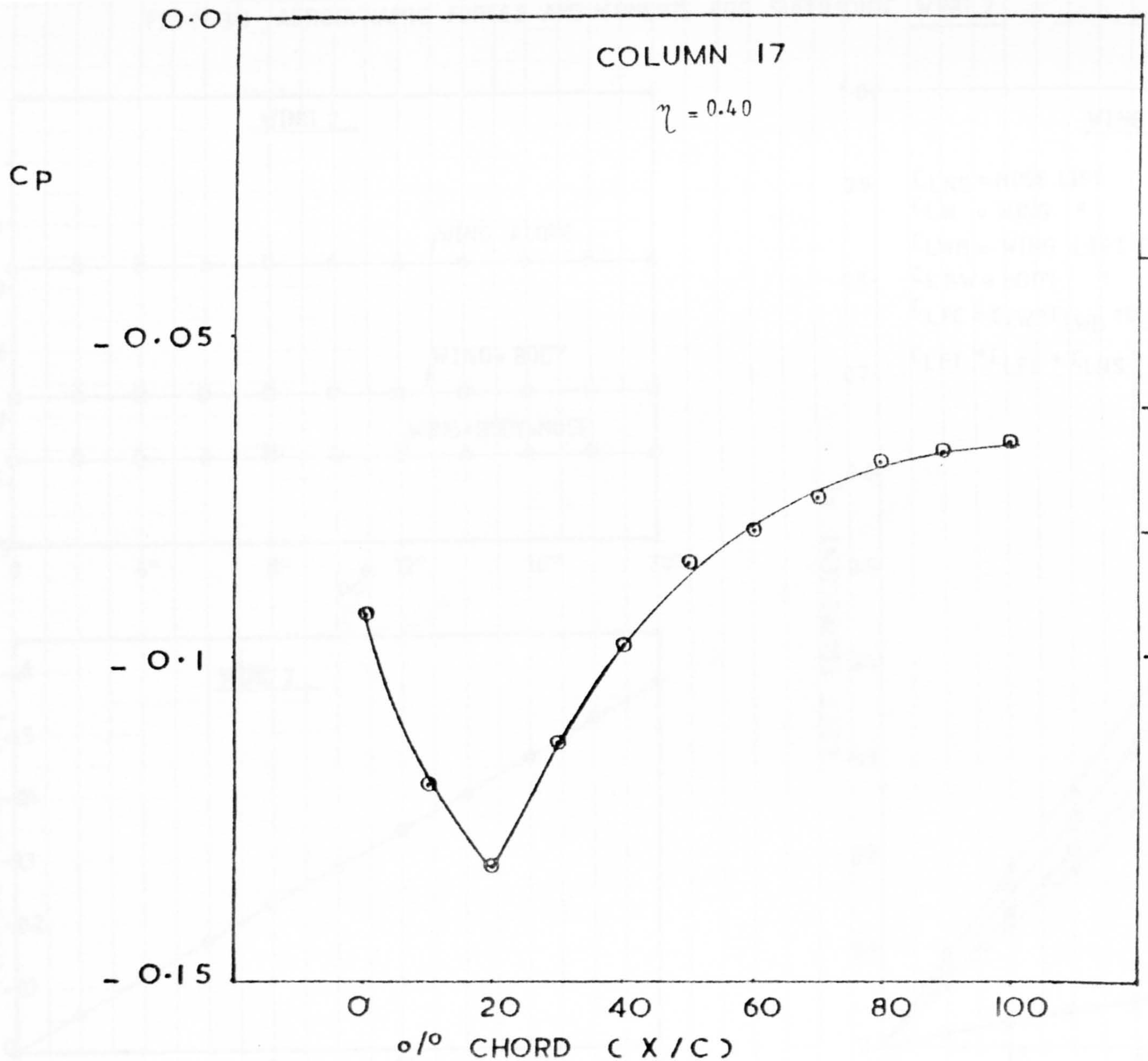

FIG.(9.33) CHORDWISE DISTRIBUTIONS PRESSURE COEFFICIENT Cp AT MID-SPAN OF THE SUPERSONIC WING 2

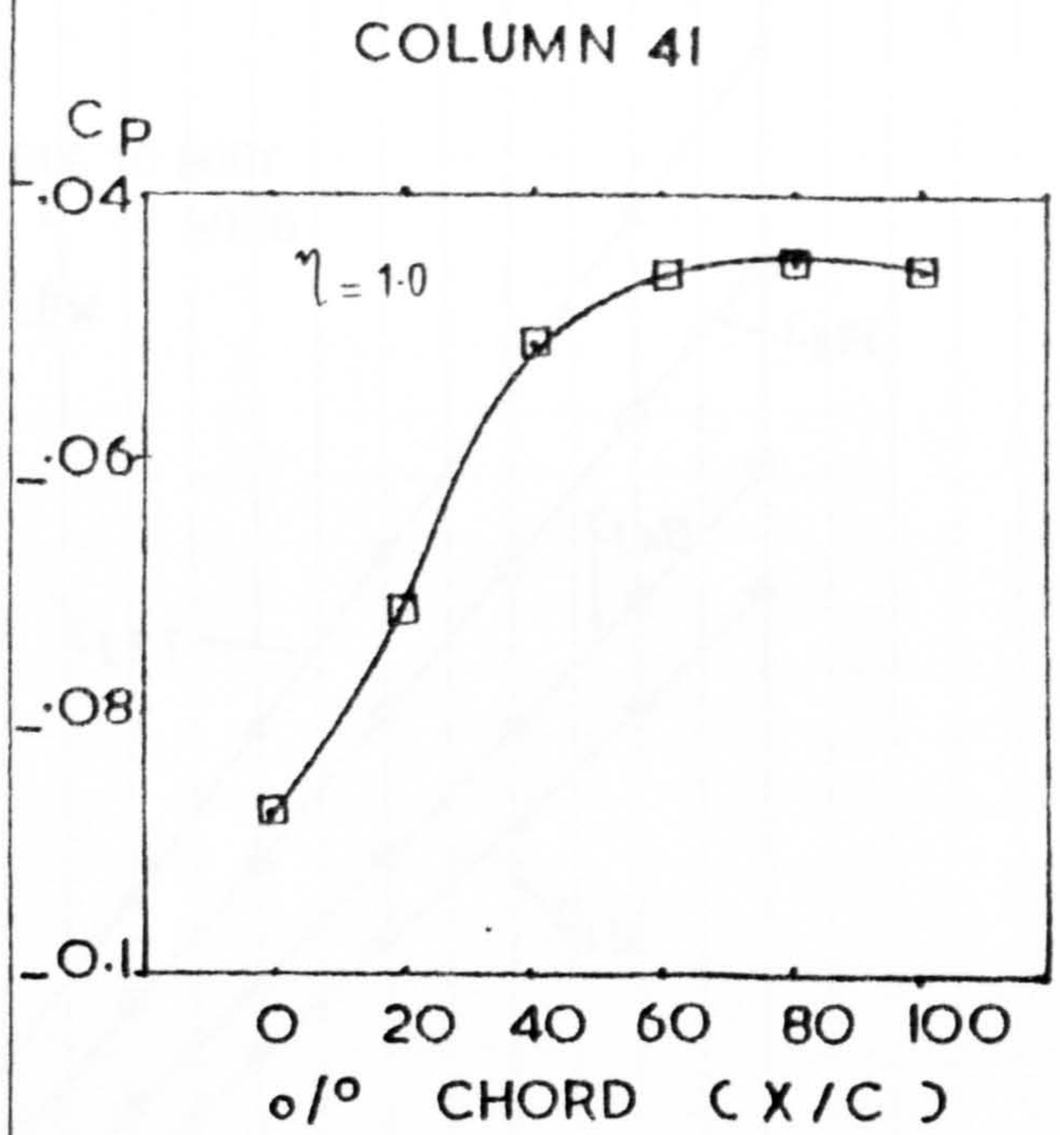

FIG.(9.33.1) CHORDWISE PRESSURE DISTRIBUTIONS AT WING TIP

FIG. (9.34) AERODYNAMIC FORCES AND MOMENTS FOR SUPERSONIC WING 2

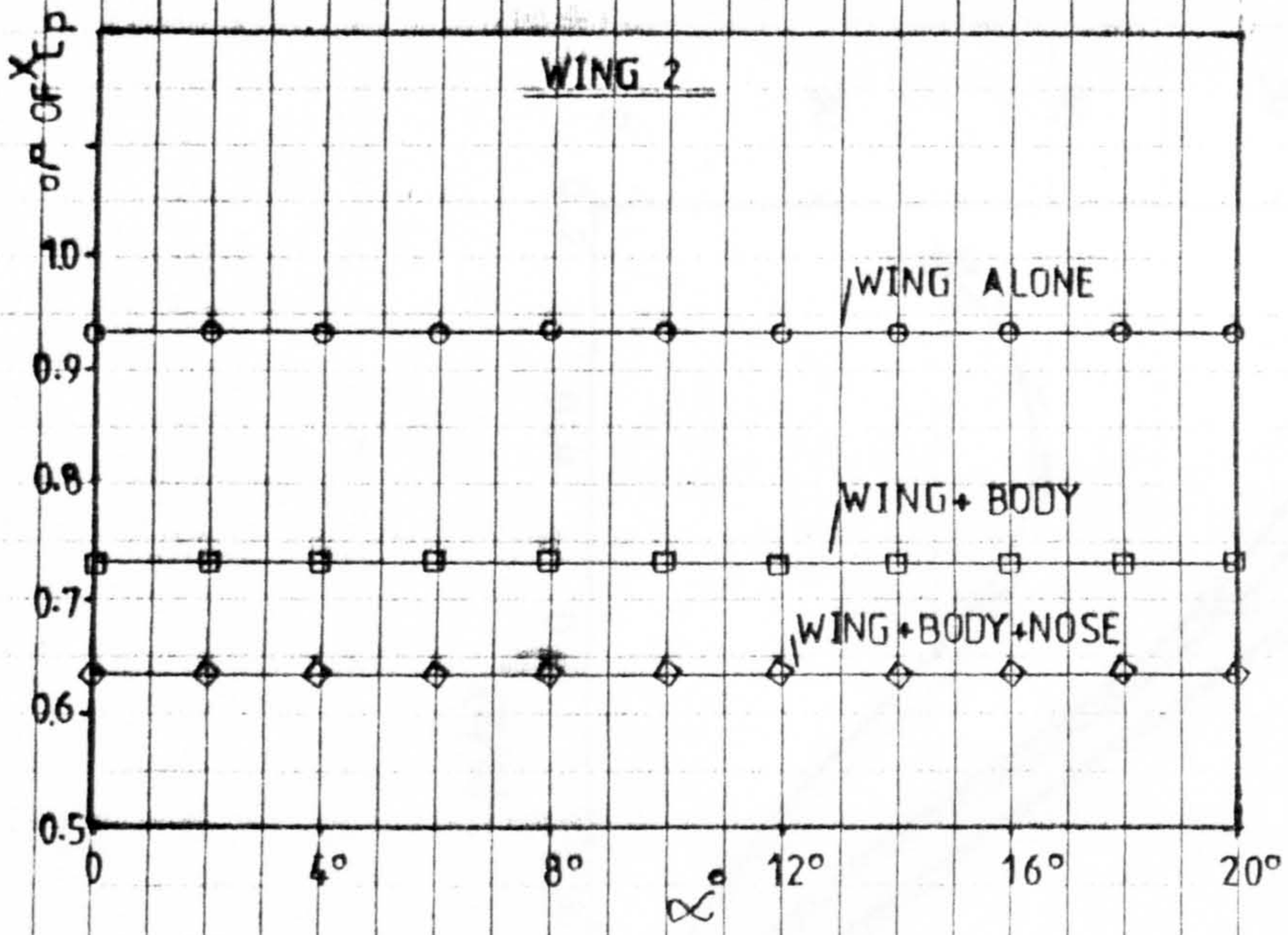

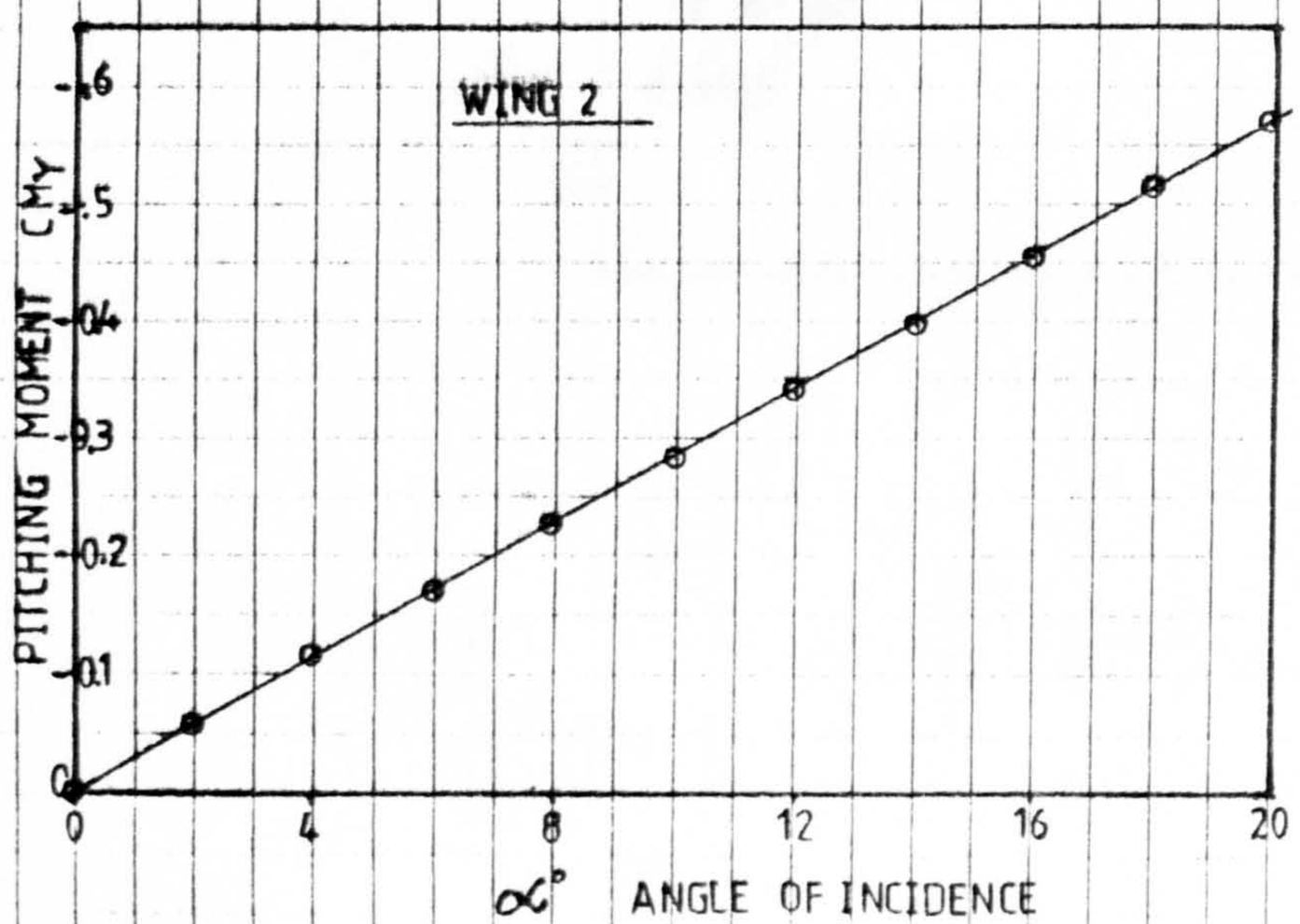

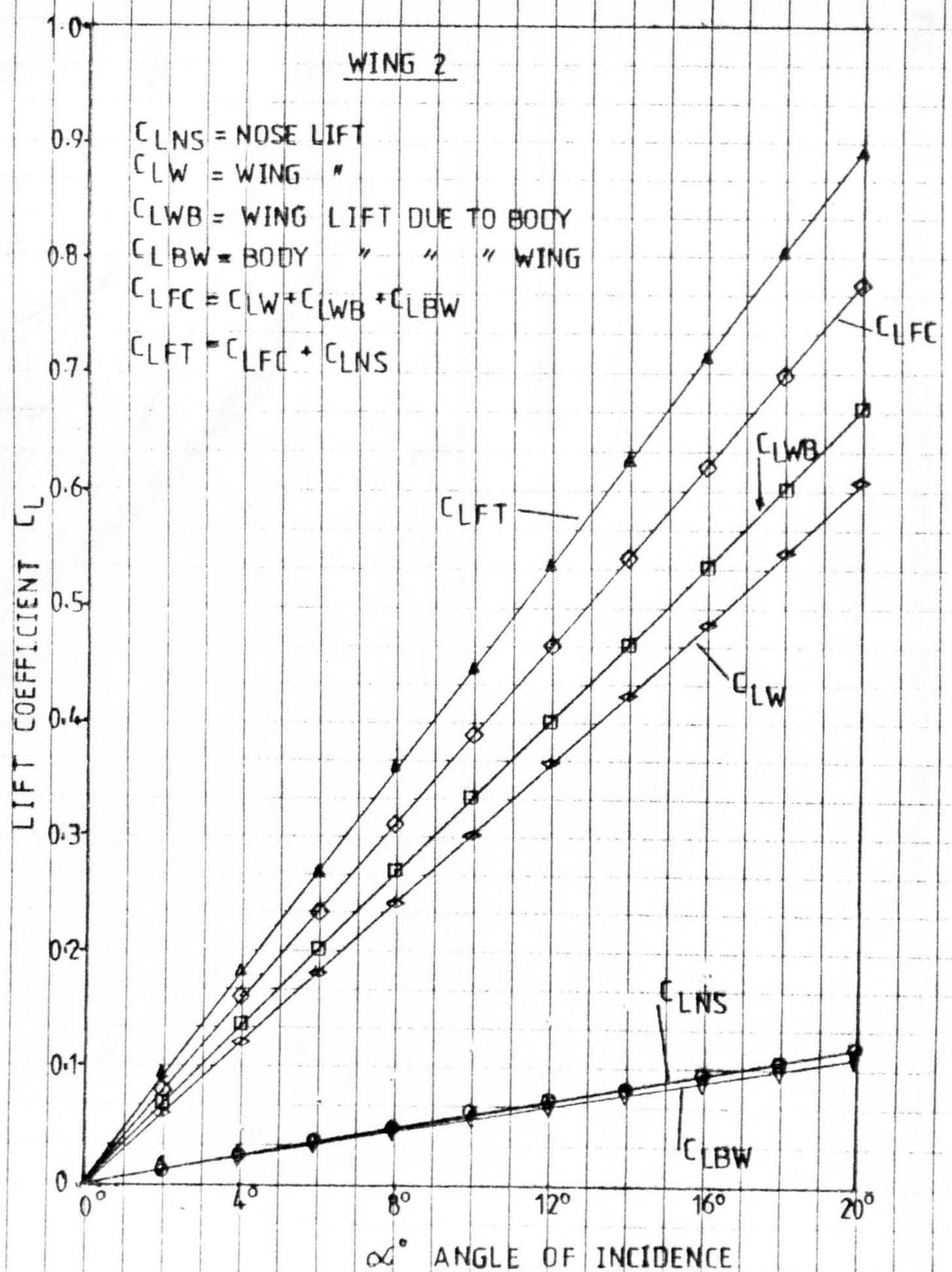

FIG. (9.35) CHORDWISE DISTRIBUTIONS OF STATIC PRESSURE ON UPPER WING SURFACE

(SUCTION)

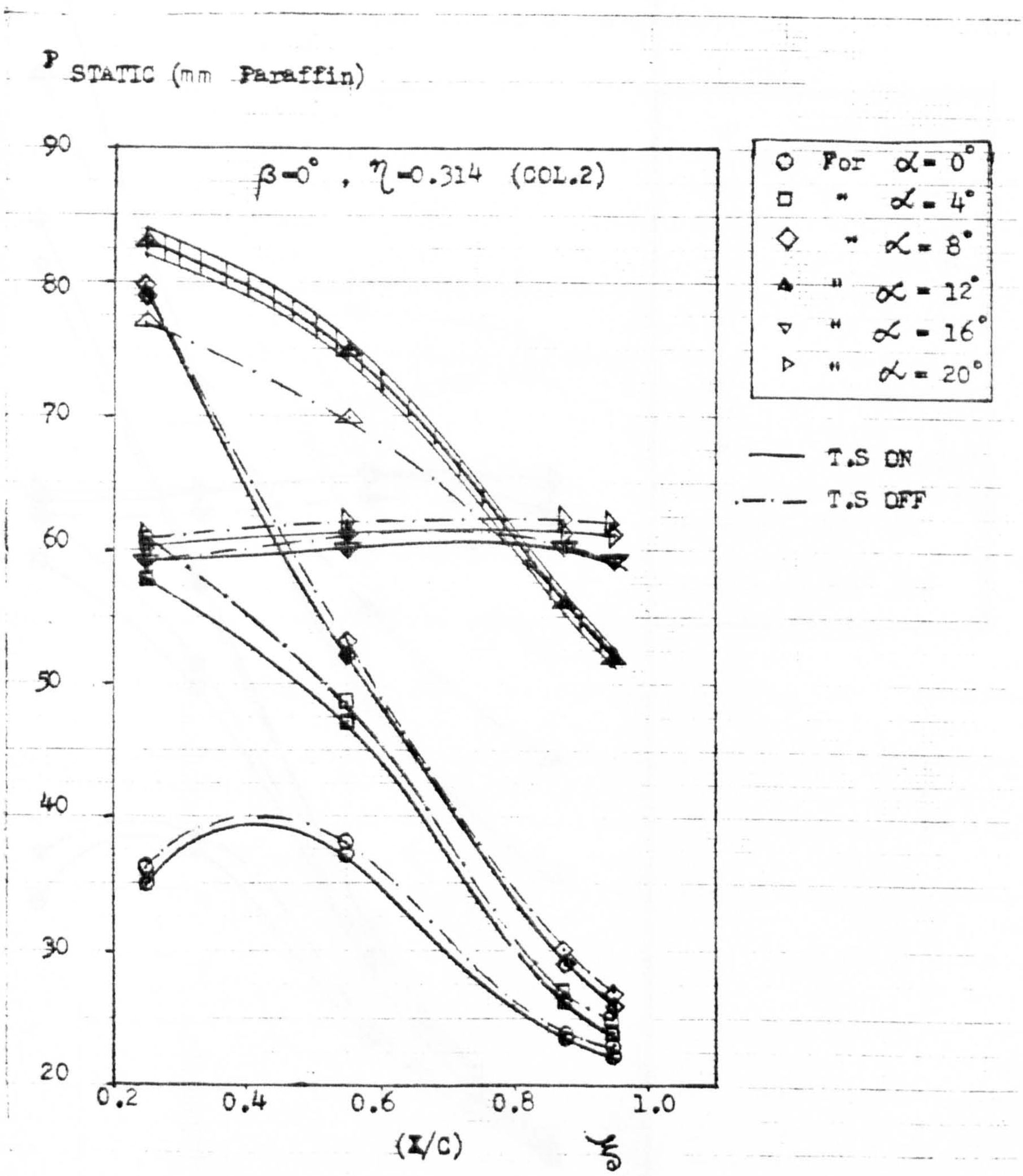

FIG. (9.36) CHORDWISE PRESSURE DISTRIBUTIONS FOR UPPER SURFACE WING

(SUCTION)

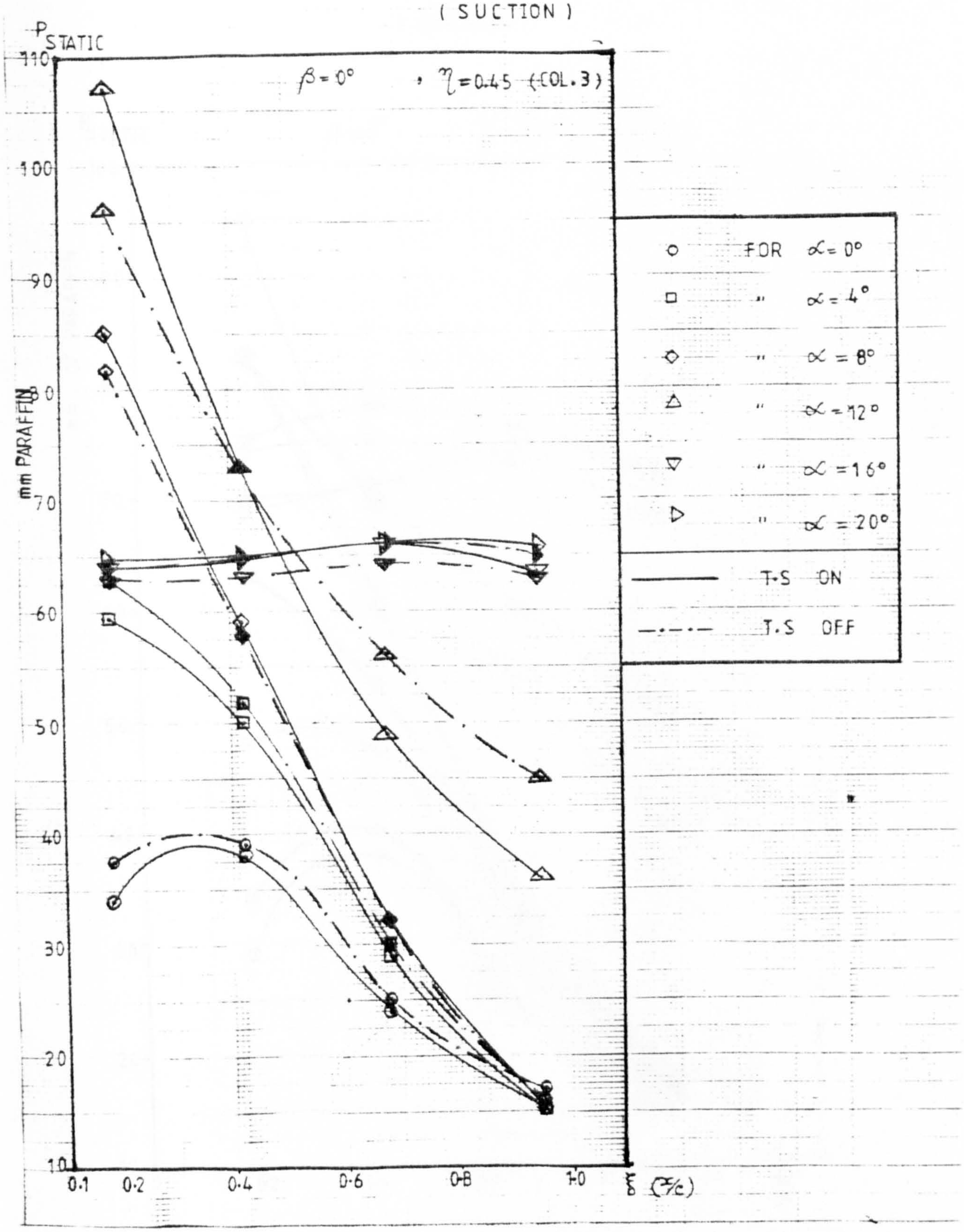

FIG. (9.37) CHORDWISE DISTRIBUTIONS OF STATIC PRESSURE ON UPPER WING SURFACE

(SUCTION)

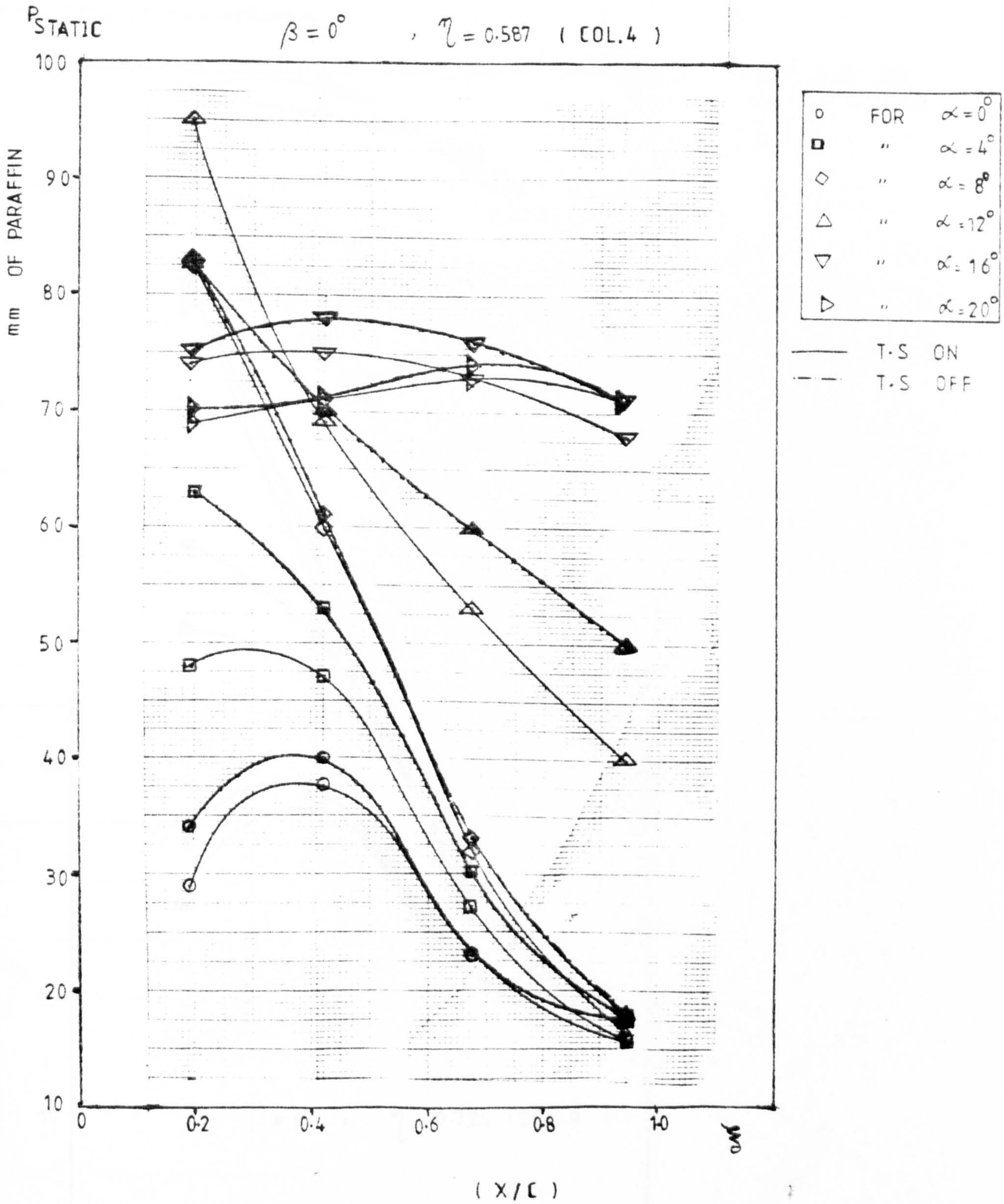

FIG. (9.38) CHORDWISE DISTRIBUTIONS OF STATIC PRESSURE ON UPPER WING SURFACE

(SUCTION)

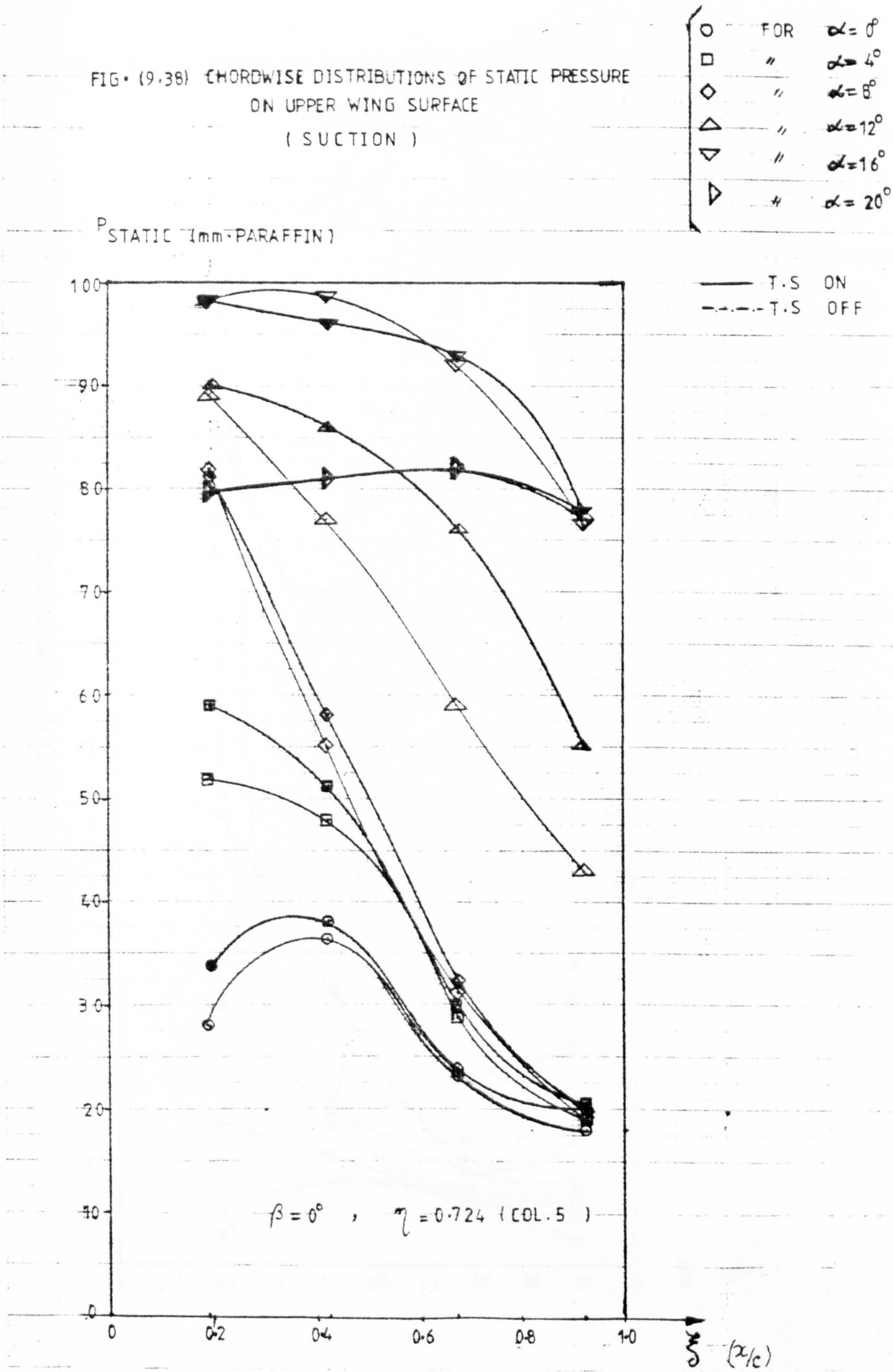

FIG (9·39) CHORDWISE DISTRIBUTIONS OF STATIC PRESSURE ON UPPER WING SURFACE

(SUCTION)

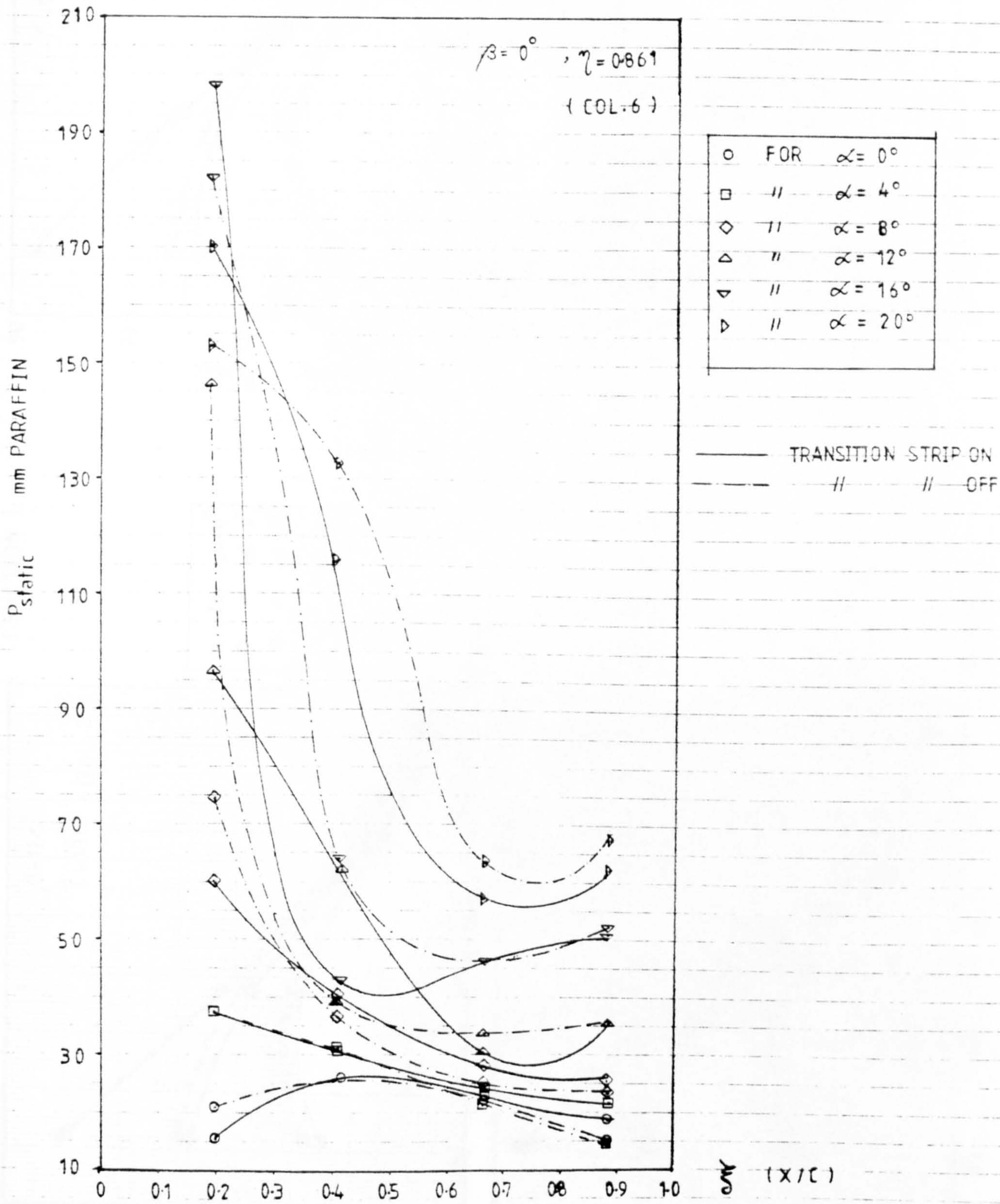

FIG.(9.40) CHORDWISE DISTRIBUTIONS OF STATIC PRESSURE ON UPPER WING SURFACE

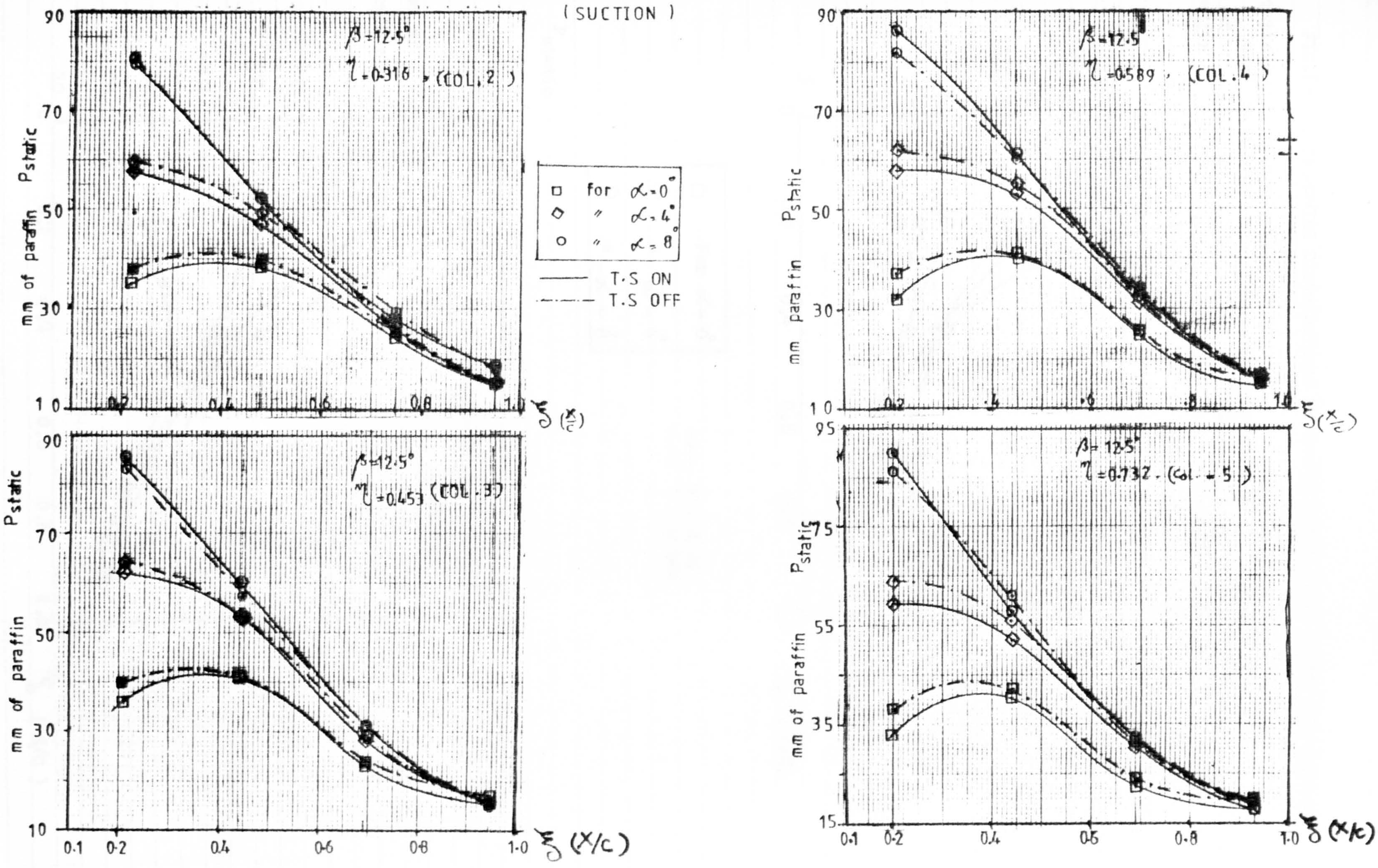

FIG.(9.41) CHORDWISE DISTRIBUTIONS OF STATIC PRESSURE ON UPPER WING SURFACE

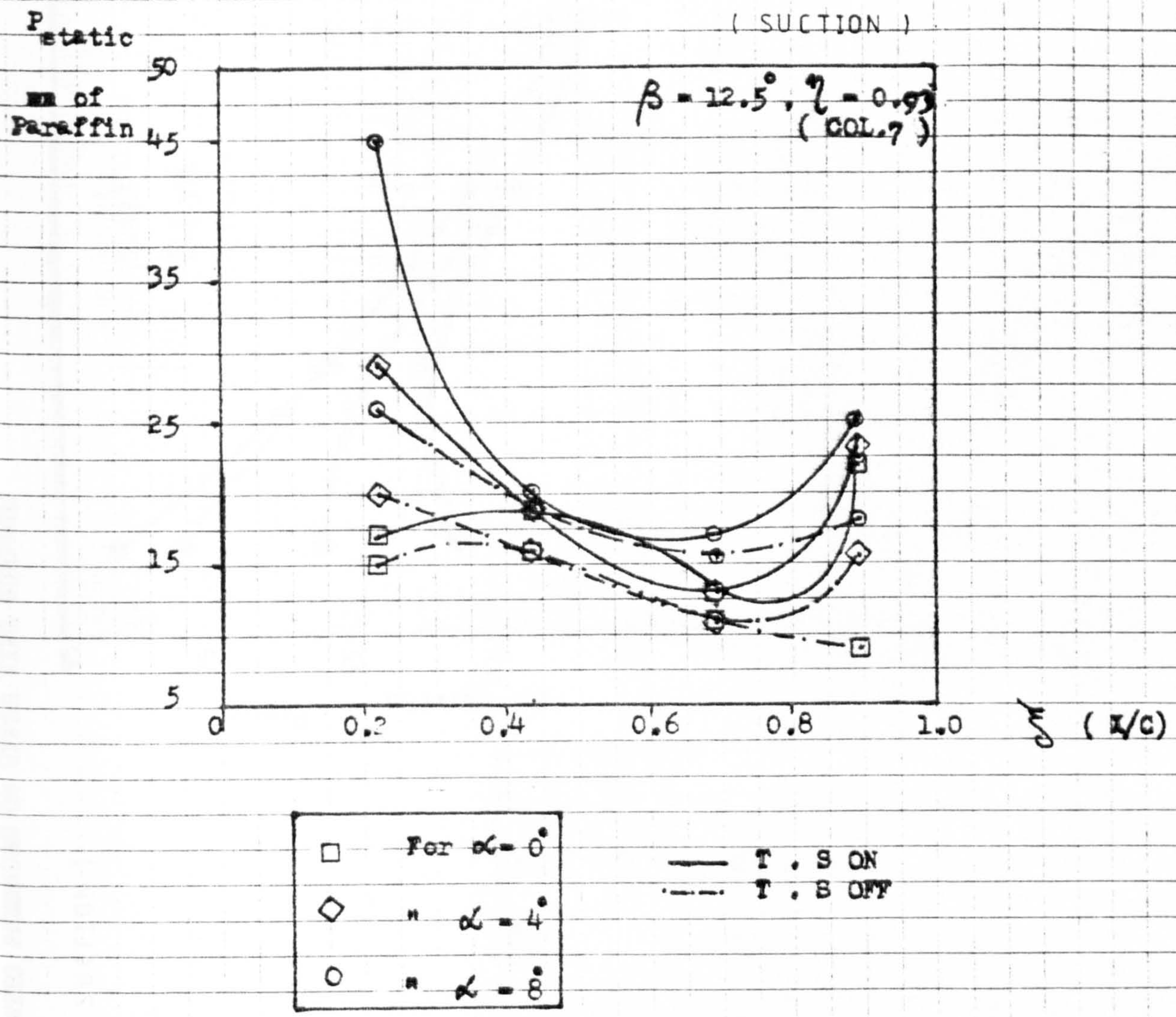

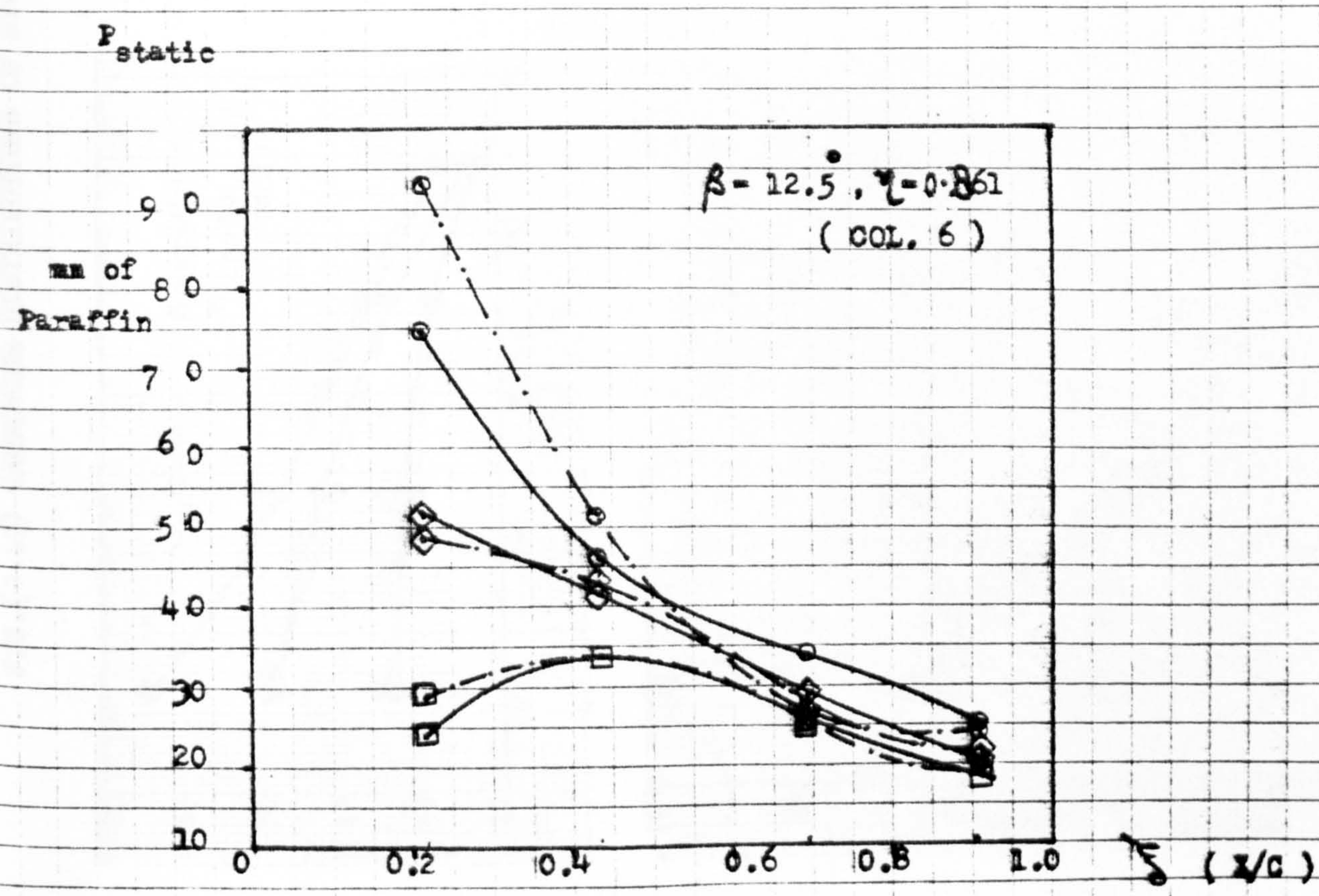

FIG.(9.42) CHORDWISE DISTRIBUTIONS OF STATIC PRESSURE ON UPPER WING SURFACE

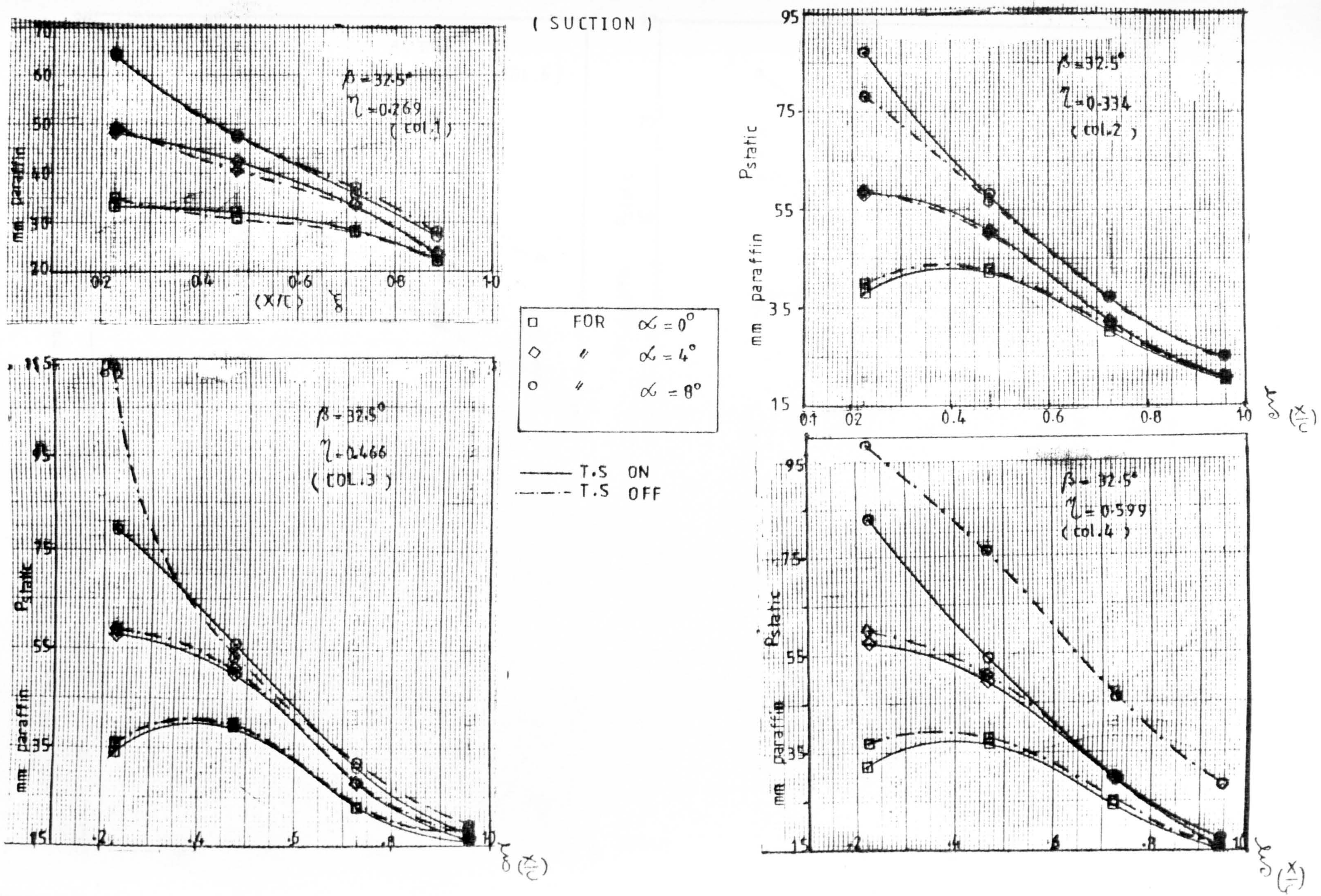

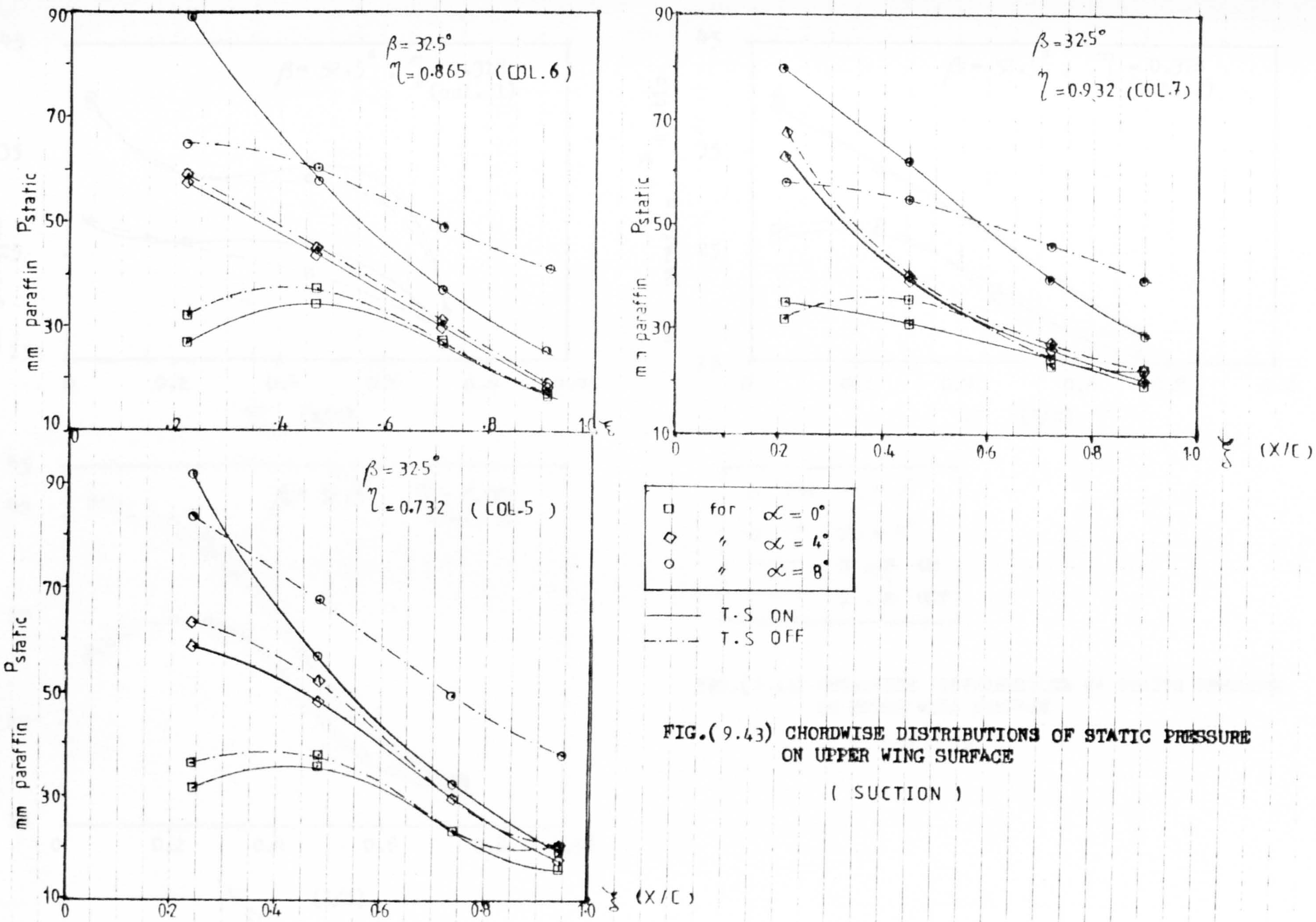

FIG.(9.43) CHORDWISE DISTRIBUTIONS OF STATIC PRESSURE ON UPPER WING SURFACE

(SUCTION)

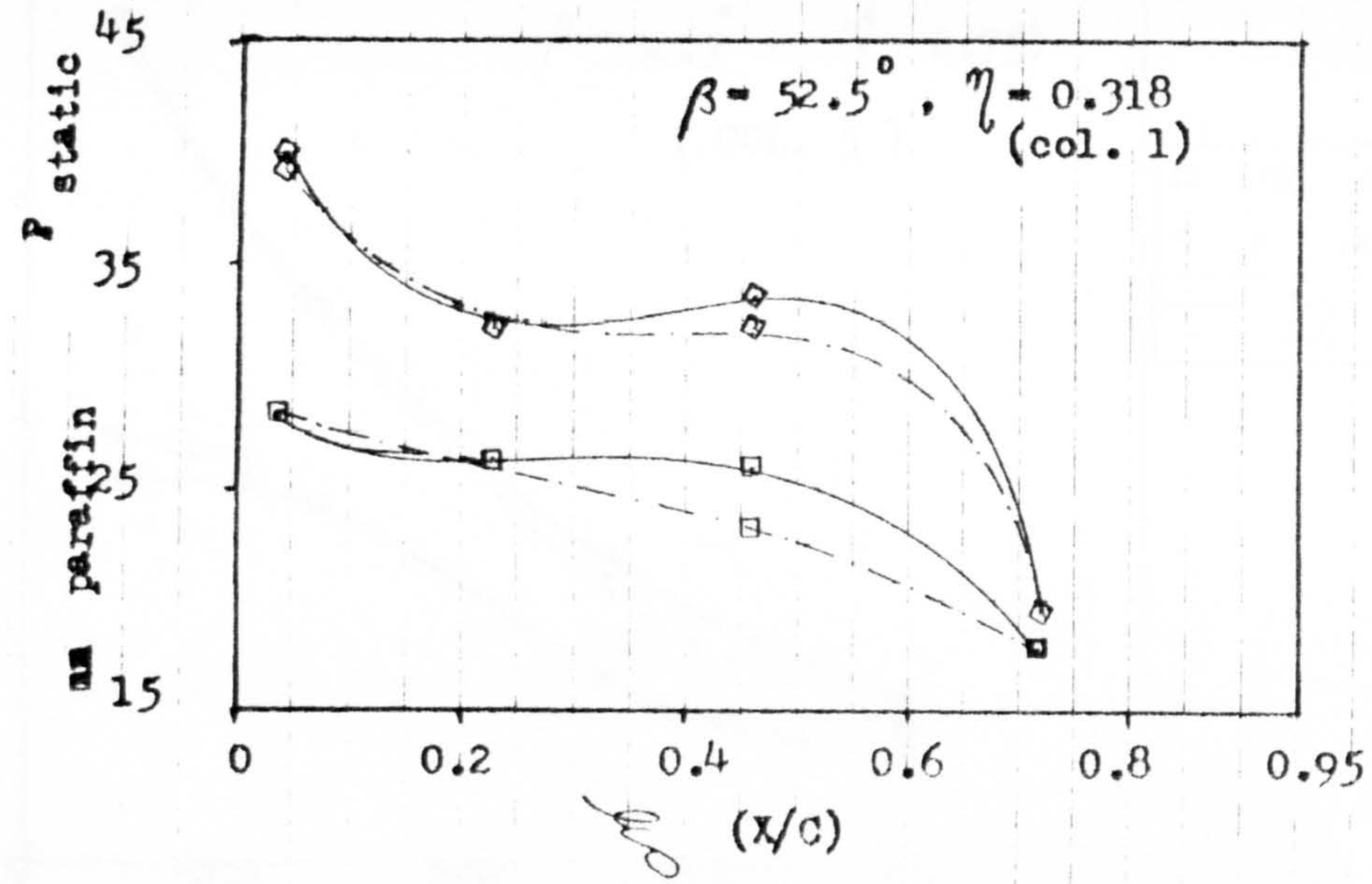

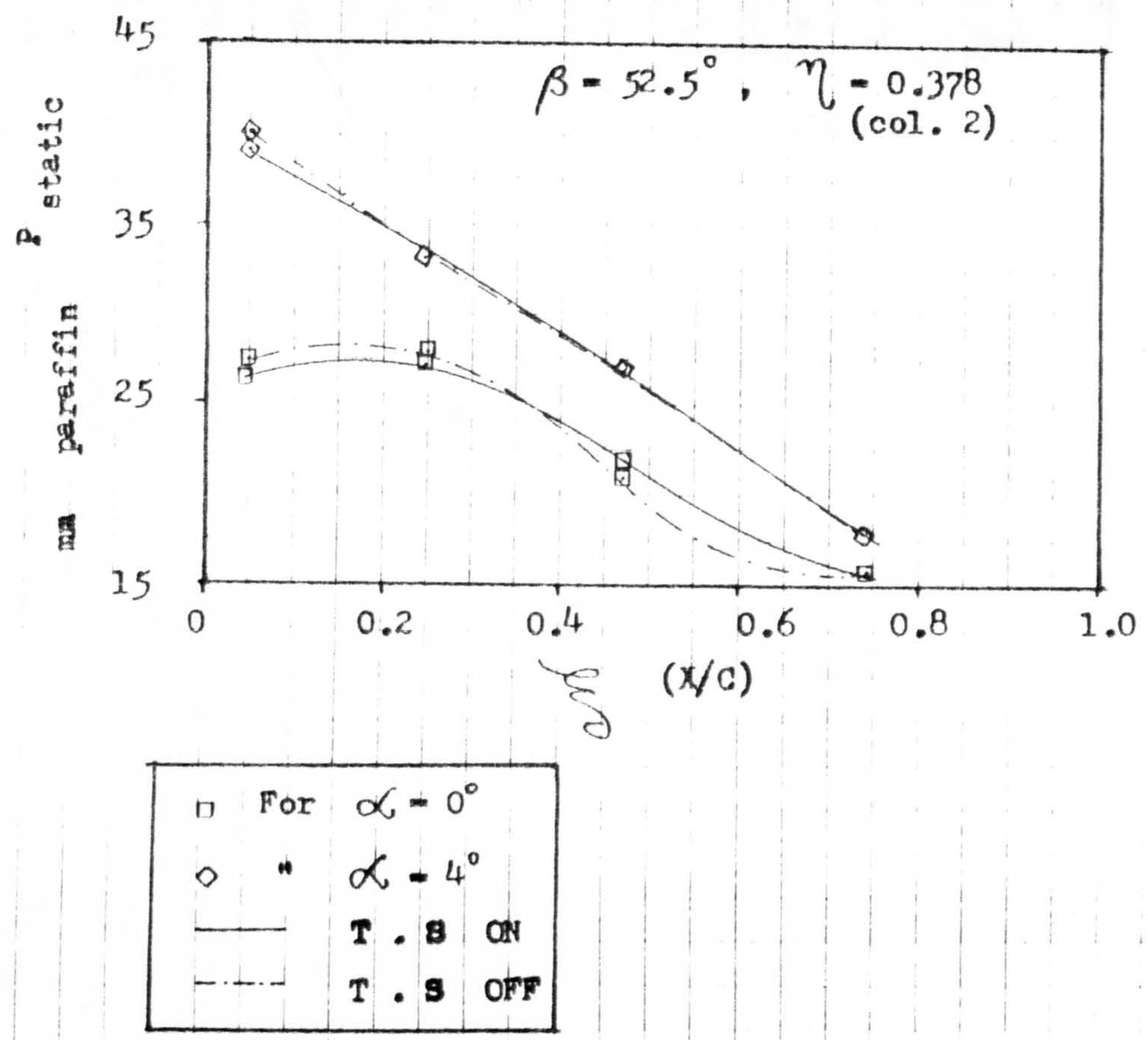

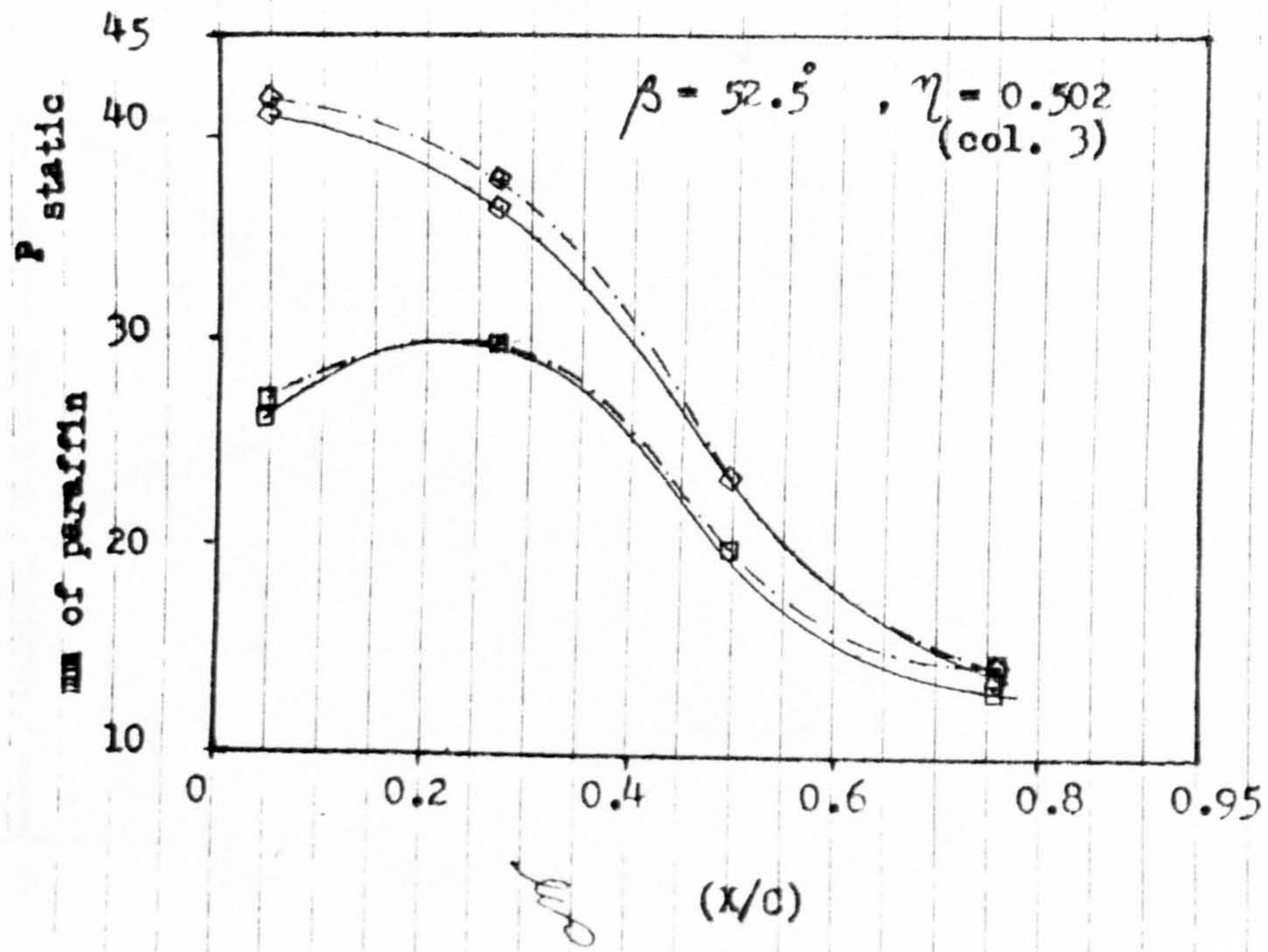

FIG.(9.44) CHORDWISE DISTRIBUTIONS OF STATIC PRESSURE ON UPPER WING SURFACE

(SUCTION)

FIG.(9.45) CHORDWISE DISTRIBUTIONS OF STATIC PRESSURE ON UPPER WING SURFACE

(SUCTION)

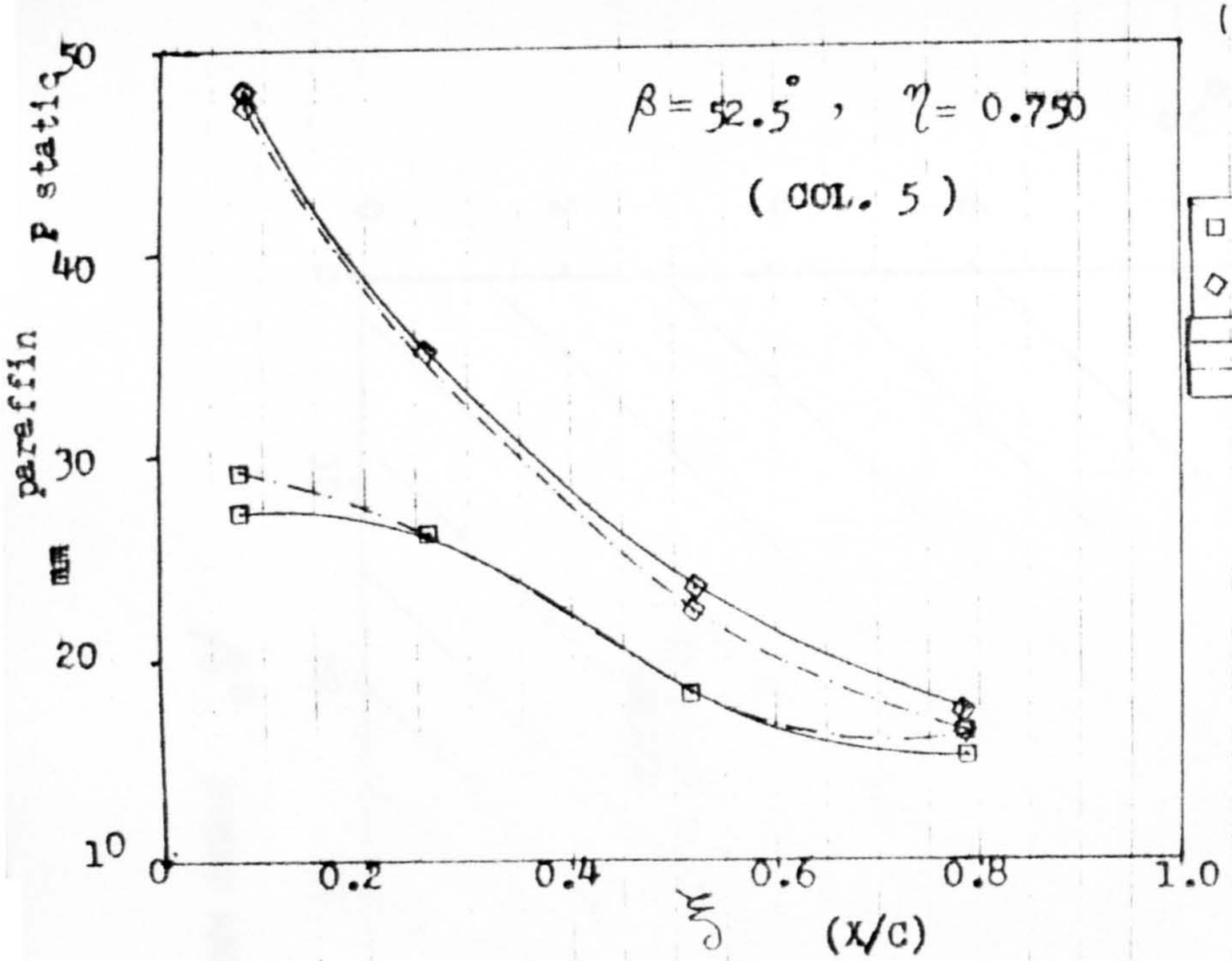

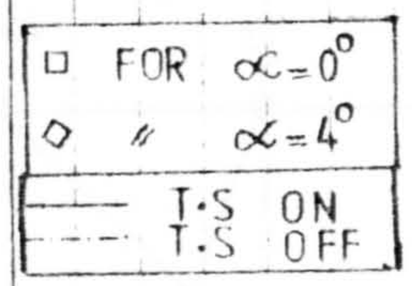

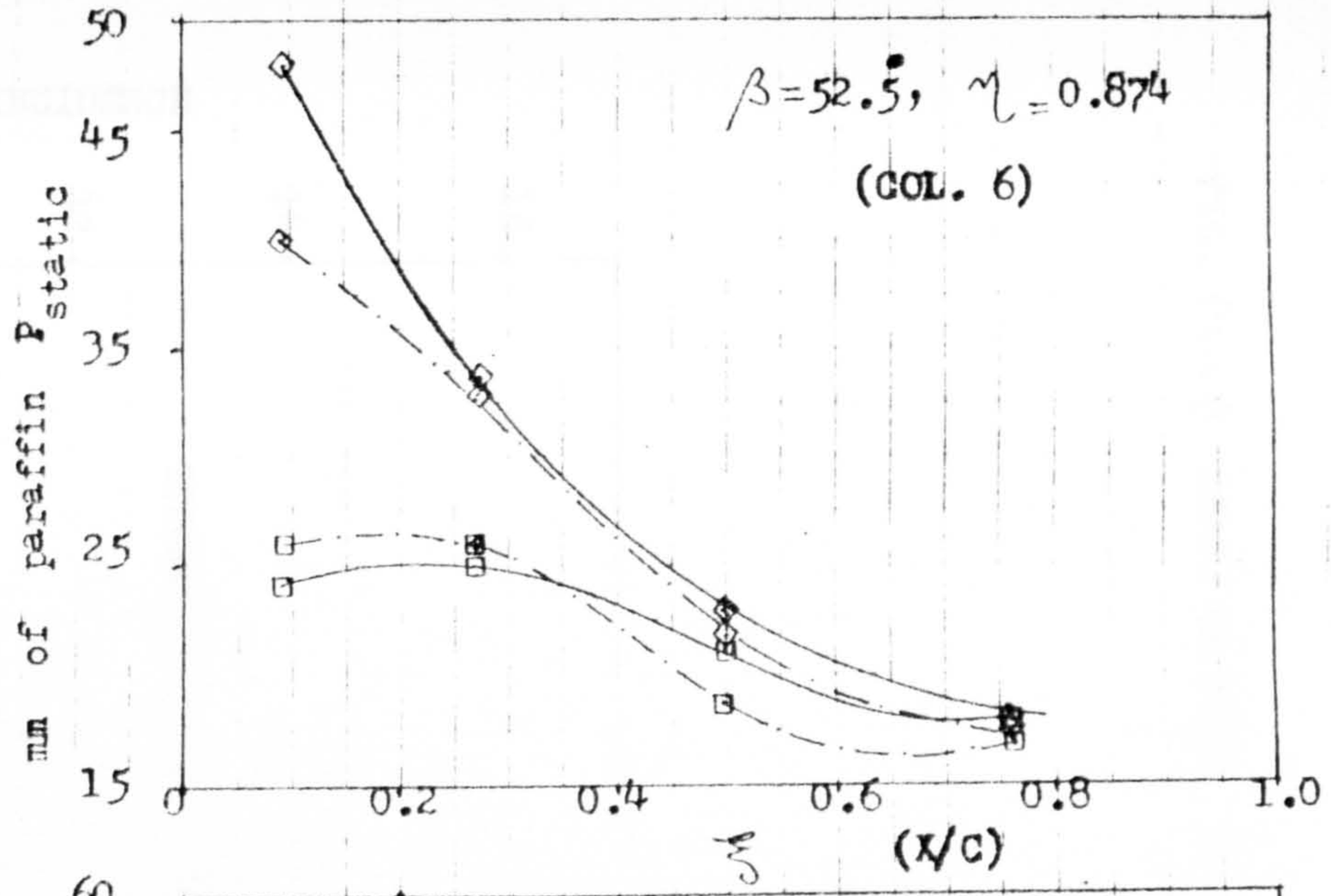

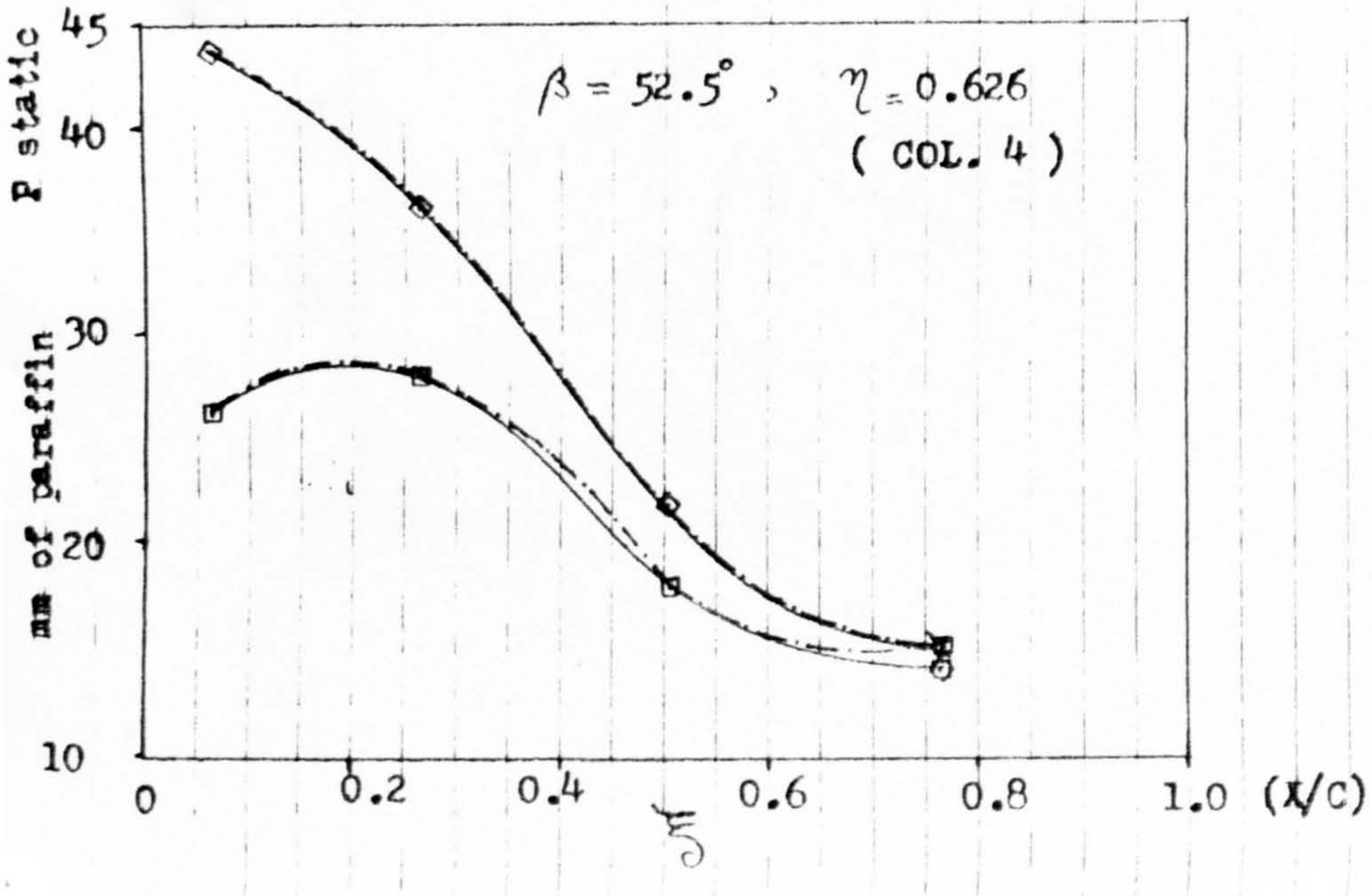

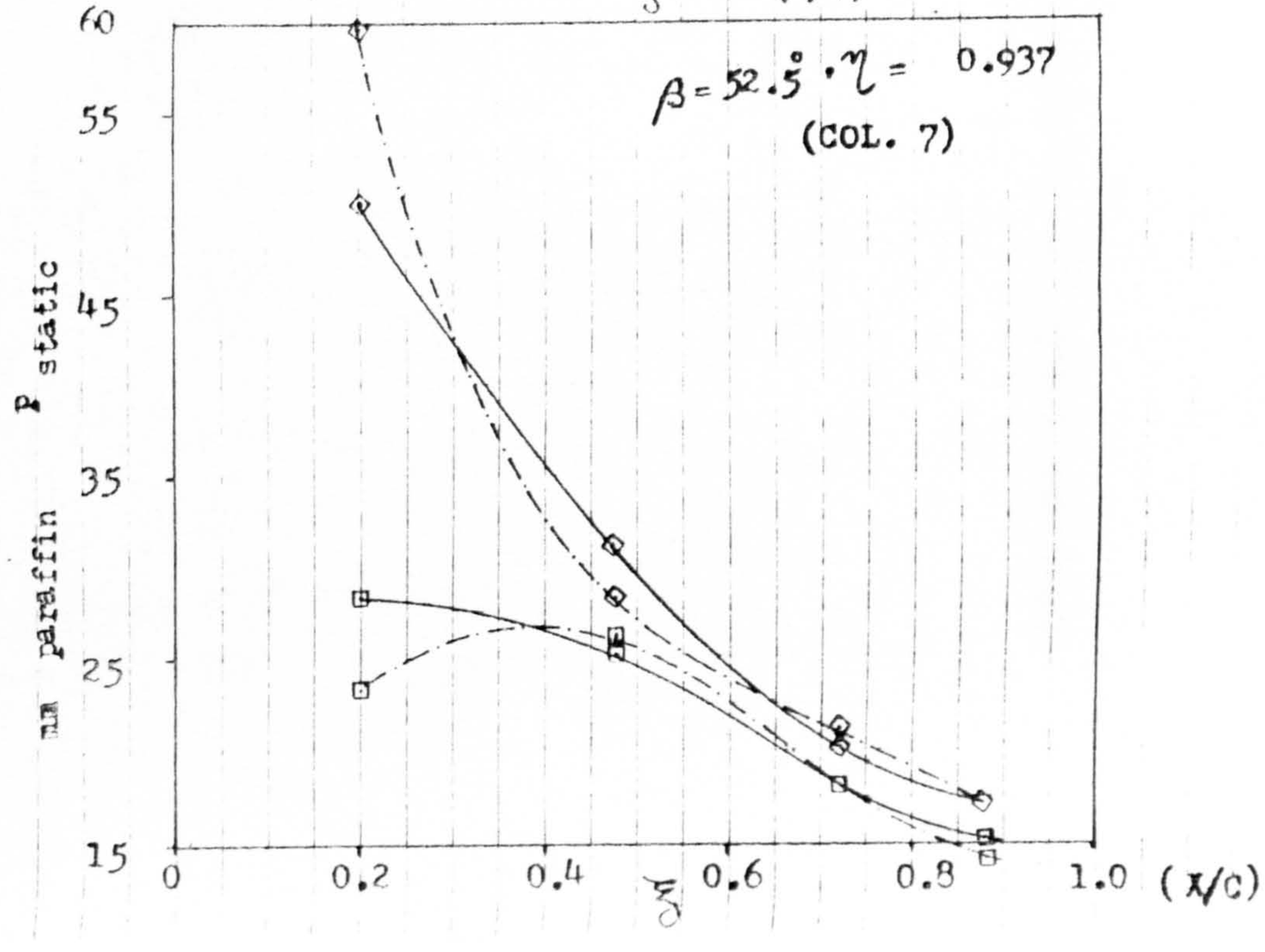

FIG. (11.46) GRAPH OF STALL CURVE FOR THE WIND TUNNEL TEST MODEL

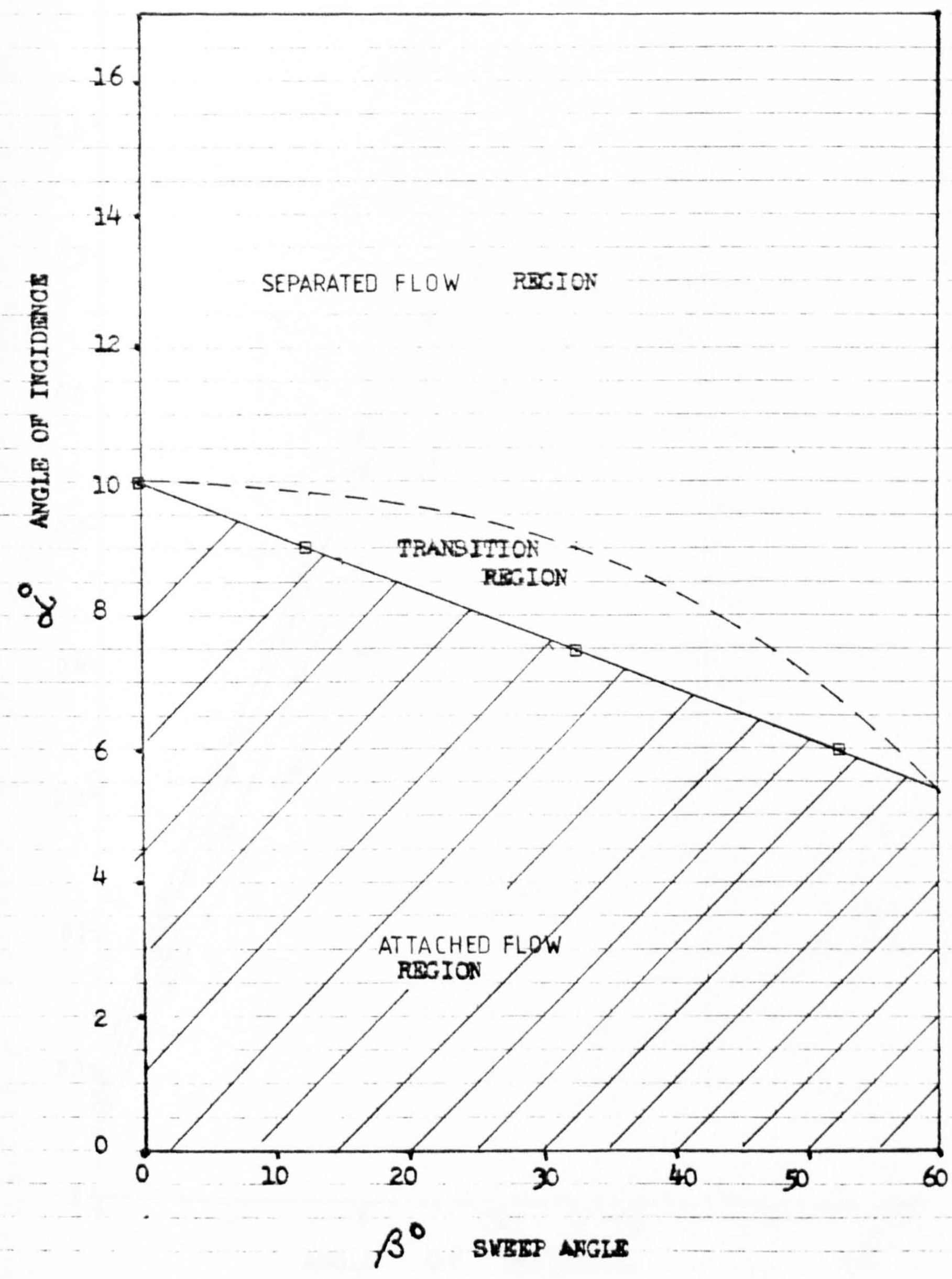

FIG.(9.47) COMPARISONS OF OVERALL LIFT COEFFICIENT V INCIDENCE ANGLE FROM EXPERIMENTAL TESTS FOR VARIABLE SWEEP WING GEOMETRIES SHOWN IN FIGS.(9.3) to (9.5)

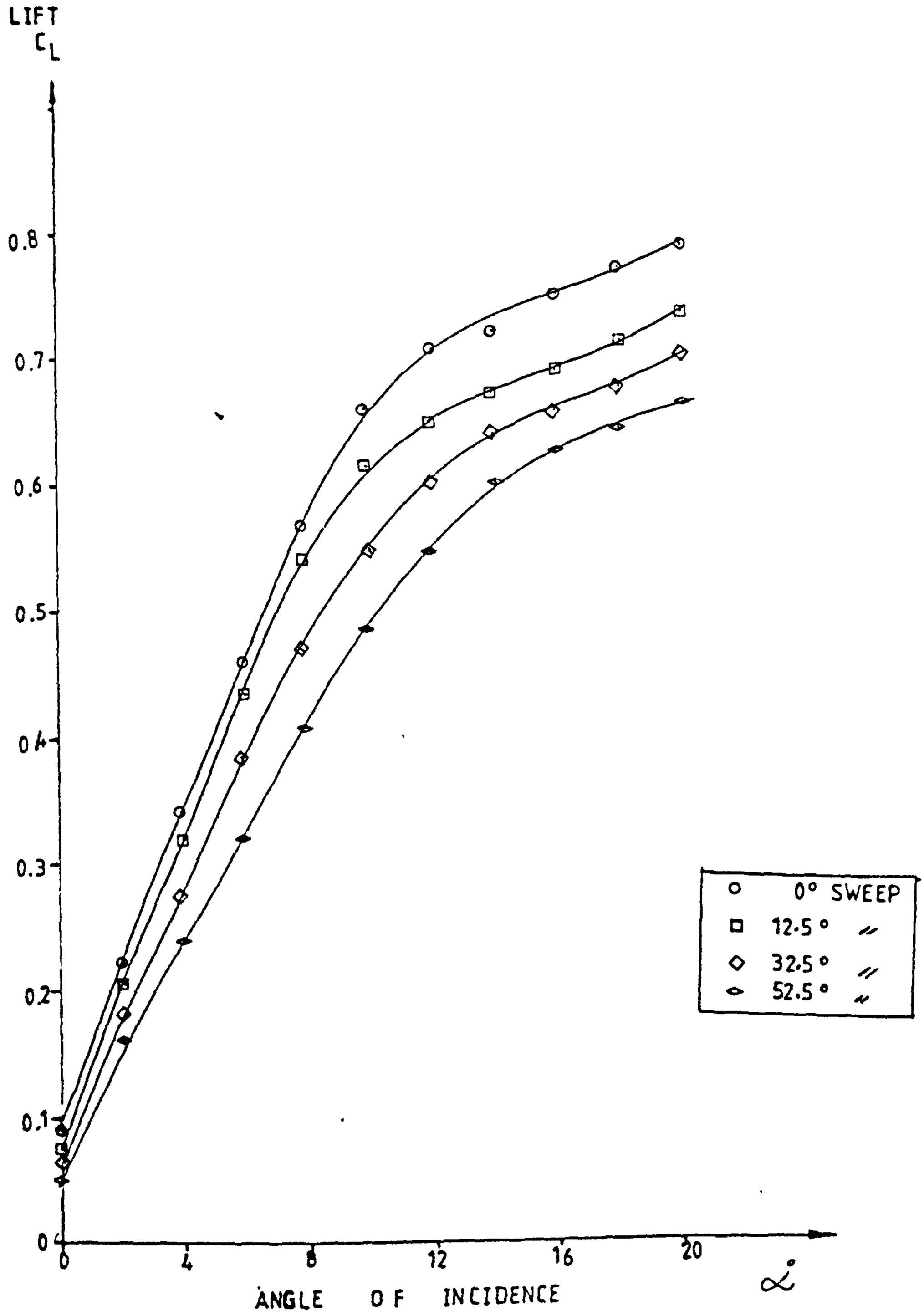

FIGS.(9.48) COMPARISONS OF OVERALL LIFT COEFFICIENT V ANGLE OF INCIDENCE FOR COMPUTED RESULTS (Quadvortex), EXPERIMENTAL RESULTS , AND THE EFFECT OF TRIPPING DEVICES ON THE WING SURFACE MODEL FOR GEOMETRIES SHOWN IN FIGS.(9.3) to (9.5)

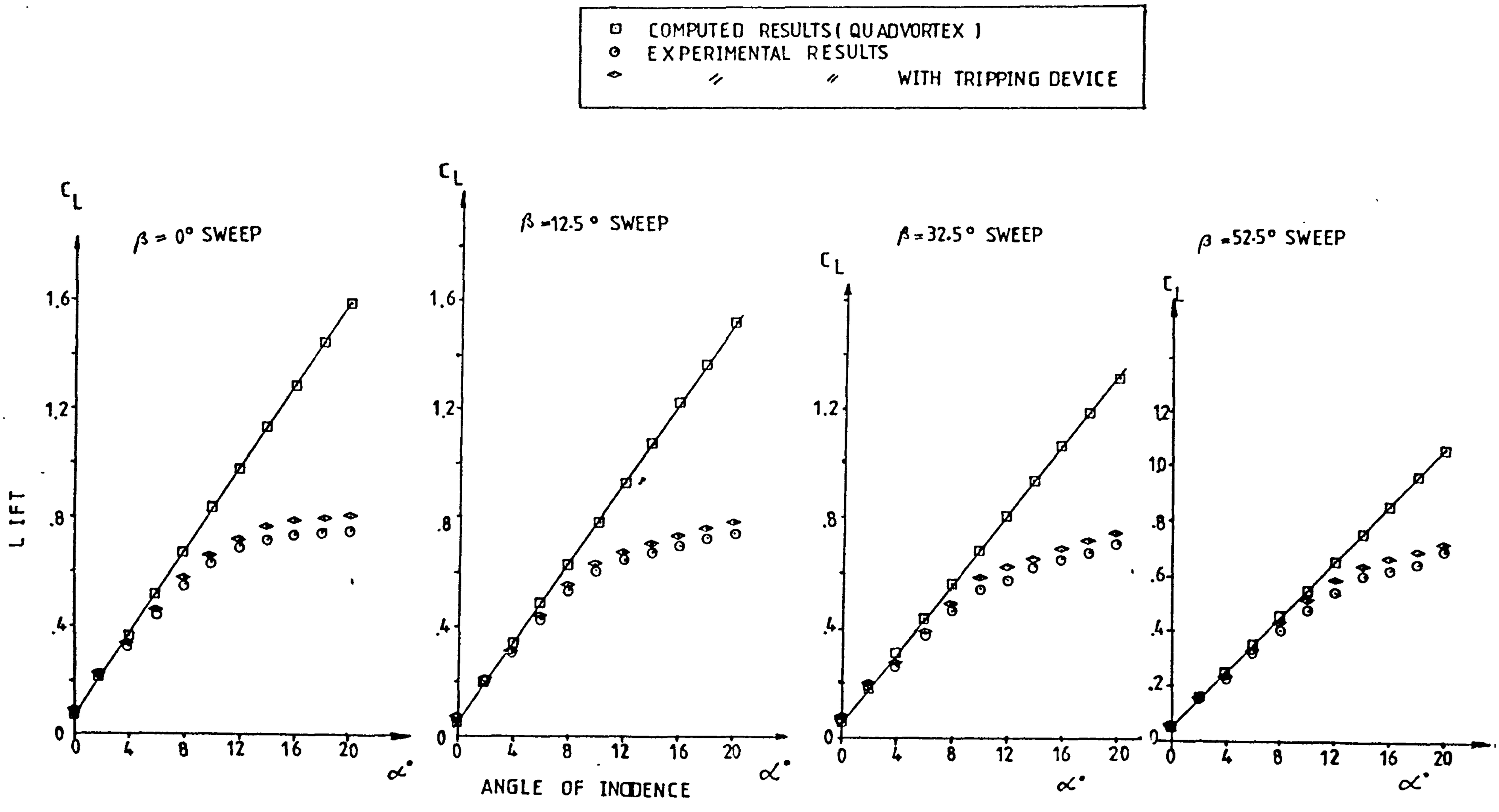

FIG.(9.49) COMPARISONS OF EXPERIMENTAL AND THEORETICAL (Quadvortex) PITCHING MOMENT C_{MY} RESULTS FOR THE GEOMETRIES SHOWN IN FIGS.(9.3) to (9.5)

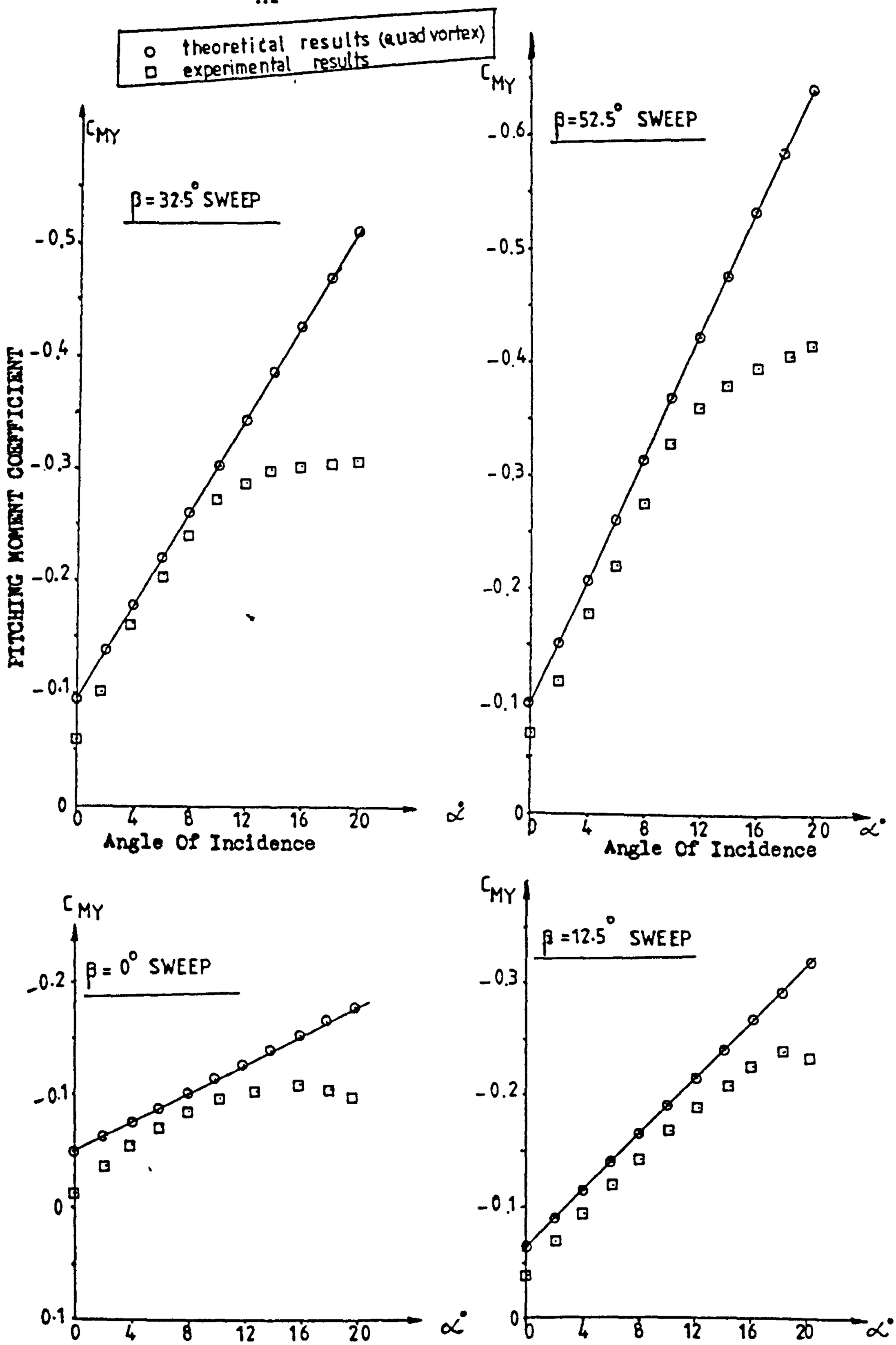

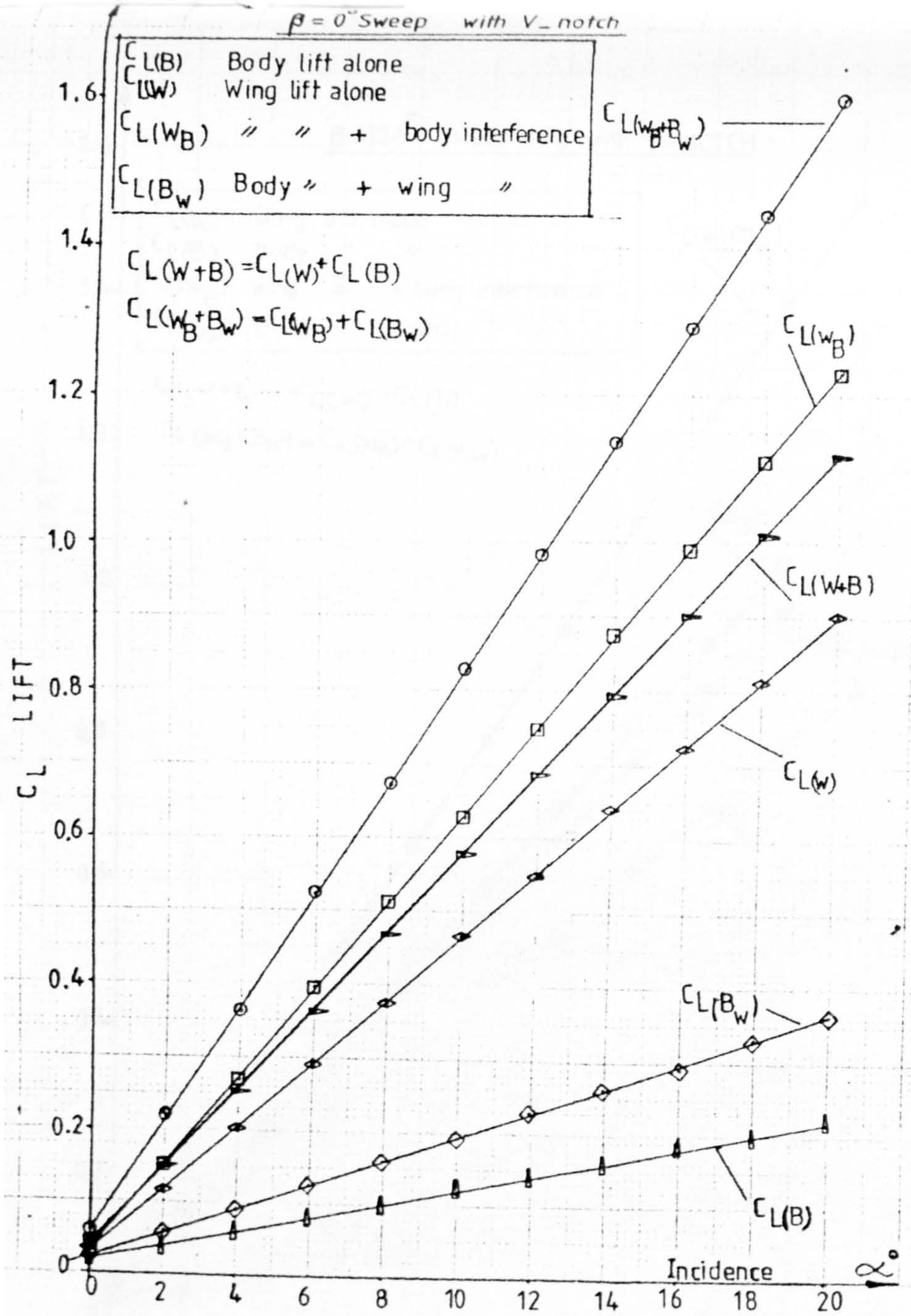

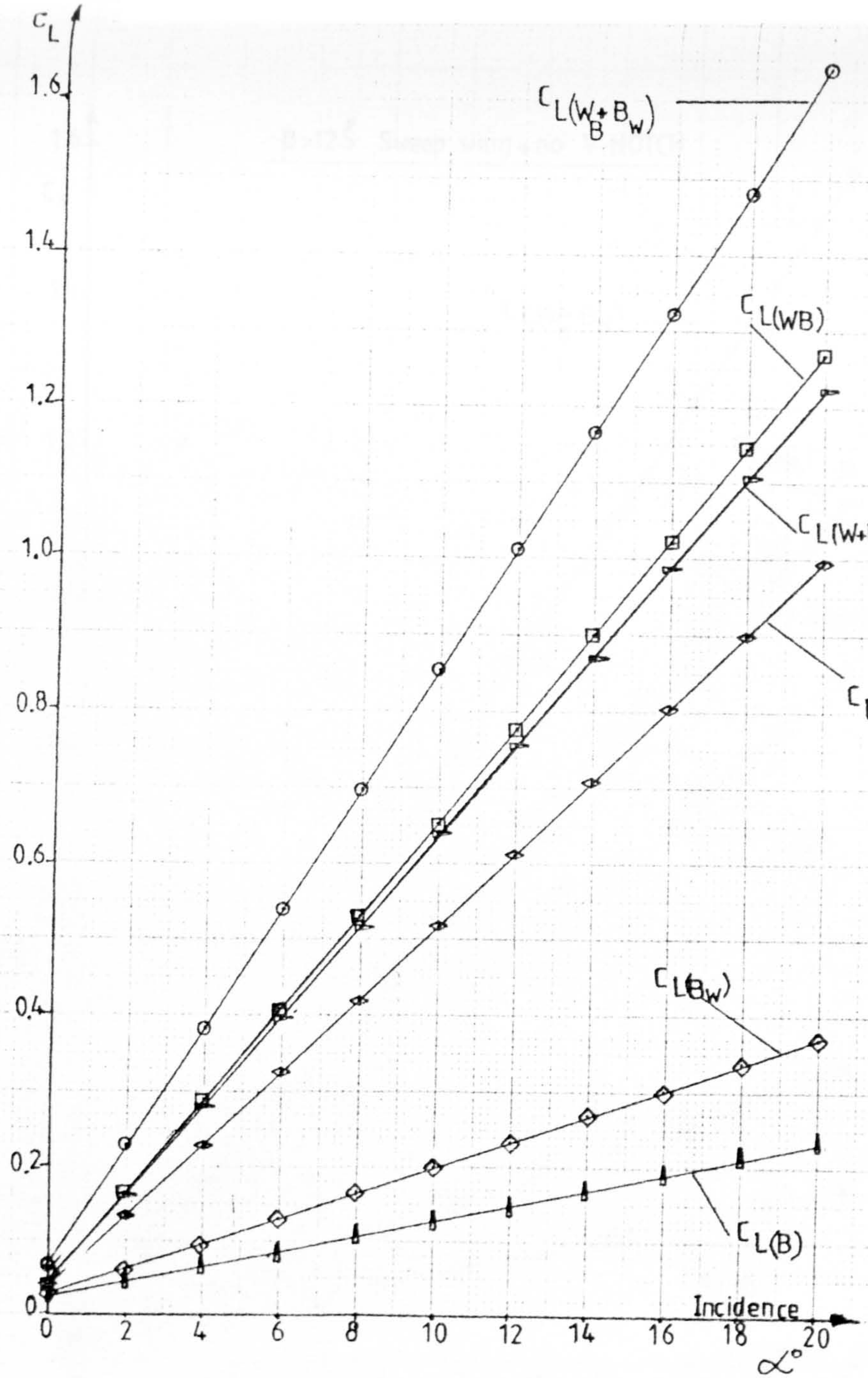

FIG. (9.50) GRAPH OF LIFT C_L - V - α FOR 0° SWEEP WING+BODY (QUADVORTEX RESULTS)

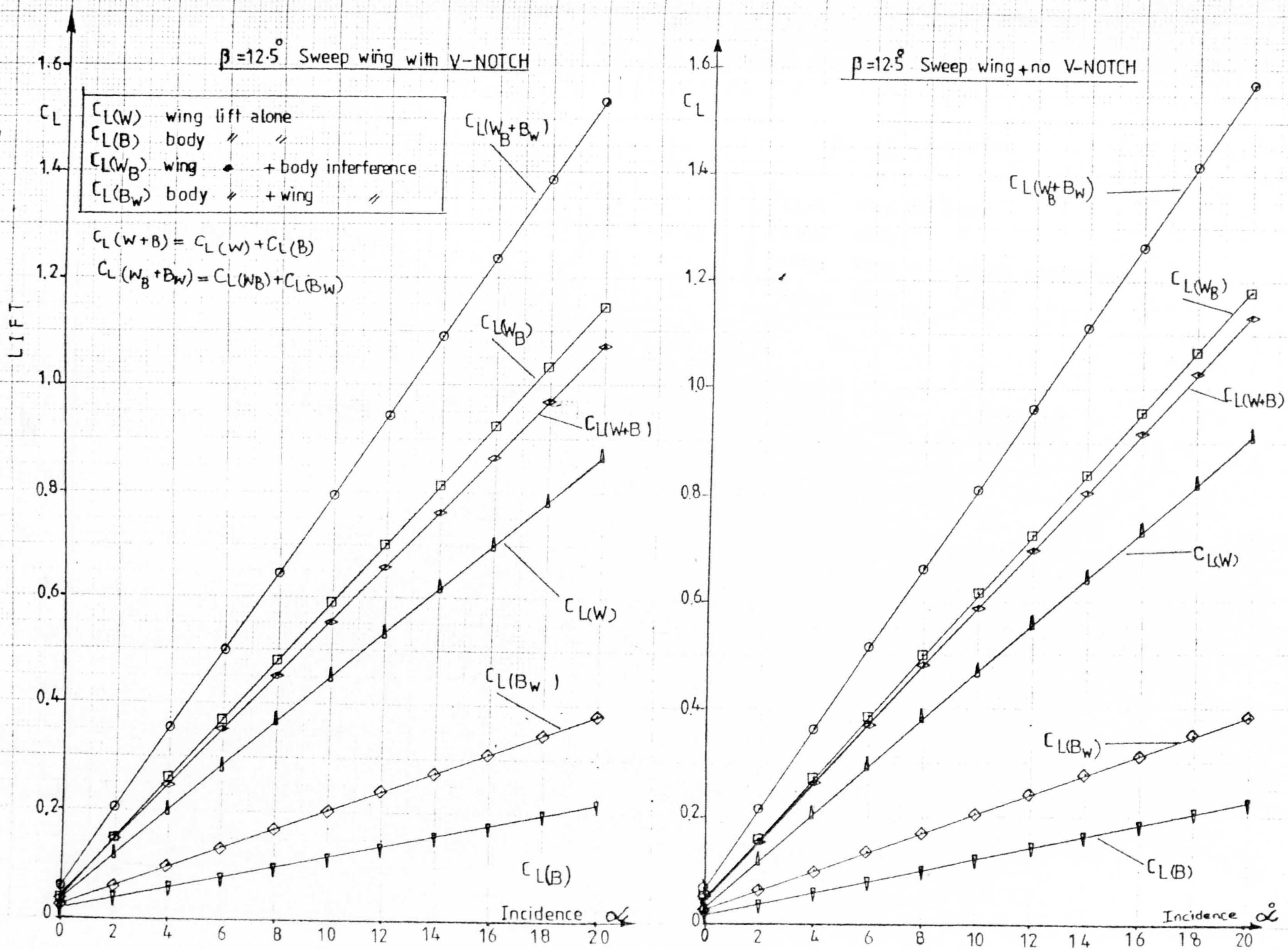

FIG. 9.51 GRAPH OF LIFT C_L V. α FOR 12·5° SWEEP WING+BODY (QUADVORTEX RESULTS)

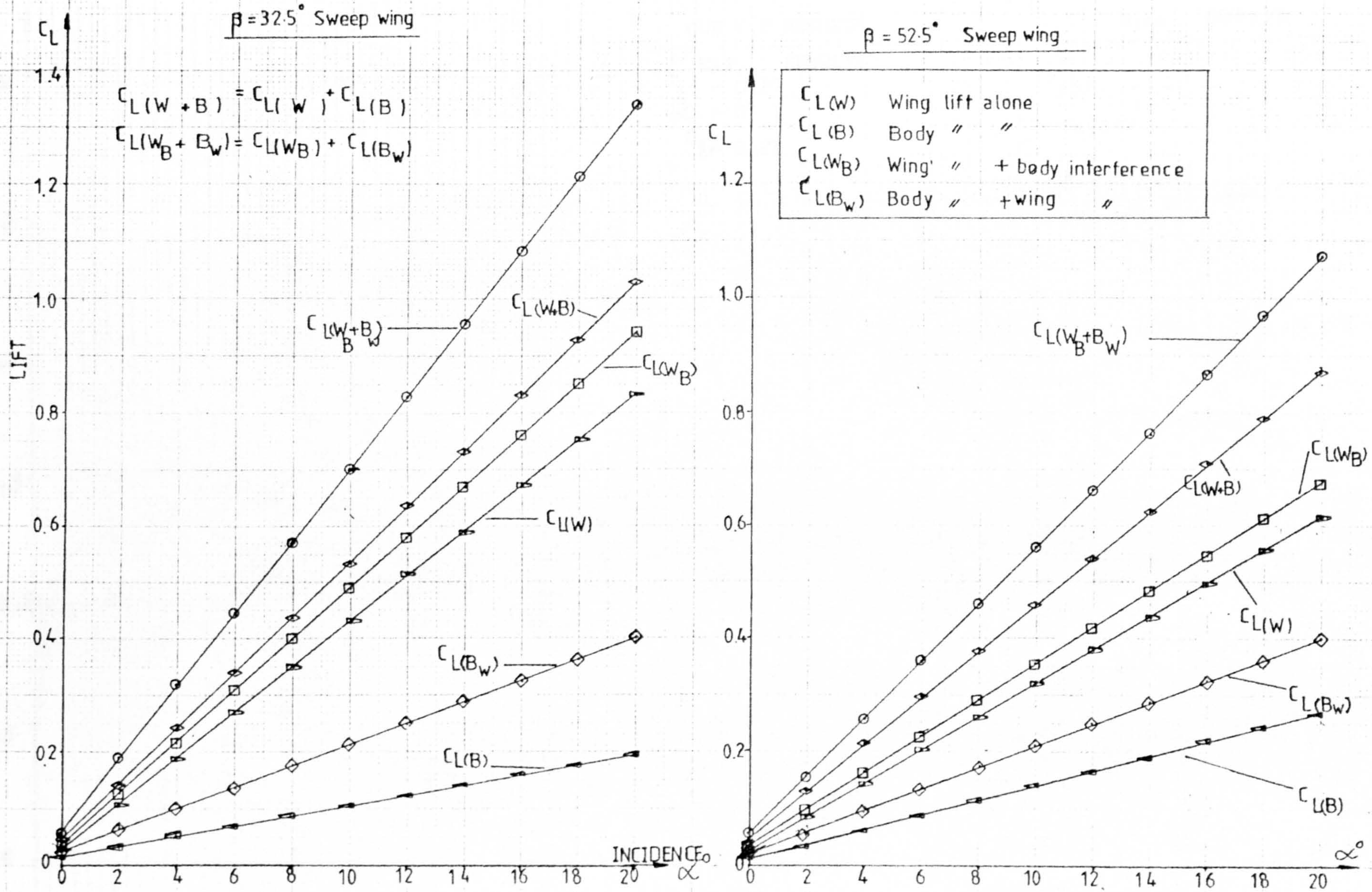

FIG (9.52) GRAPH OF LIFT $C_L \cdot V \cdot \alpha$ FOR 32·5 52·5 SWEEP WINGS+BODIES (QUADVORTEX RESULTS)

FIG.(9·53) GROSS WING COMPARISONS OF THEORETICAL AND EXPERIMENTAL RESULTS

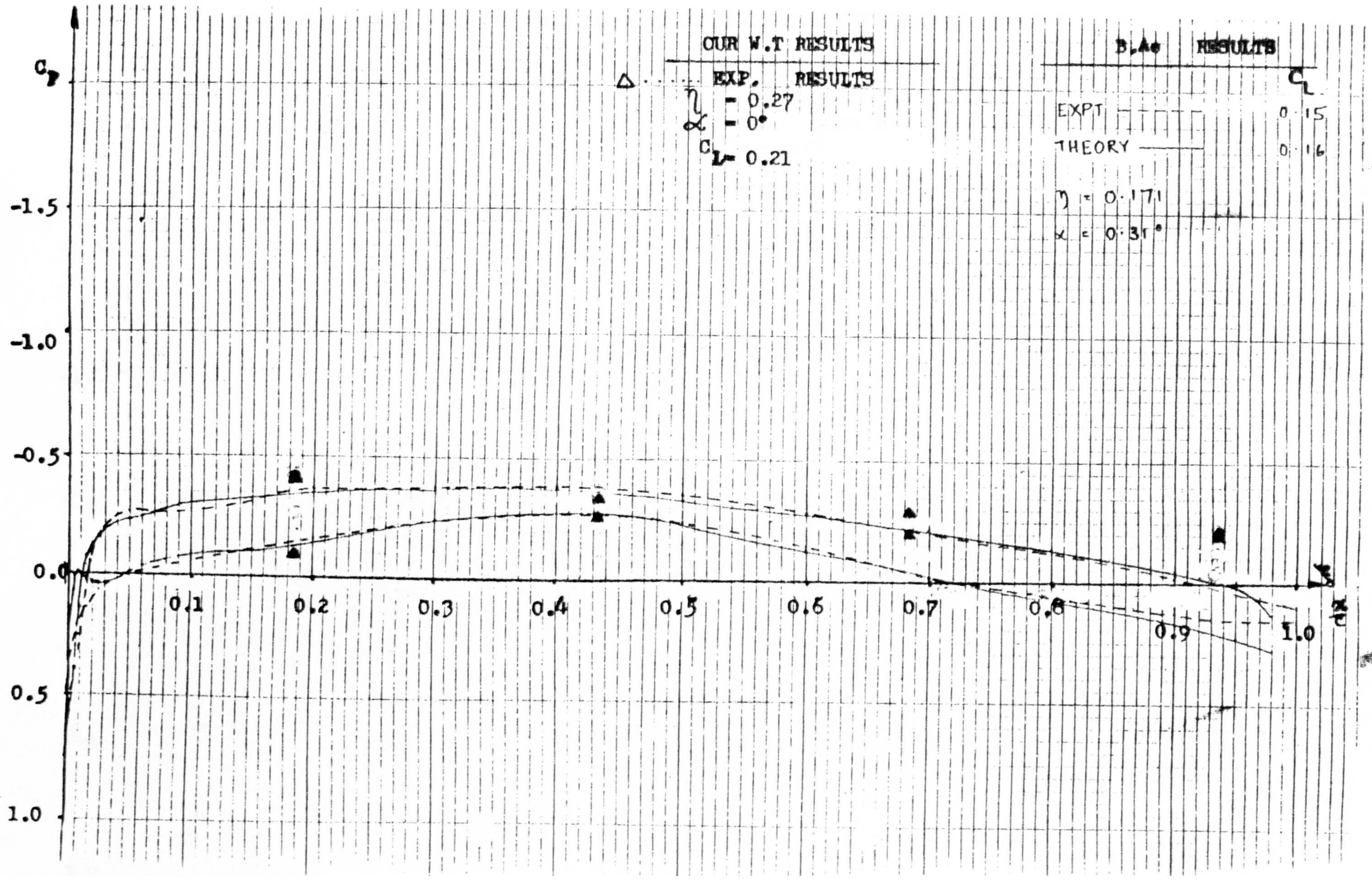

FIG(9.54) GROSS WING COMPARISONS OF THEORETICAL AND EXPERIMENTAL RESULTS

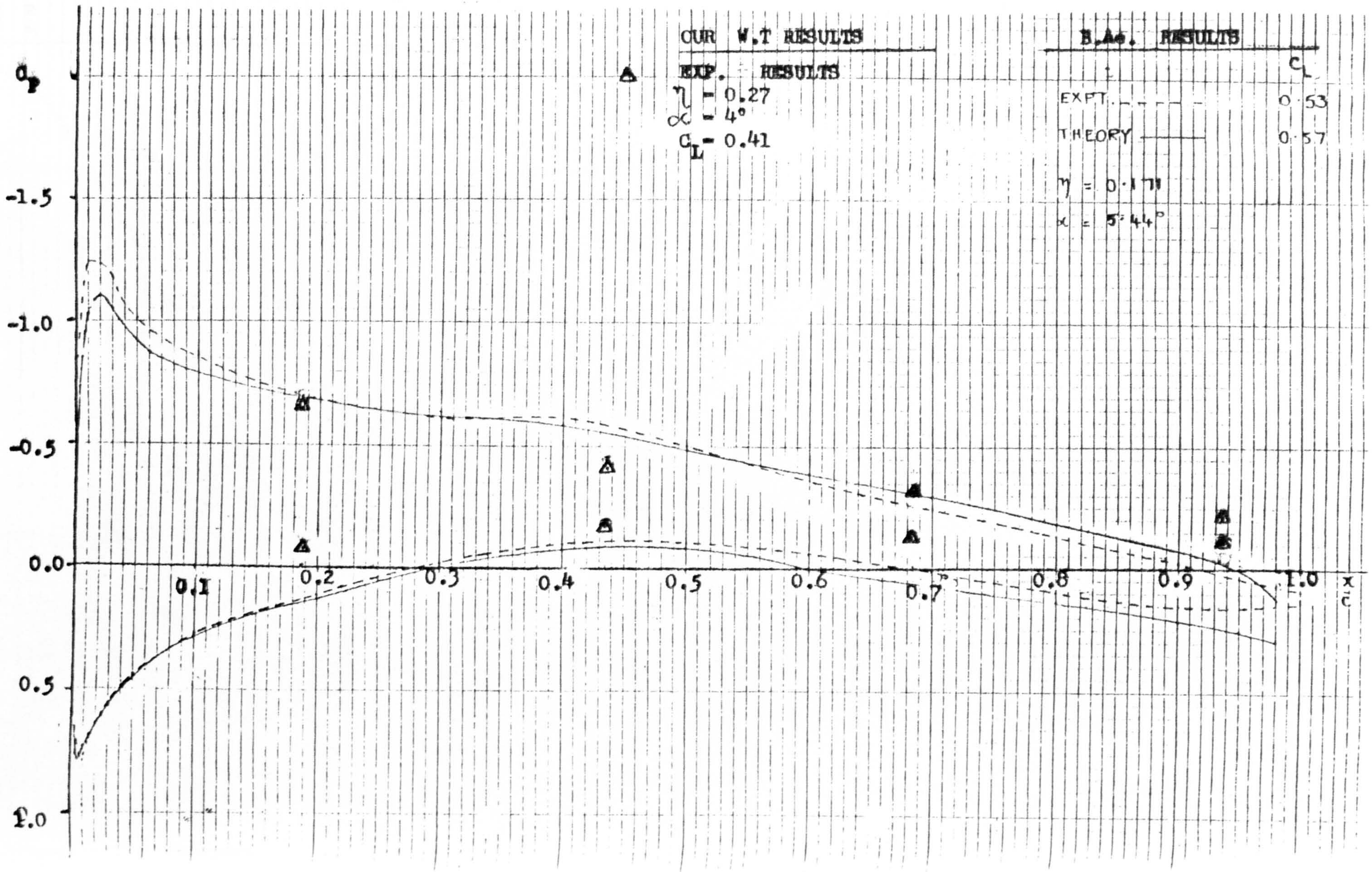

FIG.(9.55) COMPARISONS OF THEORETICAL AND EXPERIMENTAL RESULTS

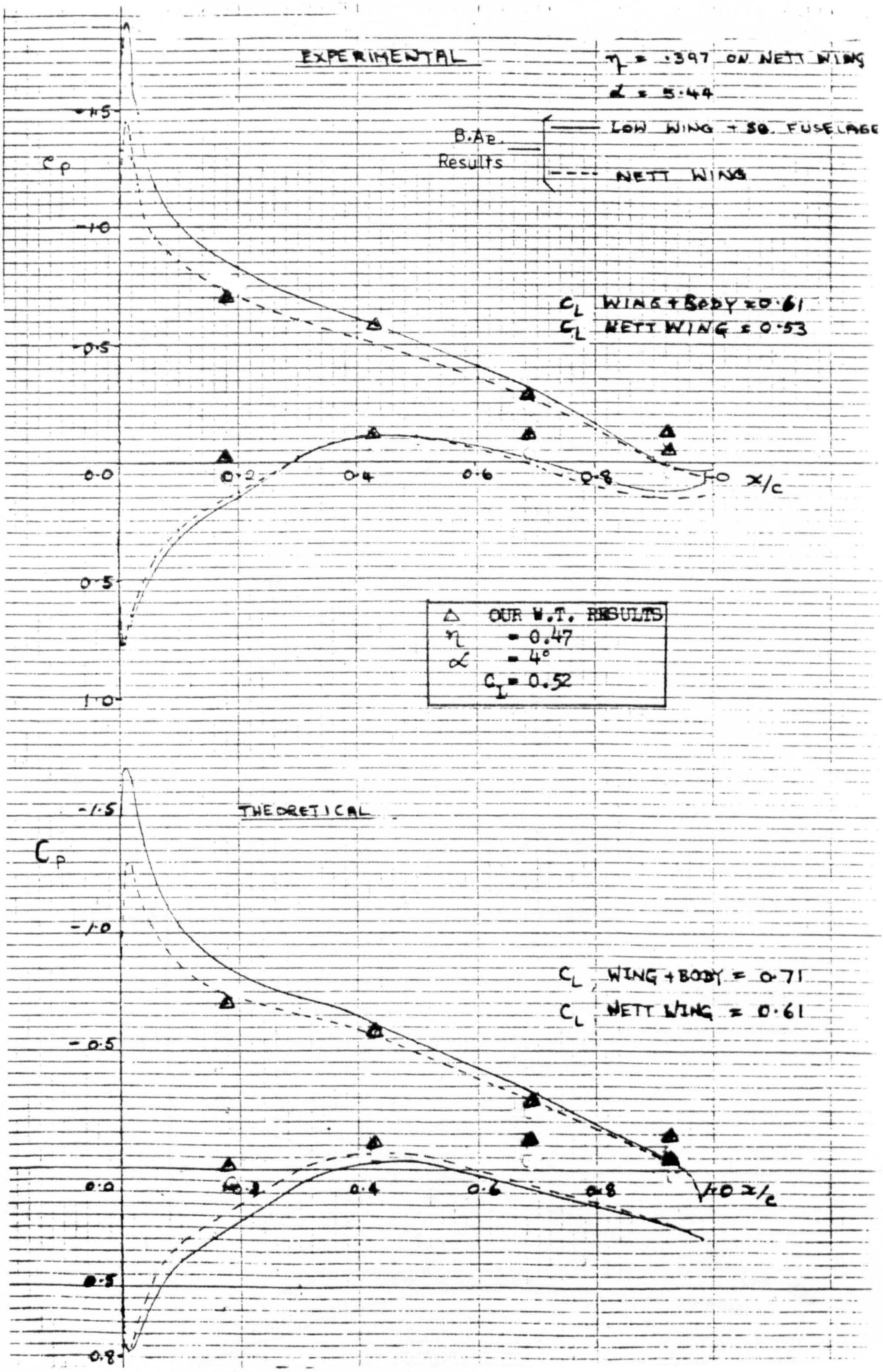

FIG. (9·56) COMPARISONS OF EXPERIMENTAL AND THEORETICAL RESULTS FOR CHORDWISE PRESSURE DISTRIBUTION

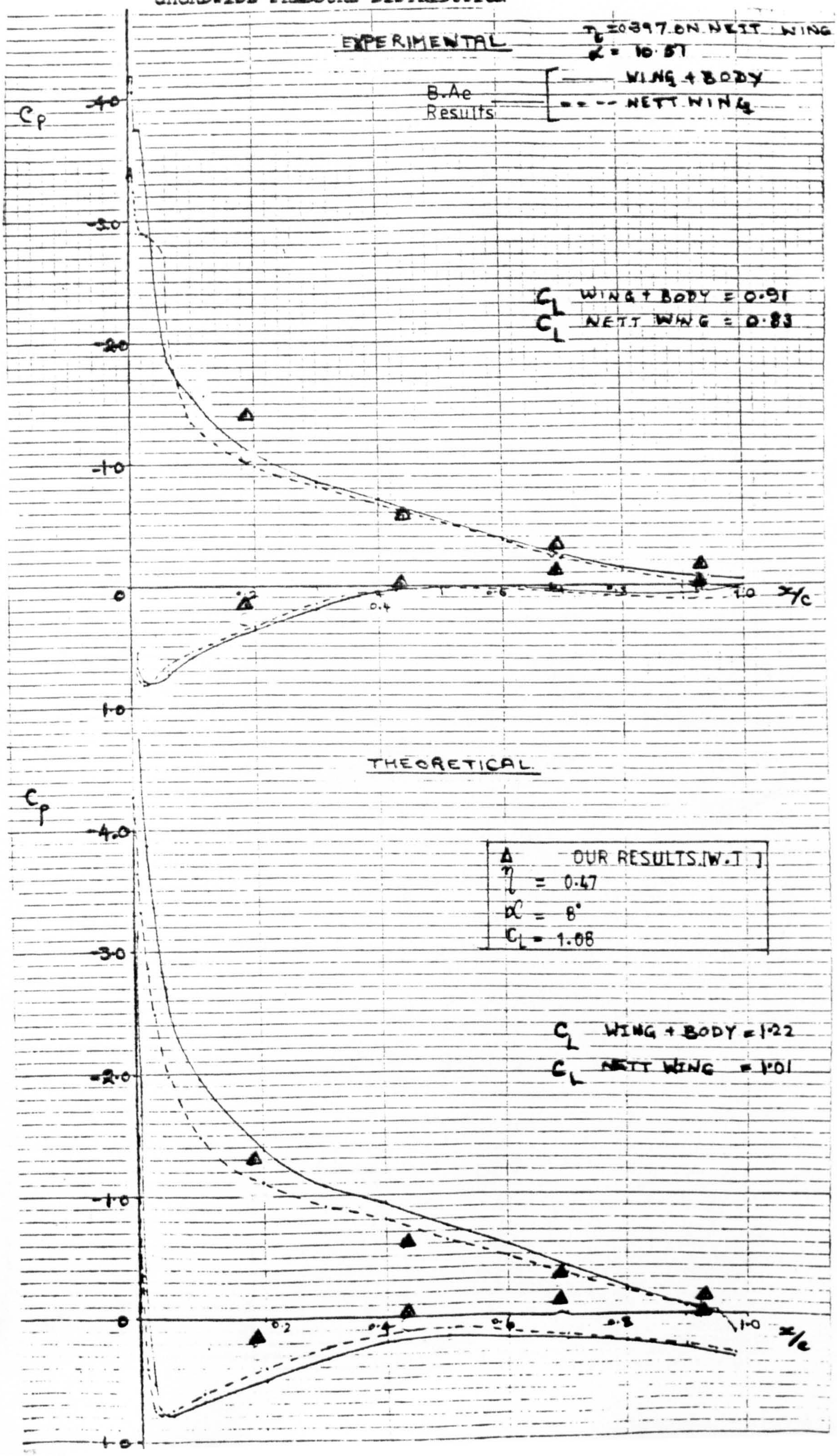

FIG.(9.57) NETT WING COMPARISONS OF CHORDWISE PRESSURE FOR THEORETICAL AND EXPERIMENTAL RESULTS

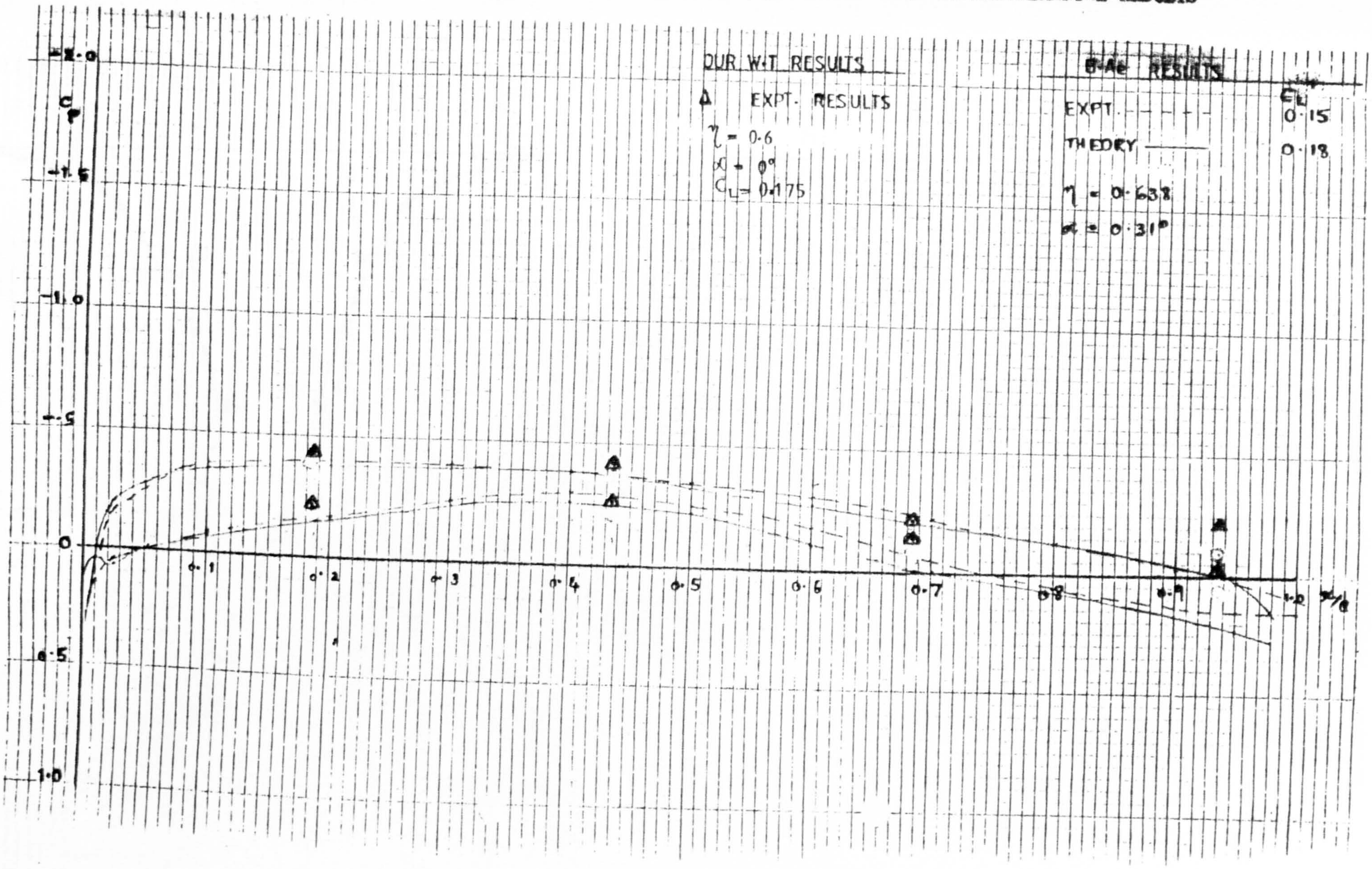

FIG.(9.58) COMPARISONS OF THEORETICAL AND EXPERIMENTAL RESULTS

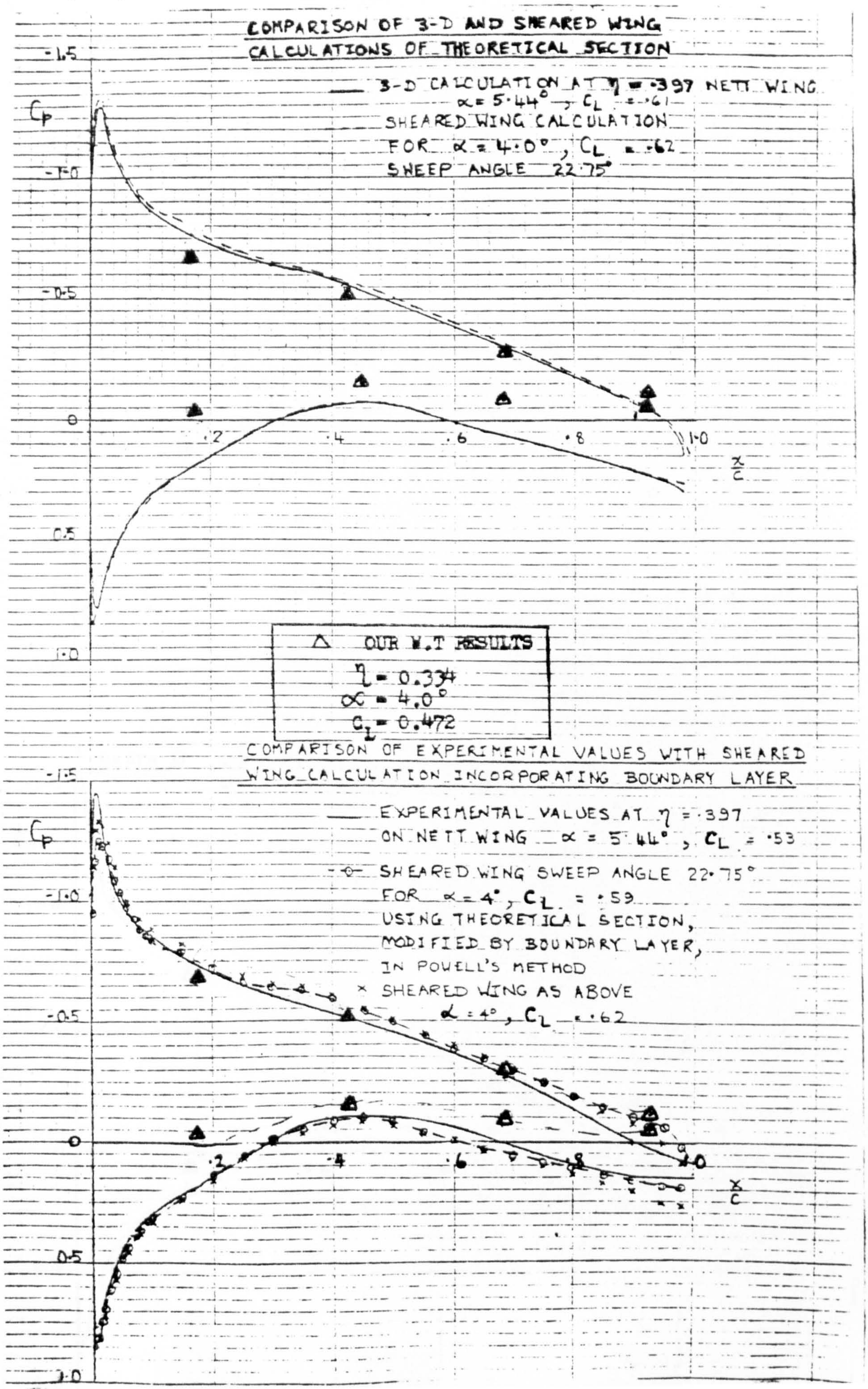

FIG.(9.59) COMPARISONS OF CHORDWISE PRESSURE DISTRIBUTION FOR EXPERIMENTAL AND THEORETICAL RESULTS

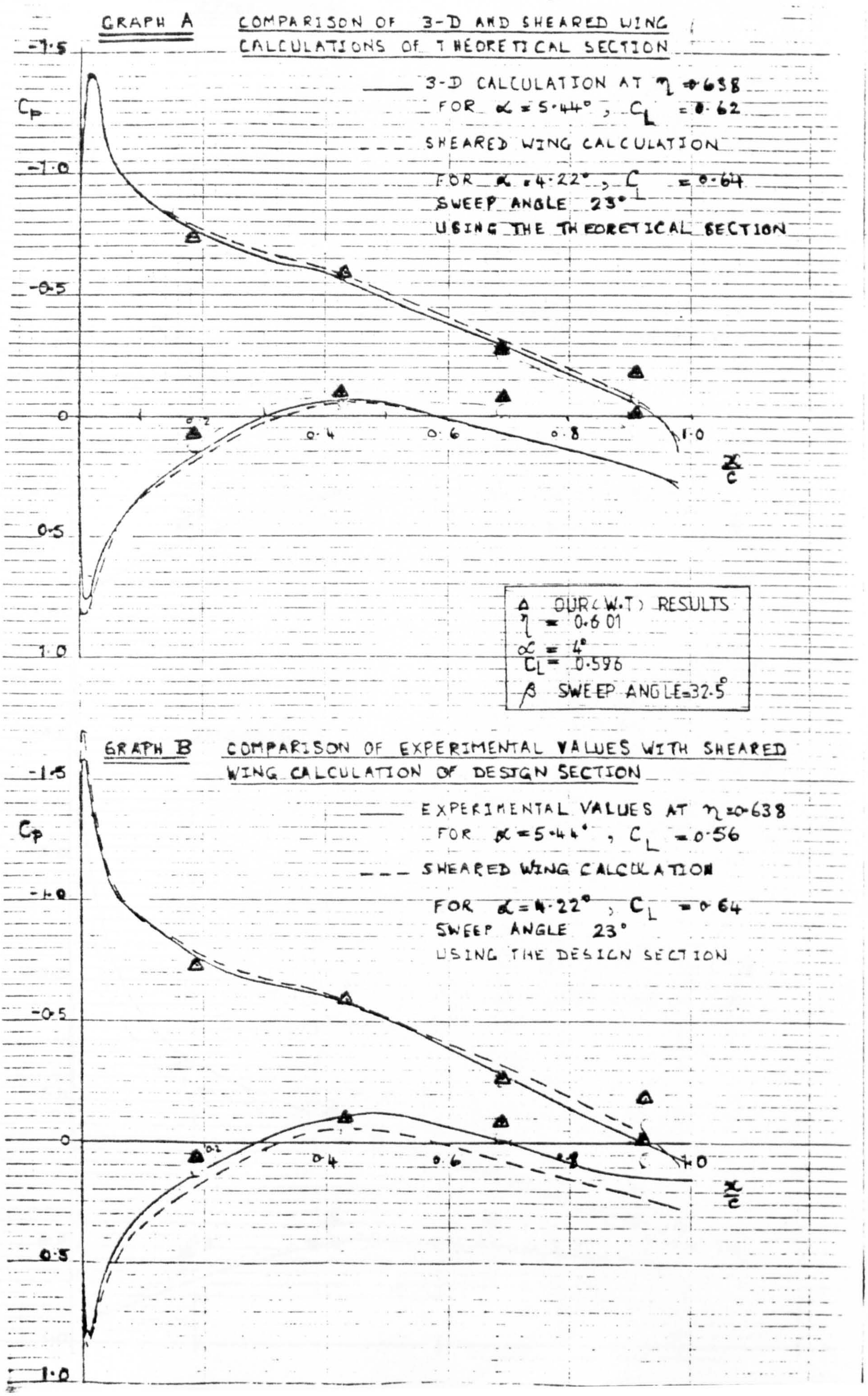

FIG.(9.60) COMPARISONS OF CHORDWISE PRESSURE DISTRIBUTION FOR EXPERIMENTAL AND THEORETICAL RESULTS

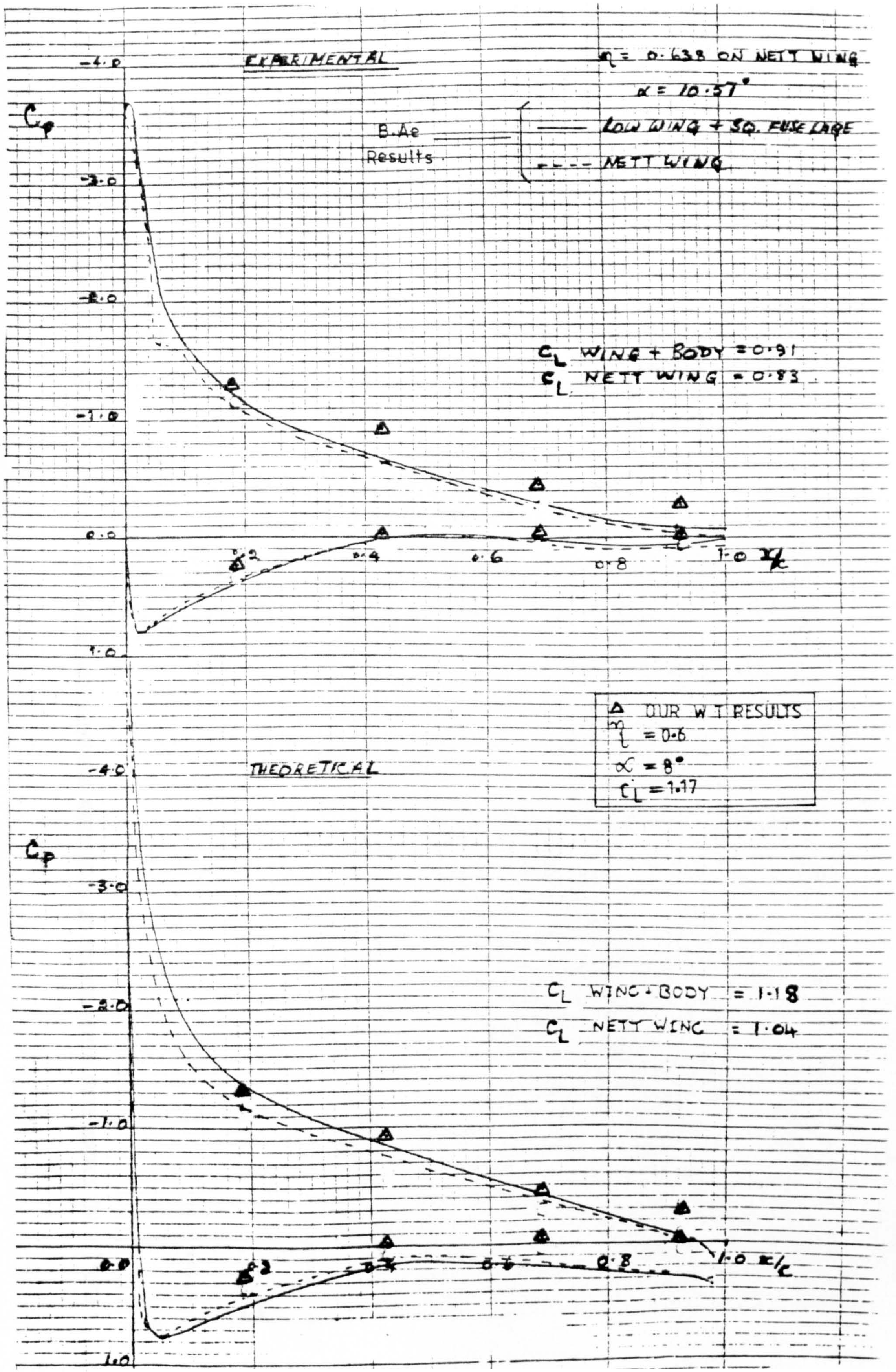

FIG.(9.61) GROSS WING COMPARISONS OF CHORDWISE PRESSURE DISTRIBUTION FOR EXPERIMENTAL AND THEORETICAL RESULTS

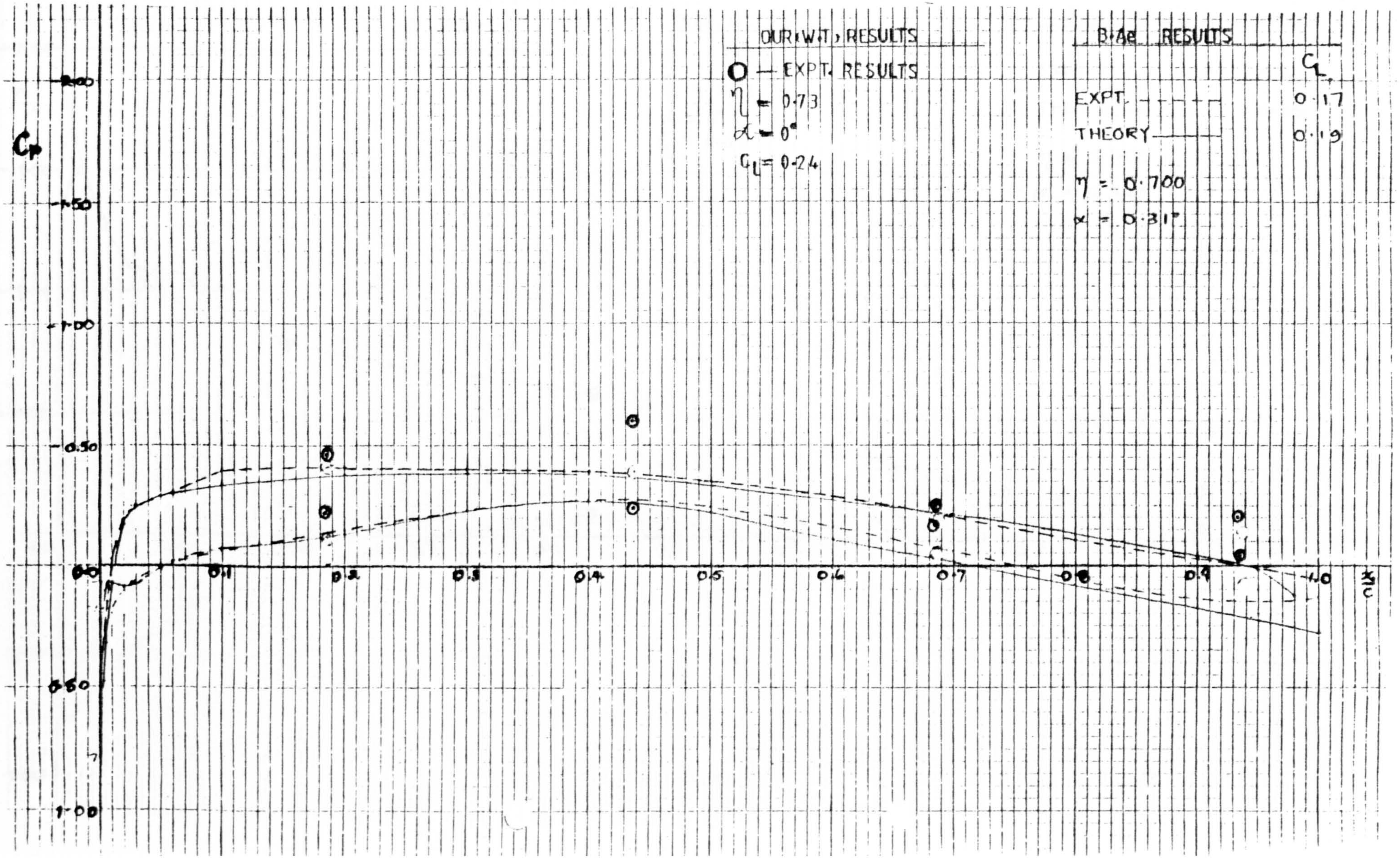

FIG.(9.62) GROSS WING COMPARISONS OF CHORDWISE PRESSURE DISTRIBUTION FOR EXPERIMENTAL AND THEORETICAL RESULTS

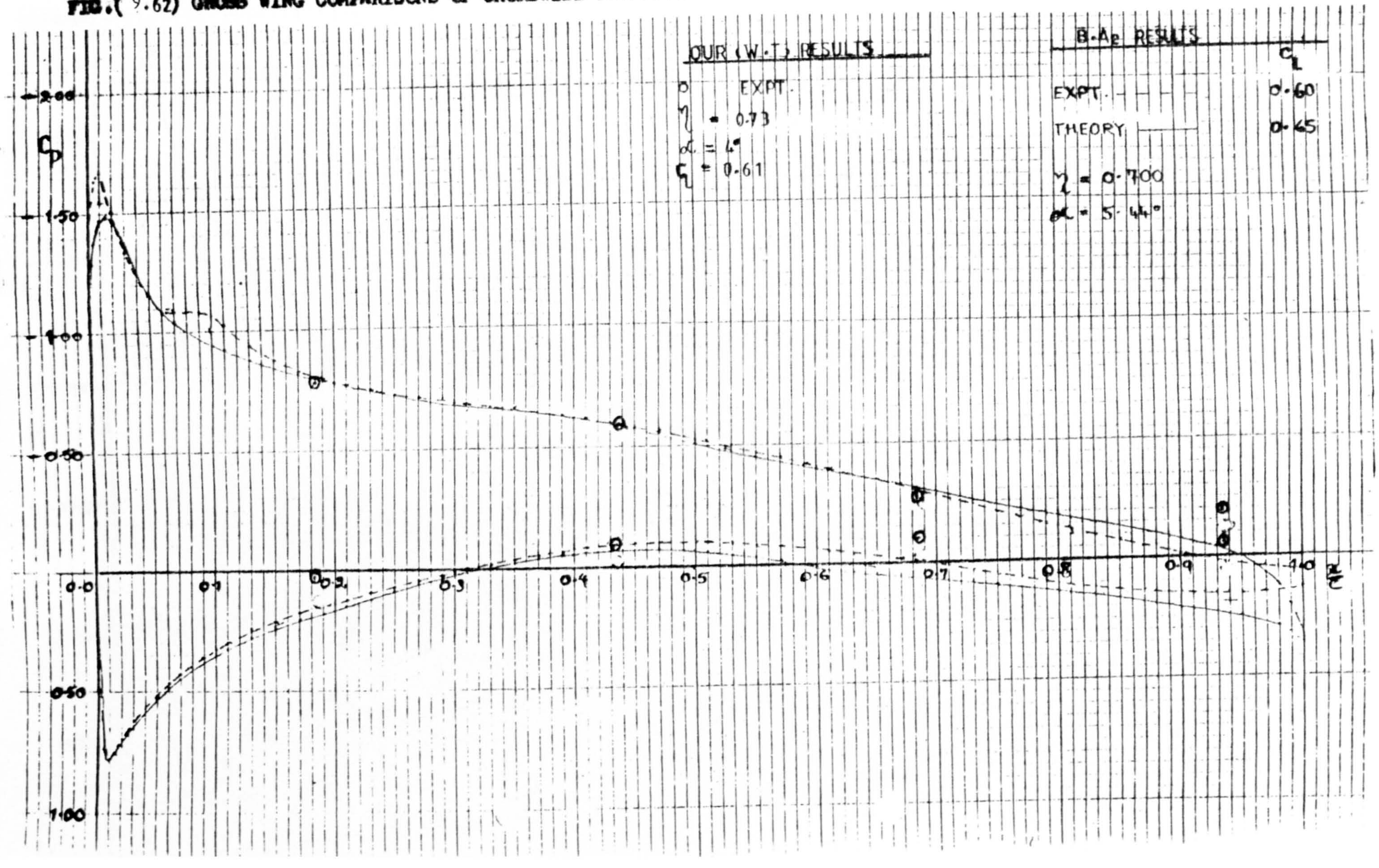

FIG.(9.63) GROSS COMPARISONS OF CHORDWISE PRESSURE DISTRIBUTION FOR EXPERIMENTAL AND THEORETICAL RESULTS

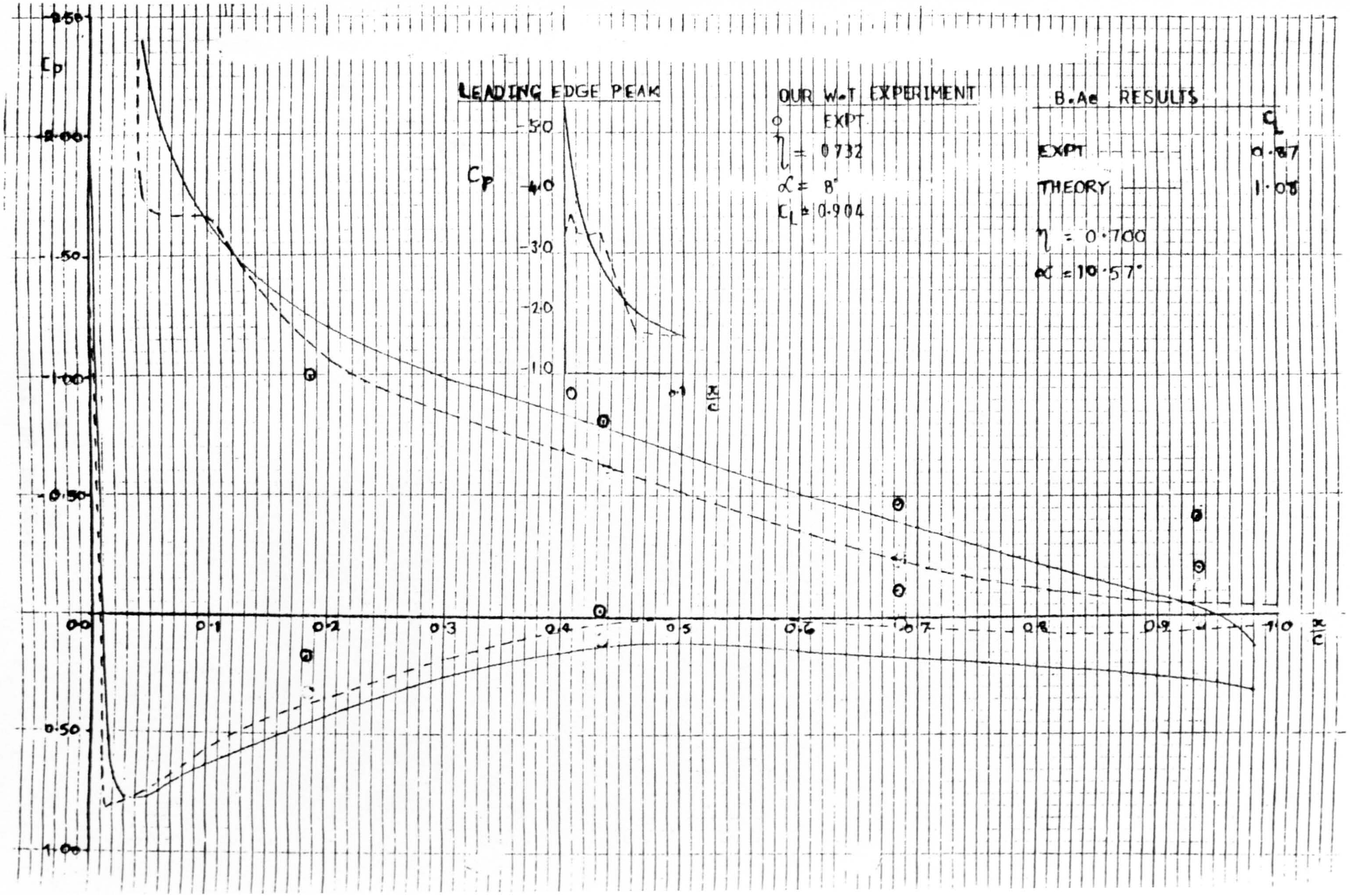

FIG.(9.64) COMPARISONS OF SECTION LIFT (FROM PRESSURE READINGS) FOR EXPERIMENTAL TESTS WITH B.Ae's RESULTS.

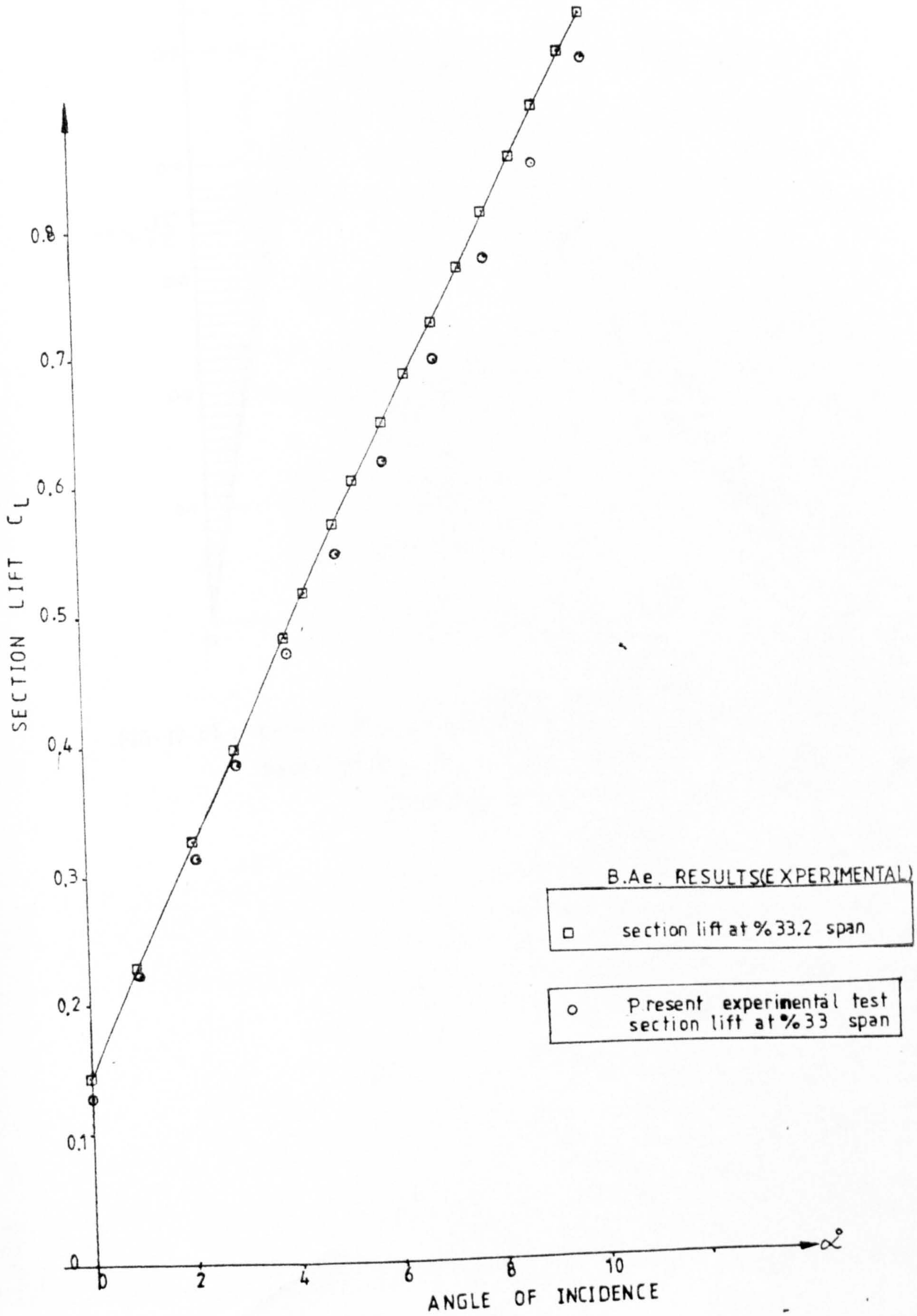

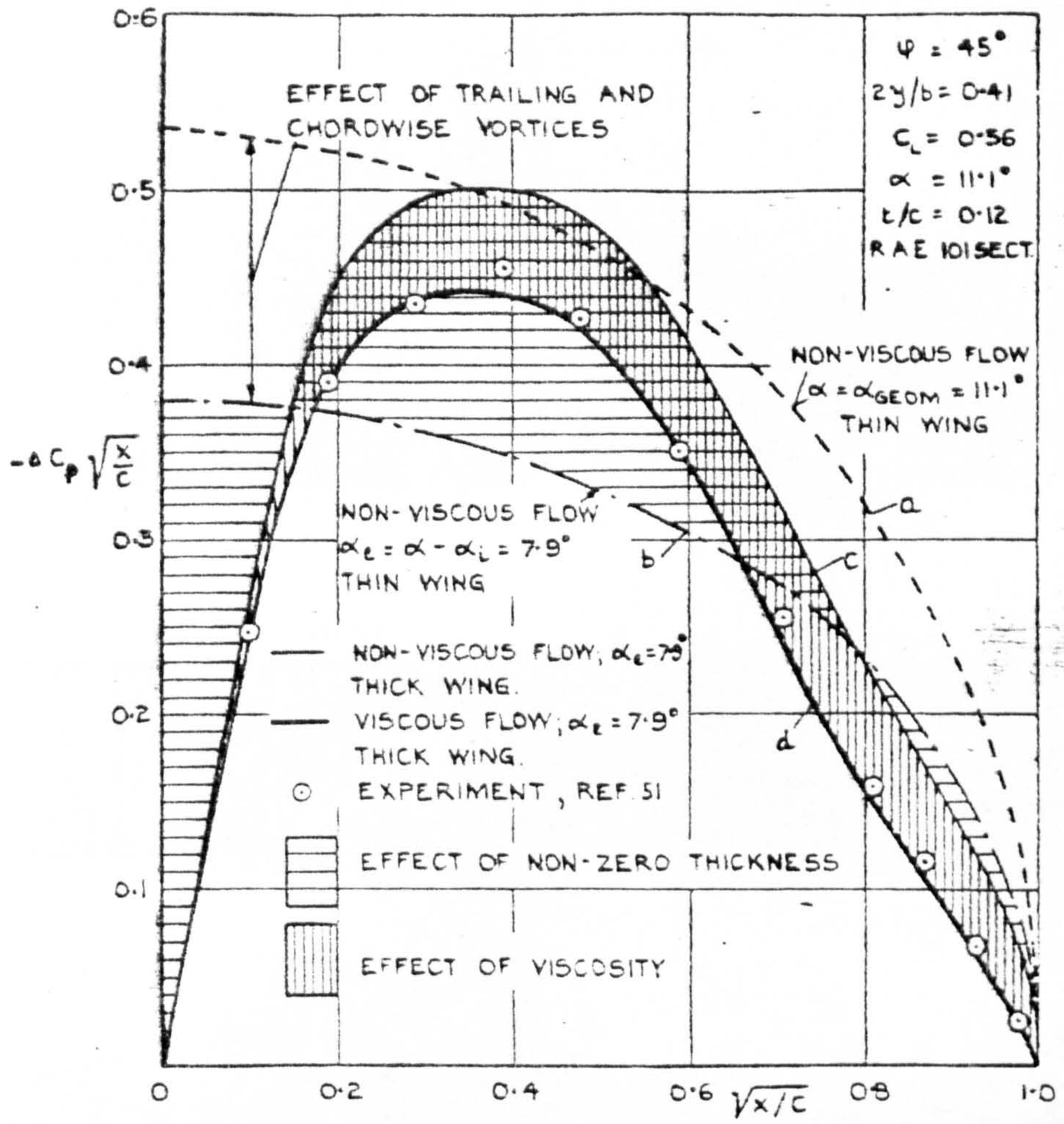

FIG. (9.65) CHORDWISE LOAD DISTRIBUTIONS AT ABOUT MID-SPAN ON A 45° SWEPT-BACK CONSTANT CHORD WING OF ASPECT RATIO 3

(FROM REF. 9.6)

$\alpha = 0^\circ$, $\beta = 0^\circ$, TRANSITION BAND OFF

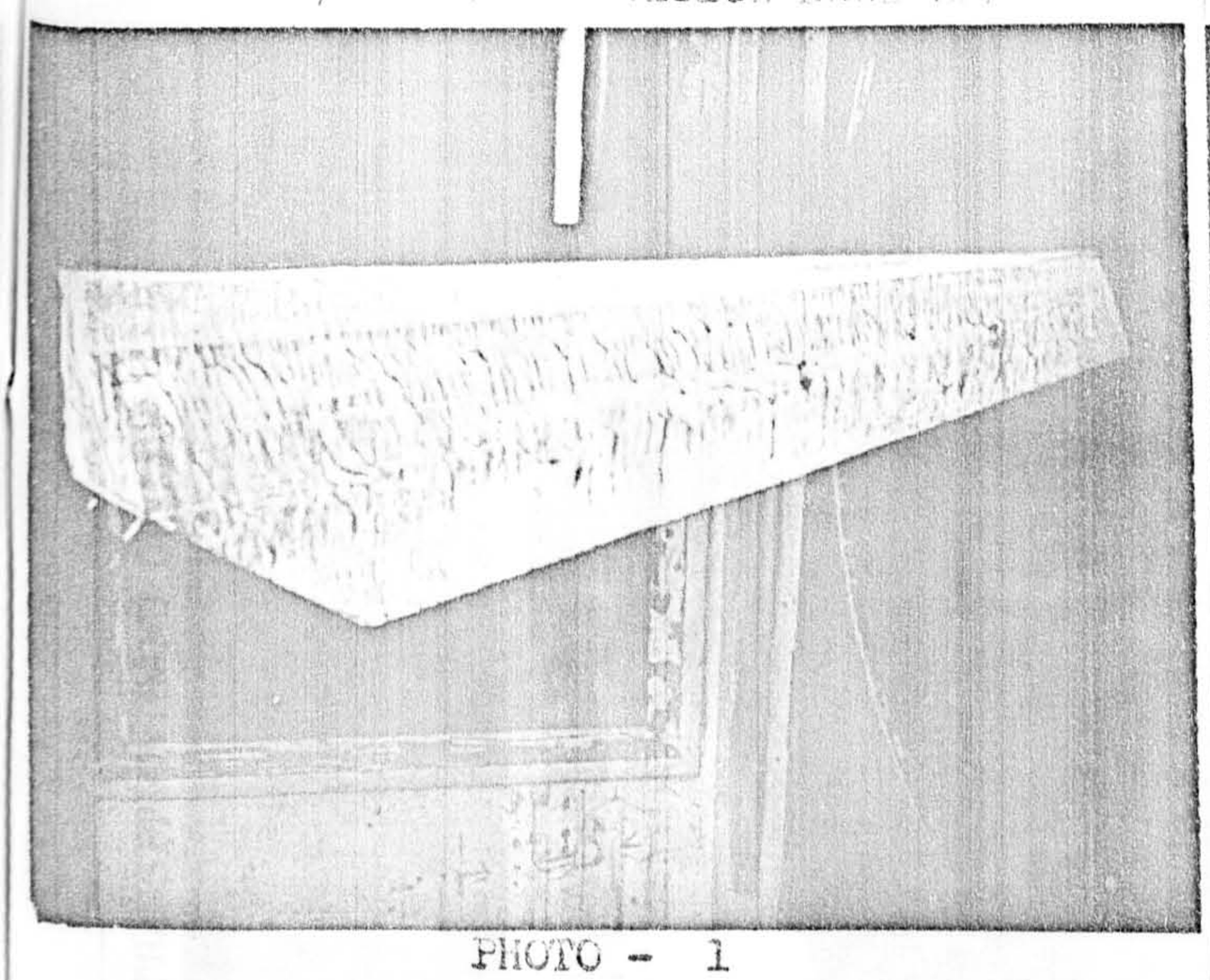

PHOTO - 1

$\alpha = 4^\circ$, $\beta = 0^\circ$, TRANSITION BAND OFF

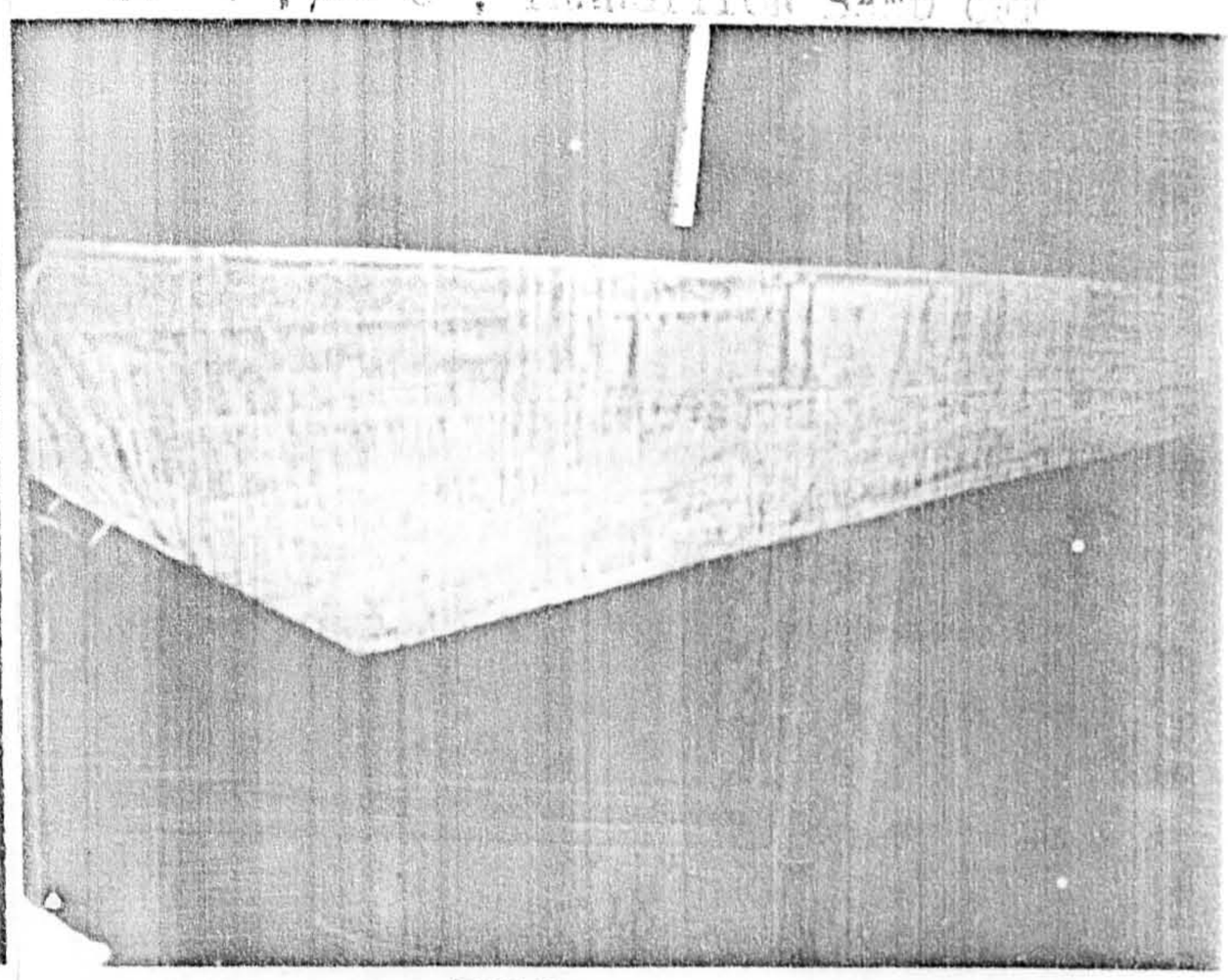

PHOTO- 2

$\alpha = 8^\circ$, $\beta = 0^\circ$, TRANSITION BAND OFF

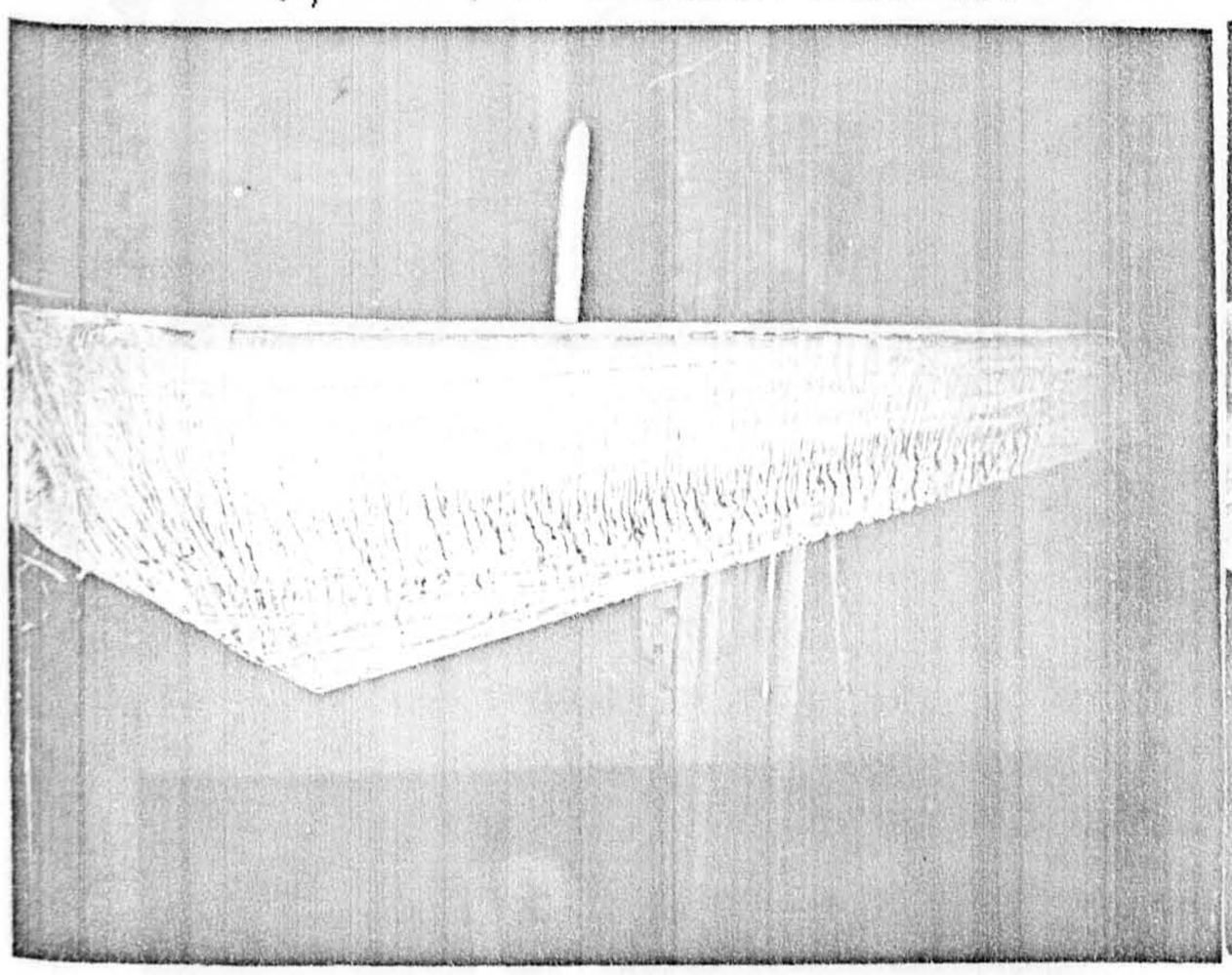

PHOTO - 3

$\alpha = 12^\circ$, $\beta = 0^\circ$, TRANSITION BAND OFF

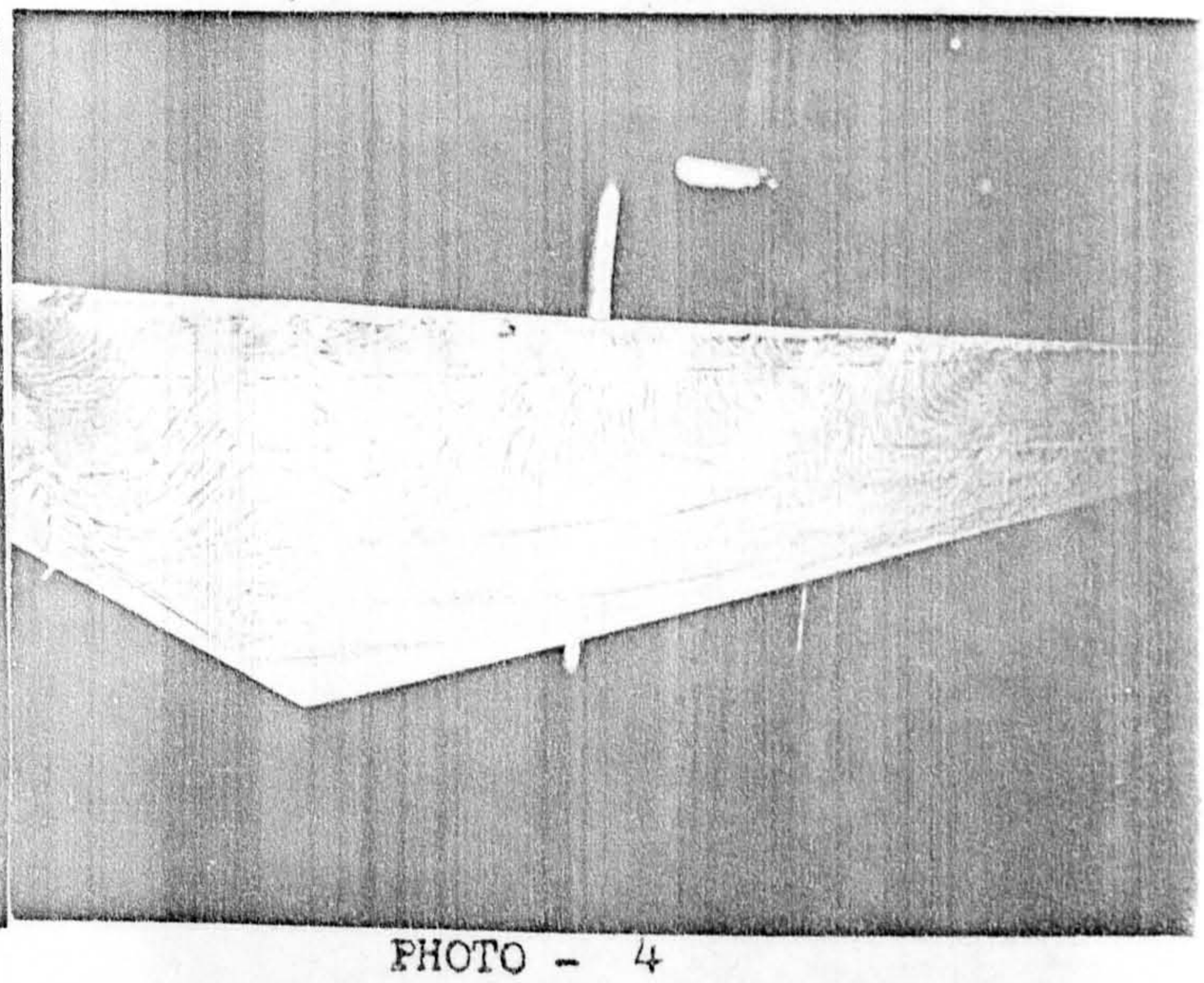

PHOTO - 4

$\alpha = 16^\circ$, $\beta = 0^\circ$, TRANSITION BAND OFF

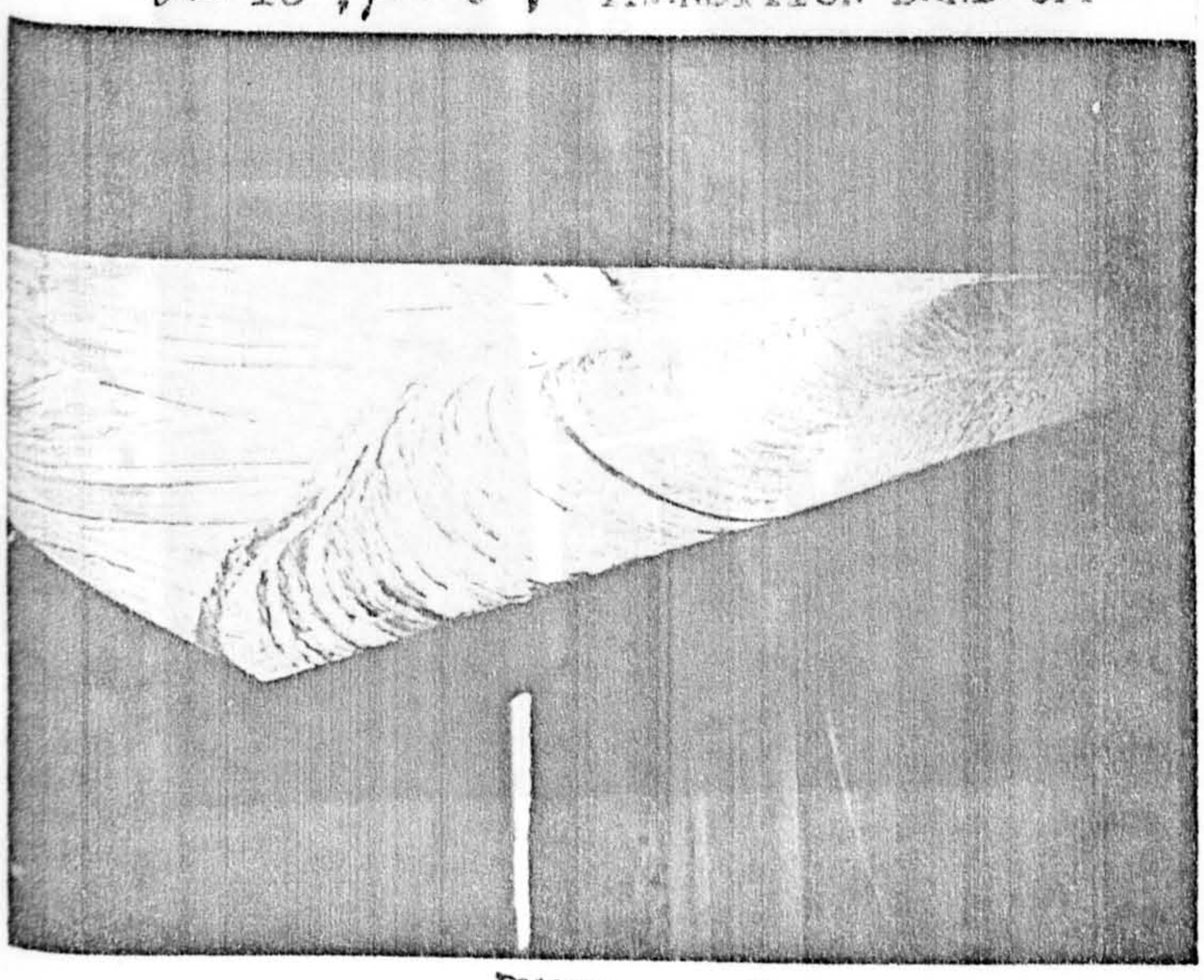

PHOTO _ 5

$\alpha = 20^\circ$, $\beta = 0^\circ$, TRANSITION BAND OFF

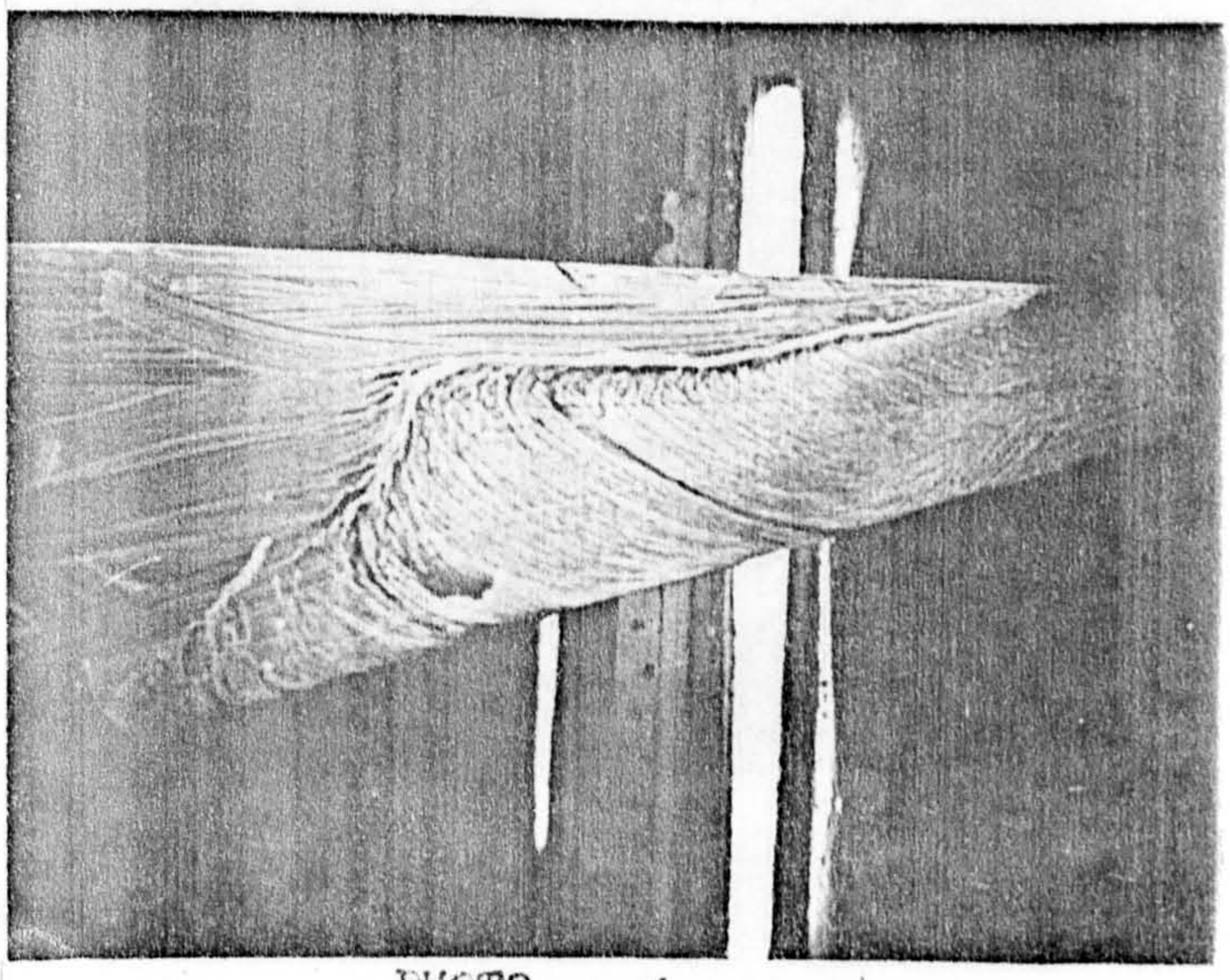

PHOTO _ 6

$\alpha = 0°$, $\beta = 0°$, TRANSITION BAND ON

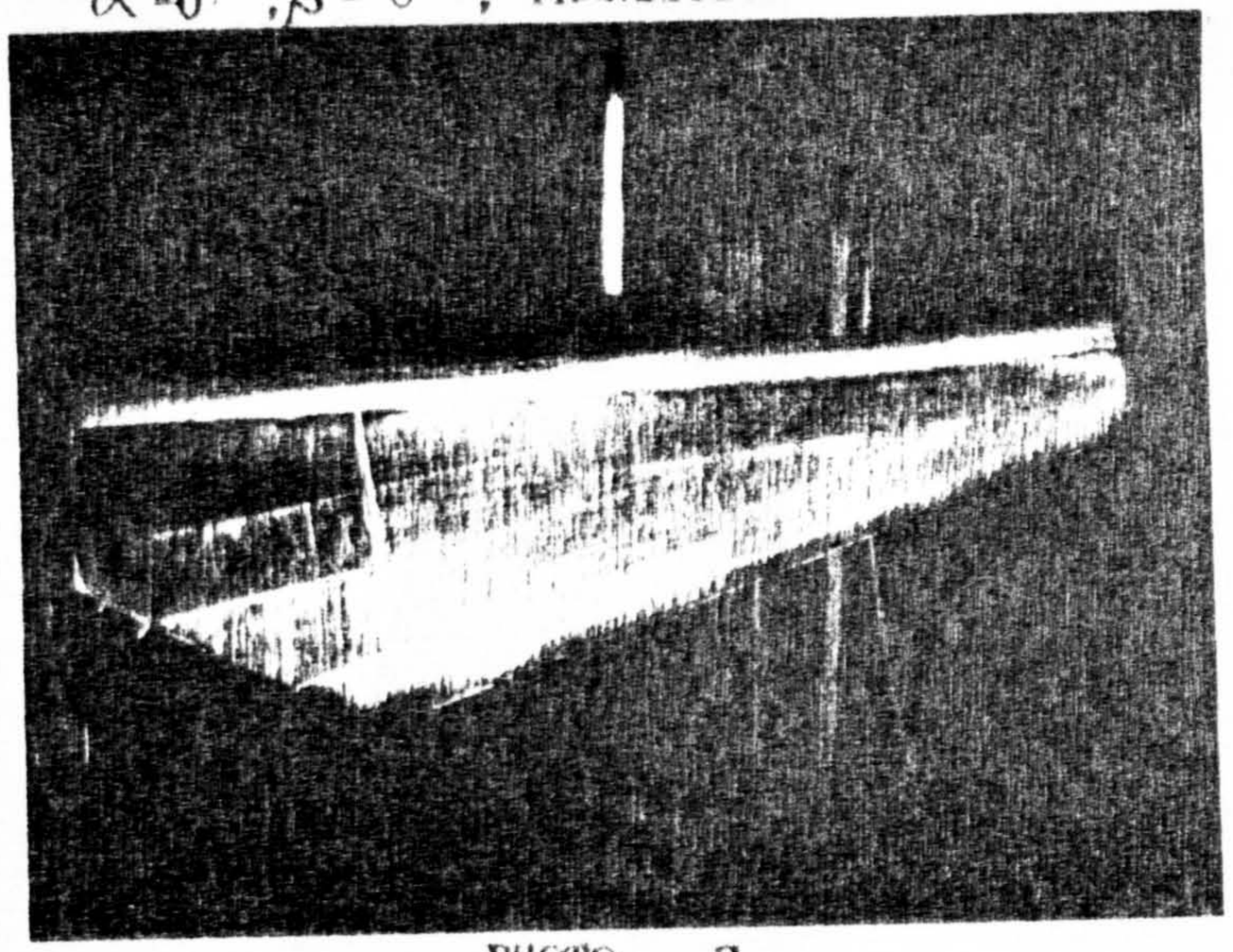

PHOTO - 7

$\alpha = 4°$, $\beta = 0°$, TRANSITION BAND ON

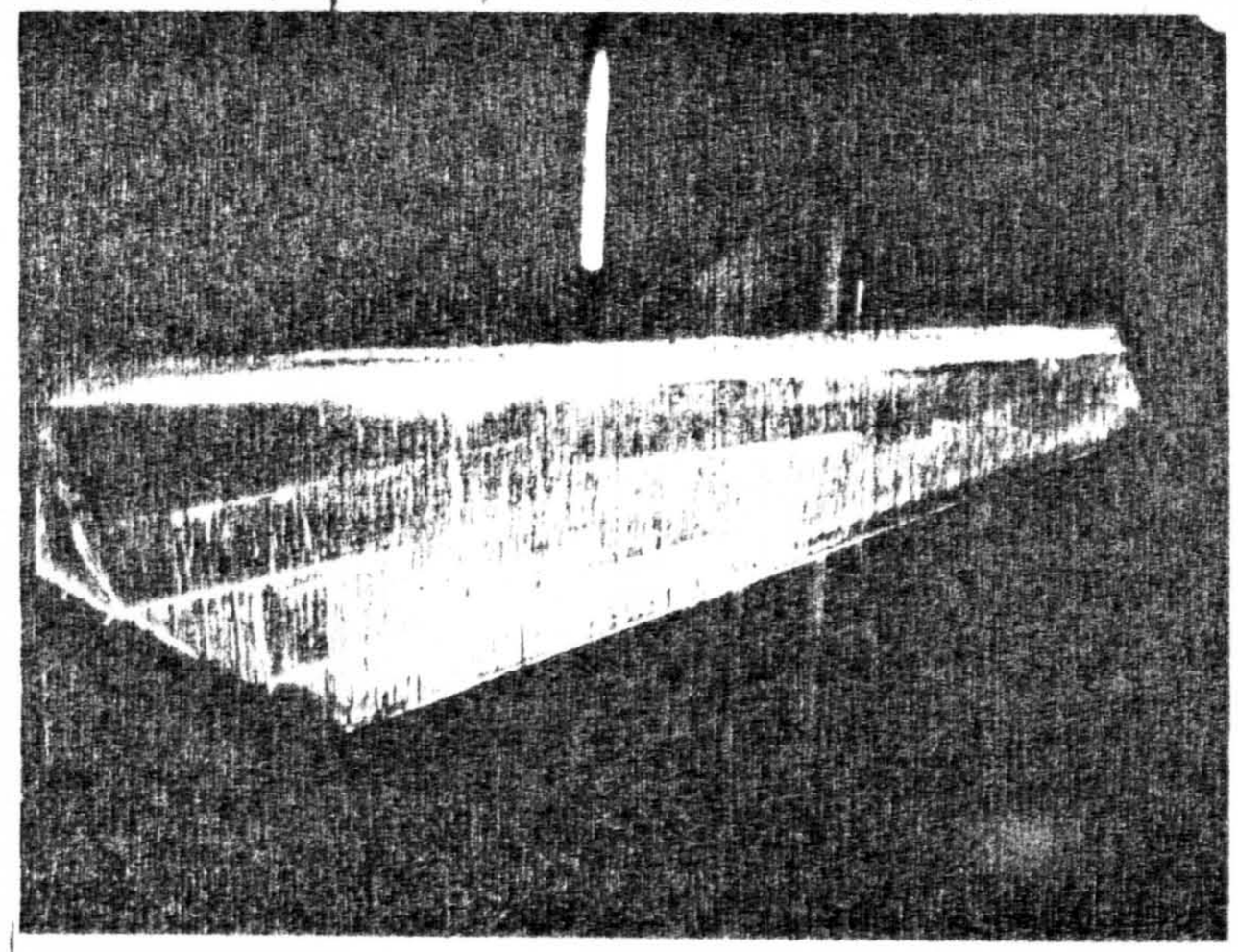

PHOTO - 8

$\alpha = 8°$, $\beta = 0°$, TRANSITION BAND ON

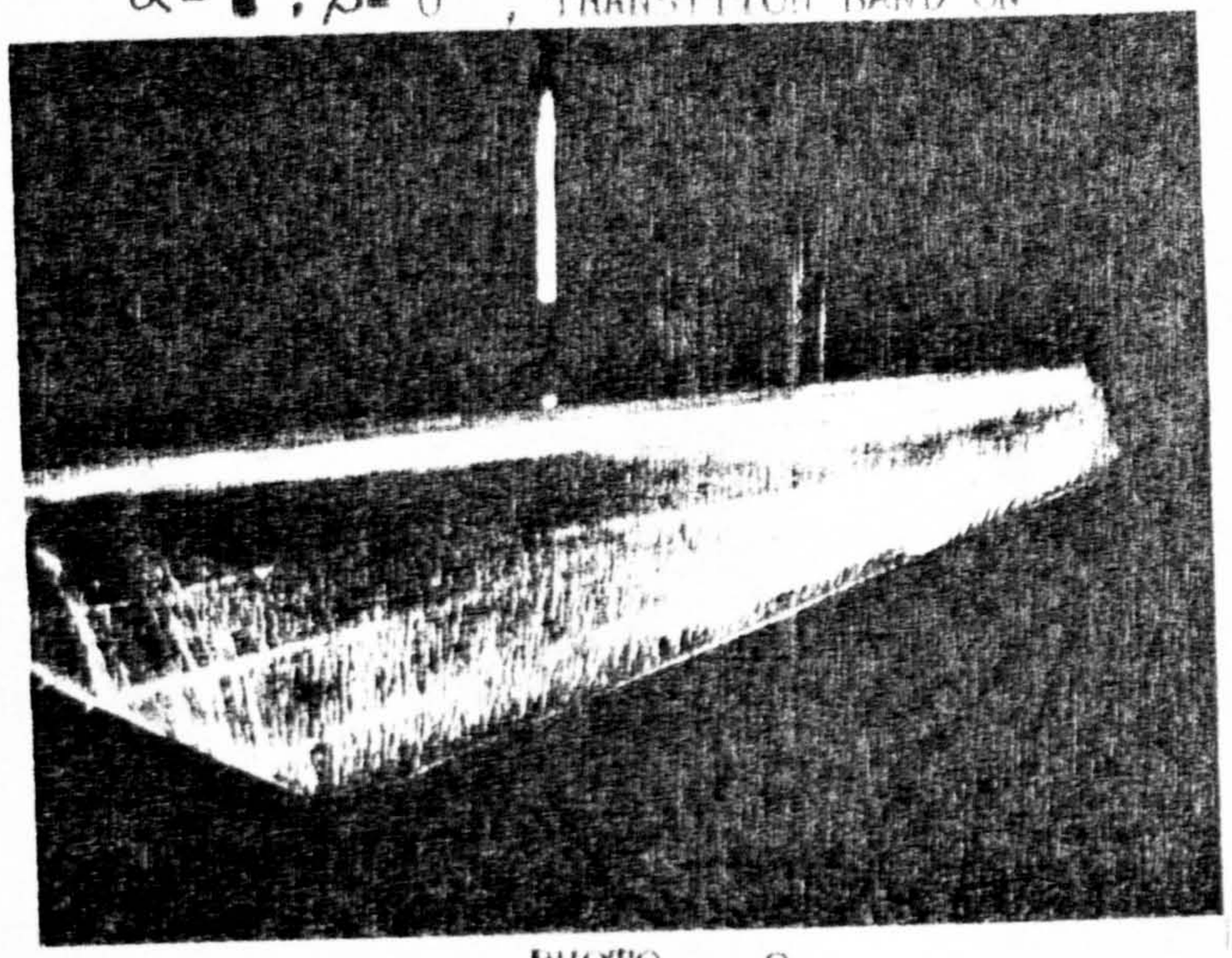

PHOTO - 9

$\alpha = 12°$ $\beta = 0°$ TRANSITION BAND ON

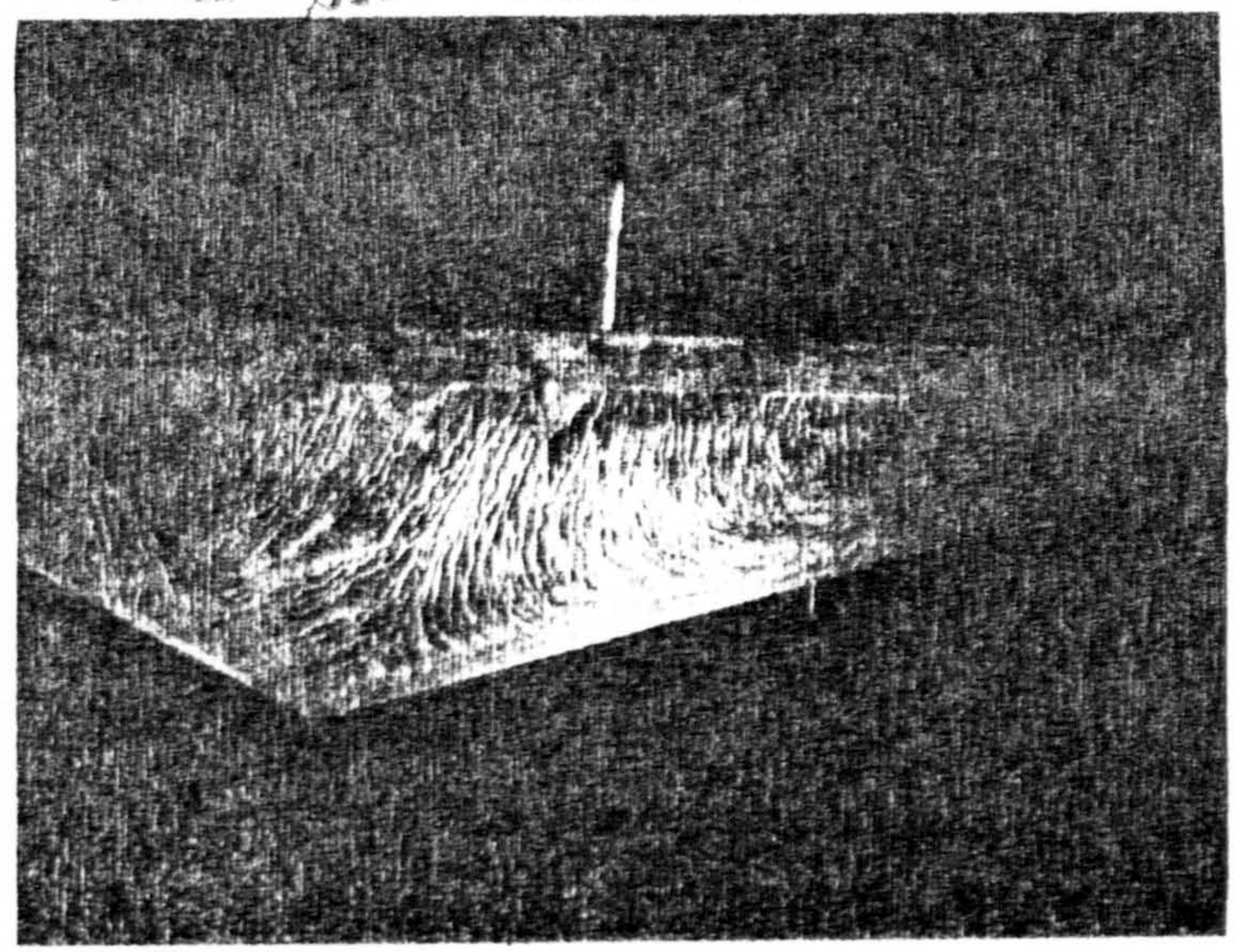

PHOTO - 10

$\alpha = 0^\circ$, $\beta = 12.5^\circ$, TRANSITION BAND OFF

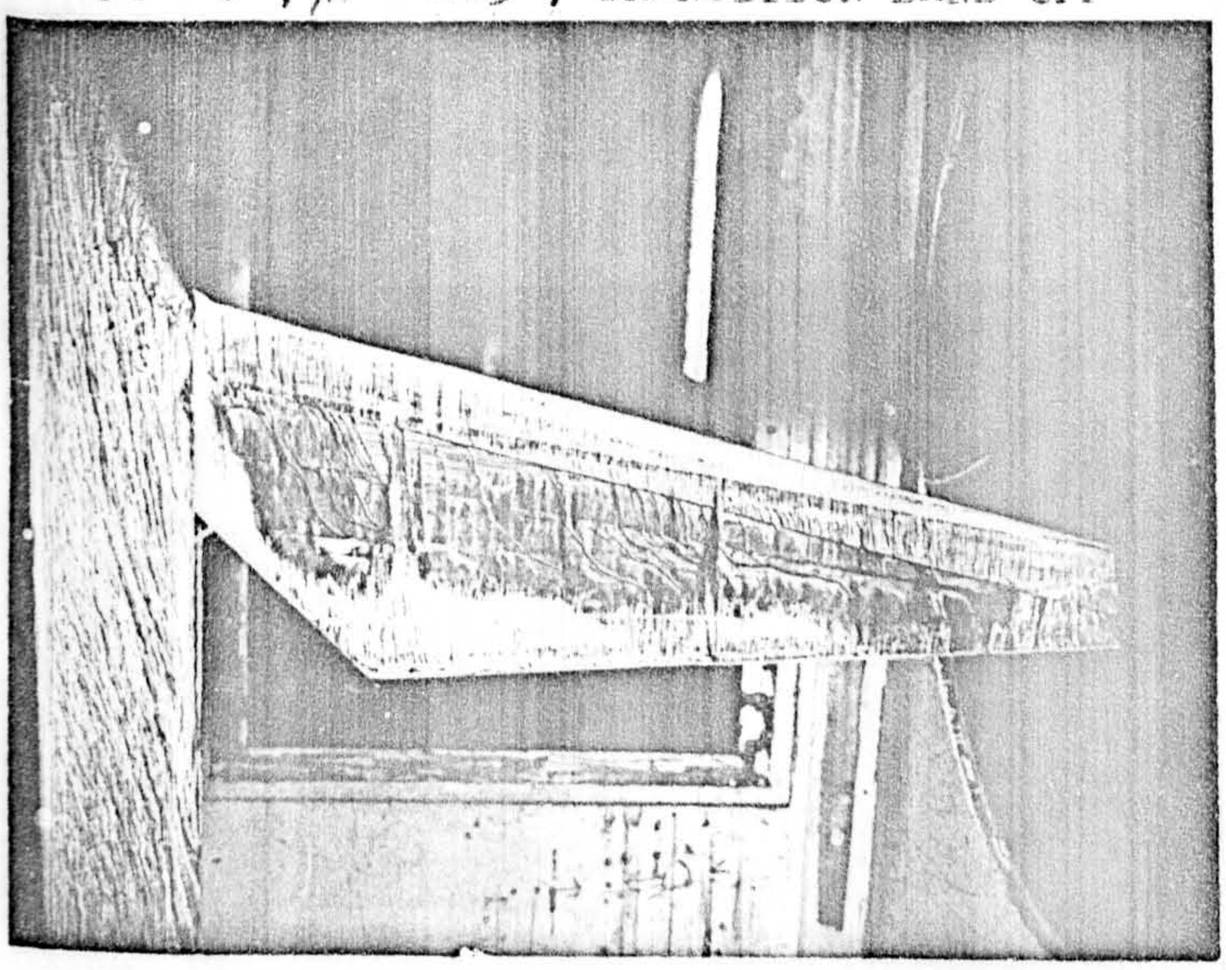

PHOTO - 11

$\alpha = 4^\circ$, $\beta = 12.5^\circ$, TRANSITION BAND OFF

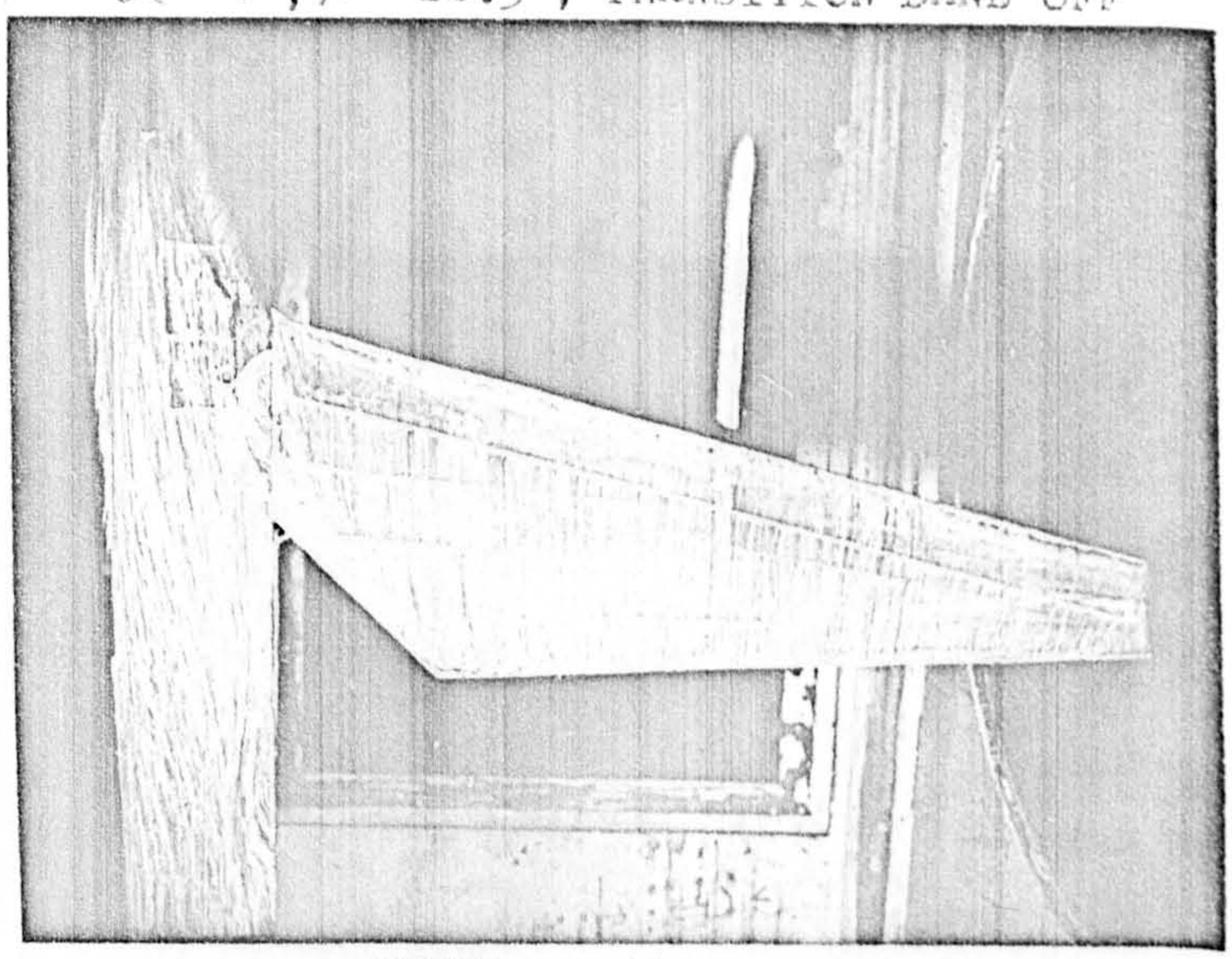

PHOTO - 12

$\alpha = 8^\circ$, $\beta = 12.5^\circ$, TRANSITION BAND OFF

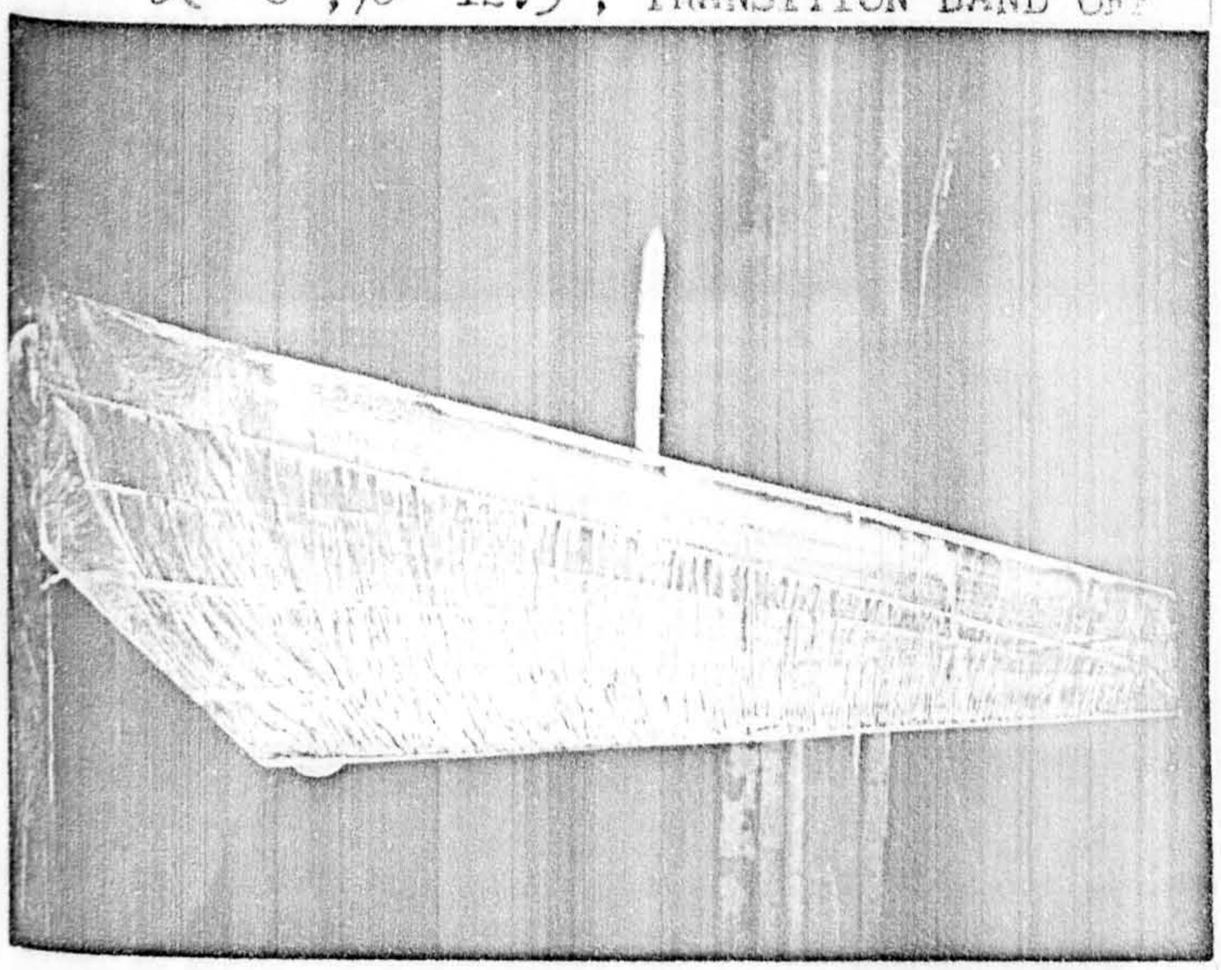

PHOTO - 13

$\alpha = 12^\circ$, $\beta = 12.5^\circ$, TRANSITION BAND OFF

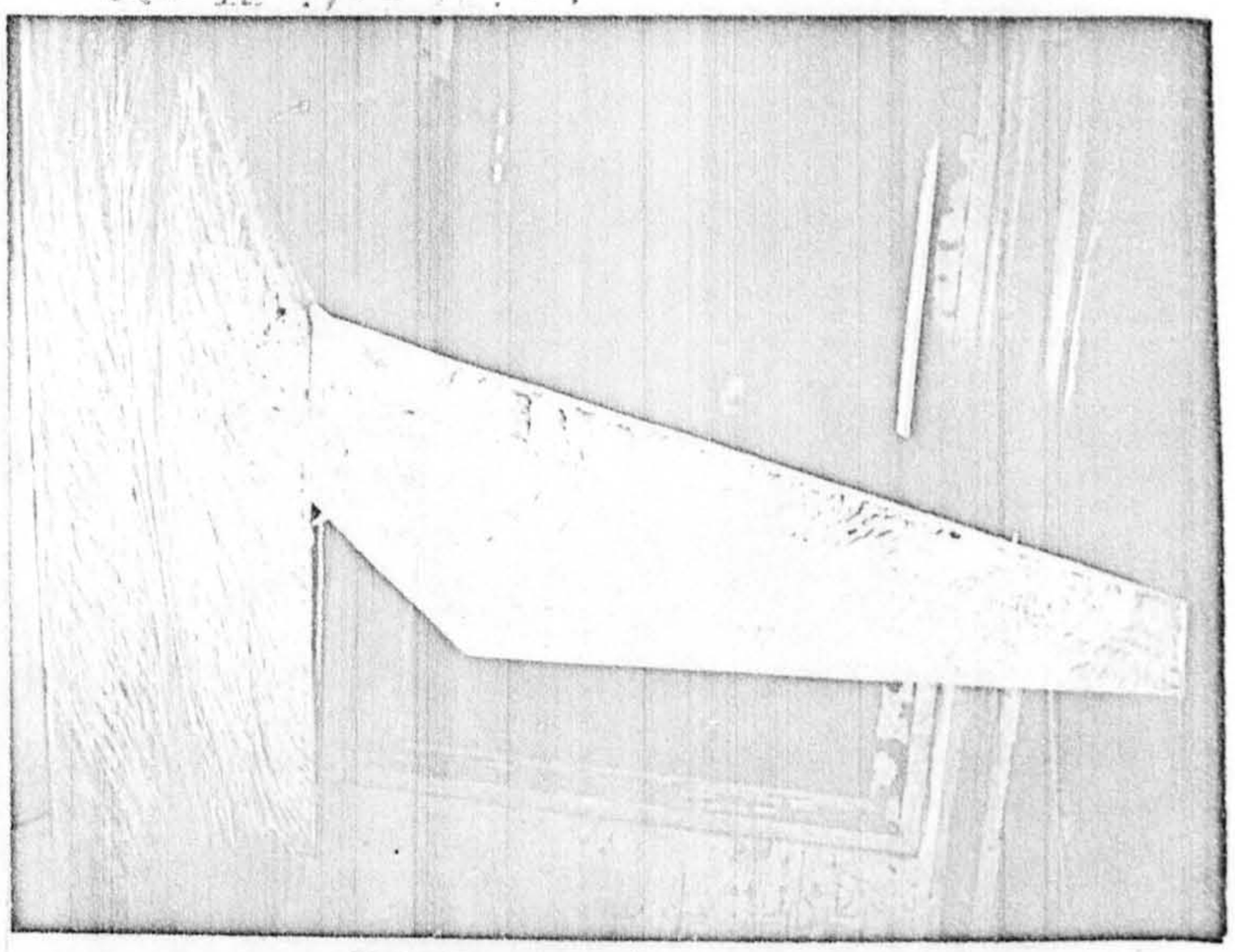

PHOTO - 14

$\alpha = 16^\circ$, $\beta = 12.5^\circ$, TRANSITION BAND OFF

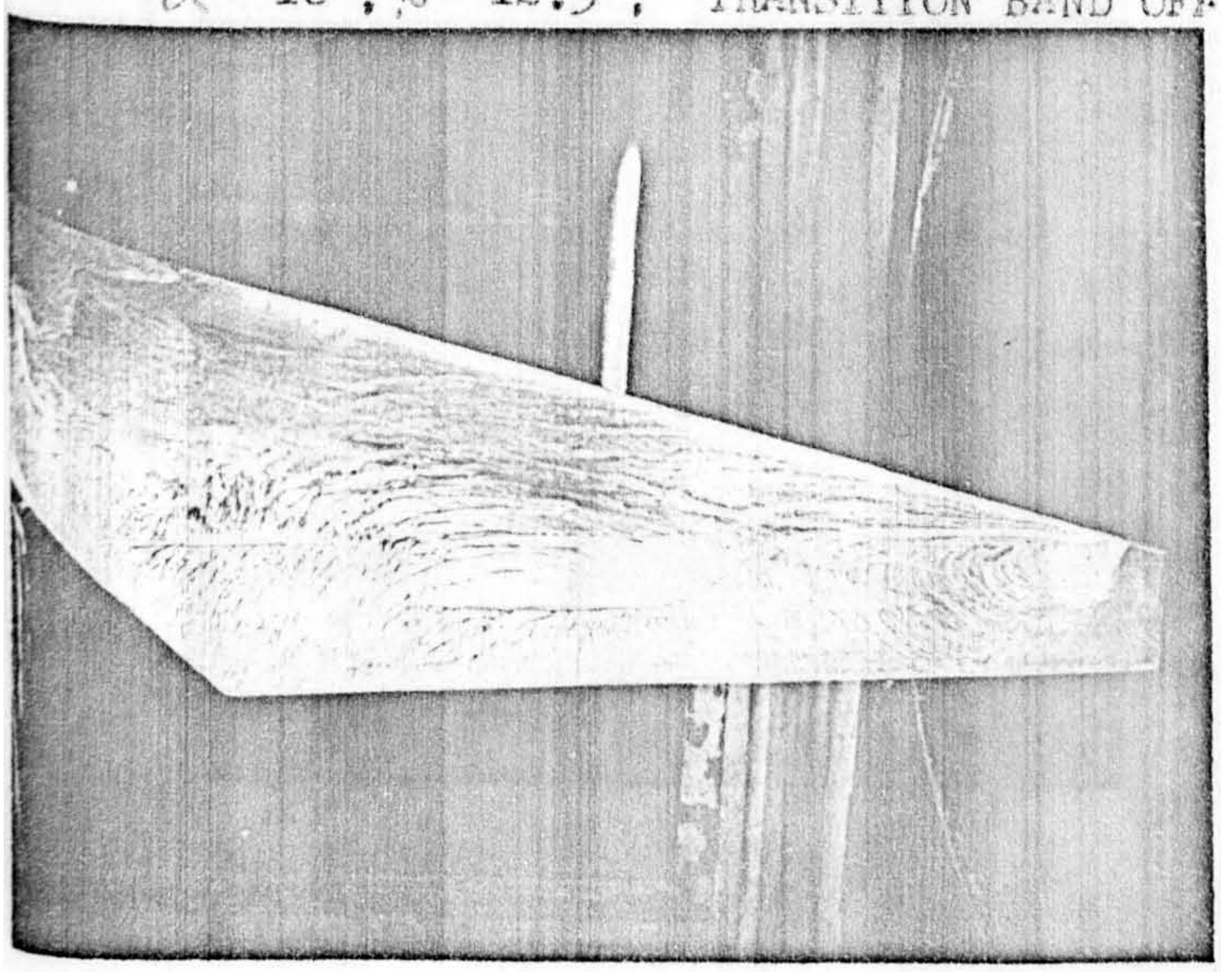

PHOTO - 15

$\alpha = 20^\circ$, $\beta = 12.5^\circ$, TRANSITION BAND OFF

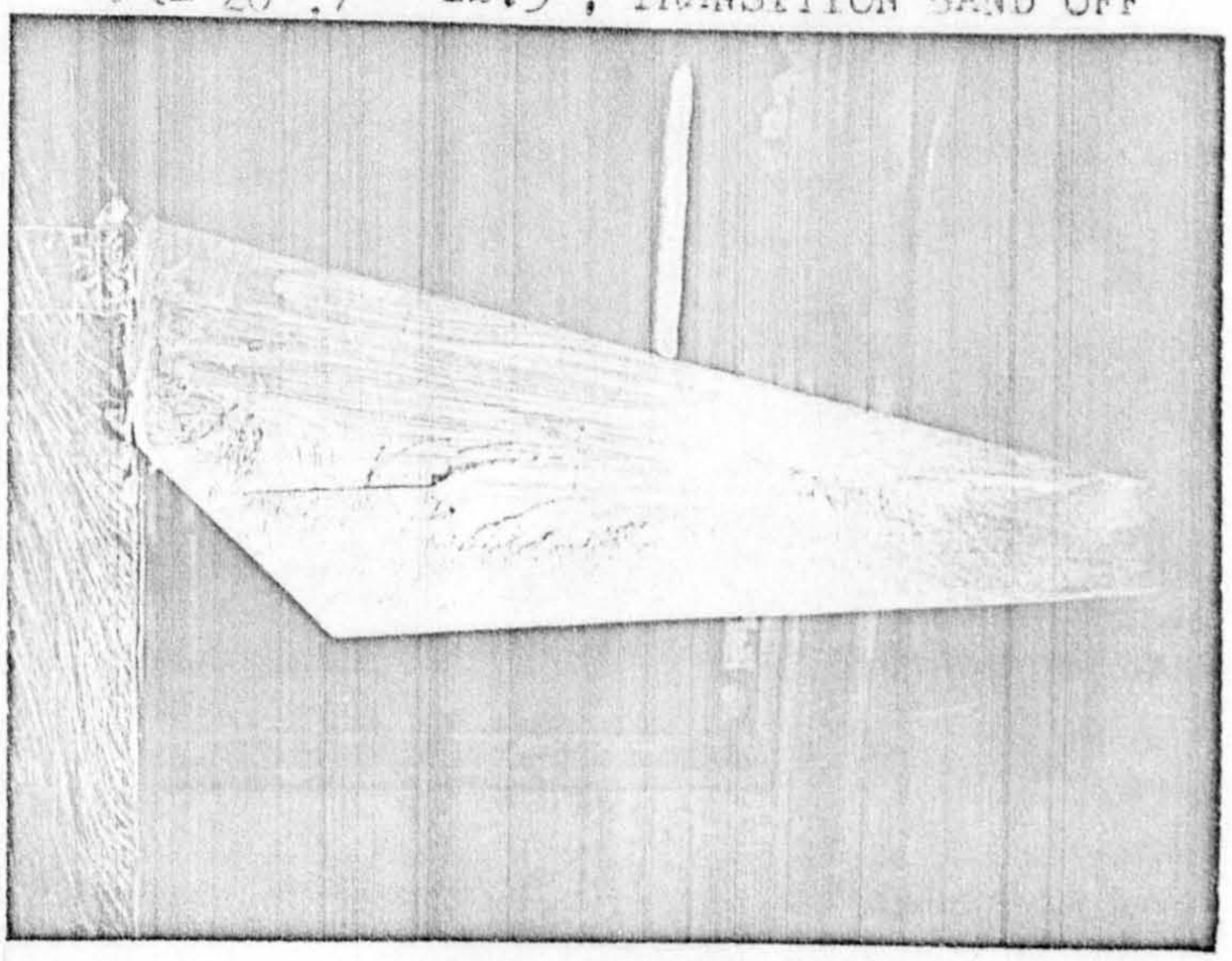

PHOTO - 16

$\alpha = 0^\circ$, $\beta = 12.5^\circ$, TRANSITION BAND ON

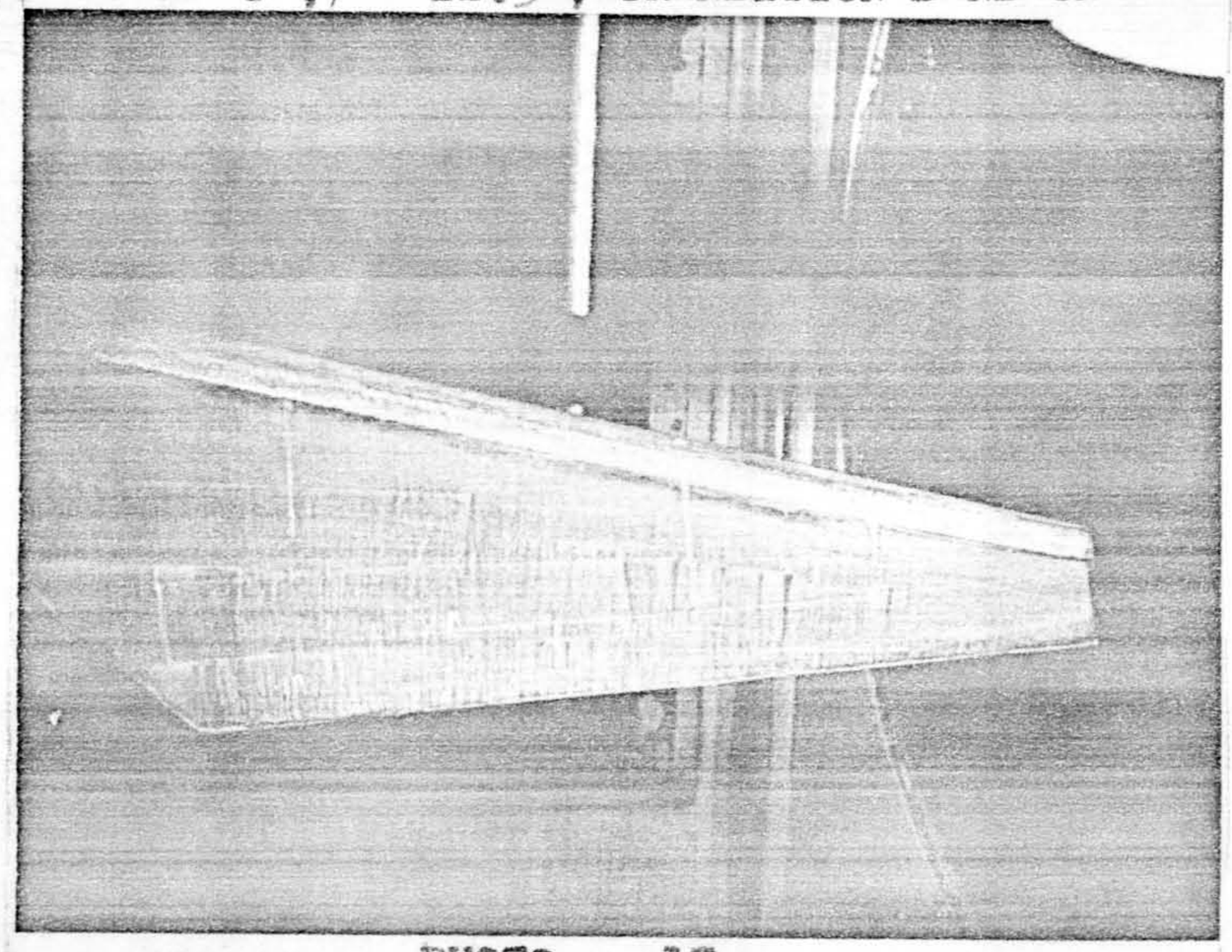

PHOTO- 17

$\alpha = 4^\circ$, $\beta = 12.5^\circ$, TRANSITION BAND ON

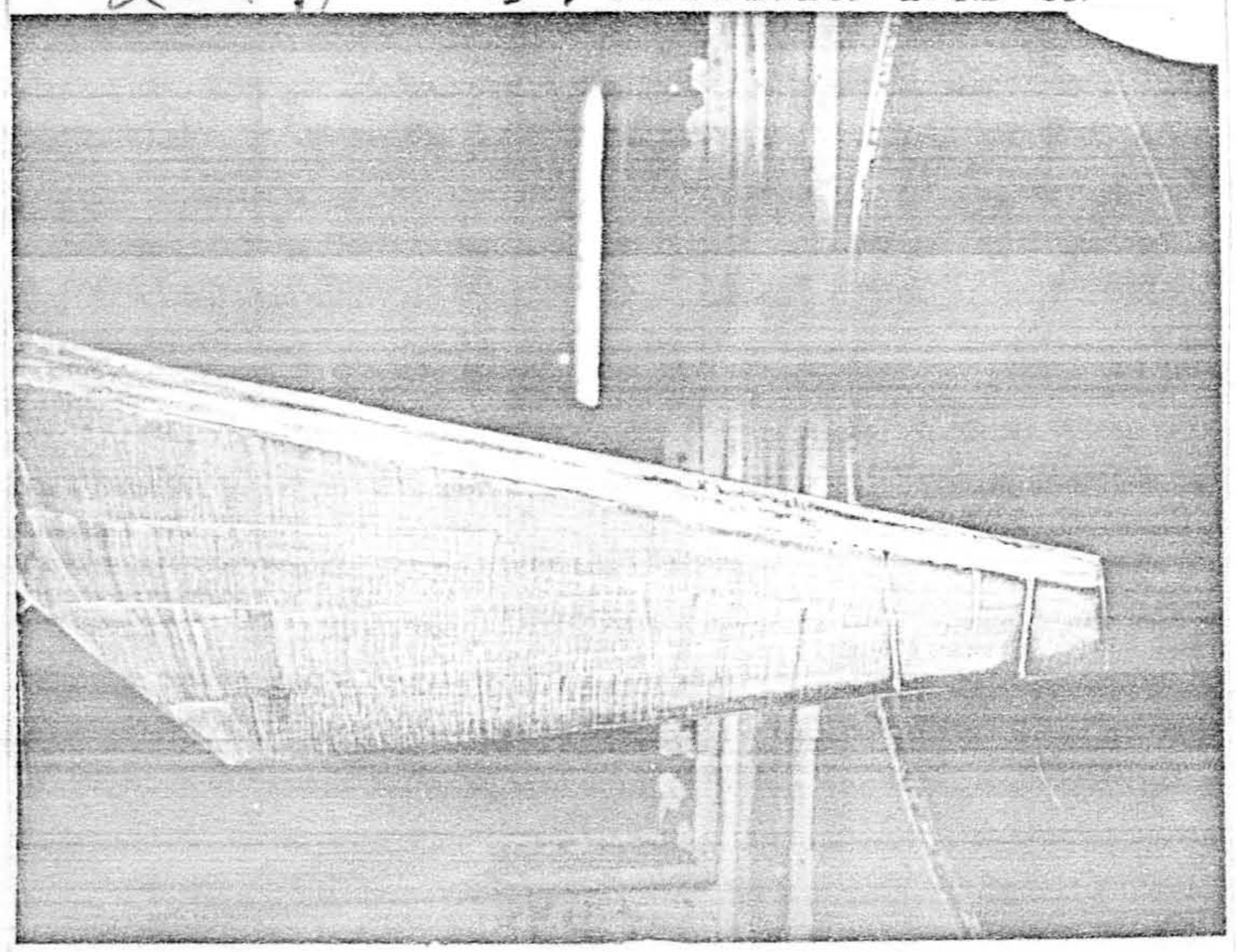

PHOTO - 18

$\alpha = 8^\circ$, $\beta = 12.5^\circ$, TRANSITION BAND ON

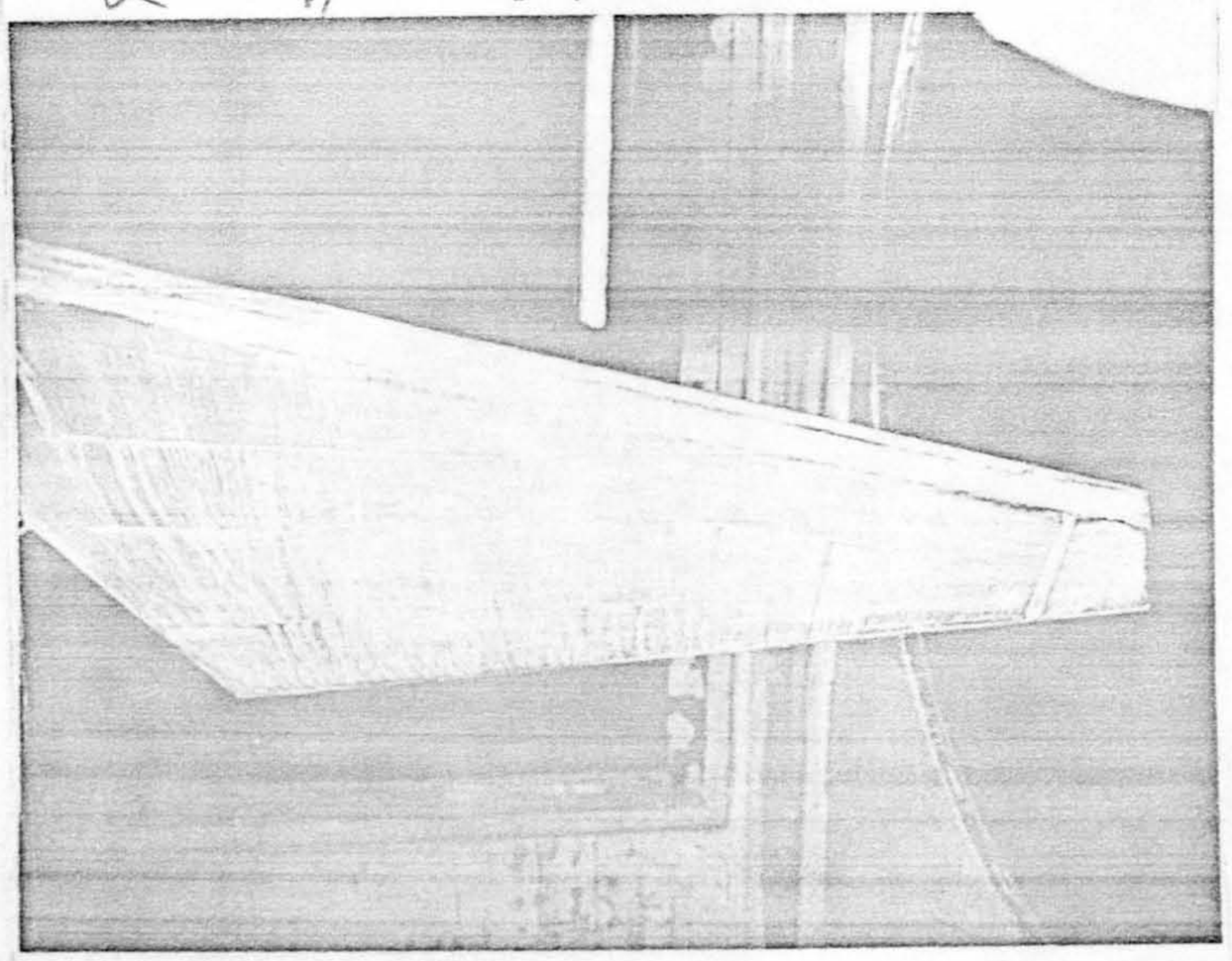

PHOTO - 19

$\alpha = 12^\circ$, $\beta = 12.5^\circ$, TRANSITION BAND ON

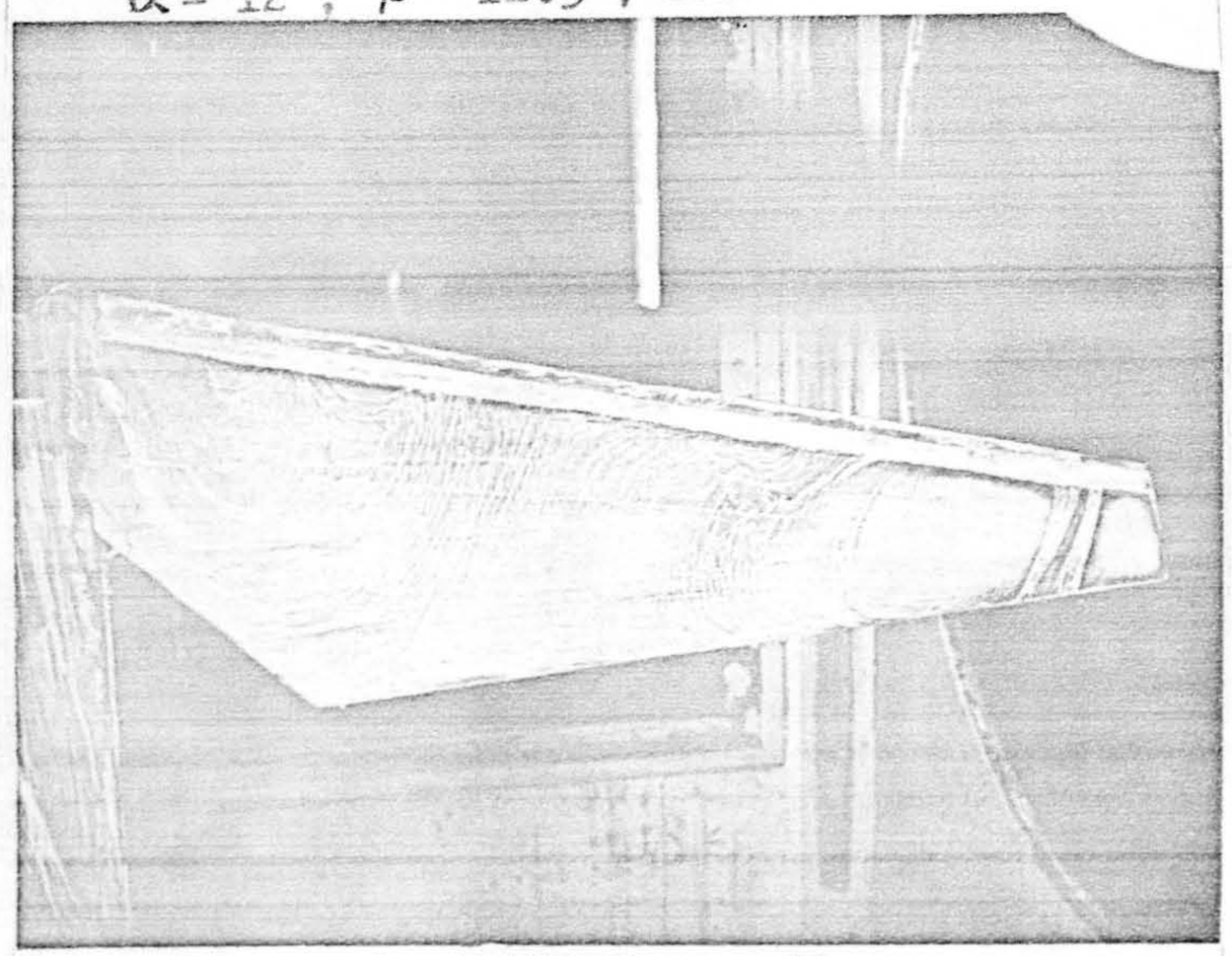

PHOTO - 20

$\alpha = 0^\circ$, $\beta = 32.5^\circ$, TRANSITION BAND OFF

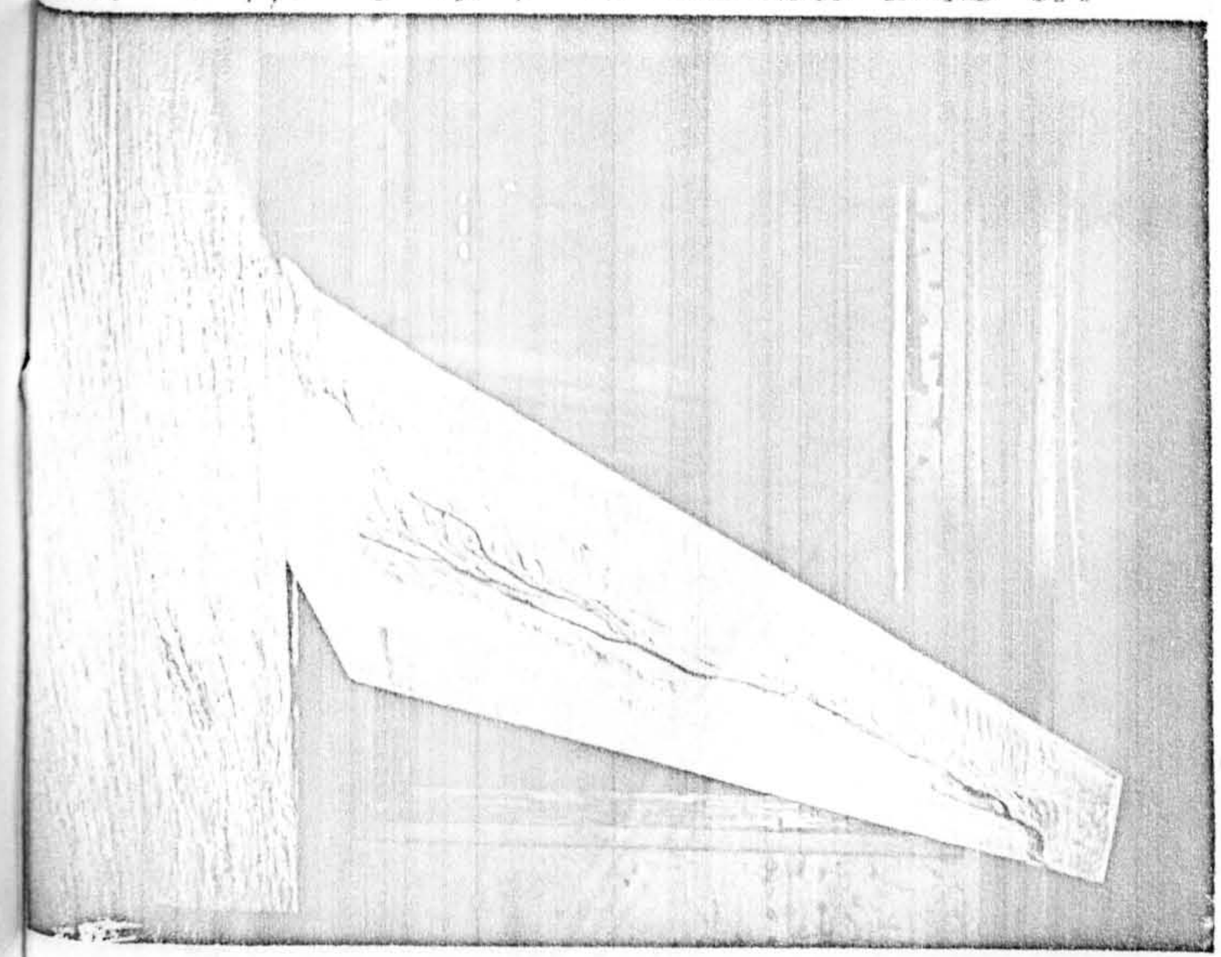

PHOTO- 21

$\alpha = 4^\circ$, $\beta = 32.5^\circ$, TRANSITION BAND OFF

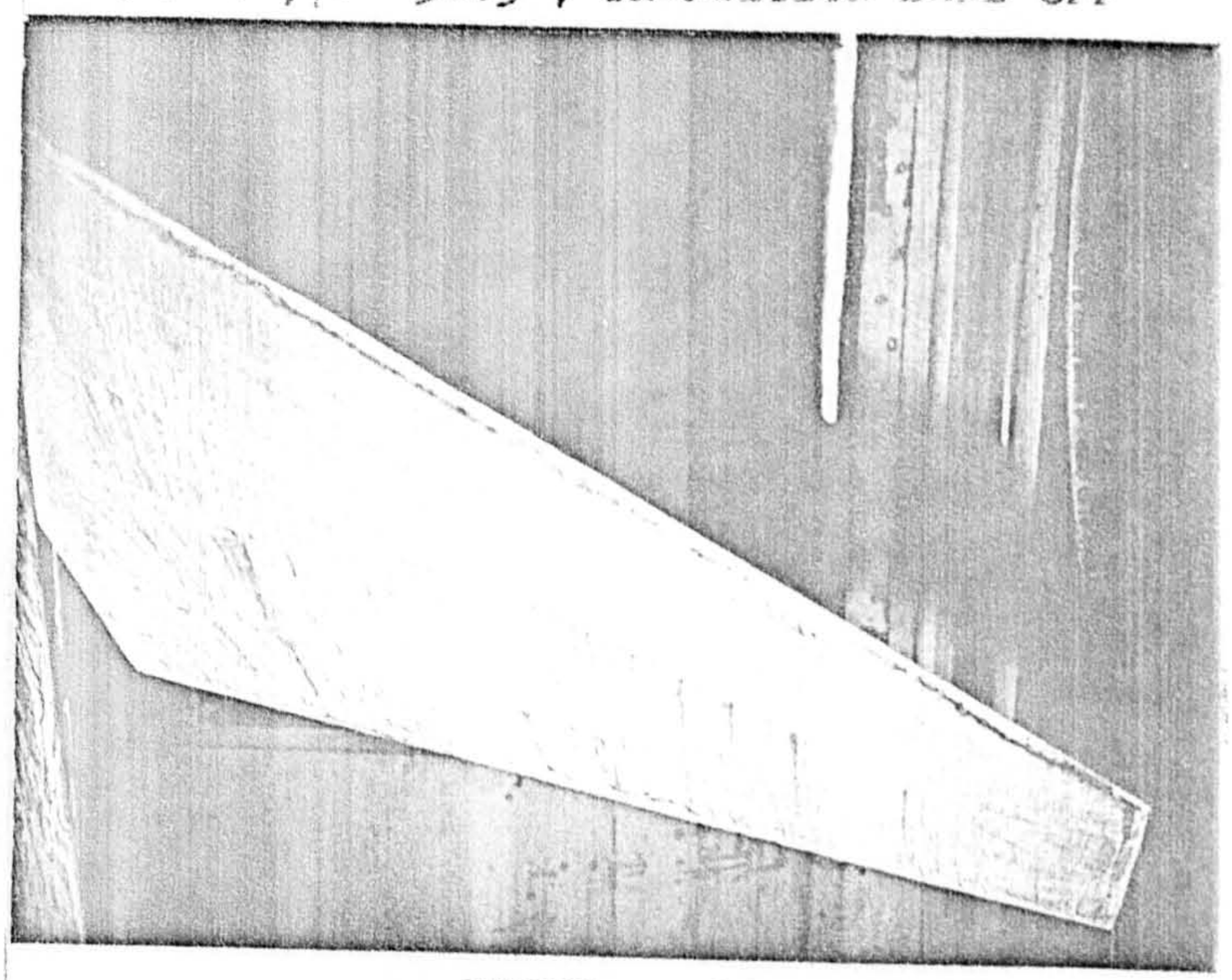

PHOTO - 22

$\alpha = 8^\circ$, $\beta = 32.5^\circ$, TRANSITION BAND OFF

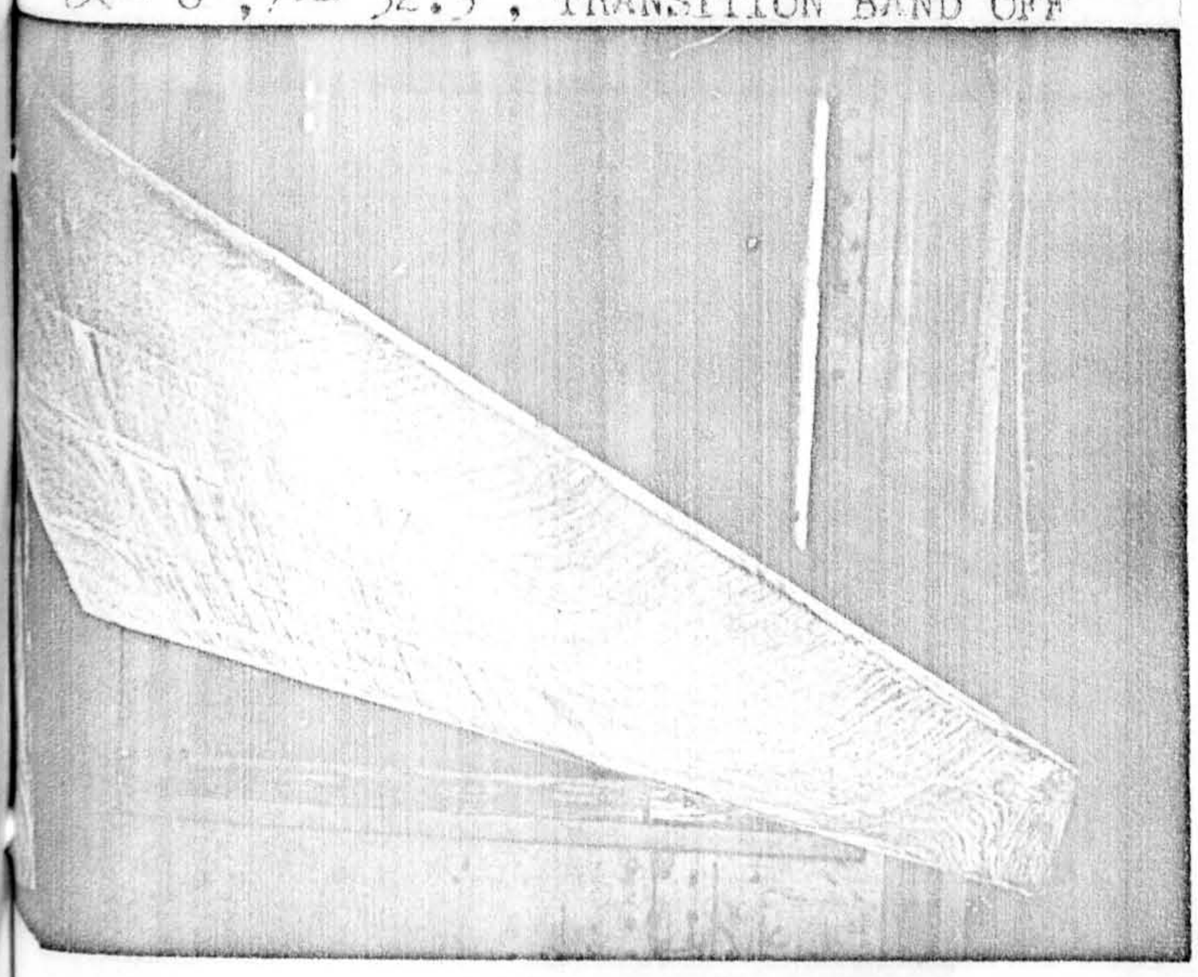

PHOTO - 23

$\alpha = 12^\circ$, $\beta = 32.5^\circ$, TRANSITION BAND OFF

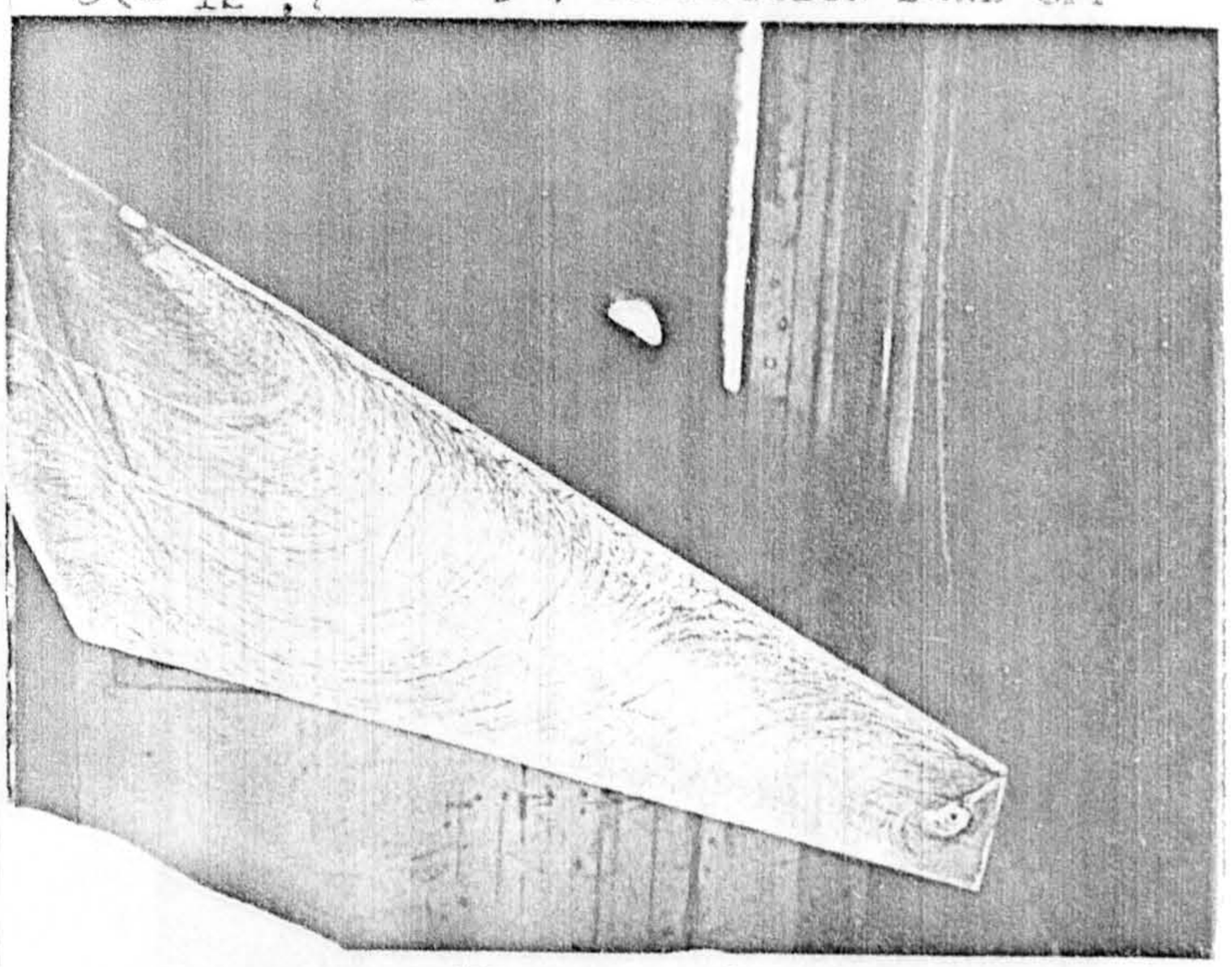

PHOTO - 24

$\alpha = 16^\circ$, $\beta = 32.5^\circ$, TRANSITION BAND OFF

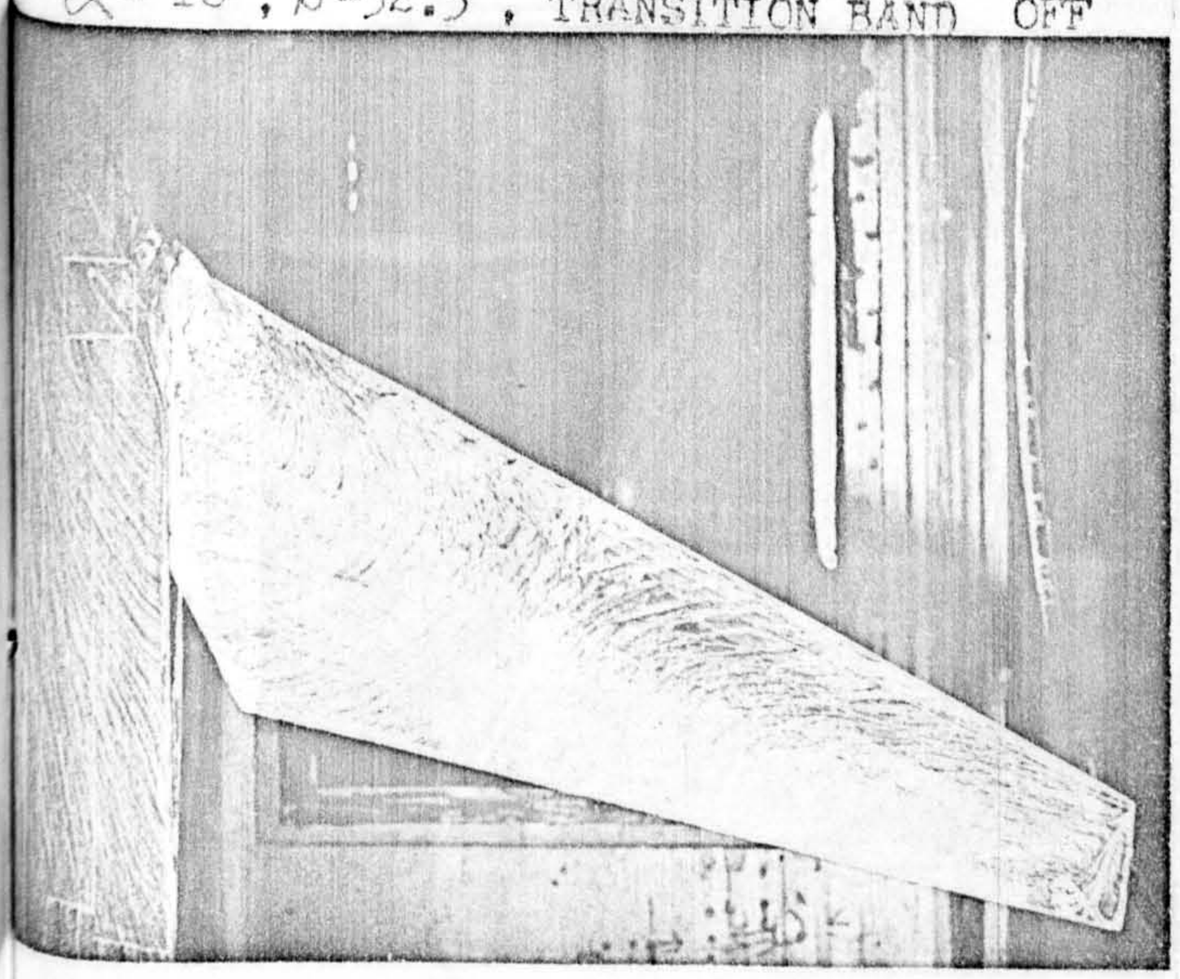

PHOTO - 25

$\alpha = 20^\circ$, $\beta = 32.5^\circ$, TRANSITION BAND OFF

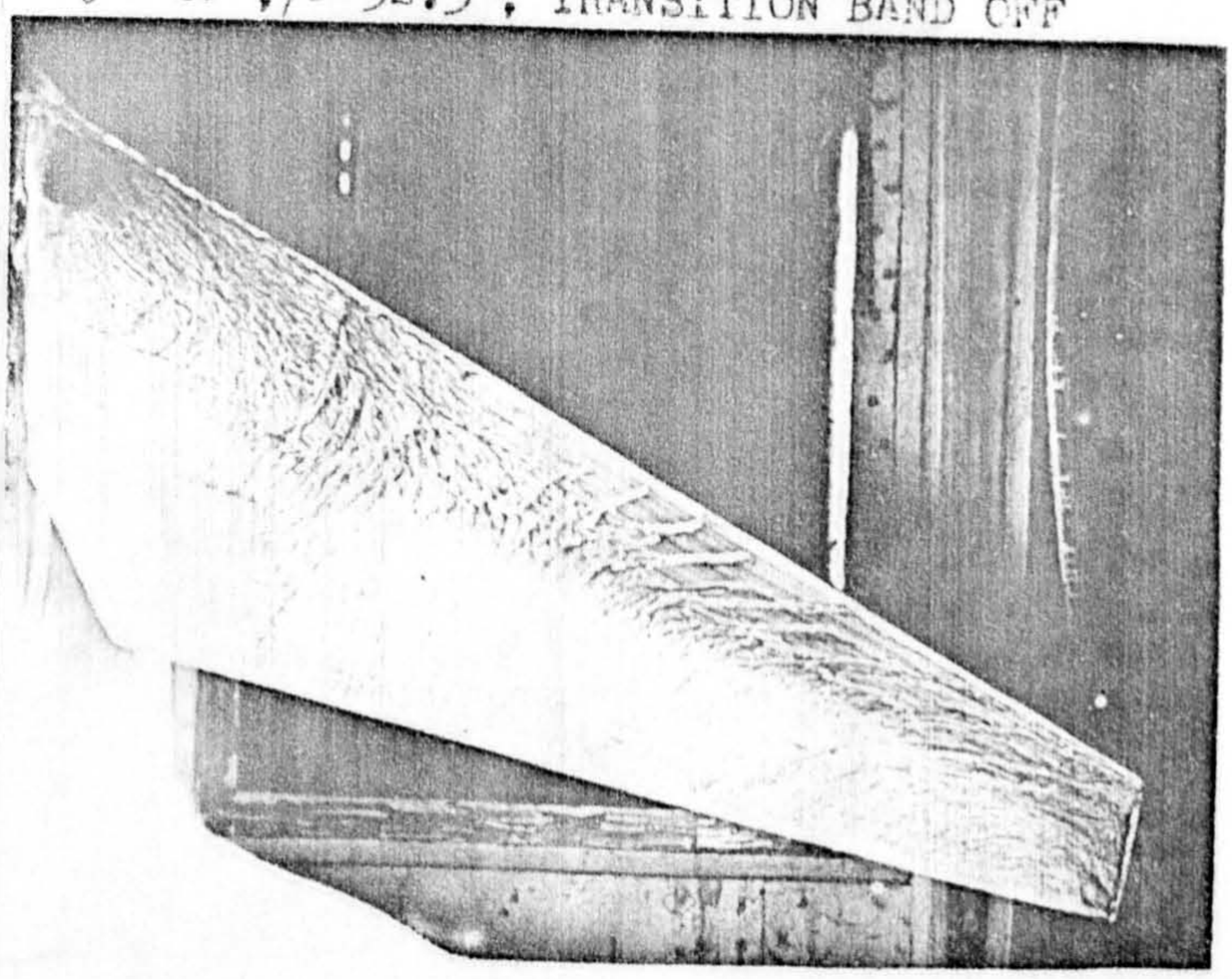

PHOTO - 26

$\alpha = 0^\circ$, $\beta = 32.5^\circ$, TRANSITION BAND ON

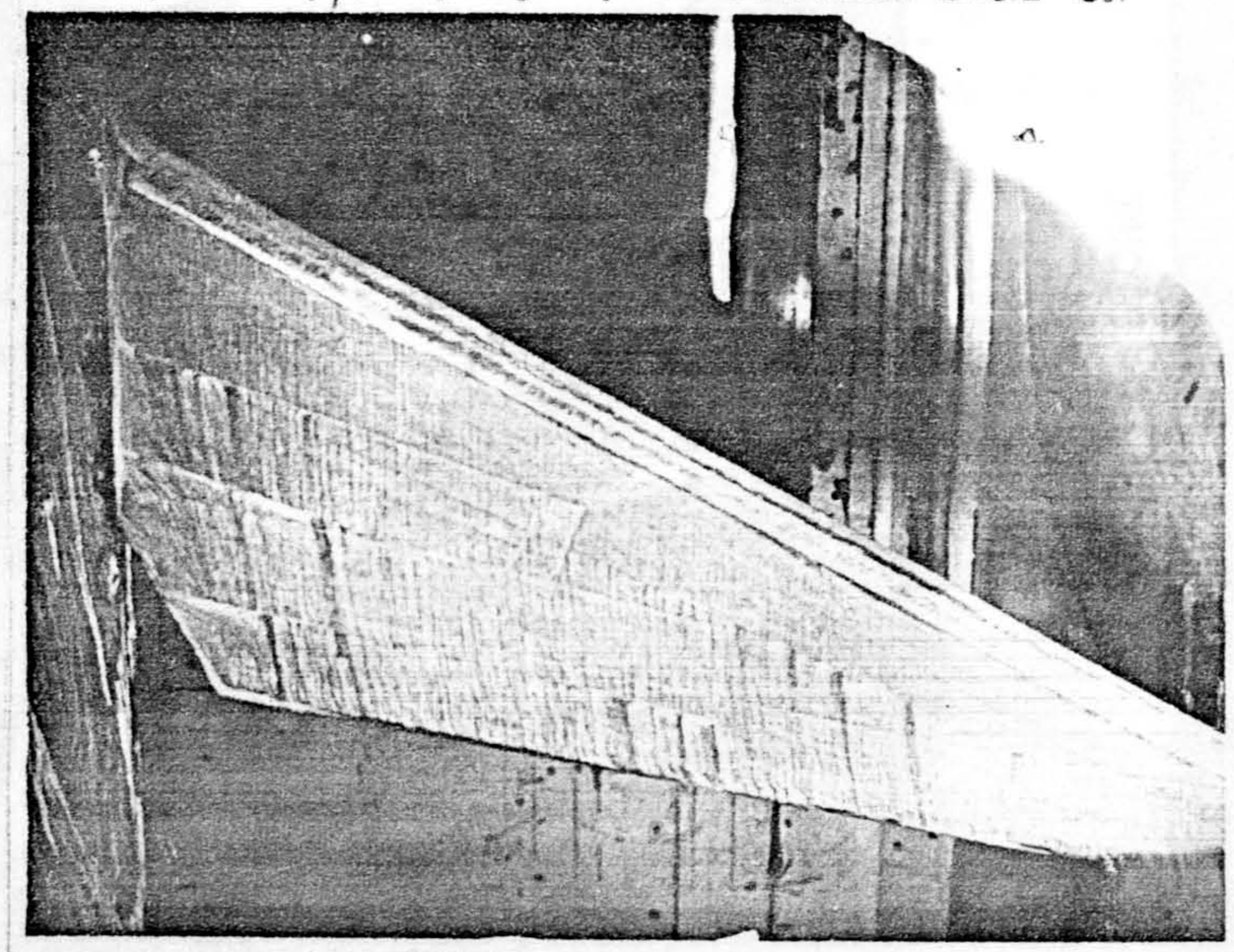

PHOTO - 27

$\alpha = 4^\circ$, $\beta = 32.5^\circ$, TRANSITION BAND ON

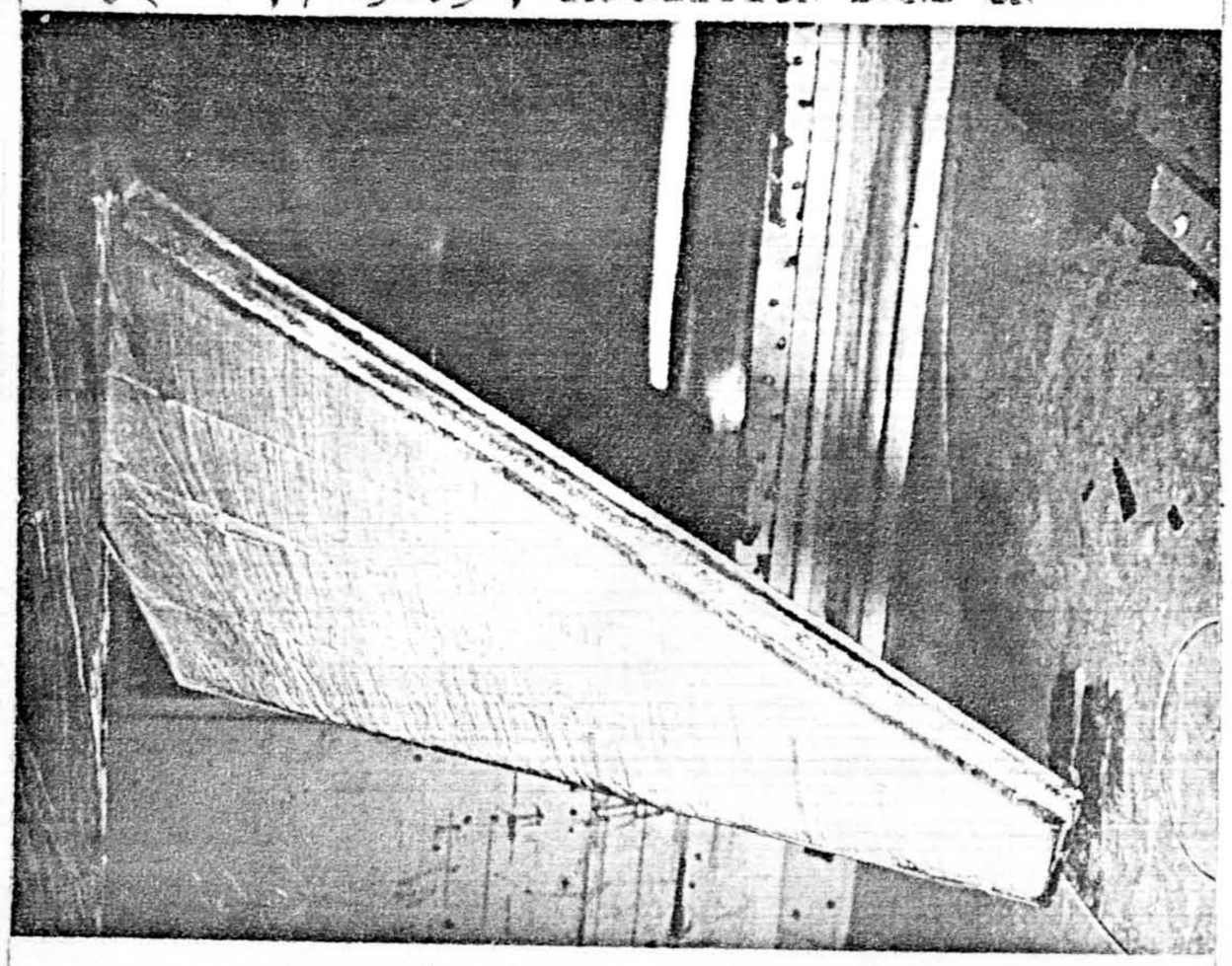

PHOTO - 28

$\alpha = 8^\circ$, $\beta = 32.5^\circ$, TRANSITION BAND ON

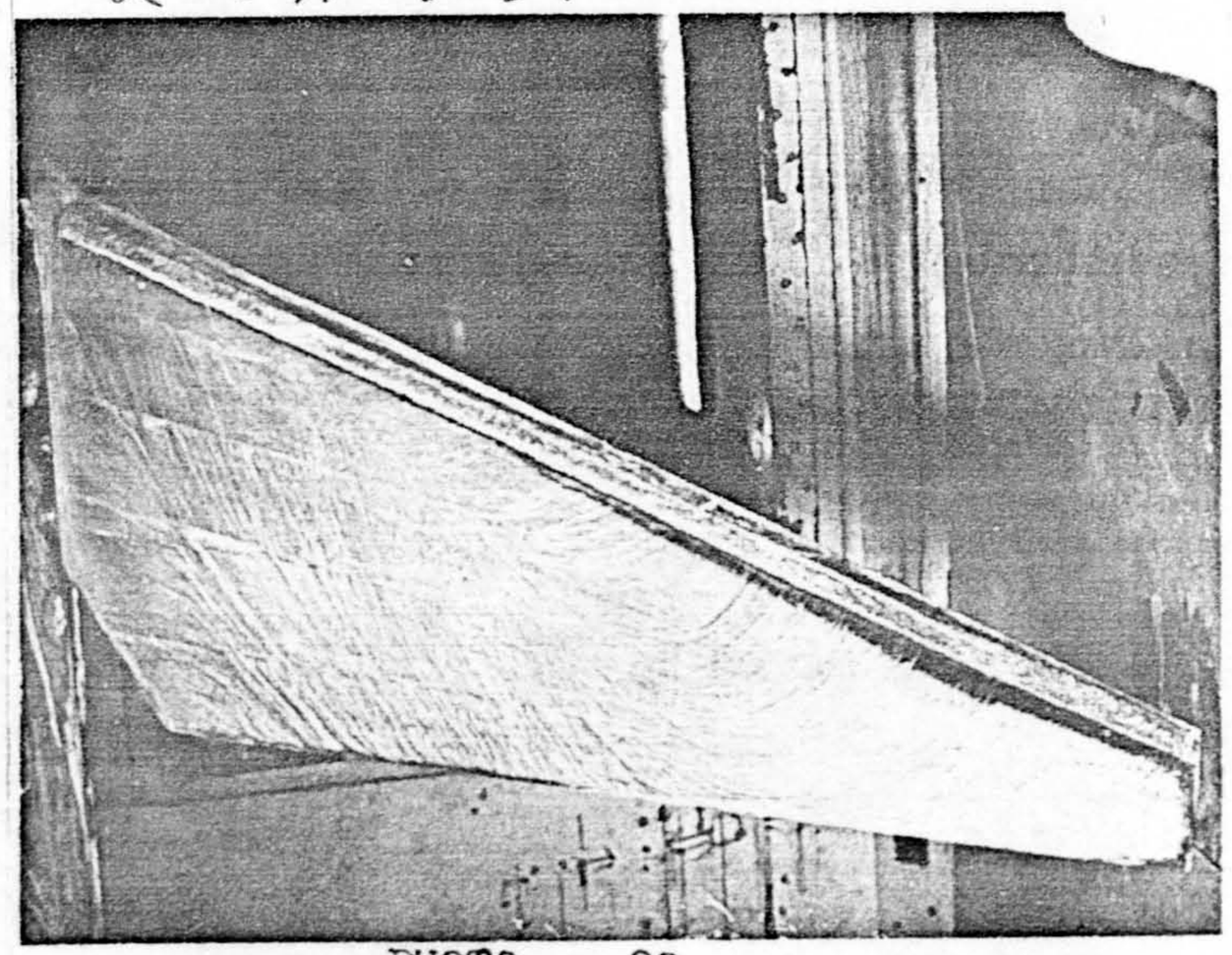

PHOTO - 29

$\alpha = 0^\circ$, $\beta = 52.5^\circ$, TRANSITION BAND OFF

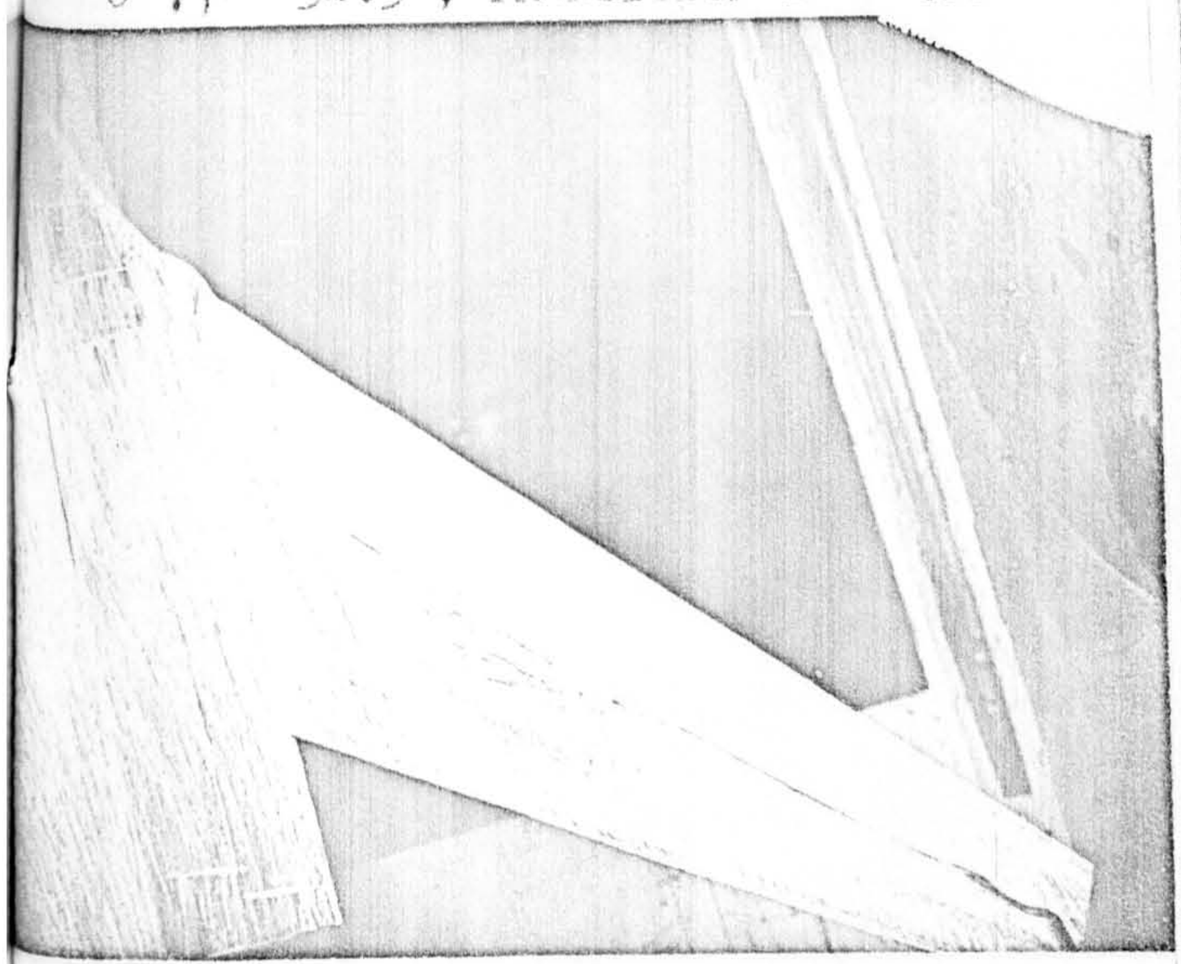

PHOTO - 30

$\alpha = 4^\circ$, $\beta = 52.5^\circ$, TRANSITION BAND OFF

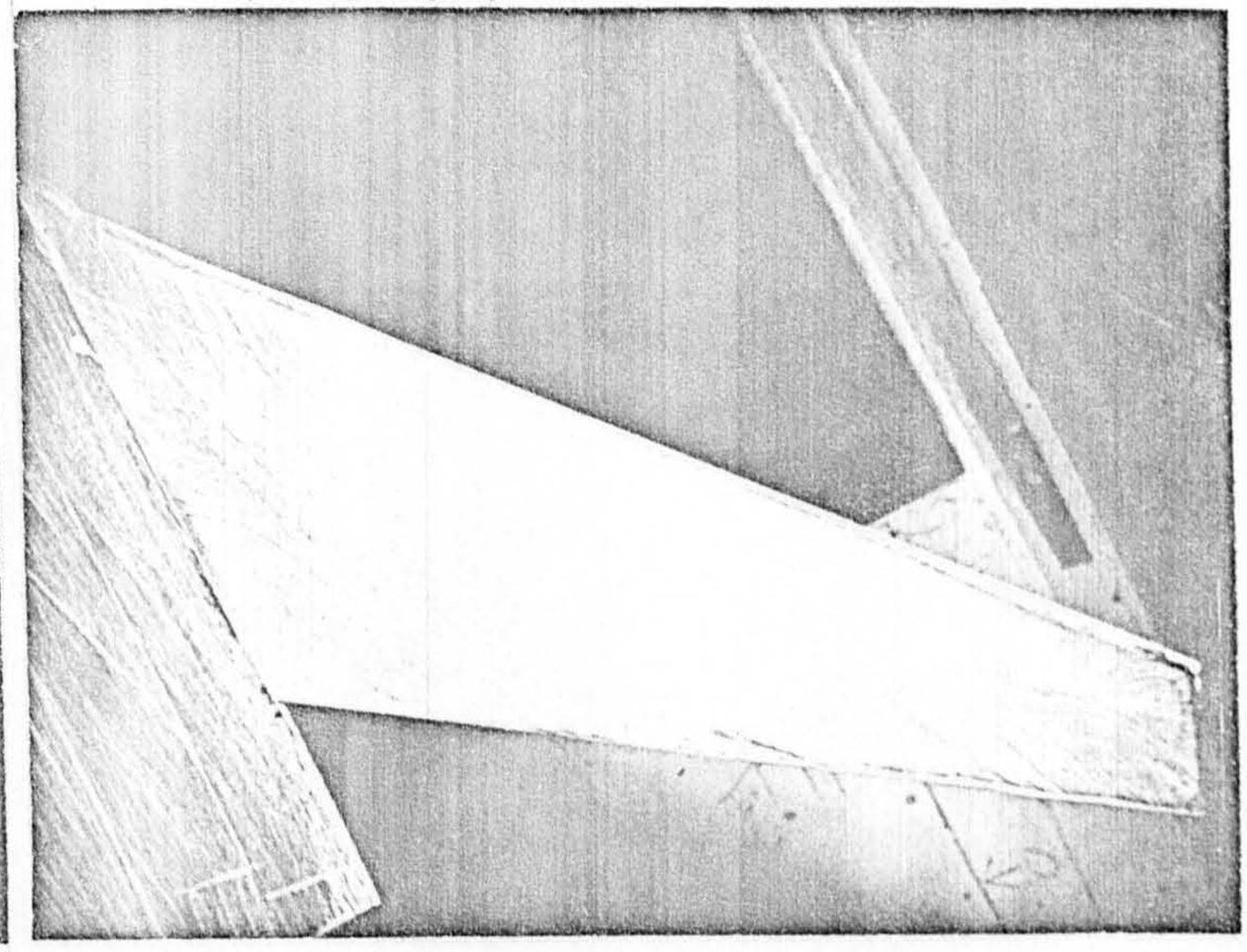

PHOTO- 31

$\alpha = 8^\circ$, $\beta = 52.5^\circ$, TRANSITION BAND OFF

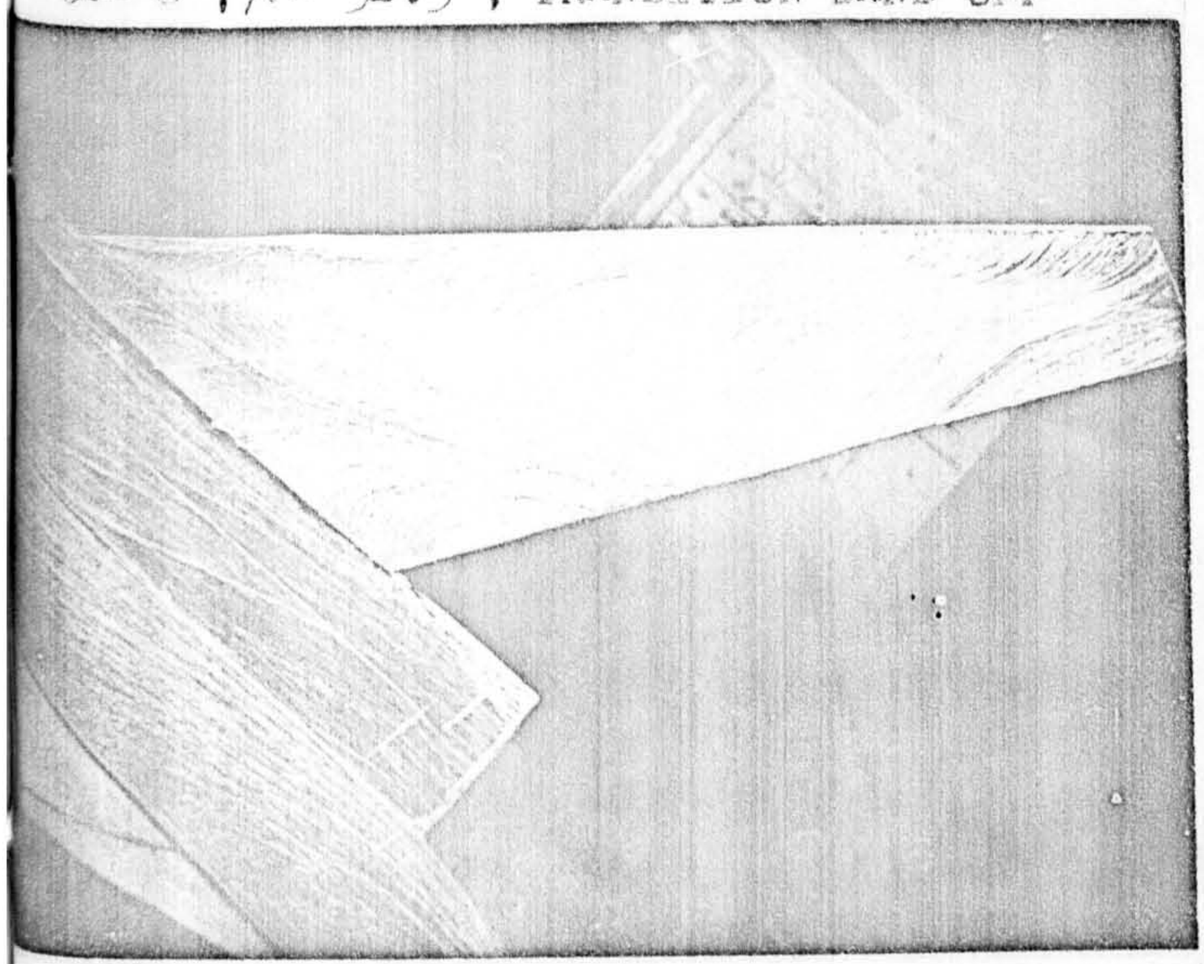

PHOTO - 32

$\alpha = 12^\circ$, $\beta = 52.5^\circ$, TRANSITION BAND OFF

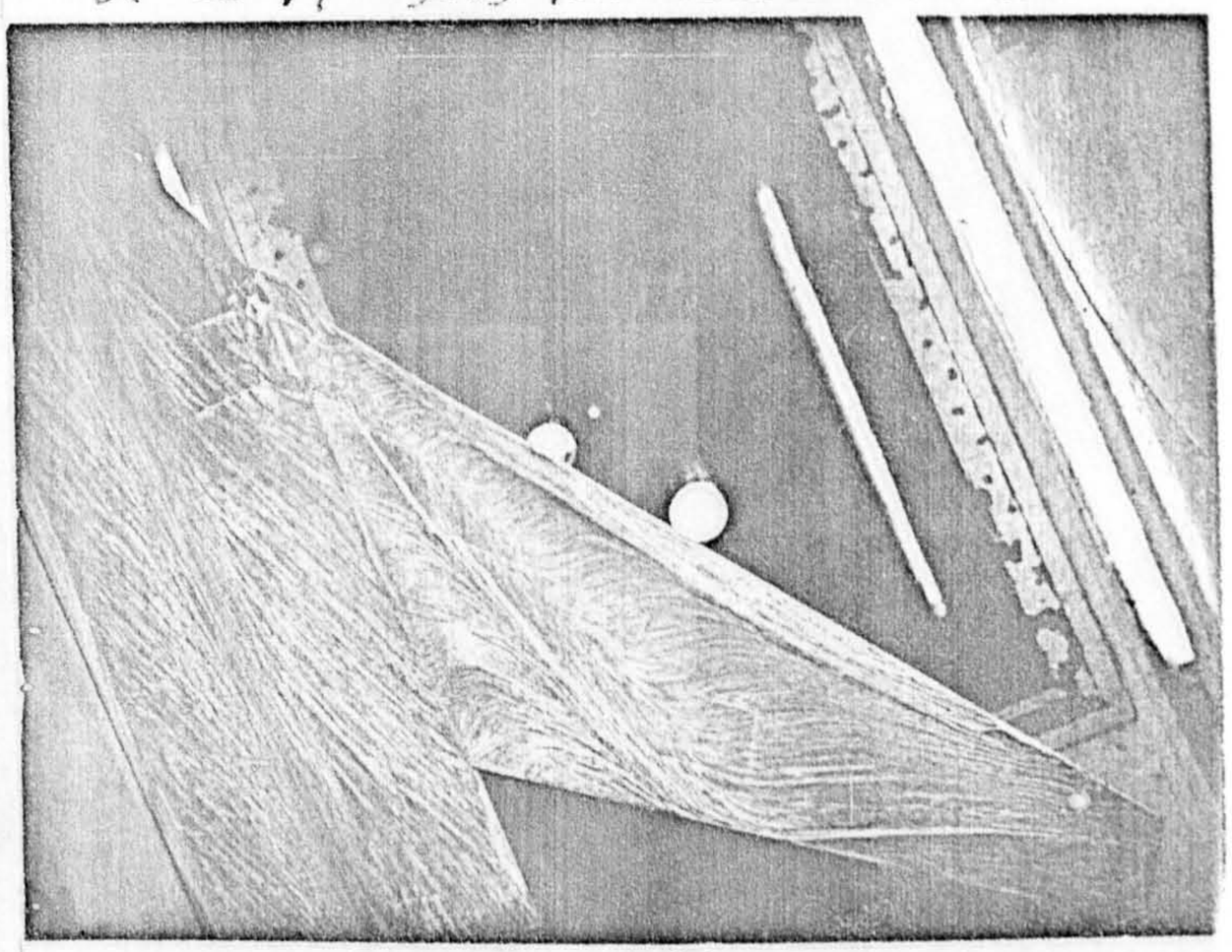

PHOTO - 33

$\alpha = 16^\circ$, $\beta = 52.5^\circ$, TRANSITION BAND OFF

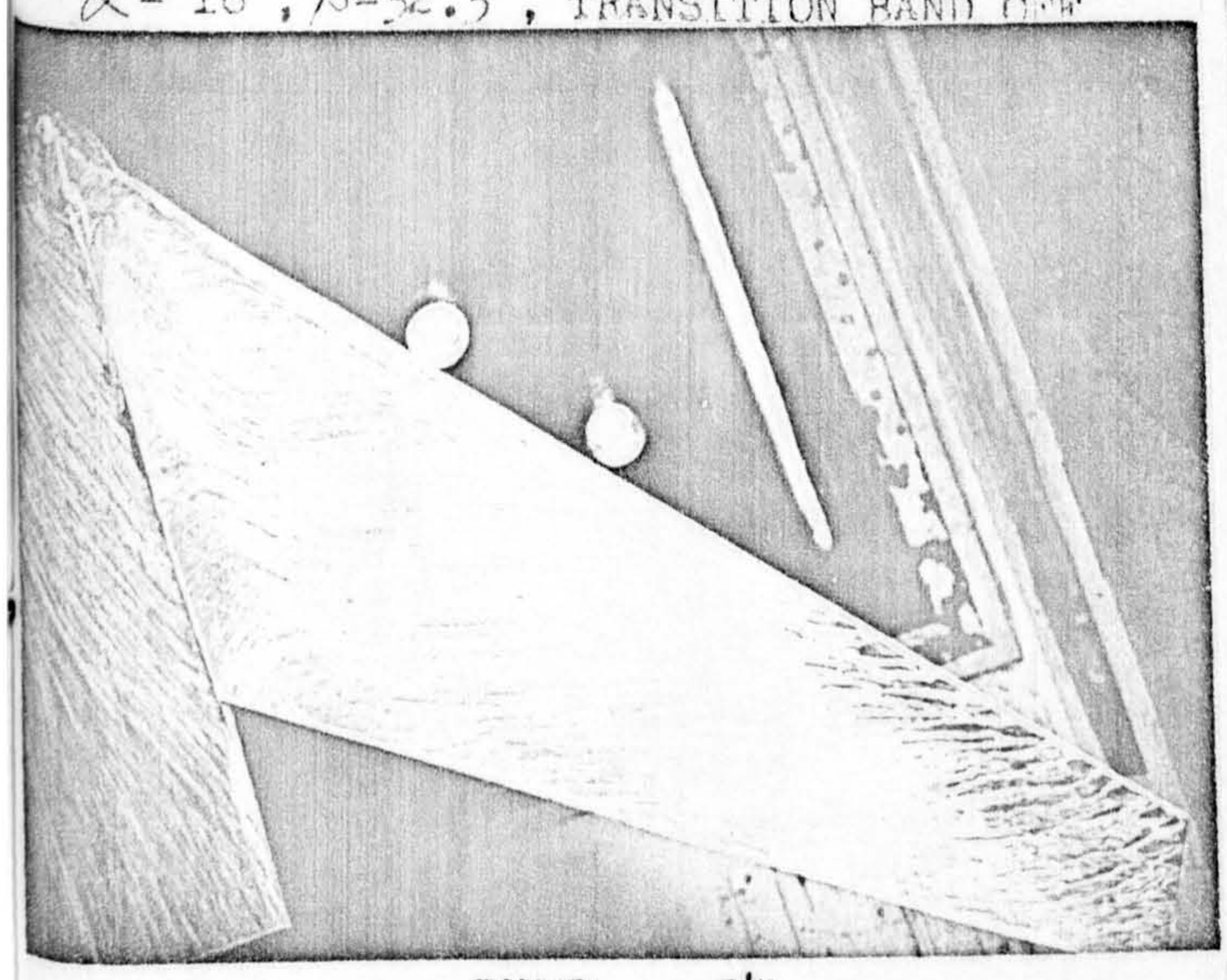

PHOTO - 34

$\alpha = 20^\circ$, $\beta = 52.5^\circ$, TRANSITION BAND OFF

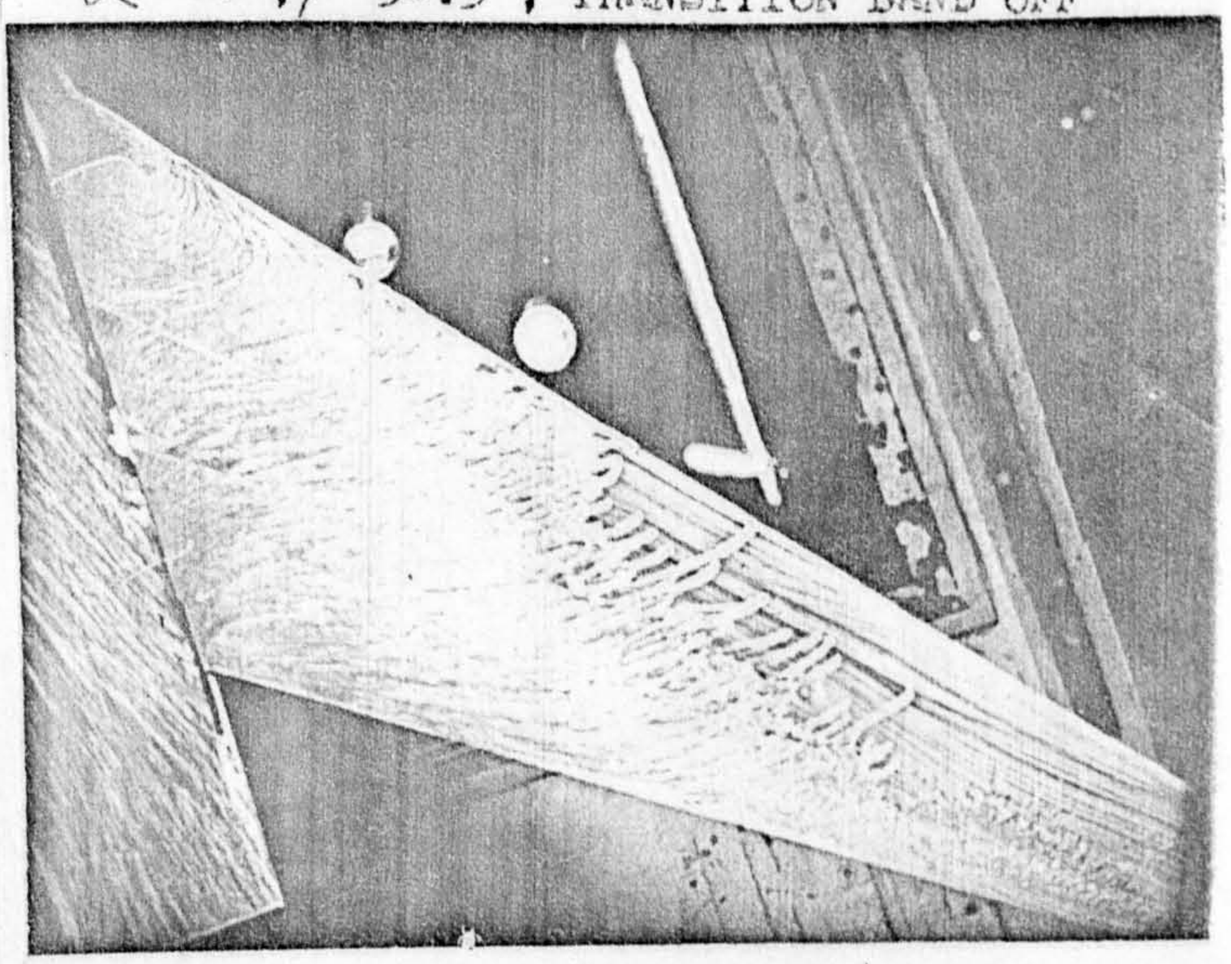

PHOTO - 35

CHAPTER 10

CONCLUDING REMARKS AND SUGGESTIONS FOR FURTHER WORK

10.1 Concluding Remarks

The work presented lies in the broad field of incompressible subsonic and supersonic wing-body interference applied to swing wing aircraft. Within this field, several important observations have been made regarding low speed wind tunnel tests and also subsonic and supersonic computational methods and the accuracies achieved. It is noted that :

(1) In low speed testing, limits for angle of incidence at various angles of sweep for fully attached flow on the model have been established by surface flow visualization.
The effects of various boundary layer transition devices on these limits has been investigated.

(2) A method for deducing section lift from only four chordwise pressure measurements is put forward and found to be acceptably accurate.

(3) The extension of the incompressible Quadvortex computation method to compressible flow has been achieved, and their results were found, to behave in the right trends as the incompressible ones.

(4) Comparison of Quadvortex predictions with experimental results both from this present work and with work at British Aerospace show that the Quadvortex method gives good accuracy for subsonic flow.

(5) An investigation of the number of panels needed for the Quadvortex method to achieve acceptable accuracy for rectangular

and 45° sweep wings has been carried out. Comparisons are made with published theoretical results due to Kuchemann and Multhopp.

(6) The use of the Allen and Sadler method for supersonic wing computation and comparisons with conical flow theory and experiments has been investigated. Finally, incorporation the Allen and Sadler method into the Nielsen method for computation of wing/body interference in supersonic flow has been completed.

In low speed wind-tunnel testing extreme care was taken to ensure that controllable errors were minimized and since good repeatability was experienced, it may therefore be implied that the present results obtained from experimental wind tunnel tests provide valuable information on the object of this research. However, there are some errors due to the wind tunnel interference and blockage which are not avoidable. Examination of the wind tunnel tests and the aerodynamic characteristics derived for the model suggests that vortices, generated on the body-wing junction, are quite large near the junction but become smaller away from the junction. This effect can be seen in their corresponding photos (1 to 35) in chapter 9. The results indicate that increasing the angle of sweep on the wing, gives a gradual decending trend in the overall lift coefficient. Wing-body interference calculations are noted to be favourable. The wing sweep had an influence on these interference effects, such that as sweep angle increases the interference become smaller.

The work concerning wing-body interference effects for subsonic flow

give a good basis for the investigation of other configurations, and consequently allow the possibility of producing a better aerodynamic design. The subsonic theoretical investigations covered a broad field of study which provides some insights and understanding of the basic principles and problems involved in interference effects. In the subsonic flow investigations, it is assumed that the flow is steady, that viscous regions are approximated by (or enclosed within) vortex sheets, external to which potential flow exists. Also the position and shape of free vortex sheets are specified at the outset.

In the supersonic investigations of wing-body interference, the Allen and Sadler results (by use of a rhombic mesh) are used for a final calculation of wing-body interference by incorporation into the Nielsen method. The corresponding comparisons of these results with conical flow theory and experimental evidence show a very good and encouraging agreement in distributions of Cp for a rectangular wing. Free stream Mach number has an influence on computational errors such that as M rises the errors become smaller. For example at M=1·7 errors of 5 % were found, but at M=2·4 these errors fall to 1·5%. This error can be made a lot smaller by decreasing the rhombus side length, so that the velocity potential is determined at enough points chordwise and spanwise to define the variations of the potentials with reasonable accuracy, bearing in mind that the potential is assumed to vary linearly along Mach cone directions in deriving the weights. It must be noted that as the rhombus side length decreases, the time taken by the main programme to compute the potentials increases rapidly with the number of

rhombuses on the planform. For example, if the mesh size is halved, there will be four times as many rhombuses on the planform, and each of these rhombuses has four times as many rhombuses in its forecone. Hence, it would be expected that the computation time would increase by a factor of sixteen. Cumulative errors tend to gain large values away from the leading edge, because if any potentials are slightly in error, this error starts propogating downstream producing a larger error, since each potential is determined by the upstream potentials. Other errors that can creep in the numerical calculation are in the Cp calculations, where finite difference equations are used for determination of this coefficient. However, the Allen and Sadler procedure in its simplified form can be used effectively to predict the pressure distribution over a wing planform in supersonic flow by using these results for the final calculations for interference of wing-body within the reliable extension of the slender body method of J. Nielsen. Using irregular rhombuses can cause an inaccuracy in the final results at lower Mach number.

10.2 Suggestions for Further Work

(1) The Quadvortex method can be developed to deal with spanwise and chordwise thickness distributions on the wing. It would also be possible to incorporate a boundary layer calculations method to determine displacement thickness and to predict separation of the flow. The modified thickness distribution could be used for a recalculation of pressures using Quadvortex.

(2) The subsonic flow method can be developed and modified so that the results are more compatible with experimental tests in order to solve for the surface pressure distributions when there are discrete vortices in the flow (as may arise in the wing-body junction or from wing strakes at moderate angles of attack). The Quadvortex method should be able to predict the velocity distributions on each panel due to the vortex flow interference and then, using boundary layer theory to in conjunction with surface velocity distribution , find separation locations theoretically. Consequently, the final results for forces and moments could be nearer to experimental tests at these higher incidences.

(3) The supersonic program (which owing to limitations in time was only tested for a few specific geometries) can be developed to deal with more general wing planforms, and a faster and more accurate method of solving the irregular

rhombuses developed, using more accurate finite difference equations for the edge regions. Also this can be developed by introducing more routines into the programme for variable sweep wing geometries with chordwise and spanwise thickness, and camber distributions for variable incidence and Mach numbers. Thus the method can be used at the design stage to optimise aircraft geometry to meet specific requirements.

Boundary layer calculations can be introduced for the viscous supersonic flow , although this may produce changes less significient than those in subsonic flows .

APPENDIX (A)

CONVERSION OF EXPERIMENTAL READINGS TO WIND AXES

A·1 CONVERSION AND CALIBRATION FACTORS FOR THE EXPERIMENTAL READINGS

Force and moment readings from the experimental tests were converted to wind axes. For this purpose, the procedure was as follows :

(1) Initial readings were corrected by taking the wind off from the wind on readings, then these readings were converted to wind axes as shown in Table (A.1).

(2) Readings from step (1) were corrected by the equipment calibration factors. Hence, coefficients of forces and moments were derived for the wind tunnel model as follows :

$$\text{FORCE COEFFICIENT} = \frac{\text{FORCE}}{1/2 \cdot \rho \cdot V^2 \cdot S} \quad , \text{ and}$$

$$\text{MOMENT COEFFICIENT} = \frac{\text{MOMENT}}{\frac{1}{2} \cdot \rho \cdot V^2 \cdot S \cdot \bar{c}} \quad ,$$

where ρ is the air density, V is air speed, S is effective lift area, $\bar{c}$ is mean chord, and also $\frac{1}{2} \cdot \rho \cdot V^2 \cdot S$ = Betz (mm H2O) $\times K_1 \times g \times S$,

where $g = 9 \cdot 81$ m/sec^2 , and K_1 is the wind tunnel calibration factor (from chapter 2).

Table (A.1) gives some details of conversion for the experimental readings as well as equipment calibration factors .

TABLE (A.1) CONVERSION TABLE

EXPERIMENTAL READINGS	CONVERTED READINGS
SIDE FORCE	LIFT
LIFT	SIDE FORCE
DRAG	DRAG
PITCHING MOMENT	YAWING MOMENT
YAWING MOMENT	PITCHING MOMENT
ROLLING MOMENT	ROLLING MOMENT

CALIBRATION FACTOR FOR THE SIX COMPONENTS MASS BALANCE MECHANISM ARE :

LIFT	$= 1000\ V_L$	N
DRAG	$= 100\ V_D$	N
SIDE FORCE	$= 1000\ V_S$	N
PITCHING MOMENT	$= 100\ V_P$	N.m
ROLLING //	$= 10\ V_R$	N.m
YAWING //	$= 10\ [V_Y - 0.024 V_D + 0.588\ V_S + 0.728\ V_S^2]$	N.m

Therefore the coefficient for pitching moment becomes :

$$C_M = C_{M1} - \frac{0.00588 C_L}{\bar{c}} \qquad \text{APPROX.}$$

APPENDIX B

COMPRESSIBILITY EFFECT IN SUBSONIC FLOW

B.1 EFFECT OF COMPRESSIBILITY ON AERODYNAMIC FORCES

B.1.1 LIFT COEFFICIENT CL_C

Deriving an integrated form of lift equation on an aerofoil in a compressible flow :

$$L_C = \tfrac{1}{2}\rho \cdot U_\infty^2 \cdot \iint \Delta C_{P_C} \cdot dx \cdot dy \quad \text{or} \quad = \frac{1}{2}\cdot\rho\cdot U_\infty^2 \cdot \frac{1}{(1-M_\infty^2)} \iint \Delta C_{P_i} \cdot dx \cdot dy \ , \qquad \text{(B.1)}$$

where $dx = \sqrt{1-M_\infty^2} \cdot d\xi$

writing R.H.S of equation (B.1) in terms of the incompressible form variations:

$$L_C = \frac{\sqrt{1-M_\infty^2}}{(1-M_\infty^2)} \cdot \frac{1}{2}\rho \cdot U_\infty^2 \iint \Delta C_{P_i} \cdot d\xi \cdot dy \ . \qquad \text{(B.2)}$$

Equation (B.2) can be simplified to give the following relationship for the lift force for a compressible condition:

$$L_c = \frac{1}{\sqrt{1-M_\infty^2}} \cdot L_i \qquad \text{(B.3)}$$

From equation (B.3) the lift coefficient can be derived for a compressible condition as follows:

Knowing that the lift coefficient is $CL_C = \dfrac{L_c(\text{lift})}{1/2 \cdot \rho \cdot U_\infty^2 \cdot S_c}$,

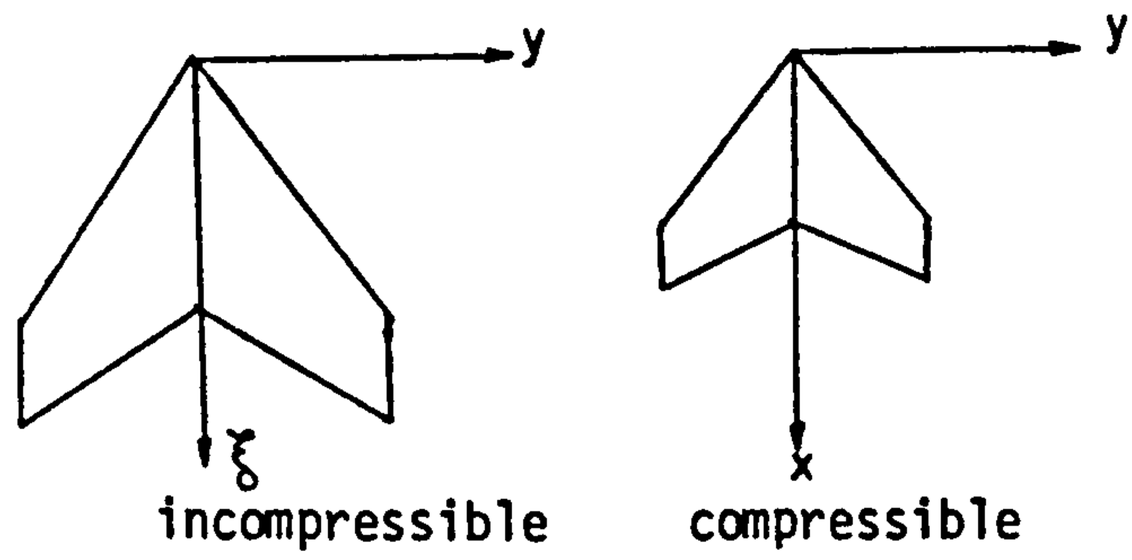

SKETCH (B.1)

where S is wing area, and

$$\frac{S_i}{S_c} = \frac{\xi \cdot y}{x \cdot y} = \frac{\xi}{x} = \frac{1}{\sqrt{1-M_\infty^2}} \qquad \text{(B.4)}$$

Substituting equation (B.4) into equation (B.3) and modifying it will give:

$$CL_c = \frac{1}{(1 - M_\infty^2)} \; CL_i \qquad \text{..... (B.5)}$$

B.1.2 DRAG COEFFICIENT CD_c

From first principles, the drag equation in an integrated form for an aerofoil in compressible flow is:

$$\text{Drag} = D_c = \frac{1}{2} \rho \, U_\infty^2 \iint \Delta Cp_c . dy . dz \qquad \text{..... (B.6)}$$

Substituting equation (3.13) into equation (B.6) gives

$$D_c = \frac{\frac{1}{2} \rho \, U_\infty^2}{(1-M_\infty^2)} \iint \Delta Cp_i . dy . dz$$

or

$$D_c = \frac{D_i}{1 - M_\infty^2} \qquad \text{..... (B.7)}$$

Now substituting equation (B.4) into equation (B.7) and putting the drag force in coefficient form gives:

$$CD_c = \frac{1}{1 - M_\infty^2} \cdot \frac{S_i}{S_c} \; \frac{D_i}{\frac{1}{2} \rho U_\infty^2 \; S_i}$$

$$CD_c = \frac{1}{(1 - M_\infty^2)^{3/2}} \cdot CD_i \qquad \text{..... (B.8)}$$

B.1.3 SIDE FORCE COEFFICIENTS CF_c

The total side force acting on a wing can be deduced by integrating the distribution of side force over the wing surface. Thus,

Total side force for compressible flow $\quad F_c = \frac{1}{2}\rho U_\infty^2 \iint \Delta Cp_c . dx . dz \qquad$ ..... (B.9)

Substituting equation (B.13) into equation (B.9) will give:

$$F_c = \frac{\sqrt{1 - M_\infty^2}}{(1 - M_\infty^2)} \cdot \frac{1}{2}\rho U_\infty^2 \iint \Delta Cp_i . d\xi . dz$$

$$F_c = \frac{1}{(1 - M_\infty^2)^{1/2}} F_i \qquad \text{..... (B.10)}$$

Now substituting equation (B.4) into equation (B.10) and modifying the side force into the coefficient of side force gives:

$$CF_c = \frac{1}{(1 - M_\infty^2)^{1/2}} \cdot \frac{1}{(1 - M_\infty^2)^{1/2}} \cdot CF_i$$

Hence $$CF_c = \frac{1}{(1 - M_\infty^2)} \cdot CF_i \qquad \text{..... (B.14)}$$

B.2 EFFECT OF COMPRESSIBILITY ON AERODYNAMIC MOMENTS

B.2.1 PITCHING MOMENT COEFFICIENT CMP_c

Again from first principles, the total pitching moment acting on the wing can be expressed as:

Pitching moment for compressible flow. $$MP_c = \frac{1}{2}\rho\, U_\infty^2 \iint \Delta Cp_c . x . dx . dy \qquad \text{..... (B.12)}$$

Substituting equation (3.13) into equation (B.12) gives:

$$MP_c = \frac{1}{2}\rho\, U_\infty^2 \frac{(1-M_\infty^2)^{1/2} \cdot (1 - M_\infty^2)^{1/2}}{(1-M_\infty^2)} \iint \Delta Cp_i . \xi . d\xi . dy$$

or $$MP_c = \frac{1}{2}\rho\, U_\infty^2 . \iint \Delta Cp_i . \xi . d\xi . dy$$

Thus $$MP_c = MP_i \qquad \text{..... (B.13)}$$

Now, substituting equation (B.4) into equation (B.13) and expressing the pitching moment in coefficient form gives:

$$CMP_c = \frac{\bar{C}_i}{C_i} \cdot \frac{S_i}{S_c} \cdot CMP_i$$

Hence $$CMP_c = \left(\frac{1}{1 - M_\infty^2}\right) . CMP_i \qquad \text{..... (B.14)}$$

B.2.2 ROLLING MOMENT COEFFICIENT CMR_c

The total rolling moment acting on the aircraft can be deduced by integrating the total forces on the surfaces in a compressible flow in the form:

Rolling Moment $$MR_c = \frac{1}{2}\rho U_\infty^2 . \iint \Delta Cp_c . y . dy . dx \qquad \text{..... (B.15)}$$

Equation (B .15) can be simplified by substitution of equation (3.13) to give:

$$MR_c = \frac{\sqrt{1 - M_\infty^2}}{(1 - M_\infty^2)} . \frac{1}{2}\rho U_\infty^2 . \quad \Delta Cp_i . y . dy . d\xi$$

Therefore

$$MR_c = \frac{1}{(1 - M_\infty^2)^{1/2}} . MR_i \qquad \text{..... (B.16)}$$

Now, substituting equation (B.4) into equation (B.16) and introducing the coefficient of moment gives:

$$CMR_c = \frac{1}{(1 - M_\infty^2)^{1/2}} . \frac{1}{(1 - M_\infty^2)} . CMR_i$$

Hence

$$CMR_c = \frac{1}{(1 - M_\infty^2)^{3/2}} \cdot CMR_i \qquad \text{..... (B.17)}$$

B.2.3 YAWING MOMENT COEFFICIENT CMY_c

Using the similar method for deriving the total yawing moment acting on wing for compressible flow:

Yawing moment $MY_c = \frac{1}{2}\rho U_\infty^2 . \iint \Delta Cp_c . y . dy . dz$ ..... (B.18)

Substituting equation (3.13) into equation (B.18) gives:

$$MY_c = \frac{1}{2}\rho U_\infty^2 . \frac{1}{(1 - M_\infty^2)} . \iint \Delta Cp_i . y . dy . dz$$

$$MY_c = \frac{1}{(1 - M_\infty^2)} . MY_i \qquad \text{..... (B.19)}$$

Now equation (B.19) can be modified by substituting equation (B.4) and converting it to coefficient form:

$$CMY_c = \frac{S_i}{S_c} \cdot \frac{\bar{C}_i}{\bar{C}_c} \frac{1}{(1 - M_\infty^2)} \iint \frac{\Delta Cp_i . y . dy . dz}{(\frac{1}{2}\rho U_\infty^2)}$$

$$CMY_c = \frac{1}{(1 - M_\infty^2)} \cdot \frac{1}{(1 - M_\infty^2)^{1/2}} \cdot \frac{1}{(1 - M_\infty^2)^{1/2}} \iint \frac{\Delta Cp_c . y . dy . dz}{\frac{1}{2} \rho . U_\infty^2}$$

$$CMY_c = \frac{1}{(1 - M_\infty^2)^2} . \; CMY_i \qquad \text{..... (B.20)}$$

All the necessary corrections for compressibility have been inserted into the subsonic program, according to the results derived in this Appendix .